

Lecture Notes in Physics

736

Wolfhard Janke

Rugged Free Energy Landscapes

Common Computational Approaches
to Spin Glasses, Structural Glasses and
Biological Macromolecules



Springer

Lecture Notes in Physics

Editorial Board

R. Beig, Wien, Austria
W. Beiglböck, Heidelberg, Germany
W. Domcke, Garching, Germany
B.-G. Englert, Singapore
U. Frisch, Nice, France
P. Hänggi, Augsburg, Germany
G. Hasinger, Garching, Germany
K. Hepp, Zürich, Switzerland
W. Hillebrandt, Garching, Germany
D. Imboden, Zürich, Switzerland
R. L. Jaffe, Cambridge, MA, USA
R. Lipowsky, Potsdam, Germany
H. v. Löhneysen, Karlsruhe, Germany
I. Ojima, Kyoto, Japan
D. Sornette, Nice, France, and Zürich, Switzerland
S. Theisen, Potsdam, Germany
W. Weise, Garching, Germany
J. Wess, München, Germany
J. Zittartz, Köln, Germany

The Lecture Notes in Physics

The series Lecture Notes in Physics (LNP), founded in 1969, reports new developments in physics research and teaching – quickly and informally, but with a high quality and the explicit aim to summarize and communicate current knowledge in an accessible way. Books published in this series are conceived as bridging material between advanced graduate textbooks and the forefront of research and to serve three purposes:

- to be a compact and modern up-to-date source of reference on a well-defined topic
- to serve as an accessible introduction to the field to postgraduate students and nonspecialist researchers from related areas
- to be a source of advanced teaching material for specialized seminars, courses and schools

Both monographs and multi-author volumes will be considered for publication. Edited volumes should, however, consist of a very limited number of contributions only. Proceedings will not be considered for LNP.

Volumes published in LNP are disseminated both in print and in electronic formats, the electronic archive being available at springerlink.com. The series content is indexed, abstracted and referenced by many abstracting and information services, bibliographic networks, subscription agencies, library networks, and consortia.

Proposals should be sent to a member of the Editorial Board, or directly to the managing editor at Springer:

Christian Caron
Springer Heidelberg
Physics Editorial Department I
Tiergartenstrasse 17
69121 Heidelberg / Germany
christian.caron@springer.com

W. Janke (Ed.)

Rugged Free Energy Landscapes

Common Computational Approaches to Spin Glasses,
Structural Glasses and Biological Macromolecules

 Springer

Editor

Wolfhard Janke
Universität Leipzig
Institut für Theoretische Physik
Postfach 100 920
04009 Leipzig
Germany
wolfhard.janke@itp.uni-leipzig.de
<http://www.physik.uni-leipzig.de/~janke>

W. Janke (Ed.), *Rugged Free Energy Landscapes: Common Computational Approaches to Spin Glasses, Structural Glasses and Biological Macromolecules*, Lect. Notes Phys. 736 (Springer, Berlin Heidelberg 2008), DOI 10.1007/ 978-3-540-74029-2

Library of Congress Control Number: 2007937508

ISSN 0075-8450

ISBN 978-3-540-74025-4 Springer Berlin Heidelberg New York

This work is subject to copyright. All rights are reserved, whether the whole or part of the material is concerned, specifically the rights of translation, reprinting, reuse of illustrations, recitation, broadcasting, reproduction on microfilm or in any other way, and storage in data banks. Duplication of this publication or parts thereof is permitted only under the provisions of the German Copyright Law of September 9, 1965, in its current version, and permission for use must always be obtained from Springer. Violations are liable for prosecution under the German Copyright Law.

Springer is a part of Springer Science+Business Media
springer.com

© Springer-Verlag Berlin Heidelberg 2008

The use of general descriptive names, registered names, trademarks, etc. in this publication does not imply, even in the absence of a specific statement, that such names are exempt from the relevant protective laws and regulations and therefore free for general use.

Typesetting: by the authors and Integra using a Springer L^AT_EX macro package
Cover design: eStudio Calamar S.L., F. Steinen-Broo, Pau/Girona, Spain

Printed on acid-free paper SPIN: 12072897 5 4 3 2 1 0

Preface

This volume on spin glasses, structural glasses and biological macromolecules collects pedagogically written lecture notes of internationally renowned experts from eight countries, who work on different physical problems but employ similar theoretical concepts and computational methods. The research into at first sight quite different physical phenomena, therefore, faces related problems, whose origin can be traced back to the difficulties of numerical simulations of systems with rugged free-energy landscapes. Many of the original publications presuppose quite specialized “common” knowledge, usually readily accessible only to the experts in each of these fields. Moreover, they are typically published in quite different sets of scientific journals. The main objective of these Lecture Notes is, therefore, to provide the necessary background material in a coherent fashion and thereby to initialize knowledge transfer of advanced methodologies across the boundaries of the disciplines. It can be anticipated that future successful computer simulation studies of static and dynamic properties of the three systems considered here as well as the further development of improved numerical algorithms will greatly profit from an interaction among researchers in these different fields.

More specifically, the merits and drawbacks of the various variants of generalized ensemble methods as employed in computational studies of glassy systems and biomolecules as well as the complicated interplay of different algorithms in combined methods are discussed from rather different viewpoints in this volume. For investigations of spin and structural glasses, the Lecture Notes should have an impact on a better understanding of their similarities in dynamical and non-equilibrium properties, which in turn are intimately related to the rugged free-energy landscape mapped out by means of equilibrium methods. And it can be hoped that the already existing expertise in the physics of glassy systems will give conceptual guidance to similar studies of biological macromolecules, such as peptides and proteins.

The contents of this volume are organized into four parts. The first three parts cover introductory material and reviews of recent research results for spin glasses, structural glasses and biological macromolecules with emphasis

on the protein folding problem. The joint theme of these chapters is rugged free-energy landscapes and computational methods to deal with this multiple-minima problem efficiently. The fourth part, finally, focuses on a detailed exposition of recent, quite general algorithmic developments that alleviate the computational problems and can be put to good use in specific applications in each of the fields considered in the first three parts.

The idea for such a volume came to us about 2 years ago at the occasion of a CECAM workshop in Lyon, France, where about 30 talks on the above topics were presented. The interdisciplinary character of the workshop was indeed very stimulating, and it became clear that an up-to-date volume like this emphasizing the close interrelations between the three fields and at the same time bridging the gap between introductory material and ongoing state-of-the-art research would be highly desirable.

Leipzig,
May 2007

Wolfgang Janke

Contents

1 Rugged Free-Energy Landscapes – An Introduction	
<i>Wolfhard Janke</i>	1
References	6

Part I Spin Glasses

2 Some Aspects of Infinite-Range Models of Spin Glasses: Theory and Numerical Simulations	
<i>Alain Billoire</i>	11
2.1 Introduction	12
2.2 The Sherrington–Kirkpatrick Model	14
2.3 Simulations Techniques	29
2.4 Finite-Size Effects for the Free Energy and the Internal Energy	36
2.5 Conclusions	43
References	44

3 The Potts Glass Model: A Scenario for the Freezing Transition of Structural Glasses?	
<i>Kurt Binder, Claudio Brangian and Walter Kol</i>	47
3.1 Introduction: A Brief Survey of Experimental Facts and Theoretical Ideas on Glass Transitions	47
3.2 The p -State Potts Glass and Its Properties in the Thermodynamic Limit for Infinite-Range Interactions	51
3.3 Monte Carlo Results for the 10-State Mean-Field Potts Glass: Static Properties	54
3.4 Finite-Size Scaling for the “Dynamic Transition” of the Potts Glass	57
3.5 Monte Carlo Study of the Short-Range 10-State Potts Glass: Do all Transitions Disappear?	60

3.6 Concluding Discussion: What have we Learned about Glass Transitions?	62
References	64

4 Domain Walls, Droplets and Barriers in Two-Dimensional Ising Spin Glasses

<i>Alexander K. Hartmann</i>	67
4.1 Experimental Realizations	68
4.2 Models	72
4.3 Ground States of Two-Dimensional Spin Glasses	76
4.4 Droplets and Domain Walls	88
4.5 Energy Barriers	96
References	104

5 Local Scale-Invariance in Disordered Systems

<i>Malte Henkel and Michel Pleimling</i>	107
5.1 Introduction	107
5.2 Local Scale-Invariance Without Disorder	115
5.3 Disordered Ferromagnets	123
5.4 Critical Ising Spin Glasses	131
5.5 Discussion	141
Note Added in Proof	143
References	143

Part II Structural Glasses

6 Transport of Mobile Particles in an Immobile Environment: Computer Simulations of Sodium Silicates

<i>Jürgen Horbach</i>	149
6.1 Introduction	149
6.2 Model and Details of the Simulation	151
6.3 The Structure of Sodium Silicates	153
6.4 Channel Diffusion	161
6.5 Mode-Coupling Theory	165
6.6 Conclusions	169
References	170

7 The Goniherdic Ising Model and Glassiness

<i>Desmond A. Johnston, Adam Lipowski and Ranasinghe P. K. C. Malmini</i>	173
7.1 (Pre-)History of the Model	173
7.2 Equilibrium Behaviour, by Various Means	178
7.3 Non-equilibrium Behaviour, Mostly by Monte Carlo Simulations	184
7.4 Variations on the Glassy and Goniherdic Themes	195
7.5 Endpiece	196
References	197

Part III Protein Folding

8 Thermodynamics of Protein Folding from Coarse-Grained Models' Perspectives

<i>Michael Bachmann and Wolfhard Janke</i>	203
8.1 Introduction	203
8.2 Why Coarse-Graining?	206
8.3 The Hydrophobic-Polar Lattice Protein Model	207
8.4 Going Off-Lattice: Folding Behavior of Heteropolymers in the AB Continuum Model	234
8.5 Peptide Aggregation	240
8.6 Summary	242
References	244

9 Exact Energy Landscapes of Proteins Using a Coarse-Grained Model

<i>Frank Dressel and Sigismund Kobe</i>	247
9.1 Introduction	247
9.2 Structural Discretization	249
9.3 Fragmentation of Protein Structures	251
9.4 Energy Function	252
9.5 Branch and Bound	256
9.6 Results	258
9.7 Summary	267
References	267

10 Protein Folding, Unfolding and Aggregation Studied Using an All-Atom Model with a Simplified Interaction Potential

<i>Anders Irbäck</i>	269
10.1 Introduction	269
10.2 Model and Methods	271
10.3 Results	274
10.4 Summary	288
References	289

11 All-Atom Simulations of Proteins

<i>Ulrich H. E. Hansmann</i>	293
11.1 Introduction	293
11.2 Energy Landscape Paving	295
11.3 Parallel Tempering	297
11.4 Multicanonical Sampling	301
11.5 Other Generalized-Ensemble Techniques	303
11.6 Helix Versus Sheet Formation	304
11.7 Structure Predictions of Small Proteins	307
11.8 Conclusions	312
References	312

Part IV Algorithmic Developments

12 Markov Chain Monte Carlo Methods for Simulations of Biomolecules

<i>Bernd A. Berg</i>	317
12.1 Introduction	317
12.2 Markov Chain Monte Carlo	318
12.3 Statistical Errors of MCMC Data	326
12.4 Generalized Ensembles for MCMC Simulations	332
12.5 Biased Markov Chain Monte Carlo	341
12.6 Conclusions and Outlook	348
References	349

13 A Different Approach to Monte Carlo Simulations in Systems with Complex Free-Energy Landscapes

<i>David P. Landau</i>	353
13.1 Introduction	353
13.2 Method	354
13.3 Applications	359
13.4 Conclusions	367
References	367

14 Generalized-Ensemble Algorithms for Protein Folding Simulations

<i>Yuji Sugita, Ayori Mitsutake and Yuko Okamoto</i>	369
14.1 Introduction	369
14.2 Generalized-Ensemble Algorithms	372
14.3 Simulation Results	396
14.4 Conclusions	402
References	403

Index	409
--------------------	-----

Rugged Free-Energy Landscapes – An Introduction

Wolfgang Janke

Institut für Theoretische Physik and Centre for Theoretical Sciences (NTZ),
Universität Leipzig, Postfach 100 920, D-04009 Leipzig, Germany
wolfgang.janke@itp.uni-leipzig.de

Understanding the static and even more the dynamical behavior of complex physical systems is one of the most challenging problems of current research in physics, chemistry and biology. Paradigmatic examples of condensed matter physics are spin glasses and structural glasses. More recently, in life sciences, the rapid advances in computational biology have added the exploration of the properties of biologically relevant macromolecules to this list. Here, the most prominent example is protein folding, but also studies of protein aggregation and adsorption to soft or hard interfaces are of great medical and technological interest. While the physics concepts underlying the behavior of spin and structural glasses are still quite close, the basic principles governing the properties of biomolecules are in many respects quite diverse. Still, there are certain joint features in all these systems which make a common treatment quite promising for future scientific advances.

The lectures in this volume are mainly centered around computational approaches. Due to the steadily increasing power of modern capability computers combined with significant algorithmic improvements over the past few years, computational physics/chemistry/biology is by now the third column of basic research tools in fundamental natural science besides the traditional analytical theory and experiments. This is nicely illustrated by the “Landau triangle” in Fig. [13.1](#) of Chap. [13](#).

Among the most prominent joint key features of the three fields considered in this volume are rugged free-energy landscapes which generate metastability and are often responsible for very slow dynamics. In computer simulation studies, this is reflected by a slow time evolution of the systems which tend to get trapped in one of these multiple minima. It is a great challenge to develop new simulation algorithms that alleviate the resulting slowing down problem. Usually a quite specific knowledge of the considered system is necessary to develop ideas for improvements. Once discovered, however, it is often possible to transfer new methods also to the related fields. In the last couple of years, precisely this mechanism has been at work concerning the rugged free-energy

landscape problem, where improvements have been discovered (and often also rediscovered) in computational physics, computational chemistry and more recently also computational biology.

To follow up these developments and take advantage of them, a fairly deep understanding of at least the basic notions and elementary properties of the specific systems is necessary. For example, the concept of “overlap parameters” is rooted in the replica theory of spin glasses, originally developed for infinite-range mean-field models of the Sherrington–Kirkpatrick type. Later the computational definition of “real replicas” and their “overlap parameters” has been carried over to short-range spin glasses of the Edwards–Anderson type. More recently, “overlap parameters” are considered in a by now quite routine fashion also in protein-folding studies to measure the distance to some given reference conformation.

Besides similarities and analogies there are, of course, also many features that distinguish the three systems. For example, the overall shapes of the free-energy landscape for the protein-folding problem and for spin glasses are quite different, see Fig. 1.1. While for proteins a funnel-like landscape with a minimum hosting the native conformation is expected, spin glasses exhibit pronounced metastability. The main difference between glasses and spin

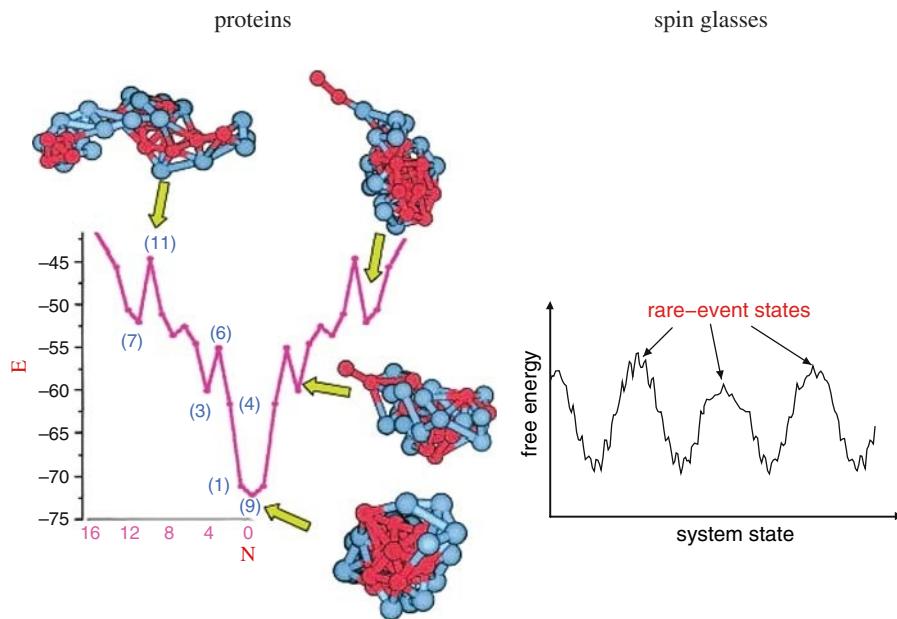


Fig. 1.1. Typical shapes of rugged free-energy landscapes in the protein-folding problem and for spin glasses. While the native protein conformation resides in the minimum of a funnel-like landscape, for spin glasses many degenerate minima are expected (the protein sketch is taken with permission from G. Srinivas, B. Bagchi: *J. Chem. Phys.* **116**, 8579 (2002))

glasses is that the glassiness of the former is caused intrinsically by structural disorder while the latter are governed by quenched, random couplings which introduce frustration and disorder. The purpose of this volume is, therefore, to stress the conceptual similarities and differences of these physically quite diverse phenomena and to prepare the reader for adopting useful methods from a neighboring field by providing introductory lecture notes explaining the basic principles of each of the three disciplines.

Part I on spin glasses [1, 2] starts in Chap. 2 with a lecture by A. Billoire, who first gives an introduction into the phenomenology of spin glasses and then explains the differences between mean-field Sherrington–Kirkpatrick and short-range Edwards–Anderson Ising spin-glass models. Next he sketches the celebrated replica field theory and discusses the controversy between the resulting replica and alternative droplet picture, which is still not yet resolved. In the main part of his lecture notes, he focuses on Monte Carlo computer simulations of the Sherrington–Kirkpatrick model, for which by now many exact (and partly even rigorous) results are available. In the data analysis, he pays particular attention to finite-size effects, which are of tremendous importance for any serious computer simulation study.

Chapter 3 is devoted in its main part to a special mean-field spin glass model, the 10-state Potts glass, where both a static and a dynamic transition occur [1]. K. Binder, C. Brangian and W. Kob discuss in their lecture notes to what extent the transitions of this model resemble the behavior of a glass-forming fluid, that is the transition to a structural glass [3, 4]. Next they turn their attention to Monte Carlo computer simulations of the 10-state Potts glass with *nearest-neighbor* interactions and provide numerical evidence that no trace of the static and dynamic glass transition observed in the mean-field limit is left in the short-range case.

In Chap. 4, A. K. Hartmann gives an in-depth introduction to exact methods for finding the ground state and the first excited states of two-dimensional Ising spin glasses. Here graph-theoretical concepts such as minimum-weight perfect-matching algorithms are explained and applied to analyses of domain walls, droplets and free-energy barriers [5]. One important conclusion is that assumptions underlying the droplet picture can be verified numerically. In the last section of this chapter, the graph-theoretical approach is extended to dynamical properties such as the scaling of the energy barriers with the size of the system.

Dynamical scaling properties and ageing in disordered systems far from equilibrium are the main subject of Chap. 5, where M. Henkel and M. Pleimling give a comprehensive overview of recent achievements [6]. Starting from simple non-glassy ferromagnets quenched to below the Curie temperature, they discuss ferromagnetically disordered magnets and spin glasses at criticality. In the latter cases, the dependence of the scaling properties on the distribution of the random, quenched couplings is carefully examined. As their main theme, particular attention is devoted to the question to what extent a recently proposed generalization of dynamical scaling to a *local* scale invariance (LSI) can

be confirmed by numerically obtained data. Two extensive tables covering a wide range of models and one collecting experimental results provide invaluable information on the state-of-the-art concerning coarsening kinetics and other dynamical properties.

In Part II on structural glasses [3, 4], J. Horbach begins in Chap. 6 with a summary of recent molecular dynamics (MD) computer simulations of various sodium silicate melts. Here the concept of percolating sodium-rich channels is introduced, which form a channel network that can be detected numerically and also experimentally by a prepeak in the static structure factor. On the theoretical side, the framework of mode-coupling theory (MCT) is discussed and applied to the calculation of coherent and incoherent scattering functions, which are explained in this article. The results are found in qualitative agreement with direct “measurements” within the molecular dynamics simulations.

Chapter 7 is devoted to a somewhat exotic and, at least in the condensed-matter community, less well-known spin model, the so-called *gonihedric* Ising model in three dimensions. In fact, historically this model had its genesis as a possible discretization of string theory in high-energy physics. Starting from the Nambu–Goto formulation over its generalization by an additional extrinsic curvature term or alternatively through the Steiner model, one eventually ends up with a discretized lattice model of the Ising type with next-to-nearest neighbor and plaquette interactions. By tuning the respective coupling constants in a way suggested by the string theory perspective, one obtains a lattice model *without* quenched coupling constants that nevertheless does exhibit genuine glassy behavior. In this sense, the “self-induced” glassiness resembles rather a structural than a spin glass [1, 2, 3, 4].

Part III of this volume deals with biological macromolecules and in particular with the computationally very demanding protein-folding problem [7, 8]. Four lecture notes take the reader through the whole hierarchy of descriptions on different length scales of resolution, from coarse-grained lattice and off-lattice models over simplified all-atom formulations to detailed atomistic models incorporating empirical force fields such as AMBER, CHARMM, ECEPP, GROMOS, etc.

In Chap. 8, M. Bachmann and I start at the coarsest level and explain in detail mesoscopic model formulations of the hydrophobic-polar type, where the 20 naturally occurring amino acids are classified into only two classes, “hydrophobic” (trying to avoid the aqueous solvent) and “polar” or “hydrophilic” (being favorably attracted by the polar solvent). When the heteropolymer chains are modeled as self-avoiding walks on a lattice, this is the so-called HP model, and for chains in the continuum with bending energy one speaks of the AB model. Using these coarse-grained formulations, computer simulation studies of protein folding and aggregation as well as of the adsorption propensity of peptides to solid substrates are discussed. Compared with detailed all-atom formulations, the simplicity of the coarse-grained models allows for a more universal description and classification of structure formation

processes resulting in various conformational pseudophases. On the methodological side, various variants of multicanonical chain-growth algorithms with population control are introduced for the lattice models and general ensemble techniques (multicanonical, parallel tempering, etc.) are employed in the continuum formulations.

Exact energy landscapes of proteins within a suitably defined coarse-grained model is the main topic of the lecture notes by F. Dressel and S. Kobe in Chap. 9. They point out that not only calculating the ground state of a protein model but also its excited states with the correct energies is a very promising but still challenging task. To tackle this problem, the use of an exact branch-and-bound algorithm is proposed that can map the whole landscape below a certain energy threshold. This allows the characterization of all states and transitions between them. As an application, results for both globular and membrane proteins are presented and compared with atomic force microscopy experiments on membrane proteins.

In Chap. 10, A. Irbäck presents his all-atom model with simplified and computationally convenient interaction potentials and implicit solvent. In contrast to detailed all-atom models, this potential is calibrated against data pertaining to folding properties of *whole* chains, rather than of small groups of atoms. The current version of the PROFASI simulation package is able to fold several sequences with about 20 amino acids, including both peptides with α -helical and β -sheet structures. Furthermore, it is demonstrated that the simulation package can reproduce the mechanical unfolding behavior of ubiquitin, a 76 amino acid protein, and finally also a successful study of the aggregation properties of the 7-amino acid fragment $A\beta_{16-22}$ of the amyloid- β peptide associated with Alzheimer’s disease is presented.

All-atom simulations of proteins using the ECEPP energy function as implemented in the SMMP simulation package are reviewed by U. H. E. Hansmann in Chap. 11. Here, also the energy landscape paving optimization algorithm “ELP” is explained, which is closely related to generalized ensemble simulation techniques, in particular in the formulation discussed by D. P. Landau in his lecture notes in Chap. 13. After reviewing applications of parallel tempering, multicanonical sampling and simulated tempering to biological macromolecules 9, as an example, the peptide with one-letter code EKAYLRT is discussed, which appears in naturally occurring proteins with significant frequency at positions of both α -helices and β -sheets, as well as the 36-residue villin headpiece subdomain HP-36, which is one of the smallest peptides that can fold autonomously.

Part IV on algorithmic developments begins in Chap. 12 with an introduction to Markov chain Monte Carlo methods by B. A. Berg. Starting out with the general idea of importance sampling and its realization by Markov chains 10, 11, local update rules such as the Metropolis and heat-bath algorithm are explained next. The basic methods are illustrated with relatively simple example simulations of Ising, Potts and $O(3)$ spin models on regular lattices. Special emphasis is put on a thorough analysis of statistical errors

of Monte Carlo data, including autocorrelation times as well as binning and Jackknife techniques, which is a “must” for any serious computer simulation study. Next generalized ensembles for Monte Carlo simulations are presented and a detailed exposition of the various tricks along the way is given. Here as application also examples from protein folding are discussed. The article closes with a section on biased Markov chain Monte Carlo methods such as the “Rugged Metropolis” algorithm, which may find useful applications to biophysics in the future.

In Chap. [3], D. P. Landau presents a more recently developed generalized-ensemble algorithm, where a random walk in energy space is performed and where the resulting density of states is modified continuously to produce a “flat” histogram. The properties of this method are first illustrated for two-dimensional Ising and Potts models, where exact or highly accurate numerical results are available for comparison. Also more elaborate applications of this so-called Wang–Landau sampling to spin glasses and biological macromolecules are sketched, and many other applications to classical and quantum statistics problems are briefly outlined.

The lecture notes by Y. Sugita, A. Mitsutake and Y. Okamoto in Chap. [4] give finally a comprehensive overview of generalized-ensemble algorithms with special emphasis on applications to biological macromolecules [9]. Here most implementations are discussed for both Monte Carlo and molecular dynamics simulations. The authors discuss the multicanonical algorithm, simulated tempering and the replica-exchange or parallel tempering method as well as several powerful combinations thereof. In three comparative case studies, they investigate the crucial question which of the various methods is the most recommendable for protein-folding studies, both with implicit and explicit solvent molecules.

Acknowledgements

I wish to thank all authors for devoting their time to these lecture notes and Dr. Christian Caron from Springer-Verlag for very patiently accompanying and supporting this project.

References

1. K. Binder, A. P. Young: *Spin glasses: experimental facts, theoretical concepts, and open questions*, Rev. Mod. Phys. **58**, 801 (1986) [3, 4]
2. A. P. Young (ed.): *Spin Glasses and Random Fields* (World Scientific, Singapore, 1998) [3, 4]
3. K. Binder, W. Kob: *Glassy Materials and Disordered Solids – An Introduction to Their Statistical Mechanics* (World Scientific, London, 2005) [3, 4]
4. E.-W. Donth: *The Glass Transition. Relaxation Dynamics in Liquids and Disordered Materials* (Springer, Berlin, 2001) [3, 4]

5. A. K. Hartmann, M. Weigt: *Phase Transitions in Combinatorial Optimization Problems* (Wiley-VCH, Weinheim, 2005) [3](#)
6. M. Henkel, M. Pleimling, R. Sanctuary (eds.): *Ageing and the Glass Transition*, Springer Lecture Notes in Physics **716** (Springer, Berlin, Heidelberg, 2007) [3](#)
7. T. E. Creighton: *Proteins: Structure and Molecular Properties* (Freeman, New York, 1993) 2nd ed. [4](#)
8. C. Branden, J. Tooze: *Introduction to Protein Structure* (Garland, New York, 1999) 2nd ed. [4](#)
9. U. H. E. Hansmann, Y. Okamoto: The generalized ensemble approach to protein folding simulations. In D. Stauffer (ed.): *Annual Reviews in Computational Physics VI* (World Scientific, Singapore, 1999), p. 129 [5](#) [6](#)
10. B. A. Berg: *Markov Chain Monte Carlo Simulations and Their Statistical Analysis* (World Scientific, Singapore, 2004) [5](#)
11. D. P. Landau, K. Binder: *A Guide to Monte Carlo Methods in Statistical Physics* (Cambridge University Press, Cambridge, MA, 2005) 2nd ed. [5](#)

Spin Glasses

Some Aspects of Infinite-Range Models of Spin Glasses: Theory and Numerical Simulations

Alain Billoire

Service de physique théorique, CEA Saclay, 91191 Gif-sur-Yvette, France
alain.billoire@cea.fr

Abstract. The expression “spin glasses” was originally coined to describe metallic alloys of a nonmagnetic metal with few, randomly substituted, magnetic impurities. Experimental evidences were obtained for a low-temperature “spin-glass” phase characterized by nonperiodic freezing of the magnetic moments (the spins) with a very slow, and strongly history dependent, response to external perturbations (this later aspect leads, more recently, to many fascinating developments). The theoretical analysis of this phenomenon leads to the celebrated Edwards–Anderson model [1] of spin glasses: classical spins on the sites of a regular lattice with random interactions between nearest neighbor spins. However, after more than 30 years of intense studies, the very nature of the low-temperature phase of the Edwards–Anderson model in three dimensions is still debated, even in the simple case of Ising spins. Two main competing theories exist: the mean field approach originating from the work of Sherrington and Kirkpatrick [2], and the so-called droplet [3] or scaling theory of spin glasses.

The mean field approach is the application to this problem of the conventional approach to phase transitions in statistical physics: one first builds a mean field theory after identifying the proper order parameter, solve it (usually a straightforward task) and then study the fluctuations around the mean field solution. Usually, fluctuations turn out to have mild effects for space dimensions above the so-called upper critical dimension (up to infinite space dimension, where mean field is exact). Below the upper critical dimension, fluctuations have major effects and nonperturbative techniques are needed to handle them. The second item of this agenda (solving the mean field equations) led, with spin glasses, to severe unexpected difficulties, and revealed a variety of new fascinating phenomena. The last step is the subject of the so-called replica field theory, which is still facing formidable difficulties.

These notes are an introduction to the physics of the infinite-range version of the Edwards–Anderson model, the so-called Sherrington–Kirkpatrick model, namely a model of classical spins that are not embedded in Euclidean space, with all pairs of spins interacting with a random interaction. If there is no more debate whether Parisi famous solution of the Sherrington–Kirkpatrick model in the infinite-volume limit is correct, much less is known, as mentioned before, about the Edwards–Anderson model in three dimensions, with numerical simulations as one of our main sources of knowledge. It is accordingly important to test the various methods of analysis

proposed for the Edwards-Anderson model, in the Sherrington-Kirkpatrick model case first.

In a first part, I motivate and introduce the Edwards-Anderson and Sherrington-Kirkpatrick models. In the second part, I sketch the analytical solution of the Sherrington-Kirkpatrick model, following Parisi. I next give the physical interpretation of this solution. This is a vast subject, and I concentrate on the major points and give references for more developments. The third part presents the numerical simulation approach and compares some numerical results to theoretical expectations. The last part, more detailed, is about the specific problem of finite size effects for the free energy, which is interesting for both theoretical and practical point of views. I have left aside several very interesting aspects, such as the problem of chaos [4, 5], the TAP approach [6] (see [7] for numerical results) and the computation of the complexity [8].

There are many books and review articles about spin glasses and related phenomena: One may start with the text book by Fischer and Hertz [9], the review by Binder and Young [10], which gives a very complete account of the situation in 1986 both experimental, theoretical and numerical with many detailed analytical computations, and (at a higher level) the book by Mézard, Parisi and Virasoro [11]. More recent references include [12] and [13]. The recent book by de Dominicis and Giardinà [14] gives a very complete exposition of the replica field theory. Reviews on various aspects of the physics of spin glasses can be found in [15, 16, 17]. The nonequilibrium behavior of spin glasses has been the subject of intense work during the recent years, see [18, 19, 20] for reviews.

2.1 Introduction

The Edwards-Anderson Ising (EAI) model is the classical Ising model with quenched random interactions. The Hamiltonian is

$$\mathcal{H} = - \sum_{\langle i,j \rangle} J_{i,j} \sigma_i \sigma_j - H \sum_i \sigma_i, \quad (2.1)$$

where the variables $\sigma_i = \pm 1$ are Ising spins living on the sites of a regular square lattice in d dimensions. H is the magnetic field. The interaction involves all nearest neighbor pairs of spins, with a strength $J_{i,j}$ that depends on the particular link $\langle i,j \rangle$. The $J_{i,j}$ s are quenched variables, namely they do not fluctuate. They have been drawn (once for ever) independently from a unique distribution $P(\mathcal{J})$ with mean J_0 and square deviation J^2 . In what follows, I will consider the case $J_0 = 0$ and choose $J^2 = 1$. The later choice is just the choice of the unit of temperature.

For a fixed set of $J_{i,j}$ s, denoted by \mathcal{J} , one can compute thermodynamic average values, for example the average internal energy $E_J = \langle E \rangle$, where the symbol $\langle \dots \rangle$ denotes the thermodynamics average (with given \mathcal{J}). In general, the results depend on \mathcal{J} , and should be averaged over the \mathcal{J} distribution. I note by $\overline{\dots}$ this disorder average.

This model was proposed [1] as a simple model that captures the essential of the physics of spin glasses, and in particular of magnetic spin glasses. Those

are alloys with magnetic impurities randomly distributed inside a nonmagnetic matrix. The interaction between the impurities is the RKKY interaction that oscillates with the distance. Since the positions of the impurities are random, their interactions are random too and one is led to the Edwards–Anderson model (see, e.g., [1, 9, 10] for more than this abrupt summary). If this very simple model is to explain convincingly the behavior of real spin glasses, its physics should obviously not depend (too much) on the specific disorder distribution used, as soon as it has zero mean and unit square deviation. This disorder distribution is usually Gaussian (this leads to simpler analytical computations) or binary with values ± 1 (this leads to faster computer programs, using the multi-spin coding technique).

The same model can be generalized to vector spins with two or three components. Those are called the XY and Heisenberg Edwards–Anderson models respectively. Most real spin glasses are indeed Heisenberg spin glasses with anisotropic interactions (due to the lattice structure, the interaction is not the rotational invariant $\sigma_i \sigma_j$).

In the zero magnetic field case ($H = 0$), there is now an agreement (based mostly on numerical simulations) between spin-glass physicists that the EAI model has no transition at finite T in two dimensions, and a transition for three dimensions and above.¹ In the low-temperature phase, the spins are frozen, with $\langle \sigma_i \rangle \neq 0$, but with a random pattern, and $\sum_i \langle \sigma_i \rangle$ is of order $1/\sqrt{N}$, where N is the number of spins. There is accordingly no spontaneous magnetization. There is no hidden magnetization either: the spins follow no periodic pattern (like, e.g., in an anti-ferromagnet), and it is furthermore very likely that the spin orientations are completely reshuffled as soon as one varies the temperature.² This is summarized by the statement: The EAI model is not a disguised ferromagnet.

The statement $\langle \sigma_i \rangle \neq 0$ needs to be made more precise. For a finite system, it means that $\langle \sigma_i \rangle$ is nonzero when observed over a time scale $t \ll t_{\text{erg}}(N)$, where $t_{\text{erg}}(N)$ is called the ergodic time. At some later time t , the system will eventually tunnel from the current equilibrium state, to a state where $\langle \sigma_i \rangle$ is reversed. However the dynamics of the EAI model is extremely slow, and $t_{\text{erg}}(N)$ is enormous in the low- T phase, as soon as one has few hundred spins, to the point that with any real spin glass, this time is much larger than the duration of any experiment.

In absence of magnetization, we have to find another order parameter for the glass order, one uses the so-called Edwards–Anderson parameter, namely

$$q_{\text{EA}} = \lim_{t \rightarrow \infty} \lim_{N \rightarrow \infty} \frac{1}{N} \sum_i \langle \sigma_i(t_0) \sigma_i(t + t_0) \rangle, \quad (2.2)$$

that is nonzero below the spin-glass transition and zero above. On a finite system, $C(t) = 1/N \sum_i \langle \sigma_i(t_0) \sigma_i(t + t_0) \rangle$ will rapidly decrease from the

¹ The value of lower the critical dimension, between 2 and 3, is not yet settled.

² This is the so-called temperature chaos effect.

starting value $C(1) = 1$ and have a plateau of height q_{EA} for a long time (of order t_{erg}) before dropping. As N grows, the plateau becomes longer and longer. The so defined q_{EA} turns out to depend weakly on \mathcal{J} for large systems. This is a so-called self-averaging quantity (see Sect. 2.2.3).

One may also consider two independent copies of the system, $\{\sigma_i^{(1)}\}$ and $\{\sigma_i^{(2)}\}$, with the same disorder instance \mathcal{J} (such copies are called real replica, or sometimes clones, in order to distinguish them from the replica of the replica method, see Sect. 2.2), and consider the probability distribution

$$P_{\mathcal{J}}(q) = \left\langle \delta \left(q - \frac{1}{N} \sum_i \sigma_i^{(1)} \sigma_i^{(2)} \right) \right\rangle, \quad (2.3)$$

namely the probability distribution of the overlap $q = 1/N \sum_i \sigma_i^{(1)} \sigma_i^{(2)}$ between the two systems. A nonzero q_{EA} corresponds to two peaks in $P_{\mathcal{J}}(q)$ centered at $q = \pm q_{\text{EA}}$. We will see later that, at least for the Sherrington–Kirkpatrick model, $P_{\mathcal{J}}(q)$ has more structure than this double peak.

Clearly, $q_{\text{EA}} = \langle M \rangle^2$ for a ferromagnet in d dimensions (still at zero magnetic field), where $\langle M \rangle$ is the spontaneous magnetization. On a finite system, $P(q)$ is made of two Gaussian centered around $\pm \langle M \rangle^2$. Between the two peaks, $P(q)$ is exponentially small [21], of order $\exp(-2\mathcal{A}L^{d-1})$, where \mathcal{A} is the interface tension, and L the linear dimension of the system.

In Ising ferromagnets, the transition happens when the magnetization M acquires a nonzero expectation value, and accordingly the susceptibility $\chi = N \langle M^2 \rangle$ becomes infinite as T decreases toward T_c . In Ising spin glasses, the spin susceptibility stays finite as $T \rightarrow T_c$, but the spin-glass susceptibility $\chi_{\text{SG}} = N \langle q^2 \rangle$ diverges. There is however a difference: In ferromagnets, one can define a connected susceptibility³ $N(\langle M^2 \rangle - \langle M \rangle^2)$ that is finite in the low T phase. For spin glasses, the analog connected susceptibility⁴ diverges, as $N \rightarrow \infty$ in the whole low- T phase.

2.2 The Sherrington–Kirkpatrick Model

This model [2] is a simplified version of the Edwards–Anderson model, where all spins are directly coupled. The Hamiltonian is

$$\mathcal{H} = - \sum_{1 \leq i < j \leq N} \frac{J_{i,j}}{\sqrt{N}} \sigma_i \sigma_j - H \sum_i \sigma_i, \quad (2.4)$$

where N is the number of spins. The $J_{i,j}$ s are again drawn from a unique probability distribution $P(\mathcal{J})$ with zero mean and unit square deviation. The

³ In this formula, $\langle M \rangle$ is to be interpreted as an average restricted over a time interval of length $\ll t_{\text{erg}}(N)$, or simply as $\langle |M| \rangle$.

⁴ It is usually defined as $\sum_{i,j} (\overline{\langle \sigma_i \sigma_i \rangle} - \overline{\langle \sigma_i \rangle} \overline{\langle \sigma_j \rangle})^2$, sometimes simply as $N(\overline{\langle q^2 \rangle} - \overline{\langle q \rangle}^2)$.

factor $1/\sqrt{N}$ will ensure a finite limit for the internal energy per spin $e_N(T)$ as $N \rightarrow \infty$. It is in some sense a model in infinite dimension since a given spin is coupled to N spins, with $N \rightarrow \infty$ in the thermodynamic limit. The model has “infinite connectivity”. The infinite connectivity will ensure that the mean field method gives the exact result. As we will show, the Sherrington–Kirkpatrick model can be solved exactly in the thermodynamic limit, and the result is independent of the choice made for the disorder distribution $P(\mathcal{J})$.

The standard method to solve this model is the famous replica trick⁵. One is interested in computing the average free energy $-\overline{\beta F_{\mathcal{J}}} = \overline{\ln Z_{\mathcal{J}}}$, where $\beta = 1/T$ is the inverse temperature, in units such that $k_B = 1$. This is done by considering the partition function of n identical uncoupled copies of the system, with the same instance of the disorder \mathcal{J} . Such copies are called replica. The partition function is simply the n th power of $Z_{\mathcal{J}}$, $Z_{\mathcal{J}}^n$. Continuing this function defined for integer $n \geq 1$ to a function of the real variable n , one has, at least for finite N ,

$$-\beta F = \overline{\ln Z_{\mathcal{J}}} = \lim_{n \rightarrow 0} \frac{\overline{Z_{\mathcal{J}}^n} - 1}{n}. \quad (2.5)$$

$Z_{\mathcal{J}}^n$ can be written as

$$\begin{aligned} Z_{\mathcal{J}}^n &= \text{Tr}_{\sigma}^{[n]} \exp(-\beta(\mathcal{H}_{\mathcal{J}}^{[n]})) \\ &= \text{Tr}_{\sigma}^{[n]} \exp(-\beta(\mathcal{H}_{\mathcal{J}}(\sigma^{(1)}) + \dots + \mathcal{H}_{\mathcal{J}}(\sigma^{(n)}))) , \end{aligned} \quad (2.6)$$

where $\sigma^{(1)}$ represents the N spins of the first replica (namely $\{\sigma_i^{(1)}\}$), $\sigma^{(2)}$ the N spins of the second replica, \dots , and $\text{Tr}_{\sigma}^{[n]}$ is the trace over the nN spin variables. The average over the $n(n-1)/2$ $J_{i,j}$ variables are independent, and the disorder average factorizes as a product of terms of the form

$$\overline{\exp\left(\frac{\beta J_{i,j} X_{i,j}}{\sqrt{N}}\right)} = \exp\left(\sum_{p=1}^{\infty} \frac{\beta^p X_{i,j}^p [J]_p}{p! N^{p/2}}\right), \quad (2.7)$$

where

$$X_{i,j} = \sigma_i^{(1)} \sigma_j^{(1)} + \sigma_i^{(2)} \sigma_j^{(2)} + \dots + \sigma_i^{(n)} \sigma_j^{(n)} = \sum_{a=1}^n \sigma_i^{(a)} \sigma_j^{(a)}, \quad (2.8)$$

and the $[J]_p$ s are the successive cumulants of the disorder distribution $P(\mathcal{J})$,

$$\begin{aligned} [J]_1 &= \overline{J}, \\ [J]_2 &= \overline{(J - \overline{J})^2}, \\ [J]_3 &= \overline{(J - \overline{J})^3}, \\ [J]_4 &= \overline{(J - \overline{J})^4} - 3\overline{(J - \overline{J})^2}^2, \\ &\dots \end{aligned} \quad (2.9)$$

⁵ There is an alternative method called the cavity method, see [11].

Since we have $\overline{J} = 0$ and $\overline{J^2} = 1$, one is led to the result

$$\overline{\exp\left(\frac{\beta J_{i,j} X_{i,j}}{\sqrt{N}}\right)} = \exp\left(\frac{\beta^2 X_{i,j}^2}{2N} + \dots\right). \quad (2.10)$$

The neglected terms in the exponent are of order $1/N^2$ and will not contribute to the thermodynamic limit⁶ and accordingly the physics is independent of the disorder distribution. One obtains for the disorder averaged partition function:

$$\begin{aligned} \overline{Z_{\mathcal{J}}^n} &= \text{Tr}_{\sigma}^{[n]} \exp\left(\frac{\beta^2}{2N} \sum_{i < j} \left(\sum_{b=1}^n \sigma_i^{(b)} \sigma_j^{(b)}\right)^2 + \beta H \sum_i \sum_{b=1}^n \sigma_i^{(b)}\right) \\ &= \text{Tr}_{\sigma}^{[n]} \exp\left(\frac{\beta^2}{2N} \sum_{a < b} \left(\sum_i \sigma_i^{(a)} \sigma_i^{(b)}\right)^2 + \beta H \sum_i \sum_{b=1}^n \sigma_i^{(b)}\right. \\ &\quad \left.+ (nN - n^2) \frac{\beta^2}{4}\right). \end{aligned} \quad (2.11)$$

The average over the disorder has been performed analytically, but now the n replicas are coupled. In order to proceed further, one uses the formula

$$\sqrt{\frac{N\beta^2}{2\pi}} \int_{-\infty}^{+\infty} dq \exp\left(-\frac{N\beta^2 q^2}{2}\right) \exp(q\beta^2 X) = \exp\left(\frac{\beta^2 X^2}{2N}\right), \quad (2.12)$$

introducing $n(n-1)/2$ auxiliary real variables $q_{a,b}$ ($a < b$), with the result

$$\begin{aligned} \overline{Z_{\mathcal{J}}^n} &= \left[\prod_{a < b} \sqrt{\frac{N\beta^2}{2\pi}} \int dq_{a,b} \right] \text{Tr}_{\sigma}^{[n]} \exp\left(-\frac{N\beta^2}{2} \sum_{a < b} q_{a,b}^2\right. \\ &\quad \left.+ \beta^2 \sum_{a < b} q_{a,b} \sum_i \sigma_i^{(a)} \sigma_i^{(b)} + \beta H \sum_i \sum_{b=1}^n \sigma_i^{(b)} + (nN - n^2) \frac{\beta^2}{4}\right). \end{aligned} \quad (2.13)$$

The variables $q_{a,b}$ have been defined for $a < b$. In the following, it will be sometimes convenient to define $q_{a,b}$ for $a \geq b$ also, as $q_{a,b} = q_{b,a}$ and $q_{a,a} = 0$. For a given replica index a , the trace over the spins factorizes as

$$\begin{aligned} &\prod_{i=1}^N \text{Tr}_{\sigma_i^{(a)}} \exp\left(\beta^2 \sum_{a < b} q_{a,b} \sum_i \sigma_i^{(a)} \sigma_i^{(b)} + \beta H \sum_i \sum_{b=1}^n \sigma_i^{(b)}\right) \\ &= \left[\text{Tr}_{S^{(a)}} \exp\left(\beta^2 \sum_{a < b} q_{a,b} S^{(a)} S^{(b)} + \beta H \sum_{b=1}^n S^{(b)}\right) \right]^N, \end{aligned} \quad (2.14)$$

⁶ They are altogether absent if the distribution is Gaussian.

where $S^{(a)}$ is any of the $\sigma_i^{(a)}$ s, or alternatively the spin of a single spin system, which is replicated n times. Thus⁷

$$\begin{aligned} \overline{Z_{\mathcal{J}}^n} = & \left[\prod_{a < b} \sqrt{\frac{N\beta^2}{2\pi}} \int dq_{a,b} \right] \exp \left(-\frac{N\beta^2}{2} \sum_{a < b} q_{a,b}^2 \right. \\ & \left. + N \log \left(\text{Tr}_S^{[n]} \left[\exp \left(\beta^2 \sum_{a < b} q_{a,b} S^{(a)} S^{(b)} + \beta H \sum_{b=1}^n S^{(b)} \right) \right] \right) + nN \frac{\beta^2}{4} \right). \end{aligned} \quad (2.15)$$

The formula has a particularly simple form, with all dependence in N explicit,

$$\overline{Z_{\mathcal{J}}^n} = \left[\prod_{a < b} \sqrt{\frac{N\beta^2}{2\pi}} \int dq_{a,b} \right] \exp(-N\beta\mathcal{A}(\{q_{a,b}\})) . \quad (2.16)$$

Up to now our derivation is exact (for a Gaussian disorder) in the $n \rightarrow 0$ limit. We now make the saddle-point (or steepest-descent) approximation, which gives the correct $N \rightarrow \infty$ behavior. Assuming the existence of a unique absolute maximum of the integrand at location $\{q_{a,b}^{SP}\}$, one has

$$\overline{Z_{\mathcal{J}}^n} \approx \exp(-N\beta\mathcal{A}(\{q_{a,b}^{SP}\})) . \quad (2.17)$$

By assumption, all partial derivatives of \mathcal{A} , $\partial\mathcal{A}/\partial q_{a,b}$, are zero at the saddle point, and the matrix of the second derivatives, the Hessian, has only non-negative eigenvalues. The free energy of the original Sherrington–Kirkpatrick model is thus simply related to the saddle point of the $q_{a,b}$ integral representation of the partition function of the n times replicated model (with a reckless interchange of limits),

$$f = \lim_{N \rightarrow \infty} \frac{F}{N} = \lim_{n \rightarrow 0} \frac{1}{n} \mathcal{A}(\{q_{a,b}^{SP}\}) . \quad (2.18)$$

Note that the saddle-point equations can be written as self-consistent equations, involving a single spin system

$$q_{a,b}^{(SP)} = \frac{\text{Tr}_S \left[S^{(a)} S^{(b)} \exp \left(\beta^2 \sum_{a < b} q_{a,b}^{(SP)} S^{(a)} S^{(b)} + \beta H \sum_{b=1}^n S^{(b)} \right) \right]}{\text{Tr}_S \left[\exp \left(\beta^2 \sum_{a < b} q_{a,b}^{(SP)} S^{(a)} S^{(b)} + \beta H \sum_{b=1}^n S^{(b)} \right) \right]} . \quad (2.19)$$

The replica method is not limited to the evaluation of the free energy. It can be used to compute the average (thermodynamic average and disorder average)

⁷ From now on, we omit the n^2 terms in the exponent since they do not contribute in the $n \rightarrow 0$ limit.

of any function of the spins. Let $\mathcal{O}(\sigma)$ be a function of the spins $\{\sigma_i\}$, we have by definition, for any disorder sample:

$$\langle \mathcal{O}(\sigma) \rangle = \frac{\text{Tr}_{\sigma}^{[1]} \mathcal{O}(\sigma^{(1)}) \exp \left(-\beta \left(\mathcal{H}_{\mathcal{J}}^{[1]} \right) \right)}{Z_{\mathcal{J}}} . \quad (2.20)$$

Multiplying both numerator and denominator by Z^{n-1} , and letting⁸ $n \rightarrow 0$, we have

$$\langle \mathcal{O}(\sigma) \rangle = \lim_{n \rightarrow 0} \text{Tr}_{\sigma}^{[n]} \mathcal{O}(\sigma^{(1)}) \exp \left(-\beta \left(\mathcal{H}_{\mathcal{J}}^{[n]} \right) \right) . \quad (2.21)$$

The right-hand side is of a form whose disorder average is readily computed using (2.10). The method is extended readily to the disorder average of products like $\langle \mathcal{O}(\sigma) \rangle \langle \mathcal{P}(\sigma) \rangle$. Introducing two real replica, we have indeed

$$\langle \mathcal{O}(\sigma) \rangle \langle \mathcal{P}(\sigma) \rangle = \frac{\text{Tr}_{\sigma}^{[2]} \mathcal{O}(\sigma^{(1)}) \mathcal{P}(\sigma^{(2)}) \exp \left(-\beta \left(\mathcal{H}_{\mathcal{J}}^{[2]} \right) \right)}{Z_{\mathcal{J}}^2} . \quad (2.22)$$

Multiplying both numerator and denominator by Z^{n-2} , and letting $n \rightarrow 0$, we have

$$\langle \mathcal{O}(\sigma) \rangle \langle \mathcal{P}(\sigma) \rangle = \lim_{n \rightarrow 0} \text{Tr}_{\sigma}^{[n]} \mathcal{O}(\sigma^{(1)}) \mathcal{P}(\sigma^{(2)}) \exp \left(-\beta \left(\mathcal{H}_{\mathcal{J}}^{[n]} \right) \right) , \quad (2.23)$$

which is again of a form whose disorder average is readily computed using (2.10).

2.2.1 Interpretation of the $q_{a,b}$ Variables

The $q_{a,b}$ variables have been introduced formally. Their value at the saddle point has a simple interpretation [22] in terms of the overlaps between real replicas as defined in (2.3). Consider two clones $\sigma^{(1)}$ and $\sigma^{(2)}$ and compute the generating function $G(y)$ ⁹

$$G(y) = \left\langle \exp \left(\frac{y\beta^2}{N} \sum_i \sigma_i^{(1)} \sigma_i^{(2)} \right) \right\rangle . \quad (2.24)$$

We have

$$\left\langle \exp \left(\frac{y\beta^2}{N} \sum_i \sigma_i^{(1)} \sigma_i^{(2)} \right) \right\rangle = \frac{1}{Z^2} \text{Tr}_{\sigma}^{(2)} \exp \left(\frac{y\beta^2}{N} \sum_i \sigma_i^{(1)} \sigma_i^{(2)} - \beta \mathcal{H}_{\mathcal{J}}^{[2]} \right) . \quad (2.25)$$

⁸ We did add $n-1$ replica to the one real replica and then let $n \rightarrow 0$.

⁹ This is a convenient way to evaluate at once the expression $\langle (1/N \sum_i \sigma_i^{(1)} \sigma_j^{(2)})^k \rangle$ for all values of k .

Multiplying the numerator and denominator by Z^{n-2} , and letting $n \rightarrow 0$, one obtains after averaging over the disorder

$$G(y) = Z^{-n} \left[\prod_{a < b} \sqrt{\frac{N\beta^2}{2\pi}} \int dq_{a,b} \right] \exp \left(y\beta^2 q_{1,2} - \frac{N\beta^2}{2} \sum_{a < b} q_{a,b}^2 \right. \\ \left. + N \log \left(\text{Tr}_S^{[n]} \left[\exp \left(\beta^2 \sum_{a < b} q_{a,b} S^{(a)} S^{(b)} + \beta H \sum_{b=1}^n S^{(b)} \right) \right] \right) + nN \frac{\beta^2}{4} \right), \quad (2.26)$$

with $Z^n = 1$ since $n \rightarrow 0$.

At leading order in $1/N$, the saddle point is y independent, and accordingly

$$\overline{\left\langle \exp \left(\frac{y\beta^2}{N} \sum_i \sigma_i^{(1)} \sigma_i^{(2)} \right) \right\rangle} = \exp \left(y\beta^2 q_{1,2}^{SP} \right). \quad (2.27)$$

If the saddle point is not symmetric, namely if the $q_{a,b}^{SP}$ s are not all equal, the solution of the saddle-point equations is degenerate, and one must average¹⁰ over all degenerate solutions, or alternatively all permutations of a and b . The correct formula is then

$$\overline{\left\langle \exp \left(\frac{y\beta^2}{N} \sum_i \sigma_i^{(1)} \sigma_i^{(2)} \right) \right\rangle} = \frac{2}{n(n-1)} \sum_{a < b} \exp \left(y\beta^2 q_{a,b}^{SP} \right), \quad (2.28)$$

where $n(n-1)/2$ is the number of $q_{a,b}$ variables. This implies the following direct relation between the disorder averaged $P(q)$ and the value of $q_{a,b}$ at the saddle point:

$$P(q) = \overline{P(q)_{\mathcal{J}}} = \overline{\left\langle \delta \left(q - \frac{1}{N} \sum_i \sigma_i^{(1)} \sigma_i^{(2)} \right) \right\rangle} \\ = \frac{2}{n(n-1)} \sum_{a < b} \delta \left(q - q_{a,b}^{SP} \right). \quad (2.29)$$

The distribution $P_{\mathcal{J}}(q)$, namely before disorder average, has an interpretation in terms of pure states. In the rigorous formulation of statistical physics (without disorder), pure states give a precise definition of thermodynamic phases directly in the infinite-volume limit (see [17] for a discussion from a physicist point of view). Pure states have the following properties:

- The clustering property: Inside a pure state, spin correlation functions factorize when the distance goes to infinity. For example, if α is a pure state, one has $\langle \sigma_x \sigma_y \rangle_{\alpha} \rightarrow \langle \sigma_x \rangle_{\alpha} \langle \sigma_y \rangle_{\alpha}$, as $|x - y| \rightarrow \infty$.

¹⁰ Since the saddle-point solution is degenerate, one must sum over the solutions in both numerators and denominators of (2.26).

- Every translationally invariant state is a convex linear combination of pure states. This means that for any A , one has $\langle A \rangle = \sum_{\alpha} w_{\alpha} \langle A \rangle_{\alpha}$, where the weights $w_{\alpha} \geq 0$, with $\sum_{\alpha} w_{\alpha} = 1$, are independent of A .

In a ferromagnet at temperature $T < T_c$, there are two T -dependent pure states corresponding to states with positive and negative magnetizations respectively, that we can call the “+” and the “−” states. A general translationally invariant state is a linear combination of these two pure states. For example, doing the infinite-volume limit (at zero magnetic field) by considering a set of finite systems of increasing sizes with periodic boundary conditions, one has $\omega_+ = \omega_- = 1/2$.

Let us assume (departing boldly from rigor) that the same decomposition holds for finite systems in the Sherrington–Kirkpatrick model for every disorder sample, namely that $\langle A \rangle = \sum_{\alpha} w_{\alpha} \langle A \rangle_{\alpha}$, for any A , where the weights and the states are (disorder) sample dependent. We introduce \mathcal{Q} , the overlap between two pure states

$$\mathcal{Q}_{\alpha,\beta} = \frac{1}{N} \sum_i \langle \sigma_i^{(1)} \rangle_{\alpha} \langle \sigma_i^{(2)} \rangle_{\beta} . \quad (2.30)$$

In a ferromagnet $\mathcal{Q}_{+,+} = \mathcal{Q}_{-,-} = \langle M \rangle^2$ and $\mathcal{Q}_{+,-} = \mathcal{Q}_{-,+} = -M^2$. We now proceed to show that the overlap between pure states is related to the clone overlap introduced in (2.3). We do this by considering successive moments of q . For the first moment, we have

$$\begin{aligned} \langle q \rangle &= \frac{1}{N} \sum_i \langle \sigma_i^{(1)} \sigma_i^{(2)} \rangle \\ &= \frac{1}{N} \sum_i \langle \sigma_i^{(1)} \rangle \langle \sigma_i^{(2)} \rangle , \end{aligned} \quad (2.31)$$

since $\sigma^{(1)}$ and $\sigma^{(2)}$ are independent systems. Introducing the pure states, this gives

$$\begin{aligned} \langle q \rangle &= \frac{1}{N} \sum_i \sum_{\alpha,\beta} \omega_{\alpha} \omega_{\beta} \langle \sigma_i^{(1)} \rangle_{\alpha} \langle \sigma_i^{(2)} \rangle_{\beta} \\ &= \sum_{\alpha,\beta} \omega_{\alpha} \omega_{\beta} \mathcal{Q}_{\alpha,\beta} . \end{aligned} \quad (2.32)$$

For the second moment, we have

$$\begin{aligned} \langle q^2 \rangle &= \frac{1}{N^2} \sum_i \sum_j \langle \sigma_i^{(1)} \sigma_j^{(1)} \sigma_i^{(2)} \sigma_j^{(2)} \rangle \\ &= \frac{1}{N^2} \sum_{i,j} \langle \sigma_i^{(1)} \sigma_j^{(1)} \rangle \langle \sigma_i^{(2)} \sigma_j^{(2)} \rangle \\ &= \frac{1}{N^2} \sum_{i,j} \sum_{\alpha,\beta} \omega_{\alpha} \omega_{\beta} \langle \sigma_i^{(1)} \sigma_j^{(1)} \rangle_{\alpha} \langle \sigma_i^{(2)} \sigma_j^{(2)} \rangle_{\beta} \end{aligned}$$

$$\approx \frac{1}{N^2} \sum_{i,j} \sum_{\alpha,\beta} \omega_\alpha \omega_\beta \left\langle \sigma_i^{(1)} \right\rangle_\alpha \left\langle \sigma_j^{(1)} \right\rangle_\alpha \left\langle \sigma_i^{(2)} \right\rangle_\beta \left\langle \sigma_j^{(2)} \right\rangle_\beta, \quad (2.33)$$

where we assumed that, since the states α and β are pure states, one has $\langle \sigma_i \sigma_j \rangle_\alpha \approx \langle \sigma_i \rangle_\alpha \langle \sigma_j \rangle_\alpha$ (we pretend that all points are far apart this is clearly not correct for $i = j$, but the error is negligible for large N). Finally,

$$\langle q^2 \rangle \approx \sum_{\alpha,\beta} \omega_\alpha \omega_\beta \mathcal{Q}_{\alpha,\beta}^2. \quad (2.34)$$

In general, one has, for any integer r ,

$$\langle q^r \rangle \approx \sum_{\alpha,\beta} \omega_\alpha \omega_\beta \mathcal{Q}_{\alpha,\beta}^r, \quad (2.35)$$

namely (still with disorder dependent ω_α s and $\mathcal{Q}_{\alpha,\beta}$ s)

$$\left\langle \delta \left(q - \frac{1}{N} \sum_i \sigma_i^{(1)} \sigma_i^{(2)} \right) \right\rangle = \sum_{\alpha,\beta} \omega_\alpha \omega_\beta \delta(q - \mathcal{Q}_{\alpha,\beta}). \quad (2.36)$$

This is a remarkable relation between a quantity relative to pure states and a quantity that is directly accessible, e.g., with Monte Carlo simulation. This relation is quite useful since there is no simple way to characterize pure states for spin glasses, in contrast to Ising ferromagnets where a pure state can be selected by simply applying an infinitesimal constant magnetic field of suitable sign.

2.2.2 Solution of the Model

We look for the absolute minimum of $\mathcal{A}(\{q_{a,b}\})$, namely the lowest stable solution of $\partial \mathcal{A} / \partial q_{a,b} = 0$ for all $q_{a,b}$ with generic n . The solution is then to be analytically continued to the limit $n \rightarrow 0$. One proceeds heuristically by first making an ansatz for the matrix $q_{a,b}$ and generic n , involving a few parameters x_i and q_i . Very surprising at first sight, the correct saddle-point solution is a maximum of \mathcal{A} with respect to the x_i s and q_i s (and not a minimum), and if several maxima are found, one should take usually the largest. Once a candidate solution is found, one should check that this solution is stable (that the Hessian has only nonnegative eigenvalues). If no satisfactory solution is found, one tries a more general ansatz (this is indeed a heuristic procedure).

The simplest ansatz is the replica symmetric (RS) ansatz [2], namely all $q_{a,b} = q_0$, and accordingly $P(q) = \delta(q - q_0)$. This ansatz has a (ferromagnetic) solution in the whole $T > 0$ half-plane, with $q_0 = 0$ and zero magnetization for $H = 0$, and $q_0 > 0$ and nonzero magnetization for $H \neq 0$. At zero magnetic field and $T < 1$, this ansatz has another solution with $q_0 \neq 0$ that should in principle be selected since it has a higher free energy than the first solution.

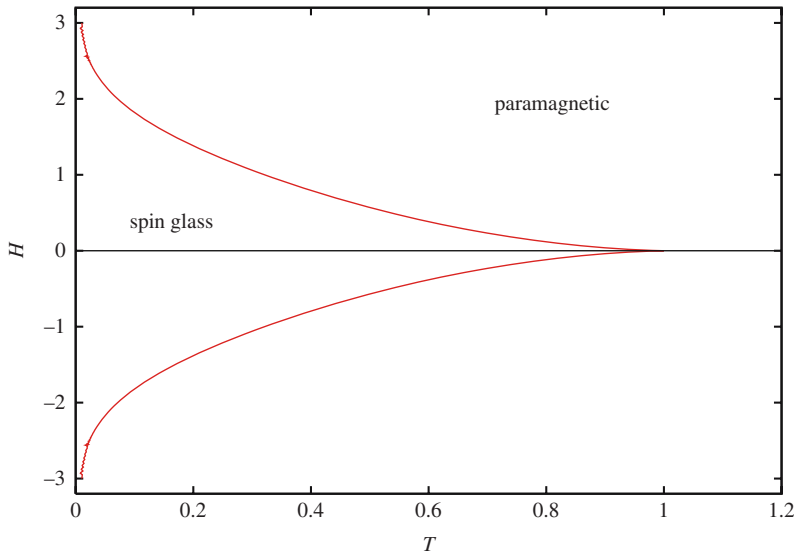


Fig. 2.1. Phase diagram of the Sherrington–Kirkpatrick model in the $T-H$ plane. The paramagnetic RS solution is valid outside of the area delimited by the AT lines and the H axis. The complementary region is the spin-glass phase, where the ∞ -RSB ansatz gives the correct result

However detailed investigation [23] of the eigenvalues of the Hessian shows that neither solution is a minimum of the integrand in (2.16), and accordingly both should be rejected, when the absolute value of H is below the so-called Almeida–Thouless (AT) line that starts at some nonzero H at $T = 0$ and reaches the $H = 0$ axis at $T_c = 1$ (see Fig. 2.1). In the rest of the half $T > 0$ plane, the paramagnetic RS solution is stable, which means heuristically that it is the correct solution.

One is thus led to a more general non replica symmetric ansatz. The correct (∞ -RSB) ansatz was found by Parisi [24, 25, 26, 27]. It is a hierarchical solution that goes in an infinite number of steps. The first step is the so-called one-step RSB ansatz. The n replica are partitioned in n/x_1 blocks of x_1 replica. At this level, x_1 is an integer and x_1 divides n . One assumes that $q_{a,b} = q_1$ if a and b are in the same block, and that $q_{a,b} = q_0$ if they do not. With this rule, we have $-\frac{n}{2}(1 - x_1)$ elements $q_{\alpha,\beta}$ (for $a > b$) with value q_1 , and $-\frac{n}{2}(x_1 - n)$ elements with value q_0 . If we plug this information into (2.29), and do formally the limit $n \rightarrow 0$, this gives

$$P(q) = x_1 \delta(q - q_0) + (1 - x_1) \delta(q - q_1), \quad (2.37)$$

which means that $P(q)$ has two peaks of weights x_1 and $1 - x_1$ respectively. Clearly, this result only makes sense if $x_1 \in [0, 1]$. We started with a $n \times n$ matrix subdivided in $x_1 \times x_1$ blocks, and then let $n \rightarrow 0$. We have to admit that in this strange limit, the integer x_1 becomes a real variable $\in [0, 1]$.

In the next step, the so-called two-step RSB ansatz, each diagonal block of size x_1 is divided in x_1/x_2 sub-blocks of size x_2 and one assumes that now $q_{\alpha,\beta} = q_2$ in the diagonal sub-blocks, and is unchanged elsewhere.

Performing this procedure k times, we introduce a subdivision $n = x_0 > x_1 > x_2 > \dots > x_{k+1} = 1$, with integer x_0, x_1, \dots, x_k , $x_0/x_1, x_1/x_2, \dots, x_{k-1}/x_k$ and to a set of values for the overlaps q_0, q_1, \dots, q_k . Then

$$P(q) = \sum_{i=0}^k (x_{i+1} - x_i) \delta(q - q_i) . \quad (2.38)$$

In order for this formula to makes sense, we have to assume that in the $n \rightarrow 0$ limit, the x_i variables become $0 = x_0 < x_1 < x_2 < \dots < x_{k+1} = 1$. Assuming now that the q_i s form an increasing sequence, one has

$$\int_0^{q_m} P(q) dq = \sum_{i=0}^m (x_{i+1} - x_i) = x_{m+1} \quad m = 0, 1, \dots, k . \quad (2.39)$$

In the $k \rightarrow \infty$ limit, assuming that the increasing sequence q_i s converges to a continuous function $q(x)$, with an inverse $x(q)$, this equation becomes

$$\int_0^q P(q') dq' = x(q) , \quad P(q) = \frac{dx}{dq} . \quad (2.40)$$

We have similarly the equation, for any integer r ,

$$-\frac{2}{n} \sum_{a \neq b} q_{a,b}^r = \sum_{i=0}^k (x_{i+1} - x_i) q_i^r \sim \int_0^1 dx q(x)^r . \quad (2.41)$$

Finally, $\mathcal{A}(q(x))$ is expressed as a (complicated) functional of $q(x)$, that should be maximized with respect to variations of the function $q(x)$ in order to give the free energy $f(T)$:

$$\begin{aligned} -f(T) &= \frac{\beta}{4} \left(1 - 2q(1) + \int_0^1 dx q^2(x) \right) \\ &+ \int_{-\infty}^{+\infty} \frac{dy}{\sqrt{2\pi q(0)}} \exp \left(-\frac{(y-H)^2}{2q(0)} \right) \phi(0, y) , \end{aligned} \quad (2.42)$$

where $\phi(0, y)$ is the solution, evaluated at $x = 0$, of the equation

$$\partial_x \phi(x, y) = -\frac{\partial_x q(x)}{2} \left[\partial_y^2 \phi(x, y) + \beta x (\partial_y \phi(x, y))^2 \right] , \quad (2.43)$$

with the boundary condition

$$\phi(1, y) = \beta^{-1} \log (2 \cosh \beta y) . \quad (2.44)$$

One can show [28] that the (∞ -RSB) solution is stable in the whole region where the paramagnetic RS solution is unstable. This means (heuristically) that we have found the correct solution for all H and $T > 0$. There is however no known closed form solution neither for $q(x)$ ¹¹ nor for the corresponding free energy $f(T)$, and most articles in the literature use approximate estimates of $q(x)$, usually based on the truncated Hamiltonian (see next section), valid for $T \approx T_c$. Precise estimates can be obtained however either by an expansion of the functional in powers of $T_c - T$, or by numerical methods (see [29] for recent very precise estimates in the $H = 0$ case, and [30] in the $H \neq 0$ case).

For $H \neq 0$, the continuous nondecreasing function $q(x)$ behaves as follows (see Fig 2.2): There exist values $0 \leq x_{\min} \leq x_{\max} \leq 1$ such that $q(x) = q_{\min} \geq 0$ for $x \in [0, x_{\min}]$, $q(x)$ increases for $x \in [x_{\min}, x_{\max}]$, and $q(x) = q_{\max}$ for $x \in [x_{\max}, 1]$. Accordingly, the function $P(q)$ has two delta function peaks located at $q(x) = q_{\min}$ and $q(x) = q_{\max}$ respectively, and is nonzero between. The transition on the AT line is continuous, with $q_{\min} \rightarrow q_{\max}$, as the AT line is approached.

The value q_{\max} is interpreted as q_{EA} , the overlap between two configurations in the same pure state:

$$q_{\text{EA}} = \frac{1}{N} \sum_i \langle \sigma_i \rangle_\alpha \langle \sigma_i \rangle_\alpha . \quad (2.45)$$

One can show that q_{EA} is independent of α . This definition is in agreement with the one given in the introduction (2.2), thanks to the wide separation of time scales in the model: A given configuration stays a very long time in the same pure state, and accordingly the correlation function $C(t)$ has a plateau of height q_{EA} .

As $H \rightarrow 0$, $q_{\min} \rightarrow 0$ and the corresponding peak disappears. When H is exactly zero, $P(q)$ which is nonzero for $0 < q_{\min} \leq q \leq q_{\max}$ for $H \neq 0$ becomes symmetric (obviously the two limits $N \rightarrow \infty$ and $H \rightarrow 0$ do not commute). At

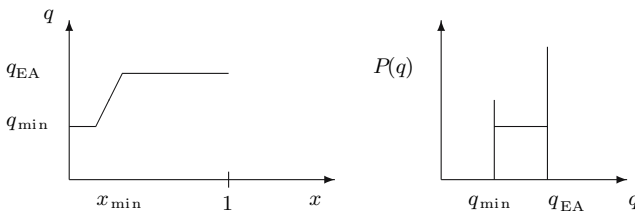


Fig. 2.2. Schematic representation of the ∞ -RSB solution for $H \neq 0$: $q(x)$ as a function of x and $P(q)$ as a function of q , with $q_{\text{EA}} = q_{\max}$. In the actual solution, the increasing portion of $q(x)$ and the corresponding continuum in $P(q)$ are not straight

¹¹ From now on, $q(x)$ denotes the solution of the saddle-point equations $q^{SP}(x)$.

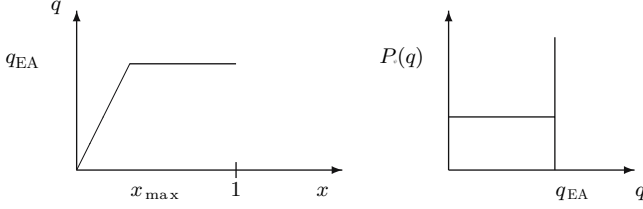


Fig. 2.3. Schematic representation of the ∞ -RSB solution for $H = 0$: $q(x)$ as a function of x and $P(q)$ as a function of q , with $q_{EA} = q_{max}$. In the actual solution, the increasing portion of $q(x)$ and the corresponding continuum in $P(q)$ are not straight. In this $H = 0$ case, $P(q)$ is symmetric in q . Only the $q > 0$ part of $P(q)$ is represented here

$H = 0$, $P(q)$ is made of two delta peaks located at $\pm q_{max} = \pm q_{EA}$ with a continuum between. As shown in [29], and in contradiction with many drawings in the literature (and Fig. 2.3), $P(q)$ has a minimum at a nonzero value of q (at least as soon as $T < 0.96 \dots$) and behaves like $a + bq^2 + c|q|^3 + \dots$, with $c \neq 0$ for small q . When $T \rightarrow T_c$, $q_{EA} \rightarrow 0$, namely the transition is continuous.

2.2.3 Properties of the Solution

Among the fascinating features of Parisi solution is ultrametricity. Taking three clones, one can show that [11, 31]

$$\begin{aligned}
 P(q_{1,2}, q_{2,3}, q_{3,1}) &= \left\langle \delta \left(q_{1,2} - \sum_{i=1}^N \sigma_i^{(1)} \sigma_i^{(2)} \right) \delta \left(q_{2,3} - \sum_{i=1}^N \sigma_i^{(2)} \sigma_i^{(3)} \right) \right. \\
 &\quad \left. \delta \left(q_{3,1} - \sum_{i=1}^N \sigma_i^{(3)} \sigma_i^{(1)} \right) \right\rangle > \\
 &= \frac{1}{n(n-1)(n-2)} \sum_{a \neq b, b \neq c, c \neq a} \delta(q_{1,2} - q_{a,b}) \\
 &\quad \delta(q_{2,3} - q_{b,c}) \delta(q_{3,1} - q_{c,a}) .
 \end{aligned} \tag{2.46}$$

The ∞ -RSB solution for the $q_{a,b}$ s has the property that this probability is zero unless the three overlaps $q_{1,2}, q_{2,3}, q_{3,1}$ satisfy the ultrametricity constraints: at least two overlaps are equal, and the third is smaller or equal to their common value. Ultrametricity generalizes to pure states, where one defines a distance between pure states α and β , as

$$\begin{aligned}
 d_{\alpha,\beta} &= \frac{1}{N} \sum_i (\langle \sigma_i \rangle_\alpha - \langle \sigma_i \rangle_\beta)^2, \\
 &= \mathcal{Q}_{\alpha,\alpha} + \mathcal{Q}_{\beta,\beta} - 2\mathcal{Q}_{\alpha,\beta} = 2(q_{EA} - \mathcal{Q}_{\alpha,\beta}) ,
 \end{aligned} \tag{2.47}$$

since all self-overlaps are equal to q_{EA} .

Another feature, of the Parisi solution is that some intensive observables are not self-averaging¹² namely some thermodynamic averages $\langle A \rangle$ retain a (disorder) sample dependence even in the large N limit, i.e., $\lim_{N \rightarrow \infty} (\overline{\langle A \rangle^2} - \overline{\langle A \rangle}^2) \neq 0$. Among self-averaging quantities are the internal energy, the free energy, the magnetization and the Edwards–Anderson order parameter q_{EA} . The order parameter distribution function $P_J(q)$ is an example of a nonself-averaging quantity. The general rule is that observables that do not involve correlations between different pure states are self-averaging, and those that involve such correlations are not self-averaging.

In order to show that the order parameter distribution function $P_J(q)$ is not self-averaging, one considers four clones and the probability $P_J(q_{1,2}, q_{3,4})$. Clearly, $P_J(q_{1,2}, q_{3,4}) = P_J(q_{1,2})P_J(q_{3,4})$ since clones are noninteracting. However, we will show that

$$\overline{P_J(q_{1,2})P_J(q_{3,4})} \neq \overline{P_J(q_{1,2})} \overline{P_J(q_{3,4})}, \quad (2.48)$$

which implies that $P_J(q)$ is not self-averaging since a self-averaging $P_J(q)$ would not depend on J for a large system. The evaluation of $\overline{P_J(q_{1,2}, q_{3,4})}$ is done by considering moments of the distribution

$$\begin{aligned} & \int dq_{1,2} q_{1,2}^r \int dq_{3,4} q_{3,4}^s \overline{P_J(q_{1,2})P_J(q_{3,4})} = \overline{q_{1,2}^r q_{3,4}^s} \\ &= \frac{1}{n(n-1)(n-2)(n-3)} \sum_{\substack{a,b,c,d \\ \text{all different}}} q_{a,b}^r q_{c,d}^s, \end{aligned} \quad (2.49)$$

with integer r and s .

We now use the very powerful property of replica equivalence, namely the observation that in Parisi solution, one has

$$\sum_b q_{a,b} \quad \text{independent of } a. \quad (2.50)$$

In order to use this property, one notes that

$$\begin{aligned} \sum_{\substack{a,b,c,d \\ \text{all different}}} q_{a,b}^r q_{c,d}^s &= \sum_{a,b} \sum_{c,d} q_{a,b}^r q_{c,d}^s - 4 \sum_{a,b,d} q_{a,b}^r q_{a,d}^s \\ &\quad + 2 \sum_{a,b} q_{a,b}^r q_{a,b}^s. \end{aligned} \quad (2.51)$$

Since the sum $\sum_{a,b,d} q_{a,b}^r q_{a,d}^s$ is unrestricted, one can write it as

¹² For a discussion of nonself-averaging in other random systems, see [\[32\]](#).

$$\sum_{a,b} q_{a,b}^r \sum_d q_{a,d}^s = \sum_{a,b} q_{a,b}^r \frac{1}{n} \sum_{c,d} q_{c,d}^s . \quad (2.52)$$

In the $n \rightarrow 0$ limit, one obtains

$$\overline{\langle q_{1,2}^r q_{3,4}^s \rangle} = \frac{1}{3} \overline{\langle q_{1,2}^{r+s} \rangle} + \frac{2}{3} \overline{\langle q_{1,2}^r \rangle} \overline{\langle q_{3,4}^s \rangle} , \quad (2.53)$$

$$\overline{P_J(q_{1,2}) P_J(q_{3,4})} = \frac{1}{3} \overline{P_J(q_{1,2}) \delta(q_{1,2} - q_{3,4})} + \frac{2}{3} \overline{P_J(q_{1,2})} \overline{P_J(q_{3,4})} , \quad (2.54)$$

in agreement with (2.48). It is interesting that the above relation can be proved rigorously [33] (the proof given in this paper is for the $r = s = 2$ case).

The method used by Parisi to solve the Sherrington–Kirkpatrick model is far from mathematical rigor, to say the less, and it took time to convince the skeptics that it does give the correct result. Very recently, however, beautifully rigorous results have been obtained. One is a rigorous proof [34] that the free energy density of the Sherrington–Kirkpatrick model has a well-defined limit as $N \rightarrow \infty$, a long awaited result that is far from trivial for a disordered model with infinite connectivity. Then the method was extended to show that the free energy of the Parisi solution is a lower bound on the free energy of the model [35], and finally to prove that it is equal to the free energy of the model [36]. More recently, a proof appeared that the AT line is indeed the boundary of the paramagnetic replica symmetric region [37].

2.2.4 Critical Exponents

At zero magnetic field, the transition at T_c is of second order, and one can define critical exponents. The order parameter is the mean overlap $\overline{\langle q \rangle}$, and one has

$$\begin{aligned} \overline{\langle q \rangle} &\propto (T_c - T)^\beta & T < T_c & \quad \text{with} \quad \beta = 1 , \\ &= 0 & T > T_c , \\ \chi_{\text{SG}} &= N \overline{\langle q^2 \rangle} , \\ &\propto (T_c - T)^{-\gamma} & T > T_c & \quad \text{with} \quad \gamma = 1 , \\ &= \infty & T < T_c . \end{aligned} \quad (2.55)$$

The values of the critical exponents are $\alpha = -1$ (the specific heat has a cusp at the critical temperature), $\beta = 1$, $\eta = 0$ (the mean field value), $\gamma = 1$, and $\nu = 1/2$. Hyperscaling holds, provided one uses the value $d = 6$ of the space dimension in the formula. This is related to the fact that $d = 6$ is the upper critical dimension of the replica field theory.

2.2.5 The Truncated Model

We have seen that for $H = 0$, the high T solution has $q_{a,b} = 0 \forall a, b$. It is accordingly natural to expand \mathcal{A} in powers of $q_{a,b}$ in (2.16). Only the terms up to the order four are usually kept, as one can show that this gives the correct critical behavior and the correct qualitative description of the low T phase. This truncated model has been very useful historically. It is also quite useful in order to study finite-size effects (see Sect. 2.4.1).

The trace over the spins is straightforward. For a given replica index, the trace is equal to zero for an odd power of the replicated spins and two for an even power. Neglecting powers of $q_{a,b}$ higher than four, one obtains the truncated model (written for $H = 0$):

$$\beta f_N = -\ln 2 - \frac{\beta^2}{4} - \lim_{n \rightarrow 0} \frac{1}{nN} \ln \int \left[\prod_{a < b} \sqrt{\frac{N}{2\pi\beta^2}} d\tilde{q}_{ab} \right] \exp(-N\beta\mathcal{L}[\tilde{q}]) , \quad (2.56)$$

$$\begin{aligned} \beta\mathcal{L}[\tilde{q}] = & \frac{\tau}{2} \sum_{a,b} \tilde{q}_{a,b}^2 - \frac{1}{6} \sum_{a,b,c} \tilde{q}_{a,b} \tilde{q}_{b,c} \tilde{q}_{c,a} \\ & - \frac{1}{8} \sum_{a,b,c,d} \tilde{q}_{a,b} \tilde{q}_{b,c} \tilde{q}_{c,d} \tilde{q}_{d,a} + \frac{1}{4} \sum_{a,b,c} \tilde{q}_{a,b}^2 \tilde{q}_{a,c}^2 - \frac{1}{12} \sum_{a,b} \tilde{q}_{a,b}^4 + \dots , \end{aligned} \quad (2.57)$$

where $\tau = (T^2 - 1)/2$. We use the notation $\tilde{q} = q\beta^2 = q/T^2$ in order to simplify the formula, and write unrestricted sums over the replica indexes, considering $\{q_{a,b}\}$ as a symmetric matrix with zero elements on the diagonal. For $T > T_c$, $\tau > 0$ and the paramagnetic solution is stable, as it should.

A further simplification, that leads to simpler analytical computations, has been proposed by Parisi in one of his seminal articles [26]. It amounts to replace (2.57) by

$$\beta\mathcal{L}[\tilde{q}] = \frac{\tau}{2} \sum_{a,b} \tilde{q}_{a,b}^2 - \frac{1}{6} \sum_{a,b,c} \tilde{q}_{a,b} \tilde{q}_{b,c} \tilde{q}_{c,a} - \frac{y}{8} \sum_{a,b} \tilde{q}_{a,b}^4 , \quad (2.58)$$

keeping only the fourth-order term that is responsible for the replica symmetry breaking and using the value $y = 2/3$. This is the Parisi approximation of the truncated model, sometimes called the truncated model, sometimes the reduced model. In most cases, this approximation has only mild effects, changing the numerical value of some coefficients. In a few cases however, it gives qualitatively wrong results.

2.2.6 Some Variant of the Model

Two variants of the Sherrington–Kirkpatrick model are worth mentioning. The first is the spherical Sherrington–Kirkpatrick model, defined by the same

Hamiltonian (2.1) as the original model, but with continuous spins σ_i obeying the spherical constraint

$$\sum_i \sigma_i^2 = N. \quad (2.59)$$

It can be exactly solved [38] in the thermodynamic limit without the use of replica. It can also be solved using the replica trick, and both methods give the same results. The physics of the spherical model is however quite different from the one of the original model: It is paramagnetic for all $T \geq 0$ and $H \neq 0$ but for the region $H = 0$ and $T \leq 1$, where the RS ansatz with nonzero q_0 gives the correct solution. On the other hand, much has been learned of the dynamics of spin-glass models from analytical studies of the spherical Sherrington–Kirkpatrick model (see e.g. [19]).

The second variant is the p -spin model [39], where all combinations of p spins are coupled together, with the Hamiltonian

$$H = - \sum_{1 \leq i_1 < i_2 < \dots < i_p \leq N} J_{i_1, \dots, i_p} \sigma_{i_1} \dots \sigma_{i_p} - H \sum_{i=1}^N \sigma_i, \quad (2.60)$$

where the J_{i_1, \dots, i_p} s are quenched independent identically distributed random variables with zero mean and square deviation $\overline{J^2} = \frac{p!}{2N^{p-1}}$. The spins are Ising spins $\sigma_i = \pm 1$. The original Sherrington–Kirkpatrick model is recovered for $p = 2$. The $p \geq 3$ p -spin model has a very different physics than the Sherrington–Kirkpatrick model: In the $H = 0$ case, by decreasing the temperature from $T = \infty$, one encounters three successive phase transitions, a purely dynamical transition, then a transition to a state with one-step RSB, and finally a transition to a state with ∞ -RSB. For details, see [39, 40]. One can define a spherical p -spin model with continuous spin variables obeying the spherical constraint [41, 42]. Many analytical results have been obtained for the latter model. Some subtle qualitative differences are found however between the original and spherical p -spin models [40].

2.3 Simulations Techniques

Spin-glass simulations are very difficult since on the one hand the dynamics is very slow, and on the other hand one needs to perform the simulation for many disorder samples. Both effects are stronger as T decreases and/or N increases. The Sherrington–Kirkpatrick model is no exception. It is furthermore much harder to simulate than finite dimension spin-glass models since one needs $O(N)$ operations to update one-spin variable, and not $O(1)$. The p -spin model is even harder with $O(N^{p-1})$ operations to update a single spin. For a simulation of the $p = 3$ p -spin model, see [43].

The best existing algorithm is called under various names, such as “Replica Monte Carlo”, “Exchange Monte Carlo” and “Parallel Tempering” [44]. This

algorithm is well known and consists in simulating n_{PT} clones of the system in parallel at temperatures $T_1 < T_2 < \dots < T_{n_{\text{PT}}}$ respectively. Two kinds of Monte Carlo moves are performed:

- Step 1 (the parallel Metropolis step): Metropolis update of each clone independently.
- Step 2 (the exchange step): Conditionally exchange of the spin configurations of all pairs of clones, with a suitable acceptance probability.

In both steps, the acceptance probability is the usual Metropolis acceptance probability. If π_x is the Boltzmann weight of state x , with energy E_x , namely $\pi_x = \exp(-E_x/T) / \sum_y \exp(-E_y/T)$, and $p_{x,y}$ the probability to go from state x at time t to state y at time $t+1$, one desires to fulfill the condition

$$\sum_x \pi_x p_{x,y} = \pi_y. \quad (2.61)$$

This condition is called balance (stationarity in the mathematical literature). Together with ergodicity (irreducibility in the mathematical literature) and the more technical condition of aperiodicity, this ensures that the Markov chains converge toward the Boltzmann distribution [45, 46, 47].

Balance is done by requiring that the probability to propose the move $p_{x,y}^{(0)}$ and the probability to accept it $a_{x,y}$ satisfy¹³ (one has clearly $p_{x,y} = p_{x,y}^{(0)} a_{x,y}$)

$$\frac{p_{x,y}^{(0)} a_{x,y}}{p_{y,x}^{(0)} a_{y,x}} = \min\{1, \exp[-(1/T)(E_x - E_y)]\}. \quad (2.62)$$

A common misconception is that after the exchange step the system is not at equilibrium, and that this introduces a bias that one may minimize by making many parallel Metropolis steps (Step 1) between each exchange step. This is not correct, balance is enough to ensure convergence toward the Boltzmann weight.

There is a considerable freedom in implementing this algorithm. The parallel Metropolis step is usually done by updating all spins, either systematically (all spins are updated one after the other) or randomly (choose one spin at random, then update it, then choose another, ...). The exchange step is usually restricted to the $n_{\text{PT}} - 1$ pairs of clones with neighboring temperatures (the acceptance rate of this exchange is higher), and can be done systematically (update the pair at temperatures T_1 and T_2 , then the pair at temperatures T_2 and T_3 , ...) or randomly. Step 2 clearly takes no time as compared to Step 1. One usually alternates the two steps, one parallel tempering step (PT step) consists accordingly of one parallel Metropolis step followed by one exchange step.

The choice of the sequence $T_1 < T_2 < \dots < T_{n_{\text{PT}}}$ leads also to considerable freedom. One constraint is that the acceptance rate of the chain

¹³ I consider the general case $p_{x,y}^{(0)} \neq p_{y,x}^{(0)}$, even if the equality usually holds.

exchange (chain of energy E at temperature T with chain of energy E' at temperature T')

$$\begin{aligned} \frac{a_{T,T'}}{a_{T',T}} &= \min\{1, \exp[-(E/T' + E'/T)] / \exp[-(E/T + E'/T')]\} \\ &= \min\{1 - \exp[-(E - E')(1/T - 1/T')]\} , \end{aligned} \quad (2.63)$$

should not be too small. The acceptance rate is thus governed by the combination $(T' - T)^2 dE/dT$, with $dE_N/dT = N de_N(T)/dT = N c_N(T)$, where $c_N(T)$ is the specific heat per spin, which is regular for all temperatures (and weakly N dependent) in the Sherrington–Kirkpatrick model. One may [48] adjust for every system size N the number n_{PT} and the values of the temperature of the clones in such a way that $(T_{i+1} - T_i)^2 N c_N(T)$, $i = 1, 2, \dots, n_{PT} - 1$ is roughly independent of i and N . There is however no guarantee that this choice is optimal, for example that it minimizes the statistical errors. A more satisfactory prescription is to maximize the number of tunnelings, namely the number of times a given clone goes from the minimal temperature to the maximal temperature (or the other way), as proposed recently in [49].

2.3.1 An Example of Monte Carlo Simulation

In what follows, I will use data generated in collaboration with Enzo Marinari [5] for $H = 0$ (with $N=64-4096$, $T \in [0.4, 1.325]$) and Barbara Coluzzi [51] for $H \neq 0$ (for N up to 3200). For the purpose of these notes, I performed additional small simulations in order to measure the number of tunnelings as a function of N . I considered $N = 64, 256$, and 1024. The temperatures of the clones are equidistant with $T = 0.4, 0.425, 0.45, \dots, 1.325$ (here $n_{PT} = 38$), with 128 disorder samples (16 for $N = 1024$), performing 400000 PT steps, starting from very well-equilibrated configurations.

As shown in Fig. 2.4, the number of tunnelings is dramatically decreasing as N grows. Figure 2.4 gives another indicator of the algorithm behavior: the spread of the distribution of times spent by a given chain at each temperature. With infinite statistics, each chain should spend the same amount of time at each temperature. I have measured for each disorder sample the maximal (pop-max) and minimal (pop-min) time spent (in unit of PT steps) by each chain at each temperature. The average time (pop-avg) is equal to $400\,000/n_{PT} = 10526$. These numbers are plotted in Fig. 2.4 as a function of N . The situation is clearly degrading as N grows. Analyzing the $N = 4096$ data of [5] (the results of a massive numerical effort, with 520 000 PT steps and $\Delta T = 0.0125$), one finds pop-min as low as 16.5.

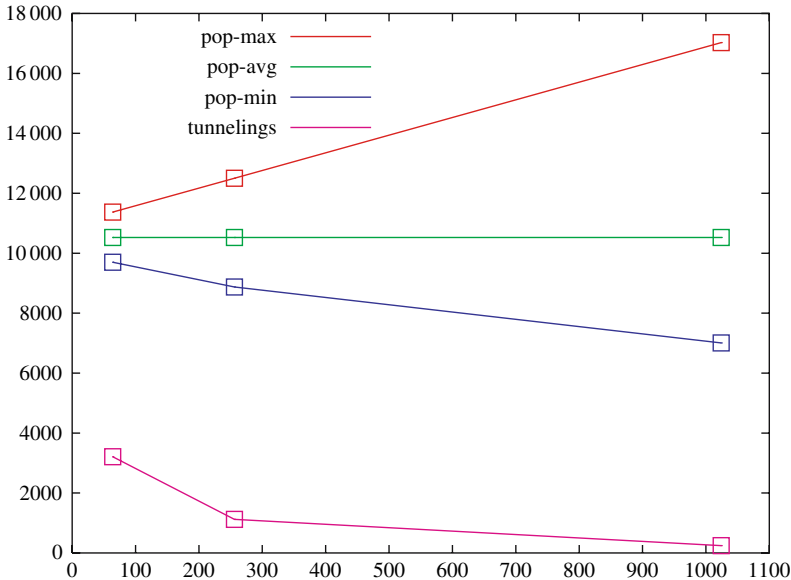


Fig. 2.4. From *top to bottom*: maximal (pop-max), average (pop-avg) and minimal (pop-min) times spent by a clone at a given temperature as a function of the number of sites. Lines have been drawn between the points to guide the eyes. The line in the bottom is the average number of tunnelings

2.3.2 Comparison with Theoretical Expectations

Figure 2.5 shows $P_J(q)$ for eight different disorder realizations, using the data of [5]. Here $N = 4096$ and $T = 0.4$, a pair of values that is at the borderline of what can be done with current algorithms and computer resources. We are well inside the spin-glass phase, and the number of spins is equal to the number of spins of a 16^3 lattice.¹⁴ These eight samples are just the eight first samples generated by our computer program, they have not been selected afterward. One sees clearly that the shape of $P_J(q)$ is strongly fluctuating from sample to sample. In view of (2.36), this is very suggestive of the existence of several (disorder dependent) pure states. The two extreme peaks correspond to the self-overlap q_{EA} (which is the same for all pure states), the other peaks correspond to cross overlaps. If the shape of $P_J(q)$ is strongly fluctuating, the position of the outmost peak is not, in agreement with the prediction that q_{EA} is self-averaging. One notes finally that the curves are reasonably symmetric, this is a very strong sign that the Monte Carlo statistics is sufficient.

The nonself-averaging of $P_J(q)$ makes the measurement of the disorder averaged $P(q)$ quite difficult on large lattices. This is exemplified in Fig. 2.6.

¹⁴ This is to say that it is a large system, by current spin-glass standards.

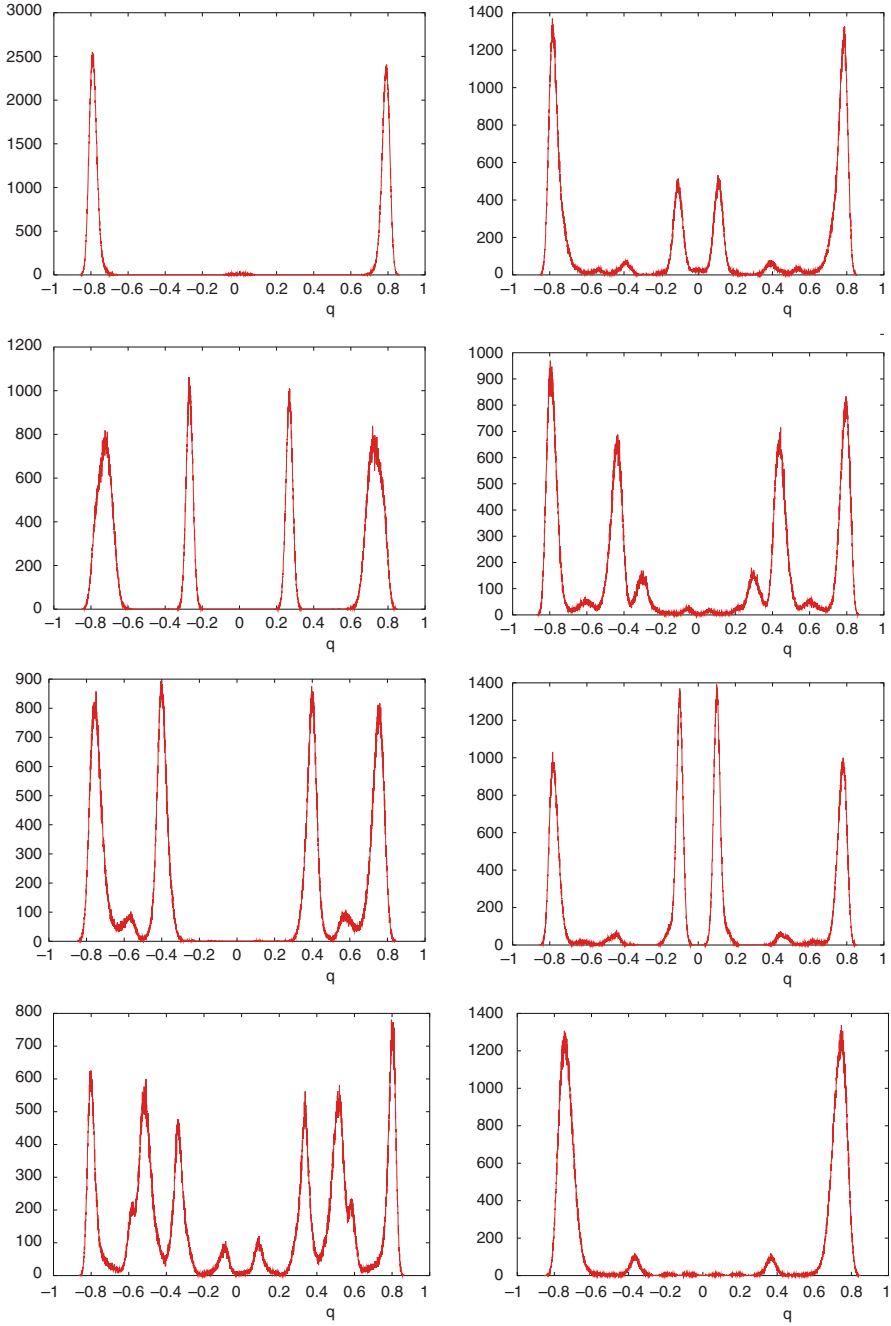


Fig. 2.5. $P_J(q)$ for eight different disorder realization. Here $N = 4096$ and $T = 0.4$

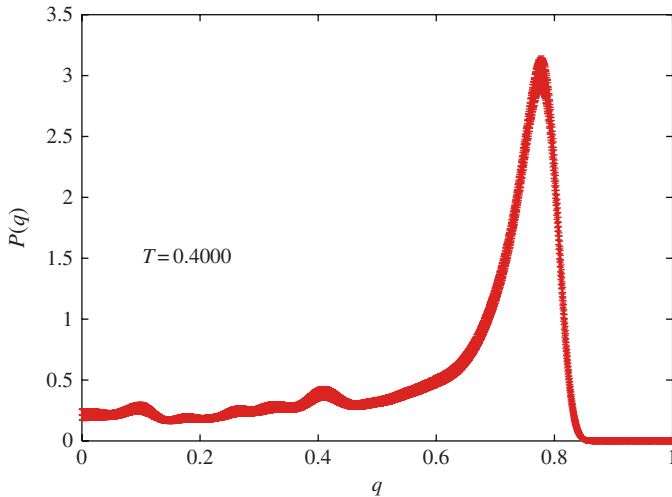


Fig. 2.6. The disorder averaged $P(q)$ for $q > 0$ and zero magnetic field. Here $N = 4096$ and $T = 0.4$. The wiggles are a fluctuation due to the finite number ($= 256$) of disorder samples. For this value of T , the infinite-volume limit of q_{EA} is [50] $q_{\text{EA}} = 0.759$

which presents our estimate of this average with all 256 disorder samples. The wiggles are artifacts due to the finite number of samples.

The Parisi solution has the quite unusual prediction that the low-temperature phase extends to nonzero H (up to the AT line). This prediction is unfortunately hard to check numerically, as can be seen in Fig. 2.7 from [51]. Even the very existence of a peak at q_{min} is not clear from the data. In order to see this peak unambiguously, one would need to satisfy two conflicting constraints, H should not be too small since the weight of the peak goes to zero as $H \rightarrow 0$. It should also not be too close to the AT line since $q_{\text{min}} \rightarrow q_{\text{max}}$ in this limit. Clearly, much larger systems would be needed in order to see a clear distinct peak at q_{min} .

A classical method to locate the critical point from numerical data uses the Binder parameter (the Kurtosis of the order parameter distribution function). For the Sherrington–Kirkpatrick model, this is

$$B_N(H, T) = \frac{1}{2} \left(3 - \frac{\overline{\langle (q - \langle q \rangle)^4 \rangle}}{\overline{\langle (q - \langle q \rangle)^2 \rangle}^2} \right). \quad (2.64)$$

Here $B(H, T)$ is defined¹⁵ in such a way that it is zero if $P_J(q)$ is Gaussian (namely at high enough temperature) and one for a two equal weight delta

¹⁵ When $H = 0$, $\langle q \rangle = 0$, and the formula simplifies substantially.

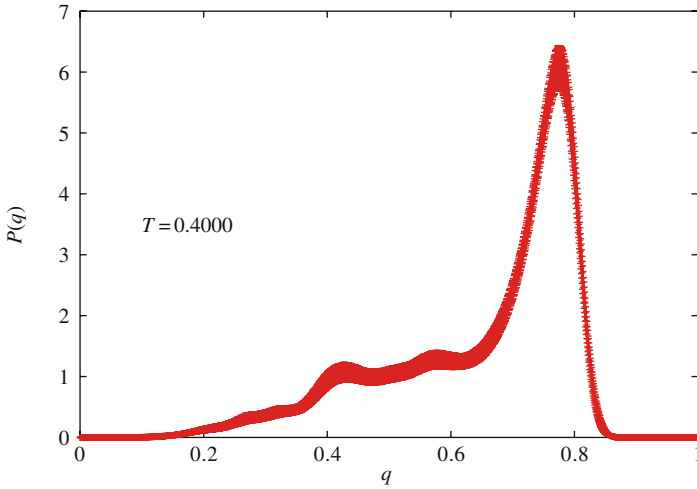


Fig. 2.7. The disorder averaged $P(q)$ for $q > 0$ at nonzero $H = 0.3$. Here $N = 3200$ and $T = 0.4$. For these values of H and T , the infinite-volume limits of q_{EA} and q_{min} are [50] $q_{\text{EA}} = 0.759$ and $q_{\text{min}} \approx 0.44$. The self-overlap q_{EA} is nearly H independent at fixed T . This is a consequence of the so-called Parisi–Toulouse hypothesis

functions distribution. In finite dimension, we know from finite-size scaling that $B_N(H, T)$ is a function of $(T - T_c(H))L^{1/\nu} = (T - T_c(H))N^{1/(\nu d)}$, and accordingly the curves for $B_N(H, T)$ drawn for different values of N should all cross at the critical point $T_c(H)$. This provides a very convenient numerical method to determine a critical point. In the Sherrington–Kirkpatrick model, finite-size scaling holds with $d = 6$ and $\nu = 1/2$ (see Sect. 2.2.4). The Binder parameter method to locate T_c works nicely at zero magnetic field, the curves for different values of N decrease monotonously as a function of T , are well separated away from T_c and cross nicely at T_c . This is not the case at nonzero magnetic field [51], at least with system sizes one can currently simulate.

It is fair to admit that, from a numerical perspective, the AT line remains elusive. This is not a problem in the Sherrington–Kirkpatrick model case since there is no doubt about the existence and exact location of this transition line. It becomes annoying, however, if one has the EAI case in mind.

I will close this section by mentioning that there are some numerical evidences for ultrametricity, in the sense that triplets of typical spin configurations (with the same disorder configuration) $\{\sigma_i^{(1)}\}, \{\sigma_i^{(2)}\}, \{\sigma_i^{(3)}\}$ do fulfill [52] the ultrametric constraint. There is, however, no numerical evidence [53] for the full treelike structure of states, as predicted by Parisi solution.

2.4 Finite-Size Effects for the Free Energy and the Internal Energy

Numerical simulations are obviously limited to finite systems, and simulations of spin glasses are indeed limited to very small systems. A detailed understanding of finite-size effects in spin-glass models is accordingly highly desirable. In what follows, I will only consider the free energy and the internal energy at zero magnetic field. I define the exponents μ and ω according to the equations

$$\begin{aligned} f_N(T) &= f(T) + B(T)N^{-\mu} + \dots \\ e_N(T) &= e(T) + C(T)N^{-\omega} + \dots, \end{aligned} \quad (2.65)$$

where $f(T)$ and $e(T)$ are the infinite-volume free energy and internal energy at temperature T .

2.4.1 Paramagnetic Phase

In the high-temperature phase, the finite-size effects for the internal energy and free energy can be obtained from the truncated model of (2.56) and (2.57). At first order, one keeps only the quadratic term in $\mathcal{L}[\tilde{q}]$, with the result

$$\begin{aligned} \beta f_N(T) &= -\ln 2 - \frac{\beta^2}{4} - \lim_{n \rightarrow 0} \frac{1}{nN} \ln \int \left[\prod_{a < b} \sqrt{\frac{N}{2\pi\beta^2}} d\tilde{q}_{ab} \right] \exp \left(-N\tau \sum_{a < b} q_{a,b}^2 \right) \\ &= -\ln 2 - \frac{\beta^2}{4} - \lim_{n \rightarrow 0} \frac{1}{nN} \ln \left[\prod_{a < b} \sqrt{\frac{1}{2\tau\beta^2}} \right] \end{aligned} \quad (2.66)$$

$$= -\ln 2 - \frac{\beta^2}{4} - \frac{1}{4N} \ln 2\tau\beta^2. \quad (2.67)$$

The neglected terms in $\mathcal{L}[\tilde{q}]$ can be included by expanding the exponent as a power series [54, 55, 56]. Each term is represented by a graph without external leg. Each line gives a factor $1/(N\tau)$, and each vertex a factor N . Introducing the number of lines $\#L$, of vertices $\#V$ and loops $\#B$ of a given graph, one finds that the graph behaves like $N^{\#V-1}(N\tau)^{-\#L} = N^{-\#B}\tau^{-\#L}$. Organizing the expansion as a loop expansion, one obtains an expansion in powers of $1/N$, with the most singular term (as $\tau \rightarrow 0$) at each order, given by the contribution of the cubic term in \mathcal{L} (for which $\#L = 3(\#B - 1)$). The development up to the $O(1/N^4)$ order (four loops) has been obtained in [54] (the terms of order $1/N^4$ are not given in the paper, but have been used in the resummation at T_c). Results up to five loops for arbitrary n but omitting the quartic terms in \mathcal{L} can be found in [56].

The internal energy is simply obtained through the equation

$$e_N(T) = \frac{d}{d\beta} f_N(T) \quad (2.68)$$

that holds also at finite N .

As one approaches the critical point, both expansions for $f_N(T)$ and $e_N(T)$ become singular, and need to be resummed. Writing symbolically the N -dependent part of $f_N(T \approx T_c)$ as

$$\begin{aligned} & - \lim_{n \rightarrow 0} \frac{1}{nN} \ln \int \left[\prod_{a < b} \sqrt{\frac{N}{2\pi}} d\tilde{q}_{ab} \right] \exp(-N(\tau Q^2 + Q^3 + Q^4)) \\ &= - \lim_{n \rightarrow 0} \frac{1}{nN} \ln \int \left[\prod_{a < b} \sqrt{\frac{(xN)^{1/3}}{2\pi}} d\tilde{q}_{ab} \right] \\ & \quad \times \exp(-(Q^2 + x^{1/2}Q^3 + x^{2/3}/N^{1/3}Q^4)), \end{aligned} \quad (2.69)$$

where $x = 1/(N\tau^3)$, we obtain the N -dependent part of $f_N(T_c)$ as the $x \rightarrow \infty$ limit of

$$\begin{aligned} & \frac{\ln N}{12N} - \frac{1}{N} \lim_{n \rightarrow 0} \frac{1}{n} \ln \int \left[\prod_{a < b} \sqrt{\frac{x^{1/3}}{2\pi}} d\tilde{q}_{ab} \right] \\ & \quad \times \exp(-(Q^2 + x^{1/2}Q^3 + x^{2/3}/N^{1/3}Q^4)). \end{aligned}$$

Treating the order four term as a perturbation, one obtains finally

$$f_N(T_c) = -\ln 2 - 1/4 + \frac{\ln N}{12N} + \frac{f_{(-1)}}{N} + \frac{f_{(-4/3)}}{N^{4/3}} + \dots, \quad (2.70)$$

$$e_N(T_c) = -\frac{1}{2} + \frac{e_{(-2/3)}}{N^{2/3}} + O(N^{-1}). \quad (2.71)$$

The behavior of the internal energy is the one expected from scaling. At a critical point, the singular part of the internal energy for a L^d system behaves¹⁶ like $L^{1/\nu-d}$. Using the values $\nu = 1/2$ and $d = 6$ (see Sect. 2.2.4), one finds that the singular part of internal energy does behave like $N^{-2/3}$. In order to obtain the values of the coefficients $f_{(-1)}$ and $e_{(-2/3)}$, one needs to handle the theory in the strong coupling $x \rightarrow \infty$ regime. This is not easy, and these values are poorly determined [54].

2.4.2 Zero Temperature

With the discovery of very efficient algorithms for determining the ground state of a spin-glass finite system (at fixed \mathcal{J}), the physics of zero temperature spin glass has blossomed in the recent years. This includes detailed

¹⁶ This follows from the scaling expression $f = 1/L^d \tilde{F}((T - T_c)L^{1/\nu})$.

studies of the finite-size effects of the internal energy. In the specific case of the Sherrington–Kirkpatrick model, good evidences have been obtained for a $1/N^{2/3}$ behavior for the internal energy for both Gaussian and binary disorder distributions [57, 58, 59, 60, 61, 62], as summarized in Table 2.1. The value $\omega = 2/3$ is exact for the spherical Sherrington–Kirkpatrick model [63].

2.4.3 Using the Guerra and Toninelli Formalism

As shown in [64], one can use the so-called Guerra and Toninelli interpolation formalism, an ingredient in the proof [34] that the free density energy of the Sherrington–Kirkpatrick model converges in the infinite-volume limit $N \rightarrow \infty$, as the basis of a powerful numerical method to compute the finite-size corrections to the free energy of the model. Guerra and Toninelli introduced the partition function

$$\begin{aligned} Z_N(t) = \sum_{\{\sigma\}} \exp & \left(\beta \left(\sqrt{\frac{t}{N}} \sum_{1 \leq i < j \leq N} J_{ij} \sigma_i \sigma_j \right. \right. \\ & + \sqrt{\frac{1-t}{N/2}} \sum_{1 \leq i < j \leq N/2} J'_{ij} \sigma_i \sigma_j \\ & \left. \left. + \sqrt{\frac{1-t}{N/2}} \sum_{N/2 < i < j \leq N} J''_{ij} \sigma_i \sigma_j \right) \right) \exp \left(\beta H \sum_i \sigma_i \right) \quad (2.72) \end{aligned}$$

that involves a parameter t that interpolates between the Sherrington–Kirkpatrick model with N sites ($t = 1$) and a system of two uncoupled Sherrington–Kirkpatrick models with $N/2$ sites ($t = 0$). The $J_{i,j}$ s, $J'_{i,j}$ s and $J''_{i,j}$ s are independent identically distributed Gaussian random numbers. It is straightforward to show that

$$\begin{aligned} \beta(f_N(T) - f_{N/2}(T)) &= \frac{\beta^2}{4} \int_0^1 dt \left\langle \left(q_{12} \right)^2 - \frac{1}{2} \left(q_{12}^{(1)} \right)^2 - \frac{1}{2} \left(q_{12}^{(2)} \right)^2 \right\rangle \\ &= \frac{\beta^2}{4} \int_0^1 dt \mathcal{D}(t) \quad \mathcal{D}(t) \leq 0, \quad (2.73) \end{aligned}$$

Table 2.1. Numerical estimates for the exponent ω at $T = 0$ for the Sherrington–Kirkpatrick model: reference, disorder distribution, maximum system size and result

	$P(\mathcal{J})$	N_{\max}	ω
Palassini [58]	Gaussian	199	0.673 ± 0.002
Bouchaud et al. [59]	± 1	300	0.66 ± 0.02
Boettcher [60]	± 1	1023	0.672 ± 0.005
Katzgraber et al. [61]	Gaussian	192	0.64 ± 0.01
Pál [62]	both	2048	$\approx 2/3$

where

$$\begin{aligned} q_{12} &= \frac{1}{N} \sum_{i=1}^N \sigma_i \tau_i, & q_{12}^{(1)} &= \frac{2}{N} \sum_{i=1}^{N/2} \sigma_i \tau_i, \\ q_{12}^{(2)} &= \frac{2}{N} \sum_{i=N/2+1}^N \sigma_i \tau_i. \end{aligned} \quad (2.74)$$

In the above formulas, the σ_i s and τ_i s are the spins of two real replica, q_{12} is the usual overlap, for the N sites system, $q_{12}^{(1)}$ and $q_{12}^{(2)}$ are the overlaps restricted to the two subsystems with $N/2$ sites. The right-hand side of (2.73) can be evaluated with Monte Carlo simulation. I use the Parallel Tempering algorithm, with $T \in [0.4, 1.3]$ and uniform $\Delta T = 0.025$. A total of 2×10^5 sweeps of the algorithm were used for every disorder sample. The quenched couplings have a binary distribution in order to speed up the computer program. Using the cumulant expansion (2.7), one can show that in the paramagnetic phase, the replacement of Gaussian couplings by binary couplings induces a leading $1/N$ correction to the free energy density of the same order as the leading finite-size correction (see below). One can argue that the effect of the binary couplings is also $1/N$ in the spin-glass phase and is thus negligible with respect to the leading $1/N^{2/3}$ finite-size correction: In the spin-glass phase, the leading finite-size correction is the same for the binary and Gaussian couplings. Systems of sizes N from 128 to 1024 have been simulated with 128 disorder samples for each system size (but for $N = 1024$, where I used 196 samples). The integration over t was done with the trapezoidal rule, with 39 nonuniformly spaced points¹⁷. Integrating with only half of the points makes a very small effect on the integrand (smaller than the estimated statistical error). The data presented at T_c (Figs. 2.9 and 2.12) include the results of an additional simulation of a system with $N = 2048$ sites, limited to the paramagnetic phase, with $T \in [1.0, 1.3]$, $\Delta T = 0.025$, with 128 disorder samples and a 15-point discretization of t .

In the low T phase, a remarkable scaling is observed if one plots the ratio $\mathcal{D}(t)/\mathcal{D}(t=0)$ as a function of $tN^{2/3}$, as shown in Fig. 2.8. It means that to a good approximation, one has $\mathcal{D}(t)/\mathcal{D}(0) = F(tN^{2/3})$, with the function $F(x)$ decaying faster than $1/x$ for large x , making the integral in (2.73) converge. One has accordingly in the low T phase $f_N - f_\infty \propto 1/N^{2/3}$.

The situation is different at T_c , as shown in Fig. 2.9, the ratio $\mathcal{D}(t)/\mathcal{D}(t=0)$ scales with a different exponent, namely like $F(tN^{1/3})$, with a large x behavior compatible¹⁸ with $F(x) \propto 1/x$, then

¹⁷ With a distribution adapted to the shape of $\mathcal{D}(t)$, that is, peaked at low t .

¹⁸ Admittedly, much larger system sizes would be needed in order to be sure that the system really obeys this asymptotic behavior.

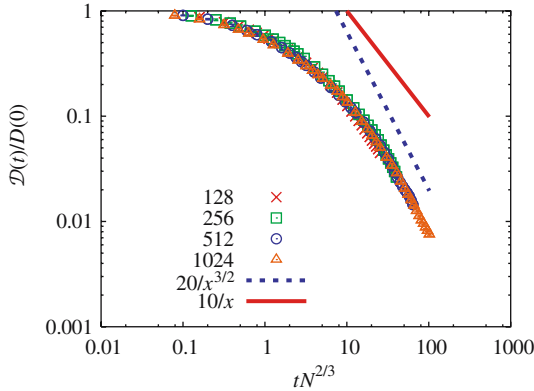


Fig. 2.8. $\mathcal{D}(t)/\mathcal{D}(0)$ as a function of $tN^{2/3}$ (both in logarithmic scale), for $T = 0.6$. The *full line* shows the $1/x$ behavior, the *dotted line* shows the $1/x^{3/2}$ behavior. Clearly $\mathcal{D}(t)$ decreases faster than $1/x$ for large x . The precise behavior of $\mathcal{D}(t)$ is not essential for my argument, as soon as $\mathcal{D}(t)$ decays faster than $1/x$

$$\begin{aligned} f_N(T) - f_{N/2}(T) &\propto \int_0^1 dt \mathcal{D}(t) = \mathcal{D}(0) \int_0^1 dt F(tN^{1/3}) \\ &\propto (1/N) \ln(N/N_0), \end{aligned} \quad (2.75)$$

for some undetermined N_0 . Use has been made of the fact that according to finite-size scaling, $\mathcal{D}(0) = -1/2 \left\langle \left(q_{1,2}^{(1)} \right)^2 \right\rangle = -1/2 \left\langle \left(q_{1,2}^{(2)} \right)^2 \right\rangle$ scales like $N^{2\beta/(d\nu)} \tilde{G}((T - T_c) N^{1/(d\nu)})$, with a finite nonzero $\lim_{x \rightarrow 0} \tilde{G}(x)$ and that

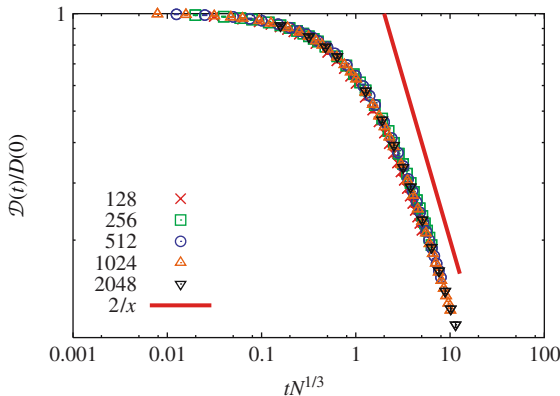


Fig. 2.9. $\mathcal{D}(t)/\mathcal{D}(0)$ as a function of $tN^{1/3}$ (both in logarithmic scale), for $T = T_c$. The *straight line* shows the expected $1/x$ behavior, in order to guide the eyes

$\beta/(d\nu) = 2/3$ (see Sect. 2.2.4). This behavior of $f_N(T) - f_{N/2}(T)$ is in agreement¹⁹ with (2.70).

Figure 2.10 shows, as a function of $1/N^{2/3}$, my estimate at $T = 0.4$ of the difference $(f_N - f_{N/2})/T$, obtained by integrating numerically (2.73), compared to the result of a linear fit $(f_N - f_{N/2})/T = -A/N^{2/3}$, with $A = 0.82 \pm 0.02$ and $\chi^2 = 4.9$. The agreement is good within estimated statistical errors. A similar agreement is obtained for other values of T in the spin-glass phase, e.g., $A = 0.39 \pm 0.01$ with $\chi^2 = 3.6$ for $T = 0.6$, and $A = 0.18 \pm 0.01$ with $\chi^2 = 33$ (a large value presumably related to the proximity of the critical point) for $T = 0.8$. The value $\omega = 2/3$ is in contradiction with the old analytical prediction of [65]. In this paper, arguments are given that relate ω to the exponent p of the first correction term in the expansion of the replicated free energy $-1/\beta \lim_{N \rightarrow \infty} 1/N \ln \overline{Z_J^n}$ in powers of n , by the equation $\omega = (p - 1)/p$. In the paramagnetic phase, it is known that there is no term in this expansion beyond the linear term, i.e., p is infinite, and thus $\omega = 1$ in agreement with the previous discussion. In the spin-glass phase Kondor [66] has found, using the truncated model of (2.56), that $p = 6$, and thus $\omega = 5/6$. The resolution of this contradiction lays presumably in the use of the Parisi approximation (2.58) in [66], and we can conjecture from our data that indeed $p = 3$.

Since the energy at zero temperature (and thus the free energy) also behaves like $1/N^{2/3}$, the most natural conclusion is that the leading finite size corrections of both $f_N(T)$ and $e_N(T)$ behave like $1/N^{2/3}$ in the whole low-temperature phase, for both binary and Gaussian distributions. This seems however to contradict the numerical results of [67]. In this paper, the

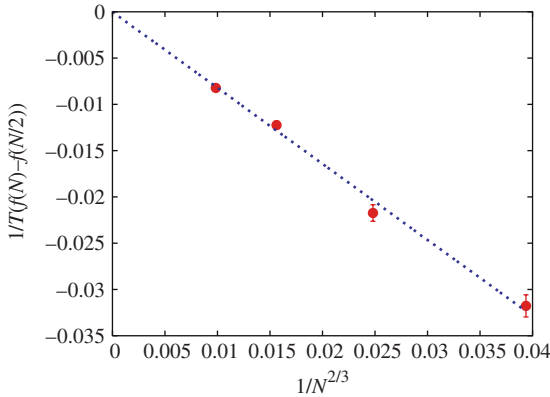


Fig. 2.10. Numerical data for $(f_N - f_{N/2})/T$ as a function of $1/N^{2/3}$, together with a numerical fit to the data of the form $(f_N - f_{N/2})/T = -A/N^{2/3}$, with $A = 0.82 \pm 0.02$ dotted line. Here $T = 0.4$, $N = 128, 256, 512$ and 1024

¹⁹ But the value of the prefactor is not predicted by my method.

internal energy of the Sherrington–Kirkpatrick model with Gaussian $P(\mathcal{J})$ has been measured with Monte Carlo simulations for values of T between $T = 0.1$ (a very low value made possible by the small sizes simulated) and $T = 1.22$, with $N = 36, 64, \dots, 196$. The data for $e_N(T)$ are fitted²⁰ as $e_N(T) = e(T) + a(T)N^{-\omega}$, with a result for ω that is compatible with $2/3$ for both $T = 0$ and $T = T_c$, but with a pronounced dip in between, in contradiction with my conjecture. Using the data for $e_N(T)$ obtained from the simulation of [5], it is quite simple to repeat the analysis of [67] for systems up to $N = 4096$ (but with binary $P(\mathcal{J})$). Figure 2.11 shows my results compared to the one of [67]. The use of larger system sizes clearly reduces the effect observed in this paper. The most likely conclusion is that the analysis of [67] is affected by systematic errors due to the small sizes used. The shape of the sub-leading corrections to the energy is not known below T_c , it is known at the critical point, however, and there the sub-leading corrections are decaying very slowly, the expansion is indeed an expansion in powers of $N^{-1/3}$, and it may not be so surprising to have difficulties finding the correct leading exponent from data with $36 \leq N \leq 196$.

Figure 2.12 shows my estimates for $(f_N - f_{N/2})/T$ at T_c as a function of $1/N$, together with the prediction of (2.70). A good agreement (with $\chi^2 = 4.3$ if one excludes the $N = 128$ data from the fit) is obtained using the value $1/N_0 = 7.8 \pm 0.2$, namely $f_{(-1)} = \ln(7.8)/12 = 0.17\dots$, within the range of results presented in [54].

The method has been extended [68] to the computation of the fluctuations of the free energy, with the result that in the spin glass phase, $\Delta^2 f_N(T) =$

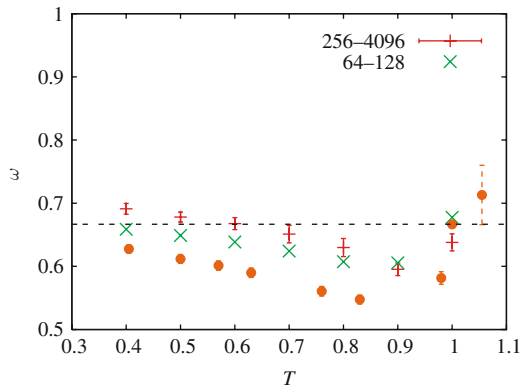


Fig. 2.11. Behavior of the finite-size exponent ω as a function of temperature for the Sherrington–Kirkpatrick model. From *top to bottom*: results of a (gnuplot) fit of the data of [5] with $4096 \geq N \geq 256$ (with estimated errors); fit of the same data with $128 \geq N \geq 64$ (without estimated errors, in order not to clutter the figure) and data from [67]

²⁰ Using the precise estimates of $e(T)$ from [29].

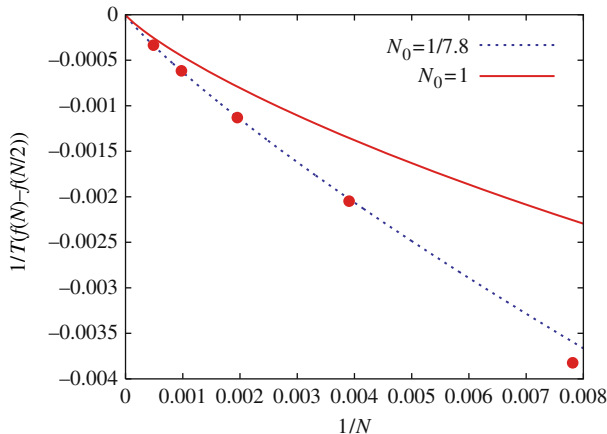


Fig. 2.12. Numerical data for $(f_N - f_{N/2})/T$ as a function of $1/N$, together with the behavior implied by the equation: $f_N/T = f_\infty/T + 1/(12N) \ln N/N_0$. The *full line* is drawn with the value $N_0 = 1$. The *dotted line* is drawn with the value $1/7.8$, from a fit to the data. Here $T = 1$, $N = 128, 256, \dots, 2048$

$\overline{f_N^2(T)} - \overline{f_N(T)}^2 \propto N^{-2\sigma}$, with $\sigma \approx 3/5$. This is definitively smaller than the value found at $T = 0$ [58, 59, 60, 61, 62], that is $\sigma \approx 3/4$.

2.5 Conclusions

The picture that emerges is the following: Above T_c the finite-size corrections of both $f_N(T)$ and $e_N(T)$ are given by series in powers of $1/N$, whose terms can be evaluated by perturbation theory. This expansion becomes singular as the critical point is approached. At the critical point, the size-dependent part of the free energy behaves like $(1/12N) \ln N/N_0$ and the size-dependent part of the internal energy as $e_{(-2/3)}/N^{2/3}$, with coefficients that are poorly determined analytically, but can be evaluated with Monte Carlo simulation. The sub-leading corrections are decaying very slowly with N . In the spin-glass phase, the data are compatible with a $1/N^{2/3}$ behavior for the leading finite size corrections of both $e_N(T)$ and $f_N(T)$.

Acknowledgements

I thank Wolfhard Janke for organizing this very pleasant CECAM workshop. My interest in the Sherrington–Kirkpatrick model stems from a continued collaboration with Enzo Marinari, whom I thank warmly. The $H \neq 0$ data have been obtained in collaboration with Barbara Coluzzi. I also thank Andrea Crisanti, Tommaso Rizzo, Helmut Katzgraber and Ian Campbell for providing

me with their numerical data. I am deeply indebted to Giorgio Parisi for many enlightening discussions.

References

1. S. F. Edwards, P. W. Anderson: J. Phys. F **5**, 965 (1975) [\[1\]](#) [\[2\]](#) [\[3\]](#)
2. D. Sherrington, S. Kirkpatrick: Phys. Rev. Lett. **35**, 1792 (1975); D. Sherrington, S. Kirkpatrick: Phys. Rev. B **17**, 4384 (1978) [\[1\]](#) [\[4\]](#) [\[2\]](#)
3. W. L. McMillan: J. Phys. C **17**, 3179 (1984); A. J. Bray, M. A. Moore: J. Phys. C **18**, L699 (1985); D. S. Fisher, D. A. Huse: Phys. Rev. B **38**, 386 (1988) [\[1\]](#)
4. T. Rizzo, A. Crisanti: Phys. Rev. Lett. **90**, 137201 (2003); T. Rizzo: J. Phys. A **34**, (2001) 5531 [\[2\]](#)
5. A. Billoire, E. Marinari: J. Phys. A **33**, L265 (2000); A. Billoire, E. Marinari: Europhys. Lett. **60**, 775 (2002) [\[2\]](#) [\[3\]](#) [\[32\]](#) [\[42\]](#)
6. D. J. Thouless, P. W. Anderson, R. G. Palmer: Phil. Mag. **35**, 593 (1977) [\[2\]](#)
7. A. Cavagna, I. Giardina, G. Parisi: Phys. Rev. Lett. **92**, 120603 (2004); T. Aspelmeier, R. A. Blythe, A. J. Bray, M. A. Moore: Phys. Rev. B **74**, 184411 (2006) [\[2\]](#)
8. A. J. Bray, M. A. Moore: J. Phys. C **13**, L469 (1980); T. Aspelmeier, A. J. Bray, M. A. Moore: Phys. Rev. Lett. **92**, 087203 (2004); G. Parisi: Lecture notes, Les Houches summer school (2005), preprint [cond-mat/0602349](#) [\[2\]](#)
9. K. H. Fischer, J. A. Hertz: *Spin Glasses* (Cambridge University Press, Cambridge, 1991) [\[2\]](#) [\[3\]](#)
10. K. Binder, A. P. Young: Rev. Mod. Phys. **58**, 4 (1986) [\[2\]](#) [\[3\]](#)
11. M. Mézard, G. Parisi, M. Virasoro: *Spin Glass Theory and Beyond* (World Scientific, Singapore, 1987) [\[2\]](#) [\[15\]](#) [\[25\]](#)
12. T. Castellani, A. Cavagna: *Spin-glass theory for pedestrians*. In lecture notes of the school: *Unifying Concepts in Glassy Physics III*, Bangalore, June 2004, J. Stat. Mech. P05012 (2005) [\[2\]](#)
13. D. Sherrington: *Spin glasses*, preprint [cond-mat/9806289](#) [\[2\]](#)
14. C. de Dominicis, I. Giardina: *Random Fields and Spin Glasses. A Field Theory Approach* (Cambridge University Press, Cambridge, 2007) [\[2\]](#)
15. N. Kawashima, H. Rieger: Recent progress in spin glasses. In *Frustrated Spin Systems*, edited by H. T. Diep (World Scientific, Singapore, 2005) [\[2\]](#)
16. E. Marinari, G. Parisi, J. Ruiz-Lorenzo: Numerical simulations of spin-glass systems. In *Spin Glasses and Random Fields*, edited by A. P. Young (World Scientific, Singapore, 1997) [\[2\]](#)
17. E. Marinari, G. Parisi, F. Ricci-Tersenghi, J. Ruiz-Lorenzo, F. Zuliani: *Replica symmetry breaking in short-range spin glasses: a review of the theoretical foundations and of the numerical evidence*, J. Stat. Phys. **98**, 973 (2000) [\[2\]](#) [\[19\]](#)
18. J.-P. Bouchaud, L. F. Cugliandolo, J. Kurchan, M. Mézard: Out of equilibrium dynamics in spin glasses and other glassy systems. In *Spin Glasses and Random Fields*, edited by A. P. Young (World Scientific, Singapore 1997) [\[2\]](#)
19. L. F. Cugliandolo: *Dynamics of glassy systems*. In lecture notes, Les Houches Summer school, July 2002 [\[2\]](#) [\[29\]](#)
20. A. Crisanti, F. Ritort: *Violation of the fluctuation-dissipation theorem in glassy systems: basic notions and the numerical evidence*, Topical Review Paper, J. Phys. A **36**, R181 (2003) [\[2\]](#)

21. B. A. Berg, A. Billoire, W. Janke: Phys. Rev. E **66**, 046122 (2002) [14](#)
22. G. Parisi, Phys. Rev. Lett. **50**, 1946 (1983) [18](#)
23. J. R. L. de Almeida, D. J. Thouless: J. Phys. A **11**, 983 (1978) [22](#)
24. G. Parisi: Phys. Lett. A **73**, 203 (1979) [22](#)
25. G. Parisi: J. Phys. A **13**, L115 (1980) [22](#)
26. G. Parisi: J. Phys. A **13**, 1101 (1980) [22](#), [28](#)
27. G. Parisi: J. Phys. A **13**, 1887 (1980) [22](#)
28. C. de Dominicis, I. Kondor: Phys. Rev. **27**, 606 (1982) [24](#)
29. A. Crisanti, T. Rizzo: Phys. Rev. E **65**, 046137 (2002) [24](#), [25](#), [42](#)
30. A. Crisanti, T. Rizzo, T. Temesvári: Eur. Phys. J. B **33**, 203 (2003) [24](#)
31. M. M'ezard, G. Parisi, N. Sourlas, G. Toulouse and M. Virasoro: J. Phys. (France) **45**, 848 (1984) [25](#)
32. S. Wiseman, E. Domany: Phys. Rev. E **58**, 2938 (1998) [26](#)
33. F. Guerra: Int. J. Mod. Phys. B **10**, 1675 (1996) [27](#)
34. F. Guerra, F. L. Toninelli: Comm. Math. Phys. **230**, 71 (2002) [27](#), [38](#)
35. F. Guerra: Comm. Math. Phys. **233**, 1 (2003) [27](#)
36. M. Talagrand: CRAS **337**, 111 (2003); M. Talagrand: Ann. Math. **163**, 221 (2006) [27](#)
37. F. Guerra: Preprint cond-mat/0604674 [27](#)
38. J. M. Kosterlitz, D. J. Thouless, R. C. Jones: Phys. Rev. Lett. **36**, 1217 (1976) [29](#)
39. E. Gardner: Nucl. Phys. B **257**, 747 (1985) [29](#)
40. A. Montanari, F. Ricci-Tersenghi: Eur. Phys. J. B **33**, 339 (2003) [29](#)
41. A. Crisanti, H.-J. Sommers: Z. Phys. B **87**, 341 (1992) [29](#)
42. A. Crisanti, H. Horner, H.-J. Sommers: Z. Phys. B **92**, 257 (1993) [29](#)
43. A. Billoire, L. Giomi, E. Marinari: Europhys. **71**, 824 (2005) [29](#)
44. K. Hukushima, K. Nemoto: J. Phys. Soc. Jpn. **65**, 1604 (1996); M. C. Tesi, E. J. Janse van Rensburg, E. Orlandini, S. G. Whittington: J. Stat. Phys. **82**, 155 (1996); E. Marinari: *Optimized Monte Carlo methods*. In *Advances in Computer Simulation*, edited by J. Kertesz, I. Kondor (Springer-Verlag, Berlin, 1997) [29](#)
45. A. D. Sokal: *Monte Carlo methods in statistical mechanics: foundations and new algorithms*. Lectures at the Cargèse Summer School on *Functional Integration: Basics and Applications*, September 1996 [30](#)
46. J. Zinn-Justin: *Quantum Field Theory and Critical Phenomena* (Clarendon, Oxford University Press, 1996), 3rd ed. [30](#)
47. O. Narayan, A. P. Young: Phys. Rev. E **64**, 021104 (2001) [30](#)
48. W. Kerler, P. Rehberg: Phys. Rev. E **50**, 4220 (1994) [31](#)
49. H. G. Katzgraber, S. Trebst, D. A. Huse, M. Troyer: J. Stat. Mech. P03018 (2006) [31](#)
50. A. Crisanti, T. Rizzo: private communication (2003) [34](#), [35](#)
51. A. Billoire, B. Coluzzi: Phys. Rev. E **68**, 026131 (2003) [31](#), [34](#), [35](#)
52. B. N. Bhatt, A. P. Young: J. Magnetism Magnetic Mater **54**, 191 (1986) [35](#)
53. S. Ciliberti, E. Marinari: J. Stat. Phys. **115**, 557 (2004); G. Hed, A. P. Young, E. Domany: Phys. Rev. Lett. **92**, 157201 (2004) [35](#)
54. G. Parisi, F. Ritort, F. Slanina: J. Phys. A **26**, 247 (1992) [36](#), [37](#), [42](#)
55. G. Parisi, F. Ritort, F. Slanina: J. Phys. A **26**, 3775 (1993) [36](#)
56. J. Yeo, M. Moore, T. Aspelmeier: J. Phys. A **38**, 4027 (2005) [36](#)
57. M. Palassini: PhD thesis, Scuola Normale Superiore di Pisa, 2000 (unpublished) [38](#)
58. M. Palassini: Preprint cond-mat/0307713 [38](#), [43](#)
59. J.-P. Bouchaud, F. Krzakala, O. Martin: Phys. Rev. B **68**, 224404 (2003) [38](#), [43](#)

- 60. S. Boettcher: Eur. Phys. J. B **31**, 29 (2003); S. Boettcher: Eur. Phys. J. B **46**, 501 (2005) [38](#), [43](#)
- 61. H. G. Katzgraber, M. Körner, F. Liers, M. Jünger, A. K. Hartmann: Phys. Rev. B **72**, 094421 (2005) [38](#), [43](#)
- 62. K. Pál: Physica A **367**, 261 (2006) [38](#), [43](#)
- 63. A. Andreanov, F. Barbieri, O. Martin: Eur. Phys. J. B **41**, 365 (2004) [38](#)
- 64. A. Billoire: Phys. Rev. B **73**, 132201 (2006) [38](#)
- 65. A. Crisanti, G. Paladin, H.-J. Sommers, A. Vulpiani: J. Phys. I (France) **2**, 1325 (1992) [41](#)
- 66. I. Kondor: J. Phys. A **16**, L127 (1983) [41](#)
- 67. H. G. Katzgraber, I. A. Campbell: Phys. Rev. B **68**, 180402(R) (2003) [41](#), [42](#)
- 68. M. Goethe, T. Aspelmeier: Preprint `cond-mat/0610028` [42](#)

The Potts Glass Model: A Scenario for the Freezing Transition of Structural Glasses?

Kurt Binder¹, Claudio Brangian¹ and Walter Kob²

¹ Institut für Physik, Johannes Gutenberg-Universität
D-55099 Mainz, Staudinger Weg 7, Germany
kurt.binder@uni-mainz.de

² Laboratoire des Colloïdes, Verres et Nanomatériaux, UMR5587 CNRS,
Université Montpellier 2, 34095 Montpellier, France
walter.kob@lcvn.univ-montp2.fr

Abstract. The question whether there is a static phase transition underlying the freezing of a supercooled fluid into a glass, or a purely dynamical transition (such as described by the mode-coupling theory of the glass transition) is briefly reviewed. The mean-field Potts glass with $p > 4$ states provides a model where both a static and a dynamic transition occur. We describe Monte Carlo simulations which provide insight into the behavior of this model and discuss how these transitions show up in systems of finite size. By studying a 10-state Potts glass with nearest-neighbor interactions on the simple cubic lattice, evidence is obtained that even at very low temperatures only short range order due to small clusters of strongly correlated Potts spins is possible. No trace of the static and dynamic glass transition found in the mean-field limit is left. Possibilities to construct models which better describe the phenomena at the glass transition of real materials are briefly discussed.

3.1 Introduction: A Brief Survey of Experimental Facts and Theoretical Ideas on Glass Transitions

It is a “grand challenge problem” of condensed matter physics to understand by which mechanism(s) a supercooled fluid transforms into an amorphous solid, and which “order parameter” distinguishes such a glassy solid from a simple “snapshot picture” of a liquid [1, 2, 3]. It is currently still a matter of debate, whether or not there exists an underlying static phase transition from a (metastable) supercooled fluid to a (metastable) ideal glass. Evidence for the existence of such a transition stems, e.g., from the so-called entropy catastrophe [4], see Fig. 5.1. If one plots the entropy difference $\Delta S(T) = S_f - S_s$ of the supercooled fluid (f) and the crystalline solid (s), one finds that it decreases strongly with decreasing temperature T . At the glass transition temperature

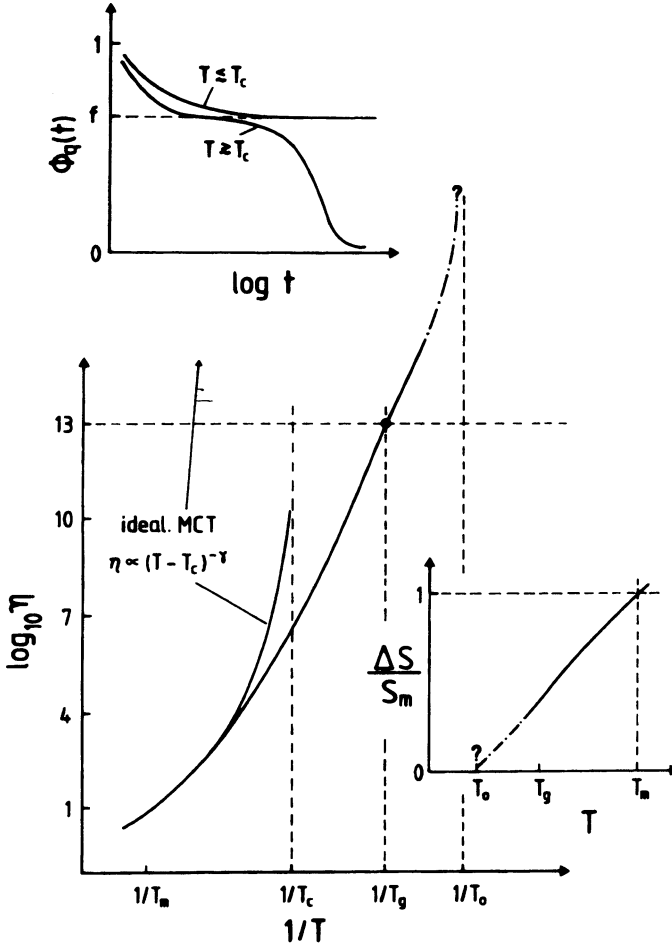


Fig. 3.1. Schematic plot of the viscosity $\eta(T)$ of the fluid as a function of inverse temperature $1/T$. The location of the melting temperature T_m , the critical temperature T_c of mode-coupling theory, the glass transition temperature T_g and the Kauzmann temperature T_0 are shown on the abscissa. The upper inset shows the time dependence of $\phi_q(t)$, the Fourier transform of correlations of density fluctuations for wave-vectors q . The lower right inset shows the entropy difference $\Delta S(T)$ in units of S_m , the entropy of fusion, plotted vs. temperature. Dash-dotted parts of the curves show hypothetical extrapolations. See text for further explanations

T_g , this difference has already decreased to about $1/3$ or even $1/4$ of its value $S_m \equiv \Delta S(T_m)$ at the melting temperature T_m . Note that T_g is empirically defined by the condition that the viscosity $\eta(T)$, which increases dramatically from small values at high temperatures ($\eta \approx 10^{-2}$ Poise) by many decades with decreasing T , has reached the value $\eta(T = T_g) = 10^{13}$ Poise. Of course,

if one assumes that the transition from the metastable supercooled fluid is associated with a divergent viscosity at a transition temperature T_{VF} with $\eta(T \rightarrow T_{\text{VF}}) \rightarrow \infty$ (and hence a divergence of the associated “structural relaxation time” τ of the fluid), such an empirical T_g will only be an *upper bound* to T_{VF} . However, since $\eta = 10^{13}$ Poise corresponds to about $\tau = 100$ s, T_g roughly corresponds to the temperature where for physically realizable cooling procedures the fluid falls out of its (metastable) equilibrium, its structure becomes frozen, and it is very difficult to experimentally measure any properties of this fluid in *metastable equilibrium* for $T < T_g$ (by “metastable”, we mean here in reference to the crystal).

It is a striking observation that a reasonable extrapolation of $\Delta S(T)$ for $T < T_g$ seems to yield a temperature T_0 , the so-called Kauzmann temperature, at which $\Delta S(T)$ actually seems to become negative [5]. This is unexpected since the ordered crystal is believed to have less entropy than the structurally disordered fluid (remember that, loosely speaking, entropy is a measure of “disorder”) and thus the vanishing of the (extrapolated) entropy $\Delta S(T)$ at $T = T_0$ is called the “Kauzmann paradox” [5]. In fact, an appropriate estimation of the configurational entropy $S_{\text{conf}}(T)$ of a lattice model for polymer melts, which can be approximated well by $\Delta S(T)$ since it is just the logarithm of the number of possible moves the system can make (apart from the vibrational motion) yields a vanishing of this entropy at a nonzero temperature T_0 [4], and extending this model to dynamics by introducing the concept of “cooperatively rearranging regions” [6] yields an estimation of the structural relaxation time $\tau(T) \propto \exp[\text{const}/(T\Delta S)]$. So if $\Delta S \propto T - T_0$, one recovers the Vogel–Fulcher law [1, 2, 3]

$$\log \eta(T) \propto \log \tau(T) \propto (T - T_{\text{VF}})^{-1} \quad (3.1)$$

with the “Vogel–Fulcher temperature” $T_{\text{VF}} = T_0$. Thus we find a close connection between the vanishing of a thermodynamic quantity (the entropy difference ΔS) and the divergence of a dynamic quantity (the viscosity η).

We emphasize that for various reasons these concepts are not generally accepted: (i) The claim that $\Delta S(T)$ cannot become negative is not generally true (actually the model of hard spheres is a simple counter example [7]); (ii) Arguments exist which show that for systems with finite interaction range the configurational entropy $S_{\text{conf}}(T > 0)$ must be nonzero and positive [8]; (iii) The approximations made for the model of [4] are actually very inaccurate and hence the vanishing of $S_{\text{conf}}(T)$ at some $T_0 > 0$ is an artifact of inappropriate approximations [9].

The “entropy theory” [4, 6] is not the only concept attributing the dramatic increase of $\eta(T)$ [or $\tau(T)$, respectively] to an underlying static phase transition. A popular alternative is to invoke the general concept of “critical slowing down” [10], attributing the growth of the relaxation time to the growth of a correlation length ξ of an appropriate glass order parameter,

$$\tau(T) \propto [\xi(T)]^z, \quad (3.2)$$

where z is a “dynamic critical exponent”. Equation (3.2) not only applies for standard second-order phase transitions [10] but also holds for “spin glasses” [11]. As is well known, spin glasses can be produced by random dilution of magnetic solids (which have competing ferro- and antiferromagnetic exchange interactions) by nonmagnetic impurities. As a result of this quenched disorder, some pairs of spins develop ferromagnetic correlations, other pairs develop antiferromagnetic ones. However, no long-range order of any conventional type can develop which is favorable for all interactions, due to this “frustration” of the interactions, the spins in the low-temperature phase get “frozen” at the “freezing temperature” T_f in some sort of random alignment. Thus, the standard spin pair correlation function $g_F(r_i - r_j) = [\langle S_i S_j \rangle]_{\text{av}}$, where $[\dots]_{\text{av}}$ stands for the averaging over the quenched disorder, i.e., the interactions between the spins, while $\langle \dots \rangle$ is the standard thermal averaging, develops at most short-range correlations. Thus, in elastic (neutron) scattering experiments, which would be the standard tool to detect magnetic orderings in solids, nothing is seen when the freezing transition is approached [11]. Nevertheless, there is a diverging correlation length $\xi_{\text{SG}}(T)$ in a spin glass, describing the decay of $g_{\text{SG}} = [\langle S_i S_j \rangle^2]_{\text{av}}$, and although the low-temperature phase of spin glasses still poses unsolved problems [12, 13], there is compelling theoretical and experimental evidence for (3.2). The large value of the exponent z is responsible for a fast increase of τ over many decades, similar to what one finds in supercooled fluids (see Fig. 3.1). Moreover, this concept can be carried over successfully to various other systems: “quadrupolar glasses” in which molecular crystals are diluted with atoms that have no electric quadrupole moment are one example [13, 14].

However, despite an intensive search for a growing correlation length $\xi_{\text{G}}(T)$ which would diverge in an supercooled fluid near the glass transition, both in experiments [15, 16] and simulations [17, 18], a clear evidence for (3.2) has not yet emerged. Although there is evidence of the presence of an increasing characteristic length scale (due to the lack of understanding which “order parameter” distinguishes the fluid from the glass, this length can only be inferred indirectly, e.g., from the range over which wall effects are felt [17]), this increase is rather weak, and there is neither evidence that this length diverges at a temperature near T_g nor that this length is the cause of the slowing down.

A more successful approach is the mode-coupling theory (MCT) of the glass transition [19, 20, 21, 22]. It is based on the concept of the so-called cage effect, i.e., the fact that in a glass-forming liquid an atom is temporarily trapped in the “cage” formed by its nearest neighbors. Within the “ideal version of MCT”, the lifetime of this cage diverges according to a power law, $\tau \propto (T/T_c - 1)^{-\gamma}$, at a critical temperature T_c , while in the “extended MCT” this divergence at T_c is rounded off, and T_c is instead only the center of a crossover region in which the temperature dependence of τ changes from power law type to Arrhenius type behavior. This cage effect shows up as a two-step relaxation of the correlation function $\phi_q(t)$ of density fluctuations

(Fig. 3.1), and is seen in experiments as well as in simulations [3, 21]. Within idealized MCT, there is a sharp (dynamical) transition at T_c from ergodic to nonergodic behavior in that the so-called nonergodicity parameter f , which is the height of the plateau in the time correlation functions (Fig. 3.1), jumps from $f = 0$ for $T > T_c$ to $f > 0$ for $T < T_c$ which implies that the density fluctuations remain frozen for $T < T_c$. Note that for generic structural glasses, this nonzero value of f appears at $T = T_c$ discontinuously.

On the other hand, the comparison with experiments and simulations shows that at T_c the actual lifetime of the plateau is still about 10 orders of magnitude smaller than at T_g , and MCT provides only scarce testable predictions in the regime $T_c \geq T \geq T_g$. While for some “fragile” glass-formers [23], T_c exceeds T_g by only 50 K, for “strong” glass-formers T_c is even in a regime that is not accessible experimentally (simulations for SiO_2 [24] show that $T_c \approx 3330$ K while $T_g = 1450$ K). Thus, at present we are still far from a complete understanding of the structural glass transition.

3.2 The p -State Potts Glass and Its Properties in the Thermodynamic Limit for Infinite-Range Interactions

The Potts glass is a generalization of the Ising spin glass, where every Ising spin can only be in two states ($\sigma_i = \pm 1$), to the case where every degree of freedom can be in one of p discrete states, $\sigma_i = 1, \dots, p$, and $i = 1, 2, \dots, N$, with $N \rightarrow \infty$.

The Hamiltonian is [25]

$$\mathcal{H} = - \sum_{i < j} J_{ij} (p \delta_{\sigma_i \sigma_j} - 1) \quad , \quad (3.3)$$

i.e., an energy pJ_{ij} is gained if a pair of spins σ_i, σ_j is in the same state. If $J_{ij} = J > 0$, we have a Potts ferromagnet [26], while drawing random J_{ij} s from a Gaussian distribution, results in the Potts glass:

$$P(J_{ij}) = [\sqrt{2\pi}(\Delta J)]^{-1} \exp\{-(J_{ij} - J_0)^2/[2(\Delta J)^2]\} \quad , \quad (3.4)$$

where ΔJ is the width of the distribution. In the infinite-range mean-field limit, every spin interacts with every other spin. To ensure a sensible thermodynamic limit, one chooses the mean interaction to be given by $J_0 = [J_{ij}]_{\text{av}} = \tilde{J}_0/(N-1)$, and the squared width by $(\Delta J)^2 \equiv [J_{ij}^2]_{\text{av}} - [J_{ij}]_{\text{av}}^2 = (\Delta \tilde{J})^2/(N-1)$. Choosing $\Delta \tilde{J} \equiv 1$ fixes the temperature scale, while the further choice $\tilde{J}_0 = 3 - p$ ensures that the model does not develop any tendency for ferromagnetic order.

For discussing the ordering of the model, it is useful to introduce the so-called simplex representation, i.e., the p states are described by $(p-1)$

dimensional vectors \mathbf{S} pointing to the corners of a p -simplex (e.g., $p = 3$: triangle; $p = 4$: tetrahedron; etc. [27]). Choosing then two “real replicas” 1, 2, i.e., two realizations of the model with identical bond configuration $\{J_{ij}\}$, the Potts spin configuration of replica 1 can be denoted by $\{\mathbf{S}_{i,1}\}$ and the one for replica 2 by $\{\mathbf{S}_{i,2}\}$. The Potts glass order parameter $q^{\mu\nu}$ is then defined as the projection of the Potts spin configurations onto one another:

$$q^{\mu\nu} = (1/N) \sum_{i=1}^N (\mathbf{S}_{i,2})^\mu (\mathbf{S}_{i,1})^\nu \quad , \quad \mu, \nu = 1, 2, \dots, p-1 \quad . \quad (3.5)$$

Because of the symmetry of the model with respect to the values of the spins, we shall only use the square root order parameter, $q \equiv \left[\frac{1}{p-1} \sum_{\mu,\nu} (q^{\mu\nu})^2 \right]^{1/2}$. For dynamic versions of the model, we shall also be interested in the spin-autocorrelation function of a single replica

$$C(t) = [N(p-1)]^{-1} \sum_{i=1}^N [\langle \mathbf{S}_i(t') \cdot \mathbf{S}_i(t' + t) \rangle]_{\text{av}} \quad . \quad (3.6)$$

The static properties of the model are then characterized by the order-parameter distribution $P(q)$ and its moments, e.g., the glass susceptibility

$$\chi_{\text{SG}} = \frac{N}{p-1} [\langle q^2 \rangle]_{\text{av}} = \frac{N}{(p-1)} \int_0^1 q^2 P(q) dq \quad . \quad (3.7)$$

While for $p = 2$, the model reduces to the Ising spin glass, which has a second-order transition at $T = T_f = 1$ where χ_{SG} diverges according to a Curie–Weiss law, $\chi_{\text{SG}} \propto 1/(1 - T_f/T)$, for $p > 4$ a very different behavior results [28, 29, 30, 31, 32, 33]: A divergence of χ_{SG} occurs only at a kind of spinodal temperature T_s , which is a stability limit of the metastable disordered phase, while glass order sets in (discontinuously) with an order parameter q_0 at a temperature T_0 , (Fig. 3.2). From a one-step replica symmetry breaking approach [28, 29, 30, 31, 32, 33] one can show that for $T < T_0$ the order-parameter distribution $P(q)$ has two-delta peaks,

$$P(q) = (T/T_0)\delta(q) + (1 - T/T_0)\delta(q - q_0), \quad T \rightarrow T_0 \quad . \quad (3.8)$$

Since near T_0 the moments $\langle q^k \rangle$ vanish continuously, $\langle q^k \rangle = (1 - T/T_0)q_0^k$, the transition is not a first-order transition in the usual sense (there is also no latent heat, the entropy has a kink at T_0). If one would extrapolate the entropy of the disordered phase, $S(T) = \ln p - (p-1)T^{-2}/4$, to temperatures below T_0 , one would find a “Kauzmann temperature” T_K where $S(T)$ vanishes (Fig. 3.2), but this does not have any physical significance whatsoever.

Very interesting is also the dynamic behavior of the model: While for $p \leq 4$, the relaxation time $\tau \equiv \int_0^\infty C(t) dt$ diverges as $T \rightarrow T_f$, i.e., one finds a standard

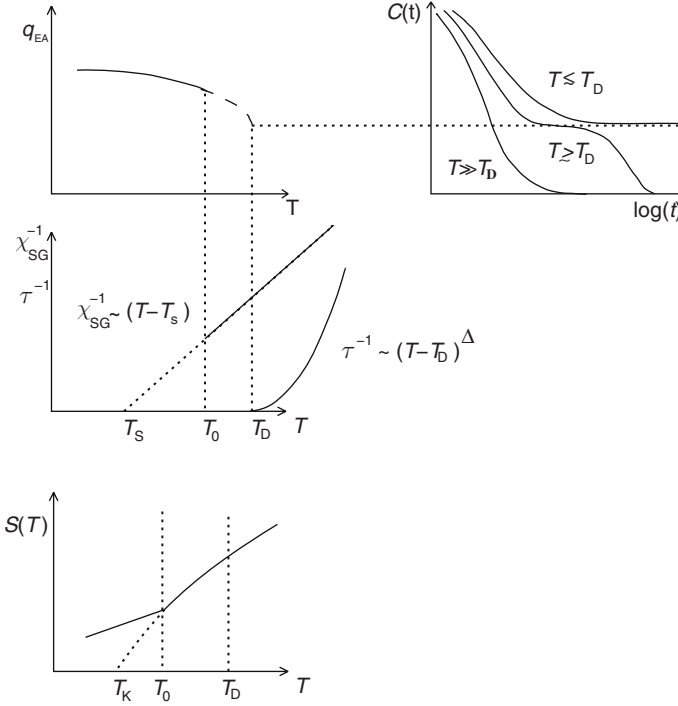


Fig. 3.2. Qualitative sketch of the mean-field predictions for the p -state Potts glass model with $p > 4$. The glass order parameter q_{EA} , which is given by the height of the plateau in the time correlation function $C(t)$ of the “Potts spins”, is nonzero only for $T < T_D$ and jumps to zero discontinuously at $T = T_D$. The spin-glass susceptibility χ_{SG} shows no anomaly whatsoever at T_D , nor does the entropy $S(T)$. At $T = T_0 < T_D$, a static phase transition occurs, $S(T)$ shows a kink, the static order-parameter distribution (which is still described by $P(q) = \delta(q)$ also for $T_0 \leq T \leq T_D$) acquires a second peak at $q \neq 0$, and therefore χ_{SG}^{-1} [(3.7)] in equilibrium is zero for all $T < T_0$, although χ_{SG}^{-1} at $T = T_0$ remains finite and nonzero. The (metastable) continuation of the high-temperature branch of χ_{SG}^{-1} would vanish at T_s , while the continuation of $S(T)$ would vanish at T_K , with $T_K/T_s = [(p-1)/\ln p]^{1/2}/2$

“critical slowing down” [10], for $p > 4$ there occurs a dynamical transition at a temperature $T_D > T_0$ [29, 30]. This dynamical transition is due to the appearance of long-lived plateaus in $C(t)$, see Fig. 3.2, and is a transition from ergodic to nonergodic behavior described by a schematic version of the same MCT [19, 20] as has been proposed for the structural glass transition! Thus one finds

$$\tau \propto (T/T_D - 1)^{-\Delta}, \quad T_D > T, \quad (3.9)$$

while for $T < T_D$ the autocorrelation time is infinite, because the phase space of the model for $T < T_D$ has split into (infinitely many) “valleys” (“ergodic components” [11]) separated by infinitely high barriers. We denote the free

energy of the system in the ℓ th valley as F_ℓ and the statistical weight of this valley as P_ℓ [note that $Z_\ell = \sum_{\lambda \in \ell} \exp(-E_\lambda/k_B T)$ where λ is a microstate belonging to the ℓ th valley, the total partition function being $Z = \sum_\ell Z_\ell$, $P_\ell = Z_\ell/Z$]. With $F = -k_B T \ln Z$, the free energy \bar{F} averaged over all valleys becomes

$$\bar{F} \equiv \sum_\ell P_\ell F_\ell = F + TI \quad \text{with} \quad I \equiv -k_B \sum_\ell P_\ell \ln P_\ell \quad , \quad (3.10)$$

where I is called the “complexity” [11]. (Since it “counts” the number of valleys in phase space, I is sometimes also called “configurational entropy” and associated with the “configurational entropy” of the Gibbs–di Marzio theory [4], but this idea is misleading since the latter deals with the total entropy $S(T)$ of the disordered phase, in the framework of the considered lattice model.) Note that $I \equiv 0$ for $T > T_D$ since there are no infinitely high barriers [and the time the system resides in a particular region of phase space is finite, see (3.9)]; in the sense of (3.10), there is only a single valley. At $T = T_D$, the complexity jumps discontinuously from zero to a finite nonzero value, but it then decreases again and vanishes at T_0 [3, 34]. This does not mean that the ordered phase for $T < T_0$ is nondegenerate: It only implies that the number of valleys increases more weakly with N than $\exp(\text{const} \times N)$ [11].

3.3 Monte Carlo Results for the 10-State Mean-Field Potts Glass: Static Properties

As described above, the Potts glass model for $p > 4$ provides a scenario where two transitions occur, an ergodic to nonergodic transition at T_D , described by MCT, and a static transition at $T_0 < T_D$, characterized by a kink in the entropy $S(T)$. Qualitatively, this is similar to the situation at the structural glass transition. Of course, there it is known that barriers hindering the escape from frozen-in states for $T < T_c$ (the critical temperature of MCT) are large but finite since “hopping processes” [3, 20, 21] do occur. A situation with finite (instead of infinite) barriers is also found in the mean-field Potts glass when the number N of Potts spins is *finite*. Moreover, the approach to the thermodynamic limit at a glass transition is of interest in its own right since it can help to understand better the nature of such transitions, and needs to be considered in the analysis of computer simulation results, which always deal with finite systems only [35, 36].

Since $q_0 \rightarrow 0$ as $q \rightarrow 4$ [$q_0 = 2(p-4)/7 + O(p-4)^2$, $T_0 - T_s \propto (p-4)^2$] [31], we choose [37, 38, 39] $p = 10$ since then $q_0 = 0.452$ is about halfway between zero and its saturation value $q_0 = 1$ [33]. In this case $T_0 = 1.1312$ also differs enough from T_s to numerically see that χ_{SG} does not diverge according to a power law when one approaches the transition from above. The entropy per

spin has decreased appreciably, but clearly is nonzero [$s(T_0)/s(T = \infty) \approx 0.236$].

Monte Carlo simulations of this model have been performed for $160 \leq N \leq 2560$ [37, 38, 39]. These simulations required significant computer resources since each spin interacts with every other spin, and the average over many samples $\{J_{ij}\}$ of the quenched disorder has to be taken [the number of samples was between $\mathcal{N} = 500$ for $N \leq 200$ and $\mathcal{N} = 50$ for $N=2560$]. At not too low temperatures, $T \geq 1$, the straightforward Metropolis algorithm [35, 36] was implemented, picking spins at random and choosing randomly an orientation for them as a trial state. For $T < 1$, “parallel tempering” [40] was used. The total computing time (in units of a single Pentium II processor with 400 MHz) needed for this study was of the order of 10 years.

Figure 3.3 shows numerical results for the entropy and inverse spin-glass susceptibility. One sees unexpectedly large finite-size effects. Only for $1/T < 0.7$ have the data converged to the results of the replica theory [25, 33]. For $1/T > 0.9$, however, it is clearly apparent that the data no longer will converge toward the replica symmetric results [25], and instead are qualitatively compatible with the results of the one-step replica symmetry breaking theory [28, 29, 30, 31, 32, 33] which have been explained in Fig. 3.2. While for

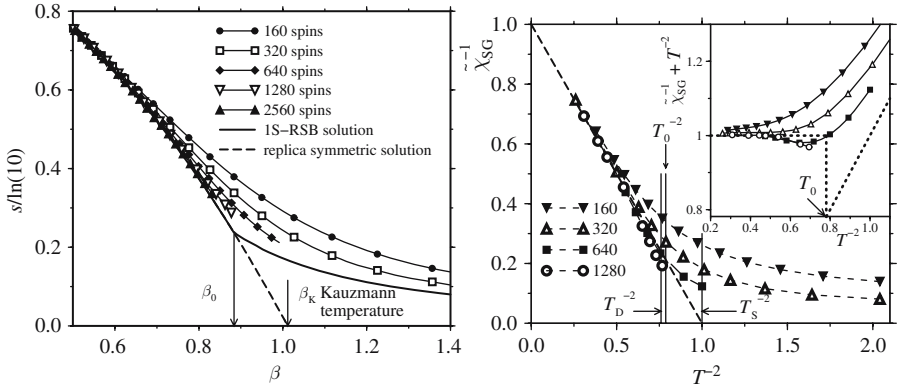


Fig. 3.3. Entropy per spin s , normalized by its high-temperature value, plotted vs. inverse temperature (*left-hand side*), for different system sizes (curves with symbols). The *bold dashed curve* and the *bold solid curve* are the replica symmetric and the one-step replica symmetry-broken solution [33], respectively. Vertical arrows indicate $\beta_0 = 1/T_0$ and $\beta_K = 1/T_K$. The *right-hand side* shows the inverse of the (reduced) spin-glass susceptibility $\tilde{\chi}_{SG}^{-1}$ (χ_{SG} is normalized by the result for noninteracting Potts spins) vs. T^{-2} . Both the location of T_D^{-2} and of T_0^{-2} are indicated by vertical straight lines. The broken straight line is the result of the replica-symmetric mean-field theory [25]. Also the location of the “spinodal temperature” T_s is indicated. Broken curves with symbols show the Monte Carlo data. The inset shows a plot of $\tilde{\chi}_{SG}^{-1} + T^{-2}$ vs. T^{-2} , to illustrate the nonmonotonic convergence to the thermodynamic limit. From Brangian et al. [38]

$T > T_0$, one finds a convergence of energy per spin $e_N(T)$ and order parameter square $\langle q^2 \rangle$ to their limits as $1/N$, for $T = T_0$ a different relation applies: $e_N(T) - e_\infty(T) \propto \langle q^2 \rangle \propto N^{-2/3}$ [38].

Particular intriguing is the behavior of $P(q)$, see Fig. 3.4. The delta function at $q = 0$ is strongly rounded and shifted to a nonzero value (note that q is defined here as root mean square value of a fluctuating quantity, see Sect. 3.2). As the temperature is lowered, this peak shifts somewhat to the right and broadens because the susceptibility increases. However, at low temperatures, the distribution develops a long tail toward large q , and there a second peak starts to grow. This behavior is very different from a second-order transition, for which the broad peak corresponding to the disordered phase bifurcates into two peaks at the transition. The *right part* of Fig. 3.4 shows that for small N the peak that develops into the delta function $\delta(q - q_0)$ only shows up as a shoulder at the wing of the broad peak representing the disordered phase, and the convergence to the two-delta function distribution, (3.8), with increasing N is apparently very slow.

For conventional phase transitions, a convenient way to estimate the location of the phase transition uses the fourth-order cumulant of the order-parameter distribution [41]. Plotting this quantity vs. temperature for several values of N , observation of a common intersection point of these curves yields an unbiased estimate of the transition temperature [35, 36, 41]. This recipe also works well for the Sherrington-Kirkpatrick Ising mean-field spin glass [11]. However, for the present case, the data (within rather larger error bars) indicate a spurious intersection point at $T \approx 1.31$, rather than at the static transition temperature $T_0 = 1.1312$ [38]. The proper extension of finite-size scaling theory to these unconventional glass transitions which are in between first and second order is hence not yet understood.

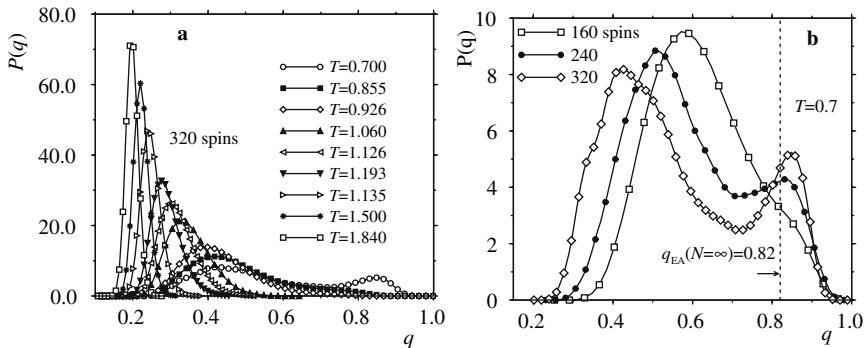


Fig. 3.4. (a) Order parameter distribution $P(q)$ vs. q for $N = 320$ and various temperatures. (b) Order parameter distribution $P(q)$ vs. q for $T = 0.7$ and three system sizes $N = 160, 240$ and 320 . The asymptotic value of the order parameter (from [33]) is included as a vertical line. From Brangian et al. [38]

3.4 Finite-Size Scaling for the “Dynamic Transition” of the Potts Glass

In order to test for the occurrence of a dynamical transition (Fig. 3.1) and the associated divergence of the relaxation time (3.9), the autocorrelation function $C(t)$ of the Potts spins (3.6) is analyzed. Figure 3.5 shows the corresponding Monte Carlo data. A surprising feature is that for $T \geq T_D$, there is no indication of the expected two-step decay (Fig. 3.2), even for N as large as $N = 1280$. Only for much lower temperatures has $C(t)$ roughly the expected type of behavior, i.e., $C(t)$ decays in two steps. Obviously, also for dynamic properties, the finite-size effects are very pronounced, apart from very high temperatures, as Fig. 3.5 shows: At $T = 1.8$, the time correlation function has nicely converged, while at $T = T_D$ size effects affect all parts of the decay of $C(t)$. To get a useful estimate of the relaxation time τ , it was hence asked how long does it take for $C(t)$ to decay down to $C(t) = 0.2$, a value distinctly below the plateau which should occur in $C(t)$ at $T = T_D$ in the thermodynamic limit. The relaxation time obtained in this way is analyzed as function of temperature in Fig. 3.6. Plotting $\log(\tau)$ vs. $1/T$, as is common practice for structural glasses (Fig. 3.6, *left part*), one finds a strongly curved behavior at high T , followed by a crossover to an Arrhenius behavior at lower temperature ($T < T_D$). The distinction here is, however, that the activation energy (which is given by the slope of the straight lines which occur for $1/T > 1/T_D$ in this plot) increases systematically with increasing N . Actually, we expect that for the present model, $\tau \rightarrow \infty$ as $T \rightarrow T_D$ from above, and τ should stay divergent for all $T < T_D$, due to the infinitely high free-energy barriers between the “valleys in phase space”.

To test for the expected divergence of τ (3.9), the data for τ are replotted in the *right part* of Fig. 3.6 in the form $\tau^{-1/\Delta}$ vs. T , using the exponent $\Delta = 2.0$ as trial value: If (3.9) holds and finite-size effects were negligible, one would see a straight line, cutting the abscissa at $T = T_D$. The *right part* of Fig. 3.6 shows that such an analysis suggests that Δ should be around $\Delta = 2$, and although there are some finite-size effects also with respect to the intersection points of the *fitted straight lines*; the apparent values $T_D(N)$ seem to converge to the correct value relatively fast.

A rather intriguing observation is the evidence for dynamical finite-size scaling (Fig. 3.7). Brangian et al. [37] suggested that τ can be expressed in the form

$$\tau = N^{z^*} \tilde{\tau}\{N(T/T_D - 1)^{\Delta/z^*}\} \quad , \quad N \rightarrow \infty, T/T_D - 1 \rightarrow 0, \quad (3.11)$$

where z^* is an exponent that describes the N -dependence of τ for $T = T_D$, and $\tilde{\tau}(\zeta)$ is a scaling function with the properties that $\tilde{\tau}(0) = \text{const}$, $\tilde{\tau}(\zeta \gg 1) \propto \zeta^{-z^*}$, so that for $T > T_D$ and large enough N the N -dependence cancels out, and (3.9) results. Figure 3.7 shows that for $z^* \approx 1.5$, this dynamic finite-size scaling is indeed compatible with the Monte Carlo results.

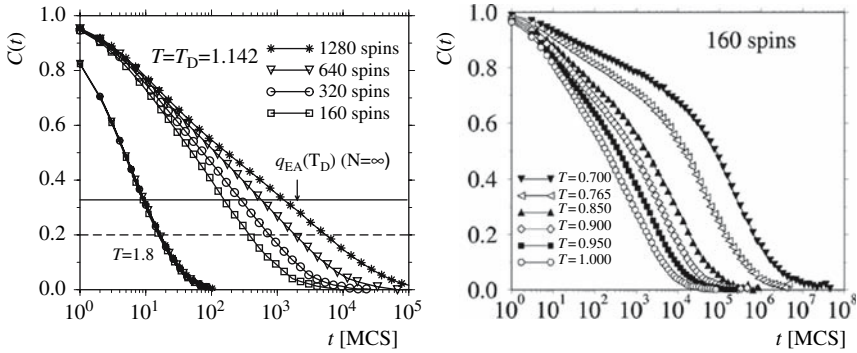


Fig. 3.5. *Left panel:* Time dependence of the autocorrelation function $C(t)$ of the Potts spins in the 10-state mean-field Potts glass for $T = 1.8$ and for $T = T_D = 1.142$ for several values of N . The *horizontal straight line* shows the theoretical value [33] of the Edwards–Anderson glass order parameter $q_{EA}(T_D)$ for $N \rightarrow \infty$. The *dashed horizontal line* shows the value $C(t = \tau) = 0.2$ that was used to define the relaxation time τ . Time is measured in units of Monte Carlo steps per spin (MCS). *Right panel:* $C(t)$ vs. t for $N = 160$ at temperatures $T < T_D$. From Brangian et al. [38]

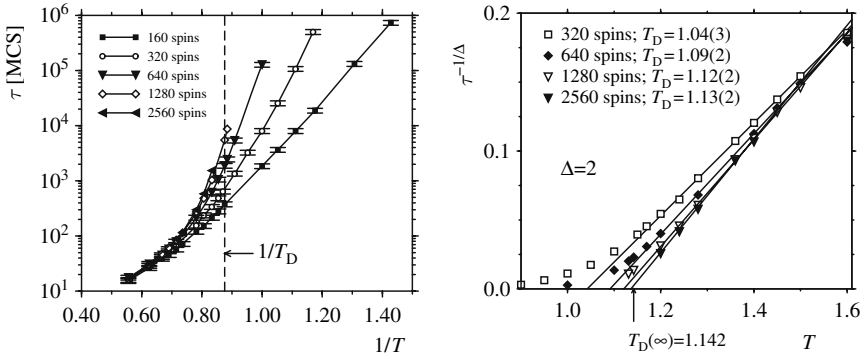


Fig. 3.6. *Left panel:* Relaxation time τ plotted vs. inverse temperature for different system sizes. The *broken vertical line* indicates the location of the dynamical transition. Note the choice of the logarithmic scale for the ordinate. *Right panel:* Temperature dependence of $\tau^{-1/\Delta}$ as a function of temperature for different system sizes, using $\Delta = 2$ as a trial value. The *bold straight lines* are fits to a subset of points with ordinate values larger than 0.03. The resulting extrapolated values for $T_D(N)$ are quoted in the figure. From Brangian et al. [38]

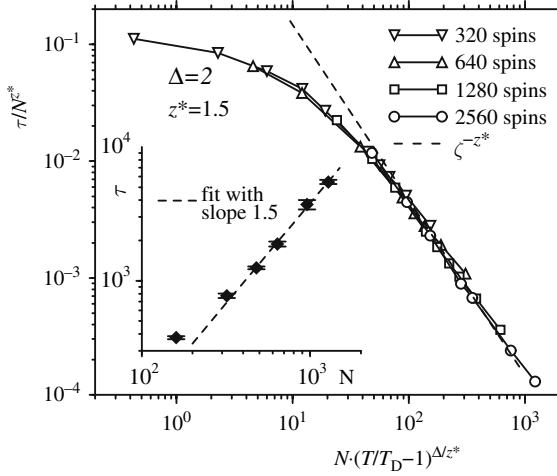


Fig. 3.7. Log-log plot of the scaled relaxation time τ/N^{z^*} vs. the scaled distance $N(T/T_D - 1)^{\Delta/z^*}$ from the dynamical transition temperature T_D . Here $z^* = 1.5$ and $\Delta/z^* = 1.3$ are chosen. The inset shows a log-log plot of $\tau(T = T_D)$ vs. N . From Brangian et al. [37]

As last point of this section, we discuss the dynamical susceptibility $\chi(t)$ [39], defined as [42]

$$\chi(t) = N[\langle q(t)^2 \rangle - \langle q(t) \rangle^2]_{\text{av}}, \quad (3.12)$$

where $q(t)$ denotes the overlap between two equilibrium configurations separated at time t . Figure 3.8 shows that $\chi(t)$ exhibits a maximum (of height χ^*) at time t^* . Using data for the largest choice of $N (= 2560)$ at temperatures high enough so that finite-size effects are minor, a compelling evidence for dynamic scaling is obtained (Fig. 3.8), i.e.,

$$\chi(t, T)/\chi^* = \tilde{\chi}(t/t^*(T)) \quad , \quad (3.13)$$

where t^* and χ^* again satisfy power laws [39], $\chi^* \propto (T - T_D)^{-1}$ and $t^* \propto (T - T_D)^{-\Delta}$, with $\Delta = 2.3 \pm 0.3$, compatible with estimate from Figs. 3.6 and 3.7. Similarly, a study of the size dependence of $\chi(t)$ at $T = T_D$ reveals again power laws, namely $\chi^* \propto N$, $t^*(T = T_D) \propto N^{z^*}$, $z^* = 1.63 \pm 0.15$ [39]. Again these estimates are consistent with the findings from the autocorrelation function of the Potts spins.

Thus, the Monte Carlo study of the $p = 10$ infinite-range Potts spin glass has revealed some unexpected features (such as very pronounced finite-size effects), but essentially the results are compatible with the theoretical expectations.

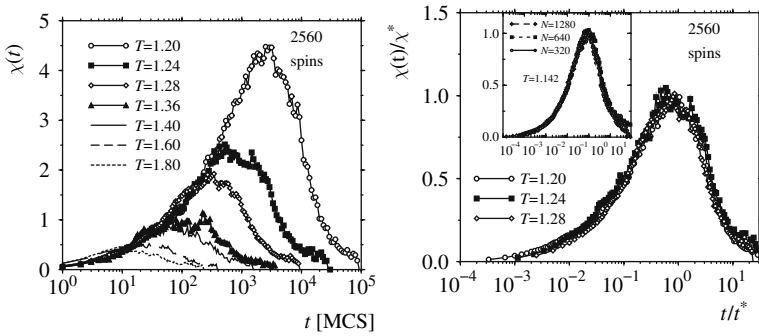


Fig. 3.8. The dynamical susceptibility $\chi(t)$ plotted vs. time for the 10-state mean-field Potts glass, for $N = 2560$, for various temperatures as indicated (*left panel*). Scaling plot of $\chi(t)/\chi^*$ vs. t/t^* (*right panel*). In the main plot, the curves are for $N = 2560$ and $T = 1.20, 1.24$ and 1.28 , respectively. The inset to the *right part* shows the same rescaling but fixed temperature $T = T_D = 1.142$ and three system sizes $N = 320, 640$ or 1080 . From Brangian [39]

3.5 Monte Carlo Study of the Short-Range 10-State Potts Glass: Do all Transitions Disappear?

While the advantage of the fully connected Potts glass, where every spin is coupled to every other spin, is the fact that it is exactly soluble via the one-step replica symmetry breaking approach [28, 29, 30, 31, 32, 33], it is clear that such an infinite range of the interaction is physically very unrealistic and does not correspond to any real material. Hence, there is the need to study what happens in models with short-range interactions. We consider here only the extreme case of a simple cubic lattice, where interactions occur only between nearest neighbors. While in the Ising spin glass, it is known [11, 12] that a static phase transition at a nonzero freezing temperature T_f does occur, although there are still controversial problems concerning the properties of the low-temperature phase [12], already for the $p = 3$ Potts glass, it was suggested that $T_f = 0$, $d = 3$ being the lower critical dimensionality for a transition (characterized by an exponential divergence of the spin-glass susceptibility χ_{SG} as $T \rightarrow 0$) [43].

Here we consider $L \times L \times L$ lattices with periodic boundary conditions for the nearest-neighbor Potts glass with $p = 10$, assuming a $\pm J$ interaction:

$$P(J_{ij}) = x\delta(J_{ij} - J) + (1 - x)\delta(J_{ij} + J) \quad . \quad (3.14)$$

To obtain $[(\Delta J)^2]_{av} = 1$, $[J_{ij}]_{av} = -1$, we choose $J = \sqrt{2}$, $x = (1 - 1/\sqrt{2})/2$, so that again no ferromagnetic ordering occurs.

Figure 3.9 shows the specific heat and the glass susceptibility as function of temperature [44, 45], giving evidence that χ_{SG} stays finite at low T , and that there are almost no finite-size effects. This is clear evidence against the

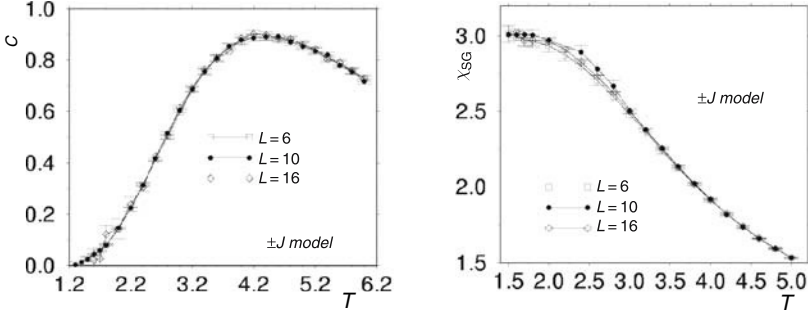


Fig. 3.9. Temperature dependence of the specific heat (*left panel*) and the spin-glass susceptibility $\chi_{SG} = N[\langle q^2 \rangle]_{av}/(p-1)$ (*right panel*) for the $p = 10$ -state nearest-neighbor \pm Potts glass {3.14}. Three choices of L are included in the figure, as indicated. From Brangian *et al.* [44]

occurrence of any static phase transition in this model. Actually, one can show [45] that the peak of the specific heat is almost entirely due to pairs of Potts spins coupled ferromagnetically, giving rise to a Schottky-like anomaly. These clusters (pairs, triples, etc.) also show up in the decay of the self-correlation function $C(t)$ of the Potts spins (Fig. 3.10). One observes a decay of $C(t)$ in several steps, and a first long-lived plateau develops at $C(t) \approx 0.6$. While at first glance this is reminiscent of MCT, an analysis of the lifetime of this plateau, τ_1 , defined from $C(t = \tau_1) = 0.4$, shows (*right part* of Fig. 3.10)

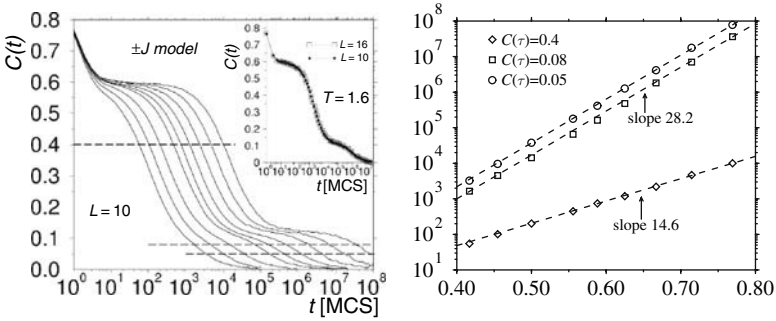


Fig. 3.10. Time-dependence of the spin autocorrelation function $C(t)$ of the $p = 10$ state nearest-neighbor \pm Potts glass (*left panel*) for temperatures (*left to right*) $T = 2.4, 2.2, 2.0, 1.8, 1.7, 1.6, 1.5, 1.4$ and 1.3 ($L = 10$). The *horizontal dashed lines* are used to define the relaxation times τ_i , see text for details. In the *inset* $C(t)$ at $T = 1.6$ for $L = 10$ and $L = 16$ are compared to show that finite-size effects are again negligible. The *right panel* shows an Arrhenius plot (τ_i , on log-scale plotted vs. $1/T$) of the relaxation times τ_i extracted from the *left part* of the figure. *Straight lines* are fits of the data to $\ln \tau = \text{const} + E_A/T$, and the activation energies E_A (slope of the lines) are quoted in the figure. From Brangian *et al.* [44]

that τ_1 does not increase according to a power law, but instead according to a simple Arrhenius law, $\tau_1 \propto \exp(E_A/k_B T)$, with $E_A = 14.6$. This value is easily understood since pairs of Potts spins coupled by ferromagnetic bonds (and connected with antiferromagnetic bonds to their environment) involve a “binding energy” $pJ = 10\sqrt{2} \approx 14.13$, which needs to be overcome when a ferromagnetic pair is broken up [cf. the definition of the Hamiltonian equations (3.3) and (3.14)]. Note that antiferromagnetic bonds lead to an energy gain if pairs are in different states, and for $p = 10$ a high degeneracy occurs for this case ($p(p-1)/2 = 45$ possibilities), and hence ferromagnetic clusters at low T are essentially decoupled from their environment. Using the concentration of ferromagnetic bonds, one can also explain the height of this plateau [45]. The second plateau in $C(t)$, Fig. 3.10, is correspondingly attributed to spins which have two neighbors to which they are coupled by ferromagnetic bonds, hence involving an energy $2p\sqrt{2} = 20\sqrt{2} \approx 28.3$, in excellent agreement with the simulation results (Fig. 3.10, right panel).

One might argue that the behavior seen in Figs. 3.9 and 3.10 is a particularity of the discrete $\pm J$ model, and it is clearly useful to study a short-range model with Gaussian distributed exchange (3.4) as well. However, the corresponding Monte Carlo results [45] also show the absence of a static glass transition for this model, down to the lowest temperatures. Of course, now the broad distribution of interaction energies causes the well-defined plateaus in $C(t)$ to disappear, unlike Fig. 3.10 one now finds a slow, strongly nonexponential decay of $C(t)$ spread out over many decades in time. Thus, also for this model, there is no evidence for a dynamical transition described by MCT.

The conclusion is that in the nearest-neighbor 10-state Potts glass both the dynamical ergodic-to-nonergodic transition and the static glass transition are completely wiped out, no trace whatsoever being left of these phenomena that are present in the mean-field models.

3.6 Concluding Discussion: What have we Learned about Glass Transitions?

In these lecture notes, the salient features of the analytical results about mean-field Potts glass models with $p > 4$ states have been summarized, and Monte Carlo results for the case $p = 10$ were presented, investigating in particular the dependence on the finite size of the system, varying N in the range $160 \leq N \leq 2560$. This model has the fascinating property that two glass transitions occur, a dynamical ergodic-to-nonergodic transition at T_D , described by idealized MCT, and a static transition at $T_0 < T_D$. The static transition involves a kink in the entropy, and the discontinuous appearance of a second peak in the order-parameter distribution, $P(q) \propto T/T_0 \delta(q) + (1 - T/T_0) \delta(q - q_0)$, at a value $q_0 > 0$. While the position of this peak appears at T_0 discontinuously, for $T \rightarrow T_0$ from below the weight of this peak vanishes continuously, and hence this transition differs from conventional first- and second-order transitions.

Both the glass susceptibility and the entropy remain finite (and nonzero) at $T \rightarrow T_0$ from above: a Kauzmann temperature at which $S(T = T_K) = 0$ can be defined by extrapolation of the high-temperature phase, but lacks physical significance. The complexity I [measuring the number of distinct valleys in phase space separated by infinitely high barriers, cf. (3.10)] should be nonzero for $T_0 < T < T_D$, however, while $I(T \rightarrow T_0) \rightarrow 0$ signals the occurrence of the static transition.

Some of these features were studied by Monte Carlo simulation and in particular the predicted dynamical transition could be characterized quantitatively, while the predicted static transition [and the two-peak structure of $P(q)$] could only be verified in a rough and qualitative way. Both static and dynamic properties are very strongly affected by finite-size effects. This latter observation (as well as the absence of a well-defined plateau in $C(t)$ for T at and above T_D , for the range of N that was accessible) differs distinctly from simulation results for atomistic models of glass-forming supercooled fluids (where a regime described by MCT is identified readily, and finite-size effects seem to be minor).

Our results cast some doubt whether the Potts glass model (and similar models, for which the scenario of Fig. 3.2 holds) is a useful qualitative model for the structural glass transition. This caveat is strengthened by the finding that in the nearest-neighbor model both the dynamical transition and the static one are completely wiped out, and only weak anomalies (and associated slow relaxation) due to small ferromagnetically coupled clusters are left. Of course, one could argue that in Potts glass models with a large but finite range of interactions or other more suitable models [46], one can expect a behavior similar to Fig. 3.2, but with the sharp transition at T_D and T_0 being replaced by slightly rounded ones. This would imply that in a plot such as Fig. 3.6 (*left part*) for $T \rightarrow T_D$ from above the relaxation time increases according to the power law (3.9), but very near T_D a crossover to an Arrhenius law (presumably) occurs, with an activation energy E_A which is large and independent of N as $N \rightarrow \infty$. While such a speculation may be tempting and supported by various arguments [46], a numerical or quantitative analytical evidence for this scenario is still missing. Clearly, more work will be needed to fully understand these problems.

Acknowledgements

These lecture notes are based on studies [37, 38, 39, 44, 45] supported by the Deutsche Forschungsgemeinschaft (DFG) under grant No. SFB262/D1. The studies have been supported by the European Community's Human Potential Programme under contract HPRN-CT-2002-00307, DYGLAGEMEM, and profited from generous grants of computer time at the CRAY T3E of the John von Neumann Institute for Computing (NIC Jülich).

References

1. J. Jäckle: Rep. Progr. Solids **49**, 171 (1986) [47](#), [49](#)
2. P. G. Debenedetti: *Metastable Liquids* (Princeton University Press, Princeton, 1997) [47](#), [49](#)
3. K. Binder, W. Kob: *Glassy Materials and Disordered Solids: An Introduction to Their Statistical Mechanics* (World Scientific, Singapore, 2005) [47](#), [49](#), [51](#), [54](#)
4. J. H. Gibbs, E. A. di Marzio: J. Chem. Phys. **28**, 370 (1958) [47](#), [49](#), [54](#)
5. W. Kauzmann: Chem. Rev. **43**, 219 (1948) [49](#)
6. G. Adam, J. H. Gibbs: J. Chem. Phys. **43**, 139 (1965) [49](#)
7. B. J. Alder, T. E. Wainwright: J. Chem. Phys. **27**, 1208 (1957) [49](#)
8. F. H. Stillinger: J. Chem. Phys. **88**, 7818 (1988) [49](#)
9. M. Wolfgangdt, J. Baschnagel, W. Paul, K. Binder: Phys. Rev. E **54**, 1535 (1996) [49](#)
10. P. C. Hohenberg, B. I. Halperin: Rev. Mod. Phys. **49**, 435 (1977) [49](#), [50](#), [53](#)
11. K. Binder, A. P. Young: Rev. Mod. Phys. **58**, 801 (1986) [50](#), [53](#), [54](#), [56](#), [60](#)
12. See the chapters by A. Billoire and A. K. Hartmann in the present Lecture Notes [50](#), [60](#)
13. K. Binder, J. D. Reger: Adv. Phys. **41**, 547 (1992) [50](#)
14. K. Binder: In *Spin Glasses and Random Fields*, edited by A. P. Young (World Scientific, Singapore, 1998), p. 99 [50](#)
15. E.-W. Donth: *The Glass Transition. Relaxation Dynamics in Liquids and Disordered Materials* (Springer, Berlin, 2001) [50](#)
16. L. Berthier, G. Biroli, J. P. Bouchaud, L. Cipelletti, D. El Masri, D. L'Hôte, F. Ladieu, M. Pierno: Science **310**, 1797 (2005) [50](#)
17. P. Scheidler, W. Kob, K. Binder: Europhys. Lett. **59**, 701 (2002) [50](#)
18. L. Berthier: Phys. Rev. E **69**, 020201 (2004) [50](#)
19. U. Bengtzelius, W. Götze, A. Sjölander: J. Phys. C **17**, 5915 (1984) [50](#), [53](#)
20. W. Götze, L. Sjögren: Rep. Progr. Phys. **55**, 241 (1992) [50](#), [53](#), [54](#)
21. W. Götze: J. Phys.: Condens. Matter **11**, A1 (1999) [50](#), [51](#), [54](#)
22. S. P. Das: Rev. Mod. Phys. **76**, 785 (2004) [50](#)
23. C. A. Angell: In *Relaxation in Complex Systems*, edited by K. L. Ngai, G. B. Wright (US Dept. Commerce, Springfield, 1985), p. 1 [51](#)
24. J. Horbach, W. Kob: Phys. Rev. B **60**, 3169 (1999) [51](#)
25. D. Elderfield, D. Sherrington: J. Phys. C **16**, L491, L971, L1169 (1983) [51](#), [55](#)
26. R. B. Potts: Proc. Camb. Phil. Soc. **48**, 106 (1952) [51](#)
27. F. Y. Wu: Rev. Mod. Phys. **54**, 235 (1982) [52](#)
28. D. J. Gross, I. Kanter, H. Sompolinsky: Phys. Rev. Lett. **55**, 304 (1985) [52](#), [55](#), [60](#)
29. T. R. Kirkpatrick, D. Thirumalai: Phys. Rev. B **37**, 5342 (1988) [52](#), [53](#), [55](#), [60](#)
30. D. Thirumalai, T. R. Kirkpatrick: Phys. Rev. B **38**, 4881 (1988) [52](#), [53](#), [55](#), [60](#)
31. G. Cwlich, T. R. Kirkpatrick: J. Phys. A **21**, 4053 (1988) [52](#), [54](#), [55](#), [60](#)
32. G. Cwlich: J. Phys. A **23**, 5029 (1990) [52](#), [55](#), [60](#)
33. E. De Santis, G. Parisi, F. Ritort: J. Phys. A **28**, 3025 (1995) [52](#), [54](#), [55](#), [56](#), [58](#), [60](#)
34. See A. Crisanti, H. Horner, H.-J. Sommers: Z. Phys. B **92**, 257 (1993) for an explicit calculation of the complexity of a related, exactly soluble model [54](#)
35. D. P. Landau, K. Binder: *A Guide to Monte Carlo Simulation in Statistical Physics* (Cambridge University Press, Cambridge, MA, 2005), 2nd ed. [54](#), [55](#), [56](#)
36. K. Binder, D. W. Heermann: *Monte Carlo Simulation in Statistical Physics. An Introduction* (Springer, Berlin, 2002), 4th ed. [54](#), [55](#), [56](#)

37. C. Brangian, W. Kob, K. Binder: Europhys. Lett. **53**, 756 (2001) [54](#), [55](#), [57](#), [59](#), [63](#)
38. C. Brangian, W. Kob, K. Binder: J. Phys. A **35**, 191 (2002) [54](#), [55](#), [56](#), [58](#), [63](#)
39. C. Brangian: Physica A **338**, 471 (2004) [54](#), [55](#), [59](#), [60](#), [63](#)
40. K. Hukushima, K. Nemoto: J. Phys. Soc. Jpn. **64**, 1604 (1996) [55](#)
41. K. Binder: Z. Phys. B **43**, 119 (1981) [56](#)
42. S. Franz, G. Parisi: J. Phys.: Condens. Matter **12**, 6335 (2000) [59](#)
43. M. Scheucher, J. D. Reger, K. Binder, A. P. Young: Phys. Rev. B **42**, 6881 (1990) [60](#)
44. C. Brangian, W. Kob, K. Binder: Europhys. Lett. **59**, 546 (2002) [60](#), [61](#), [63](#)
45. C. Brangian, W. Kob, K. Binder: J. Phys. A **36**, 10847 (2003) [60](#), [61](#), [62](#), [63](#)
46. M. P. Eastwood, P. G. Wolynes: Europhys. Lett. **60**, 587 (2002) [63](#)

Domain Walls, Droplets and Barriers in Two-Dimensional Ising Spin Glasses

Alexander K. Hartmann

Institut für Theoretische Physik, Friedrich-Hund Platz 1, 37077
Göttingen, Germany
hartmann@physik.uni-goettingen.de

Abstract. This chapter is devoted to spin glasses, a vast class of disordered magnetic materials [1, 2, 3, 4, 5]. Spin glasses are prototypical systems widely studied in condensed matter physics and statistical mechanics. A lot of research has been devoted to such systems, more than 10 000 scientific publications about spin glasses exist. The reason for this strong interest is that spin glasses exhibit a very puzzling behavior at low temperatures, which is still not completely understood. Furthermore, the theoretical treatment of these systems has led to many advances, with considerable impact on other cross-disciplinary applications such as neural networks [6], error-correcting codes [7], or optimization problems [8].

Here, we start with a general introduction, mentioning some fundamental experiments. Then we describe the standard model for spin glasses, the Edwards–Anderson Ising model, and mention some results of theoretical treatments, in particular the opposing *mean-field* and *droplet* pictures. The main part of this contribution is devoted to the numerical treatment of two-dimensional spin glasses with short-range interactions. These systems are special because they do not exhibit an ordered phase at low temperature. This means that the behavior for finite-size systems and small temperatures can be probably very well described by the droplet picture.

Here, two-dimensional spin glasses are studied via ground-state (GS) calculations. In the main algorithmic part, it is shown that the ground-state problem for planar spin glasses can be mapped on the *minimum-weight perfect-matching problem*, a classical graph-theoretic problem from computer science. For this problem, efficient algorithms are available. In the next section, it is shown that using this approach not only true (classical) ground states but also different types of excitations can be calculated. It is shown that by comparing the results for different types of excitations, important assumptions made by the droplet picture can be verified. In the last section, the presented approach is extended, such that also dynamical properties of two-dimensional spin glasses can be probed, namely the scaling of energy barriers with the system size.

4.1 Experimental Realizations

A spin glass can be created using well-known materials: Just take a lattice of a non-magnetic conducting material such as gold and randomly replace a small fraction x of the gold by magnetic iron ($\text{Fe}_x\text{Au}_{1-x}$). To see the spin-glass behavior in an experiment, the system is subjected to a weak magnetic field h and the resulting magnetization m is measured, i.e., one obtains the linear magnetic susceptibility $\chi = \left. \frac{\partial m}{\partial h} \right|_{h \rightarrow 0}$. When studying χ as a function of temperature T , one observes a peak at a very low temperature T_G . An example is shown in Fig. 4.1, the figure is taken from [9]. Usually T_G is of the order of 10 K, the exact value depends on the concentration x of the iron and on the way the sample is prepared. This peak is an indication of a phase transition.

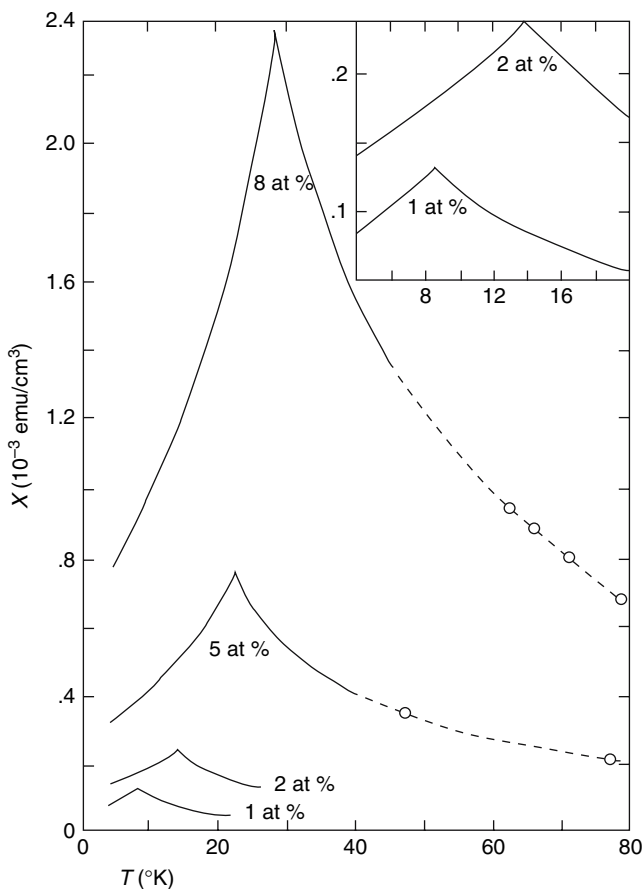


Fig. 4.1. Magnetic susceptibility χ for $\text{Au}_x\text{Fe}_{1-x}$ at low temperatures. A cusp depending on the concentration x is observed. The inset magnifies the region 0–20 K. The figure is taken from [9] with permission from J. A. Mydosh

This is in contrast to standard phase transitions, like in a pure ferromagnetic system without disorder, since the susceptibility exhibits just a cusp, but not a divergence. Also when measuring the specific heat $C(T)$, a smooth behavior around T_G is found, only a broad maximum usually at higher temperatures can be observed. This is again in strong contrast to usual phase transitions. A signature of a thermodynamic phase transition, i.e., a divergence of some quantity, is found when, e.g., measuring the *non-linear* susceptibility χ_{nl} [5]. χ_{nl} is measured by applying a magnetic field h and observing the resulting magnetization according to $M(h) = \chi_l h + \chi_{nl} h^3 + O(h^5)$. When performing a neutron-scattering experiment, one finds that below the transition temperature T_G , spin glasses do not exhibit any spatial (e.g., ferro- or antiferromagnetic) order of the orientation of the spins. Nevertheless, the spin-glass phase exhibits some kind of order in equilibrium, which is characterized by frozen local magnetic moments, visible through strong correlations between neighboring spins. The exact nature of this ordering is still subject to discussion. More details are given in Sect. 4.2.

Even more puzzling are *aging* experiments, where spin glasses are examined out of equilibrium with respect to the time evolution and to the history of the system. During such an experiment, the dynamic susceptibility $\chi(\omega)$ is measured via applying an alternating magnetic field $h(t) = h_0 \sin(\omega t)$ and measuring the resulting time-dependent magnetization $m(t) = m_0 \sin(\omega t + \phi)$, m_0 being the amplitude and ϕ the phase shift with respect to the applied field. The (linear) frequency-dependent susceptibility $\chi(\omega)$ is defined as usual via $m(t) = \chi(\omega)h(t)$, i.e., $m_0 \sin(\omega t + \phi) = \chi(\omega)h_0 \sin(\omega t)$. Using complex numbers ($\sin \alpha \rightarrow \exp(i\alpha) = \cos \alpha + i \sin \alpha$), $\chi'(\omega), \chi''(\omega)$ being the real and imaginary part of $\chi(\omega)$, respectively, and with $\chi \equiv \frac{\partial m_0}{\partial h_0} \approx \frac{m_0}{h_0}$, one obtains $\chi(\omega) = \chi'(\omega) + i\chi''(\omega) = \chi \cos \phi + i\chi \sin \phi$. Note that a non-vanishing imaginary part is related to dissipative processes in the sample.

A cartoon of a typical aging experiment is shown in Figs. 4.2 and 4.3. First, in a reference experiment, a spin glass (e.g., $\text{CdCr}_{1.7}\text{In}_{0.3}\text{S}_4$ [10, 11]) is cooled from a temperature above the transition temperature to a temperature well below, see *left* of Fig. 4.2. The cooling is performed with constant cooling rate of the order of 0.001 K/s. When, e.g., looking at $\chi''(\omega)$ (here $\omega = 0.1$ Hz), a peak very close to the phase transition can be observed. When reaching a low temperature (around 5 K), the system is heated up again. When still measuring χ'' , one observes that the data points are exactly the same as measured during the cooling.

Next, the result of an *aging experiment* is shown. Here, the same material is again cooled with constant rate, but at some temperature below T_G , the cooling is stopped for a while (2000 s here), see *left* of Fig. 4.3. Again, χ'' is measured. One observes (*right* of Fig. 4.3) that during this pause, the system ages, i.e., χ'' decreases slowly as a function of time, visible as a *vertical line* in the plot. The reason is that the material is not in equilibrium and converges toward an equilibrium situation while it is held at constant temperature. When the cooling is continued, χ'' does not decrease further, instead it *increases* for

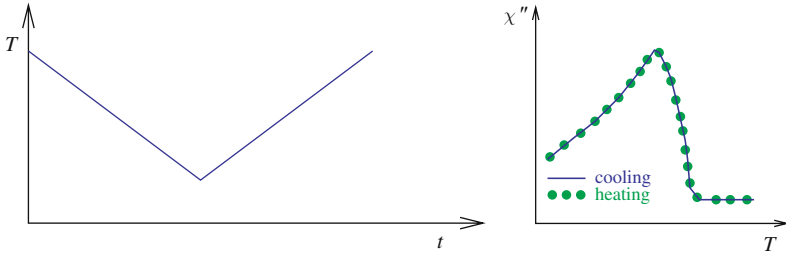


Fig. 4.2. Cartoons for reference out-of-equilibrium experiment. *Left:* Cooling schedule for the reference experiment. First, the sample is cooled down with constant rate 0.001 K/s, then heated up with the same rate. *Right:* Dynamic magnetic susceptibility χ'' for $\text{CdCr}_{1.7}\text{In}_{0.3}\text{S}_4$ (measured at 0.1 Hz) for cooling (line) and heating (symbols)

a while. At some lower temperature, χ'' has converged back to the value that was found for the reference experiment at the same temperature. Hence, it seems that the system has “forgotten” that cooling was stopped for a while. This effect is called *rejuvenation*. Finally, like in the reference experiment, the system is heated up again with constant heating rate. No pause is performed. Nevertheless, when measuring χ'' , the data points follow more or less the curve of the cooling/aging run, in particular the dip around the temperature, where cooling was stopped for a while, is found again. Hence, the system has indeed “remembered” that it has aged at a certain temperature, although from the measurements at lower temperatures, it seemed to have forgotten. This effect is the so-called *memory effect*. Such and other puzzling experiments are among the reasons that spin glasses have attracted so much attention in the past. Since many unsolved puzzles exist in this field, this interest will probably continue.

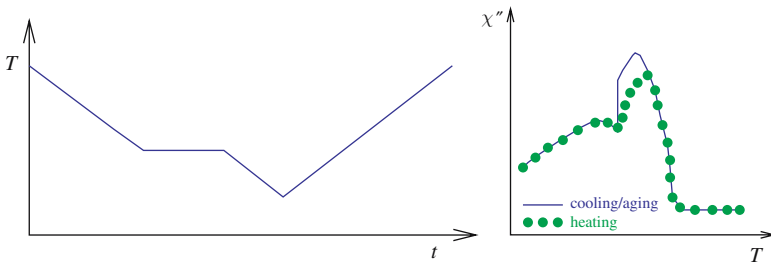


Fig. 4.3. Cartoons for aging experiment. *Left:* Cooling schedule for the aging experiment. First, the sample is cooled down with constant rate 0.001 K/s. The cooling is stopped below T_G for 2000 s and then continued. Finally, the system heated up with the constant rate. *Right:* Dynamic magnetic susceptibility χ'' for $\text{CdCr}_{1.7}\text{In}_{0.3}\text{S}_4$ (measured at 0.1 Hz) for cooling/aging (line) and heating (symbols)

The basic reason for this strange behavior is the type of interaction which is present in spin glasses. The behavior of the $\text{Fe}_x\text{Au}_{1-x}$ alloy studied in Fig. 4.4 is governed by the indirect-exchange interaction, usually called RKKY (Ruderman, Kittel, Kasuya, Yosida) interaction. Placing a magnetic spin \mathbf{S}_i (iron) in a sea of conducting electrons, results in a damped oscillation of the susceptibility as a function of the distance from the spin. Another spin \mathbf{S}_j placed at distance r will create the same kind of oscillations resulting in an energy $H = -J(r)\mathbf{S}_i \cdot \mathbf{S}_j$ where

$$J(r) \sim \frac{\sin(2k_{\text{f}}r)}{(2k_{\text{f}}r)^4} - \frac{\cos(2k_{\text{f}}r)}{(2k_{\text{f}}r)^3} \quad (4.1)$$

(k_{f} : Fermi momentum of the conductor) which at larger distances r reduces to $J(r) \sim \frac{\cos(2k_{\text{f}}r)}{(2k_{\text{f}}r)^3}$, see Fig. 4.4. The main point is that the sign of the interaction changes with distance. In the iron–gold alloy, since the iron is placed randomly in the gold host, each spin interacts with some spins ferromagnetically and with others antiferromagnetically. As a consequence, some pairs of spins prefer to be parallel aligned while other pairs favor an antiparallel orientation. At low temperatures, this mixed interactions create a frozen non-regular pattern of the orientations of the spins, explaining why no spatial order of the spins can be detected using neutron scattering.

Apart from the RKKY interaction, there are other ways of creating interactions with different signs: Some types of systems exhibit super exchange and others dipolar interactions. The system $\text{CdCr}_{1.7}\text{In}_{0.3}\text{S}_4$ presented above, in the context of aging and rejuvenation, is an example of an insulating system with ferromagnetic (super-)exchange interaction between nearest neighbors of magnetic Cr ions and an antiferromagnetic interaction between next-nearest neighbors. This variety of spin-glass behavior yielding interactions leads to a huge number of materials showing spin-glass behavior at low temperatures, more details can be found in [4]. Also there are several different mechanisms creating disorder: In the case of $\text{Fe}_x\text{Au}_{1-x}$, the randomness is obtained by placing the iron atoms at random chosen sites of a lattice. Also amorphous metallic alloys such as GdAl_2 and YFe_2 show spin-glass behavior. For another class of systems, all sites of a regular lattice are occupied by magnetic ions, but of two different types A/B, which again results in varying signs

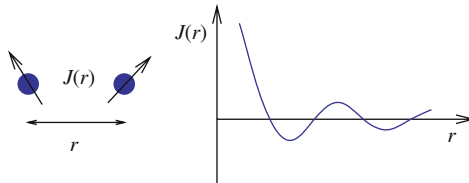


Fig. 4.4. The RKKY (Ruderman, Kittel, Kasuya, Yosida) interaction sketched: strength of the interaction of two spins with distance r in a sea of conducting electrons

and strengths of the bonds connecting nearest neighbors. Examples of such *random-bond* systems are $\text{Fe}_{1-x}\text{Mn}_x\text{TiO}_3$ and $\text{Rb}_2\text{Cu}_{1-x}\text{Co}_x\text{F}_4$. Note that in these cases, the signs of different close-by bonds are not independent because the disorder is again created via random occupation of sites. Here, the system $\text{Rb}_2\text{Cu}_{1-x}\text{Co}_x\text{F}_4$ is of particular interest. The magnetic ions Cu/Co are located at the sites of a simple square lattice [12], with a relatively large inter-layer distance. Hence, the inter-layer interactions are rather weak, making the system in the range of concentrations $0.2 < x < 0.4$ a realization of a two-dimensional spin glass, i.e., an experimental realization of the systems studied theoretically in this contribution [1]. Furthermore, since Co^{2+} ions exhibit a strong uniaxial anisotropy, all spins are directed along the c -axis for concentrations $x > 0.06$, making this system an *Ising system*. Experiments [12] measuring the non-linear susceptibility show that $\text{Rb}_2\text{Cu}_{1-x}\text{Co}_x\text{F}_4$ has $T_G = 0$ K in the spin-glass region.

4.2 Models

As we have seen in the previous section, the main ingredients constituting a spin glass are *mixed signs of interactions* and *disorder*. As a consequence, there are inevitably spins which cannot fulfill all constraints imposed by their neighbors and the connecting bonds, i.e., there will be some ferromagnetic bonds connecting antiparallel spins and vice versa. One says, it is not possible to *satisfy* all bonds. This situation is called *frustration*; the concept was introduced by Toulouse [13]. In Fig. 4.5, an example of a small frustrated system is shown.

For a theoretical model, it is not necessary to include all details of a system, e.g., the complicated RKKY interaction together with random positions of the magnetic atoms. Instead, for the *EA model* [14], N magnetic spins are placed on a *regular* lattice, e.g., a quadratic ($N = L^2$) or cubic ($N = L^3$) lattice of linear extension L . This is also the case for the random-bond systems

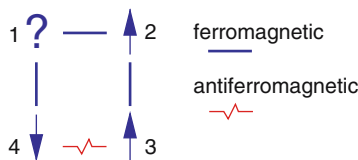


Fig. 4.5. A frustrated system of four spins at lowest energy. The *straight lines* represent ferromagnetic interactions, i.e., favoring parallel orientation of the adjacent spins, while the *zigzag line* represents an antiferromagnetic interaction. No matter which orientation spin 1 chooses, one of the bonds connecting it to its neighbors is not satisfied. Bonds 2–3 and 3–4 are satisfied

¹ For $x < 0.2$, the system behaves ferromagnetically and for $x > 0.4$ antiferromagnetically.

mentioned in the previous section. Here, we consider systems with a high magnetic anisotropy, where only one coordinate of the spin vector is relevant. This means, we study *Ising spins*, where we have in scale-free units $\sigma_i = \pm 1$. During the years, it was found in analytical and numerical studies that most fundamental phenomena occurring in spin glasses are found even for Ising systems, although systems with vector spins ($x-y$ model, Heisenberg model) have a somehow more complicated behavior.

In the EA model, only nearest-neighbor interactions are considered. Since the positions of the spins are regular and there is only one type of magnetic ions assumed, we have to incorporate randomness in a different way. This is achieved in the EA model by making the *interactions* random like in the above described $\text{Rb}_2\text{Cu}_{1-x}\text{Co}_x\text{F}_4$ system, but unlike in the experimental system, all bonds are uncorrelated in the model. The Hamiltonian is given by

$$H \equiv - \sum_{\langle i,j \rangle} J_{ij} \sigma_i \sigma_j . \quad (4.2)$$

The sum $\langle i, j \rangle$ runs over all pairs of nearest neighbors, and J_{ij} denotes the strength of the bond connecting spins i and j . It is also possible to add a term describing the interaction with an external field B , here we will concentrate on the case $B = 0$. Note that without a magnetic field, the Hamiltonian (4.2) has a spin-flip symmetry. This means, for each configuration $\{\sigma_i\}$, the configuration $\{-\sigma_i\}$, which is obtained from reversing all spins, has the same energy.

This Hamiltonian has also a broad range of applications going beyond spin glasses. Models involving similar energy formulas have been developed, e.g., for representing neural networks [6], social systems [15, 16, 17] or stock markets [18].

For each realization of the disorder, the values J_{ij} of the bonds are drawn according to a given probability distribution. Very common are the Gaussian distribution and the bimodal $\pm J$ distribution, which have the following probability densities:

$$p_G(J) = \frac{1}{\sqrt{2\pi}} \exp\left(-\frac{J^2}{2}\right), \quad (4.3)$$

$$p_{\pm J}(J) = 0.5\delta(J-1) + 0.5\delta(J+1). \quad (4.4)$$

Once the values of the bonds are fixed for a realization, they keep their values throughout the whole calculation or simulation, one speaks of *quenched disorder*. A two-dimensional sample system is shown in Fig. 4.6. Note that for a realization with bimodal distribution, a large degeneracy occurs, while for the Gaussian distributions, except the spin-flip symmetry, no degeneracy occurs, also for the ground state. Since the system is random itself, to calculate physical quantities such as magnetization or energy, one has to perform not only a thermal average but also an average over different realizations of the disorder.

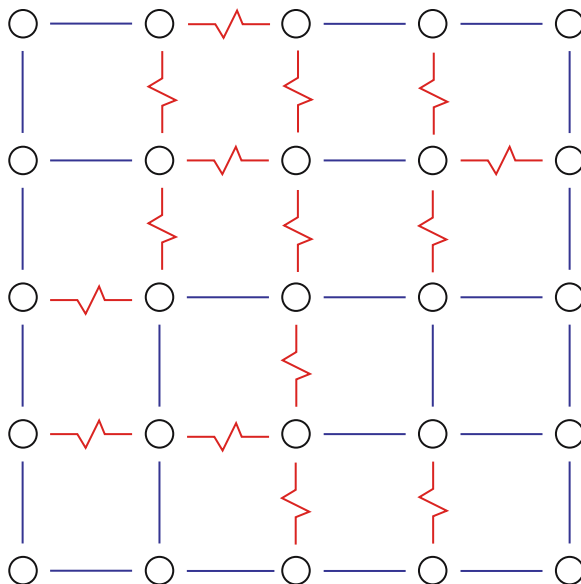


Fig. 4.6. A two-dimensional spin glass with bond disorder. Spins are placed on the sites of a regular grid. They interact with their neighbors, the interaction is random, either ferromagnetic or antiferromagnetic. Here, a bimodal $\pm J$ is assumed, hence all bonds have $|J_{ij}| = J$

Computer simulations of the EA model [1, 19] reproduce the main results found in experiments: a peak in susceptibility, a smooth behavior of the specific heat and frozen configurations of the spins. Also several results from aging experiments have been found by simulations as well, although a true replication of the above-mentioned memory and rejuvenation experiments is not possible via the time scales accessible in computer experiments. Therefore, one can conclude that even the simple EA model incorporates the main properties constituting a spin glass.

On the other hand, analytically it is very hard to treat the EA model [2, 3]. Since it is actually impossible to solve the simple cubic ferromagnet analytically, the reader may imagine that due to the additional average over the disorder involving varying sign of the bonds, only very raw approximations could be performed successfully for spin glasses. Nevertheless, there is a special spin-glass model, which was introduced by Sherrington and Kirkpatrick also in 1975 [20], the SK model. Its Hamiltonian is similar to the EA model, see (4.2), but it includes interactions between *all* $N(N-1)/2$ pairs of spins. This means that the spins do not have any positions in space, the system does not have a dimension. Usually, one says the system is infinite-dimensional because in the thermodynamic limit, each spin has infinitely many “neighbors”. The model is denoted as the *mean-field* (MF) model as well, since the MF approximation is exact here. For a Gaussian distribution of the interactions, the SK model

has been solved analytically through the use of several enhanced techniques by Parisi in the 1980s [2]. The main property of the solution is that a complicated energy landscape is obtained which organize the state-space in a hierarchy with infinitely many levels in the thermodynamic limit. In particular, there are many low-energy states, which are mutually very different from each other. For more details, see the contribution of Alain Billoire in Chap. 2 of this volume.

One of the great unsolved questions in spin-glass physics is, whether, or to what extent, the properties of the MF model are present also for finite-dimensional spin glasses. There is an opposing theory, the so-called *droplet* picture [21, 22, 23, 24, 25]. The droplet picture assumes that the low-temperature behavior is governed by droplet-like excitations. A droplet consists of a compact area of spins which are reversed with respect to a GS. Typical excitations of linear spatial extent l are assumed to cost an energy

$$\Delta E \sim l^\theta, \quad (4.5)$$

θ being a characteristic exponent, see Fig. 4.7. Note that *typical* here means that they dominate the thermodynamic behavior. This means, at finite temperature, that a droplet has minimum free energy for a given length scale l of the droplet. For $T = 0$, the minimum free energy requirement translates to a minimum-energy condition. The surface of a droplet is assumed to have a fractal dimension $d_s < d$, where d is the space dimension. Note that the surface of the droplet is at the same time a domain wall (DW) in the system, separating the spins having one ground-state orientation from the domain of spins having the opposite orientation. Furthermore, it is usually assumed that the scaling behavior of the energy ΔE of different types of excitations, e.g., droplets and other domain walls, which can be induced by changing the boundary conditions, are described by the same exponent θ . The similarity and simplicity of all excitations means that the energy landscape is dominated by two large valleys, with the two GS at the bottom of these valleys.

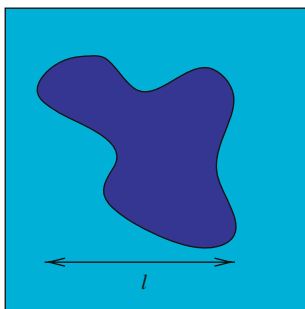


Fig. 4.7. A droplet is a compact excitation above the ground state of linear extension l . The energy of a typical droplet scales like l^θ

The most recent studies of three-dimensional spin glasses [26, 27, 28, 29, 30, 31] led to the conclusion that these systems exhibit properties of both MF and droplet pictures, which was denoted as TNT (“trivial–non-trivial”) picture.

Nevertheless, for two-dimensional spin glasses with nearest-neighbor interactions, there is no spin-glass phase at non-zero temperature [32, 33, 34, 35, 36]. For finite-size systems and small temperatures, this means that the behavior can be probably very well described by the droplet picture. This can be verified by performing ground-state calculations for the classical Hamiltonian (4.2). Note that these GSs are unphysical, in the sense that no quantum effects are included, hence the true behavior of a two-dimensional spin glass close to zero temperature will look different. Nevertheless, we will see in the subsequent sections that from the classical GS calculations, one can learn a great deal about the behavior of 2d spin glasses even at non-zero temperatures $T > 0$. In the next section, the GS algorithm is explained.

4.3 Ground States of Two-Dimensional Spin Glasses

The calculation of exact ground states [37, 38, 39, 40] for two-dimensional Ising spin glasses can be performed by algorithms that exhibit a running time, which grows polynomially with system size N . Note this is in contrast to higher dimensional spin glasses, where the ground-state calculation is *NP-hard* [41]. This is a certain class of problems in theoretical computer science [42], where all known algorithms to solve a problem exhibit a running time, which grows in the worst case exponentially with the system size. Here, we restrict ourselves to planar systems, since in this case, a so-called *matching algorithm* can be applied, which is a standard method in the field of algorithmic graph theory. The resulting running time for a system of $N = L^2$ spins is $O(N^2 \log N)$ using the approach presented here, this means that large system sizes of more than one million spins can be treated [43].

We will start by defining and explaining the necessary notions from graph theory, in particular the matching problem is introduced. Next, we explain how the ground-state problem for planar spin glasses can be mapped onto the matching problem. Within the mapping, also the shortest path problem will arise. Both, matching and shortest-path problems can be solved using standard algorithms from algorithmic graph theory [44, 45, 46, 47]. Therefore, the algorithms will not be explained here, only details of the mapping are given.

Definition 1. An (undirected) graph G is an ordered pair $G = (V, E)$, where V is a set and $E \subset V \times V$. An element of V is called a vertex or node. An element $e = \{i, j\} \in E$ is called an edge or arc. In a physical context, where

edges represent interactions between particles, edges are often called bonds. Note that $\{i, j\}$ and $\{j, i\}$ denote the same edge².

Usually we restrict ourselves to *finite* graphs, i.e., the set of nodes and the set of edges are finite. Now, a couple of notations are introduced. For an edge $\{i, j\} \in E$, we call j a *neighbor* of i (and vice versa). Both nodes are *adjacent* to each other. The set $N(i)$ of neighbors of i is given by $N(i) = \{j | \{i, j\} \in E\}$. The degree $d(i)$ of node i is the number of neighbors, i.e., the cardinality of the set of neighbors: $d(i) = |N(i)|$. A vertex with degree 0 is called *isolated*. A graph where each vertex is connected to all other vertices, i.e., the graph $G = (V, V \times V)$, is called a *complete graph*.

A *path* from v_1 to v_k is a sequence of vertices v_1, v_2, \dots, v_k which are connected by edges: $\{v_i, v_{i+1}\} \in E \forall i = 1, 2, \dots, k-1$. The *length* of the path is $k-1$, i.e., the number of edges along the path. If $v_1 = v_k$, the path is called *closed*. If no node except the first and the last one appears twice in a closed path, it is called a *cycle*. Finally, a graph that can be drawn on a paper such that no two edges intersect is called a *planar graph*.

Example 1. In Fig. 4.8, the graph $G = (\{1, 2, 3, 4, 5, 6\}, \{\{1, 3\}, \{3, 4\}, \{4, 1\}, \{4, 2\}, \{6, 1\}\})$ is shown. The nodes are represented by circles and the edges by lines connecting the circles. The graph has six vertices and five edges; e.g., nodes 3 and 4 are adjacent. The set of neighbors of vertex 1 is $N(1) = \{3, 4, 6\}$. Thus, node 1 has degree 3 while node 2 has only degree 1. Node 5 is isolated. The graph contains the path 6, 1, 4, 3 from node 6 to node 3 of length 3 and the cycle 1, 3, 4, 1.

The interactions of the Hamiltonian (4.2) can be represented by a graph G , where the sites of the lattice, holding the spins, are the vertices $i \in V$, and the interactions are the edges $e \in E$ (bonds). Since the strength of the interaction varies from edge to edge, we have to attach *edge weights*. This leads to

Definition 2. A weighted graph $G = (V, E, \omega)$ is a graph with edge weights $\omega : E \rightarrow \mathbb{R}$.

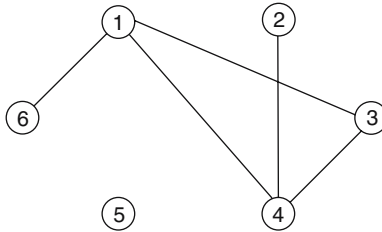


Fig. 4.8. An undirected graph

² For *directed* graphs, edges have an orientation. An edge from vertex i to vertex j is denoted as (i, j) , and it is different from an edge (j, i) from j to i .

Hence, for the spin-glass Hamiltonian, we have $\omega(\{i, j\}) = J_{ij}$. For each subset of edges $L \subset E$, we define the weight of the subset as the sum of the weights of the edges in the subset: $w(L) = \sum_{e \in L} w(e)$. One can interpret the weights of the edges as distances between two adjacent vertices. In this case, if the edges $L = \{\{v_i, v_{i+1}\} | i = 1, \dots, k-1\}$ connect the k vertices v_1, \dots, v_k of a path, the length of the path is now $w(L)$ instead of just $k-1$, the value for unweighted graphs. The *shortest path problem* is to find the shortest path in a graph connecting two given vertices i and j . This is a standard problem in algorithmic graph theory, and can be solved conveniently using, e.g., the Dijkstra algorithm [45]. We will need shortest path calculations below as auxiliary tools. The main algorithmic problem we have to solve is to obtain a so-called minimum-weight perfect matching on a graph G'' , which is derived from the interaction graph. Before we explain the construction of G'' step by step, we define matchings in general.

Definition 3. Given a graph $G = (V, E)$, a matching $M \subset E$ is a subset of edges, such that no two edges in M are incident to the same vertex [48, 49], i.e., for all vertices $i \in V$, we have $i \in e$ for at most one edge $e \in M$.

An edge contained in a given matching is called *matched*, other edges are *free*. A vertex belonging to an edge $e \in M$ is *matched*, others are *exposed* or *free*. If $e = \{i, j\}$ is matched, then i and j are called *mates*.

A matching M of maximum cardinality is called *maximum-cardinality matching*. A matching is *perfect* if it leaves no exposed vertices, hence it is automatically a maximum-cardinality matching. On the other hand, not every maximum-cardinality matching is perfect. The matching of minimum cardinality is trivially always the empty set.

Example 2. Matching

In Fig. 4.9, a sample graph is shown. Edges contained in the matching are indicated by *thick lines*. The matching shown in the *left half* is $M = \{\{1, 4\}, \{2, 5\}\}$. This means, e.g., edge $\{1, 4\}$ is matched, while edge $\{3, 4\}$ is free. Vertices 1, 2, 4 and 5 are matched, while vertices 3 and 6 are exposed. In the *right half* of the figure, a perfect matching $M = \{\{1, 5\}, \{2, 6\}, \{3, 4\}\}$ is shown, i.e., there are no exposed vertices.

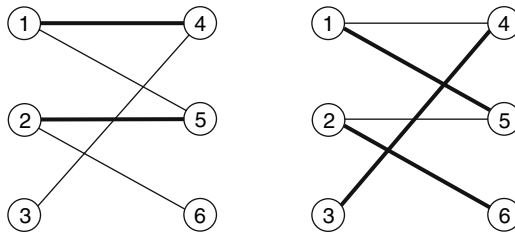


Fig. 4.9. Example graph for matching, see text

Having a weighted graph $G = (V, E, w)$, we consider also *weighted matchings*, with the weight of a matching given by the sum of the weights of all matched edges.

Definition 4. *M is a maximum-weight (minimum-weight) matching if its total weight assumes a maximum (minimum) with respect to all possible matchings.*

M is a maximum-weight (minimum-weight) perfect matching if its total weight assumes a maximum (minimum) with respect to (only) all perfect matchings.

Now, we turn back to the planar two-dimensional spin glasses and show step by step how the calculation of GSs of (4.2) can be mapped on the minimum-weight perfect-matching problem [37]. We start with the two-dimensional spin glass with free boundary conditions in all directions, shown in Fig. 4.6. We assume a configuration where all spins are “up”, i.e., $\sigma_i = +1 \forall i \in V$. This means all ferromagnetic bonds will be satisfied, since all pairs of interacting spins are trivially in the same orientation, while all antiferromagnetic bonds are not satisfied. Since there are 25 ferromagnetic bonds with $J_{ij} = +J$ and 15 antiferromagnetic bonds with $J_{ij} = -J$, the total energy of the configuration is $E = -25J + 15J = -10J$. Now, we draw *dashed lines* perpendicular to all non-satisfied bonds, the result is shown in Fig. 4.10.

This set of perpendicular *dashed lines* can be seen as subset of edges in a new *dual* graph $G' = (V', E')$, which is now defined. The vertices of G' consist of the set of all elementary cycles p with four edges, i.e., of length four. These cycles are called *plaquettes*. In general, a set of plaquettes is defined as a (non-unique) subset P of all cycles of a graph such that each possible cycle can be composed from a symmetric difference (i.e., $A \Delta B = (A \cup B) \setminus (A \cap B)$ for sets A, B) of members from some P . One can show [37] that a set $L \subset E$ of unsatisfied bonds is physical, i.e., corresponds to a spin configuration, if each frustrated (unfrustrated) plaquette contains an odd (even) number of edges in L . In case of free boundary conditions in all directions, as in the graph in Fig. 4.6, the “large” cycle surrounding the system, i.e., consisting of the boundary spins of the full system, is a member of V' , while for periodic boundary conditions only in the x direction, the two cycles containing all spins at the top and all spins at the bottom, respectively, are added. By adding these two “extra” plaquettes, each bond of the original graph is contained in exactly two cycles of V' . This allows to choose the edges in E' as those elements $\{p_1, p_2\}$, where in the original graph G , the plaquettes p_1 and p_2 have exactly one bond in common (denoted as $J(p_1, p_2)$), i.e., all neighboring plaquettes. Since each edge $\{p_1, p_2\}$ in G' corresponds exactly to the bond $J(p_1, p_2)$ crossed in G , we can assign also weights to the edges of G' by choosing $w'(\{p_1, p_2\}) = |J(p_1, p_2)|$. We will show below that this choice is useful. As an example, in the *top* of Fig. 4.11, the resulting graph G' for G from Fig. 4.6 is shown (without edge weights). Note that for the $\pm J$ model, we have the

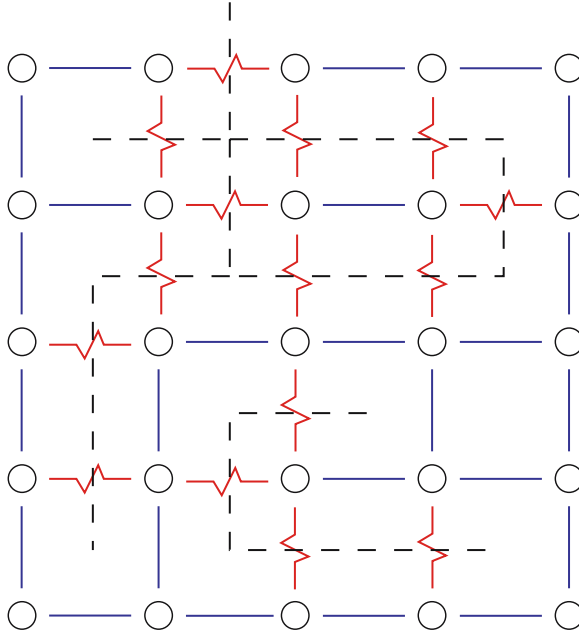


Fig. 4.10. The two-dimensional spin glass, having free boundary conditions in all directions, from Fig. 4.6. All spins are assumed to be “up” $\sigma_i = 1$. *Dashed lines* are drawn perpendicular to unsatisfied edges, which are the antiferromagnetic edges in this case

weight $w'(\{p_1, p_2\}) = J$ for all edges. In the *bottom*, G' for a graph similar to the graph of Fig. 4.6 is shown, except that it has periodic boundary conditions in the x direction.

Note that this construction, as presented here, is only for planar graphs. One could define a dual G' also for a spin interaction graph with periodic boundary conditions in all directions, but in this case, one cannot use G' in connection with a matching problem to calculate the GS. We will show an example at the end of this section.

In Fig. 4.12, the graph from Fig. 4.10 is repeated, but now the vertices of G' are also shown. In addition, the frustrated plaquettes are marked by capital letters, i.e., those plaquettes which contain an odd number of negative bonds. Note that also the large plaquette A surrounding the system is frustrated. Hence, the set of *dashed lines* represents a subset \mathcal{L} of edges from E' . Since they cross the bonds of G which are unsatisfied in configuration $\{\sigma_i\}$, we can rewrite the energy $H(\{\sigma_i\})$ as

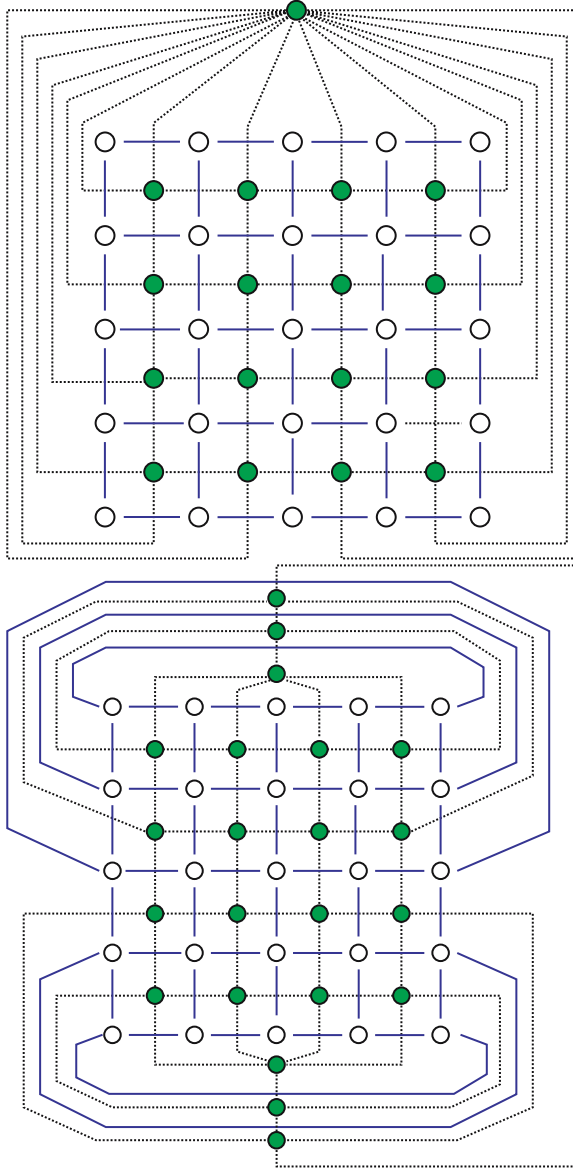


Fig. 4.11. The dual graph G' for the graph from Fig. 4.6. The plaquettes p are represented by *filled circles* inside the elementary cycles. The large plaquette surrounding the system is represented by a circle outside the graph G . The edges of the dual G' are denoted by *dashed lines*. Note that we draw the bonds of G here just as *thin lines*, irrespectively of their sign and magnitude. In the *top*, G' is shown for free boundary conditions in all directions (as in Fig. 4.6), in the *bottom* for the case where G had periodic boundary conditions in the x direction

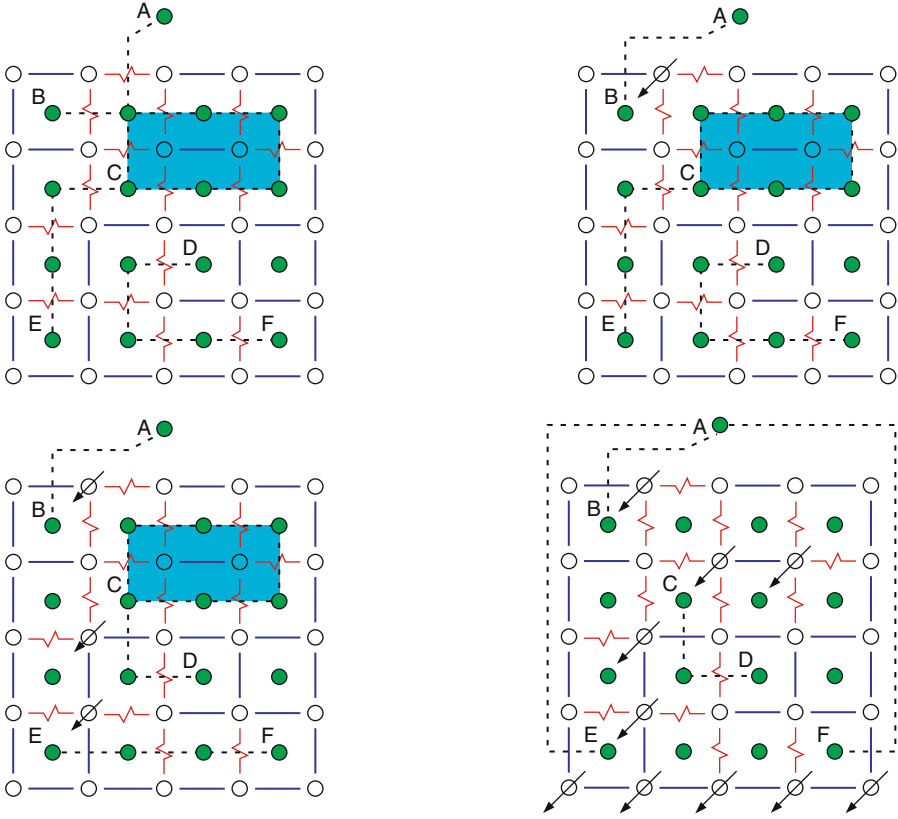


Fig. 4.12. The two-dimensional spin glass with free boundary conditions from Fig. 4.6 In the *top left*, all spins are assumed to be “up” $\sigma_i = 1$. Dashed lines indicate the edges present in the set \mathcal{L} of the dual graph $G' = (V', E')$ (see text). All edges in E' are either contained in paths connecting frustrated plaquettes (denoted by capital letters) or in cycles (*shaded area*). In the *top right*, the situation is shown, which arises, when the second spin in the top row is flipped. In the *lower left*, in addition the second spins of the third and fourth row are flipped. In the *lower right*, a GS is shown

$$\begin{aligned}
 H(\{\sigma_i\}) &= \sum_{e' \in \mathcal{L}} w'(e') - \sum_{e' \in E' \setminus \mathcal{L}} w'(e') \\
 &= 2 \sum_{e' \in \mathcal{L}} w'(e') - \sum_{e' \in E'} w'(e') \\
 &= 2w'(\mathcal{L}) - w'(E').
 \end{aligned} \tag{4.6}$$

Therefore, in this expression, each unsatisfied bond $\{i, j\}$ of the original graph G , corresponding to an edge $e' \in \mathcal{L}$, contributes a positive energy $w'(e') = |J_{ij}|$ and each satisfied bond, corresponding to an edge $e' \in E' \setminus \mathcal{L}$,

contributes a negative energy $-w'(e') = -|J_{ij}|$. Note that in the second line, the second term is a constant which does not depend on the spin configuration.

If we now take a closer look at Fig. 4.12, we observe that *all* edges from \mathcal{L} either are contained in paths joining frustrated plaquettes or are contained in cycles. Here, we have paths from A to B, from C to E and from D to F, and a cycle of length 6 (*shaded area*). Note that this way to describe \mathcal{L} is not unique. First, one can always restrict the description in a way that each edge from \mathcal{L} is contained in exactly one path or cycle. Still there are ambiguities, e.g., one could also describe the situation by a path from B to C and another (very long) path from A to E, without having a cycle in this case. It is not important that several ways to describe a spin configuration via paths and cycles are existing, it is only important that they exhibit the same set \mathcal{L} , hence the same energy.

This description via cycles and paths joining frustrated plaquettes is not only valid for this special configuration $\sigma_i = 1$, but it is valid for *all possible* spin configurations. If we flip, for example, the second spin in the *top row*, we change the state of all neighboring bonds satisfied \leftrightarrow unsatisfied. This means that the path connecting the frustrated plaquette B in the *upper left corner* with the frustrated plaquette A is just redirected, see *upper right* of Fig. 4.12. Previously, the weight of the path from A to B contributed two edges to \mathcal{L} and a value $2J$ to $w(\mathcal{L})$, now it contributes just one edge and the weight J . Therefore, the total energy is decreased to $E = -26 + 14 = -12$.

In a similar way, the configuration changes, when in the third and fourth rows each time the second spin is flipped; see *lower left* of Fig. 4.12. Still, all frustrated plaquettes are connected pairwise, but now there are paths from C to D and from E to F, where path $C \rightarrow D$ contributes a weight $2J$ and path $E \rightarrow F$ contributes a weight $3J$ to the total weight. Hence, the energy is now $E = -28 + 12 = -16$.

We are finally interested in obtaining a GS. Looking at (4.6), one observes that minimizing the energy is equivalent to minimizing the total weight $w(\mathcal{L})$ of edges in \mathcal{L} . We have already decreased the total weight by the spin flips shown before. Also, we can decrease the total energy always by removing *all* cycles in \mathcal{L} . This is achieved by just flipping all spins surrounded by each cycle. Here, when we flip, the two spins in the *shaded area*, we remove six edges from \mathcal{L} , hence decreasing the energy to $E = -34 + 6 = -28$. There, we see that in a GS, no cycle will exist. Hence, a ground-state configuration can be described by a set \mathcal{L} of edges from E' which form paths connecting frustrated plaquettes. Each frustrated plaquette is connected to exactly one other frustrated plaquette. Finally, to minimize (4.6), these paths will be of minimum weight. If one calls the weights “distances”, this means that the frustrated plaquettes are connected by shortest paths in the GS. We see that in the *lower left* Fig. 4.12, E and F are connected by a path of weight (distance) $3J$. This can be further decreased by flipping all spins on the bottom row, leading to a path of weight $2J$ from E to F. Note that the path now includes plaquette A. We observe that one has again alternative but equivalent

descriptions of the situation, e.g., one could say that A to E and B to F are connected by paths in G' . The ground-state energy is $E = -35 + 5 = -30$.

To conclude, to obtain a GS, we just have to consider the frustrated plaquettes pairwise. Each frustrated plaquette is connected to exactly another frustrated plaquette. This means, we are looking for a perfect matching of frustrated plaquettes. Since the energy directly corresponds to the weight of the matching, we are looking for a minimum-weight perfect matching to obtain a GS. To formalize this, the graph $G'' = (F', F' \times F')$ is defined. The set F' of vertices just contains the frustrated plaquettes from V' , hence $F' \subset V'$. The graph G'' is a *complete* graph because in $F' \times F'$ all possible edges $\{f_1, f_2\}$ ($f_1, f_2 \in F'$) are contained. We assign weights by choosing $w''(\{f_1, f_2\})$ as the weight of the minimum-weight (shortest) path from f_1 to f_2 in G' . Hence, to obtain the GS of the two-dimensional spin glass, *two* optimizations have to be performed.

- First, the calculation of all minimum-weight (shortest) paths in G' between all pairs of frustrated plaquettes. For this purpose, a standard shortest path algorithm, e.g., the Dijkstra algorithm can be used from the literature [44, 45]. As example, in Fig. 4.13, the graph G'' obtained from G' for our example is shown.
- Second, a selection of the minimum-weight perfect matching of frustrated plaquettes, where the edge weights of the complete graph G'' are the

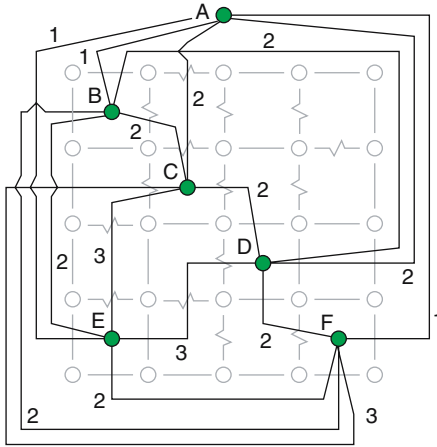


Fig. 4.13. The complete graph G'' of frustrated plaquettes obtained from G' . Each edge $\{f_1, f_2\}$ carries a weight w'' which is the minimum weight (shown in units of J) among all paths from f_1 to f_2 in G' . The edges are drawn in a way that they cross the edges of G' corresponding to a minimum weight. When interpreting the weights as distances, this is the length of a shortest path from f_1 to f_2 . Note that for G' , where all edge weights have value J , the length weight is just the number of edges

minimum-weights of the paths obtained in the first step. The calculation of minimum-weight perfect matchings is a problem which can be solved quickly on a computer, meaning that the running time increases only polynomially with the system size in the worst case. Again, standard algorithms from computer science can be applied here [46, 47]. Since these algorithms are rather complicated, at least in case of efficient implementations, we recommend to use existing computer programs from scientific libraries, e.g., the LEDA library [50]. The LEDA matching algorithm has a running time $O(nm \log n)$ for a graph with n vertices (here $n = |F'|$) and m edges (here $m = |F' \times F'| = |F'|^2$). You should note that these matching algorithms work only for integer weights. Hence, if systems with Gaussian disorder are treated, one has to choose a rather large value of J , e.g., $J = 10^4$ and truncate all weights to integer numbers. On the other hand, J should not be too large because otherwise integer overflows occur³.

Finally, a ground-state configuration can be obtained from the minimum-weight perfect matching. Exactly those bonds are not satisfied (in G), which are crossed by the minimum-weight paths in G' connecting the matched frustrated plaquettes (in G''). Note that due to the connection to shortest paths, due to the fact that each frustrated plaquette cannot be matched to more than one other plaquette and due to the minimality of the matching, it is impossible that more than one of the selected paths crosses a bond. The spins are then obtained, by first selecting (say) the upper-left spin either up or down. This corresponds to the trivial degeneracy due to the spin-flip symmetry of the Hamiltonian. Then one runs systematically through the lattice and sets neighbors of already set spins either to the same (if the connecting bond is satisfied ferromagnetic or unsatisfied antiferromagnetic) or to the opposite (if the connecting bond is unsatisfied ferromagnetic or satisfied antiferromagnetic) orientation. Note that the minimum-weight paths are sometimes not unique. For example, the path connecting plaquettes E to F can go through the bonds to the left or below of E , also either to the right or below of F . Hence, the ground-state spin configuration can also be non-trivially degenerate. Another source of degeneracy is that multiple minimum-weight matchings might exist, but not all different matchings lead to different spin configurations, see e.g., the *lower right part* of Fig. 4.12. More on how to treat degeneracy, you can find in [51]. Here, we will consider only systems with Gaussian disorder, which do not exhibit a degeneracy except the trivial two-fold.

Before the algorithm is summarized, it is outlined how a speed up can be obtained. For a system of size $N = L \times L$, there are $O(N) = O(L^2)$ frustrated plaquettes. Since the graph G'' is complete, it exhibits $m \in O(L^4)$ edges. This leads to a rather strongly increasing running time of $O(L^6 \log L^4)$,

³ For the LEDA library, the subroutine returns the actual weight of the minimum-weight perfect matching, which can be a rather large value. Since we do not need the value of this weight, only the matching itself, there is no harm if an overflow occurs here. But inside the matching subroutine, an overflow must not occur.

although it is still bounded by a polynomial. For the minimum-weight perfect matchings, one observes that for random samples, “almost never” edges in G'' with “large” weight are contained in matchings. Hence, one can safely remove all edges from G'' with a weight larger than some w_{\max} . For maximum performance, this can be done already when calculating the shortest paths. Hence, one has to suitably modify the above-mentioned Dijkstra algorithm, such that paths which extend beyond a length of w_{\max} are not considered any more. Fortunately, the Dijkstra algorithm is quite simple, such that one can implement it, including the modification, oneself. From numerical experiments, testing whether the result depends on w_{\max} , one finds that $w_{\max} = 6J$ is a safe value for the $\pm J$ and the Gaussian spin glass⁴.

Hence, to summarize, the calculation of a GS of a planar Ising spin glass is performed as follows, for each realization of the bonds:

1. Construct the dual graph $G' = (V', E')$. The vertices V' are the elementary four-bond plaquettes p (plus one or two large “extra” plaquettes, see above) and the edges E' connect neighboring plaquettes (p_1, p_2) . Each edge carries a weight $|J(p_1, p_2)|$, where $J(p_1, p_2)$ is the edge common to p_1 and p_2 .
2. Determine frustrated plaquettes among the $p \in V'$.
3. Calculate the minimum-weight (shortest) paths in G' up to weight (length) w_{\max} using the modified Dijkstra shortest path algorithm.
4. Construct graph $G'' = (F', E'')$ with frustrated plaquettes f as vertices. All pairs of frustrated plaquettes are connected by edges $\{f_1, f_2\} \in E''$, where the minimum-weight (shortest) path from f_1 to f_2 in G' has a weight (length) lower or equal to w_{\max} . These edges in G'' carry the weight (length) of the corresponding paths (in G').
5. Calculate a minimum-weight perfect matching M on G'' .
6. Determine the unsatisfied edges in G as the edges crossed by paths in G'' connecting frustrated plaquettes which are matched in M .
7. Calculate a spin configuration from the matching. Start by setting one arbitrarily chosen spin to randomly “up” (+1) or “down” (−1). Iteratively, set neighbors of already determined spins according to the state (satisfied/unsatisfied) of the bonds connecting the pairs of spins.

This section is closed by an example, showing that the above presented algorithm does not work for non-planar systems. Consider for example a two-dimensional system with periodic boundary conditions in both directions. The graph representing these interactions is not planar, but can be drawn on the surface of a torus, see Fig. 4.14. For simplicity, we now assume that all interactions are ferromagnetic, except one “shaded” column of parallel bonds, which wraps around the system. This corresponds to a ferromagnet with periodic

⁴ Note that there are more general models, e.g., the $\pm J$ random-bond model, where the fraction of ferromagnetic and antiferromagnetic bonds is not equal. For those models, usually w_{\max} must be a bit higher.

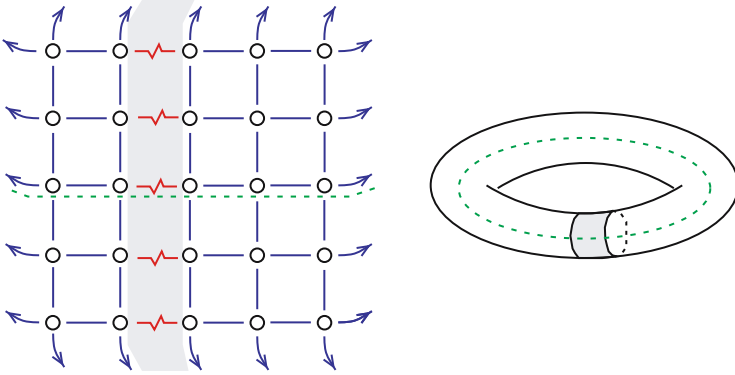


Fig. 4.14. A two-dimensional system with periodic boundary conditions in both directions (*left*). All bonds are ferromagnetic except one column of parallel antiferromagnetic bonds (*shaded area*) wrapping top-down around the system. The *dashed line* represents a loop wrapping left-right around the system. This system can be drawn on a torus (*right*)

boundary conditions in one direction and, realized by the column of antiferromagnetic bonds, antiperiodic boundary conditions in the other direction. Note that each bond is contained in exactly two four-bond plaquettes, hence this is true in particular for the antiferromagnetic bonds. Furthermore, each plaquette, which is contained in this “shaded” column wrapping around the system, contains exactly two antiferromagnetic bonds. All other four-bond plaquettes are purely ferromagnetic. This means that there are no frustrated four-bond plaquettes at all. Nevertheless, it is not possible to satisfy all bonds. Since full ferromagnetic order (all spins pointing into the same direction) is a GS of the system, exactly all antiferromagnetic bonds are unsatisfied in this case. Thus, the GS configuration, which contains unsatisfied edges, cannot correspond to a matching of frustrated four-bond plaquettes because there are none of them.

The mathematical reason behind this failure of the matching approach [37] is briefed as follows. For any graph, there is always a set of plaquettes P , i.e., according to the definition given above, each cycle in the graph can be composed from a symmetric difference of members from P . For the two-dimensional system with periodic boundary conditions, the four-bond plaquettes are not enough. For example, a circular cycle which wraps left/right around the system (*dashed line* in Fig. 4.14) cannot be composed from a symmetric difference of the four-bond plaquettes. Note that this circular cycle is frustrated. This means, for the system shown in Fig. 4.14, that also a cycle wrapping left-right around the system and a cycle wrapping top-bottom around the system have to be present in P , in addition to all four-bond plaquettes. This means there are inevitable bonds which are contained in (at least) three plaquettes, i.e., the graph G' cannot be constructed and the approach presented in this chapter fails.

4.4 Droplets and Domain Walls

As already indicated at the beginning of this contribution, not only obtaining true ground states is interesting, but the calculation of excited states using ground-state algorithms is one major task to understand the behavior of two-dimensional spin glasses. One possible general approach consists of these three steps:

1. Calculate the GS $\{\sigma_i^{(0)}\}$ of a given realization and the GS energy E_0 .
2. Modify some of the couplings so that the GS is changed.
3. Calculate the GS $\{\sigma_i^{(m)}\}$ of the modified system, which is usually a low-lying excited state of the original realization. The ground-state energy of the modified system is denoted by $E_0^{(m)}$.

Note that the algorithm presented in the last chapter breaks the spin-flip symmetry by choosing the upper left spin “up”, hence indeed a unique GS can be assumed here. Here, we will consider two types of excited states, *domain walls* and *droplets*, which play a major role in the theoretical study of spin glasses. Other types of excitations, which can be generated using ground-state algorithms in the same spirit, are discussed in the literature [27, 52, 53].

A DW spanning the whole system can be generated, e.g., by switching the boundary conditions from periodic to antiperiodic in one direction. This is done by taking one column of bonds, e.g., those which “wrap around the system boundaries”, and inverting the sign of all bonds in this column, see Fig. 4.15.

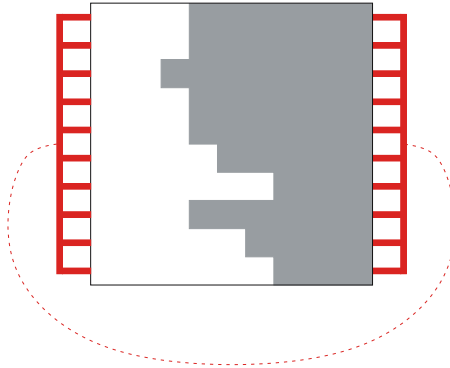


Fig. 4.15. Method used to generate DWs. After calculating the GS, the signs of all bonds connecting the pairs of spins in the first and last column (represented here by the *thick broken line*) are inverted. In this way, two domains are generated; one, where the spins still have their GS orientations (indicated by the *light area*); another, where the spins have opposite sign with respect to the GS (*dark area*). Note that the DW separating the two domains runs not necessarily “in the middle” of the system. Hence, for some realizations, the DW might even cross the line of inverted bonds

After calculating the GS with the modified system, the pairs of spins touching most⁵ of the modified bonds will have a relative orientation to each other, which is different from the GS obtained with the original bonds previously. In this way, two domains are generated; one, where the spins have their GS orientation; another, where the spins have opposite sign with respect to the GS. Note that *inside* the domains, all pairs of adjacent spins still have the relative GS orientation to each other. The two domains are separated by the DW⁶, which will adjust in a manner that the total energy is minimized. Hence, the GS energy of the modified system is locally everywhere the same as in $\{\sigma_i^{(0)}\}$, except at the DW. Thus, when calculating the energy difference between the GS energies E_0 of the original system and E_0^m of the modified system, one obtains exactly the energy of the DW: $\Delta E \equiv E_0^m - E_0$.

What can we learn from the behavior of the domain-wall energy? We will see that this approach allows us to determine whether an ordered phase can exist at low temperature. The basic idea is that the inversion of the bonds in one column corresponds roughly to a real-space renormalization [54, 55] of the system [56]. This means that one takes blocks of b^d spins, and replaces them by one *block spin*. One would like the renormalized system to be described by the same type of interactions as the original system. This means that the interactions between all members of two different blocks of spins are replaced by just one pair interaction between the two block spins. In general, one can determine the value of the interaction between two spins by calculating the energy of the system, flipping one spin, calculating again the energy and taking (half) the difference between the two energies, see Fig. 4.16. This flipping of one block spin corresponds to switching the boundary conditions from periodic to antiperiodic [56]. The only difference is that now the block size is of the

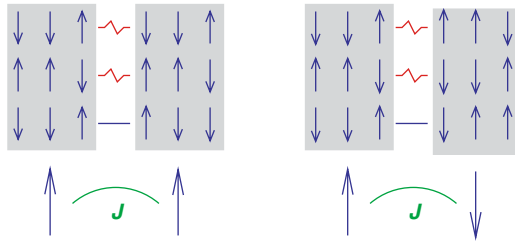


Fig. 4.16. Groups of b^d spins are grouped together in *block spins*, here $b = 3$ and $d = 2$. One can determine the value of the effective coupling $J(b)$ between the block spins by calculating twice, first with both block spins parallel ($E_1 = -J(b)S_1S_2 = -J$), then with both block spins antiparallel ($E_2 = +J(b)$), hence $J(b) = (E_2 - E_1)/2$

⁵ The DW generated might cross the modified bonds. At these few positions, the adjacent spins have still the relative GS orientation.

⁶ Formally, when comparing with the original GS, the two domains are also separated by a second DW which is just a straight line along the modified bonds, but this DW does not contribute to the energy change.

order of the full system size, i. e., $b \sim L$, and that the system consists of just two block spins. In this case, it is not a priori defined, which spins belong to which block, because the DW will be the boundary between the two block spins. Hence, the block spins do not have hypercubic shape, and the block spin size is not exactly $L/2$, but the spirit of the procedure of generating DWs is similar to the renormalization approach, and the size of the block spins is of order $O(L)$.

Since the original system is characterized by a quenched disorder, this will be the same for the renormalized system as well, but the distribution might be different. When averaging over many different realizations of the disorder, one will obtain distributions $P_L(\Delta E)$ of domain-wall energies, i. e., describing renormalized coupling strengths $J(L)$. Going to larger and larger system sizes L when calculating the domain-wall energy corresponds to taking larger and larger block spins. What will we learn from the behavior of $P_L(\Delta E)$? First, we consider the first moment, i. e., the average. Switching all bonds in one column sometimes decreases the ground-state energy with respect to the original system, but sometimes the energy is increased. Since no case is particularly favored, the distributions $P_L(\Delta)$ will be symmetric with mean zero for all sizes L , so this does not give any information about the coupling of the block spins. Instead, a measure for the strength of the interaction distribution will be the width of the distribution, or, equivalently, the behavior of the absolute value $|\Delta E|$. This is the same as for the original distributions (4.3), (4.4), where the mean is zero, and the width (and also mean of $|J_{ij}|$) is proportional to the coupling strength J . From simple scaling arguments [21, 56] and in numerical experiments, one finds a power-law behavior $|\Delta E| \sim L^\theta$, where θ is the so-called *stiffness exponent*, see below. If $\theta < 0$, then the interactions become weaker with growing block size. This means, in the limit of infinitely large blocks, the block spins are no longer coupled, hence the system behaves paramagnetically at any finite temperature, i. e., $T_G = 0$. For this case, one can easily understand the power-law behavior and relate the stiffness exponent θ to the correlation-length exponent ν . Hence, we assume that approaching $T_G = 0$, the correlation length $\xi(T)$ diverges algebraically, like in standard second-order phase transitions, according to $\xi \sim (T/J)^{-\nu}$. When looking at the system of block spins of size b , with effective couplings $J(b)$, we measure the correlation length $\xi(b) \sim (T/J(b))^{-\nu}$. On the other hand, since all distances (in terms of spins) between block spins in the rescaled system are the measured distances in the original system divided by b , we have $\xi(b) = \xi/b$. Combining these two equations, and using $b \sim L$ for the domain-wall calculations, we get a power-law behavior $J(L)/J = T\xi(L)^{1/\nu}/J = T(\xi/L)^{1/\nu}/J = L^{-1/\nu}$, i. e., $\theta = -1/\nu$.

A power-law behavior of the average DW energy is indeed observed for the $d = 2$ EA model with Gaussian distribution of the interactions, where $\theta \approx -0.28$ [32, 34, 36, 56, 57], see Fig. 4.17. For the bimodal model, $\theta = 0$ was obtained. This corresponds to $\nu = \infty$, which agrees with computer

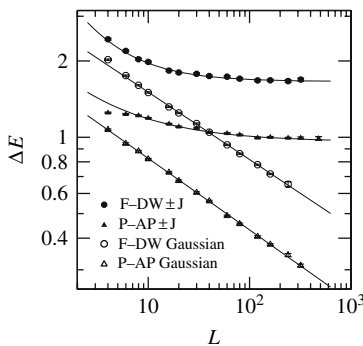


Fig. 4.17. Scaling of the DW energy as function of system size for Gaussian (*open symbols*, power-law behavior) and bimodal (*filled symbols*, convergence to constant) disorder. For both cases, two different ways of changing the boundary conditions were used. First, the method discussed here (“P-AP”) is applied. The other approach works by first choosing free boundary conditions and then introducing strong bonds to force the spins on opposite sides to be antiparallel with respect to the GS orientations. For details see [34]. The two different approaches lead, in the case of Gaussian disorder, to slightly different values of θ from the finite-size data. Using the *aspect-ratio scaling*, i.e., studying systems of sizes $L \times M$ with $L \gg M$ leads [57] to a universal exponent $\theta = -0.287$ in the thermodynamic limit

simulations⁷ of the bimodal $\pm J$ spin glass at finite temperatures, where it was found that the correlation length diverges exponentially, i.e., faster than any polynomial [35]. For larger dimensional spin glasses, where no polynomially running exact algorithms exist, positive values have been obtained, e.g., $\theta(d = 3) \approx 0.19$ [56, 59, 60] resp. $\theta(d = 4) \approx 0.65$ [61, 62]. For these systems, the couplings become stronger under renormalization, hence an ordered phase can exist at low temperatures, until entropic effects become too strong at higher temperature. Hence, we have seen that the calculation of DWs via optimization algorithms allows us to determine whether an ordered phase can exist at low temperatures. Now, we turn to the second kind of excitation discussed here, i.e., droplets.

As mentioned in Sect. 4.2, droplets are connected clusters of spins, which are reversed with respect to the GS, and which are of minimum free energy. For $T = 0$, the minimum free energy requirement translates to minimum energy conditions. This allows us to verify the scaling assumption (4.5) of the droplet scaling theory by GS calculations. We will consider two-dimensional spin glasses with free boundary conditions for the rest of this chapter.

A traditional approach of generating droplets was used by Kawashima and Aoki within a Monte Carlo simulation [63]. They first calculated the GS heuristically with an algorithm based on gradually “cooling” the system. Then, they

⁷ On the other hand, recent studies [58] claim that also for the $\pm J$ model, the correlation length diverges algebraically.

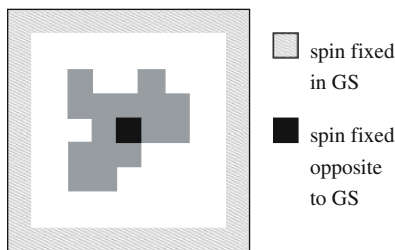


Fig. 4.18. Basic method to generate a droplet. After calculating the GS, fix the spins at the boundary in their GS orientation and fix one central spin in opposite GS orientation. A GS calculation with the fixed spins results in a droplet (black/grey area), consisting of spins opposite to the original GS orientations (white/shaded area)

recalculated the GS with the constraints that the spins on the boundary keep their GS orientation, while a central spin is flipped, see Fig. 4.18. Fixing the spins can be achieved by introducing strong local fields acting on the spins, with the direction of the fields chosen to point along the desired direction, hence one has to apply a Hamiltonian with a linear field term⁸. Since the droplet energy decreases with droplet size (since $\theta < 0$), for each given system the droplets become as large as possible at small temperature. Hence, this approach generates droplets of the order of the system size, i. e., $l \sim L$. Using this approach, small systems up to $L = 50$ with a Gaussian distribution of the interactions could be studied, and a scaling $\Delta E \sim L^{\theta'}$ of the droplet energy with $\theta' = -0.45(1)$ was found, which is significantly different from $\theta \approx -0.28$.

Since the range of system sizes in the work of Kawashima and Aoki is limited to $L \leq 50$, their result might have been an artifact of too-small sizes. Using matching algorithms, one can study much larger sizes. Unfortunately, it is not possible to treat local magnetic fields, i. e., one cannot fix a spin in some orientation. But it is possible to mimic this kind of generation of droplets in the following way. After obtaining the GS, several *hard bonds* are introduced. A hard bond is a bond with a high value of the absolute strength (one can imagine $J_{\text{big}} \sim 10^5 J$ or $J_{\text{big}} = 2N \times \max_{\langle i,j \rangle} \{J_{ij}\}$). The strength of a hard bond is so large such that the bond will be satisfied in *all* subsequent GS calculations⁹. Most of the hard bonds are used to ensure that neighboring spins i_0, j_0 have the same relative orientation as in the GS $\{\sigma_i^{(0)}\}$, i. e., one replaces bond $J_{i_0 j_0}$ by a bond with the value $J'_{i_0 j_0} = J_{\text{big}} \sigma_{i_0}^{(0)} \sigma_{j_0}^{(0)}$. An *inverted* hard bond has the opposite sign, i. e., it forces two neighboring spins to take orientations, which are different relative to the ground state orientations. This

⁸ Alternatively, one can just ignore the fixed spins in the second GS calculation and leave their current orientations. Then, the fixed spins act as local fields to their neighbors.

⁹ When working with a maximum weight w_{max} of the edges in the graph G'' of frustrated plaquettes, see p. 86, it is sufficient to chose $J_{\text{big}} > w_{\text{max}}$.

means in a GS calculation with the inverted hard bond, exactly one of the two spins will flip with respect to $\{\sigma_i^{(0)}\}$, the other spin will keep its previous GS orientation. Note that the subsystem of all hard bonds together must not exhibit frustration because no hard bond should be broken when a new GS is calculated.

Now we describe in detail which hard bonds are introduced to obtain droplets. First, all boundary spins are fixed relative to each other by introducing hard bonds around the border, see Fig. 4.19. The signs of these hard bonds are chosen such that they are compatible with the GS orientations of the spins they connect. This keeps the spins on the boundary in their GS orientations. In addition, one single inverted hard bond is introduced near the center of the system. In a subsequent GS calculation, with all other bonds not altered, this forces a DW to run through the inverted hard bond. Since the domain wall cannot go to the boundary because of the presence of the other hard bonds, it must close onto itself. Hence, a kind of droplet is generated, called *single-bond droplet*. The difference to the Kawashima/Akoi droplets is that the position of the DW of the droplet is pinned at one position, while within the Kawashima/Akoi approach, the DW can adjust without constraint.

This shows up in the results. The energy of this droplet is the energy of the resulting configuration calculated using the original bond configuration (i.e., without hard bonds), the original GS energy being deduced. In Fig. 4.20, the average droplet energy is shown as a function of system size for $L = 6$ to $L = 240$, averaged over more than 3000 samples for each size. A double-logarithmic plot (not shown) shows a curvature, which is not compatible with a convergence of the droplet energy to zero, but compatible with a convergence to a non-zero energy. This seems plausible because the choice that a certain bond, i.e., the inverted hard bond in the modified system, has to belong to the

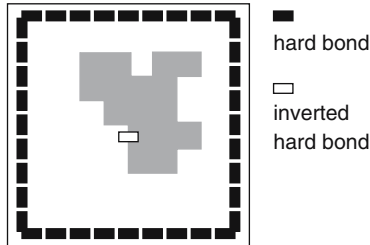


Fig. 4.19. Example of the generation of a droplet via introducing hard bonds (*small black rectangles*) and one inverted hard bond (*small white rectangle*), after the GS of the system has been obtained. The following GS calculation including the hard bonds generates two domains, one where the spins have the GS orientation (*white area*), one where the spin have the opposite GS orientation (*dark area*). A DW separates these domains and is forced to run through the inverted hard bond, and it must not run through the other hard bonds. Hence, a closed DW of minimum energy is generated, i.e., a certain droplet

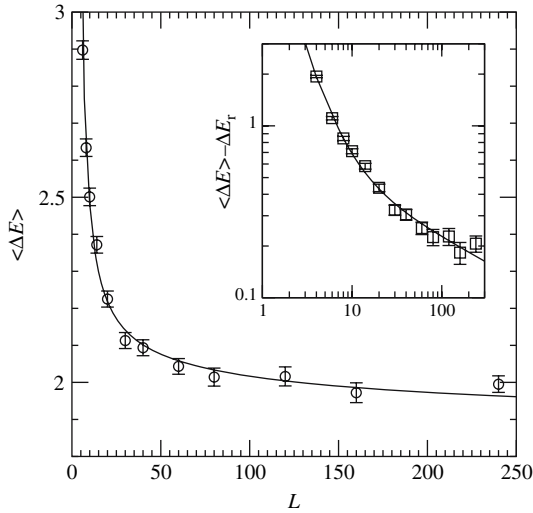


Fig. 4.20. Average energy of *single-bond* droplets. The line shows a fit to the function $E(L) = E_r + AL^\theta + BL^{-\omega}$ with $\theta = -0.29$ resulting in $\Delta E_r = 1.79(6)$ and $\omega = -1.8(2)$. The inset shows the same data with the limiting energy ΔE_r subtracted in a double logarithmic plot

minimum domain wall, imposes a penalty on the energy of the droplet. This energy should be of the order of the coupling constant $J = 1$. And indeed, when fitting to a function

$$E(L) = E_r + AL^\theta + BL^{-\omega} \quad (4.7)$$

with fixing $\theta = -0.29$ to the DW value, one obtains $E_r = 1.79(6)$ and $\omega = 1.8(2)$, with a fair quality of the fit [64], $Q = 0.14$. Hence, the leading behavior of the convergence toward a constant energy is compatible with the finite-size scaling of the DW energy shown above, as assumed by the droplet theory.

Nevertheless, one can generate droplets such that they mimic much better the approach of Kawashima and Aoki. For this purpose, instead of one single inverted hard bond, another line of hard bonds is created which runs from the middle of (say) the left border to a pre-chosen center spin, again fixing the bond's spins in their relative GS orientations. Next, the sign of exactly *one* hard bond on this line is inverted, see Fig. 4.21. Also in this case, a GS of the modified realization is calculated. With respect to the original GS, the result is a minimum energy excitation, fulfilling the constraints that it contains the center spin, that it does not run beyond the boundary and that it has a surface which runs through the hard bond which has been inverted. Hence, it will be a constrained droplet.

Note that this procedure alone does not generate the droplets as defined above because the border of the droplet is constrained to run through the

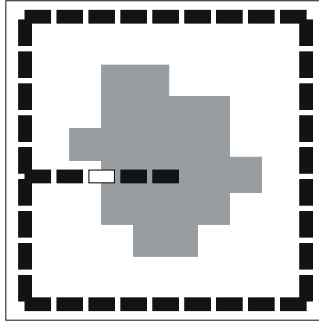


Fig. 4.21. Method used to generate the *cross* droplets. After calculating the GS, several hard bonds (*thick lines*) are introduced, one hard bond is inverted (see triangle), leading to the appearance of an excitation (*dark inner area*)

inverted hard bond, while it can fluctuate freely for the original droplets. Therefore, for each realization, this procedure is iterated over all the bonds which are located on the line from the boundary to the center, when in each case exactly one hard bond is inverted. Among all $L/2$ excitations generated in this way, the one exhibiting the lowest energy is selected as the minimum energy droplet. Hence, the DW of a such defined droplet must cross the imaginary line between the left boundary and the center spins exactly once, and may fluctuate freely everywhere else. Therefore, to introduce even more flexibility of the DW, the full procedure is iterated over all four choices of lines of bonds running from the left, right, top and bottom boundary to the center spin. This means, for each realization finally the true minimum droplet is selected as that one having the minimum energy among all $2L - 2$ excitations generated in this way. This approach generates droplets, called *cross droplets*, which are very similar to the droplets of Kawashima and Aoki, except that no droplets can be generated, where the boundary fluctuates freely in all four directions at the same time. However, it was found that these strongly fluctuating droplets play a minor role [65]; their influence on the final result is smaller than the fluctuations resulting from the statistics.

Using this approach, droplets in systems up to size $L = 160$ could be studied [65]. This is smaller than the range of sizes studied for the DWs because here many, i.e., $2L - 2$, GS calculations are necessary to obtain just one droplet. For small sizes, see Fig. 4.22, the result was exactly the same as that found by Kawashima and Aoki. But at intermediate sizes a crossover occurs, and for larger sizes a power-law behavior is found, which is indeed compatible with $\theta' = \theta \approx -0.28$. This means, by going to larger system sizes, one central proposition of the droplet scaling theory could be verified for two-dimensional spin glasses.

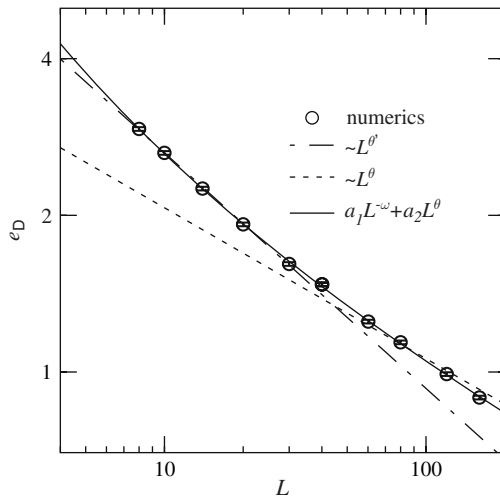


Fig. 4.22. Average *cross* droplet energy E as a function of the system size. The *dashed straight lines* represent algebraic functions with exponents $\theta' = -0.47$ and $\theta = -0.29$, while the *full curved line* represents the function from (4.7) with $E_r \equiv 0$, $\omega = 1$, $\theta = -0.29$

4.5 Energy Barriers

So far, we have been concerned with the static properties of two-dimensional spin glasses at zero temperature, i.e., we have calculated ground states and excitations using a matching approach. In this section, we want to address dynamical properties. We do *not* perform dynamic simulations, instead we look at properties of the configuration landscape which are responsible for the dynamical behavior. Particular obstacles to fast dynamics are *energy barriers* in the configuration landscape. In thermal equilibrium, the probability to surmount a barrier increases exponentially with the barrier height [66].

In order to assess how the dynamic time scales behave as a function of system size, one can look at the scaling behavior of such energy barriers. It is generally assumed that the barrier to be surmounted to create a droplet of linear extent L has an energy which scales as L^ψ where $\theta \leq \psi \leq d - 1$ for dimension d . The argument for these inequalities goes as follows: the barrier must be at least as large as the energy required to create the domain, hence $\theta \leq \psi$; the upper limit is due to the fact that the barrier must be lower than the energy of a compact droplet with a non-fractal surface containing the same number of reversed spins [24]. While many numerical studies have been done to calculate the exponent θ , the author is aware of only one direct numerical estimate of ψ and that was for two dimensions [68]. It was equal to the upper bound i.e., $\psi = d - 1$, but only small systems were studied ($L \leq 6$).

To find numerically the lowest barrier between two given states is [67] also an NP-hard problem like the GS calculation in higher dimensions (see

beginning of Sect. 4.3), even in two dimensions. Hence, it is not possible to address this problem exactly for larger than tiny sizes. Here, we will present a hierarchical approach to calculate approximate minimum barriers. The basic operational tool will be again the GS calculation via the matching approach, including the introduction of additional constraints via suitably placed hard bonds.

Next, the general idea of the algorithm is explained. Then, it is shown how it is implemented for two-dimensional spin glasses. Finally, a result for the scaling of the barrier height with the system size L is presented.

Given are two configurations $\sigma_1^{(0)}, \sigma_2^{(0)}$. The general goal is to find a (so-called *reaction*) *path* in configuration space between $\sigma_1^{(0)}, \sigma_2^{(0)}$ whose energy E_{\max} at the highest point along the path is as low as possible, i.e., a minimum path in that sense. The energy barrier is then $\Delta E_B = E_{\max} - H(\sigma_1^{(0)})$. A standard example from biophysics is the path between a folded and an unfolded configuration of a protein. The standard way to describe the transition between the two configurations is by using a *reaction coordinate* $\tau \in [\tau_1, \tau_2]$, which parametrizes in some way (see below) the configurations $\sigma(\tau)$ along the path. For a protein, the reaction path could be the bond angle for a crucial side group which has to be rotated for the folding. In our case, for the two-dimensional spin glasses, we do *not* know the reaction path in advance, we only have $\sigma(\tau_1) = \sigma_1^{(0)}, \sigma(\tau_2) = \sigma_2^{(0)}$. The main ingredient of the approach here will be a method to select one “physical” reaction coordinate τ which characterizes the transition very well and leads to a good approximation of the minimum reaction path.

Once the reaction coordinate is available, the basic operation is to calculate a ground state of the system constraint to a given value of the reaction coordinate. One can now get a rough idea of the transition, if one varies τ between τ_1 and τ_2 and generates a finite set of values $\tau \in \{\tau_1 = \tau^0 < \tau^1 < \dots < \tau^{k-1} < \tau^k = \tau_2\}$. For each of these values, using the ground-state calculation, we then obtain minimum energy configurations σ^i ($i = 1, \dots, k$) with a minimization under the constraint $\tau = \tau^i$.

Hence, we get a set of energies $H(\sigma^i)$, which is a coarse-grained picture of the energy landscape encountered during the reaction path, see *upper figure* in Fig. 4.23. Technically, this coarse-grained path is determined by the set of *constraints* C^i which fix the path at $\tau = \tau^i$. Since the description of the path via constraints is more general, and in particular more suitable for our spin-glass problem, we will use this description. The reaction path so obtained is a reasonably good approximation for the true minimum reaction path because a ground state was calculated (under the given constraints) for each intermediate point. This is the *first basic idea* of our approach. This first coarse-grained path we denote as the path on *level one*. Nevertheless, the quality of the result depends on a good choice of τ , which is straightforward for the case of two-dimensional spin glasses, see below.

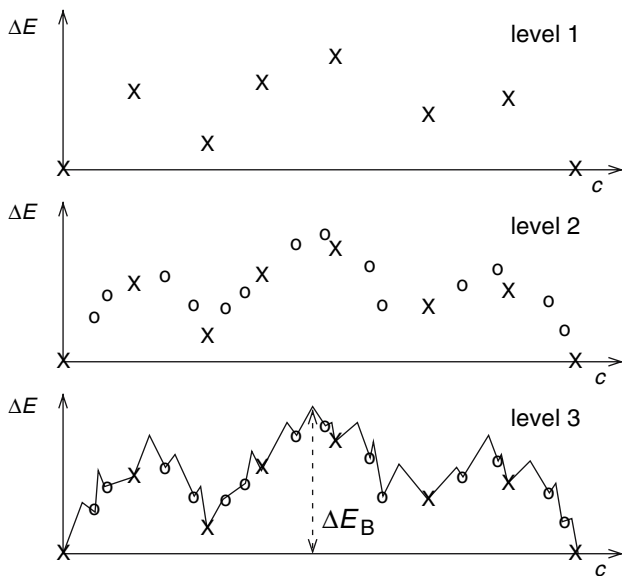


Fig. 4.23. Excitation energies ΔE for sequences of configurations σ generated by the algorithm

Now, it might be the case for two adjacent configurations σ^i, σ^{i+1} that these configurations are again separated by a high-energy barrier. An energy barrier might occur, if σ^i, σ^{i+1} differ by more than one variable. In general, for such a case, one can apply the same algorithm recursively for all adjacent configurations σ^i, σ^{i+1} where it is necessary. This is the *second basic idea* of our approach. Note that the reaction coordinate on the next level might be different from the reaction coordinate on the previous level, as it will be the case for two-dimensional spin glasses. For the protein example, the reaction coordinate might be the orientation of another side group. By considering *all* pairs of adjacent configurations σ^i, σ^{i+1} , as a result, one obtains the reaction path with higher level of details, i.e., a reaction path on *level two*. This leads to a refined picture of the energy landscape, see *middle figure* in Fig. 4.23. Note that within the optimization, the constraints which have appeared on the upper level will be also suitably included, i.e., $\tau \in [\tau^i, \tau^{i+1}]$ when looking at the case $\sigma^i \rightarrow \sigma^{i+1}$. This guarantees that one does not move “outside” the range of adjacent configurations from the previous level.

The whole approach is iterated on lower levels, leading to finer and finer descriptions of the reaction path and of the energy landscape along the path, see *lower figure* in Fig. 4.23. This is repeated until one is sure that there is no high-energy barrier between two adjacent configurations. For Ising spin systems, this is achieved when one arrives at the level of single-spin flips.

Next, it is shown explicitly, how the calculation of minimum barriers for two-dimensional spin glasses is performed. Rather than studying the barriers

to create droplets of order of the system size L , we will consider the computationally simpler task of determining upper bounds for the barrier separating the two ground states (GSs) related by a flip of all spins. This represents the highest barrier in the system and thus determines the longest time scale of the dynamics. It is equivalent to sweeping a DW through the system. Both types of barriers should be equivalent for two-dimensional spin glasses since DWs and droplets seem to share the same exponents, as we have seen in the previous section.

We will consider a system with free boundary condition. The bonds are drawn from a Gaussian distribution (4.3) of couplings with zero mean and unit width, which guarantees that the system just has two GSs $\{\sigma^0\}$ and $\{-\sigma^0\}$. We define the barrier to be the energy required to invert all spins in the GS within the context of single spin-flip dynamics, as in [68], i.e., the reaction path goes from $\{\sigma^0\}$ to $\{-\sigma^0\}$. Each trajectory of reversal is characterized by the highest maximum in the trajectory having energy ΔE_B , in excess of the GS energy, and the minimum barrier height is $E_B = \min(\Delta E_B)$, where the minimum is over all the possible trajectories.

All spin configurations can be described by the set of spins having $\{\sigma^0\}$ orientation, while the remaining spins have the $\{-\sigma^0\}$ orientation. Hence, each configuration is equivalent to a set of domain walls (DWs) separating the two GS orientations. Since these so defined DWs have always positive energies, our search for low-energy paths can be restricted to configurations which are separated by just *one* DW. Therefore, each configuration is described by one DW w which we assume to start and end somewhere at the (free) boundary. The path from $\{\sigma^0\}$ to $\{-\sigma^0\}$ will be equivalent to w sweeping, say, from left to right through the system via single spin flips. For our implementation, we will allow only that each spin flips exactly once along the reaction path, i.e., the DW cannot fluctuate back and forth. This is another major approximation, and as a consequence, we can finally only obtain an upper bound for the minimum barrier height ΔE_B instead of the true one.

The basic idea of the implementation of the approach for two-dimensional spin glasses is to use the position of one part of the DW wall as reaction coordinate. For level one of the energy-landscape hierarchy, we fix (“pin”) the DW, say, at different positions at the top boundary of the system and move this position from left to right through the system. The remaining part of the DW is allowed to adjust freely such that its energy becomes minimal. On higher levels of the iteration, a DW is moved between two given DWs which are adjacent on the preceding level. The process is repeated hierarchically until a sequence of N single spin flips from $\{\sigma^0\}$ to $\{-\sigma^0\}$ is obtained.

The calculation of the GS under certain constraints will be performed similarly to the calculation of droplets presented in the previous section. Hence, again the matching algorithm is applied and the constraints are implemented via hard bonds, some of them being inverted. In the previous section, DWs were introduced via inverting the boundary conditions in one direction. Equivalently, and more suitably for our purpose here, we introduce a horizontal line

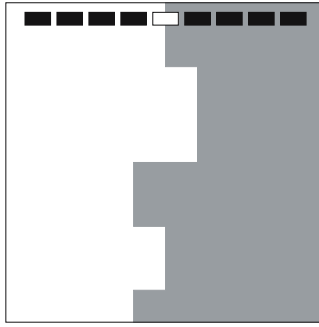


Fig. 4.24. Example of the generation of a DW via introducing hard bonds (*small black rectangles*) and one inverted hard bond (*small white rectangle*), after the GS of the system has been obtained. The DW separates these domains and is forced to run through the inverted hard bond, and it must not run through the other hard bonds

of hard bonds connecting all spins in the top row. If we calculated with this changed realization a new GS, we would get exactly the same GS again. To get something new, we furthermore invert exactly one of the hard bonds, say the bond J_{l_0, l_0+1} somewhere in the middle of the top row, see Fig. 4.24. Now we compute the GS of this changed realization. The inverted hard bond guarantees that spins l_0 and $l_0 + 1$ have opposite relative orientations to the original GS. Hence, a DW originates between spins l_0 and $l_0 + 1$. The other (non-inverted) hard bonds guarantee that all other spins at the top row have the same relative orientations as in the GS. This means, the DW has to leave the system at one of the other free boundaries, e.g., at the bottom row as shown in the example. Since the DW is obtained from another GS calculation, its energy is minimized under the constraint that its starting location is pinned between spin l_0 and $l_0 + 1$ and that it does not terminate at the top row. Everything else will be adjusted such that the energy is minimal. In the resulting configuration, all spins to the left of the DW will have one GS orientation, and all spins to the right of the DW will have the opposite GS orientation.

The basic idea to construct the reaction path on level one is to consider all possible positions of the inverted hard bond along the horizontal line, running from left to right, such that the DW is swept from left to right as well. This generates a sequence of DWs, see Fig. 4.25, describing the path on level one. The refinement of the path and the energy landscape is obtained by recursively finding sequences of DWs on level $n + 1$ which interpolate between adjacent DWs on level n again using straight lines along which an inverted hard bond is moved. We only use a generalization here: For the interpolation between pairs of DWs on lower levels below level 1, either a horizontal or a vertical line of hard bonds may be used, see below.

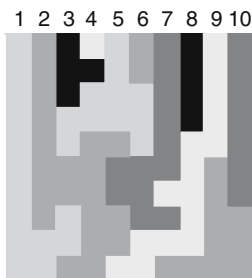


Fig. 4.25. A sample sequence of DWs generated by considering all different positions of the inverted hard bond along the *top horizontal line*, corresponding to level one of calculation of the reaction path. The different shaded regions show the different parts of the domains flipped when the i th bond is inverted. Hence, for the inverted bond at the leftmost position (connecting spins 1 and 2), the resulting GS exhibits a domain consisting of part 1 with one GS orientation, and another domain consisting of parts 2–10 with the other GS orientation. For the inverted bond connecting spins 2 and 3, the two domains consist of parts 1, 2 and 3–10, respectively, etc. The sequence of DWs generated in this way describes on a coarse-grained level the order in which one moves from one GS to the other GS

Note that also the initial situation on the first level of the above described hierarchy, i.e., the GSs $c_1^{(0)} = \{\sigma^0\}$ and $c_2^{(0)} = -\{\sigma^0\}$ can be described in the DW picture via two straight-line DWs being located at (“behind”) the left and right borders of the system, respectively. One can imagine that these initial configurations correspond to the situations where the DW has not yet entered the system, and where the DW has finally left the system, respectively. Hence, the task is on all levels of the hierarchy to interpolate between two DWs.

This means in general, two DWs w_1, w_2 are passed to the subroutine, called *seq*, which calculates on each level the path. Furthermore, we pass constraints C such that the bonds left of w_1 and right of w_2 are hard bonds (i.e., no hard bonds at all on level one). These hard bonds cause the spins left of w_1 and right of w_2 to be frozen independently into relative GS orientations. Thus, all subsequent DWs calculated on higher levels will run between w_1 and w_2 . This guarantees in the end that the domain wall does not fluctuate back and forth. Technically, it also accelerates the subsequent GS calculations considerably because hard bonds do not have to be considered during the minimization. The basic idea is now to generate a (partial) reaction path interpolating between w_1 and w_2 , i.e., to sweep a DW from w_1 to w_2 from left to right, by pinning it at one location through an inverted hard bond and moving the inverted hard bond such that it moves the DW from w_1 to w_2 . This is achieved here by *seq* by determining the longest straight (*horizontal* or *vertical*) separation between w_1 and w_2 which lies completely inside the region without hard bonds. Let $k + 1$ be the length of this separation. To construct sequences of constraints leading to this behavior, we add (inverted) hard bonds, such that the DW is effectively moved. Formally, we do this by

denoting with i_1, \dots, i_k, i_{k+1} the spins along this line, and by i_0 and i_{k+2} the spins which are reached when extending the separation in both directions by one spin. Then *seq* finally returns the sequence $\{C^1, \dots, C^k\}$ of constraints, which are defined as follows: C^l ($l = 1, \dots, k$) consists of the hard bonds $\{(i_0, i_1), (i_1, i_2), \dots, (i_k, i_{k+1}), (i_{k+1}, i_{k+2})\}$ where exactly the bond (i_l, i_{l+1}) is inverted¹⁰, the others are not inverted, see Fig. 4.26.

Thus, for the subsequent GS calculations with the constraints $C^l \cup C$, each time a domain wall is generated, which lies in the region between w_1 and w_2 and is forced by the inverted hard bond to run exactly between spins i_l and i_{l+1} , the DW is pinned between i_l and i_{l+1} . Going with l from 1 to k , each time calculating the GS, results in a sequence of DWs interpolating between w_1 and w_2 . For all pairs of adjacent domain walls generated in this way, the same procedure is continued recursively at the next level.

The hierarchical procedure stops for all pairs w_1, w_2 which are separated only by a line of spins of width 1. For this case, one can just flip in the region between w_1 and w_2 one spin after the other starting at one end. Hence, the full algorithm finally outputs a sequence of single spin flips corresponding to the movement of a DW from one end of the system to the other.

For each flipped spin, the energy of the configuration is calculated, and at the end the maximum ΔE_{\max} among the N energies is considered. An example of the corresponding energy landscape sampled by this sequence is shown in Fig. 4.27.

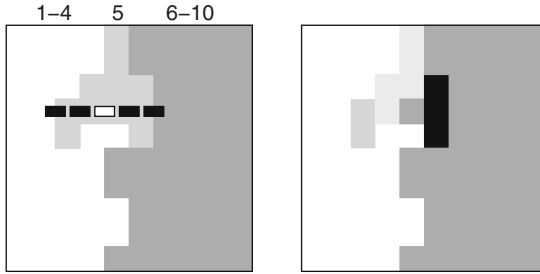


Fig. 4.26. Example of the operation of the algorithm. *Left*: two adjacent DWs (generated on level one) shown together with the line of hard bonds (*horizontal black line*) generated by *seq*, with the inverted hard bond (*white part of line*) (i_k, i_{k+1}) , corresponding to C^k . The hard bonds left of the left DW and right of the right DW are not shown for clarity. After a new GS calculation with additional constraints C^k , a DW will result, which runs between the two shown DWs and exactly through the inverted hard bond. The resulting sequence of “interpolating” DWs obtained after performing the GS calculation could look like that on the *right*, where the different domains are shown in different shades for better visibility

¹⁰ If one of the “extra” spins i_0 or i_{k+2} does not exist, the corresponding bonds do not occur. This happens always on the first level, where the separation spans the entire system, i.e., in this case, the line of hard bonds starts at i_1 and ends at i_{k+1} .

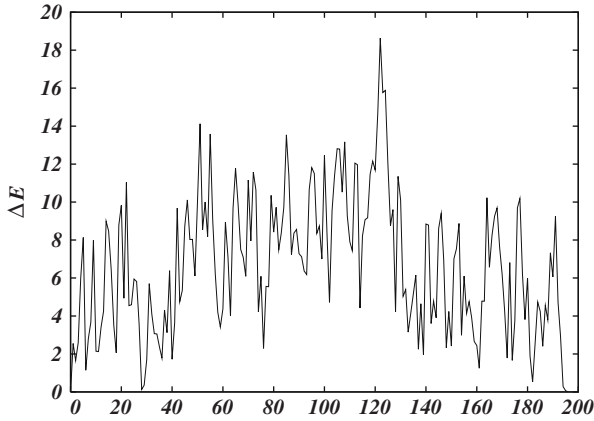


Fig. 4.27. An example of the energy landscape explored by our algorithm for $L = 14$; the exponent ψ is associated with the scaling of the maximum energy found in the sequence

Finally, a result [69] of the application of the method is shown. Since $O(L^2)$ optimum matchings have to be performed for each system, only smaller sizes can be treated in comparison to single domain-wall calculations. Here, results are shown for system sizes in the range $8 \leq L \leq 40$, and for each size, 1000 independent realizations of the bonds J_{ij} were considered. The average quantities $\langle \Delta E_{\max} \rangle$ as a function of system size is shown in Fig. 4.28. The quantity can be fitted by an algebraic function $\sim L^\psi$ with $\psi = 0.54 \pm 0.01$. Since this value provides an upper bound for the true value of ψ , it can be concluded that the exponent is clearly different from its upper bound $d-1 = 1$.

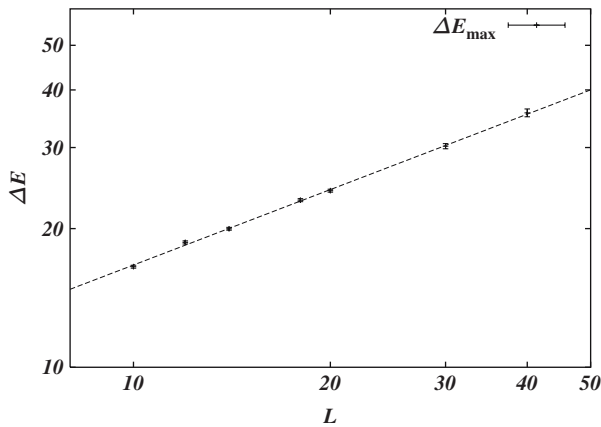


Fig. 4.28. Average barrier energy as obtained by the algorithm, being an upper bound for the true lowest barrier height

Acknowledgements

The author thanks C. Amoruso, A. J. Bray, A. C. Carter, J. Houdayer, M. A. Moore and A. P. Young for interesting collaborations in this field of two-dimensional spin glasses. Furthermore, he is grateful to O. Melchert and E. O. Yewande for critically reading the manuscript. This work was supported by the *Volkswagen-Stiftung* (Germany) within the program “Nachwuchsgruppen an Universitäten”, from the Paderborn Center for Parallel Computing in Germany, and from the European Community via the DYGLAGEMEM program.

References

1. K. Binder, A. P. Young: Rev. Mod. Phys. **58**, 801 (1986) [67](#), [74](#)
2. M. Mezard, G. Parisi, M. A. Virasoro: *Spin Glass Theory and Beyond* (World Scientific, Singapore, 1987) [67](#), [74](#), [75](#)
3. K. H. Fischer, J. A. Hertz: *Spin Glasses* (Cambridge University Press, Cambridge, MA 1991) [67](#), [74](#)
4. J. A. Mydosh: *Spin Glasses: An Experimental Introduction* (Taylor and Francis, London, 1993) [67](#), [71](#)
5. A. P. Young (ed.): *Spin Glasses and Random Fields* (World Scientific, Singapore, 1998) [67](#), [69](#)
6. B. Müller, J. Reinhardt: *Neural Networks – An Introduction* (Springer-Verlag, Berlin, Heidelberg, 1991) [67](#), [73](#)
7. N. Sourlas: In, edited by: *From Statistical Physics to Statistical Inference and Back* P. Grassberger, J.-P. Nadal (Kluwer Academic, Amsterdam, 1994) [67](#)
8. A. K. Hartmann, M. Weigt: *Phase Transitions in Combinatorial Optimization Problems* (Wiley-VCH, Weinheim, 2005) [67](#)
9. Y. Cannella, J. A. Mydosh: Phys. Rev. B **6**, 4220 (1972) [68](#)
10. S. Miyashita, E. Vincent: Eur. Phys. J. B **22**, 203 (2001) [69](#)
11. V. Dupuis, E. Vincent, J.-P. Bouchaud, J. Hammann, A. Ito, H. Aruga Katori: Phys. Rev. B **64**, 174204 (2001) [69](#)
12. C. Dekker, A. F. M. Arts, H. W. de Wijn: J. Appl. Phys. **63**, 4334 (1988) [72](#)
13. G. Toulouse: Commun. Phys. **2**, 115 (1977) [72](#)
14. S. F. Edwards, P. W. Anderson: J. Phys. F **5**, 965 (1975) [72](#)
15. G. A. Kohring: J. Phys. I **6**, 301 (1996) [73](#)
16. R. Floriana, S. Galam: Eur. Phys. J. B **16**, 189 (2000) [73](#)
17. M. Pasquini, M. Serva: Phys. Rev. E **63** 056109 (2001) [73](#)
18. J. Maskawa: Physica A **311**, 563 (2002) [73](#)
19. H. Rieger: In *Annual Reviews of Computational Physics*, Vol. II, edited by D. Stauffer (World Scientific, Singapore, 1995), pp. 295–341 [74](#)
20. D. Sherrington, S. Kirkpatrick: Phys. Rev. Lett. **51**, 1791 (1975) [74](#)
21. W. L. McMillan: J. Phys. C **17**, 3179 (1984) [75](#), [90](#)
22. A. J. Bray, M. A. Moore: J. Phys. C **18**, L699 (1985) [75](#)
23. D. S. Fisher, D. A. Huse: Phys. Rev. Lett. **56**, 1601 (1986) [75](#)
24. D. S. Fisher, D. A. Huse: Phys. Rev. B **38**, 373, 386 (1988) [75](#), [96](#)
25. A. Bovier, J. Fröhlich: J. Stat. Phys. **44**, 347 (1986) [75](#)

26. F. Krzakala, O. C. Martin: Phys. Rev. Lett. **85**, 3013 (2000) [76](#)
27. M. Palassini, A. P. Young: Phys. Rev. Lett. **85**, 3017 (2000) [76](#), [88](#)
28. F. Krzakala, O. C. Martin: Europhys. Lett. **53**, 749 (2001) [76](#)
29. H. G. Katzgraber, M. Palassini, A. P. Young: Phys. Rev. B **63**, 184422 (2001) [76](#)
30. M. Palassini, A. P. Young: Phys. Rev. B **63**, 140408(R) (2001) [76](#)
31. A. K. Hartmann, F. Ricci-Tersenghi: Phys. Rev. B **66**, 224419 (2002) [76](#)
32. H. Rieger, L. Santen, U. Blasum, M. Diehl, M. Jünger, G. Rinaldi: J. Phys. A **29**, 3939 (1996) [76](#), [90](#)
33. N. Kawashima, H. Rieger: Europhys. Lett. **39**, 85 (1997) [76](#)
34. A. K. Hartmann, A. P. Young: Phys. Rev. B **64**, 180404 (2001) [76](#), [90](#), [91](#)
35. J. Houdayer: Eur. Phys. J. B **22**, 479 (2001) [76](#), [91](#)
36. A. C. Carter, A. J. Bray, M. A. Moore: Phys. Rev. Lett. **88**, 077201 (2002) [76](#), [90](#)
37. I. Bieche, R. Maynard, R. Rammal, J. P. Uhry: J. Phys. A **13**, 2553 (1980) [76](#), [79](#), [87](#)
38. U. Derigs, A. Metz: Math. Prog. **50**, 113 (1991) [76](#)
39. F. Barahona, R. Maynard, R. Rammal, J. P. Uhry: J. Phys. A **15**, 673 (1982) [76](#)
40. A. K. Hartmann, H. Rieger: *Optimization Algorithms in Physics* (Wiley-VCH, Berlin, 2001) [76](#)
41. F. Barahona: J. Phys. A **15**, 3241 (1982) [76](#)
42. M. R. Garey, D. S. Johnson: *Computers and Intractability* (Freeman, San Francisco, 1979) [76](#)
43. R. G. Palmer, J. Adler: Int. J. Mod. Phys. C **10**, 667 (1999) [76](#)
44. R. Sedgewick: *Algorithms in C* (Addison-Wesley, Reading, MA, 1990) [76](#), [84](#)
45. T. H. Cormen, S. Clifford, C. E. Leiserson, R. L. Rivest: *Introduction to Algorithms* (MIT Press, Cambridge, MA, 2001) [76](#), [78](#), [84](#)
46. W. J. Cook, W. H. Cunningham, W. R. Pulleyblank, A. Schrijver: *Combinatorial Optimization* (John Wiley & Sons, New York, 1998) [76](#), [85](#)
47. B. Korte, J. Vygen: *Combinatorial Optimization – Theory and Algorithms* (Springer, Berlin, Heidelberg, 2000) [76](#), [85](#)
48. R. L. Graham, M. Grötschel, L. Lovász: *Handbook of Combinatorics* (Elsevier Science Publishers, Amsterdam, 1995) [78](#)
49. L. Lovász, M. D. Plummer: *Matching Theory* (Elsevier Science Publishers, Amsterdam, 1986) [78](#)
50. K. Mehlhorn, S. Näher: *The LEDA Platform of Combinatorial and Geometric Computing* (Cambridge University Press, Cambridge, MA, 1999); see also <http://www.algorithmic-solutions.de> [85](#)
51. J. W. Landry, S. N. Coppersmith: Phys. Rev. B **65**, 134404 (2002) [85](#)
52. A. K. Hartmann, A. P. Young: Phys. Rev. B **66**, 094419 (2002) [88](#)
53. A. K. Hartmann, M. A. Moore: Phys. Rev. B **69**, 104409 (2004) [88](#)
54. N. Goldenfeld: *Lectures on Phase Transitions and the Renormalization Group* (Addison Wesley, Reading, MA, 1992) [89](#)
55. J. Cardy: *Scaling and Renormalization in Statistical Physics* (Cambridge University Press, Cambridge, MA, 1996) [89](#)
56. A. J. Bray, M. A. Moore: J. Phys. C **17**, L463 (1984) [89](#), [90](#)
57. A. K. Hartmann, A. J. Bray, A. C. Carter, M. A. Moore, A. P. Young: Phys. Rev. B **66**, 224401 (2002) [90](#), [91](#)
58. T. Jorg, J. Lukic, E. Marinari, O. C. Martin: Preprint cond-mat/0601480 [91](#)
59. W. L. McMillan: Phys. Rev. B **30**, 476 (1984)
60. A. K. Hartmann: Phys. Rev. E **59**, 84 (1999)
61. A. K. Hartmann: Phys. Rev. E **60**, 5135 (1999)

- 62. K. Hukushima: Preprint `cond-mat/9903391`
- 63. N. Kawashima, T. Aoki: J. Phys. Soc. Jpn. **69** (Suppl. A) 169 (2000); see also N. Kawashima: Preprint `cond-mat/9910366` [91](#)
- 64. Q is the probability that the value of χ^2 is worse than in the current fit; see W. H. Press, S. A. Teukolsky, W. T. Vetterling, B. P. Flannery: *Numerical Recipes in C* (Cambridge University Press, Cambridge, MA, 1995) [94](#)
- 65. A. K. Hartmann, M. A. Moore: Phys. Rev. Lett. **90**, 127201 (2003) [95](#)
- 66. H. A. Kramers: Physica **7**, 284 (1940) [96](#)
- 67. A. A. Middleton: Phys. Rev. E **59**, 2571 (1999) [96](#)
- 68. T. R. Gawron, M. Cieplak, J. R. Banavar: J. Phys. A **24**, L127 (1991) [96](#) [99](#)
- 69. C. Amoruso, A. K. Hartmann, M. A. Moore: Phys. Rev. B **73**, 184405 (2006) [103](#)

Local Scale-Invariance in Disordered Systems

Malte Henkel¹ and Michel Pleimling²

¹ Laboratoire de Physique des Matériaux, Université Henri Poincaré Nancy I,
B.P. 239, F - 54506 Vandœuvre-lès-Nancy Cedex, France


henkel@lpm.u-nancy.fr

² Department of Physics, Virginia Polytechnic Institute and State University,
Blacksburg, VA 24061-0435, USA

Michel.Pleimling@vt.edu

Abstract. Dynamical scaling and ageing in disordered systems far from equilibrium is reviewed. Particular attention is devoted to the question to what extent a recently introduced generalization of dynamical scaling to local scale-invariance can describe data for either non-glassy systems quenched to below T_c or for spin glasses at criticality. The dependence of the scaling behaviour on the distribution of the random couplings is discussed. It is shown that finite-time corrections to scaling can become quite sizable in these systems. Numerically determined ageing quantities are confronted with available experimental results.

5.1 Introduction

Understanding cooperative phenomena far from equilibrium poses one of the most challenging research problems of present-day many-body physics. At the same time, the practical handling of many of these materials has been pushed to great sophistication, and a lot of practical knowledge about them exists since prehistoric times. Paradigmatic examples of such system are glasses. In many cases, they are made by rapidly cooling (“quenching”) a molten liquid to below some characteristic temperature-threshold. If this cooling happens rapidly enough, normal crystallization no longer takes place, and the material remains in some non-equilibrium state. These non-equilibrium states may at first and even second sight look very stationary – everyone has probably seen in archaeological museums intact specimens of Roman glass or even older tools from the Paleolithic or old Stone Age – after all, obsidian or fire-stone is a quenched volcanic melt. But since the material is not at equilibrium, at least in principle it is possible (and it does happen very often in practice) that over time the properties of the material change – in other words, the material ages. 

¹ Recall that *physical ageing* as it is understood here comes from reversible microscopic processes, whereas chemical or biological ageing may come from the action of essentially irreversible (bio-)chemical processes.

The properties of such non-equilibrium systems depend on time – their *age* – since they were brought out of equilibrium, and this is colloquially referred to as *ageing behaviour*.

Although the first systematic studies of ageing were carried out in the by now classic experiments of Struik [1] in polymeric glasses, it has been realized in recent years that very similar phenomena already occur in non-disordered and non-frustrated systems which hence are also commonly referred to as *ageing*. In order to present the essence of the ageing phenomenon, we begin by considering a simple Ising model made from spin variables $\sigma_i = \pm 1$ attached to each site i of a hypercubic lattice and an interaction as given by the classical Hamiltonian with the usual nearest-neighbour interactions

$$\mathcal{H} = -J \sum_{(i,j)} \sigma_i \sigma_j, \quad (5.1)$$

where $J > 0$ is the exchange integral and the sum extends over pairs of nearest neighbours. In $d > 1$ dimensions, this system has a phase-transition at some critical temperature $T_c > 0$ which separates a disordered phase at high temperatures with a single thermodynamically stable state from an ordered phase at low temperatures with two thermodynamically stable equilibrium states. It is well established that such simple Ising models may be used to discuss uniaxial magnets, binary alloys or even liquid crystals. The motion of the spins is generated by coupling the model to a thermal bath of temperature T . A possible way of realizing this is through the so-called heat-bath dynamics which is defined by the stochastic rule

$$\sigma_i(t + \Delta t) = \pm 1 \quad \text{with probability } [1 \pm \tanh(h_i(t)/T)]/2, \quad (5.2)$$

where Δt is the time increment, the local time-dependent field is $h_i(t) = \sum_{y(i)} \sigma_{y(i)}(t)$ and $y(i)$ runs over the nearest neighbours of the site i . It is well known that this rule satisfies detailed balance and hence the system evolves towards the equilibrium probability distribution $P_{\text{eq}} = Z^{-1} \exp(-\mathcal{H}/T)$, where Z is the canonical partition function [2, 3, 4]. The system is prepared at some initial temperature T_{ini} far above the critical temperature $T_c > 0$. The initial time $t = 0$ is defined by coupling the system to the thermal bath at some low temperature $T \leq T_c$ and starting the dynamics. During the simulation, the temperature T is kept fixed and one observes the time-dependence of observables such as correlation functions or susceptibilities.²

Qualitatively, the behaviour of the system can be illustrated through the equilibrium free energies at the temperatures T_{ini} and T , see Fig. 5.1. Before the quench, the system is at equilibrium with respect to the initial temperature $T_{\text{ini}} \gg T_c$ and sits at the minimum of the free energy, as indicated by the

² The chosen dynamics is such that the total average magnetization $M(t) = \langle \sigma(t) \rangle = \sum_i \langle \sigma_i(t) \rangle$ remains at its initial value $M(0) = 0$. Throughout, we shall always use this initial condition unless explicitly stated otherwise.

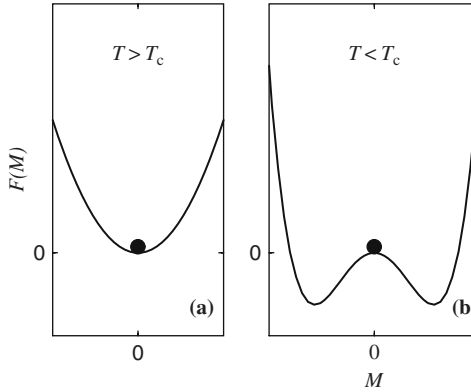


Fig. 5.1. Free energy $F(M)$ as a function of the magnetization M of a simple ferromagnet at (a) an initial high temperature $T > T_c$ before the quench and (b) after the quench to a low temperature $T < T_c$

black ball in Fig. 5.1a. If one would perturb this system slightly, it would relax rapidly, i.e. with a finite relaxation time $0 < \tau < \infty$, towards this unique equilibrium state. On the other hand, immediately after the quench, the system did not yet have the time to evolve, but with respect to the new equilibrium, its free energy is no longer minimal, see Fig. 5.1b. Rather, two new local minima of the free energy appear, which correspond to the two equivalent ordered states of the system. Because of the competition between these two new equivalent equilibrium states, the system as a whole cannot relax rapidly to one of them but rather undergoes a slow dynamics, with formally infinite relaxation times. Locally, each spin will be subject to the time-dependent field $h_i(t)$ coming from its neighbours, and this field will tilt the balance between the two equivalent equilibrium states of Fig. 5.1b in favour of one or the other. Physically, this means that the system will rapidly decompose into ordered domains, and the slow long-time dynamics of this domain growth will be determined by the motion of the domain walls between these ordered domains. This slow (non-exponential) dynamics is the *first defining property* of ageing systems.

Another aspect of this non-equilibrium dynamics (since in a spatially infinite system, none of the equilibrium states will be reached in a finite time) becomes apparent if one considers a quantity like the two-time autocorrelation function of spins at site i at times t and s

$$C(t, s) = \langle \sigma_i(t) \sigma_i(s) \rangle, \quad (5.3)$$

which by spatial translation-invariance is independent of the chosen site i . In Fig. 5.2a, data for $C(t, s)$ plotted over against the time difference $t - s$ are displayed for the three-dimensional Ising model. We see that the data depend on *both* $t - s$ and s , hence time-translation invariance is broken and

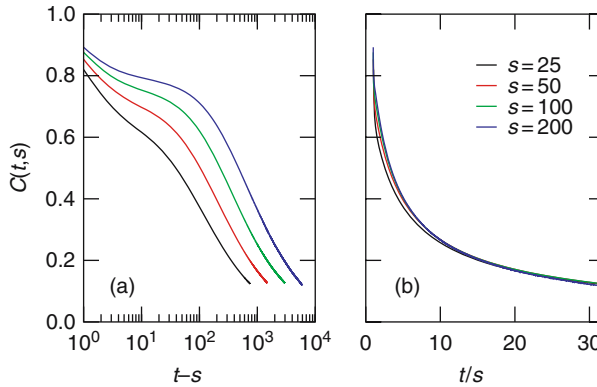


Fig. 5.2. (a) Ageing and (b) dynamical scaling of the two-time autocorrelation function $C(t, s)$ in the three-dimensional Glauber–Ising model quenched to $T = 3 < T_c$, for several values of the waiting time s

the system ages. Furthermore, with increasing values of the waiting time s , the system becomes “stiffer” and a plateau close to the equilibrium value $C_{\text{eq}} = M_{\text{eq}}^2$ develops when $t - s$ is not too large before the correlations fall off rapidly when $t - s \rightarrow \infty$. Together with the slow dynamics mentioned above, this breaking of time-translation invariance is the *second defining property* of ageing systems. In principle, this could mean that the details of the dynamics of ageing systems might depend on the entire prehistory of the sample under study, which would make any attempt to formulate a general theory for such systems hopeless. However, a great simplification, due to dynamical scaling, is apparent in Fig. 5.2b where the *same* data for $C(t, s)$, when plotted over t/s , neatly collapse onto a single curve, if only the time s is large enough and also $t - s$ is not too small. Since in domain coarsening of simple magnets, one expects that the linear size of the ordered domains is $L = L(t) \sim t^{1/z}$ when t is large enough and z is the dynamical exponent [5], the collapse in Fig. 5.2b means that $C(t, s) = f(L(t)/L(s))$, or in other words $L(t)$ is the only relevant length scale at time t . Dynamic scaling (although more general forms for $L(t)$ than simple power laws are of course possible) is the *third essential property* of ageing systems.

These three basic properties of ageing systems are also found in glassy systems. An important property of glasses is the presence of frustrations which prevent the relaxation of all local degrees of freedom. In consequence, the free-energy landscape of glasses can be very complex, with many local minima. The classic example for ageing behaviour was observed by Struik [1] in studying the mechanical properties of polymeric glasses which after a quench from the molten phase to low temperatures (i) relax very slowly (typical time scale of years), (ii) show clear evidence of the breaking of time-translation invariance and furthermore, (iii) the experimental data for the time-dependent creep curves of the mechanical response can all be mapped onto a single master

curve. Remarkably, that master curve turned out to be *the same* for materials as different as polymers such as PVC or PMMA, sugar or even metals like lead! Evidently, there are *universal* scaling functions in ageing which exactly because of their universality one may hope to be able to understand theoretically. Returning to simple magnets, that universality in the kinetics of coarsening (with a non-conserved order-parameter) after a quench to $T < T_c$ is captured through the celebrated Allen–Cahn equation [6] which states that the velocity v of the domain walls which separate the ordered domains is related to the curvature K in d dimensions via the purely geometric relationship $v = (d - 1)K$, quite independently of any details of the interactions of the spins.

The microscopic evolution which underlies the above statements about the properties of macroscopic observables is illustrated in Fig. 5.3. In the *first column*, snapshots of configurations of the two-dimensional Glauber–Ising model without disorder are shown for three different times after the quench from a fully disordered initial configuration into the ordered phase. Clearly, ordered domains form very rapidly and continue to grow up to the system size. In order to appreciate the effects of disorder, we next consider a random-bond Ising model defined by the classical Hamiltonian

$$\mathcal{H}_{\text{dis}} = - \sum_{(i,j)} J_{i,j} \sigma_i \sigma_j , \quad (5.4)$$

where the $J_{i,j}$ are random variables uniformly distributed over the interval $[1 - \varepsilon/2, 1 + \varepsilon/2]$ with $0 < \varepsilon \leq 2$. Snapshots from this two-dimensional model are shown for $\varepsilon = 2$ and $T = 0.7 < T_c$ in the *middle column* of Fig. 5.3. Again, detectable ordered domains form rapidly, but compared to the non-disordered Glauber–Ising model, although the clusters look broadly similar, one sees that the growth of the clusters proceeds much more slowly. Finally, we consider an Ising spin glass, which can again be defined by the Hamiltonian (5.4) but now the random couplings $J_{i,j} = \pm 1$ can take both positive and negative values with equal probabilities. The *right column* in Fig. 5.3 illustrates the evolution of the three-dimensional Ising spin glass with binary disorder ($J_{i,j} = \pm 1$ with equal probability) at the temperature $T = 0.8 < T_c$. It is clear that the presence of both ferromagnetic and antiferromagnetic interactions no longer permits the formation of ordered clusters, and with respect to the two other cases, the evolution appears considerably slower. We shall formalize this later on when we discuss the growth laws of the time-dependent characteristic length.

Universality as seen in experiments [11] or manifest in the Allen–Cahn equation may signal the presence of deeper dynamical symmetries. In this review, we shall describe the available evidence which points to the possibility that the well-established dynamical scaling found in ageing systems may be included into a larger group of *local* scale-transformations. As a necessary preparation, we shall begin by briefly recalling the main features of dynamical scaling. The

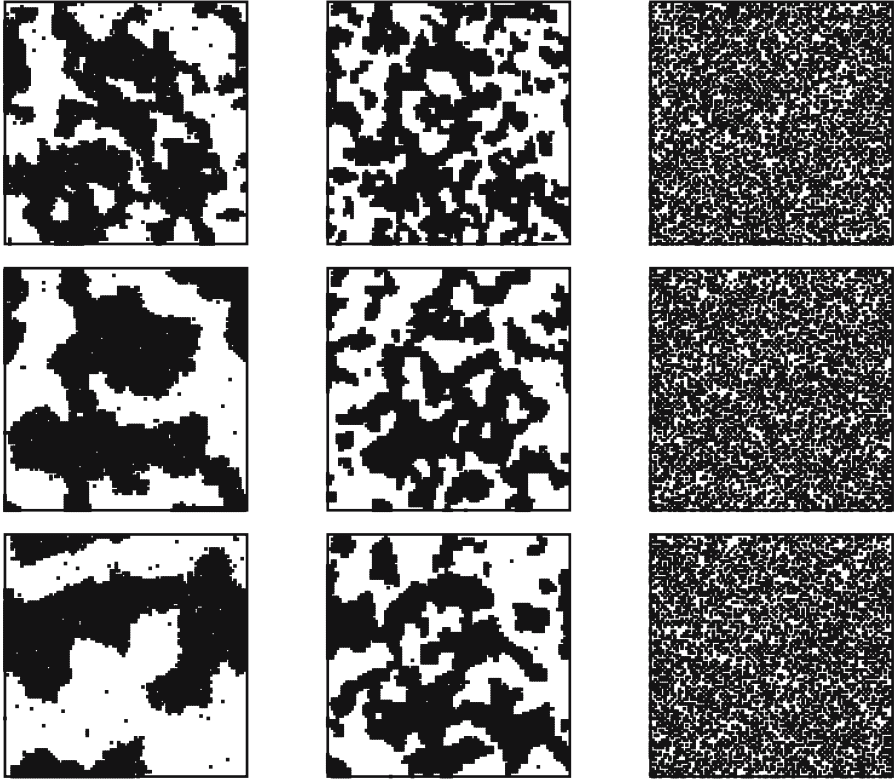


Fig. 5.3. Snapshots illustrating the growth of clusters in three variants of the kinetic Ising model, at times $t = 25, 100$ and 225 after the quench, from *top to bottom*. The *left column* shows the two-dimensional Glauber-Ising model without disorder quenched to $T = 1.5 < T_c$ and the *middle column* shows the random bond Ising model in two dimensions with $\varepsilon = 2$ and $T = 0.7 < T_c$. The *right column* shows a section of the three-dimensional Ising spin glass with binary disorder at $T = 0.8 < T_c$

topic has been under intensive study, see [5, 7, 8, 9, 10, 11, 12, 13, 14, 15] for reviews.

It is useful to discuss the properties of the coarse-grained order-parameter, denoted by $\phi(t, \mathbf{r})$ at time t at the location \mathbf{r} . Most of our discussion is for the case that the order-parameter is *non-conserved* by the dynamics and that the initial state is totally disordered with $\langle \phi(0, \mathbf{r}) \rangle = 0$, unless explicitly stated otherwise. It has become common to study ageing behaviour through the two-time autocorrelation and (linear) autoresponse functions

$$C(t, s) = \langle \phi(t, \mathbf{r}) \phi(s, \mathbf{r}) \rangle \sim s^{-b} f_C(t/s), \quad (5.5)$$

$$R(t, s) = \left. \frac{\delta \langle \phi(t, \mathbf{r}) \rangle}{\delta h(s, \mathbf{r})} \right|_{h=0} \sim s^{-1-a} f_R(t/s), \quad (5.6)$$

where $h(s, \mathbf{r})$ is the magnetic field conjugate to ϕ at time s and location \mathbf{r} . The scaling behaviour is expected to apply in the so-called *ageing regime* where

$$t, s \gg t_{\text{micro}} \quad \text{and} \quad t - s \gg t_{\text{micro}} , \quad (5.7)$$

where t_{micro} is a microscopic time scale. We emphasize the importance of the third condition for the validity of dynamical scaling. This makes the above qualitative observations drawn from Fig. 5.2 more precise. In particular, we see in Fig. 5.2 that for *finite* values of s , scaling is not perfect: Indeed corrections to dynamical scaling are detectable when $t/s \approx 1$.

The distance of such systems from a global equilibrium state can be measured through the fluctuation–dissipation ratio, defined as [16]

$$X(t, s) := TR(t, s) \left(\frac{\partial C(t, s)}{\partial s} \right)^{-1} . \quad (5.8)$$

At equilibrium, $X(t, s) = 1$ from the fluctuation–dissipation theorem. One often considers the limit fluctuation–dissipation ratio³

$$X_\infty := \lim_{s \rightarrow \infty} \left(\lim_{t \rightarrow \infty} X(t, s) \right) = \lim_{y \rightarrow \infty} \left(\lim_{t, s \rightarrow \infty} X(t, s) \Big|_{y=t/s} \right) . \quad (5.9)$$

For quenches to below T_c , one usually has $X_\infty = 0$ but for *critical* quenches onto $T = T_c$, it has been proposed by Godrèche and Luck that X_∞ should be a *universal* number [17] since it can be written as a ratio of two scaling amplitudes. The universality of X_∞ has been thoroughly confirmed for systems relaxing towards equilibrium steady-states and can be theoretically validated in a field-theoretical setting, see [10, 12] for recent reviews. On the other hand, we mention here that quite similar scaling behaviour is also found for systems containing irreversible chemical reactions and hence relaxing towards non-equilibrium steady-states. In that case, the definitions of $X(t, s)$ and of X_∞ have to be reconsidered, see [15] for a recent review.

Furthermore, in writing Eqs. (5.5) and (5.6), it was tacitly assumed that the scaling derives from the algebraic time-dependence of a single characteristic length scale growing algebraically with time $L(t) \sim t^{1/z}$ which measures the linear size of correlated or ordered clusters and where z is the dynamic exponent. That is indeed the case for simple magnets whose kinetics may be described in terms of a simple Ising model, e.g. with Glauber-type dynamics, where it can even be shown that $z = 2$ [5, 18]. Then the above forms (5.5) and (5.6) define the non-equilibrium exponents a and b and the scaling functions $f_C(y)$ and $f_R(y)$. For large arguments $y \rightarrow \infty$, one generically expects

$$f_C(y) \sim y^{-\lambda_C/z} , \quad f_R(y) \sim y^{-\lambda_R/z} , \quad (5.10)$$

where λ_C and λ_R , respectively, are known as autocorrelation [19, 20] and autoresponse exponents [21].

³ The order of the limits is crucial, since $\lim_{t \rightarrow \infty} (\lim_{s \rightarrow \infty} X(t, s)) = 1$.

While in non-disordered magnets with short-ranged initial conditions, one usually has $\lambda_C = \lambda_R$, this is not necessarily so if either of these conditions is relaxed. From a field-theoretical point of view, it is known that for a non-conserved order-parameter, the calculation of $\lambda_{C,R}$ requires an independent renormalization and hence one cannot expect to find a scaling relation between these and equilibrium exponents (including z) [22]. On the other hand, the values of the exponents a and b are known. For quenches to $T = T_c$, the relevant length scale is set by the time-dependent correlation length $L(t) \sim \xi(t) \sim t^{1/z}$, and this leads to $a = b = (d - 2 + \eta)/z$, where η is a standard equilibrium exponent. For quenches into the ordered phase $T < T_c$, one usually observes simple scaling of $C(t, s) = f_C(t/s)$, hence $b = 0$ [4]. The value of a depends on whether the equilibrium correlator is short- or long-ranged, respectively. These may be referred to as classes S and L, respectively, and one has, see e.g. [7, 24, 25]

$$C_{\text{eq}}(\mathbf{r}) \sim \begin{cases} e^{-|\mathbf{r}|/\xi} \\ |\mathbf{r}|^{-(d-2+\eta)} \end{cases} \implies \begin{cases} \text{class S} \\ \text{class L} \end{cases} \implies a = \begin{cases} 1/z \\ (d - 2 + \eta)/z \end{cases}. \quad (5.11)$$

Examples for short-ranged models (class S) include the Ising or Potts models in $d > 1$ dimensions (and $T < T_c$), while all systems quenched to criticality, or the spherical model or the two-dimensional XY model below the Kosterlitz–Thouless transition are examples for long-ranged systems (class L).

The values of these exponents are collected in Table 5.1. They have been extensively confirmed in many numerical studies, see [24, 25, 26, 27, 28, 29] and are reproduced in all known analytically solvable models.

In Sect. 5.2, we recall some of the main facts related to an extension of dynamical scaling towards a local scale-invariance (LSI). We do so first for a dynamical exponent $z = 2$, consider later possible extensions for $z \neq 2$ and finally review applications to non-disordered systems. In Sect. 5.3, we discuss the scaling of responses and correlators in disordered, but non-glassy systems and shall present the available evidence that LSI should be extendable to this

Table 5.1. Values of the non-equilibrium exponents a , b and z for non-conserved ferromagnets with $T_c > 0$ and a vanishing initial magnetization

	a	b	z	Class
$T = T_c$	$(d - 2 + \eta)/z$	$(d - 2 + \eta)/z$	z_c	L
$T < T_c$	$(d - 2 + \eta)/z$	0	2	L
$T < T_c$	$1/z$	0	2	S

The non-trivial critical-point value z_c is model-dependent

⁴ This needs no longer be the case when the ageing close to a free surface is considered [23].

class of systems. In Sect. 5.4, we consider the critical Ising spin glass, present evidence that its non-equilibrium properties depend on the distribution of the coupling constants and show to what extent the data can be explained in terms of LSI. We summarize in Sect. 5.5

5.2 Local Scale-Invariance Without Disorder

In equilibrium critical phenomena, it is well known that the standard scale-invariance can, under quite weak conditions, be extended to a *conformal* invariance. Roughly, a conformal transformation is a scale-transformation $\mathbf{r} \mapsto b\mathbf{r}$ with a space-dependent rescaling factor $b = b(\mathbf{r})$ (such that angles are kept unchanged). In particular, in two dimensions, conformal invariance allows to derive from the representation theory of the conformal (Virasoro) algebra the possible values of the critical exponents, to set up a list of possible universality classes, to calculate explicitly all n -point correlation functions and so on, see [30, 31, 32, 33]. One might wonder whether a similar extension might be possible at least in some instances of dynamical scaling and further ask *whether response functions or correlation functions might be found from their covariance under some generalized dynamical scaling with a space-time-dependent rescaling factor $b = b(t, \mathbf{r})$* [34, 35]?

We shall first consider the case of phase-ordering where $L(t) \sim t^{1/z}$ with $z = 2$ is known [5] and later describe how this might be generalized to more general values of $z \neq 2$. In particular, we enquire what can be said about the scaling functions $f_{C,R}(y)$ in a model-independent way.

A useful starting point is to consider the symmetries of the free diffusion (or free Schrödinger) equation

$$2\mathcal{M}\partial_t\phi = \Delta\phi, \quad (5.12)$$

where $\Delta = \nabla \cdot \nabla$ is the spatial Laplacian and the “mass” \mathcal{M} plays the role of a kinetic coefficient. Indeed, it was already shown by Lie more than a century ago that this equation has more symmetries than the obvious translation- and rotation-invariances. Consider the so-called *Schrödinger group* defined through the space-time transformations

$$t \mapsto t' = \frac{\alpha t + \beta}{\gamma t + \delta}, \quad \mathbf{r} \mapsto \mathbf{r}' = \frac{R\mathbf{r} + \mathbf{v}t + \mathbf{a}}{\gamma t + \delta}, \quad \alpha\delta - \beta\gamma = 1, \quad (5.13)$$

where $\alpha, \beta, \gamma, \delta, \mathbf{v}, \mathbf{a}$ are real (vector) parameters and R is a rotation matrix in d spatial dimensions. The group acts projectively on a solution ϕ of the diffusion equation through $(t, \mathbf{r}) \mapsto g(t, \mathbf{r})$, $\phi \mapsto T_g\phi$

$$(T_g\phi)(t, \mathbf{r}) = f_g(g^{-1}(t, \mathbf{r}))\phi(g^{-1}(t, \mathbf{r})), \quad (5.14)$$

where g is an element of the Schrödinger group and the companion function reads [36, 37]

$$f_g(t, \mathbf{r}) = (\gamma t + \delta)^{-d/2} \exp \left[-\frac{\mathcal{M}}{2} \frac{\gamma \mathbf{r}^2 + 2R\mathbf{r} \cdot (\gamma \mathbf{a} - \delta \mathbf{v}) + \gamma \mathbf{a}^2 - t\delta \mathbf{v}^2 + 2\gamma \mathbf{a} \cdot \mathbf{v}}{\gamma t + \delta} \right]. \quad (5.15)$$

It is then natural to include also arbitrary phase shifts of the wave function ϕ within the Schrödinger group $\text{Sch}(d)$. In what follows, we denote by \mathfrak{sch}_d the Lie algebra of $\text{Sch}(d)$. The Schrödinger group so defined is the largest group which maps *any* solution of the free Schrödinger equation (with \mathcal{M} fixed) onto another solution. For a simple illustration, consider the case $d = 1$ and define the Schrödinger operator

$$\mathcal{S} := 2M_0 X_{-1} - Y_{-1/2}^2. \quad (5.16)$$

The Schrödinger Lie algebra $\mathfrak{sch}_1 = \langle X_{-1,0,1}, Y_{-\frac{1}{2},\frac{1}{2}}, M_0 \rangle$ is spanned by the infinitesimal generators of temporal and spatial translations ($X_{-1}, Y_{-1/2}$), Galilei-transformations ($Y_{1/2}$), phase shifts (M_0), space–time dilatations with $z = 2$ (X_0) and so-called special transformations (X_1). Explicitly, the generators read [34]

$$\begin{aligned} X_n &= -t^{n+1} \partial_t - \frac{n+1}{2} t^n r \partial_r - \frac{n(n+1)}{4} \mathcal{M} t^{n-1} r^2 - \frac{x}{2} (n+1) t^n, \\ Y_m &= -t^{m+1/2} \partial_r - \left(m + \frac{1}{2} \right) \mathcal{M} t^{m-1/2} r, \\ M_n &= -\mathcal{M} t^n. \end{aligned} \quad (5.17)$$

Here x is the scaling dimension and \mathcal{M} is the mass of the scaling operator ϕ on which these generators act. The non-vanishing commutation relations are

$$\begin{aligned} [X_n, X_{n'}] &= (n - n') X_{n+n'}, \quad [X_n, Y_m] = \left(\frac{n}{2} - m \right) Y_{n+m}, \\ [X_n, M_{n'}] &= -n' M_{n+n'}, \quad [Y_m, Y_{m'}] = (m - m') M_{m+m'}. \end{aligned} \quad (5.18)$$

The invariance of the diffusion equation under the action of \mathfrak{sch}_1 is now seen from the following commutators which follow from the explicit form (5.17)

$$\begin{aligned} [\mathcal{S}, X_{-1}] &= [\mathcal{S}, Y_{\pm 1/2}] = [\mathcal{S}, M_0] = 0, \\ [\mathcal{S}, X_0] &= -\mathcal{S}, \quad [\mathcal{S}, X_1] = -2t\mathcal{S} - (2x - 1)M_0. \end{aligned} \quad (5.19)$$

Therefore, for any solution ϕ of the Schrödinger equation $\mathcal{S}\phi = 0$ with scaling dimension $x = 1/2$, the infinitesimally transformed solution $\mathcal{X}\phi$ with $\mathcal{X} \in \mathfrak{sch}_1$ also satisfies the Schrödinger equation $\mathcal{S}\mathcal{X}\phi = 0$ [36, 38, 39]. For applications to ageing, we must consider the so-called *ageing algebra* $\mathfrak{age}_1 = \langle X_{0,1}, Y_{-\frac{1}{2},\frac{1}{2}}, M_0 \rangle \subset \mathfrak{sch}_1$ (without time-translations) which is a true subalgebra of \mathfrak{sch}_1 . Extensions to $d > 1$ are straightforward.

What is the usefulness of knowing dynamical symmetries of free, simple diffusion for the understanding of non-equilibrium kinetics? One way of setting up the problem would be to write down a stochastic Langevin equation for

the order-parameter. The simplest case is usually considered to be a dynamics without macroscopic conservation laws (model A), where one would have [40]

$$2\mathcal{M}\frac{\partial\phi}{\partial t} = \Delta\phi - \frac{\delta\mathcal{V}[\phi]}{\delta\phi} + \eta, \quad (5.20)$$

where \mathcal{V} is the Ginzburg–Landau potential and η is a Gaussian noise which describes the coupling to an external heat-bath and the initial distribution of ϕ . At first sight, there appear to be no non-trivial symmetries since the noise term η is incompatible with a Galilei-invariant equation (5.20). To understand this physically, consider a magnet which is at rest with respect to a homogeneous heat-bath at temperature T . If the magnet is moved with a constant velocity with respect to the heat-bath, the effective temperature will now appear to be direction-dependent, and the heat-bath is no longer homogeneous. However, that difficulty can be avoided as follows [41]: *split the Langevin equation into a “deterministic” part with non-trivial symmetries and a “noise” part and then show using these symmetries that all averages can be reduced exactly to averages within the deterministic, noiseless theory.* Technically, one first constructs in the standard fashion (Janssen-de Dominicis procedure) [42, 43] the associated stochastic field-theory with action $J[\phi, \tilde{\phi}]$, where $\tilde{\phi}$ is the response field associated to the order-parameter ϕ . Second, decompose the action into two parts

$$J[\phi, \tilde{\phi}] = J_0[\phi, \tilde{\phi}] + J_b[\tilde{\phi}], \quad (5.21)$$

where

$$J_0[\phi, \tilde{\phi}] = \int_{\mathbb{R}_+ \times \mathbb{R}^d} dt d\mathbf{r} \tilde{\phi} \left(2\mathcal{M}\partial_t\phi - \Delta\phi + \frac{\delta\mathcal{V}}{\delta\phi} \right) \quad (5.22)$$

contains the terms coming from the “deterministic” part of the Langevin equation (\mathcal{V} is the self-interacting “potential”) whereas

$$J_b[\tilde{\phi}] = -T \int_{\mathbb{R}_+ \times \mathbb{R}^d} dt d\mathbf{r} \tilde{\phi}(t, \mathbf{r})^2 - \frac{1}{2} \int_{\mathbb{R}^{2d}} d\mathbf{r} d\mathbf{r}' \tilde{\phi}(0, \mathbf{r}) a(\mathbf{r} - \mathbf{r}') \tilde{\phi}(0, \mathbf{r}') \quad (5.23)$$

contains the terms coming either from the noisy coupling to the heat-bath or else from the average over the disordered initial conditions [43]. It was assumed here that $\langle\phi(0, \mathbf{r})\rangle = 0$ and $a(\mathbf{r})$ denotes the initial two-point correlator

$$a(\mathbf{r}) := C(0, 0; \mathbf{r} + \mathbf{r}', \mathbf{r}') = \langle\phi(0, \mathbf{r} + \mathbf{r}')\phi(0, \mathbf{r}')\rangle = a(-\mathbf{r}), \quad (5.24)$$

while the last relation follows from spatial translation-invariance which we shall admit throughout. Averages are of course calculated from the functional integral

$$\langle A \rangle = \int \mathcal{D}\phi \mathcal{D}\tilde{\phi} A[\phi, \tilde{\phi}] e^{-J[\phi, \tilde{\phi}]}. \quad (5.25)$$

It is instructive to consider briefly the case of a free field, where $\mathcal{V} = 0$. Variation of (5.21) with respect to $\tilde{\phi}$ and ϕ , respectively, then leads to the equations of motion

$$2\mathcal{M}\partial_t\phi = \Delta\phi + T\tilde{\phi}, \quad -2\mathcal{M}\partial_t\tilde{\phi} = \Delta\tilde{\phi}. \quad (5.26)$$

The first one of those might be viewed as a Langevin equation if $\tilde{\phi}$ is interpreted as a noise. Comparison of the two equations of motion (5.26) shows that if the order-parameter ϕ is characterized by the “mass” \mathcal{M} (which by physical convention is positive), then the associated response field $\tilde{\phi}$ is characterized by the *negative* mass $-\mathcal{M}$. This characterization remains valid beyond free fields.

We now concentrate on actions $J_0[\phi, \tilde{\phi}]$ which are Galilei-invariant. This means that if $\langle \cdot \rangle_0$ denotes the averages calculated only with the action J_0 , the Bargman superselection rules [44]

$$\left\langle \underbrace{\phi \dots \phi}_n \underbrace{\tilde{\phi} \dots \tilde{\phi}}_m \right\rangle_0 \sim \delta_{n,m} \quad (5.27)$$

hold true. It follows that both response and correlation functions can be exactly expressed in terms of averages with respect to the deterministic part alone. For example (we suppress for notational simplicity the spatial coordinates) [41]

$$R(t, s) = \left. \frac{\delta \langle \phi(t) \rangle}{\delta h(s)} \right|_{h=0} = \langle \phi(t) \tilde{\phi}(s) \rangle = \langle \phi(t) \tilde{\phi}(s) e^{-J_b[\tilde{\phi}]} \rangle_0 = \langle \phi(t) \tilde{\phi}(s) \rangle_0, \quad (5.28)$$

where the “noise” part of the action was included in the observable and the Bargman superselection rule (5.27) was used. In other words, *the two-time response function* $R(t, s) = R_0(t, s)$ *does not depend explicitly on the “noise” at all!* The correlation function is reduced similarly [41]

$$\begin{aligned} C(t, s; \mathbf{r}) &= T \int_{\mathbb{R}_+ \times \mathbb{R}^d} du d\mathbf{R} \left\langle \phi(t, \mathbf{r} + \mathbf{y}) \phi(s, \mathbf{y}) \tilde{\phi}(u, \mathbf{R})^2 \right\rangle_0 \\ &+ \frac{1}{2} \int_{\mathbb{R}^{2d}} d\mathbf{R} d\mathbf{R}' a(\mathbf{R} - \mathbf{R}') \left\langle \phi(t, \mathbf{r} + \mathbf{y}) \phi(s, \mathbf{y}) \tilde{\phi}(0, \mathbf{R}) \tilde{\phi}(0, \mathbf{R}') \right\rangle_0. \end{aligned} \quad (5.29)$$

Only terms which depend explicitly on the “noise” remain – recall the vanishing of the “noiseless” two-point function $\langle \phi(t) \phi(s) \rangle_0 = 0$ because of the Bargman superselection rule. Using mathematical methods explained in [45] and restricting to a disordered initial state $a(\mathbf{r}) = a_0 \delta(\mathbf{r})$, the resulting three-point function can be calculated. It is satisfying that $\lambda_C = \lambda_R$ follows [41], in agreement with an earlier derivation [5].

Therefore, the dynamical symmetries of non-equilibrium kinetics are characterized by the “deterministic” part of Langevin equation. This result only depends on the Galilei-invariance of the “deterministic” part (provided that ϕ and $\tilde{\phi}$ transform projectively through (5.14)). Clearly, linear equations are Galilei-invariant in this sense. On the other hand, the question is considerably

more complicated for non-linear equations. For the purposes of this review, it is sufficient to state that deterministic non-linear diffusion/Schrödinger equations with \mathbf{age}_1 or \mathbf{sch}_1 as a dynamical symmetry and sufficiently general to be applicable to phase-ordering kinetics have been explicitly constructed [46, 47]. In particular, it has been shown that independently of the form of the potential the same representation of \mathbf{age}_d or \mathbf{sch}_d applies, in agreement with universality. We refer to the literature for the details.

Since all quantities of interest will reduce to some kind of response function, one may calculate them from the *requirement that they transform covariantly under the action ageing subgroup* (with Lie algebra \mathbf{age}_d) obtained from the Schrödinger group when leaving out time-translations. We shall concentrate here on the two-time autoresponse function $R(t, s) = \langle \phi(t) \tilde{\phi}(s) \rangle$ built from so-called quasi-primary [30] scaling operators ϕ and $\tilde{\phi}$ which transform according to the generators of the ageing algebra. Then the requirement of covariance of R reduces to the two conditions $X_0 R(t, s) = X_1 R(t, s) = 0$. Since time-translations are not included in the ageing group, the generators X_n can be generalized from (5.17) to the following form

$$X_n = -t^{n+1} \partial_t - \frac{n+1}{2} t^n r \partial_r - \frac{(n+1)n}{4} \mathcal{M} t^{n-1} r^2 - \frac{x}{2} (n+1) t^n - \xi n t^n, \quad n \geq 0, \quad (5.30)$$

where ξ is a new quantum number associated with the field ϕ on which the generators X_n act. Consequently, a quasi-primary scaling operator which transforms covariantly under the ageing algebra is characterized by the triplet (x, ξ, \mathcal{M}) . The last term in (5.30) can only be present for systems out of an equilibrium state. In particular, the requirement of time-translation invariance and $[X_1, X_{-1}] = 2X_0$ lead to $\xi = 0$ and any representation of \mathbf{sch}_d must have $\xi = 0$. In addition, the last commutator in (5.19) must be replaced by $[\mathcal{S}, X_1] = -2t\mathcal{S} - (2x + 2\xi - 1)M_0$. The meaning of ξ can be understood by integrating the generators X_n in order to recover the finite, non-infinitesimal transformations. Then it follows that if $\xi \neq 0$, lattice observables are related to the quasi-primary fields Φ of ageing invariance according to $\phi_{\text{lattice}}(t) \mapsto \mathfrak{a}^{-x} t^\xi \Phi(t)$ with an additional time-dependent factor [48] and where \mathfrak{a} is a lattice constant. Rather than being an exotic exception, this extension of the Schrödinger transformations seems to occur quite generically, the best-known example being the one-dimensional Glauber–Ising model at zero temperature. For further examples, see Table 5.3. Finally, solving the two differential equations for R gives the explicit form of $R(t, s)$, see (5.34) below.

While this discussion was carried out explicitly for the case $z = 2$, it is tempting to try and generalize this idea to more general values of z . In this way, the notion of *local scale-transformation* has been introduced, which is based on the following main assumptions [35]:

1. In principle, the following conformal time-transformations should be included

$$t \mapsto t' = \frac{\alpha t + \beta}{\gamma t + \delta}, \quad \alpha\delta - \beta\gamma = 1. \quad (5.31)$$

For applications to ageing, however, time-translations generated by β must be left out (generalizing the restriction $\mathfrak{sch}_d \rightarrow \mathfrak{age}_d$).

2. The generator X_0 of scale-transformations is

$$X_0 = -t\partial_t - \frac{1}{z}r\partial_r - \frac{x}{z}, \quad (5.32)$$

where x is the scaling dimension of the quasi-primary operator on which X_0 is supposed to act. Physically, this implies that there is a single relevant length scale $L(t) \sim t^{1/z}$.

3. Spatial translation-invariance is required.

Generators for infinitesimal local scale-transformations have been explicitly constructed [35]. In almost all cases, however, it turned out that terms containing certain fractional derivatives are needed. Skipping over the details of their construction which can be found in the literature, it is sufficient here to state that one can show that the linear equation $\mathcal{S}_z\phi = 0$ with the generalized Schrödinger operator

$$\mathcal{S}_z = -\lambda\partial_t + (\nabla_r^2)^{z/2}, \quad (5.33)$$

where λ is a constant, satisfies with the generators of local scale-transformations commutation relations quite similar to (5.19) which establishes local scale-invariance as a dynamical symmetry of that linear equation [35, 49, 50]. Attempts to suppress the fractional terms in the generators of local scale-transformations lead either to $\lambda \rightarrow 0$ or to $\lambda \rightarrow \infty$ (there is an exception if $z = 1$ [35]). Explicit tests have recently been performed for $z = 4$ in models of kinetic growth described by the Mullins–Herring equation [49] and the kinetic spherical model with conserved order-parameter [50]. Further tests in the long-ranged spherical model where z can be continuously tuned through a control parameter were recently carried out [51]. On the other hand, a systematic derivation of an analogue of the Bargman superselection rules for $z \neq 2$ is still lacking and indeed constitutes one of the most important open questions to be overcome for a further development of the theory.

Local scale-invariance (LSI) assumes in particular that the two-time response functions transform covariantly under these local scale-transformations, hence $X_0R = X_1R = 0$. This leads to the following prediction for the autore-sponse [35, 41, 48, 52]

$$R(t, s) = \langle \phi(t)\tilde{\phi}(s) \rangle = s^{-1-a}f_R(t, s), \quad f_R(y) = f_0 y^{1+a'-\lambda_R/z}(y-1)^{-1-a'}, \quad (5.34)$$

where the exponents $a, a', \lambda_R/z$ are related to $x, \xi, \tilde{x}, \tilde{\xi}$ and f_0 is a normalization constant [5]. Spatio-temporal responses can be found similarly, with the result

⁵ We point out that the prediction (5.34) as well as the explicit form (5.30) of X_n , valid for $z = 2$, assume that the mean order-parameter $\langle \phi(0, \mathbf{r}) \rangle = m_0 = 0$ at the initial moment when the quench to $T < T_c$ or $T = T_c$ is made.

Table 5.2. Magnetic systems quenched into the coexistence phase ($T < T_c$) which satisfy (5.34) with the exponents $a = a'$ and λ_R

model	d	z	$a = a'$	λ_R	Ref.
Ising	2	2	1/2	1.26(1)	[55]
	2	2	$\simeq 0.5$	1.24(2)	[29, 56]
	3	2	1/2	1.60(2)	[55]
Potts-3	2	2	0.49	1.19(3)	[29, 56]
Potts-8	2	2	0.51	1.25(1)	[29, 56]
XY	3	2	0.5	1.7	[28]
XY spin-wave	≥ 2	2	$d/2 - 1$	d	angular response [41]
spherical	> 2	2	$d/2 - 1$	$(d - \alpha)/2$	$C_{\text{ini}}(\mathbf{r}) \sim \mathbf{r} ^{-d-\alpha}$ [21, 57]
long-range	> 2	σ	$d/\sigma - 1$	$d/2$	$0 < \sigma < 2$
spherical	≤ 2	σ	$d/\sigma - 1$	$d/2$	$0 < \sigma < d$ [58]
random-bond Ising	2	$2 + \varepsilon/T$	$1/z(T, \varepsilon)$	$\lambda_R(T, \varepsilon)$	disordered [59]

d is the spatial dimension and the numbers in brackets estimate the numerical uncertainty in the last digit(s). In the spherical model, long-range initial conditions are included and in the long-range spherical model, the exchange couplings decay as $J_r \sim |\mathbf{r}|^{-d-\sigma}$. In the bond-disordered Ising model, the couplings are taken homogeneously from the interval $[1 - \varepsilon/2, 1 + \varepsilon/2]$. Then $z = z(T, \varepsilon) = 2 + \varepsilon/T$ [54] and one observes roughly $1.3 \lesssim \lambda_R(T, \varepsilon) \lesssim 1.7$

$$R(t, s; \mathbf{r}) = \left. \frac{\delta \langle \phi(t, \mathbf{r}) \rangle}{\delta h(s, \mathbf{0})} \right|_{h=0} = R(t, s) \Phi \left(|\mathbf{r}|(t - s)^{-1/z} \right), \quad (5.35)$$

where $\Phi(u) = \exp(-\frac{1}{2}\mathcal{M}u^2)$ if $z = 2$. For $z \neq 2$, the function $\Phi(u)$ has to be found from a known fractional differential equation [35, 49, 50].

Starting with [53], the prediction (5.34) has been reproduced in many different spin systems and we list examples quenched to below criticality in Table 5.2 and quenched to the critical point in Table 5.3. For $T < T_c$, it is found empirically that $a = a'$ in all examples considered so far.⁶ We point out that agreement with local scale-invariance (5.34) is not only obtained for systems where the dynamical exponent is $z = 2$ but that rather there exist quite a few examples where z can become considerably larger or smaller than 2. It must be remembered, however, that the above derivation of (5.34) for a stochastic Langevin equation has for the time being only been carried out for $z = 2$ and the justification of $X_0 R = X_1 R = 0$ remains an open problem for $z \neq 2$ in general although the result (5.34) seems to work remarkably well. It is non-trivial that a relatively simple extension of dynamical scaling should be capable of making predictions which can be reproduced in physically quite different systems.

A few comments are still needed: (i) for the XY model in the spin-wave approximation (Table 5.2), (5.34) holds for the response of the angular

⁶ Recall that $M_{\text{TRM}}(t, s)$ in direct space is not very sensitive to $a - a'$ and that most numerical studies were carried out in this setting. A considerably more sensitive test looks at M_{TRM} in momentum space [65].

Table 5.3. Systems quenched to a critical point of their stationary state which satisfy (5.34) with the exponents a , a' and λ_R/z

model	d	a	$a' - a$	λ_R/z		Ref.
random walk		-1	0	0		[16]
OJK-model		$(d-1)/2$	-1/2	$d/4$		[52, 60, 61]
Ising	1	0	-1/2	1/2		[62, 63, 64]
	2	0.115	-0.187(20)	0.732(5)		[48, 65]
	3	0.506	-0.022(5)	1.36		[48, 65]
XY	3	0.52	0	1.34(5)		[28]
spherical	< 4	$d/2 - 1$	0	$d/2 - \alpha/4 - 1/2$	L	[21]
$d > 2$	> 4	$d/2 - 1$	0	$(d - \alpha)/4 + 1/2$	L	[21]
	< 4	$d/2 - 1$	0	$3d/4 - 1$	S	[17]
	> 4	$d/2 - 1$	0	$d/2$	S	[17]
CSM	> 2	$d/4 - 1$	0	$(d+2)/4$		[50]
disordered Ising	$4 - \varepsilon$	$1 - \frac{1}{2}\sqrt{\frac{6\varepsilon}{53}}$	0	$3 - \frac{1}{2}\sqrt{\frac{6\varepsilon}{53}}$	$O(\varepsilon)$, log	[66, 67, 68]
FA	> 2	$1 + d/2$	-2	$2 + d/2$		[69]
	1	1	-3/2	2		[69, 70]
Ising spin glass	3	0.060(4)	-0.76(3)	0.38(2)	see Sect. 5.4	[52, 71]
contact process	1	-0.681	+0.270(10)	1.76(5)	$t/s \gtrsim 1.1$	[48, 72, 73]
	> 4	$d/2 - 1$	0	$d/2 + 2$		[74]
NEKIM	1	-0.430(4)	0	1.9(1)		[75]
BCP	≥ 1	$d/2 - 1$	0	$d/2$		[47, 76]
BPCP	> 2	$d/2 - 1$	0	$d/2$	$\alpha \leq \alpha_C$	[47, 76]

d is the spatial dimension and the numbers in brackets estimate the uncertainty in the last digit(s). CSM stands for the spherical model with a conserved order-parameter, FA denotes the Frederikson–Andersen model, NEKIM is the non-equilibrium kinetic Ising model and BCP and BPCP denote the bosonic contact and pair-contact processes, respectively. In the BPCP, dynamical scaling only holds along a part of the critical line. In the spherical model, long-range initial correlations $C_{\text{ini}}(\mathbf{r}) \sim |\mathbf{r}|^{-d-\alpha}$ were considered. If $d + \alpha > 2$, these reduce to short-ranged initial correlations (denoted S), but for $d + \alpha < 2$, a new class L arises. In those models described by a Langevin equation, the simple white noise $\langle \eta(t, \mathbf{r}) \eta(s, \mathbf{r}') \rangle = 2T \delta(\mathbf{r} - \mathbf{r}') \delta(t - s)$ was used, with the only exception of the CSM. In the Ising spin glass, a bimodal disorder was used

variable $\phi = \phi(t, \mathbf{r})$ which is related to the XY spin through $\mathbf{S} = (\cos \phi, \sin \phi)$. Magnetic responses have a different scaling form [27, 77]. (ii) In the critical disordered Ising model (Table 5.3), one finds a logarithmic scaling form $R(t, s) = (r_0 + r_1 \ln(t - s)) f_R(t/s)$ [66, 67, 68] such that the computed $f_R(y)$ is consistent with (5.34) to one-loop order, or up to terms of order $O(\varepsilon)$. (iii) Finally, a two-loop calculation of the critical non-conserved $O(n)$ -model

does produce in $4 - \varepsilon$ dimensions an expression for $f_R(y)$ which is incompatible with (5.34) [78] and a similar result is anticipated in $2 + \varepsilon$ dimensions [79], although the one-loop results are still compatible [78, 79, 80]. Should one conclude from these studies that for $T = T_c$ the prediction (5.34) and by implication local scale-invariance can only hold approximatively? This might well be a subtle question. Deviations between (5.34) and the field-theoretical studies typically arise when $t/s \approx 1$. However, in this region the field-theoretical results for $f_R(y)$ do not agree with the ones of non-perturbative numerical studies [65]. Since the perturbative expansion usually carried out in field-theoretical studies does not necessarily take care of the Galilei-invariance, it is necessary to carefully check that the truncation of the ε -series does not introduce slight inaccuracies. Only after this has been done (for example by re-summing the ε -series) and checked by comparing with non-perturbative data can meaningful quantitative statements on the scaling functions be made. (iv) Throughout, it was implicitly assumed that the order-parameter vanishes initially. Systematic studies on what happens when this condition is relaxed are only now becoming available [79, 81, 82, 83]. These extensions might be particularly important for chemical kinetics [15] and the existing simulations for directed percolation (or the contact process) may well turn out to be an example where the initial non-vanishing value of the order-parameter influences the form of scaling functions such as $f_R(y)$ [72, 73, 74, 83]. From that point of view, it is surprising that (5.34) could describe any part of the data of $f_R(y)$ as well as it does. (v) We did not include growth models since their analysis from the point of view of LSI is just beginning [49, 50].

If $z = 2$, it is also possible, using (5.29), to derive explicit predictions for the two-time correlation function [41, 84]. These have been tested in some exactly solvable models [41, 48], the two-dimensional Ising model [84] and the two-dimensional q -states Potts model with $q = 2, 3, 8$ [29, 56]. Extensions to $z = 4$ have been studied very recently [49, 50].

Finally, let us mention that the prediction (5.35) for the space-time response has been verified for $z = 2$ through numerical simulations of two- and three-dimensional Ising models undergoing phase-ordering [25] and from the exact solutions of the 1D Glauber–Ising model [62, 63, 64] at $T = 0$, the spherical model in $d > 2$ dimensions [17, 21] and the long-range spherical model [51, 58].

5.3 Disordered Ferromagnets

We now take up the discussion of disordered systems. Rather than going directly to spin glasses, it may be useful to consider first disordered, but not frustrated systems, such that the random exchange couplings $J_{i,j} \geq 0$ in models such as (5.4).

We point out that a disorder in the exchange couplings, as introduced in the random-bond model (5.4), can have quite different consequences

than a random site dilution, as described by a classical Hamiltonian $\mathcal{H} = -J \sum_{(i,j)} \varepsilon_i \varepsilon_j \sigma_i \sigma_j$ where $\varepsilon_i \in \{0, 1\}$ are random variables selected according to a control parameter p . Provided that on average $\overline{J_{i,j}} = 1$, the critical temperature in the presence of bond disorder will not change much. For a site-diluted model, however, the phase-transition should disappear once the non-magnetic sites (where $\varepsilon_i = 0$) will begin to percolate. Here, we shall mainly restrict attention to random-bond disorder and shall furthermore restrict to the case of quenched, that is immobile, disorder.

The first question to be addressed concerns the existence and the detailed form of dynamical scaling, as expressed through the time-dependence $L = L(t)$ of the linear size of the clusters. The physical picture is as follows [85], see also the *middle column* of Fig. 5.3. Initially, small clusters will form and start to grow. These early stages are still unaffected by the presence of the disorder which will only begin to be felt once the average cluster size has become of the same order as the mean distance between two impurities. Then the domain walls will become trapped close to the disorder-induced defects and their motion will slow down correspondingly. Rather than being described by purely geometric considerations as it can be done through the Allen–Cahn equation for non-disordered systems, the impurities act as energy barriers to the domain growth, hence the pinning centers are localized in energetically favourable positions, which explains the slowing-down of the kinetics. Phenomenologically, for a non-conserved order-parameter, one still expects that the basic curvature-reducing mechanism is applicable, leading to [85, 86]. This yields

$$\frac{dL(t)}{dt} = \frac{D(L, T)}{L(t)}, \quad (5.36)$$

where the diffusion constant $D = D(L, T)$ now depends on the domain scale $L = L(t)$ and the temperature T . For a constant D , one is back to the non-disordered case, with $L(t) \sim t^{1/2}$. For thermally activated motion, one should have

$$D(L, T) \simeq D_0 \exp(-E_B/T), \quad (5.37)$$

where $E_B = E_B(L)$ is the barrier energy. Huse and Henly [85] have argued long ago that the barrier energy should depend on the domain size algebraically, $E_B(L) \simeq E_0 L^\psi$, where the exponent $\psi = (2\zeta + d - 3)/(2 - \zeta)$, where ζ is the domain-wall roughness exponent. For example, in two dimensions, it is known that $\zeta = \frac{2}{3}$, hence $\psi = \frac{1}{4}$. Inserting into (5.36) leads to [85]

$$L(t) = \left(\frac{T}{E_0}\right)^{1/\psi} \mathcal{L}\left(\frac{t}{t_0}\right), \quad \mathcal{L}(\tau) = \begin{cases} \frac{2}{\psi} \tau & ; \tau \ll 1 \\ (\ln \tau)^{1/\psi} & ; \tau \gg 1, \end{cases} \quad (5.38)$$

which describes the qualitative change of behaviour between the initial regime and a second regime of slower growth for larger times.

We now compare this result with the available experimental evidence collected in Table 5.4. Although there is a general qualitative agreement about a change from a relatively fast kinetics seen at not too late times [87, 88, 89]

Table 5.4. Experimental results on the growth of the domain size $L(t)$ in some disordered, but non-glassy systems in two dimensions

material	model	$L(t)$	ψ	T_c [K]	Ref.
Rb ₂ Co _{0.60} Mg _{0.40} F ₄	diluted Ising antiferromagnet	$A + B(\ln t)^{1/\psi}$	0.28 (15[K]/ T)	20	[87]
tryglycine sulfate (TGS)	ferroelectric	$\sim (t - t_0)^{1/z}$	if $T \lesssim 15[\text{K}]$ $z \approx 3$	322	[88, 89]
	conserved	$\sim (\ln t)^{1/\psi}$	$1/4$		
Rb ₂ Cu _{0.89} Co _{0.11} F ₄	random-bond	$(\ln t)^{1/\psi}$	0.20(5)	4.93(5)	[90]
	Ising		$T = 3.9[\text{K}]$		
ZLI 4792 (Merck) (liquid crystal)	random-bond	$(\ln t)^{1/\psi}$	$1/4$		[91]
	Ising				

For Rb₂Co_{0.60}Mg_{0.40}F₄ a different temperature-dependent exponent ψ is found close to T_c . For TGS the order-parameter is conserved

to slowing-down of the kinetics at later times, quantitatively the situation remains a little ambiguous. In the published work known to us, data were usually compared to a logarithmic law $L(t) \sim (\ln t)^{1/\psi}$, which rather than being an objective statement might simply come from the fact that the prediction (5.38) of Huse and Henley [85] has been around for quite some time. On the other hand, there is some experimental information which is not consistent with (5.38), if it can be taken at face value. For example, in at least one system, the effective exponent depends on temperature [87] while a constant $\psi = \frac{1}{4}$ is theoretically expected in two dimensions [85]. Indeed, it has been argued that in site-diluted Ising models, because of the fractal nature of the domains boundaries, the energy barriers should rather depend logarithmically on $L(t)$, viz. $E_B(L) = \varepsilon \ln(1 + L)$ [54, 92, 93]. Inserting this into (5.36) leads to an algebraic law $L(t) \sim t^{1/z}$ where the effective z crosses over from $z = \frac{1}{2}$ for short times to

$$z = z(T, \varepsilon) = 2 + \varepsilon/T \quad (5.39)$$

for late times. In at least one experiment, data were explicitly seen to be also compatible with an algebraic growth law [88, 89].

For a conserved order-parameter, a similar discussion can be carried out. It can be shown that for algebraic energy barriers the result (5.38) remains unchanged [85], whereas for logarithmic barriers one finds again algebraic growth $L(t) \sim t^{1/z}$ with $z = z(T, \varepsilon) = 3 + \varepsilon/T$ [54, 94].

Theoretical work has among others studied a random-bond Ising model defined by the classical Hamiltonian

$$\mathcal{H}_{\text{dis}} = - \sum_{(i,j)} J_{i,j} \sigma_i \sigma_j, \quad (5.40)$$

where the $J_{i,j}$ are random variables uniformly distributed over the interval $[1 - \varepsilon/2, 1 + \varepsilon/2]$ and where a non-conserved dynamics was created via

a Metropolis or heat-bath algorithm. For examples, estimates for $L(t)$ extracted from the single-time spatio-temporal correlation function were seen to be in full agreement with the prediction (5.39) of logarithmic energy barriers [54, 94]. The same conclusions are obtained from the dynamical scaling behaviour of two-time quantities [59], see also below. It would be desirable to compare existing experimental data with the possibility of logarithmic energy barriers. If the discrepancy between the information extracted from experiments and theoretical simulations should persist, it could mean that the usually considered theoretical models are not realistic enough for a quantitative description of real disordered materials.

We here discuss the thermoremanent magnetization $M_{\text{TRM}}(t, s)$ which is obtained when quenching the system in presence of a small magnetic field. The magnetic field is cut after the waiting time s and the decay of the magnetization is then monitored as a function of time. The thermoremanent magnetization is related to the response $R(t, s)$ through

$$M_{\text{TRM}}(t, s) = h_0 \int_0^s du R(t, u) , \quad (5.41)$$

where h_0 is the amplitude of the small magnetic field. The interest in this integrated response function comes from the fact that a direct calculation of the functional derivative which defines R produces extremely noisy data, in contrast to the measurement of M_{TRM} where the noise is to a large extent smoothed out by the integration.

From our experience with the scaling of $M_{\text{TRM}}(t, s)$ in the phase-ordering of simple magnets, we expect the scaling behaviour [24, 25]

$$M_{\text{TRM}}(t, s) = r_0 s^{-a} f_M(t/s) + r_1 s^{-\lambda_R/z} g_M(t/s) , \quad g_M(y) \simeq y^{-\lambda_R/z} . \quad (5.42)$$

Note that we have here included the leading correction term $\sim s^{-\lambda_R/z} g_M(t/s)$ which can become quite sizeable in systems undergoing phase-ordering and which must be subtracted off before a reliable determination of the scaling function $f_M(y)$ is possible. In the framework of LSI, an analytical expression for $f_M(y)$ is readily derived from (5.34) with $a = a'$ and reads (${}_2F_1$ is a hypergeometric function)

$$f_M(y) = y^{-\lambda_R/z} {}_2F_1 \left(1 + a, \frac{\lambda_R}{z} - a; \frac{\lambda_R}{z} - a + 1; \frac{1}{y} \right) . \quad (5.43)$$

The expected scaling behaviour (5.42) of the linear response has been studied through large-scale numerical simulations [59]. As an example, Fig. 5.4 shows data obtained for $\varepsilon = 0.5$ and $T = 1$. This is a case where the finite-time correction to the leading behaviour $\sim s^{-a} f_M(t/s)$ is negligible, i.e., $r_1 \approx 0$ in (5.42). Plotting $M_{\text{TRM}}(ys, s)$ against s in a log-log plot nicely verifies the expected scaling behaviour and yields in addition an estimate for the ageing exponent a , see Table 5.5. It is worth noting that the estimates are in complete

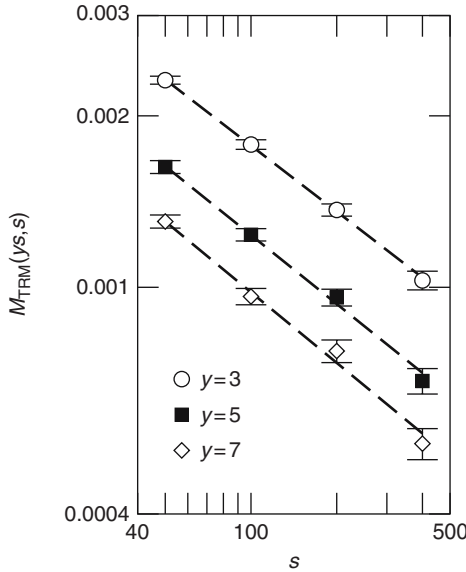


Fig. 5.4. Thermoremanent magnetization $M_{\text{TRM}}(ys, s)$ of the two-dimensional random-bond Ising model (5.40) as a function of s for $\varepsilon = 0.5$ and $T = 1.0$ and different values of y

agreement with the relation $a(T, \epsilon) = 1/z(T, \epsilon)$ expected for systems of class S as discussed in Sect. 5.1, where the dynamical exponent z is given by (5.39). This confirms the conclusion of [54, 94] that the random-bond Ising model shows simple ageing and furthermore $L(t) \sim t^{1/z}$ with $z = z(T, \epsilon)$ given by (5.39).

We also compiled in Table 5.5 the estimates [59] for the non-universal constants r_0 and r_1 as well as for the exponent λ_R/z which governs the asymptotic behaviour of the scaling function $f_M(y) \sim y^{-\lambda_R/z}$.

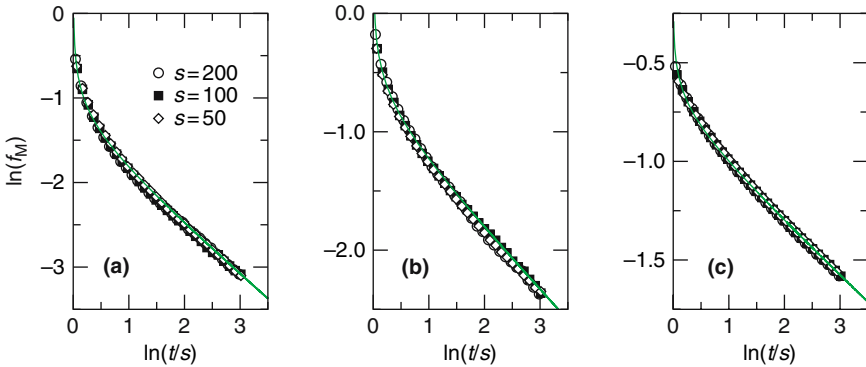
The random-bond Ising model is very well suited for investigating in detail the possible applicability of the theory of local scale-invariance to non-trivial systems undergoing phase-ordering. This is of course due to the fact that the dynamical exponent can be continuously changed by changing the distribution of the couplings and/or the temperature, yielding values of z much larger than the value $z = 2$ encountered in non-disordered ferromagnets undergoing phase-ordering. We have seen in Sect. 5.2 for what models the data for $M_{\text{TRM}}(t, s)$ agree with LSI, see Table 5.2. Figure 5.5 compares for three different cases the computed scaling function f_M of the thermoremanent magnetization with the LSI prediction (5.43). The same comparison was made for $\varepsilon = 0.5, T = 1$, $\varepsilon = 1, T = 0.6$, and $\varepsilon = 2, T = 1$ in our original paper [59]. It has to be recalled that prior to this comparison the values of the exponents entering into (5.43) and also the normalization are already fixed. We see that the form of the scaling function (after subtraction of the above-mentioned finite-time

Table 5.5. Quantities describing the dynamical scaling behaviour of the linear response M_{TRM} in the bond-disordered two-dimensional Ising model for different values of ϵ and different temperatures T

ϵ	T	a	λ_R/z	r_0	r_1	$1/z$
0.5	1.0	0.398(5)	0.61(1)	0.021(1)	0	0.400
	0.8	0.382(4)	0.595(10)	0.020(1)	0	0.381
	0.6	0.353(4)	0.58(1)	0.022(1)	0	0.353
	0.4	0.310(5)	0.52(1)	0.029(2)	0.008(1)	0.308
1.0	1.0	0.330(5)	0.51(1)	0.021(1)	-0.009(1)	0.333
	0.8	0.308(4)	0.49(1)	0.019(1)	-0.006(1)	0.308
	0.6	0.277(6)	0.46(1)	0.020(1)	-0.007(1)	0.273
	0.4	0.22(1)	0.375(10)	0.026(2)	-0.014(3)	0.222
2.0	1.0	0.24(2)	0.33(1)	0.048(2)	-0.048(4)	0.250
	0.8	0.22(2)	0.30(1)	0.093(3)	-0.042(4)	0.222
	0.6	0.17(2)	0.27(1)	0.194(4)	-0.033(3)	0.188

The last column is obtained from equation (5.39) and should be compared with the numerical estimates for the exponent a

correction, if needed) is perfectly described by LSI, and this is the case for all values of ϵ and T investigated. This is a very remarkable result as it suggests that the idea of extending dynamical scaling to local, space- and time-dependent, scaling is capable of reproducing faithfully the linear responses of very different systems characterized by very different values of the dynamical exponent.

**Fig. 5.5.** Comparison of the numerically determined scaling functions $f_M(t/s)$ of the two-dimensional random-bond Ising model with the LSI prediction (5.43) (full lines) for (a) $\epsilon = 0.5$ and $T = 0.6$, (b) $\epsilon = 1$ and $T = 1$ and (c) $\epsilon = 2$ and $T = 0.6$

Having looked at the evidence in favour of simple scaling of $M_{\text{TRM}}(t, s)$, it may be useful here to take a slightly broader point of view. Indeed, in the discussion of glassy systems, people often describe the scaling of, say, the two-time correlation function as follows, e.g. [95]

$$C(t, s) = C_{\text{st}}(t - s) + C_{\text{age}}(t, s) \quad (5.44)$$

such that the stationary part satisfies $\lim_{t \rightarrow \infty} C_{\text{st}}(t) = 0$ and furthermore $\lim_{t-s \rightarrow \infty} (\lim_{s \rightarrow \infty} C_{\text{st}}(t - s)) = q_{\text{EA}}$, where q_{EA} is the Edwards–Anderson order-parameter for glasses. On the other hand, the ageing part is assumed to read

$$C_{\text{age}}(t, s) = \mathcal{C} \left(\frac{h(t)}{h(s)} \right), \quad h(t) = h_0 \exp \left[\frac{1}{A} \frac{t^{1-\mu} - 1}{1 - \mu} \right], \quad (5.45)$$

where \mathcal{C} is a scaling function, μ is a free parameter and h_0 and A are constants. Conventionally, one refers to the case $0 < \mu < 1$ as *subageing*, the limit case $\mu \rightarrow 1$ as (full or simple) *ageing* and the case $\mu > 1$ as *superageing*. However, it has been shown by Kurchan [96] that, given that the positive function $\mathcal{C}(u)$ decreases strictly monotonously with u , the case $\mu > 1$ is incompatible with an elementary property of the autocorrelation function, namely that if there is a strong correlation between times t_1 and $t_2 > t_1$ and as well a strong correlation between times t_2 and $t_3 > t_2$, then there must exist a strong correlation between times t_1 and t_3 . Hence *superageing is impossible* [96].

There is a nice argument which explains the origin of the form (5.44), (5.45) [97]. It relies on the observation that if $C(t, s)$ is plotted over against $t - s$, a plateau is observed, see also Fig. 5.2a. Furthermore, according to Zippold et al. [98], the transition towards the scaling regime occurs at a time difference $t - s \sim t^\zeta$, where $0 < \zeta < 1$ describes this change of behaviour [7]. Hence, close to the plateau, one can assume

$$C(t, s) = q_{\text{EA}} + t^{-\alpha} g_1((t - s)t^{-\zeta}) + \dots, \quad (5.46)$$

where α is some exponent and g_1 a scaling function. Now, consider $t - s = xt^\zeta$ and take the limit $t \rightarrow \infty$ and then $x \gg 1$. Then, to leading order

$$C(t, s) = \mathcal{C} \left(\frac{h(t)}{h(s)} \right) \simeq \mathcal{C} \left(1 + xt^\zeta \frac{d \ln h(t)}{dt} \right) \simeq q_{\text{EA}} + c_{\text{age}}^{(1)} \left(xt^\zeta \frac{d \ln h(t)}{dt} \right)^{\mathfrak{b}}, \quad (5.47)$$

where \mathfrak{b} is a further exponent which can be worked out for certain model spin glasses [97]. Comparing (5.46) and (5.47), the dependences on t and on x can be separated which in particular leads to $d \ln h(t)/dt = A^{-1} t^{-\mu}$, where $\mu = \zeta + \alpha/\mathfrak{b}$ and A is a separation constant. Then (5.45) follows directly [97]. In particular, this means that other phenomenological forms which have been discussed in the past can be eliminated.

⁷ Explicitly, $\zeta = 4/(d + 2)$ in the d -dimensional spherical model and $\zeta = 4/5$ in the spherical spin glass [98].

After these preparations, we turn to a discussion of ageing properties of the autocorrelation function in disordered ferromagnets. Indeed, recent studies of $C(t, s)$ in bond-diluted [59] and in site-diluted [99] Ising models quenched to below the critical points showed surprising and at first sight unexpected features. In Fig. 5.6a, we show data [59] for the two-dimensional random-bond Ising model plotted over t/s . In clear contrast with non-disordered simple magnets, no clear scaling is seen. At first sight, one might be tempted to introduce a non-vanishing ageing exponent b , see (5.5), but since the curves for $C(t, s)$ increase with s , the effective values of $b = b_{\text{eff}}$ fitted to the data will turn out to be negative [59, 99]. If true, that would imply that for $s \rightarrow \infty$ the autocorrelator $C(t, s)$ would grow unboundedly, which is impossible. It is therefore necessary to re-examine whether the standard scaling form of simple ageing is applicable. Indeed, in a recent study of the randomly site diluted Ising model [99], the more general scaling form (5.44), (5.45) was used and fitted values of μ in the range $\mu \approx 1.03 - 1.04$ were reported, implying the so-called superageing behaviour [99]. Although a good collapse of the data can be obtained this way, the arguments raised by Kurchan [96] and quoted above make it doubtful that the conclusion of [99] can be accepted at face value. Indeed, in using scaling forms such as (5.5), one has to be careful about the possibility of finite-time corrections to scaling. We illustrate the presence of strong corrections to scaling in Fig. 5.6b [100] for the case $\varepsilon = 2$ and $T = 1$, for several values of

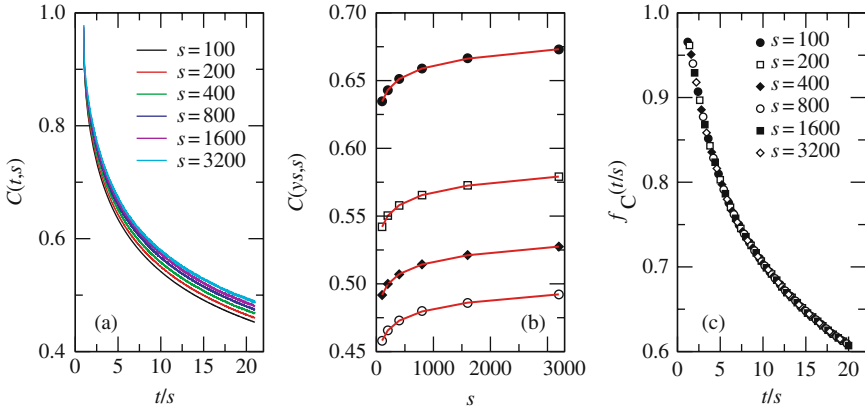


Fig. 5.6. (a) Autocorrelation $C(t, s)$ versus t/s for various waiting times s in the random-bond Ising model with $\varepsilon = 2$ and $T = 1$. (b) Plot of $C(ys, s)$ for the same parameters and $y = 5, 10, 15, 20$ (from top to bottom). The data can be perfectly fitted by the scaling form (5.48) with $b' = 0.075$, which illustrates the existence of important finite-time corrections. (c) The scaling function $f_C(t/s)$ obtained after subtracting off the finite-time corrections from the autocorrelation, again for $\varepsilon = 2$ and $T = 1$, in agreement with simple ageing of the autocorrelation

$y = t/s$. Clearly, the data are perfectly described by the extended scaling form

$$C(ys, s) = f_C(y) - s^{-b'} g_C(y) \quad (5.48)$$

(hence with $b = 0$) and with $b' > 0$. Subtracting off the leading correction term yields a perfect scaling behaviour (5.5) according to simple ageing as shown in Fig. 5.6: [100], quite analogous with the standard scaling expected for simple magnets quenched to below their critical point.

In conclusion, the random-bond Ising model apparently ages in much the same way as a simple magnet. The prediction of Table 5.1 for the exponents a, b in class S systems holds true for this non-glassy disordered system as well, but the value of the dynamical exponent $z = z(T, \varepsilon)$ (and also of $\lambda_{C,R}$) becomes dependent on temperature and on the distribution of the couplings. The form of the response function agrees with the prediction of LSI, for a large range of values of z . It would be very interesting to check these conclusions in other systems.

5.4 Critical Ising Spin Glasses

The disordered ferromagnet studied in the previous section can be viewed as intermediary between the simple, non-disordered magnets and the disordered and highly frustrated spin glasses. In the following, we discuss to what extent the results obtained for the disordered ferromagnets can be extended to glassy systems. We thereby shall concentrate on the Ising spin glass, with a static Hamiltonian $\mathcal{H} = -\sum_{(i,j)} J_{i,j} \sigma_i \sigma_j$. Here $\sigma_i = \pm 1$ are the usual Ising spins and the nearest-neighbour couplings $J_{i,j}$ are random variables. We shall consider three different distributions of the couplings: (i) the *bimodal distribution* with

$$P_B(J_{i,j}) = [\delta(J_{i,j} - J) + \delta(J_{i,j} + J)]/2, \quad (5.49)$$

(ii) the *Gaussian distribution* with

$$P_G(J_{i,j}) = \exp(-J_{i,j}^2/2J^2)/(J\sqrt{2\pi}) \quad (5.50)$$

and (iii) the *Laplacian distribution* with

$$P_L(J_{i,j}) = \exp(-\sqrt{2} |J_{i,j}/J|)/(J\sqrt{2}). \quad (5.51)$$

All distributions are symmetric with zero mean and variance $\langle J_{i,j}^2 \rangle / J^2 = 1$. The dynamics of the model is given by a master equation where the rates are chosen according to heat-bath dynamics. It is by now established, see e.g. [11] for a review, that for $d > 2$ dimensions this model undergoes an equilibrium phase-transition between a paramagnetic and a frustrated spin-glass phase. There has been considerable debate on the precise relationship between the relevant time and length scales for quenches below the spin-glass critical

temperature T_c . It has been attempted to summarize the present state of knowledge into the form [101]

$$t(L) \sim L^z \exp \left(\frac{\Delta_0}{T} \left(\frac{L}{\xi(T)} \right)^\psi \right), \quad (5.52)$$

where Δ_0 is an energy scale of order T_c , ψ is a barrier exponent and $\xi(T)$ is the equilibrium correlation length at temperature T . This form has been used to fit successfully simulation data in the three-dimensional and in the four-dimensional Edwards–Anderson model [101, 102]. Although the typical length scales are merely of the order of a few lattice sizes, see e.g. [103], the relaxation times are sufficiently large for a dynamical scaling to set in. While the expression (5.52), if correct, points towards a crossover behaviour between a simple power-law scaling and an exponential scaling for $T < T_c$ in spin glasses as would follow from the droplet model, it also suggests that at criticality simple power-law scaling (in the sense discussed above in Sect. 3) should prevail.

From now on we consider the three- and the four-dimensional Ising spin glass quenched to $T = T_c$ from a fully disordered initial state and discuss the dynamical scaling behaviour of critical two-time quantities. We consider two classes of observables: (a) thermoremanent magnetization where h is constant up to a single jump and (b) alternating susceptibility, where $h = h(t)$ is oscillatory.

5.4.1 Thermoremanent Magnetization

Let us first verify that the standard scaling forms (5.5) and (5.6) for the auto-correlation and the autoresponse are indeed observed in *critical* spin glasses. From the data shown in Fig. 5.7 for the case of a bimodal distribution of the couplings in three dimensions, we conclude that both the correlation (Fig. 5.7a) and integrated response (Fig. 5.7b) are consistent with a power-law scaling. Similar results are obtained [71, 104] for the two other distributions, both in three and four space dimensions.

From the slopes of Fig. 5.7, we obtain the estimates for the exponents a and b gathered in Table 5.6. Interestingly, we observe that $a = b$ within our numerical errors for a fixed choice of the distribution of the couplings, but that the results for different distributions are different. Even more intriguingly, other critical non-equilibrium dynamical quantities, as for example the exponent λ_C/z describing the decay of the correlations in the long-time limit or the limit value of the fluctuation–dissipation ratio (5.8), also vary strongly and systematically with the form of the interaction distribution, see Table 5.6 and Fig. 5.7c [104]. Here, we emphasize the diagnostic usefulness of the *universal* limit fluctuation–dissipation ratio X_∞ whose numerical estimates vary up to a factor of 2 between the various distributions. Having excluded the most probable sources of systematic errors [104], we interpret the numerical

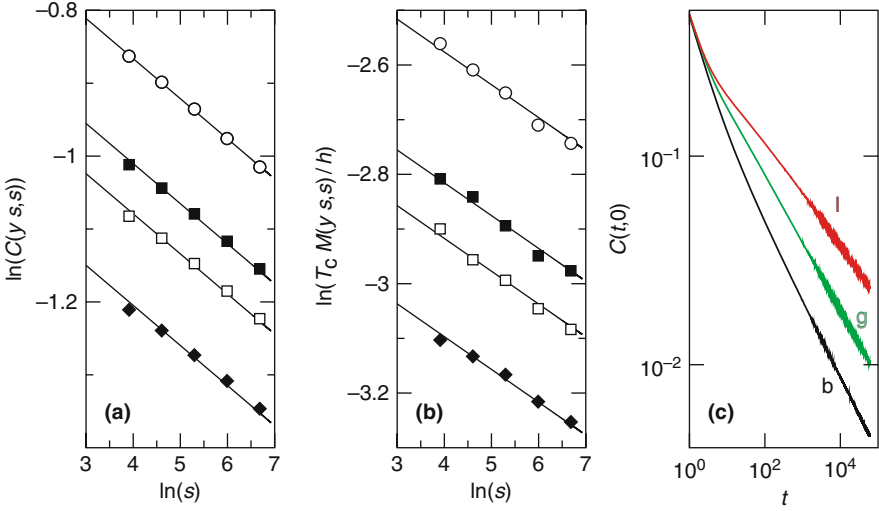


Fig. 5.7. Scaling of (a) the autocorrelation function $C(y, s)$ and (b) the thermoremanent magnetization $M(y, s)$ of the critical three-dimensional Edwards–Anderson spin glass with a bimodal distribution of the couplings for (from *top to bottom*) $y = 5, 8, 10, 15$. The *full curves* are $C(y, s) = c_0 s^{-b}$ and $M(y, s) = m_0 s^{-a}$, where c_0, m_0 were fitted to the numerical data. (c) Temporal evolution of the autocorrelation $C(t, 0)$ in the three-dimensional cases (b: bimodal, g: Gaussian, l: Laplacian)

data as strong evidence that in spin glasses critical out-of-equilibrium quantities do depend on the exact form of the distribution of the couplings⁸. It is not yet clear whether this intriguing property is only a purely dynamical effect. Whereas in the past some studies of static critical quantities observed a similar dependence on the distribution of the couplings [105], recent studies yielded for the different distributions values which agree within error bars [106, 107].

Let us now turn to the scaling functions themselves. Plotting the rescaled autocorrelator $s^b C(t, s)$ versus the scaling variable t/s yields a nice data collapse compatible with a simple power-law scaling $L(t) \sim t^{1/z}$ [71, 104]. In Fig. 5.8, we show the two-time scaling of the integrated response where again a collapse of the data in terms of a simple power-law scaling is observed. The fact that both the autocorrelator and the thermoremanent magnetization can be described in terms of such a power-law scaling is evidence in favour of the time-dependent length scale (5.52). In principle, one would like to extract an exponent λ'_R/z from the slopes of the thermoremanent magnetization. It turns out that the values of λ'_R/z thus obtained are significantly different from the ones found for λ_C/z . For example, for the Ising spin glass with a

⁸ We recall that a similar result was already seen for the disordered, but unfrustrated, Ising model in Sect. 3.

Table 5.6. Non-equilibrium quantities of the critical Ising spin glass for bimodal, Gaussian and Laplacian distributions of the nearest-neighbour couplings in $d = 3$ and $d = 4$ dimensions

bimodal				
d	a	b	λ_C/z	X_∞
3	0.060(4)	0.056(3)	0.362(5)	0.12(1)
4	0.18(1)	0.180(5)	0.615(10)	0.20(1)
Gaussian				
d	a	b	λ_C/z	X_∞
3	0.044(1)	0.043(1)	0.320(5)	0.09(1)
4	0.169(4)	0.171(2)	0.58(1)	0.175(10)
Laplacian				
d	a	b	λ_C/z	X_∞
3	0.033(3)	0.032(2)	0.259(2)	0.055(2)
4	0.143(5)	0.140(3)	0.54(1)	0.13(1)

bimodal distribution of the couplings, one finds $\lambda'_R/z = 0.45$ (resp. 0.72) in three (resp. four) dimensions. On the other hand, since X_∞ is finite, one must have $\lambda_R = \lambda_C$, but it may be necessary to go to very large values of $y = t/s$ in order to see this. Indeed, if one considers larger values of $y = t/s$ as is shown in the insets of Fig. 5.8ab, one observes a passage from an effective exponent λ'_R/z at intermediate values of the scaling variable y to the truly asymptotic value λ_R/z at larger values of y . Because of this passage from an effective exponent λ'_R/z at intermediate values of $y = t/s$ to the truly asymptotic value for larger y , we cannot expect the LSI equation (5.43) to describe the scaling function $f_M(y)$ for all values of $y = t/s$. In Fig. 5.8(a) and (b), we compare the numerical data, in both three and four dimensions with the prediction (5.43) where we have inserted the values of the exponents a and λ'_R/z . We find a nice agreement of the prediction (5.43) of local scale-invariance with our data for $y = t/s$ not too large, but for very large arguments, the precise behaviour of the scaling function $f_M(y)$ cannot be fully reproduced.

5.4.2 Alternating Susceptibility

An interesting possibility to further test the behaviour of critical spin-glass models consists of working with a time-dependent (oscillating) magnetic field and to study simultaneously the dependence on time and on the imposed oscillation angular frequency ω . For a harmonic magnetic field, it is common to consider the real and the imaginary part of the magnetic susceptibility

$$\begin{aligned}
\chi'(\omega, t) &= \int_0^t du R(t, u) \cos(\omega(t - u)) , \\
\chi''(\omega, t) &= \int_0^t du R(t, u) \sin(\omega(t - u)) ,
\end{aligned} \tag{5.53}$$

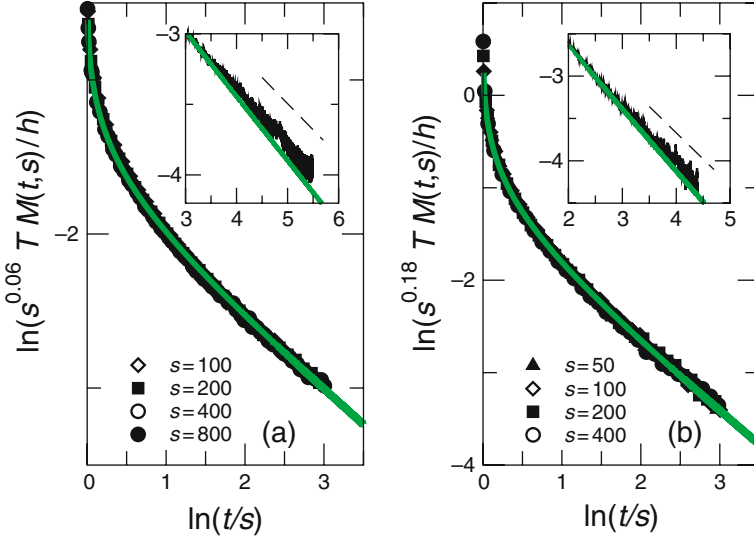


Fig. 5.8. Scaling of the thermoremanent magnetization in the Edwards–Anderson spin glass at criticality with a bimodal distribution of the couplings in (a) three and (b) four dimensions. The *full curve* is the prediction (5.43) of local scale-invariance. The results of very long runs for a single waiting time are shown in the insets where (a) $s = 100$ in three dimensions and (b) $s = 25$ in four dimensions

where $R(t, s)$ is the linear response discussed above. In this setting, $1/\omega$ provides the second time scale, the natural scaling variable is $y = \omega t$ and the scaling regime should be reached in the limit $\omega \rightarrow 0$ and $t \rightarrow \infty$. In many experiments and simulations, one averages over at least one period of the oscillating field, see e.g. [108]. Then in a great variety of glass-forming substances quenched to below or near to their glass transition point, one observes good but not always perfect evidence for an ωt -scaling behaviour of the following form of the period-averaged dissipative (imaginary) part [109, 110]

$$\overline{\chi''}(\omega, t) = \chi''_{\text{st}}(\omega) + \chi''_{\text{age}}(\omega, t), \quad \chi''_{\text{age}}(\omega, t) \simeq A''_{\text{age}} (\omega t)^{-b''}, \quad (5.54)$$

where χ''_{st} is thought of as a “stationary” contribution while the ageing behaviour is described by χ''_{age} . The amplitude A''_{age} and the exponent b'' are obtained from fits to the experimental data. Similar scaling forms have been proposed for the dispersive (real) part $\overline{\chi'}$ but in practice the imaginary part is usually easier to measure. It is usually thought that $b' = b''$.

Assuming the validity of LSI, we have derived the scaling relation [52]

$$b' = b'' = a - a' \quad (5.55)$$

where a' is the exponent defined in (5.34). Hence, this method gives direct access to the exponent $a - a'$ and should be useful for future direct tests of whether a and a' are really different.

In order to derive (5.55), we notice the central role played by the time difference $\tau = t - u$ in (5.54) [24]. Depending on its value either an equilibrium behaviour or else an ageing behaviour is obtained. Recall from Sect. 3 that there is a time scale $t_p \sim t^\zeta$ with $0 < \zeta < 1$ on which the transition between the two regimes occurs [98] such that $R(t, s) \simeq R_{\text{eq}}(t - s)$ for $t - s \lesssim t_p$ and $R(t, s) = s^{-1-a} f_R(t/s)$ as given in (5.34) for $t - s \gtrsim t_p$. In addition, one measures for $u \approx t$ the response with respect to a change in the initial conditions and then instead of (5.34) one expects $R \approx R_{\text{ini}}(t) \sim t^{-\lambda_R/z}$ [5]⁹. We therefore must introduce a further time scale t_ε such that $t - t_\varepsilon = O(1)$. Splitting the integral into three terms corresponding to these three regimes, one has

$$\begin{aligned}
\chi''(\omega, t) &= \int_0^t d\tau R(t, t - \tau) \sin \omega \tau \\
&= \int_0^{t_p} d\tau R(t, t - \tau) \sin \omega \tau + \int_{t_p}^{t_\varepsilon} d\tau R(t, t - \tau) \sin \omega \tau \\
&\quad + \int_{t_\varepsilon}^t d\tau R(t, t - \tau) \sin \omega \tau \\
&\simeq \int_0^{t_p} d\tau R_{\text{eq}}(\tau) \sin \omega \tau + t^{-a} \int_{t_p/t}^{t_\varepsilon/t} dv f_R \left(\frac{1}{1-v} \right) \frac{\sin \omega t v}{(1-v)^{1+a}} \\
&\quad + t^{-\lambda_R/z} \int_{t_\varepsilon}^t d\tau c_0 \sin \omega \tau \\
&= \chi_1''(\omega) + t^{-a} \int_0^1 dv f_R \left(\frac{1}{1-v} \right) \frac{\sin \omega t v}{(1-v)^{1+a}} + O \left(t^{-\lambda_R/z} \right) \\
&= \chi_1''(\omega) + t^{-a} \chi_2''(\omega t) + O \left(t^{-\lambda_R/z} \right). \tag{5.56}
\end{aligned}$$

In the third line, we used the asymptotic forms of $R(t, s)$ as described above. This means that the crossover between the equilibrium and the ageing regimes is assumed to be very rapid. While this is certainly correct for simple magnets, its validity in spin glasses is far from obvious. In the last line, we restricted ourselves to the long-time limit $t \rightarrow \infty$. Here, the function $\chi_1''(\omega)$ merely depends on the equilibrium form of the linear response $R_{\text{eq}}(t, s)$. It also becomes clear that the often-found stationary term in the *integrated* response [7, 8, 11, 109, 110, 111, 112, 113, 114] does not necessarily require the separation of a similar “stationary” part in the response function $R(t, s)$ itself. An analogous expression can be derived for $\chi'(\omega, t)$.

We now insert the prediction Eqs. (5.34) of LSI. Then the scaling functions read, together with their leading behaviour as $y \rightarrow \infty$ [52],

⁹ A similar argument is used in the derivation of (5.42) and (5.43) [24, 25].

$$\begin{aligned}
\chi_2''(y) &= f_0 B \left(1 - a', \frac{\lambda_R}{z} - a \right) y^{1-a} \\
&\quad \times {}_2F_3 \left(\frac{1-a'}{2}, \frac{2-a'}{2}; \frac{3}{2}, \frac{1-a-a'}{2} + \frac{\lambda_R}{2z}, \frac{2-a-a'}{2} + \frac{\lambda_R}{2z}; -\frac{y^2}{4} \right) \\
&\simeq f_1'' y^{a'-a} + f_2'' y^{-\lambda_R/z} \sin \left(y + \frac{\pi}{2} [a - \lambda_R/z] \right), \tag{5.57}
\end{aligned}$$

$$\begin{aligned}
\chi_2'(y) &= f_0 B \left(-a', \frac{\lambda_R}{z} - a \right) y^{-a} \\
&\quad \times {}_2F_3 \left(\frac{-a'}{2}, \frac{1-a'}{2}; \frac{1}{2}, \frac{-a-a'}{2} + \frac{\lambda_R}{2z}, \frac{1-a-a'}{2} + \frac{\lambda_R}{2z}; -\frac{y^2}{4} \right) \\
&\simeq f_1' y^{a'-a} + f_2' y^{-\lambda_R/z} \cos \left(y + \frac{\pi}{2} [a - \lambda_R/z] \right), \tag{5.58}
\end{aligned}$$

where ${}_2F_3$ is a hypergeometric function and $f_{1,2}'$ and $f_{1,2}''$ are known constants proportional to the normalization constant f_0 . We see that there appear terms which decrease monotonously with y but that there are also oscillating terms. They are described by different exponents and must be extracted by a different experimental setup. The oscillating terms follow the oscillations of the external field, and the decrease of the oscillation amplitude gives a direct access to the exponent λ_R/z . On the other hand, in many experiments, the data are averaged over one or several periods of the external field. For y sufficiently large, the contribution of the oscillating term in (5.57) and (5.58) vanishes after averaging and then only a simple algebraic component remains, which permits to extract the exponent $a - a'$. For period-averaged data or else if $\lambda_R/z \geq a - a'$, the leading behaviour for large arguments is

$$\chi_2'(y) \sim \chi_2''(y) \sim y^{a'-a} \tag{5.59}$$

and the scaling relations (5.55) follow. Since the new exponent a' enters in (5.55), this suggests that no scaling relation between $b' = b''$ and the other ageing exponents, with a' excluded, exists.

We now describe a test [52] of the predictions (5.57) and (5.58) in the three-dimensional Ising spin glass with bimodal disorder, quenched to its critical point $T_c \approx 1.19$. In order to study the alternating susceptibility far from equilibrium, we prepared the system in an uncorrelated initial state (corresponding to an infinite initial temperature) before quenching it to the critical point at time $t = 0$. At the same time, an external oscillating magnetic field

$$h(t) = h_0 \cos \omega t \tag{5.60}$$

was switched on, with its amplitude fixed at $h_0 = 0.05$ which is well inside the linear-response regime. We consider different values of the angular frequency $\omega = 2\pi/p$ with p ranging from 50 to 1600. Numerically, the in-phase and the out-of-phase susceptibilities are given by the expressions [115]

$$\chi''(\omega, t) = m(t) \sin \omega t, \quad \chi'(\omega, t) = m(t) \cos \omega t \tag{5.61}$$

with $m(t) = \sum_i \sigma_i(t)$, but the equilibrium parts of χ'' and χ' must be subtracted off [52].

In Figs. 5.9 and 5.10 [52], we compare the expected scaling behaviour of the ageing part

$$\chi'' = \chi''(\omega t) \quad \text{and} \quad \chi' = \chi'(\omega t). \quad (5.62)$$

For the larger values of p , corresponding to the smaller values of ω , one observes a very good data collapse for both quantities, which furnishes clear evidence in favour of a power-law scaling at $T = T_c$. The value $a = 0.060(4)$ determined previously from the decay of the thermoremanent magnetization [71, 104] was used. For smaller values of p , the collapse is less good. It is possible that for the corresponding values of ω the dynamical scaling regime is not yet reached.

The data shown in these two figures can in principle be compared directly with the analytical predictions (5.57) and (5.58), *provided* however, that the positions of maxima of χ'' and χ'_2 are shifted by the amount $\Delta y \approx -0.45$ when compared with the positions obtained in the analytical treatment of the previous section. Where this shift comes from is not understood. It is possible, however, that the crossover between the equilibrium and the ageing regimes is not almost instantaneous in contrast to what we assumed in the derivation of (5.56).

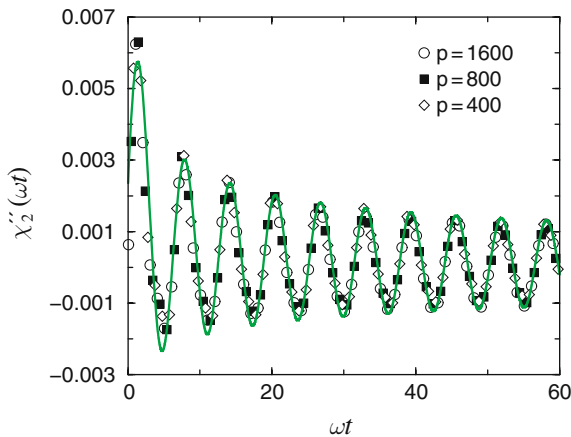


Fig. 5.9. Scaling of the dissipative part $\chi''_2(\omega t)$ of the alternating susceptibility as function of the scaling variable ωt for different angular frequencies $\omega = 2\pi/p$ with $p = 1600, 800$ and 400 . The *full curve* is the theoretical prediction (5.57) with $f_0 = 0.002$ and $a' = -0.70$ but which has also been shifted horizontally by $y \rightarrow y + \Delta y$, with $\Delta y = -0.45$, see text. Statistical error bars are smaller than the symbol sizes

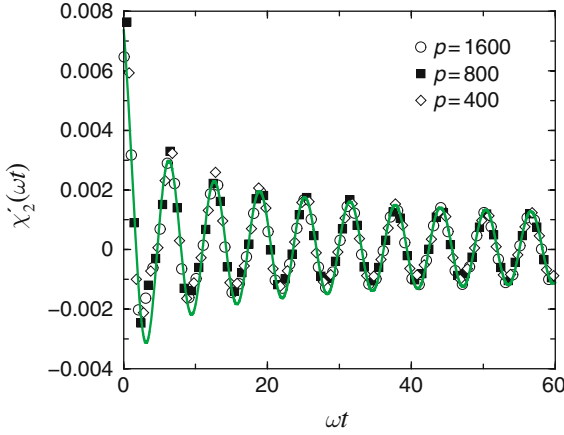


Fig. 5.10. The same as in Fig. 5.9 but now for the dispersive part $\chi'_2(\omega t)$. The full curve is the shifted theoretical prediction (5.58) with $f_0 = 0.002$ and $a' = -0.70$

Since both a and λ_R/z were known before [71, 104] the only free parameters in this comparison are the amplitude f_0 and the exponent a' . The final estimates are [52]

$$a' = -0.70(3) \quad , \quad f_0 = 0.00203(1) \quad (5.63)$$

and the fit is compared to the data in the figures. These values (5.63) of the parameters describe consistently both χ''_2 and χ'_2 . Although some discrepancies are observed for small values of $y = \omega t$, the overall agreement between the simulation and the shifted theoretical prediction is very good. Clearly, LSI captures an essential part of the ageing behaviour of critical spin glass models.

We finish with a discussion of existing experimental results on the scaling of the alternating susceptibility. A detailed discussion of a possible scaling of the alternating susceptibility was presented by Suzuki and Suzuki for the short-ranged Ising spin glass $\text{Cu}_{0.5}\text{Co}_{0.5}\text{Cl}_2\text{-FeCl}_3$ graphite bi-intercalation compound [110]. After a rapid quench to below the glass temperature $T_g = 3.92(11)$ K, they measure $\chi''(\omega, t)$ for fixed ω and find that their (period-averaged) data are well-fitted by the power-law

$$\overline{\chi''}(\omega, t) = \chi''_0(\omega) + A''(\omega)t^{-b''} \quad (5.64)$$

While the fitted exponent b'' depends only slightly on ω , they further show evidence for a power-law $A''(\omega) = A''_0\omega^{-\mu''}$ and find that “...the value of μ'' is almost the same as that of b'' ” [110]. In this way, they arrive at the ωt -scaling form

$$\overline{\chi''}(\omega, t) = \chi''_0(\omega) + A''_0(\omega t)^{-b''} \quad (5.65)$$

and a similar form for $\overline{\chi'}(\omega, t)$ where “... b' and b'' are of the same order at the same temperature” [110]. Experimentally measured values of the exponent

b'' (and also b') of some materials are collected in Table 5.7. Comparing the experimental results of Suzuki and Suzuki [110] with the theoretical scaling form (5.56), one sees:

1. The experimental evidence for a pure ωt -scaling indicates that the exponent a must indeed be very small.
2. When considering the leading behaviour for $y = \omega t$ large (their data go up to $y \lesssim 10^6$ [110]) and recalling that the experimental data are averaged over at least one period of the external field, one can read off

$$b'' = a - a', \quad \mu'' = -a' \quad (5.66)$$

and the observed [110] near equality $b'' \approx \mu''$ is again consistent with a being negligibly small.

3. The data are consistent with the theoretically requested relation $b' = b''$.

Similar values of b'' were observed for several other materials, quite independently of the precise physical nature as can be seen from Table 5.7, but the errors are still too large to permit a discussion of the universality of the exponents. However, the experimental data are in many of these systems at least as well described by a logarithmic scaling as expected from the droplet theory [109, 117, 116]. Furthermore, in several systems also strong deviations from a simple ωt -scaling were found, see [120]. Finally, we mention that in systems like β -hydroquinol-clathrate [113] or even simple liquids like glycerol [121] a

Table 5.7. Measured values of the exponents b'' and b' in several glassy materials, using the scaling form (5.54)

material	$T_g(K)$	$T(K)$	b''	b'	Ref.	
$\text{Cu}_{0.5}\text{Co}_{0.5}\text{Cl}_2\text{-FeCl}_3$ – GBIC	3.92(11)	3.25	0.01(4)	0.08(3)	[110]	Ising
		3.5	0.017(32)	0.05(2)		spin glass
		3.75	0.16(3)	0.20(2)		
		3.85	0.15(3)			
		3.95	0.16(4)	0.20(2)		
$\text{Fe}_{0.5}\text{Mn}_{0.5}\text{TiO}_3$	20.7	15	0.14(3)		[116, 117]	Ising
		19	0.14(3)			spin glass
$\text{CdCr}_{1.7}\text{In}_{0.3}\text{S}_4$	16.7	12	0.18(3)		[116, 117]	Heisenberg
		14	0.18(3)			spin glass
$\text{CdCr}_{2x}\text{In}_{2-2x}\text{S}_4$ $x = 0.95$	70	8	0.2		[117, 118]	disordered
		67	0.2			ferromagnet
$\text{Pb}(\text{Mg}_{1/3}\text{Nb}_{2/3})\text{O}_3$	$x = 0.90$	50	0.20		[117, 119]	
		~ 220	$\lesssim 220$	0.17	[111]	relaxor
theory	$(T = T_c)$					ferroelectric
			0.76(3)	0.76(3)	[52]	Ising
						spin glass

Here T_g stands for the glass transition temperature, and T is the temperature where the data were taken. For $\text{Fe}_{0.5}\text{Mn}_{0.5}\text{TiO}_3$ and $\text{CdCr}_{1.7}\text{In}_{0.3}\text{S}_4$, the relation $b' = b''$ was assumed. The simulational results in the critical Ising spin glass are also included

power-law dependence of the form $\chi''_{\text{age}} \sim t^{-a}$ or $\chi'_{\text{age}} \sim t^{-a}$ was observed. All in all, it is at present not completely clear why one should find a simple ωt -scaling of the alternating susceptibility whereas subageing is frequently admitted for the thermoremanent magnetization.

A last important observation follows from comparing the experimental data for the exponents $b' = b'' \approx 0.1 - 0.2$ for all the 3D materials studied so far with the theoretical estimate $b'' \simeq 0.76$ derived from the 3D Ising spin glass with binary disorder. The values are very far from each other and this huge difference calls for an explanation. Could this be seen as an indication that the spin glass models considered by theorists only capture imperfectly what is going on in real materials?

5.5 Discussion

The available evidence for universality in the ageing behaviour seen in either glassy materials, disordered systems or else simple many-body systems without disorder may be taken, in combination with dynamical scaling, as suggestive of the existence of deeper dynamical symmetries in such systems. We have advocated here the point of view that such a new symmetry might be sought through an extension of standard dynamical scaling towards a local scale-invariance. The present formulation of the theory has been built around dynamical scaling as it occurs in full ageing, but this was mainly for reasons of technical simplicity and one could consider different forms of dynamical scaling, with a modified form of the Lie algebra generator X_0 , if required.

Even within this specific context, it is in principle possible to generalize in many different ways. For that reason, it is important to be able to test quantitatively some of the consequences of local scale-invariance. Here, the calculation of the two-time response function $R(t, s)$ is one of the easiest tasks and has the advantage that prediction are relatively easy to test in simulations, for example by considering an integrated response such as the thermoremanent magnetization $M_{\text{TRM}}(t, s)$.

The central idea of LSI is the decomposition of the stochastic Langevin equation into a *deterministic part* which can possess local scale-invariance and into a *noise part* which does break this. Remarkably, the noise part is usually built in such a way that any n -point function of the full theory can be reduced exactly to a certain m -point function of the noiseless theory (where $m \geq n$). This reduction depends on the Bargman superselection rules which are proved only for $z = 2$ at the time of writing. Then the symmetries of the noiseless part yield conditions on the form of the m -point functions. In certain cases, such as the two-time response functions, these constraints are enough to fix the functional form, see (5.34).

In models where the deterministic part of the Langevin equation is *linear*, LSI can be proven, for example in the spherical model [41], the 1D Glauber–Ising model [41, 48], bosonic particle-reaction models [47] or certain simple

growth models [49, 50]. Furthermore, there is a systematic way to construct LSI-invariant non-linear equations [46, 47]. Since these are not identical to the Langevin equations, one usually starts from [40], numerical evidence for those systems is crucial, in the absence of exact solutions.

In order to be able to carry out meaningful tests, one must first show that simple ageing (on which LSI is built) holds true. For non-conserved ferromagnets this is thought to be certain [5], and we have discussed the evidence that this remains so for disordered, non-glassy Ising models. In most numerically studied systems, only $M_{\text{TRM}}(t, s)$ has been compared with LSI. Provided that corrections to scaling are treated carefully, in all cases the results are consistent with LSI, see Tables 5.2 and 5.3. The fact that $M_{\text{TRM}}(t, s)$, as measured in a *noisy* system, is consistent with the integral of (5.34) found from the symmetries of the *noiseless* theory, even if $z \neq 2$, is a strong indication that an extension of the Bargman superselection rules to $z \neq 2$ should exist.

At present, the only other observables measured have been space-time responses and autocorrelations in the two- and three-dimensional Ising models [55, 84] and in the two-dimensional Potts- q models ($q = 2, 3, 8$) [29]. It would be important to consider different quantities, e.g. alternating susceptibilities.

When turning to critical spin glasses, although there is evidence that simple ageing applies, the agreement of the data with LSI was only partial. It should be recalled that the analysis performed relied on a rapid change between quasi-static and scaling behaviour, which might be an oversimplification. Remarkably, in the presence of disorder, we have seen evidence that the non-equilibrium exponents may depend on the distribution of the random exchange couplings $J_{i,j}$, independently on whether the system was glassy or not. Since this is a highly controversial issue, further tests would be most welcome.

At present, the available evidence¹⁰ from both analytical solved models and numerical studies supports the predictions of local scale-invariance for the two-time response (and in some cases also correlation) functions. This suggests that the kind of Langevin equation used in the description of these models should possess a fundamental, hitherto unsuspected and non-trivial dynamical symmetry underlying certain stochastic Langevin equations. Already the present examples show that the calculation of time-dependent quantities such as the thermoremanent magnetization is considerably simplified and leads to results not available as yet by other methods. Local scale-invariance, similar in spirit to the tremendously successful techniques of conformal field-theory, has the potential of leading to a much more profound understanding of non-equilibrium critical phenomena.

Finally, comparison of simulational results with experimental evidence for both glassy and non-glassy systems (see Tables 5.5 and 5.7) points to some systematic differences which need to be clarified.

¹⁰ Of course, models such as the celebrated zero-range process, see [122, 123], which lacks a proper spatial structure should be excluded from this kind of consideration.

Acknowledgements

We thank Wolfhard Janke for his invitation to write this review, F. Baumann, I. A. Campbell, S. B. Dutta, T. Enss, A. Gambassi, A. R  thlein and J. Unterberger for fruitful collaborations on the th  matique reviewed here and acknowledge the support by the Deutsche Forschungsgemeinschaft through grant no. PL 323/2. This work was also supported by the franco-german binational programme PROCOPE and by CINES Montpellier (projet pmn2095).

Note Added in Proof

Recently, generalised Bargman superselection rules could be derived for any $z \neq 2$. Consequently, the treatment of the noise directly extends to arbitrary values of z . The predictions for R and C agree with exactly solved models [49, 50, 51] and with numerical data on the space-time response and correlators in the 2D disordered Ising model [100].

References

1. L. C. E. Struik: *Physical Ageing in Amorphous Polymers and Other Materials* (Elsevier, Amsterdam, 1978) [108, 110, 111]
2. N. G. van Kampen: *Stochastic Processes in Physics and Chemistry* (North Holland, Amsterdam, 1992), 2nd ed. [108]
3. O. Narayan, A. P. Young: Phys. Rev. E **64**, 021104 (2001) [108]
4. R. Zwanzig: *Nonequilibrium Statistical Mechanics* (Oxford University Press, Oxford, 2001) [108]
5. A. J. Bray: Adv. Phys. **43**, 357 (1994) [110, 112, 113, 115, 118, 136, 142]
6. S. M. Allen, J. W. Cahn: Acta Metall. **27**, 1085 (1979) [111]
7. M. E. Cates, M. R. Evans (eds.): *Soft and Fragile Matter* (IOP Press, Bristol, 2000) [112, 114, 136]
8. L. F. Cugliandolo: In *Slow Relaxation and Non-Equilibrium Dynamics in Condensed Matter*, Les Houches Session 77, July 2002, edited by J.-L. Barrat, J. Dalibard, J. Kurchan, M. V. Feigel'man (Springer, Berlin, 2003) [112, 136]
9. C. Godr  che, J.-M. Luck: J. Phys.: Condens. Matter **14**, 1589 (2002) [112]
10. A. Crisanti, F. Ritort: J. Phys. A **36**, R181 (2003) [112, 113]
11. N. Kawashima, H. Rieger: In *Frustrated Magnetic Systems*, edited by H. Diep (World Scientific, Singapore, 2004) [112, 131, 136]
12. P. Calabrese, A. Gambassi: J. Phys. A **38**, R181 (2005) [112, 113]
13. A. Gambassi: J. Phys. Conf. Series **40**, 13 (2006) [112]
14. M. Henkel, M. Pleimling, R. Sanctuary (eds.): *Ageing and the Glass Transition*, Springer Lecture Notes in Physics **716** (Springer, Berlin, Heidelberg, 2007) [112, 144, 145, 146]
15. M. Henkel: J. Phys.: Condens. Matter, **19**, 065101 (2007) [112, 113, 123]
16. L. F. Cugliandolo, J. Kurchan, G. Parisi: J. Physique I **4**, 1641 (1994) [113, 122]
17. C. Godr  che, J.-M. Luck: J. Phys. A **33**, 9141 (2000) [113, 122, 123]

18. A. J. Bray, A. D. Rutenberg: Phys. Rev. E **49**, R27 (1994); A. D. Rutenberg, A. J. Bray: E **51**, 5499 (1995) [113](#)
19. D. S. Fisher, D. A. Huse: Phys. Rev. B **38**, 373 (1988) [113](#)
20. D. A. Huse: Phys. Rev. B **40**, 304 (1989) [113](#)
21. A. Picone, M. Henkel: J. Phys. A **35**, 5575 (2002) [113](#), [121](#), [122](#), [123](#)
22. H. K. Janssen, B. Schaub, B. Schmittmann: Z. Phys. B **73**, 539 (1989) [114](#)
23. F. Baumann, M. Pleimling: J. Phys. A **39**, 1981 (2006) [114](#)
24. M. Henkel, M. Paessens, M. Pleimling: Europhys. Lett. **62**, 644 (2003) [114](#), [126](#), [136](#)
25. M. Henkel, M. Paessens, M. Pleimling: Phys. Rev. E **69**, 056109 (2004) [114](#), [123](#), [126](#), [136](#)
26. C. Chatelain: J. Phys. A **36**, 10739 (2003) [114](#)
27. S. Abriet, D. Karevski: Eur. Phys. J. B **37**, 47 (2004) [114](#), [122](#)
28. S. Abriet, D. Karevski: Eur. Phys. J. B **41**, 79 (2004) [114](#), [121](#), [122](#)
29. E. Lorenz, W. Janke: Europhys. Lett. **77**, 10003 (2007) [114](#), [121](#), [123](#), [142](#)
30. A. A. Belavin, A. M. Polyakov, A. B. Zamolodchikov: Nucl. Phys. B **241**, 333 (1984) [115](#), [119](#)
31. J. L. Cardy: In *Fields, Strings and Critical Phenomena*, Les Houches XLIX, edited by E. Brézin, J. Zinn-Justin (North Holland, Amsterdam, 1990) [115](#)
32. P. di Francesco, P. Mathieu, D. Sénéchal: *Conformal Field Theory* (Springer, Berlin, Heidelberg, 1997) [115](#)
33. M. Henkel: *Conformal Invariance and Critical Phenomena*, (Springer, Berlin, Heidelberg, 1999) [115](#)
34. M. Henkel: J. Stat. Phys. **75**, 1023 (1994) [115](#), [116](#)
35. M. Henkel: Nucl. Phys. B **641**, 405 (2002) [115](#), [119](#), [120](#), [121](#)
36. U. Niederer: Helv. Phys. Acta **45**, 802 (1972) [115](#), [116](#)
37. M. Perroud: Helv. Phys. Acta **50**, 233 (1977) [115](#)
38. H. A. Kastrup: Nucl. Phys. B **7**, 545 (1968) [116](#)
39. C. R. Hagen: Phys. Rev. D **5**, 377 (1972) [116](#)
40. P. Hohenberg, B. I. Halperin: Rev. Mod. Phys. **49**, 435 (1977) [117](#), [142](#)
41. A. Picone, M. Henkel: Nucl. Phys. B **688**, 217 (2004) [117](#), [118](#), [120](#), [121](#), [123](#), [141](#)
42. C. de Dominicis, L. Peliti: Phys. Rev. B **18**, 353 (1978) [117](#)
43. H. K. Janssen: In *From Phase Transitions to Chaos*, edited by G. Györgyi et al. (World Scientific, Singapore, 1992), p. 68 [117](#)
44. V. Bargman: Ann. of Math. **56**, 1 (1954) [118](#)
45. M. Henkel, J. Unterberger: Nucl. Phys. B **660**, 407 (2003) [118](#)
46. S. Stoimenov, M. Henkel: Nucl. Phys. B **723**, 205 (2005) [119](#), [142](#)
47. F. Baumann, S. Stoimenov, M. Henkel: J. Phys. A **39**, 4095 (2006) [119](#), [122](#), [141](#), [142](#)
48. M. Henkel, T. Enss, M. Pleimling: J. Phys. A **39**, L589 (2006) [119](#), [120](#), [122](#), [123](#), [141](#)
49. A. Röthlein, F. Baumann, M. Pleimling: Phys. Rev. E **74**, 061604 (2006); *E76*, 019901 (2007) erratum [120](#), [121](#), [123](#), [142](#), [143](#)
50. F. Baumann, M. Henkel: J. Stat. Mech., p. 1012 (2007) [120](#), [121](#), [122](#), [123](#), [142](#), [143](#)
51. F. Baumann, S.B. Dutta, M. Henkel: J. Phys. A **40**, 7389 (2007) [120](#), [123](#), [143](#)
52. M. Henkel, M. Pleimling: J. Phys.: Condens. Matter **17**, S1899 (2005) [120](#), [122](#), [135](#), [136](#), [137](#)
53. M. Henkel, M. Pleimling, C. Godrèche, J.-M. Luck: Phys. Rev. Lett. **87**, 265701 (2001) [121](#)
54. R. Paul, S. Puri, H. Rieger: Europhys. Lett. **68**, 881 (2004) [121](#), [125](#), [126](#), [127](#)
55. M. Henkel, M. Pleimling: Phys. Rev. E **68**, 065101(R) (2003) [121](#), [142](#)
56. W. Janke: In [124](#), p. 207 [121](#), [123](#)
57. T. J. Newman, A. J. Bray: J. Phys. A **23**, 4491 (1990) [121](#)
58. S. A. Cannas, D. A. Stariolo, F. A. Tamarit: Physica A **294**, 362 (2001) [121](#), [123](#)

59. M. Henkel, M. Pleimling: Europhys. Lett. **76**, 561 (2006) [121](#), [126](#), [127](#), [130](#)
60. L. Berthier, J. L. Barrat, J. Kurchan: Eur. Phys. J. B **11**, 635 (1999) [122](#)
61. G. F. Mazenko: Phys. Rev. E **69**, 016114 (2004) [122](#)
62. C. Godrèche, J.-M. Luck: J. Phys. A **33**, 1151 (2000) [122](#), [123](#)
63. E. Lippiello, M. Zanetti: Phys. Rev. E **61**, 3369 (2000) [122](#), [123](#)
64. M. Henkel, G. M. Schütz: J. Phys. A **37**, 591 (2004) [122](#), [123](#)
65. M. Pleimling, A. Gambassi: Phys. Rev. B **71**, 180401(R) (2005) [121](#), [122](#), [123](#)
66. P. Calabrese, A. Gambassi: Phys. Rev. B **66**, 212407 (2002) [122](#)
67. G. Schehr, R. Paul: Phys. Rev. E **72**, 016105 (2005) [122](#)
68. G. Schehr, R. Paul: J. Phys. Conf. Series **40**, 27 (2006) [122](#)
69. P. Mayer, S. Léonard, L. Berthier, J. P. Garrahan, P. Sollich: Phys. Rev. Lett. **96**, 030602 (2006) [122](#)
70. P. Mayer: PhD thesis, King's college London (2004) [122](#)
71. M. Henkel, M. Pleimling: Europhys. Lett. **69**, 524 (2005) [122](#), [132](#), [133](#), [138](#), [139](#)
72. T. Enss, M. Henkel, A. Picone, U. Schollwöck: J. Phys. A **37**, 10479 (2004) [122](#), [123](#)
73. H. Hinrichsen: J. Stat. Mech., L06001 (2006) [122](#), [123](#)
74. J. J. Ramasco, M. Henkel, M. A. Santos, C. A. de Silva Santos: J. Phys. A **37**, 10497 (2004) [122](#), [123](#)
75. G. Ódor: J. Stat. Mech., L11002 (2006) [122](#)
76. F. Baumann, M. Henkel, M. Pleimling, J. Richert: J. Phys. A **38**, 6623 (2005) [122](#)
77. L. Berthier, P. C. W. Holdsworth, M. Sellitto: J. Phys. A **34**, 1805 (2001) [122](#)
78. P. Calabrese, A. Gambassi: Phys. Rev. E **66**, 066101 (2002) [123](#)
79. A. A. Fedorenko, S. Trimper: Europhys. Lett. **74**, 89 (2006) [123](#)
80. P. Calabrese, A. Gambassi: Phys. Rev. E **65**, 066120 (2002) [123](#)
81. A. Annibale, P. Sollich: J. Phys. A **39**, 2853 (2006) [123](#)
82. P. Calabrese, A. Gambassi, F. Krzakala: J. Stat. Mech., P06016 (2006) [123](#)
83. F. Baumann, A. Gambassi: J. Stat. Mech., P01002 (2007) [123](#)
84. M. Henkel, A. Picone, M. Pleimling: Europhys. Lett. **68**, 191 (2004) [123](#), [142](#)
85. D. A. Huse, C. L. Henley: Phys. Rev. Lett. **54**, 2708 (1985) [124](#), [125](#)
86. Z. W. Lai, G. F. Mazenko, O. T. Valls: Phys. Rev. B **37**, 9481 (1988) [124](#)
87. H. Ikeda, Y. Endoh, S. Itoh: Phys. Rev. Lett. **64**, 1266 (1990) [124](#), [125](#)
88. V. Likodimos, M. Labardi, M. Allegrini: Phys. Rev. B **61**, 14440 (2000) [124](#), [125](#)
89. V. Likodimos, M. Labardi, X. K. Orlik, L. Pardi, M. Allegrini: Phys. Rev. B **63**, 064104 (2001) [124](#), [125](#)
90. A. G. Schins, A. F. M. Arts, H. W. de Wijn: Phys. Rev. Lett. **70**, 2340 (1993) [125](#)
91. D. K. Shenoy, J. V. Selinger, K. A. Grüneberg, J. Naciri, R. Shashidhar: Phys. Rev. Lett. **82**, 1716 (1999) [125](#)
92. C. L. Henley: Phys. Rev. Lett. **54**, 2030 (1985) [125](#)
93. R. Rammal, A. Benoit: Phys. Rev. Lett. **55**, 649 (1985) [125](#)
94. R. Paul, S. Puri, H. Rieger: Phys. Rev. E **71**, 061109 (2005) [125](#), [126](#), [127](#)
95. E. Vincent: In [14](#), p. 7 [129](#)
96. J. Kurchan: Phys. Rev. E **66**, 017101 (2002) [129](#), [130](#)
97. A. Andreanov, A. Lefèvre: Europhys. Lett. **76**, 919 (2006) [129](#)
98. W. Zippold, R. Kühn, H. Horner: Eur. Phys. J. B **13**, 531 (2000) [129](#), [136](#)
99. R. Paul, G. Schehr, H. Rieger: Phys. Rev. E **75**, 030104 (2007) [130](#)
100. F. Baumann, M. Henkel, M. Pleimling, in preparation; F. Baumann, thèse de doctorat Nancy/Erlangen (2007) [130](#), [131](#), [143](#)

101. J.-P. Bouchaud, V. Dupuis, J. Hammann, E. Vincent: Phys. Rev. B **65**, 024439 (2001) [132](#)
102. L. Berthier, J.-P. Bouchaud: Phys. Rev. B **66**, 054404 (2002) [132](#)
103. H. Yoshino, K. Hukusghima, H. Takayama: Phys. Rev. B **66**, 064431 (2002) [132](#)
104. M. Pleimling, I. A. Campbell: Phys. Rev. B **72**, 184429 (2005) [132](#), [133](#), [138](#), [139](#)
105. L. W. Bernardi, I. A. Campbell: Phys. Rev. B **56**, 5271 (1997) [133](#)
106. T. Jörg: Phys. Rev. B **73**, 224431 (2006) [133](#)
107. H. G. Katzgraber, M. Körner, A. P. Young: Phys. Rev. B **73**, 224432 (2006) [133](#)
108. M. Picco, F. Ricci-Tersenghi, F. Ritort: Eur. Phys. J. B **21**, 211 (2001) [135](#)
109. P. E. Jönsson, H. Yoshino, P. Nordblad, H. Agura Katori, A. Ito: Phys. Rev. Lett. **88**, 257204 (2002) [135](#), [136](#), [140](#)
110. I. S. Suzuki, M. Suzuki: Phys. Rev. B **68**, 094424 (2003) [135](#), [136](#), [139](#), [140](#)
111. E. V. Colla, L. K. Chao, M. B. Weissman, D. D. Viehland: Phys. Rev. Lett. **85**, 3033 (2000) [136](#), [140](#)
112. V. Dupuis, F. Bert, J.-P. Bouchaud, J. Hammann, F. Ladieu, D. Parker, E. Vincent: Pramana J. Phys. *64*, 1109 (2005) [136](#)
113. M. Rheinstädter, K. Knorr, H. Rieger: Phys. Rev. B **69**, 144427 (2004) [136](#), [140](#)
114. G. F. Rodriguez, G. G. Kenning, R. Orbach: Phys. Rev. Lett. **91**, 037203 (2003) [136](#)
115. J.-O. Andersson, T. Jonsson, J. Mattsson: Phys. Rev. B **54**, 9912 (1996) [137](#)
116. V. Dupuis, E. Vincent, J.-P. Bouchaud, J. Hammann, A. Ito, H. A. Katori: Phys. Rev. B **64**, 174204 (2001) [140](#)
117. V. Dupuis: Thèse de doctorat (Paris XI Orsay, 2002) [140](#)
118. V. Dupuis, E. Vincent, M. Alba, J. Hammann: Eur. Phys. J. B **29**, 19 (2002) [140](#)
119. E. Vincent, V. Dupuis, M. Alba, J. Hammann, J.-P. Bouchaud: Europhys. Lett. **50**, 674 (2000) [140](#)
120. E. V. Colla, L. K. Chao, M. B. Weissman: Phys. Rev. B **63**, 134107 (2001) [140](#)
121. R. L. Leheny, S. R. Nagel: Phys. Rev. B **57**, 5154 (1998) [140](#)
122. M. R. Evans, T. Hanney: J. Phys. A **38**, R195 (2005) [142](#)
123. C. Godrèche: In [14](#), p. 261 [cond-mat/0604276] [142](#)

Structural Glasses

Transport of Mobile Particles in an Immobile Environment: Computer Simulations of Sodium Silicates

Jürgen Horbach^{1,2}

¹ Institut für Physik, Johannes Gutenberg–Universität Mainz, Staudinger Weg 7, D–55099 Mainz, Germany
juergen.horbach@dlr.de

² Institut für Materialphysik im Weltraum, Deutsches Zentrum für Luft-und Raumfahrt, Linder Höhe, D-51147 Köln, Germany

Abstract. Molecular dynamics (MD) simulations of various sodium silicate melts, $(\text{Na}_2\text{O})_x(\text{SiO}_2)$ with $x = 2, 3, 20$, are presented. In these systems, the mobility of sodium ions is much higher, often by orders of magnitude, than that of the silicon and oxygen atoms forming a tetrahedral network structure. We show that the high mobility of sodium is intimately related to the chemical ordering in sodium silicates. A network of percolating sodium-rich channels is formed in the static structure that serve as diffusion channels for the sodium ions. This channel network is revealed in static structure factors by a prepeak at the wavenumber $q = 0.95 \text{ \AA}^{-1}$. Inelastic neutron scattering experiments of sodium silicate melts, done at temperatures as high as 1600 K, confirm the existence of the latter prepeak. The channel diffusion of sodium ions yields a peculiar behavior of time-dependent density–density correlation functions, the so-called intermediate scattering functions. Whereas the incoherent scattering function for sodium, $F_{\text{Na}}^{\text{s}}(q, t)$, detects the fast sodium ion diffusion, the coherent scattering function for Na–Na correlations, $F_{\text{NaNa}}(q, t)$, decays on the slow time-scale of the Si–O matrix. This reflects the hopping motion of sodium ions between sodium sites, thereby $F_{\text{NaNa}}(q, t)$ describing site–site correlations. Numerical calculations in the framework of mode-coupling theory (MCT) are presented which use the partial static structure factors from the MD simulations as an input. The MCT results are in qualitative agreement with those from MD simulations.

6.1 Introduction

In multicomponent glassforming systems, a time-scale separation between different chemical components may occur. Paradigms of such systems are alkali silicate melts [1, 2, 3]. Here, the tetrahedral Si–O network is partially disrupted by the alkali ions, accompanied by a high alkali ion mobility. More than 20 years ago, it has been suggested by Angell and others [4, 5, 6] that there are “preferential pathways” in the static structure through which the alkali ions

can easily move, thus explaining the high mobility of alkali ions. If the latter “pathways” exist, it should be possible to identify them by structural quantities. Moreover, it should be possible to predict the dynamics, in particular the fast transport of alkali ions in a quasi-frozen Si–O network, from the equilibrium structure. The investigation of such a structure–dynamics relation in sodium silicates is addressed in the following. This review is based on results from molecular dynamics (MD) computer simulations, inelastic neutron scattering, and calculations in the framework of mode-coupling theory (MCT) [7].

A characteristic feature of amorphous mixtures of SiO_2 with other oxides such as Na_2O , K_2O , MgO , CaO , or Al_2O_3 is the appearance of characteristic length scales that go beyond that of the distance between atoms that are nearest neighbors. These length scales are often reflected by prepeaks in static structure functions. Examples for such prepeaks have been found in neutron scattering experiments and Molecular Dynamics (MD) computer simulations: Gaskell et al. [8] were able to measure the partial structure factors of a calcium silicate glass by means of neutron scattering and found a peak around a wavenumber $q = 1.3 \text{ \AA}^{-1}$. In sodium silicate melts of different compositions, a similar prepeak was found around $q = 0.95 \text{ \AA}^{-1}$ both in neutron scattering [9, 10] and MD simulation [11, 12, 13]. As evidenced by MD simulation studies [13, 14, 15], also in structure factors of aluminium silicate melts a prepeak occurs at $q = 0.5 \text{ \AA}^{-1}$. All these features stem from an inhomogeneous distribution of the cations on length scales of the order of 5–15 \AA .

For sodium silicates, it has been shown that the prepeak around $q = 0.95 \text{ \AA}^{-1}$ is intimately related to the high mobility of sodium ions in these systems [16, 17]. The structure that leads to this prepeak is that of a percolating network of sodium-rich channels, serving as “preferential pathways” for the sodium diffusion. In these channels, there are characteristic sodium ion sites that provide a hopping motion of the sodium ions from site to site. Note that the latter hopping motion has been identified in various simulations of alkali silicates [4, 11, 18, 19, 20, 21, 22].

In order to “prove” the structure–dynamics relation, a microscopic theory is desirable which is able to predict the dynamics from structural quantities. Such a theory is the MCT of the glass transition which has been developed to describe structural relaxation in glassforming liquids [7]. MCT uses structural input, in particular the partial static structure factors, to predict the temperature dependence of time-dependent density correlation function from which also transport coefficients can be extracted. Thereby, the structural input can be provided by MD simulations and then the MCT predictions for the dynamics can be tested against those from MD. This program has been performed for different models of glassforming systems, ranging from hard-sphere systems and systems with a hard-sphere like structure [23, 24, 25, 26, 27] to liquids with orientational degrees of freedom [28, 29, 30]. In all these cases, MCT was able to predict the dynamics on a qualitative level and, e.g., in the case of hard-sphere systems, also on a quantitative level. Even in the case

of silica (SiO_2), MCT was able to predict Debye–Waller factors to within a few percent [31]. In a recent study [32], MCT was applied to sodium silicates, and it was shown that MCT reproduces the time-scale separation in sodium silicates. The results of this study are reviewed below.

The rest of these lecture notes is organized as follows: In Sect. 6.2, we describe the model for sodium silicates that is used in the present study, and we give the main details of the simulation. Section 6.3 is then devoted to the structure of sodium silicates. Here, we first describe the structural quantities that are calculated (in particular static structure functions of concentration densities), before we present results both from MD simulations and inelastic neutron scattering. Section 6.4 is then on the MD results of dynamic correlation functions, and in Sect. 6.5, the MD is compared to MCT calculations.

6.2 Model and Details of the Simulation

In order to model the interactions between the atoms in sodium silicate melts, we use a simple pair potential proposed by Kramer et al. [33] which is based on the BKS potential for pure silica [34]. The details of the Kramer potential as well as the modifications that we have introduced can be found in [11, 33]. MD simulations with the latter potential yield results for structural and dynamic quantities that agree well with experimental data [11, 13], and also ab initio simulations (Car–Parrinello molecular dynamics) of $(\text{Na}_2\text{O})_4(\text{SiO}_2)$ lead to comparable results for structural quantities when compared to molecular dynamics simulations with our potential [35].

In the following, we consider mainly the systems $(\text{Na}_2\text{O})_2(\text{SiO}_2)$ [NS2] and $(\text{Na}_2\text{O})_{20}(\text{SiO}_2)$ [NS20] as well as SiO_2 , which contain 33.3, 4.8, and 0 mol% Na_2O , respectively. In all three cases, the density was kept constant at $\rho = 2.37 \text{ g/cm}^3$. The simulations were done for systems of 8064 particles in the case of the sodium silicates and of 8016 particles in the case of SiO_2 . The equations of motion were integrated with the velocity form of the Verlet algorithm [36, 37] using a time step of 1.6 fs for the integration. The different systems were investigated in fully equilibrated melt states as well as below the glass transition temperatures of the simulations. During the equilibration, the temperature was kept constant by coupling the systems to a stochastic heat bath, and after the equilibration, the runs were continued in the micro-canonical ensemble to measure the static and dynamic quantities of interest. The temperature ranges investigated were $4000 \text{ K} \geq T \geq 2100 \text{ K}$ for NS2, $6100 \text{ K} \geq T \geq 2500 \text{ K}$ for NS20, and $6100 \text{ K} \geq T \geq 2750 \text{ K}$ for SiO_2 . The longest equilibration runs, i.e., the runs at the lowest temperatures in the latter ranges, lasted over 1.5 million time steps for NS2, 5 million time steps for NS20, and 12 million time steps for SiO_2 . Thus, at the lowest temperatures, the typical relaxation times of the systems under consideration were in the range between 2.5 and 20 ns. The glass samples were produced by cooling

the systems from the lowest melt temperature to 0 K with a cooling rate of about 10^{12} K/s. In order to improve the statistics, two independent runs were done at each temperature. More details on the simulations can be found in [11, 12, 17, 38].

Figure 6.1 shows the temperature dependence of the pressure for the different runs (the *solid lines* correspond to states below the glass transition temperature of the simulation, and the *symbols* correspond to states of the equilibrated melt). The behavior of $p(T)$ is very similar in SiO_2 and NS20. This means probably that the small Na_2O content in NS20 does not affect the structure of the SiO_4 network very strongly. Around 4800 K in SiO_2 and 4400 K in NS20, we find a minimum in $p(T)$ which corresponds to a density maximum in a constant pressure simulation (see the simulation of Vollmayr et al. [39]). A density maximum is also an experimentally well-known property, but the measured value at which the density maximum occurs is at a much lower temperature, namely around 1820 K [40, 41]. As we can also infer from Fig. 6.1 the behavior of $p(T)$ for NS2 is very different from that of SiO_2 : In this case, no anomaly is visible anymore and the pressure increases with increasing temperature. The pressure of the NS2 system is 0.57 GPa at $T = 2100$ K, and it becomes negative slightly below 2000 K. Note that simulations at $\rho = 2.5 \text{ g/cm}^3$ [42] show that the pressure is close to zero at $T = 300$ K, in very good agreement with experiment [43]. However, one should keep in mind that the thermal history of experimental samples is very different from that of our computer glass. The simulation produces glass samples at

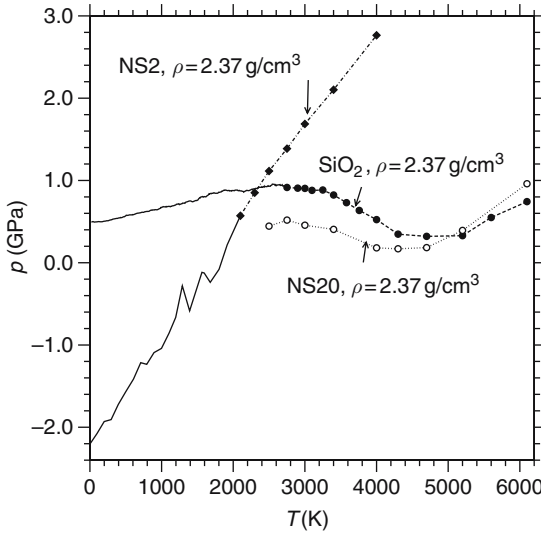


Fig. 6.1. Temperature dependence of the pressure for the indicated systems. The *symbols* correspond to states of fully equilibrated melts, whereas the *solid lines* correspond to simulations below the glass transition

a much higher cooling rate than the experiment. Thus, one may expect that the agreement is not as perfect as it seems at first glance.

6.3 The Structure of Sodium Silicates

6.3.1 Basic Quantities

Now we define static correlation functions with which we analyze the structure of sodium silicates. We follow the paper by Bl  try [44] that generalizes the Bhatia–Thornton formalism [45] for two component systems to systems with arbitrarily many components. Of course, our interest in this work is in systems with three chemical components. In particular, we derive the structure factors of concentration densities since these quantities are useful to identify structural order on intermediate length scales.

Consider a mixture of n chemical species that contains a total number of $N = \sum_{\alpha=1}^n N_{\alpha}$ particles, with N_{α} the number of particles of species α . The local number density in reciprocal space for particles of type α is defined as follows:

$$\rho_{\alpha} = \sum_{k=1}^{N_{\alpha}} \exp(i\mathbf{q} \cdot \mathbf{r}_k), \quad (6.1)$$

with \mathbf{q} the wavevector and \mathbf{r}_k the position of particle k of type α . The partial structure factors are given by [46]

$$S_{\alpha\beta}(q) = \frac{1}{N} \langle \rho_{\alpha}(\mathbf{q}) \rho_{\beta}(-\mathbf{q}) \rangle. \quad (6.2)$$

Note that, in this equation, we assume that the system is isotropic and thus, each of the $S_{\alpha\beta}(q)$ depends only on the magnitude of wavevector \mathbf{q} . Obviously, the functions $S_{\alpha\beta}(q)$ are symmetric, i.e., $S_{\alpha\beta}(q) = S_{\beta\alpha}(q)$, and therefore, there are $n(n+1)/2$ independent partial structure factors. For $q \rightarrow \infty$, the functions $S_{\alpha\beta}(q)$, as defined by (6.2), approach $x_{\alpha} = N_{\alpha}/N$ for $\alpha = \beta$ and zero for $\alpha \neq \beta$. We show below that concentration–concentration structure factors can be written as linear combinations of the partial structure factors $S_{\alpha\beta}(q)$.

The local concentration variables for particles of type α are given by

$$c_{\alpha}(\mathbf{q}) = \rho_{\alpha}(\mathbf{q}) - x_{\alpha} \sum_{\beta=1}^n \rho_{\beta}(\mathbf{q}). \quad (6.3)$$

The densities $c_{\alpha}(\mathbf{q})$ describe the local deviation from a homogeneous concentration distribution of particles of type α (thus, if ρ_{α} is equal to N_{α}/N for $\alpha = 1, \dots, n$ the variables c_{α} vanish). The partial structure factors that correspond to the concentration fluctuations $c_{\alpha}(\mathbf{q})$ follow a similar definition as the partial structure factors for the number densities:

$$S_{c_\alpha c_\beta}(q) = \frac{1}{N} \langle c_\alpha(\mathbf{q}) c_\beta(-\mathbf{q}) \rangle . \quad (6.4)$$

Again these functions are symmetric, i.e., $S_{c_\alpha c_\beta}(q) = S_{c_\beta c_\alpha}(q)$. Moreover, the sum rule

$$\sum_{\beta=1}^n S_{c_\alpha c_\beta}(q) = 0 \quad (6.5)$$

follows directly from the definition (6.4).

For the case $n = 2$, one has $c_1 = -c_2$ and thus $S_{c_1 c_1}(q) = S_{c_2 c_2}(q)$. Furthermore, (6.5) yields $S_{cc}(q) = S_{c_1 c_1}(q) = -S_{c_1 c_2}(q)$. Thus, for $n = 2$, only one independent concentration–concentration structure factor $S_{cc}(q)$ exists which can be expressed as a linear combination of the partial structure factors given by (6.2),

$$S_{cc}(q) = x_2^2 S_{11}(q) + x_1^2 S_{22}(q) - 2x_1 x_2 S_{12}(q) . \quad (6.6)$$

Note that for $q \rightarrow \infty$, this correlation function approaches $x_1 x_2$.

The case $n = 3$ is slightly more complicated. Now, the functions $S_{\alpha\beta}(q)$ with $\alpha = \beta$ are given by the following linear combinations of the partial structure factors for the number densities:

$$\begin{aligned} S_{c_1 c_1}(q) &= (x_2 + x_3)^2 S_{11}(q) - 2x_1(x_2 + x_3)[S_{12}(q) + S_{13}(q)] \\ &\quad + x_1^2[S_{22}(q) + 2S_{23}(q) + S_{33}(q)] , \end{aligned} \quad (6.7)$$

$$\begin{aligned} S_{c_2 c_2}(q) &= (x_1 + x_3)^2 S_{22}(q) - 2x_2(x_1 + x_3)[S_{12}(q) + S_{23}(q)] \\ &\quad + x_2^2[S_{11}(q) + 2S_{13}(q) + S_{33}(q)] , \end{aligned} \quad (6.8)$$

$$\begin{aligned} S_{c_3 c_3}(q) &= (x_1 + x_2)^2 S_{33}(q) - 2x_3(x_1 + x_2)[S_{13}(q) + S_{23}(q)] \\ &\quad + x_3^2[S_{11}(q) + 2S_{12}(q) + S_{22}(q)] . \end{aligned} \quad (6.9)$$

Each of the $S_{c_\alpha c_\beta}(q)$ with $\alpha \neq \beta$ can be written as a linear combination of the three $S_{c_\alpha c_\alpha}(q)$,

$$S_{c_1 c_2}(q) = \frac{1}{2}[S_{c_3 c_3}(q) - S_{c_1 c_1}(q) - S_{c_2 c_2}(q)] , \quad (6.10)$$

$$S_{c_1 c_3}(q) = \frac{1}{2}[S_{c_2 c_2}(q) - S_{c_1 c_1}(q) - S_{c_3 c_3}(q)] , \quad (6.11)$$

$$S_{c_2 c_3}(q) = \frac{1}{2}[S_{c_1 c_1}(q) - S_{c_2 c_2}(q) - S_{c_3 c_3}(q)] . \quad (6.12)$$

Thus, the latter functions do not contain any additional information and so we consider only the correlation functions (6.7)–(6.9) in the following.

6.3.2 Simulated Structure Factors for Sodium Silicates

As we have mentioned in the introduction, the sodium ions disrupt partially the tetrahedral Si–O network. This can be directly recognized in the partial

structure factors $S_{\alpha\beta}(q)$ (defined by (6.2)). Three of them, i.e., the ones for the NaNa, NaO, and SiNa correlations, are shown in Fig. 6.2a for NS2 at $T = 2100$ K. Different from the structure factors for pure SiO_2 , a peak around 1.7 \AA^{-1} is absent which would indicate the tetrahedral network structure. Note that a peak at 1.7 \AA^{-1} is also observed in the SiSi, SiO, and OO correlations in NS2. However, it has a much smaller amplitude than in SiO_2 [11]. An interesting feature in Fig. 6.2a is an additional peak around $q_1 = 0.95 \text{ \AA}^{-1}$ which is not present in structure factors of pure SiO_2 . The length scales that correspond to q_1 are of the order of $6\text{--}7 \text{ \AA}$, and this is about the distance between next-nearest Na–Na or Si–Na neighbors [11]. In NS20 (Fig. 6.2b), one can still identify peaks around q_1 although they have moved to a slightly smaller q in $S_{\text{NaNa}}(q)$ and to a slightly larger q in $S_{\text{SiNa}}(q)$ and $S_{\text{NaO}}(q)$.

In order to elucidate the structure that underlies the peak at q_1 , we turn now our attention to the behavior of the structure factors $S_{c_\alpha c_\alpha}(q)$ for SiO_2 , NS20, and NS2. We have seen in Sect. 6.2 that these quantities can be calculated as linear combinations of the partial structure factors $S_{\alpha\beta}(q)$ (see (6.7)–(6.9)).

Figure 6.3 shows the functions $S_{c_\alpha c_\alpha}(q)$, $\alpha \in \{\text{Si}, \text{O}, \text{Na}\}$, for NS2 at different temperatures. As we can infer from the figure, in all three cases, the temperature dependence is relatively weak: At $T = 4000$ K, the curves exhibit already all the features that are present at $T = 2100$ K and $T = 300$ K. In $S_{c_{\text{Si}}c_{\text{Si}}}(q)$ and $S_{c_{\text{Na}}c_{\text{Na}}}(q)$, there are peaks around $q_2^{\text{Si}} = 2.72 \text{ \AA}^{-1}$ and $q_2^{\text{Na}} = 2.18 \text{ \AA}^{-1}$, respectively. These peaks reflect the chemical ordering in

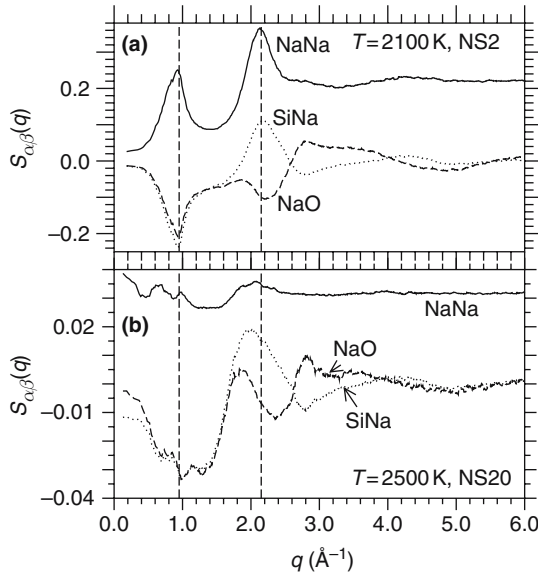


Fig. 6.2. Partial structure factors $S_{\text{NaNa}}(q)$ (solid lines), $S_{\text{SiNa}}(q)$ (dotted lines), and $S_{\text{NaO}}(q)$ (dashed lines) for (a) NS2 at $T = 2100$ K and (b) NS20 at $T = 2500$ K

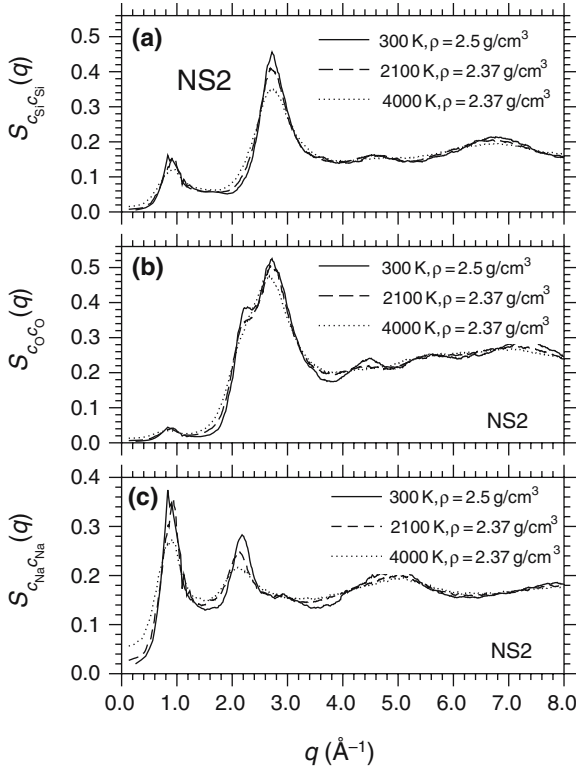


Fig. 6.3. Structure functions of the concentration densities for NS2 at the indicated temperatures and densities. (a) $S_{c_{\text{Si}}c_{\text{Si}}}(q)$, (b) $S_{c_{\text{O}}c_{\text{O}}}(q)$, (c) $S_{c_{\text{Na}}c_{\text{Na}}}(q)$

NS2: Between nearest cation neighbors, there is always a shell of oxygen atoms, i.e., strong fluctuations in the local concentrations of the cations occur on lengths of the order of the nearest cation–oxygen distance. And indeed, the lengths $2\pi/q_2^{\text{Si}} \approx 2.3 \text{ \AA}$ and $2\pi/q_2^{\text{Na}} \approx 2.9 \text{ \AA}$ that correspond respectively to the peaks at q_2^{Si} and at q_2^{Na} are approximately the locations of the first minima in the partial pair correlation functions for the Si–O and Na–O correlations, respectively [11, 38]. In $S_{c_{\text{O}}c_{\text{O}}}(q)$, there is an overlap of the peaks at q_2^{Si} and q_2^{Na} . This is reasonable since the oxygen atoms are distributed both around silicon and sodium atoms.

As we further see in Fig. 6.3, in all of the three structure functions, there is a peak at $q_1 = 0.95 \text{ \AA}^{-1}$ that we have already identified in the partial structure factors. The appearance of this prepeak in structure factors of concentration densities reveals a microsegregation into sodium-rich regions and the tetrahedral Si–O network: A Na–O rich network is formed that percolates through the SiO_2 structure, and the characteristic length scale of this sodium-rich network is given by $\approx 2\pi/q_1 = 7 \text{ \AA}$. It is reasonable that the concentration fluctuations as reflected by q_1 are weaker in $S_{c_{\text{O}}c_{\text{O}}}(q)$ because

the oxygen atoms can only distinguish between Na and Si rich regions through their different chemical ordering around the cationic species.

It is now interesting to see how the $S_{c_\alpha c_\alpha}(q)$ look like in NS20, i.e., a system with a relatively low Na₂O content of 4.8 mol%. As we can infer from Fig. 6.4, the temperature dependence of $S_{c_{\text{Si}c_{\text{Si}}}}(q)$ and $S_{c_{\text{O}c_{\text{O}}}}(q)$ is again relatively weak. Only minor changes occur from 4000 to 2500 K. In this figure, we also include $S_{cc}(q)$ for SiO₂ at $T = 2750$ K (as calculated by (6.6)). The curve that corresponds to this function is essentially on top of the curves for $S_{c_{\text{Si}c_{\text{Si}}}}(q)$ and $S_{c_{\text{O}c_{\text{O}}}}(q)$ for NS20 at $T = 2500$ K. So obviously, the presence of the sodium atoms in NS20 does not affect the structure of the SiO₂ network significantly (and this is also in agreement with the aforementioned behavior of the pressure in NS20 and SiO₂). A peculiar feature in the curves of Fig. 6.4a and b is a shoulder around 1.7 \AA^{-1} which indicates the tetrahedral network structure. Note that this feature is much more pronounced in the structure factors for the number densities and appears there as a peak around 1.7 \AA^{-1} (see [38, 39] and references therein).

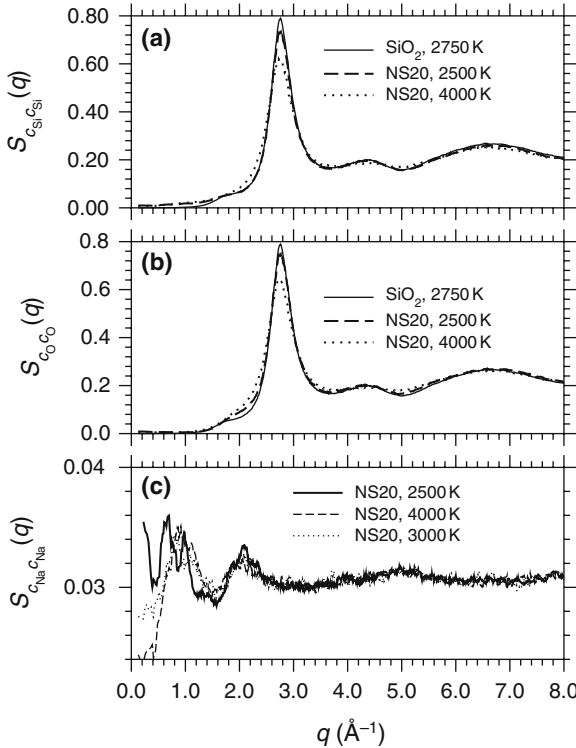


Fig. 6.4. Structure functions of the concentration densities for NS20 at the indicated temperatures and densities. (a) $S_{c_{\text{Si}c_{\text{Si}}}}(q)$, (b) $S_{c_{\text{O}c_{\text{O}}}}(q)$, (c) $S_{c_{\text{Na}c_{\text{Na}}}}(q)$. In (a) and (b) also $S_{cc}(q)$ as defined by (6.6) is shown for SiO₂

Very interesting is the behavior of $S_{c_{\text{Na}c_{\text{Na}}}}(q)$ in NS20: At high temperatures, i.e., at $T = 3000$ and 4000 K, there is still a peak around $q_1 = 0.95 \text{ \AA}^{-1}$ although the Na_2O content is very small. At $T = 2500$ K, the peak at q_1 splits into two peaks, one at $q = 0.7 \text{ \AA}^{-1}$ and the other one at $q = 1.0 \text{ \AA}^{-1}$. The occurrence of two characteristic length scales on a nanoscopic scale reveals that the distribution of sodium ions becomes more heterogeneous at low temperatures and this might be an indicator that at $T = 2500$ K, Na_2O and SiO_2 are not miscible anymore, and thus we see the early stages of a phase separation. This is supported by the fact that $S_{c_{\text{Na}c_{\text{Na}}}}(q)$ seems to increase strongly in the limit $q \rightarrow 0$. Note that it is also a well-known experimental fact that NS20 is immiscible at typical melt temperatures [47].

6.3.3 Experiment Versus Simulation

The MD simulations presented in the previous section yield the emergence of an inhomogeneous distribution of sodium ions on intermediate length scales that is reflected in a prepeak around $q_1 = 0.95 \text{ \AA}^{-1}$ in various static structure factors. In this section, we address the question whether the latter prepeak appears also in real sodium silicate melts. To this end, we present the results of a study on $(\text{Na}_2\text{O})_3(\text{SiO}_2)$ [NS3] using a combination of inelastic neutron scattering and MD simulations [10]. Note that the properties of NS3 are very similar to those of NS2 which is evident both from simulation and experiment [9, 10, 11, 48]. Thus, the conclusion that is drawn below holds also for NS2.

The inelastic neutron scattering experiments were performed at room temperature (i.e., $T = 293$ K) and on liquid samples at temperatures between 1200 and 1600 K on the neutron time-of-flight spectrometer IN6 of the Institut Laue-Langevin in Grenoble [9, 10]. In these measurements, the elastic structure factor $S(q, \omega = 0)$ (with ω the frequency) can be extracted (see below) was determined, from which in good approximation the static structure factor $S(q)$. This quantity can be also measured in the simulation. To this end, the time-dependent dynamic structure factor $S(q, t)$ has to be determined, which is defined by

$$S(q, t) = \frac{N}{\sum_{\alpha} N_{\alpha} b_{\alpha}^2} \sum_{\alpha, \beta} b_{\alpha} b_{\beta} S_{\alpha\beta}(q, t), \quad \alpha, \beta \in \{\text{Si, Na, O}\} \quad (6.13)$$

with

$$S_{\alpha\beta}(q, t) = \frac{1}{N} \sum_{k=1}^{N_{\alpha}} \sum_{l=1}^{N_{\beta}} \langle \exp[i\mathbf{q} \cdot (\mathbf{r}_k(t) - \mathbf{r}_l(0))] \rangle, \quad (6.14)$$

$\mathbf{r}_i(t)$ the position vector of particle i at time t . In (6.13), b_{α} denotes the experimental coherent scattering lengths of particle species α . The elastic structure factors can be estimated by the equation $S(q, \omega = 0) = f(q)S(q)$ (with $S(q) \equiv S(q, t = 0)$) where the Debye–Waller factor $f(q)$ can be

determined by fitting in the β -relaxation regime the normalized quantity $F(q, t) = S(q, t)/S(q)$ to a von Schweidler law (for details see [17, 49]).

Figure 6.5 displays the elastic structure factor of glassy and viscous NS3 as seen by inelastic neutron scattering. As discussed before, the maximum at 1.7 \AA^{-1} corresponds to the disrupted tetrahedral Si–O network structure in sodium silicates. With increasing temperature, the elastic scattered intensity at this wave-vector is decreasing at the expense of an increasing inelastic scattering. In contrast, $S(q, \omega = 0)$ displays an emerging prepeak around 0.95 \AA^{-1} which grows with increasing temperature. Although we have identified this prepeak above also in the simulation, the growth of this peak with increasing temperature seems to be in contradiction to the simulation data: For a monoatomic system, a change in the structure that is due to thermal expansion would lead – beside a slight shift of the peak positions towards a smaller q value – to a decreasing intensity of the peak height with increasing temperature. Thus, the emerging prepeak in the elastic structure factors as shown in Fig. 6.5 does not seem to be merely caused by thermal expansion but might be related to a change in the underlying structure, in contrast to the simulation results seen in Fig. 6.3. However, this behavior of the experimental elastic structure factors can be clarified by the MD simulations.

The simulations were done at various densities for systems of $N = 8064$ particles ($N_{\text{Si}} = 2016$, $N_{\text{Na}} = 1344$, and $N_{\text{O}} = 4704$). As before for NS2 and NS20, the potential proposed by Kramer et al. [33] was used. At the densities 2.2 and 2.37 g/cm^3 , systems at the temperature $T = 2100 \text{ K}$, i.e., in the liquid state, were equilibrated for 3.3 ns followed by microcanonical production runs of the same length. In each case, two independent runs were done in order to improve the statistics. The equilibrated systems at the density $\rho = 2.37 \text{ g/cm}^3$ were also quenched to a glass state at $T = 300 \text{ K}$ using a cooling rate

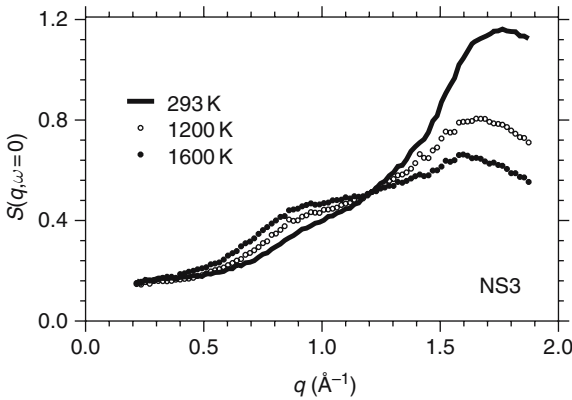


Fig. 6.5. Elastic structure factor of NS3 from inelastic neutron scattering for different temperatures, as indicated

of about 10^{12} K/s. In the latter simulation, the pressure was kept constant at ambient pressure which yielded a density of 2.46 g/cm^3 at 300 K. Note that the densities $\rho = 2.2 \text{ g/cm}^3$ and $\rho = 2.46 \text{ g/cm}^3$ are close to the experimental densities at $T = 2100 \text{ K}$ and $T = 300 \text{ K}$, respectively [43].

Figure 6.6 displays the neutron scattering elastic structure factor of NS3 as determined from the simulation. We observe a similar behavior as in the neutron scattering experiment: Around 1.7 \AA^{-1} , the elastic scattered intensity decreases with increasing temperature, and around 0.95 \AA^{-1} a shoulder is present at $T = 2100 \text{ K}$ which is nearly absent in the glass at $T = 300 \text{ K}$. Also shown in Fig. 6.6 is the elastic structure factor at the density of 2.37 g/cm^3 at $T = 2100 \text{ K}$. Here, the shoulder around 0.95 \AA^{-1} has a smaller amplitude than in the corresponding case at the experimental density. This gives evidence that the possible structural changes leading to a more pronounced appearance of the feature around 0.95 \AA^{-1} in $S(q, \omega = 0)$ are not due to a change in temperature, but due to the change in the density. Thus, the question arises whether the shoulder around 0.95 \AA^{-1} is related to structural features that tend to disappear with increasing density.

The puzzling behavior of the elastic structure factors can be easily clarified by the partial static structure factors $S_{\alpha\beta}(q)$. Three of these functions are shown in Fig. 6.7 (at the experimental densities for different correlations, as indicated): A well-pronounced peak is present in $S_{\text{SiNa}}(q)$ and $S_{\text{NaNa}}(q)$ at $T = 2100 \text{ K}$ and at $T = 300 \text{ K}$. Thus, the structure that leads to the peak at $q_1 = 0.95 \text{ \AA}^{-1}$ does not at all disappear with increasing density. That the feature at q_1 seems to be absent in $S(q, \omega = 0)$ at 300 K is due to the fact that $S(q, \omega = 0)$ is a linear combination of six different partial structure factors: On the one hand, positive and negative contributions cancel each other (note the negative

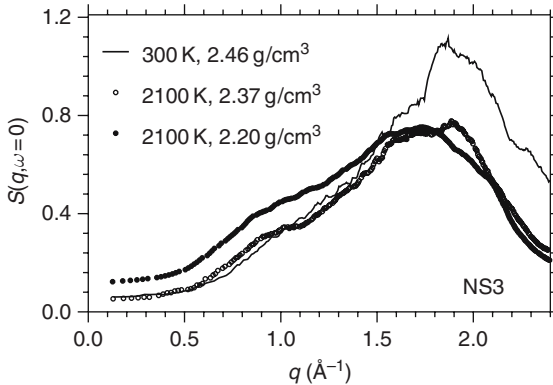


Fig. 6.6. Elastic structure factor of sodium trisilicate as obtained by molecular dynamics simulation (see text) weighted with the neutron scattering lengths: Note the emerging prepeak at $\simeq 0.9 \text{ \AA}^{-1}$ with decreasing density

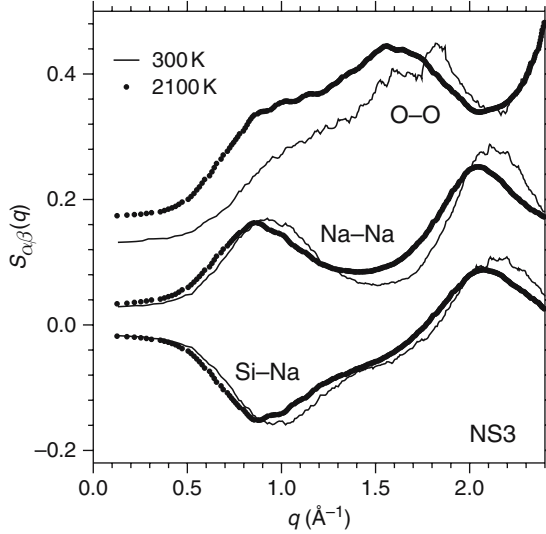


Fig. 6.7. Partial structure factors $S_{\text{OO}}(q)$, $S_{\text{NaNa}}(q)$, $S_{\text{SiNa}}(q)$ as obtained by the simulation in glassy and liquid sodium trisilicate at experimental densities. $S_{\text{OO}}(q) + 0.1$ for clarity

amplitude of $S_{\text{SiNa}}(q)$ at q_1), and on the other hand, due to the overlap with the peak around $q_2 = 1.7 \text{ \AA}^{-1}$, $S_{\text{OO}}(q)$ exhibits only a shoulder at q_1 which is less pronounced at $T = 300 \text{ K}$. Because oxygen is the majority component (about 60% of the particles in NS3) and the coherent scattering length of oxygen is significantly larger than that of sodium and silicon ($b_{\text{O}}/b_{\text{Si}} \approx 1.4$ and $b_{\text{O}}/b_{\text{Na}} \approx 1.6$), $S_{\text{OO}}(q)$ gives the major contribution to $S(q, \omega = 0)$ and thus, the changes in $S_{\text{OO}}(q)$ are the main cause for the emerging prepeak in the experimental and simulated $S(q, \omega = 0)$ with increasing temperature and decreasing density, respectively.

The results presented in this section demonstrate how computer simulations can be used to elucidate experimental data. This requires a molecular dynamics model that describes the real system accurately. Then, since the MD provides more detailed information than the experiment, new insight can be gained on material's properties, in our case the intermediate range order in sodium silicates.

6.4 Channel Diffusion

We now turn our attention to the dynamics in sodium silicates. Figure 6.8 shows an Arrhenius plot of the self-diffusion constants D_{α} ($\alpha = \text{Si}, \text{O}, \text{Na}$) for SiO_2 , NS20, and NS2. We recognize from the figure that the dynamics in

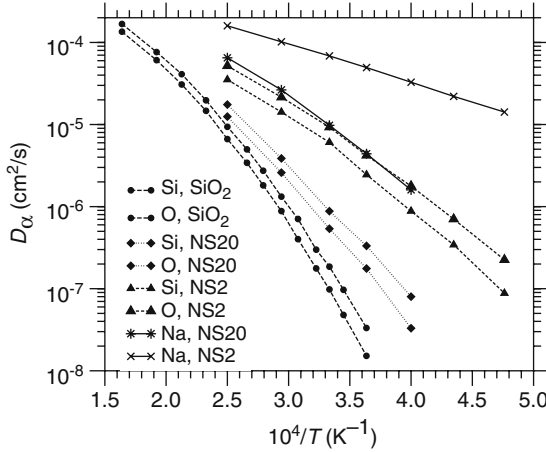


Fig. 6.8. Arrhenius plot of self-diffusion constants D_α ($\alpha = \text{Si, O, Na}$) for SiO_2 , NS20, and NS2, as indicated

sodium silicates is faster than in SiO_2 . For instance, at $T = 2750$ K, the silicon diffusion constant for NS20 is almost one order of magnitude larger than that for SiO_2 . In the case of NS2, D_{Si} is even two orders of magnitude higher than in SiO_2 . Moreover, a significant time-scale separation between the sodium motion and that of the Si–O network is evident: Even above 2000 K, D_{Na} is up to two orders of magnitude higher than D_{Si} and D_{O} . Whereas D_{Na} for NS2 follows an Arrhenius law (with an activation energy of 0.93 eV [11]), the temperature dependence of D_{Na} for NS20 is non-Arrhenius and more similar to that of D_{Si} and D_{O} . This indicates that the mechanism for the sodium diffusion changes from NS20 to NS2.

Now, we address the question whether the time-scale separation in NS2 can be related to the structure, in particular to the prepeak seen at $q_1 = 0.95 \text{ \AA}^{-1}$ in static structure factors. To this end, we follow an idea of Jund et al. [19], and we divide the simulation box into 48^3 small cubes with a linear size of about 1 \AA (note that the linear dimension of the simulation box is $L = 48.653 \text{ \AA}$). Then we calculate the probability $P(t)$ that a cube which does not contain a sodium ion at time zero is also not visited by a sodium ion until a later time t . The time dependence of $P(t)$ is shown in the inset of Fig. 6.9. Even after 2.5 ns, more than 50% of the cubes have not yet been visited by sodium ions (note that after this time, the mean squared displacement of the Na atoms is more than 45 \AA^2 , thus these atoms have moved already over a large distance). From this observation, one can infer that the sodium diffusion is restricted to a subspace within the Si–O network.

In order to analyze the structure of this subspace, we define a “Swiss cheese” structure factor $S_{\text{sc}}(q, t)$ as follows: We assign to each cube which has not been visited by a sodium atom until time t a point, and we compute the static structure factor of $N_{\text{sc}}(t) = P(t)(48^3 - N_{\text{Na}})$ points:

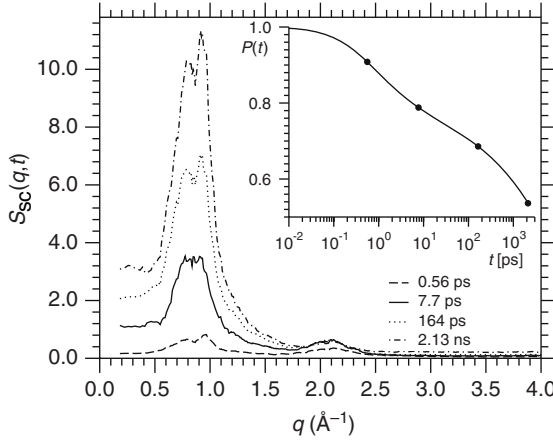


Fig. 6.9. “Swiss cheese” structure factor $S_{sc}(q, t)$ for the sodium free regions at $T = 2100$ K for $t = 0.56, 7.7, 164$ ps, and 2.13 ns. The inset shows the probability $P(t)$ that a cube which is sodium free at time zero remains sodium free until time t . The *circles* on the curve for $P(t)$ are at the times at which $S_{sc}(q, t)$ is shown

$$S_{sc}(q, t) = \frac{1}{N_{sc}(t)} \sum_{k,l=1}^{N_{sc}(t)} \exp(i\mathbf{q} \cdot (\mathbf{r}_k - \mathbf{r}_l)) . \quad (6.15)$$

This quantity is shown in Fig. 6.9 for four different times: $t = 0.56, 7.7, 164$ ps, and 2.13 ns. We see that $S_{sc}(q, t)$ has peaks at $q_1 = 0.95 \text{ \AA}^{-1}$ and $q_2 = 2.15 \text{ \AA}^{-1}$ which are also the prominent features in $S_{NaNa}(q)$, the static structure factor for the NaNa correlations [11]. With increasing time, the height of the peak at q_1 in $S_{sc}(q, t)$ increases quickly. Note that this peak decreases again on time-scales where the Si–O matrix starts to reconstruct itself significantly. In Sect. 3.2, we have associated the prepeak at q_1 (e.g., in the partial static structure factors) to sodium-rich regions that percolate through the Si–O network. Now, we see that this structure on intermediate length scales is reflected in the sodium dynamics. It provides a network of diffusion channels that enable the high mobility of the sodium ions.

The motion of the sodium ions, which is restricted to a subspace (the network of diffusion channels), is accompanied by a peculiar behavior of dynamic structure factors for the sodium correlations, namely the sodium–sodium (coherent) and the sodium-self (incoherent) correlation functions [46, 49], $F_{\alpha\alpha}(q, t) = S_{\alpha\alpha}(q, t)/S_{\alpha\alpha}(q)$ and $F_{\alpha}^s(q, t)$ in the case $\alpha = \text{Na}$. In Fig. 6.10, these functions are displayed for three different wave-vectors: $q = 0.94, 2.0$, and 2.75 \AA^{-1} . From this figure, we infer immediately a surprising result: At $q = 0.94 \text{ \AA}^{-1}$, i.e., at the characteristic q value of the sodium channel structure, $F_{NaNa}(q, t)$ decays on a time-scale which is two orders of magnitude larger than the one for $F_{Na}^s(q, t)$. This result can be rationalized by the idea that the sodium atoms move quickly between preferential sites, since this type

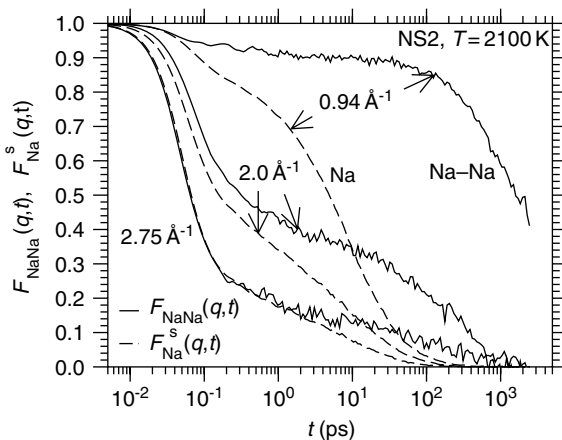


Fig. 6.10. Coherent intermediate scattering functions $F_{\text{NaNa}}(q, t)$ (solid lines) and incoherent intermediate scattering functions $F_{\text{Na}}^s(q, t)$ (dashed lines) at $T = 2100$ K for the indicated values of q

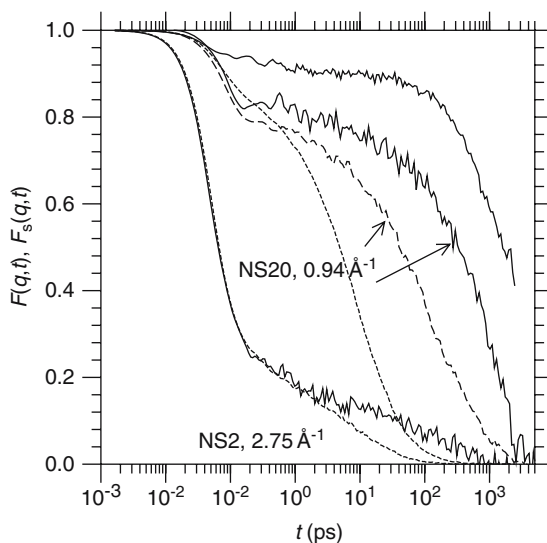


Fig. 6.11. Coherent intermediate scattering functions $F_{\text{NaNa}}(q, t)$ (solid lines) and incoherent intermediate scattering functions $F_{s,\text{Na}}(q, t)$ (dashed lines) for the indicated values of q . The bold lines correspond to NS20 at $T = 2500$ K, whereas the thin lines are for NS2 at $T = 2100$ K. For NS20 at $T = 2500$ K also $F_{\text{SiSi}}(q, t)$ at $q = 0.94 \text{ \AA}^{-1}$ is shown (bold dotted line)

of motion gives rise to a fast decorrelation of the incoherent function, whereas it does not affect the coherent one. Only on the time-scale of the relaxation of the Si–O matrix does the coherent function start to decay. Note that the slow decay of $F_{\text{NaNa}}(q, t)$ is most pronounced around q_1 . For different q , the function decays significantly faster as can be seen from the other curves shown in Fig. 6.10. In NS20, $F_{\text{NaNa}}(q, t)$ decays also significantly slower around q_1 than $F_{\text{Na}}^s(q, t)$. However, the effect is much less pronounced than in NS2 in this case (see Fig. 6.11). This is due to the structural changes from NS2 to NS20. In NS20, a system of diffusion channels may still exist, but due to the small Na_2O concentration, these channels are not forming a percolating network structure anymore.

6.5 Mode-Coupling Theory

In previous sections, we have shown evidence that the time-scale separation in sodium silicates is intimately related to the presence of intermediate range order in the static structure. A prepeak at $q_1 = 0.95 \text{ \AA}^{-1}$ found in partial static structure factors (and in the functions $S_{c_\alpha c_\alpha}(q)$) is due to a structure of percolating sodium channels that act as diffusion channels for the fast sodium transport. However, up to now, we have only put forward that there is some structure–dynamics relation, but we have no “proof” that the dynamics can be predicted from structural quantities such as the partial static structure factors. A theoretical framework in which this is possible (at least in principle) is mode-coupling theory (MCT) [7, 49]. Using information about the equilibrium structure as an input, the MCT equation yields the intermediate scattering functions $F_{\alpha\beta}(q, t)$ (in our case $\alpha, \beta = \text{Si, O, Na}$). In the following, results of MCT calculations for NS2 and NS20 are presented that use the partial static structure factors from the simulation as an input. Note that the MCT equations also require the input of static triplet correlation functions. In our case, these functions were set to zero, approximating three-point correlation functions by a convolution approximation [7]. However, in the case of SiO_2 [31], it was shown that the latter triplet correlations are important. We shall keep this in mind, when we discuss the MCT results. For more details on the MCT calculations, we refer the reader to [32]. Details on the numerical solution of the MCT equations can be found in [50].

MCT predicts an idealized glass transition, i.e., a divergence of relaxation times at a critical temperature T_c . This transition is smeared out in real systems. Nevertheless, the value of T_c can be extracted from experimental or MD data, by fitting the data to various scaling predictions of the theory [7]. The value for T_c , that is obtained this way, is usually smaller than the value calculated within the theory. This is also the case here: A scaling analysis of simulation data yields $T_c \approx 3330 \text{ K}$ for silica [38] and 2000 K for NS2 [17]. The respective values from MCT calculations are $T_c \approx 3983$ and 3105 K . In order to compare dynamical data that show the same degree of slowing down, i.e.,

the same separation between the structural relaxation time-scale and the time scale of molecular short-time motion, we compare MD data for temperature T with MCT data at a different (higher) temperature T_{MCT} . This is then the only free parameter in our comparison.

First, we discuss the results for NS2: MD results at $T = 2100$ K together with MCT results at $T_{\text{MCT}} = 3410$ K for $F_{\text{NaNa}}(q, t)$ and $F_{\text{Na}}^s(q, t)$ at different values of q are shown in Fig. 6.12. The comparison is done at the latter temperatures, since at these temperatures the coherent relaxation times as obtained from MD and MCT are very similar at q_1 (see also below). As we have already seen in Sect. 6.4, at q_1 MD yields a much faster decay of Na–self correlations than of NaNa correlations, e.g., at $T = 2100$ K, the decay of $F_{\text{Na}}^s(q, t)$ is two orders of magnitude faster. MCT underestimates this separation, but it still gives a factor of about 50 between the two time-scales, thus describing correctly the fast sodium dynamics in NS2 on a qualitative level. At $q = 2.05 \text{ \AA}^{-1}$, the time-scale separation is smaller, but still $\tau/\tau^s \approx 20$ for the MD data. Here, the MCT result, $\tau/\tau^s \approx 14$, is even closer to the simulation value.

Although, the theory reproduces well many features seen in the MD, also discrepancies are evident. First, the heights of the plateaus seen in the correlation functions at intermediate times differ. They are connected to the Debye–Waller factors, for which in the case of silica [31] the agreement was quantitative with static triplet correlations taken into account, but qualitative only without them (as in our case). We therefore expect this first problem to be curable by providing better static structure input. A second problem is the

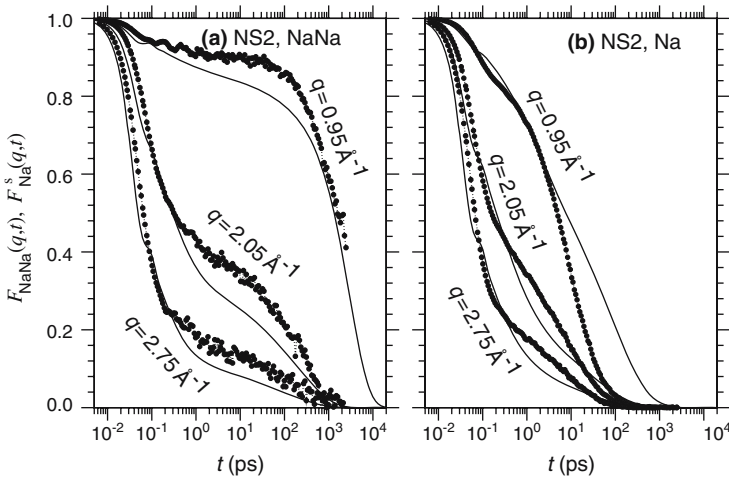


Fig. 6.12. Normalized sodium–sodium intermediate scattering functions, $F_{\text{NaNa}}(q)$ (left panel), and sodium–self intermediate scattering functions, $F_{\text{Na}}^s(q, t)$ (right panel), for NS2. The symbols are MD results for $T = 2100$ K; the solid lines are MCT results for $T_{\text{MCT}} = 3410$ K; q values are indicated

shape of the correlators, especially the sodium-self correlators at long times: for example, for $q_1 = 0.95 \text{ \AA}^{-1}$, MCT predicts a long, extremely stretched decay from 0.6 to zero over more than two decades in time, which is not observed in the simulation.

To test the wave-vector dependence of the dynamics in more detail, we turn to a discussion of structural relaxation times for the coherent, $\tau_\alpha(q)$, and the incoherent correlators, $\tau_\alpha^s(q)$. We define them through fits of stretched exponentials to the correlation functions, $F_{\alpha\alpha}(q, t) \approx A_\alpha(q) \exp[-(t/\tau_\alpha(q))^{\beta_\alpha(q)}]$ at long times, with $\beta_\alpha(q) < 1$ and $A_\alpha(q) < 1$, and similarly for $F_\alpha^s(q, t)$. This yields a reasonable description of the dynamics for $t \approx 1 \text{ ps}$. In Fig. 6.13, coherent and incoherent relaxation times are plotted for oxygen and sodium. MD and MCT results are shown as *symbols* and *lines*, respectively. The coherent relaxation times are, at fixed q , all of the same order of magnitude, and they almost coincide around $q \approx 1 \text{ \AA}^{-1}$, the region corresponding to the main structural features of the system (note that this holds also for $\tau_{Si}(q)$). The values obtained from MCT and those from MD are in good agreement given that we only have temperature as an adjustable parameter. In particular, their

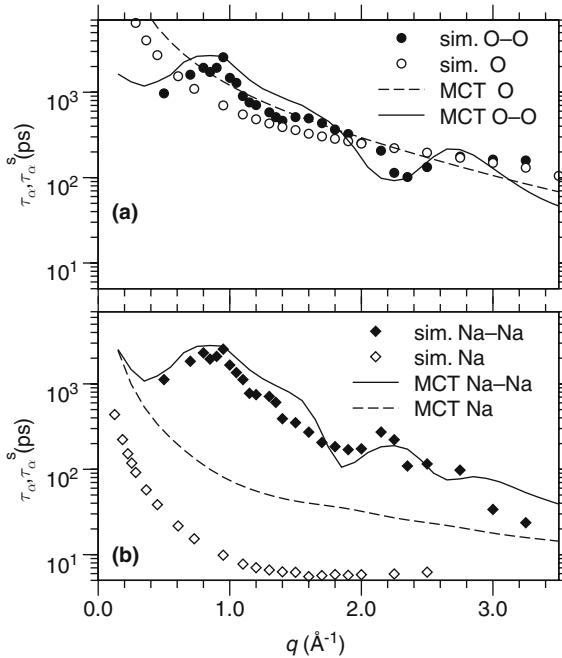


Fig. 6.13. Structural relaxation times $\tau_\alpha(q)$ for coherent density relaxation functions $F_{\alpha\alpha}(q, t)$ and $\tau_{Na}^s(q)$ for the incoherent density relaxation function $F_{Na}^s(q, t)$, (a) $\tau_O(q)$ and $\tau_O^s(q)$, (b) $\tau_{Na}(q)$ and $\tau_{Na}^s(q)$. As indicated, *symbols* are simulation results ($T = 2100 \text{ K}$) and *lines* are MCT results ($T = 3410 \text{ K}$). See text for the definition of $\tau_\alpha(q)$ and $\tau_\alpha^s(q)$

subtle q dependence is reproduced. The oxygen-self relaxation time $\tau_O^s(q)$ is of the same order as the corresponding coherent one, $\tau_O(q)$, except for $q \rightarrow 0$. This is what one expects in a typical glassforming liquid. On the contrary, the sodium-self relaxation time $\tau_{Na}^s(q)$ is much smaller than all other structural relaxation times, both in the MCT and the MD results. Even if the MCT results for this quantity are systematically higher than the MD data (reflecting the difference in shape of $F_{Na}^s(q, t)$ in Fig. 6.12), this confirms that MCT indeed predicts the fast sodium dynamics in NS2 from the equilibrium structure alone.

We now investigate the effect of sodium concentration on the dynamics by discussing simulation and MCT results for NS20. Figure 6.14 shows the coherent and incoherent sodium-density correlators for this system, similar to the NS2 results shown in Fig. 6.12. The main effect of reducing the sodium concentration from NS2 to NS20 on the dynamics is that the sodium-self relaxation now is appreciably slower, as is evident from the right-hand panel in Fig. 6.14. The relaxation time obtained from the MD data, is $\tau_{Na}^s(q = 0.95 \text{ \AA}^{-1}) \approx 10^3$ ps, similar to the $\tau_{Na}(q)$ value at that q , i.e., all relaxation times, including that of the sodium-self correlations, are now of the same order of magnitude at fixed q . MCT again somewhat overestimates the sodium-self relaxation times, but the overall sodium-concentration effect is well explained by the theory.

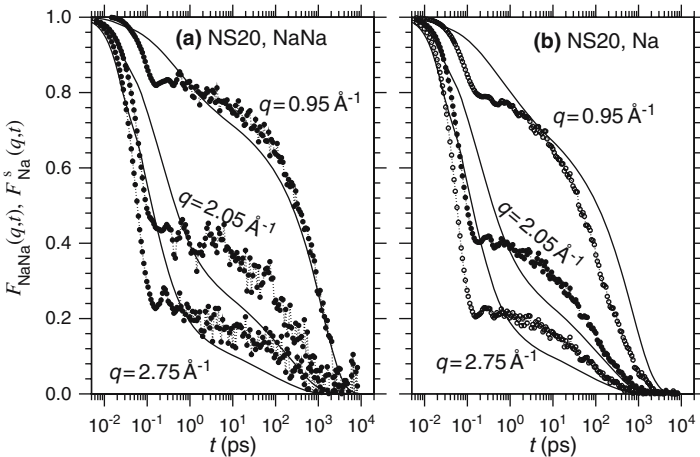


Fig. 6.14. Normalized sodium-sodium intermediate scattering functions, $F_{NaNa}(q)$ (left panel), and sodium-self intermediate scattering functions, $F_{Na}^s(q, t)$ (right panel), as in Fig. 6.12 but for NS20. MD results (symbols) are for $T = 2500\text{K}$, MCT results (solid lines) for $T_{MCT} = 4000\text{K}$

Also for NS20, the shape of $F_{\text{Na}}^s(q, t)$ predicted by MCT is different from that observed in MD. But here, the discrepancy is found largely in the form of the relaxation toward the plateau, while the further deviations visible in Fig. 6.14 are ascribable to the error in those plateau values as explained above. The observation of deviations at relatively short times, compared to the structural relaxation time, is typical for comparisons between MCT and Newtonian dynamics MD simulations [23, 26].

In summary, we have shown that MCT is able to reproduce the decoupling of time-scales between the sodium self-dynamics and the much slower relaxation of the Si–O network. Since MCT only makes use of the partial structure factors $S_{\alpha\beta}(q)$, this shows that indeed a structure–dynamics relation holds for the fast ion transport in sodium silicates. One may expect that MCT yields a better description on a quantitative level, if static triplet correlations are taken into account. However, the computational effort to obtain them by simulation is enormous [31].

6.6 Conclusions

In this review, we have presented different approaches to clarify the high diffusivity of sodium ions in different sodium silicates. MD simulations reveal that the different chemical ordering of Si and Na leads to a microsegregation on length scales of about 6–7 Å. This structural feature is reflected in a prepeak in static concentration–concentration correlation functions as well as in the partial static structure factors. The existence of this prepeak is confirmed by state-of-the-art measurements using inelastic neutron scattering [9, 10]. The structure that underlies the microsegregation in sodium silicates provides the existence of diffusion channels in the static structure, thus supporting the idea of “preferential pathways” for the fast sodium diffusion: The sodium motion is restricted to a subspace within the Si–O network. That there is really a structure–dynamics relation in sodium silicates is demonstrated by MCT calculations that use the partial structure factors of the simulation as an input.

Acknowledgements

This review is based on collaborative work with Kurt Binder, Florian Kargl, Walter Kob, Andreas Meyer, and Thomas Voigtmann. It is a great pleasure to thank them for a very pleasant and fruitful collaboration. This work was supported by Schott Glas and the Deutsche Forschungsgemeinschaft, grant number HO2231/2-1/2. Generous grants of computing time at the NIC Jülich are gratefully acknowledged.

References

1. J. R. Johnson, R. H. Bristow, H. H. Blau: *J. Am. Ceram. Soc.* **34**, 165 (1951) [149](#)
2. Y. P. Gupta, T. B. King: *Trans. Metal. Soc. AIME* **237**, 1701 (1966) [149](#)
3. M. Braedt, G. H. Frischat: *Phys. Chem. Glasses* **29**, 214 (1988) [149](#)
4. C. A. Angell, P. A. Cheeseman, S. Tamaddon: *J. Phys. (Paris)* **C9-43**, 381 (1982) [149](#), [150](#)
5. M. D. Ingram: *Philos. Mag. B* **60**, 729 (1989) [149](#)
6. G. N. Greaves: *J. Non-Cryst. Solids* **71**, 203 (1985) [149](#)
7. For reviews of the theory and tests of MCT, see, e.g., L. Sjögren, W. Götze: *Rep. Prog. Phys.* **55**, 241 (1992); W. Götze: *J. Phys.: Condens. Matter* **11**, A1 (1999) [150](#), [165](#)
8. P. H. Gaskell, M. C. Eckersley, A. C. Barnes, P. Chieux: *Nature* **350**, 675 (1991) [150](#)
9. A. Meyer, H. Schober, D. B. Dingwell: *Europhys. Lett.* **59**, 708 (2002) [150](#), [158](#), [169](#)
10. A. Meyer, J. Horbach, W. Kob, F. Kargl, H. Schober: *Phys. Rev. Lett.* **93**, 027801 (2004) [150](#), [158](#), [169](#)
11. J. Horbach, W. Kob: *Phil. Mag. B* **79**, 1981 (1999); J. Horbach, W. Kob, K. Binder: *Chem. Geol.* **174**, 87 (2001) [150](#), [151](#), [152](#), [155](#), [156](#), [158](#), [162](#), [163](#)
12. J. Horbach, W. Kob, K. Binder: *J. Phys.: Condens. Matter* **15**, S903 (2003) [150](#), [152](#)
13. K. Binder, J. Horbach, W. Kob, A. Winkler: *Comp. Sci. Eng.* **5** (2), 60 (2003) [150](#), [151](#)
14. A. Winkler, J. Horbach, W. Kob, K. Binder: *J. Chem. Phys.* **120**, 384 (2004) [150](#)
15. P. Pflöiderer, J. Horbach, K. Binder: *Chem. Geol.* **229**, 186 (2006) [150](#)
16. J. Horbach, W. Kob, K. Binder: *Phys. Rev. Lett.* **88**, 125502 (2002) [150](#)
17. J. Horbach, W. Kob: *J. Phys.: Condens. Matter* **14**, 9237 (2002) [150](#), [152](#), [159](#), [165](#)
18. J. Oviedo, J. F. Sanz: *Phys. Rev. B* **58**, 9047 (1998) [150](#)
19. P. Jund, W. Kob, R. Jullien: *Phys. Rev. B* **64**, 134303 (2001) [150](#), [162](#)
20. E. Sunyer, P. Jund, W. Kob, R. Jullien: *J. Non-Cryst. Solids* **307-310**, 939 (2002) [150](#)
21. A. N. Cormack, J. Du, T. R. Zeitler: *Phys. Chem. Chem. Phys.* **4**, 3193 (2002) [150](#)
22. H. Lammert, M. Kunow, A. Heuer: *Phys. Rev. Lett.* **90**, 215901 (2003) [150](#)
23. M. Nauroth, W. Kob: *Phys. Rev. E* **55**, 657 (1997) [150](#), [169](#)
24. W. Kob, M. Nauroth, F. Sciortino: *J. Non-Cryst. Solids* **307-310**, 181 (2002) [150](#)
25. A. B. Mutiara, H. Teichler: *Phys. Rev. E* **64**, 046133 (2001) [150](#)
26. G. Foffi, W. Götze, F. Sciortino, P. Tartaglia, Th. Voigtmann: *Phys. Rev. E* **69**, 011505 (2004) [150](#), [169](#)
27. Th. Voigtmann, A. M. Puertas, M. Fuchs: *Phys. Rev. E* **70**, 061506 (2004) [150](#)
28. L. Fabbian, A. Latz, R. Schilling, F. Sciortino, P. Tartaglia, C. Theis: *Phys. Rev. E* **60**, 5768 (1999) [150](#)
29. C. Theis, F. Sciortino, A. Latz, R. Schilling, P. Tartaglia: *Phys. Rev. E* **62**, 1856 (2000) [150](#)
30. S.-H. Chong, F. Sciortino: *Phys. Rev. E* **69**, 051202 (2004) [150](#)
31. F. Sciortino, W. Kob: *Phys. Rev. Lett.* **86**, 648 (2001) [151](#), [165](#), [166](#), [169](#)
32. Th. Voigtmann, J. Horbach: *Europhys. Lett.* **74**, 459 (2006) [151](#), [165](#)
33. G. J. Kramer, A. J. M. de Man, R. A. van Santen: *J. Am. Chem. Soc.* **64**, 6435 (1991) [151](#), [159](#)
34. B. W. H. van Beest, G. J. Kramer, R. A. van Santen: *Phys. Rev. Lett.* **64**, 1955 (1990) [151](#)

35. S. Ispas, M. Benoit, P. Jund, R. Jullien: Phys. Rev. B **64**, 214206 (2001) [151](#)
36. M. P. Allen, D. J. Tildesley: *Computer Simulation of Liquids* (Clarendon Press, Oxford, 1987) [151](#)
37. D. Frenkel, B. Smit: *Understanding Molecular Simulation: From Algorithms to Applications*, 2nd ed. (Academic Press, San Diego, 2002) [151](#)
38. J. Horbach, W. Kob: Phys. Rev. B **60**, 3169 (1999) [152](#), [156](#), [157](#), [165](#)
39. K. Vollmayr, W. Kob, K. Binder: Phys. Rev. B **54**, 15808 (1996) [152](#), [157](#)
40. R. Brückner: J. Non-Cryst. Solids **5**, 123 (1970) [152](#)
41. C. A. Angell: Science **193**, 1121 (1976) [152](#)
42. J. Horbach: Unpublished [152](#)
43. O. V. Mazurin, M. V. Streltsina, T. P. Shvaiko-Shvaikowskaya: *Handbook of Glass Data, Part A: Silica Glass and Binary Silicate Glasses* (Elsevier, Amsterdam, 1983) [152](#), [160](#)
44. J. Blétry: Z. Naturforsch. **31a**, 960 (1976) [153](#)
45. A. B. Bhatia, D. E. Thornton: Phys. Rev. B **28**, 3004 (1970) [153](#)
46. J.-P. Hansen, I. R. McDonald: *Theory of Simple Liquids* (Academic Press, London, 1986) [153](#), [163](#)
47. O. V. Mazurin, E. A. Porai-Koshits: *Phase Separation in Glass* (Elsevier, Amsterdam, 1984) [158](#)
48. R. Knoche, D. B. Dingwell, F. A. Seifert, S. L. Webb: Phys. Chem. Minerals **116**, 1 (1994) [158](#)
49. K. Binder, W. Kob: *Glassy Materials and Disordered Solids – An Introduction to Their Statistical Mechanics* (World Scientific, London, 2005) [159](#), [163](#), [165](#)
50. W. Götze, Th. Voigtmann: Phys. Rev. E **67**, 021502 (2003) [165](#)

The Gonihedric Ising Model and Glassiness

Desmond A. Johnston¹, Adam Lipowski² and Ranasinghe P. K. C. Malmini³

¹ Department of Mathematics and the Maxwell Institute for Mathematical Sciences, Heriot-Watt University, Riccarton Edinburgh, EH14 4AS, Scotland
d.a.johnston@ma.hw.ac.uk

² Faculty of Physics, Adam Mickiewicz University, 61-614 Poznań, Poland
lipowski@amu.edu.pl

³ Department of Mathematics, University of Sri Jayewardenepura, Gangodawila, Sri Lanka
malmini@sjp.ac.lk

Abstract. We review a class of 3D lattice spin models in which planar Peierls boundaries between $+$ and $-$ spins can be created at zero energy cost. These so-called Gonihedric Ising models have (in general) specially tuned nearest neighbour, next-to-nearest neighbour and plaquette interactions, which endow the models with some novel properties both in and out of equilibrium.

After reviewing the genesis of the models in string theory, we discuss investigations of both their equilibrium and non-equilibrium behaviours by various analytical and numerical means. The purely plaquette variant of the model displays all the standard indications of glassy behaviour without any recourse to quenched disorder, whilst still possessing a crystalline low-temperature phase in equilibrium.

7.1 (Pre-)History of the Model

The Gonihedric 3D Ising model is a lattice spin model in which planar Peierls boundaries between $+$ and $-$ spins can be created at zero energy cost. Instead of weighting the *area* of Peierls boundaries as the case for the usual 3D Ising model with nearest-neighbour interactions, the *edges*, or “bends” in an interface are weighted, a concept which is related to the intrinsic curvature of the boundaries in the continuum.

The model is a generalised Ising model living on a cubic 3D lattice with nearest neighbour, next to nearest-neighbour and plaquette interactions. The ratio between the couplings of these three terms is fixed to a one-parameter family which endows the model with unusual properties both in and out of equilibrium. Of particular interest for the discussion here will be that the model manifests all the indications of glassy behaviour without any recourse to quenched disorder, whilst still possessing a crystalline low-temperature phase in equilibrium.

In these notes, we follow a roughly chronological order by first reviewing the background to the formulation of the model, before moving on to the elucidation of the equilibrium phase diagram by various means and then to the investigation of the non-equilibrium, glassy behaviour of the model. We apologise in advance for our narrow focus on things Gonihedric at the expense of other lattice models with glassy behaviour since the aim is to concentrate on giving an overview of the Gonihedric Ising model in 3D.

The model has an unusual genesis since it was originally introduced as a potential discretisation of string theory. The Nambu–Goto [1] action (or Hamiltonian in statistical mechanical language) in bosonic string theory is given by the area swept out by the string worldsheet as it moves through spacetime. Directly discretising euclideanised versions of this action produced ensembles of surfaces, i.e. string worldsheets, which were dominated by collapsed and irregular configurations such as that in Fig. 7.1 and which were

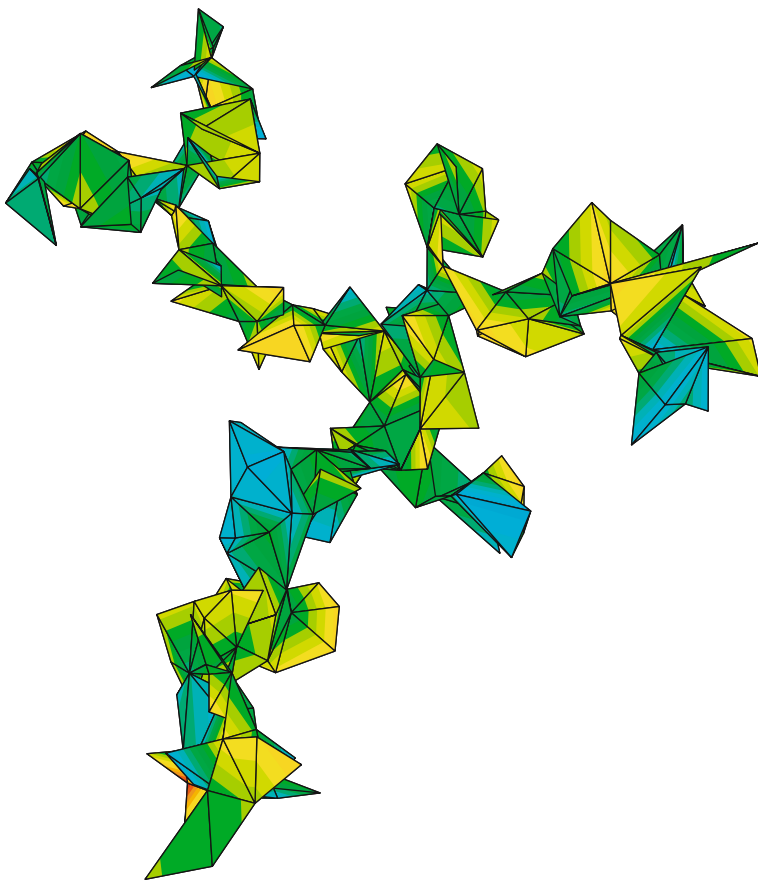


Fig. 7.1. A typical collapsed triangulated surface resulting from a simulation of the Gaussian Hamiltonian in (7.1)

unsuitable for taking any sort of continuum limit [2]. This was presumably a reflection of the well-known tachyonic instability of the bosonic string and therefore not entirely unexpected. The interest was in whether any straightforward modifications of such Hamiltonians did allow a continuum limit, and hence some insight into stable string theories in physical dimensions.

Discretising the Polyakov [3] form of the string action, which is equivalent to the Nambu–Goto formulation, by triangulating an embedded surface gives the simple Gaussian Hamiltonian

$$H = \frac{1}{2} \sum_{\langle ij \rangle} (\mathbf{X}_i - \mathbf{X}_j)^2, \quad (7.1)$$

where the vectors \mathbf{X}_i live on the vertices of the triangulated surface and determine where the vertices sit in the embedding space. The sum $\langle ij \rangle$ is carried out over the edges of the triangulation and in principle one should also sum over different triangulations of the surface as a discretised version of the sum over metrics in the continuum string theory with the Polyakov action. In any case, the observed behaviour of surfaces turns out to be rather similar in ensembles with and without this sum. One possibility for stabilising the surfaces produced by such Hamiltonians is to add an extrinsic curvature term as suggested first in the continuum by Polyakov and Kleinert [4], which acts to prevent the surfaces collapsing,

$$H = \frac{1}{2} \sum_{\langle ij \rangle} (\mathbf{X}_i - \mathbf{X}_j)^2 + \lambda \sum_{\Delta_i, \Delta_j} (1 - \mathbf{n}_i \cdot \mathbf{n}_j), \quad (7.2)$$

where the $\mathbf{n}_i, \mathbf{n}_j$ are normals on adjacent triangles Δ_i, Δ_j . The second term tends to align the normals on adjacent triangles and hence to “stiffen” or flatten out the surface [5], at least over short-length scales, see Fig. 7.2. The issue for Monte Carlo simulations is to determine whether this flattening is also effective on macroscopic length scales.

Another possibility, which also uses a geometrical concept and which has some appealing features from the string theory point of view [6], is to take an action proportional to the linear size of a surface – a notion first introduced by Steiner [7]. This can be discretised as

$$H = \frac{1}{2} \sum_{\langle ij \rangle} |\mathbf{X}_i - \mathbf{X}_j| \theta(\alpha_{ij}), \quad (7.3)$$

on triangulated surfaces, where $\theta(\alpha_{ij}) = |\pi - \alpha_{ij}|$ with α_{ij} denoting the dihedral angle between the embedded neighbouring triangles with a common link $\langle ij \rangle$. The $\theta(\alpha_{ij})$ term also acts to flatten out the surfaces [8]. The elements making up these various possible surface Hamiltonians are shown in Fig. 7.3. The origin of the word Gonihedric is a combination of the Greek words *gonia* for angle (referring to the dihedral angle) and *hedra* for base or face (referring to the adjacent triangles).

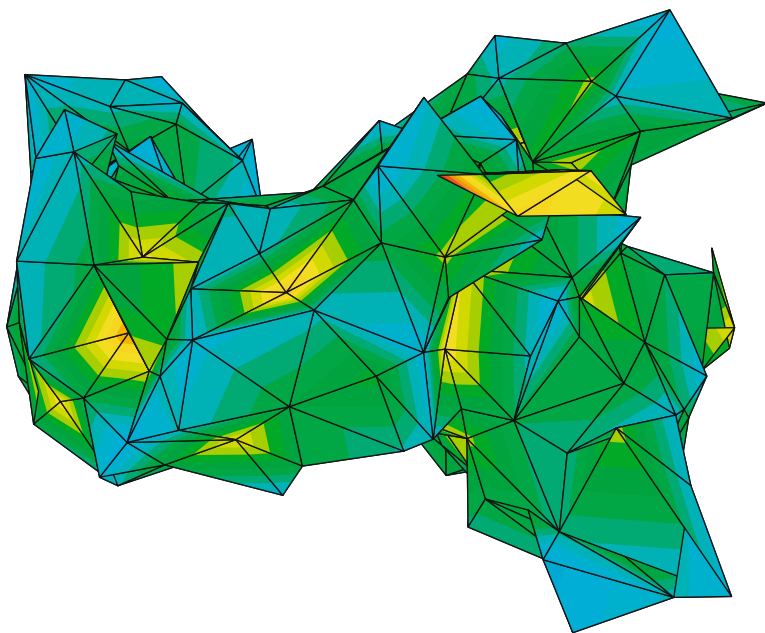


Fig. 7.2. A typical uncollapsed triangulated surface resulting from a simulation of the Gaussian plus extrinsic curvature Hamiltonian in (7.2) with $\lambda = 1.1$

Savvidy and Wegner posed the question of how to translate the essential features of such a Hamiltonian to a surface composed of plaquettes on a cubic (or hypercubic) lattice [9]. This was motivated by the observation that it was possible to rewrite the Hamiltonian for an ensemble of such surfaces by using the geometrical spin cluster boundaries of a suitable generalised Ising model with nearest neighbour, next to nearest-neighbour and plaquette interactions to define the surfaces and their appropriate energies. It is generally much easier to simulate an Ising spin model than a gas of surfaces so one might expect

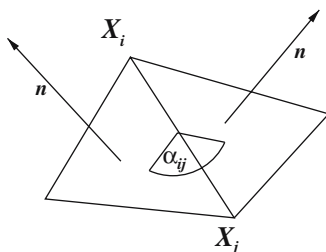


Fig. 7.3. Two adjacent triangles in a triangulation of a surface with a common edge $\langle ij \rangle$, showing the normals \mathbf{n} , the co-ordinates of the endpoints $\mathbf{X}_{i,j}$ and the dihedral angle α_{ij}

some advantages, both numerical and analytical, from such a reformulation of the system.

On a fixed cubic lattice all the edge lengths $|\mathbf{X}_i - \mathbf{X}_j|$ will be identical, so the statistical weight of a surface configuration will be entirely determined by the $\theta(\alpha_{ij}) = |\pi - \alpha_{ij}|$ factors, where the α_{ij} are restricted to multiples of $\pi/2$ radians. In other words, the statistical weight of a plaquette surface configuration will be determined entirely by the number of bends and self-intersections it contains. There is no (bare) weight for the area of a plaquette in the surfaces in contrast to the usual 3D Ising model with only nearest-neighbour interactions.

The generalised Ising models which are used in the construction are of the form

$$H = J_1 \sum_{\langle ij \rangle} \sigma_i \sigma_j + J_2 \sum_{\langle\langle i, j \rangle\rangle} \sigma_i \sigma_j + J_3 \sum_{[i, j, k, l]} \sigma_i \sigma_j \sigma_k \sigma_l, \quad (7.4)$$

where the Hamiltonian contains nearest neighbour ($\langle i, j \rangle$), next to nearest neighbour ($\langle\langle i, j \rangle\rangle$) and round a plaquette ($[i, j, k, l]$) terms. The couplings in such models can be related to the energy cost for a plaquette in the Peierls interface β_A , a right-angled bend between two such adjacent plaquettes, β_C , and the energy cost, β_I , for the intersection of four plaquettes having a link in common

$$\begin{aligned} \beta_A &= 2J_1 + 8J_2, \\ \beta_C &= 2J_3 - 2J_2, \\ \beta_I &= -4J_2 - 4J_3. \end{aligned} \quad (7.5)$$

General cases of such Hamiltonians and their equivalent surface formulations had been studied in some detail by Cappi et al. [10] and found to have a very rich phase structure for generic choices of the couplings, including homogeneous, lamellar, disordered and bicontinuous phases. The Gonihedric model constitutes a particular one-parameter slice in this space of Hamiltonians:

$$H = -2\kappa \sum_{\langle ij \rangle} \sigma_i \sigma_j + \frac{\kappa}{2} \sum_{\langle\langle i, j \rangle\rangle} \sigma_i \sigma_j - \frac{1-\kappa}{2} \sum_{[i, j, k, l]} \sigma_i \sigma_j \sigma_k \sigma_l, \quad (7.6)$$

and for such a ratio of couplings $\beta_A = 0$, which is the desired zero weight for plaquette area suggested by translating the Hamiltonian of (7.3). The energy of the spin cluster boundaries for this Gonihedric model on a cubic lattice is simply given by

$$E = n_2 + 4\kappa n_4, \quad (7.7)$$

where n_2 is the number of links where two plaquettes on a spin cluster boundary meet at a right angle, n_4 is the number of links where four plaquettes meet at right angles and κ is a free parameter which determines the relative weight of a self-intersection of the surface.

The particular ratio of couplings in (7.6) also introduces a novel semi-global symmetry into the Hamiltonian, as we discuss in the next section. This is related to a zero-temperature high-degeneracy point where it is possible to flip non-intersecting planes of spins at zero energy cost. This symmetry is further enhanced at $\kappa = 0$ where the action becomes a purely plaquette term

$$H = -\frac{1}{2} \sum_{[i,j,k,l]} \sigma_i \sigma_j \sigma_k \sigma_l, \quad (7.8)$$

and *any* plane of spins, even intersecting ones, may be flipped at zero energy cost at $T = 0$, which suggests a highly degenerate ground state for the $\kappa = 0$ Gonihedric model. Series expansions and cluster variational calculations, described below, show that the degeneracy of the Hamiltonian is broken in the free energy for $\kappa \neq 0$, indicating a ferromagnetic low-temperature phase in this case, but the nature of the order in the low-temperature phase for $\kappa = 0$ remains rather mysterious.

7.2 Equilibrium Behaviour, by Various Means

In what follows, we use the standard definitions of quantities such as the magnetisation

$$M = \frac{1}{L^3} \sum_i \sigma_i \quad (7.9)$$

and the Binder cumulant

$$U = 1 - \frac{\langle M^4 \rangle}{3\langle M^2 \rangle^2}, \quad (7.10)$$

in discussing critical properties, where the $\langle \rangle$ brackets denote thermal averages.

The energy $\langle E \rangle$ is just given by the average of the Hamiltonian, the specific heat C by the variance of the energy and the susceptibility χ by the variance of the magnetisation. The scaling exponents are then defined by the singular properties of these quantities at the critical point(s) of the model

$$C = B + C_0 t^{-\alpha}, \quad M = M_0 t^\beta, \quad \chi = \chi_0 t^{-\gamma}, \quad \xi = \xi_0 t^{-\nu}, \quad (7.11)$$

where $t = |(T - T_c)/T_c|$ is the reduced temperature, ξ is the correlation length and ν is the correlation length exponent, giving the divergence of the correlation length at criticality.

These can also be recast as finite-size scaling relations

$$C = B' + C'_0 L^{\alpha/\nu}, \quad M = M'_0 L^{-\beta/\nu}, \quad \chi = \chi'_0 L^{\gamma/\nu} \quad (7.12)$$

for lattices of linear extent L , which is more convenient when T_c is not known exactly, which is usually the case.

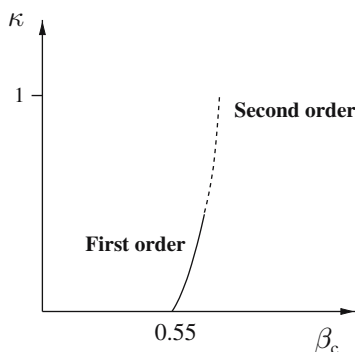


Fig. 7.4. The phase transition line as κ is varied

Various methods have been used to investigate the phase diagram of the Gonihedric model, ranging from generalised mean-field techniques, through cluster variational calculations to Monte Carlo simulations. The gross phase structure of the Gonihedric model was apparent even in the earliest Monte Carlo work [11], and is shown schematically in Fig. 7.4. For $\kappa = 0$ and small values of κ , there is a first-order transition [12], signified by a jump in the energy, E , at the transition point and first-order (volume) scaling in the specific heat.

As κ was increased, the transition softened to second order, but Monte Carlo simulations and other approaches have struggled to produce a consistent set of critical exponents. The first direct Monte Carlo simulations [11], for instance, found $\nu = 1.2(1)$, $\gamma = 1.60(2)$, $\beta = 0.12(1)$ when $\kappa = 1$, but later work using the scaling of the surface tension of a spin interface [13] obtained $\nu = 0.44(2)$ and $\gamma/\nu = 2.1(1)$.

Other approaches also gave results at variance with these: a low-temperature expansion by Pietig and Wegner found $\alpha = 0.62(3)$, $\beta = 0.040(2)$ and $\gamma = 1.7(2)$ at $\kappa = 1$ [14]; whilst Cirillo et al. [15] found $\beta = 0.062(3)$ and $\gamma = 1.41(2)$ using a combination of the cluster variational method and Padé approximants (“CVPAM”) [16].

These cluster variational calculations, ground-state enumerations and mean-field calculations all use a similar starting point – the decomposition of the lattice into elementary cubes and we now discuss these methods in some detail since they are useful in sketching out the phase structure. Indeed, the cluster variational method, allied with Padé approximant techniques has succeeded in providing a very plausible picture of the Gonihedric phase diagram by looking at an extended two-parameter Hamiltonian.

One of the elementary cubes from the 3D cubic lattice is shown in Fig. 7.5. The full lattice Hamiltonian may be written as a sum over individual cube Hamiltonians

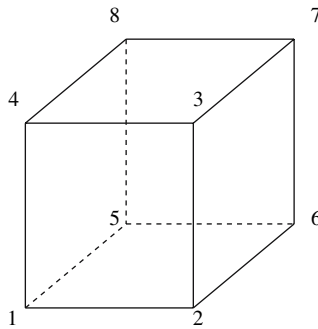


Fig. 7.5. The ground-state and mean-field analyses of the Gonihedric model require working with elementary cubes rather than single sites to capture the various possible spin configurations

$$h_c = \frac{\kappa}{2} \sum_{\langle i,j \rangle} \sigma_i \sigma_j - \frac{\kappa}{4} \sum_{\langle\langle i,j \rangle\rangle} \sigma_i \sigma_j + \frac{1-\kappa}{4} \sum_{[i,j,k,l]} \sigma_i \sigma_j \sigma_k \sigma_l \tag{7.13}$$

which differs from the full Hamiltonian by the symmetry factors in front of each term. If the lattice can be tiled by a cube configuration minimising the individual h_c , then the ground-state energy density is $E_0 = \min h_c$.

We list some of the inequivalent spin configurations on a single cube and their multiplicities in Table 7.1. In the list of spins, the first column represents one face of the cube and the second the other and the notation ψ_0, \dots is borrowed from [10]. The antiferromagnetic image of a configuration is obtained by flipping the three nearest neighbours and the spin at the other end of the cube diagonal from a given spin and is denoted by an overbar.

With the Gonihedric values of the couplings, there is a freedom to flip spin planes in the ground state as ψ_0 , which would represent a ferromagnetic state when used to tile the lattice, and ψ_6 which would represent flipped spin layers, have the same energy for any value of κ . The degeneracy increase when $\kappa = 0$, the club of states of energy $-3/2$ is now composed of $\psi_0, \psi_{\bar{0}}, \psi_6, \psi_{\bar{6}}$.

Table 7.1. Elementary cube ground-state energies

State	Top	Bottom	Energy	Multiplicity
ψ_0	++	++	$-3/2 - 3\kappa/2$	2
	++	++		
$\psi_{\bar{0}}$	-+	+-	$-3/2 + 21\kappa/2$	2
	+-	-+		
ψ_6	--	++	$-3/2 - 3\kappa/2$	6
	--	++		
$\psi_{\bar{6}}$	++	--	$-3/2 + 5\kappa/2$	6
	--	++		

This degeneracy means that the definition of an order parameter for the low-temperature phase is a moot point. The standard magnetisation M will not serve at zero temperature as is clear from consideration of the ground-state energies above since the freedom to flip spin planes means that it is identically zero. As we have noted, it appears that this symmetry is broken for $\kappa \neq 0$ at non-zero temperature, but in Monte Carlo simulations the magnetisation is still indistinguishable from zero, presumably because of the difficulty of removing such flipped planes within the timespan of the simulation. Even staggered magnetisations do not suffice as order parameters as the interlayer spacing between the flipped planes of spins can be arbitrary.

One possibility on a finite lattice is to force the model into the ferromagnetic phase with a suitable choice of boundary conditions such as fixed boundary conditions. Although this allows the use of a standard magnetic order parameter, it does some violence to both the scaling properties and the ground-state structure itself. The corrections to first-order scaling, for example, are much stronger with fixed boundary conditions than with the more familiar periodic boundary conditions (see Table 7.2), although simulations of the $\kappa = 0$ model with fixed boundary conditions have given good agreement with this scaling [17].

The approach taken to enumerating the ground states by splitting the lattice into elementary cubes can also be applied to mean-field theory for the model and to extensions of mean-field theory such as the cluster variational method. In the mean-field approximation, the spins are replaced by the average site magnetisations, and an entropy term is introduced to give the free energy. In the Gonihedric model, the total mean-field free energy may be written as the sum of elementary cube free energies $\phi(m_C)$,

$$\begin{aligned} \phi(m_C) = & -\frac{\kappa}{2} \sum_{\langle i,j \rangle \subset C} m_i m_j + \frac{\kappa}{4} \sum_{\langle\langle i,j \rangle\rangle \subset C} m_i m_j - \frac{1-\kappa}{4} \sum_{[i,j,k,l] \subset C} m_i m_j m_k m_l \\ & + \frac{1}{16} \sum_{i \subset C} [(1+m_i) \ln(1+m_i) + (1-m_i) \ln(1-m_i)], \end{aligned} \quad (7.14)$$

Table 7.2. Scaling laws for periodic versus fixed boundary conditions for the critical temperature, maxima of the specific heat and susceptibility and minimum of the Binder cumulant. In all cases a d -dimensional cubic lattice of length L is considered

	PBC	FBC
$\beta_c^{\text{peaks}}(L) =$	$\beta_c(\infty) + \frac{\theta_1}{L^d} + O(\frac{1}{L^{2d}})$	$\beta_c(\infty) + \frac{a_1}{L} + O(\frac{1}{L^2})$
$C_{\text{max}}(L) =$	$\gamma_0 + \gamma_2 L^d + O(\frac{1}{L^d})$	$c_0 + c_2 L^d + O(L^{d-1})$
$\chi_{\text{max}}(L) =$	$\delta_0 + \delta_2 L^d + O(\frac{1}{L^d})$	$e_0 + e_2 L^d + O(L^{d-1})$
$U_{\text{min}}(L) =$	$\Phi_0 + \frac{\Phi_1}{L^d} + O(\frac{1}{L^{2d}})$	$B_0 + \frac{B_1}{L} + O(\frac{1}{L^2})$

where m_C is the set of the eight magnetisations of the elementary cube. This in turn gives a set of eight mean-field equations

$$\frac{\partial \phi(m_C)}{\partial m_i} \Big|_{(i=1\dots 8)} = 0 \quad (7.15)$$

(one for each corner of the cube) rather than the familiar single equation for the standard nearest-neighbour Ising action.

If we solve these equations iteratively, we arrive at zeroes for a paramagnetic phase or various combinations of ± 1 for the magnetised phases on the eight cube vertices, and the mean-field ground state is then given by gluing together the elementary cubes consistently to tile the complete lattice, in the manner of the ground-state discussion. Carrying out this program gives a rather simple mean-field phase diagram for the Gonihedric model with action (7.6), with a single transition from a paramagnetic phase to a degenerate “layered” phase that is pushed down to $\beta = 0$ at large κ . The low-temperature phase is generically of the $\psi_{0,6}$ type, apart from $\kappa = 0$ where we see a $\psi_{0,\bar{6}}$ phase that is degenerate with these. A more sophisticated treatment using the cluster variational method, described below, suggests that the layered phase has a slightly higher free energy than the ferromagnetic phase so the low-temperature phase is in fact the ferromagnetic one when the model is in the regime with a continuous transition.

The cluster variation method, or CVM for short, is based on a truncation of the cluster (cumulant) expansion of the free energy density functional on which the variational formulation of statistical mechanics is based [18]. Unlike mean-field theory, it generally locates rather accurately the boundaries between different phases in complex phase diagrams and, using the recently proposed cluster variation – Padé approximant method, one can extract non-classical, precise estimates of the critical exponents.

For the Gonihedric model, it is again possible to use the cube approximation of the CVM, in which the maximal clusters are the elementary cubic cells of our simple cubic lattice; for this approximation, the free energy density functional has the form

$$\begin{aligned} \phi[\rho_8] = & \text{Tr}(\rho_8 H_8) + \frac{1}{\beta} \left[\text{Tr} \mathcal{L}(\rho_8) - \frac{1}{2} \sum_{\text{plaquettes}} \text{Tr} \mathcal{L}(\rho_{4,\text{plaquette}}) \right. \\ & \left. + \frac{1}{4} \sum_{\text{edges}} \text{Tr} \mathcal{L}(\rho_{2,\text{edge}}) - \frac{1}{8} \sum_{\text{sites}} \text{Tr} \mathcal{L}(\rho_{1,\text{site}}) \right], \end{aligned} \quad (7.16)$$

where H_8 is the contribution of a single cube to the Hamiltonian, $\mathcal{L}(x) = x \ln x$, ρ_α with $\alpha = 8, 4, 2, 1$ denotes the cube (respectively plaquette, edge, site) density matrix, and the sums in the entropy part are over all plaquettes (edges, sites) of a single cube.

Since the cluster variation method can be viewed as a generalised mean-field theory, it is clear that it can give only classical predictions for the critical exponents. In order to overcome this difficulty, one can use the cluster

variation–Padè approximant method (CVPAM), which has proven to be a quite accurate technique for extracting exponents. The basic idea of the CVPAM is that, since the CVM gives for Ising-like models very accurate results far enough from the critical point, one can try to extrapolate these results in order to study the critical behaviour. In order to determine the critical exponent of an order parameter M , for example, one calculates $M(\beta)$ with the CVM up to a temperature at which the error can be estimated to be very small (typically of order 10^{-5}), and then constructs, by a simple interpolation, Padè approximants for the logarithmic derivative of $M(\beta)$: the pole and the corresponding residue of each Padè approximant are then estimates for the critical temperature and for the critical exponent respectively [16].

The CVPAM calculations give a phase diagram whose topology agrees with Monte Carlo simulations [15]. The value for the magnetic exponent is found to be $\beta = 0.062 \pm 0.003$. Another important observation from the CVPAM calculations is that at finite temperatures there is a violation of the flip symmetry of the Gonihedric Hamiltonian when $\kappa \neq 0$, so that in the ordered region of the model the ferromagnetic phase is always stable with respect to the lamellar phase.

Applying CVPAM methods to a slight extension to the Gonihedric Hamiltonian gives useful insight into the nature of the phase diagram [19]. The Hamiltonian is modified to

$$H = - \sum_{\langle ij \rangle} \sigma_i \sigma_j - j \sum_{\langle\langle ij \rangle\rangle} \sigma_i \sigma_j - \frac{1-\kappa}{4\kappa} \sum_{[ij,k,l]} \sigma_i \sigma_j \sigma_k \sigma_l, \quad (7.17)$$

with a second parameter j which reduces to the Gonihedric model, with suitably rescaled couplings, when $j = -0.25$. The CVPAM calculations (and independent transfer-matrix calculations [20]) for this modified Hamiltonian give a phase diagram whose $\kappa = 1$ slice is shown in Fig. 7.6.

The structure of this phase diagram gives some strong hints as to why the critical exponent measurements in Monte Carlo simulations have been so inconsistent. The *dotted line* in Fig. 7.6 is the usual 3D ferromagnetic Ising transition, along which the standard 3D Ising critical exponents such as

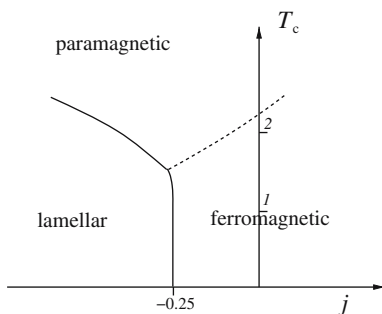


Fig. 7.6. A $\kappa = 1$ slice of the two-parameter Hamiltonian phase diagram

$\nu = 0.6294$ would be observed. The line separating the lamellar and ferromagnetic phases appears to be bent slightly to the left according to both CVPAM and transfer-matrix calculations. The observed Goni-hedric model transition will thus be strongly influenced by crossover effects close to the endpoint of the standard Ising line which is near, but not exactly at, $j = -0.25$.

In such a case, we would expect the correlation length to diverge as

$$\xi \sim N^{\pm} t^{-\nu}, \quad (7.18)$$

where the new feature is the critical amplitude, which is given by

$$N^{\pm} \propto \Delta^{(-\dot{\nu}+\nu)/\phi}, \quad (7.19)$$

with $\dot{\nu}$ and ν being the tricritical and 3D Ising values for the correlation length exponent respectively, and $\Delta = j + 0.25$. While CVPAM and transfer-matrix calculations [19, 20] are both in agreement with this general picture, the values obtained for the tricritical exponents and crossover exponent do not agree, the transfer-matrix calculations finding $\dot{\nu} = 0.45(15)$ and $\phi = 0.6(2)$, whereas the CVPAM calculation finds $\phi = 1.1(1)$.

In summary, while the general features of the Goni-hedric model equilibrium phase diagram are understood both for $\kappa = 0$ and $\kappa \neq 0$ and a plausible tricritical/crossover scaling scenario has been advanced to describe the observed values of the critical exponents, these have still not been determined with any great degree of certainty. It is also difficult to define a suitable magnetic order parameter for the low-temperature phase as the flip symmetry of the Hamiltonian means that the standard magnetisation will be zero in the ground state. Although both low-temperature expansions and CVPAM calculations of the free energy strongly suggest that this symmetry is broken for non-zero κ at finite temperature, the standard magnetisation is still measured to be zero in the low-temperature phase in Monte Carlo simulations for $\kappa \neq 0$. The flip symmetry appears to be unbroken for the $\kappa = 0$ (pure plaquette) case, so the low-temperature phase for this is highly degenerate.

A further difficulty which has been observed in attempting to extract critical exponents via Monte Carlo simulations is the very long autocorrelation times which the model exhibits, as was first remarked in [21]. These have the effect of smearing out the observed critical singularities and rendering the extraction of critical exponents problematic. With this in mind, we now turn to the non-equilibrium properties.

7.3 Non-equilibrium Behaviour, Mostly by Monte Carlo Simulations

On heuristic grounds, we would expect slow dynamics in the Goni-hedric model since the destruction of a spin droplet will require an activation energy because of the weighting of any new edges in the Goni-hedric Hamiltonian; for an

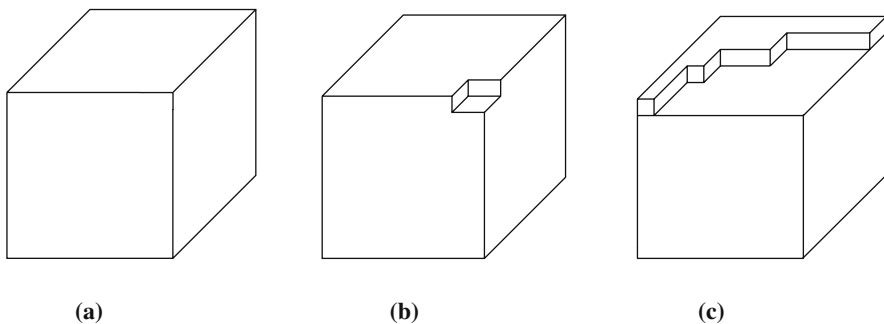


Fig. 7.7. Destroying a cubic excitation, by “nibbling” away the edges has an activation energy in the Gonihedric model

illustration see Fig. 7.7. Indeed, when $\kappa = 1$ the plaquette term drops out and one is left with

$$H = -2 \sum_{\langle ij \rangle} \sigma_i \sigma_j + \frac{1}{2} \sum_{\langle \langle i, j \rangle \rangle} \sigma_i \sigma_j , \quad (7.20)$$

which represents a particular case of a class of models with competing nearest neighbour and next-nearest neighbour interactions formulated by Shore and Sethna specifically to investigate slow dynamics [22]. We will denote such models with generic coupling ratios as Shore and Sethna models below. The Gonihedric Hamiltonian with $\kappa = 1$ displays some differences in its dynamics compared with the generic case.

Hand in hand with such slow dynamics and energy barriers, we would also expect to see metastability in the model, and this is backed up by both CVPAM calculations and direct integration in Monte Carlo simulations to obtain the free energy. For $\kappa = 0$ the CVPAM calculations of the free energy show a region of metastability both above and below the first-order transition point at $\beta = T^{-1} \sim 0.55$ [15], c.f. Fig. 7.8. To calculate the free energy of the model in a Monte Carlo simulation [23] shown in Fig. 7.9, we used the following equations:

$$\begin{aligned} \phi_{\text{low}-T} &= E - T \int_0^T \frac{C}{T} dT , \\ \phi_{\text{high}-T} &= -Ts(\infty) + T \int_0^{1/T} E d\left(\frac{1}{T}\right) . \end{aligned} \quad (7.21)$$

In the above equation, C and E denote the specific heat and internal energy, respectively (measured using the standard formulae in the Monte Carlo simulation), and $s(\infty) = \ln(2)$ is the entropy per site at infinite temperature.

We also find, see Fig. 7.10 and as advertised earlier, that the lamellar low-temperature phase has a higher free energy than the ferromagnetic phase when $\kappa = 1$ indicating that the true low-temperature phase is ferromagnetic

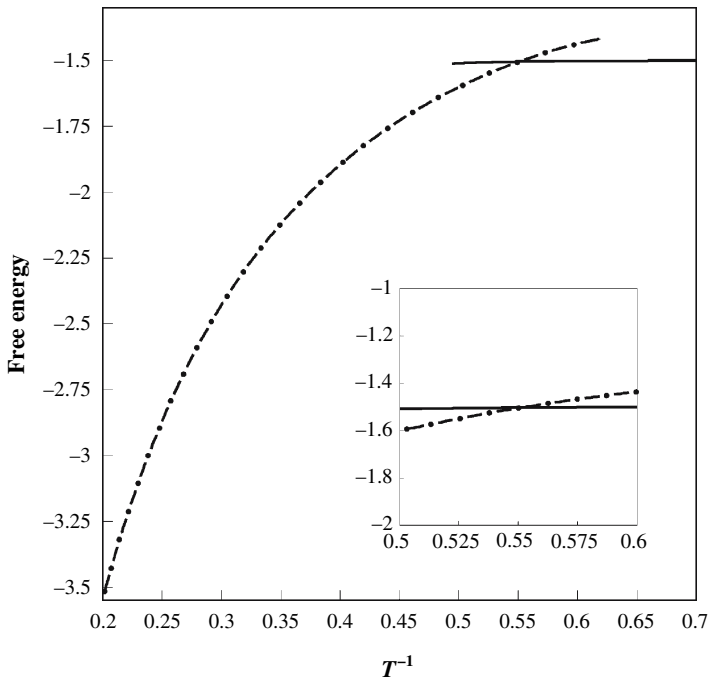


Fig. 7.8. The free energy from a CVPAM calculation when $\kappa = 0$. The *solid line* is the low-temperature phase and the *dashed dotted line* the high-temperature paramagnetic phase

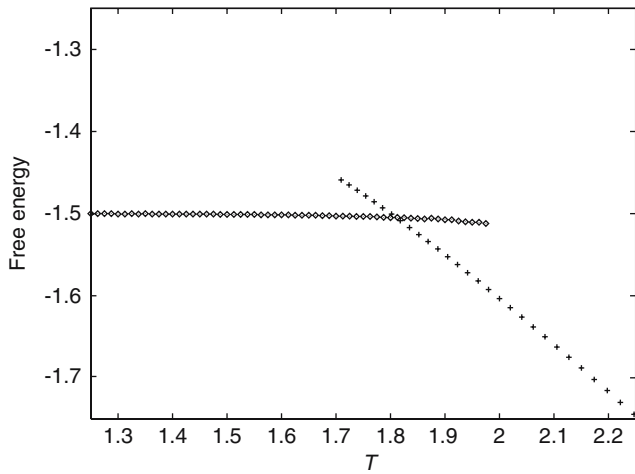


Fig. 7.9. The free energy from a Monte Carlo simulation when $\kappa = 0$. The transition point and the region of metastability are both in excellent agreement with the CVPAM calculation of Fig. [7.8](#)

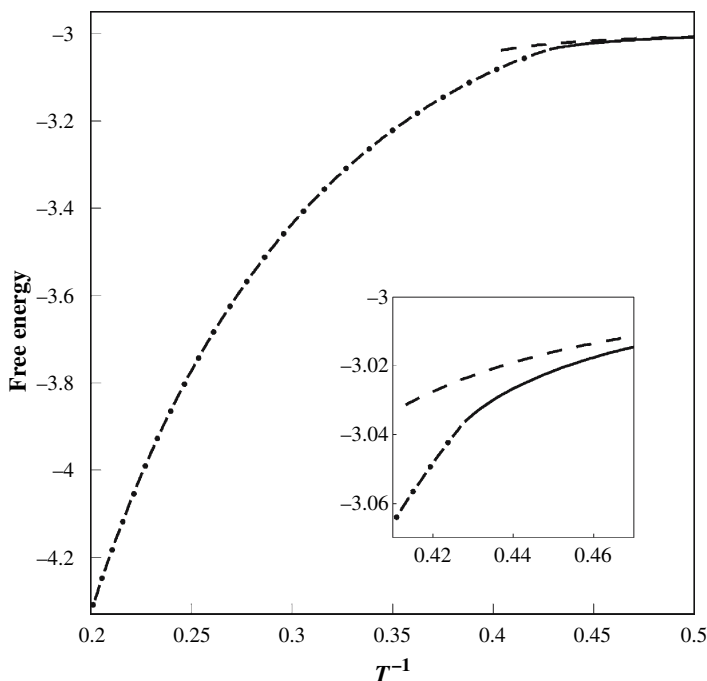


Fig. 7.10. The free energy from a CVPAM calculation when $\kappa = 1$. The *solid line* is the ferromagnetic phase, the *dashed dotted line* the high-temperature paramagnetic phase and the *dashed line* the lamellar phase

in this case, although this does not appear to be realised within the time scale of Monte Carlo simulations carried out so far.

Qualitative numerical experiments provide plenty of evidence for interesting dynamical behaviour in the model, particularly with respect to quenches [23]. In the $\kappa = 0$ case to study the evolution of a random configuration quenched to low temperature, one can measure the energy excess $\delta E(t) = E(t) - E_0$ over the ground-state energy E_0 . One expects that the inverse of this quantity sets the characteristic length scale of the system $l(t)$, which roughly corresponds to the average size of domains. There is convincing evidence that the generic behaviour in many systems with non-conservative dynamics and scalar order parameter (i.e. conditions which are satisfied here) $l(t)$ increases asymptotically in time as $l(t) \sim t^n$ and $n = 1/2$. However, in some systems, $l(t)$ is known to increase much more slowly in time, even logarithmically $l(t) \sim \log(t)$. These rather exceptional systems include some random (at the level of the Hamiltonian) systems, and also the Shore and Sethna models at sufficiently low temperatures. It is the energy barriers developing in these systems during the coarsening which cause such a slow increase of $l(t)$, so the Gonihedric model would also be a good candidate for such behaviour.

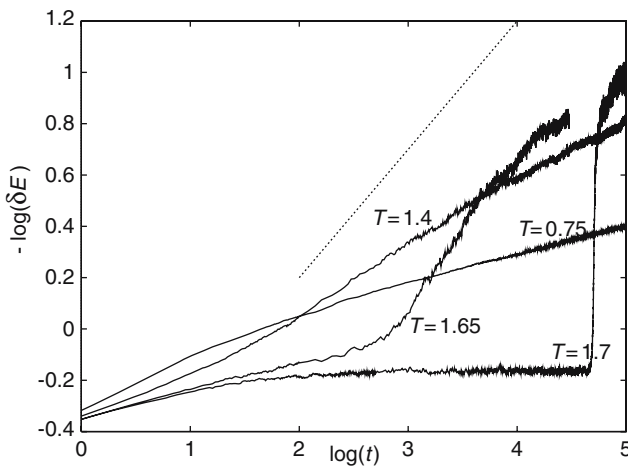


Fig. 7.11. The excess energy over the ground state versus time during a quench to various temperatures. The *dotted line* represents generic coarsening behaviour with an exponent of $1/2$

The log-log plot of $1/\delta E(t)$ as a function of time for the Gonihedric model with $\kappa = 0$ is shown in Fig. 7.11. The presented results are obtained for $L = 40$ but very similar behaviour was observed for $L = 30$. From Fig. 7.11, it is clear that for $T = 0.75$ and 1.4 the asymptotic slopes of the curves are much smaller than $1/2$ and there is a tendency for these curves to bend downwards. Taking into account the absence of models with n considerably smaller than $1/2$ and the existence of energy barriers in the Gonihedric model of basically the same nature as in the Shore and Sethna model, suggests that for the examined temperatures the characteristic length asymptotically increases logarithmically in time. It would appear that such a slow increase of $l(t)$ takes place even for $T = 1.65$ and 1.7 , but the behaviour of $l(t)$ for these temperatures is obscured by the metastability effects, since before collapsing into the glassy phase the system remains in the liquid state for some time.

The difference between the Gonihedric model and the Shore and Sethna model becomes clear when we approach the lower boundary of the metastable region which we roughly estimate to lie at $T = T_1 \sim 1.7$ by *increasing* the temperature. In the Shore and Sethna model for temperatures below the critical point but above a corner-rounding transition, thermal fluctuations roughen corners of domains, and energy barriers are no longer relevant. Consequently, the standard coarsening dynamics with $n = 1/2$ is restored, and the system rapidly evolves towards the low-temperature phase. On the contrary, in the Gonihedric model for $1.7 < T < 1.95$ a random quench does not even evolve towards the low-temperature phase but remains disordered.

The region of metastability can also be investigated through measuring various characteristic times by imposing different initial and boundary

conditions and monitoring the evolution towards a final state. To check the decay time associated with the stability of the high-temperature “liquid” phase (τ_{liq}), a random initial configuration can be used and then simulated at lower temperature until the energy reaches a sufficiently small value. To estimate τ_{liq} around 100 independent runs were necessary. The results for $T = 1.75$ are shown in Fig. 7.12 and they suggest that the escape time increases at least exponentially with the system size, which is at first sight surprising for a model with finite range interactions.

A later order of magnitude calculation [24] for the size of a critical droplet (one that would grow and eventually take over the whole system with the stable phase) in the Gonihedric model by Swift et al. showed that the results discussed here were for system sizes comparable or smaller than such a droplet, so the system size itself was setting the scale of energy barriers, leading to the observed exponential growth in lifetimes. The energy barrier Δ to forming a droplet of size R would be

$$\Delta = A\sigma R^{d-1} - B\delta f R^d \quad (7.22)$$

in d dimensions, where σ is the surface tension between stable and metastable phases, δf is the bulk free energy difference between the two phases and A and B are determined by the geometry of the droplet. Maximising Δ gives the critical radius R^*

$$R^* = \frac{A(d-1)\sigma}{B\delta f d} . \quad (7.23)$$

At low T in 3D, this gives a time scale for the nucleation of such a critical droplet of the form

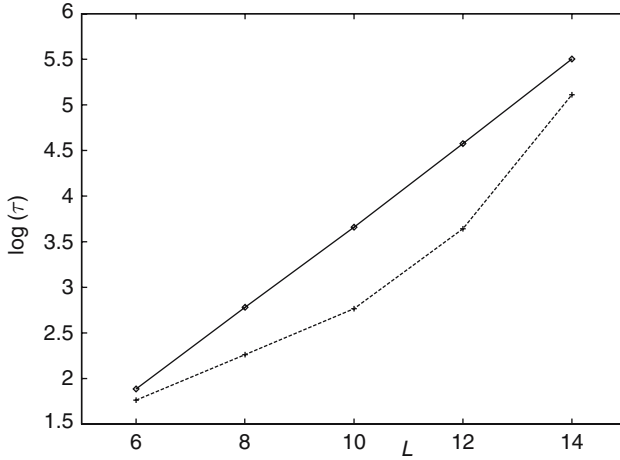


Fig. 7.12. The size dependence of the logarithm of the escape times τ_{liq} (□) and τ_{+-} (+). Calculation of τ_{liq} and τ_{+-} was done for $T = 1.75$ and $T = 1.8$, respectively

$$\tau \sim \exp(4A^3\sigma^3/27B^2\delta f^2T) \quad (7.24)$$

and inserting plausible estimates for σ and δf in the $\kappa = 0$ Gonihedric model gives $R^* = 25$ for cubic droplets and $\tau \sim 10^{47}$ Monte Carlo steps.

To check the stability of the low-temperature “crystal” phase, one should measure the time (τ_+) needed for the crystal to be transformed into the liquid. It would be particularly interesting to examine the size dependence of τ_+ for $1.8 < T < 1.95$, i.e. for temperatures where the crystal is metastable. It was found, however, that this quantity increases very rapidly with the system size, and in this temperature range, it is virtually impossible to increase the system size beyond $L = 6$. The stability of this phase might be also inferred from measurements of the time (τ_{+-}) needed to shrink a cubic excitation of size L . This technique parallels that which has already been applied to the Shore and Sethna model: The initial configuration has “up” spins at the boundary of the cube of size $L + 2$ (which are kept fixed) and “down” spins inside this cube. Simulations are performed until the magnetisation of the interior of the cube decays to zero and the time needed for such a run is recorded. To calculate τ_{+-} at a given temperature, 100 independent runs were again made. The results for $T = 1.8$ suggest that τ_{+-} increases approximately exponentially with L , whereas above the corner-rounding transition in the Shore and Sethna model, one expects $\tau_{+-} \sim L^2$, in which case the data in Fig. 7.12 would bend noticeably downwards.

Other analogous numerical experiments may be carried out for non-zero κ and the tentative picture which emerges [25] is shown in Fig. 7.13. The salient features are that generic Shore and Sethna models with competing nearest neighbour and next-nearest neighbour interactions have logarithmically slow low-temperature dynamics, with a transition to standard $t^{1/2}$ coarsening behaviour above a corner rounding transition at T_{cr} . For the Gonihedric model with a continuous transition (e.g. $\kappa = 1$), simulations suggest that this corner rounding transition is pushed close to (or may even be at) the equilibrium critical temperature T_c . The $\kappa = 0$ Gonihedric model displays rather different

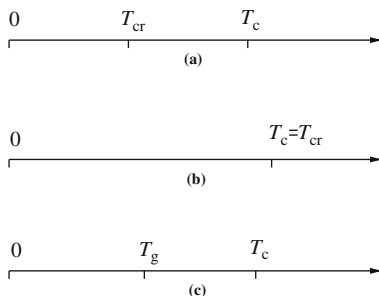


Fig. 7.13. The phaselines for the Shore and Sethna model (a), the Gonihedric model with a continuous transition (b) and the Gonihedric model with a first-order transition (in particular $\kappa = 0$) (c)

properties. In this case, there is a region of strong metastability on either side of a first-order equilibrium transition at T_c . We tentatively identify the lower boundary of the region of metastability with a glass transition temperature T_g . We now discuss why it is tempting to do so.

Glassy effects in simulations are usually discerned by looking at appropriate two-time quantities such as the spin–spin autocorrelation

$$C(t, t_w) = \left\langle \frac{1}{N} \sum_i \sigma_i(t_w) \sigma_i(t + t_w) \right\rangle, \quad (7.25)$$

where $N = L^3$ and t_w is the *waiting time* before measurements are commenced. Both normal coarsening and glassy dynamics are expected to display strong waiting time dependence (“aging”), but one may distinguish the type I aging dynamics seen in coarsening from the type II aging seen in glassy systems by looking at the overlap distribution function

$$Q(t_w + t, t_w + t) = \left\langle \frac{1}{N} \sum_i \sigma_i^{(1)}(t + t_w) \sigma_i^{(2)}(t + t_w) \right\rangle. \quad (7.26)$$

This is measured by relaxing the system from a disordered state for a time t_w at which point it is cloned into two sets of spins, $\{\sigma^{(1)}\}$ and $\{\sigma^{(2)}\}$, and evolved with independent random numbers for a further time t . One finds that $Q(t_w + t, t_w + t) \rightarrow 0$ as $C(t, t_w) \rightarrow 0$ in type II aging – the heuristic idea being that no matter when the two systems are separated, their configurations continue to move apart, which is suggestive of a truly rugged free energy landscape as found in glasses. If this were not the case, as in type I aging, one would find $Q(t_w + t, t_w + t) \rightarrow q$ for some constant q as $C(t, t_w) \rightarrow 0$. For the $\kappa = 0$ Gonihedric Ising model type II, aging is clearly seen with these criteria [24, 25, 26].

A further glassy feature is the behaviour of energy autocorrelation [24]

$$A(t, t_w) = \langle E(t_w) E(t + t_w) \rangle \quad (7.27)$$

for $T_g < T < T_c$. It is found that a stretched exponential form

$$A(t, t_w) \sim A_0 \exp \left(- \left(\frac{t}{\tau} \right)^\beta \right) \quad (7.28)$$

fits this quite well, where the relaxation time diverges as

$$\tau \sim \frac{A}{T - T^*} \quad (7.29)$$

and the value for T^* is very close to the measured value for T_g . The exponent β is temperature dependent and has been measured to fall in the range 0.6–0.8.

Furthermore, numerical cooling experiments suggest that it is possible that the Gonihedric model with $\kappa = 0$ may be displaying not just glassy behaviour,

but *ideal* glassy behaviour [27]. Some time ago, Anderson proposed that the glassy transition, which is a kinetic phenomenon, might be related in the limit of vanishingly small cooling rate with a thermodynamic transition [28]. It is found that for the Goni-hedric Ising model, the peak in the specific heat of the liquid occurs at, or very close to, the temperature at which the internal energy jumps under very slow cooling. The specific heat shown in Fig. 7.14 is a thermodynamic quantity. It was calculated in a (standard) quasi-equilibrium manner: After fixing a temperature, we relaxed the system and then measured the variance of the internal energy. The sharp peak seen in Fig. 7.14 indicates a thermodynamic-like singularity in this model.

On the other hand, an almost vertical drop of the internal energy under continuous cooling, shown in Fig. 7.15, indicates the dynamic, glassy transition. The results were obtained by simulating the model under continuous cooling with a constant cooling rate r and initial temperature $T_0 = 2.1$ ($T_0 > T_g$). This means that temperature as a function of time is given by $T = T_0 - rt$. Calculations were performed for several system sizes L in order to ensure that L was sufficiently large. For example, for $r = 0.02$, the system size $L = 30$ is sufficient to obtain size-independent results, but for $r = 0.00002$, we had to take $L = 70$. One can see that although r decreases by three decades, the zero-temperature energy approaches the ground-state energy very slowly and that lowering the cooling rate r sharpens the transition. At first sight, one might expect that in the limit $r \rightarrow 0$, the transition becomes infinitely sharp and coincides exactly with thermodynamic singularity at the peak of the specific heat. However, as we have seen, the metastability of the liquid

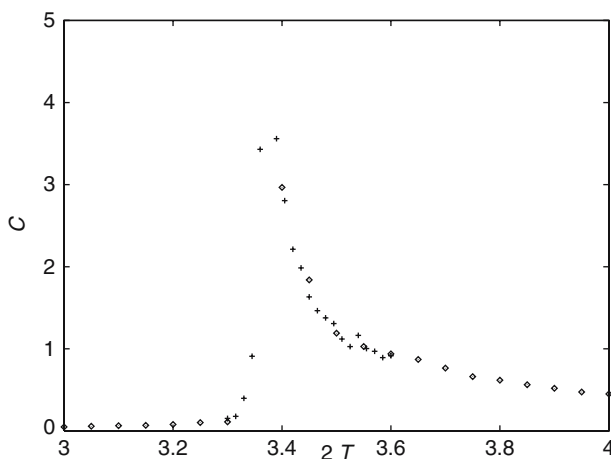


Fig. 7.14. The specific heat C as a function of temperature T calculated from the variance of the internal energy for $L = 24$ (\diamond) and $L = 40$ ($+$). At each temperature, the system was relaxed for 10^3 Monte Carlo steps and then measurements were performed during 10^4 Monte Carlo steps

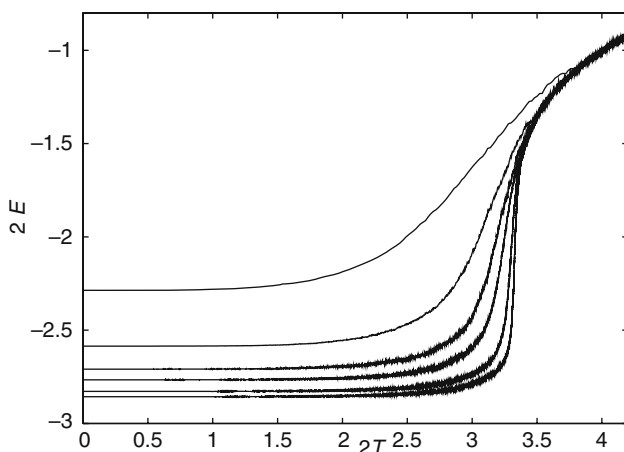


Fig. 7.15. The internal energy E as a function of temperature for (from the top) $r = 0.02, 0.002, 0.0005, 0.0002, 0.00005$ and 0.00002

is a finite (but large) time/size effect and neither the peak nor the internal energy drop can be made perfectly sharp.

Anderson's idea has had a rather limited experimental support. The main problem is that under slow cooling, real liquids do not get trapped in the glassy phase, but instead tend to crystallise. The reason for this is that when liquid is cooled below the melting point, it becomes metastable, and within a finite time due to heterogeneous or homogeneous crystal nucleation, it then crystallises. Only under sufficiently fast cooling can the crystal nucleation be avoided and the liquid trapped in the glassy state. In this context, the Gonihedric model with plaquette interactions appears to correspond to an almost ideal glass with an extremely large lifetime for the metastable state.

A final subject which merits further investigation is the nature of the self-induced disorder in the glassy phase. To get some insight into the $\kappa = 0$ case, it is possible to look at the distribution of unsatisfied plaquettes in the glassy phase (i.e. plaquettes contributing energy above the ground state) [29]. A random high-temperature sample was slowly cooled down to zero temperature, and the final configuration was used to locate unsatisfied plaquettes, and their spatial distribution is shown in Fig. 7.16. For comparison, we also present similar simulations for the $\kappa = 2$ case. One can see that in both cases, the energy from these unsatisfied plaquettes is concentrated in linear segments (around 90% in both cases for slow cooling). Interestingly, low-temperature excitations observed in the 3D Edwards–Anderson *spin* glass is

$$H = - \sum_{\langle ij \rangle} J_{ij} \sigma_i \sigma_j , \quad (7.30)$$

where the nearest neighbour couplings $\{J_{ij}\}$ are quenched Gaussian random variables with zero mean and unit variance, which appear to have a rather

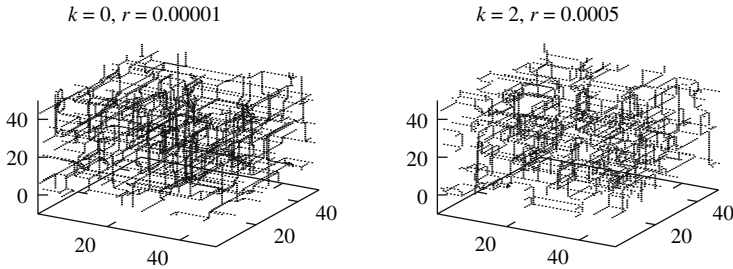


Fig. 7.16. A distribution of unsatisfied plaquettes in the zero-temperature glassy phase. Simulations were made for the system size $L = 100$

similar stringy structure [30]. It is possible that the self-induced disorder in the $\kappa = 0$ Gonihedric model gives rise to similar characteristics for the excitations as the quenched disorder which is imposed a priori in the finite-dimensional spin glass.

A further point of contact with spin glasses is that a spin glass version of the $\kappa = 0$ Hamiltonian (still on a 3D cubic lattice)

$$H = -J_{\square} \sum_{[i,j,k,l]} \sigma_i \sigma_j \sigma_k \sigma_l, \quad (7.31)$$

where the J_{\square} are now quenched random variables, was also found to display numerous common properties with structural glasses [31]. Many of the observed numerical features seen in simulations of this model, such as the stretched exponential correlations and divergence of the autocorrelation time, are extremely similar to those discussed here for the $\kappa = 0$ Gonihedric model. The inference from this might be that the additional quenched disorder arising from the J_{\square} may be gratuitous since the plaquette Hamiltonian on its own is enough to give the same, or very similar, behaviour.

Self-induced disorder has been posited before as a mechanism for glassy behaviour in various deterministic mean-field models. One well-known example is the Hamiltonian originally formulated by Golay [32],

$$H = -\frac{J_0^2}{2N} \sum_{k=1}^{N-1} \left[\sum_{i=1}^{N-k} \sigma_i \sigma_{i+k} \right]^2, \quad (7.32)$$

in the context of obtaining binary sequences with small autocorrelations. It was shown that many of the properties of the deterministic Hamiltonian in (7.32) were reproduced by the disordered Hamiltonian

$$H = -\frac{1}{2N} \sum_{k=1}^{N-1} \left[\sum_{i,j=1}^N J_{ij}^{(k)} \sigma_i \sigma_j \right]^2, \quad (7.33)$$

where the $J^{(k)}$ were random connectivity matrices [33]. The contrasting feature for the Gonihedric model is that the self-induced disorder is appearing with finite-range couplings.

The non-equilibrium, dynamical properties of the Gonihedric Ising model thus display many interesting features both for $\kappa = 0$ and $\kappa \neq 0$. For the case of $\kappa = 0$ (the purely plaquette action), there are clear parallels with the observed behaviour of real glass formers, so it offers an appealing lattice model for investigations of glassy dynamics by virtue of its simplicity. Indeed, there may also be similarities with finite-dimensional spin glasses, as we have seen above.

7.4 Variations on the Glassy and Gonihedric Themes

There are a plethora of other lattice models which can be formulated to display glassy properties [34, 35]. In many cases, these have trivial static Hamiltonians of the form

$$H = \sum_{i=1}^N n_i, \quad (7.34)$$

where the $n_i = 0, 1$ are defined on each site of a cubic lattice of linear size L , which has periodic boundary conditions and can be thought of as labelling the (im)mobility of a site. The interesting (glassy) behaviour is induced in these cases via constrained dynamics.

Other models may possess a non-trivial Hamiltonian, but a trivial equilibrium phase diagram. Nonetheless, the dynamical properties of such models may still be of interest. The 2D Gonihedric Ising model is one such case

$$\mathcal{H}_{\text{gonih}}^{2D} = -\kappa \sum_{\langle i,j \rangle} \sigma_i \sigma_j + \frac{\kappa}{2} \sum_{\ll i,j \gg} \sigma_i \sigma_j - \frac{1-\kappa}{2} \sum_{[i,j,k,l]} \sigma_i \sigma_j \sigma_k \sigma_l,$$

where the form is similar to the 3D model, but the relative weights of the terms differ. This is constructed to weight the corners of 2D spin clusters, rather than their edge length, which is the effect of the standard 2D Ising action. Via a mapping to the 8-vertex model, it is possible to show that the 2D Gonihedric Hamiltonian does not display a static phase transition. Just as for the trivial Hamiltonian models with constraints, the dynamics displays many interesting features [36].

We have concentrated exclusively on Ising spins here. It is also possible to define a 3D Gonihedric Potts models

$$\begin{aligned} H = & -2\kappa \sum_{x,\mu>0} (2\delta_{\sigma_x, \sigma_{x+\mu}} - 1) + \frac{\kappa}{2} \sum_{x,\mu \neq \nu, \mu>0} (2\delta_{\sigma_x, \sigma_{x+\mu+\nu}} - 1) \\ & - \frac{1-\kappa}{2} \sum_{x,\mu \neq \nu, \mu>0, \nu>0} (2\delta_{\sigma_x, \sigma_{x+\mu}} \delta_{\sigma_{x+\nu}, \sigma_{x+\mu+\nu}} - 1) \times \end{aligned}$$

$$(2\delta_{\sigma_x, \sigma_{x+\nu}} \delta_{\sigma_{x+\mu}, \sigma_{x+\mu+\nu}} - 1)(2\delta_{\sigma_x, \sigma_{x+\mu+\nu}} \delta_{\sigma_{x+\nu}, \sigma_{x+\mu}} - 1), \quad (7.35)$$

where the spin variables $\{\sigma\}$ now take on q values [37]. In this case, the model appears to retain a first-order equilibrium transition for larger κ than with Ising spins, but the dynamical properties of the model remain to be investigated.

The idea that multi-spin, specifically plaquette, interactions give rise to self-induced disorder might also be applied to models with continuous spins, such as gauge glasses. The standard 3D gauge glass Hamiltonian is of the form [38]

$$H = - \sum_{\langle i, j \rangle} \cos(\theta_i - \theta_j + A_{ij}), \quad (7.36)$$

where the A_{ij} are quenched, random variables uniformly distributed in $[0, 2\pi]$. A plaquette interaction of the form

$$H = - \sum_{[i, j, k, l]} \cos(\theta_i - \theta_j + \theta_k - \theta_l) \quad (7.37)$$

would presumably give rise to a similar sort of frustration as the quenched disordered $\{A_{ij}\}$.

A final avenue for further research might be the dual model to the $\kappa = 0$ Gonihedric action, which may be written in several equivalent forms including

$$H_{\text{dual}} = \sum_{\xi} [A^{\chi}(\xi)A^{\chi}(\xi + \chi) + A^{\eta}(\xi)A^{\eta}(\xi + \eta) + A^{\zeta}(\xi)A^{\zeta}(\xi + \zeta)] , \quad (7.38)$$

where $A^{\chi} = (1, 1, -1, -1)$, $A^{\eta} = (1, -1, 1, -1)$ and $A^{\zeta} = (1, -1, -1, 1)$ are one-dimensional irreducible representations of the fourth-order Abelian group and ξ, η, ζ are unit vectors in the dual lattice. The spins may also be considered as Ising (± 1) spins if we set $A^{\zeta} = A^{\chi} A^{\eta}$, which gives the following Hamiltonian

$$\begin{aligned} H_{\text{dual}} = & \sum_{\xi} [A^{\chi}(\xi)A^{\chi}(\xi + \chi) + A^{\eta}(\xi)A^{\eta}(\xi + \eta) \\ & + A^{\chi}(\xi)A^{\eta}(\xi)A^{\chi}(\xi + \zeta)A^{\eta}(\xi + \zeta)] . \end{aligned} \quad (7.39)$$

This is recognisable as a strongly anisotropically coupled Ashkin–Teller model. It is possible that consideration of this dual model might shed some light on the definition of an order parameter in the original Hamiltonian and also suggests an intriguing link with *anisotropic* scaling properties.

7.5 Endpiece

Gonihedric 3D Ising models have had an interesting past and display novel properties both in equilibrium and dynamically. The $\kappa = 0$ (plaquette) Gonihedric Hamiltonian appears to provide a simple lattice model with similar

behaviour to structural glass formers, which also has some connections with spin glasses in spite of the absence of quenched disorder. Even after some fairly extensive investigation by Monte Carlo simulations and other means over recent years, many features of the models still remain in need of clarification. They may well have an interesting future ahead of them too.

Acknowledgements

DAJ would like to thank G. Savvidy for an elementary Greek lesson, and for many discussions over the years on the Gonihedric model. DAJ's work was partially supported by EU RTN-Network "ENRAGE": *Random Geometry and Random Matrices: From Quantum Gravity to Econophysics* under grant No. MRTN-CT-2004-005616. Many of the results described here were obtained in collaboration with D. Espriu, E. Cirillo, G. Gonnella and A. Pelizzola, who have all contributed to the understanding of the model.

References

1. Y. Nambu: Lectures at the Copenhagen Symposium 1970; T. Goto: Prog. Theor. Phys. **46**, 1560 (1971) [174](#)
2. B. Durhuus, J. Fröhlich, T. Jonsson: Nucl. Phys. B **225**, 185 (1983); T. Eguchi, H. Kawai: Phys. Lett. B **114**, 247 (1982); J. Ambjørn, B. Durhuus, J. Fröhlich: Nucl. Phys. B **257**, 433 (1985); D. Boulatov, V. Kazakov, I. Kostov, A. Migdal: Nucl. Phys. B **275**, 241 (1986); A. Billoire, F. David: Nucl. Phys. B **275**, 617 (1986); J. Jurkiewicz, A. Krzywicki, B. Petersson: Phys. Lett. B **168**, 273 (1986) [175](#)
3. A. M. Polyakov: Mod. Phys. Lett. A **2**, 893 (1987); J. Distler, H. Kawai: Nucl. Phys. B **323**, 330 (1989); F. David: Mod. Phys. Lett. A **3**, 1651 (1988) [175](#)
4. A. M. Polyakov: Nucl. Phys. B **268**, 406 (1986); H. Kleinert: Phys. Lett. B **174**, 335 (1986); W. Helfrich: J. Phys. (France) **46**, 1263 (1985); F. Alonso, D. Espriu: Nucl. Phys. B **283**, 393 (1987); H. Kleinert: Phys. Rev. Lett. **58**, 1915 (1987) [175](#)
5. S. M. Catterall: Phys. Lett. B **220**, 207 (1989); C. F. Baillie, D. A. Johnston, R. D. Williams: Nucl. Phys. B **335**, 469 (1990); C. Baillie, S. Catterall, D. Johnston, R. Williams: Nucl. Phys. B **348**, 543 (1991); M. Baig, D. Espriu, J. F. Wheeler: Nucl. Phys. B **314**, 609 (1989); J. Ambjørn, B. Durhuus, T. Jonsson: Nucl. Phys. B **316**, 526 (1989); M. Bowick, P. Coddington, L. Han, G. Harris, E. Marinari: Nucl. Phys. B **394**, 791 (1993); K. Anagnostopoulos, M. Bowick, P. Coddington, M. Falcioni, L. Han, G. Harris, E. Marinari: Phys. Lett. B **317**, 102 (1993); M. Bowick, S. Catterall, M. Falcioni, G. Thorleifsson, K. Anagnostopoulos: J. Phys. I (France) **6**, 1321 (1996); M. Baig, D. Espriu: Nucl. Phys. (Proc. Suppl.) **30**, 779 (1993); J. F. Wheeler, P. W. Stephenson: Phys. Lett. B **302**, 447 (1993); J. F. Wheeler: Nucl. Phys. B **458**, 671 (1996) [175](#)
6. R. V. Ambartzumian, G. S. Sukiasian, G. K. Savvidy, K. G. Savvidy: Phys. Lett. B **275**, 99 (1992); G. K. Savvidy, K. G. Savvidy: Int. J. Mod. Phys. A **8**,

- 3393 (1993); G. K. Savvidy, K. G. Savvidy: *Mod. Phys. Lett. A* **8**, 2963 (1993); J. Ambjørn, G. K. Savvidy, K. G. Savvidy: *Nucl. Phys. B* **486**, 390 (1997) [175](#)
7. J. Steiner: *Gesammelte Werke*, Vol. 2, Berlin (1927) 171 [175](#)
8. C. Baillie, D. Espriu, D. Johnston: *Phys. Lett. B* **305**, 109 (1993); C. Baillie, A. Irbäck, W. Janke, D. Johnston: *Phys. Lett. B* **325**, 45 (1994) [175](#)
9. G. K. Savvidy, F. J. Wegner: *Nucl. Phys. B* **413**, 605 (1994); G. K. Savvidy, K. G. Savvidy: *Phys. Lett. B* **324**, 72 (1994); G. K. Savvidy, K. G. Savvidy, P. G. Savvidy: *Phys. Lett. A* **221**, 233 (1996); G. K. Savvidy, K. G. Savvidy: *Phys. Lett. B* **337**, 333 (1994); G. K. Savvidy, K. G. Savvidy, F. J. Wegner: *Nucl. Phys. B* **443**, 565 (1995); G. K. Bathas, E. Floratos, G. K. Savvidy, K. G. Savvidy: *Mod. Phys. Lett. A* **10**, 2695 (1995); G. K. Savvidy, K. G. Savvidy: *Mod. Phys. Lett. A* **11**, 1379 (1996); G. Koutsoumbas, G. K. Savvidy, K. G. Savvidy: *Phys. Lett. B* **410**, 241 (1997); J. Ambjørn, G. Koutsoumbas, G. K. Savvidy: *Europhys. Lett.* **46**, 319 (1999); G. Koutsoumbas, G. K. Savvidy: *Mod. Phys. Lett. A* **17**, 751 (2002) [176](#)
10. A. Cippi, P. Colangelo, G. Gonella, A. Maritan: *Nucl. Phys. B* **370**, 659 (1992) [177](#), [180](#)
11. D. Johnston, R. K. P. C. Malmini: *Phys. Lett. B* **378**, 87 (1996) [179](#)
12. M. Baig, D. Espriu, D. Johnston, R. K. P. C. Malmini: *J. Phys. A* **30**, 405 (1997) [179](#)
13. M. Baig, D. Espriu, D. Johnston, R. K. P. C. Malmini: *J. Phys. A* **30**, 7695 (1997) [179](#)
14. R. Pietig, F. Wegner: *Nucl. Phys. B* **466**, 513 (1996); *B* **525**, 549 (1998) [179](#)
15. E. Cirillo, G. Gonnella, A. Pelizzola, D. Johnston: *Phys. Lett. A* **226**, 59 (1997) [179](#), [183](#), [185](#)
16. A. Pelizzola: *Phys. Rev. E* **49**, 2503(R) (1994); A. Pelizzola: *Physica A* **211**, 107 (1994); A. Pelizzola: *J. Magn. Magn. Mat.* **140–144**, 1491 (1995); A. Pelizzola: *Phys. Rev. E* **53**, 5825 (1996) [179](#), [183](#)
17. M. Baig, J. Clua, D. A. Johnston, R. Villanova: *Phys. Lett. B* **585**, 180 (2004) [181](#)
18. R. Kikuchi: *Phys. Rev.* **81**, 988 (1951); *G. An. J. Stat. Phys.* **52**, 727 (1988); T. Morita: *J. Stat. Phys.* **59**, 819 (1990) [182](#)
19. E. Cirillo, G. Gonnella, A. Pelizzola: *Phys. Rev. E* **55**, 17(R) (1997) [183](#), [184](#)
20. Y. Nishiyama: *Phys. Rev. E* **70**, 026120 (2004) [183](#), [184](#)
21. R. Hellmann, A. Ferrenberg, D. P. Landau, R. Gerling: In *Computer Simulation Studies in Condensed Matter Physics IV*, edited by D. P. Landau, K. Mon, H.-B. Schüttler (Springer-Verlag, Berlin, 1993) [184](#)
22. J. D. Shore, J. P. Sethna: *Phys. Rev. B* **43**, 3782 (1991) [185](#)
23. A. Lipowski: *J. Phys. A* **30**, 7365 (1997); A. Lipowski, D. Johnston: *J. Phys. A* **33**, 4451 (2000) [185](#), [187](#)
24. M. Swift, H. Bokil, R. Travasso, A. Bray: *Phys. Rev. B* **62**, 11494 (2000) [189](#), [191](#)
25. A. Lipowski, D. Johnston, D. Espriu: *Phys. Rev. E* **62**, 3404 (2000) [190](#), [191](#)
26. P. Dimopoulos, D. Espriu, E. Jané, A. Prats: *Phys. Rev. E* **66**, 056112 (2002) [191](#)
27. A. Lipowski, D. Johnston: *Phys. Rev. E* **61**, 6375 (2000) [192](#)
28. P. W. Anderson: In *Ill Condensed Matter*, edited by R. Balian, R. Maynard, G. Toulouse (North Holland, Amsterdam, 1979) [192](#)
29. A. Lipowski, D. Johnston: *Phys. Rev. E* **65**, 017103 (2002) [193](#)
30. J. Lamarcq, J.-P. Bouchaud, O. C. Martin, M. Mezard: *Europhys. Lett.* **58**, 321 (2002) [194](#)
31. D. Alvarez, S. Franz, F. Ritort: *Phys. Rev. B* **54**, 9756 (1996) [194](#)

- 32. M. Golay: IEEE **IT-23**, 43 (1977); M. Golay: IEEE **IT-28**, 543 (1982); J. Bernasconi: J. Phys. (France) **48**, 559 (1987) [194](#)
- 33. J. Bouchaud, M. Mézard: J. Phys. I (France) **4**, 1109 (1994) [195](#)
- 34. F. Ritort, P. Sollich: Adv. Phys. **52**, 219 (2003) [195](#)
- 35. R. Jack, J. Garrahan: J. Chem. Phys. **123**, 164508 (2005); R. Jack, J. Garrahan, D. Chandler: J. Chem. Phys. **125**, 184509 (2006) [195](#)
- 36. D. Espriu, A. Prats: Phys. Rev. E **70**, 046117 (2004); R. Jack, L. Berthier, J. Garrahan: Phys. Rev. E **72**, 016103 (2005); D. Espriu, A. Prats: J. Phys. A **39**, 1743 (2006) [195](#)
- 37. P. Dimopoulos, G. Koutsoumbas, G. Savvidy: Phys. Lett. A **318**, 499 (2003) [196](#)
- 38. H. Katzgraber, A. Young: Phys. Rev. B **66**, 224507 (2002) [196](#)

Protein Folding

Thermodynamics of Protein Folding from Coarse-Grained Models' Perspectives

Michael Bachmann and Wolfhard Janke

Institut für Theoretische Physik and Centre for Theoretical Sciences (NTZ),
Universität Leipzig, Postfach 100 920, D-04009 Leipzig, Germany
{michael.bachmann,wolfhard.janke}@itp.uni-leipzig.de

Abstract. Folding and aggregation of proteins, the interaction between proteins and membranes, as well as the adsorption of organic soft matter to inorganic solid substrates belong to the most interesting challenges in understanding structure and function of complex macromolecules. This is reasoned by the interdisciplinary character of the associated questions ranging from the molecular origin of the loss of biological functionality as, for example, in Alzheimer's disease to the development of organic circuits for biosensory applications. In this lecture, we focus on the analysis of mesoscopic models for protein folding, aggregation, and hybrid systems of soft and solid condensed matter. The simplicity of the coarse-grained models allows for a more universal description of the notoriously difficult problem of protein folding. In this approach, classifications of structure formation processes with respect to the conformational pseudophases are possible. This is similar in aggregation and adsorption processes, where the individual folding propensity is influenced by external forces. The main problem in studies of conformational transitions is that the sequences of amino acids, which built up the proteins, are necessarily of finite length and, therefore, a thermodynamic limit does not exist. Thus, structural transitions are not phase transitions in the strict thermodynamic sense and the analysis of pseudouniversal aspects is intricate, as apparently small-system effects accompany all conformational transitions and cannot be neglected.

8.1 Introduction

Proteins are linear chains of amino acids connected by covalent peptide bonds. Twenty types of amino acids, mainly differing in the molecular structure of their side chains, were identified in bioproteins. Since bioproteins typically consist of hundreds to thousands of amino acids, the number of possible amino acid sequences is extremely large. Considering, for example, a chain of only 100 amino acids, the number of possible sequences (i.e., primary structures) is of order 10^{130} , but this is only one side of the medal. The main importance of proteins lies in their function in a biological organism, and this function is inseparably connected with the geometrical structure of a protein, i.e., its

folded, native conformation which is usually divided into secondary, tertiary, and quaternary substructures [1, 2]. The required stability of this native state against thermal and other environmental fluctuations rules out most of the possible sequences [3]. It is not yet understood how the relatively small number of relevant proteins, e.g., about 10^5 in the human body, has been selected by nature in an evolutionary process [4].

The physical interactions responsible for the folding of a protein into its native structure are in principle known. The complexity of the macromolecule with up to ten thousands of atoms, however, makes precise predictions of the energetically most-favored structure based on *ab initio* quantum-mechanical calculations practically impossible. This is due to the long-range overlap of many-body electronic orbitals and the screening by the positively charged cores. The problem is indeed still more complex as the natural environment of proteins is a polar aqueous solvent. For this reason, classical models with hundreds of effective parameters (“force fields”) have been developed in the past decades in order to predict native structures and to study folding dynamics in computer simulations [5]. Despite the simplifications, these models are still highly complex and hard to manage even by means of sophisticated algorithms and powerful capability computers. Furthermore, it turned out that folding and misfolding depend sensitively on the choice of the force field parameters, with the consequence that predictions of different established models do not frequently coincide. Another problem is that investigations of these models require enormous computational capacities. For this reason and the fact that folding times in nature range from milliseconds to seconds, molecular dynamics simulations (MD) for studying the deterministic folding dynamics are currently widely useless as the timescale of nano- to microseconds of reliable MD simulations is orders of magnitudes smaller.

It should be noted, however, that MD is quite successful in studies of biological short-time processes, where the biological function of proteins can be studied. Fascinating examples, where MD proved to be highly successful, are the penetration of water molecules into a cell through aquaporin being a membrane protein [6] and the ATP synthase, a process, where the catalytic subunits of F1, embedded into the membrane F0 proton channel, partially act as rotating “molecular motor” that promotes dehydration of ADP and P to ATP [7]. Such studies require that the native folds of the proteins must be known as these are used as *input*. For considering thermodynamics, Monte Carlo simulations of these all-atom models are much more promising, in particular by applying sophisticated generalized-ensemble algorithms [8]. Nonetheless, the enormous efforts required to obtain trustworthy results with these models strongly limit the systematic exposure of the general principles behind protein folding processes, which necessitates comparative studies of an appropriate set of different sequences.

In these lecture notes, we therefore follow a different approach and discuss minimalistic, coarse-grained protein models. Coarse-graining of models, i.e., increasing relevant length scales by reducing the number of microscopic

degrees of freedom, has proved to be very successful in polymer science. Although specificity is much more sensitive for proteins, since details (charges, polarity, etc.) and differences of the amino acid side chains can have strong influences on the fold, mesoscopic approaches are also of essential importance for the basic understanding of conformational transitions affecting the folding process. It is also the only possible approach for systematic analyses such as the evolutionarily significant question why only a few sequences in nature are “designing”, i.e., relevant for selective functions. On the other hand, what is the reason why proteins prefer a comparative small set of target structures, i.e., what explains the preference of designing sequences to fold into the *same* three-dimensional structure? All these questions are widely still unanswered.

As a first step toward their solution, we discuss in the first part simple hydrophobic–polar (HP) lattice models, where only the most characteristic hydrophobic or polar nature of the 20 naturally occurring amino acids is taken into account and the linear chain is modeled by a self-avoiding walk. Such models allow a comprising analysis of both, the conformation *and* sequence space, e.g., by exactly enumerating all combinatorial possibilities. Other important aspects in lattice model studies are the identification of lowest-energy conformations of comparatively long sequences and the characterization of the folding thermodynamics.

In the second part, we focus on simple AB off-lattice models, where similar to the HP model (for historical reasons) *A* symbolizes hydrophobic and *B* polar regions of the protein, whose conformations are modeled by polymer chains governed by bending energy and van der Waals interactions. These models allow for the analysis of different mutated sequences with respect to their folding characteristics. Here, the idea is that the folding transition is a kind of pseudophase transition which can in principle be described by one or a few order-like parameters. Depending on the sequence, the folding process can be highly cooperative (single-exponential), less cooperative depending on the height of a free-energy barrier (two-state folding), or even frustrating due to the existence of different barriers in a metastable regime (crystal or glassy phases). These characteristics known from functional proteins can be recovered in the AB model, which is computationally much less demanding than all-atom formulations and thus enables throughout theoretical analyses.

Such coarse-grained models enable a broader view on the general problem of protein folding, but for precise, specific predictions, their applicability is limited. In analogy to magnetic systems, they are rather comparable with the Ising model for ferromagnets or the Edwards-Anderson Ising model for spin glasses. It should also be remarked that, due to their nontrivial simplicity, coarse-grained models are also a perfect testing ground for newly developed algorithms.

8.2 Why Coarse-Graining?

Functional proteins in a biological organism are typically characterized by a unique three-dimensional molecular structure, which makes the protein selective for individual functions, e.g., in catalytic, enzymatic, and transport processes. In most cases, the free-energy landscape is believed to exhibit a rough shape with a large number of local minima and, for functional proteins, a deep, funnel-like global minimum. This assumed complexity is the reason why it is difficult to understand how the random-coil conformation of covalently bonded amino acids – the sequence is generated in the ribosome according to a certain genetic sequence in the DNA – spontaneously folds into a well-defined stable “native” conformation. Furthermore, it is expected that there are only a small number of folding paths from any unfolded conformation to this final fold.

Protein folding follows a strict hierarchy at different length scales. The so-called primary structure, i.e., the sequence of amino acids in the linear chain is provided by the ribosome. Since subsequent amino acids are uniformly linked by a covalent peptide bond independent of the geometrical structure of the protein, the typical length scale of the primary structure is a single amino acid. The next level is secondary structures such as α -helices, β -sheets, and turns. The main reason for the formation of these structures is backbone hydrogen bonding which typically involves segments of several subsequent amino acids. Therefore, the scale of secondary structures is determined by the typical segment sizes, which are of the order of ten amino acids. Consequently, secondary-structure formation is the first step in protein folding. This is followed by the formation of global, single-domain tertiary structures. In fact, this process is what renders protein folding special. The main driving force for the folding of a complex domain, i.e., of up to hundreds of amino acids, is an effective cooperative intrinsic interaction between many amino acid side chains and which is strongly influenced by the solubility properties (in particular its polarization) of the aqueous solvent the protein resides in. Roughly, amino acid side chains can be classified as polar, hydrophobic, and neutral. While polar residues favor contact with polar water molecules, hydrophobic acids avoid contact with water which results in an effective attraction between hydrophobic side chains. In consequence, this attractive force leads to the formation of a highly compact hydrophobic core, which is screened from the solvent by a shell of polar amino acids. For very large proteins, the final stage in the folding process is the arrangement of several domains in a quaternary structure.

Thus, the most complex process in protein folding is the formation of tertiary hydrophobic-core structures. Although atomic details, e.g., van der Waals volume exclusion separating side chains in linear and ring structures, polarizability, and partial charges, noticeably influence the folding process and the native fold, it should be possible to understand certain aspects of the folding characteristics, at least qualitatively, by means of coarse-grained

models which are based on a few effective parameters. In the following, we investigate this question within the two minimalistic HP lattice and AB off-lattice heteropolymer models.

8.3 The Hydrophobic–Polar Lattice Protein Model

The simplest model for a qualitative description of protein folding is the lattice hydrophobic-polar (HP) model [9]. In this model, the continuous conformational space is reduced to discrete regular lattices and conformations of proteins are modeled as self-avoiding walks restricted to the lattice. Assuming that the hydrophobic interaction is the most essential force toward the native fold, sequences of HP proteins consist of only two types of monomers (or classes of amino acids): Amino acids with high hydrophobicity are treated as hydrophobic monomers (H), while the class of polar (or hydrophilic) residues is represented by polar monomers (P). In order to achieve the formation of a hydrophobic core surrounded by a shell of polar monomers, the interaction between hydrophobic monomers is attractive and short range. In the standard formulation of the model [9], all other interactions are neglected. Variants of the HP model also take into account (weaker) interactions between H and P monomers as well as between polar monomers [4].

Although the HP model is extremely simple, it has been proven that identifying native conformations is an NP-complete problem in two and three dimensions [10]. Therefore, sophisticated algorithms were developed to find lowest-energy states for chains of up to 136 monomers. The methods applied are based on very different algorithms, ranging from exact enumeration in two dimensions [11, 12] and three dimensions on cuboid (compact) lattices [4, 13, 14, 15], and hydrophobic-core construction methods [16, 17] over genetic algorithms [18, 19, 20, 21, 22], Monte Carlo simulations with different types of move sets [23, 24, 25, 26], and generalized ensemble approaches [27] to Rosenbluth chain-growth methods [28] of the “Go with the Winners” type [29, 30, 31, 32, 33, 34, 35]. With some of these algorithms, thermodynamic quantities of lattice heteropolymers were studied as well [14, 27, 31, 34, 35, 36].

8.3.1 The HP Model

A monomer of an HP sequence $\sigma = (\sigma_1, \sigma_2, \dots, \sigma_N)$ is characterized by its residual type ($\sigma_i = P$ for polar and $\sigma_i = H$ for hydrophobic residues), the position $1 \leq i \leq N$ within the chain of length N , and the spatial position \mathbf{x} to be measured in units of the lattice spacing. A conformation is then symbolized by the vector of the coordinates of successive monomers, $\mathbf{X} = (\mathbf{x}_1, \mathbf{x}_2, \dots, \mathbf{x}_N)$. We denote by $x_{ij} = |\mathbf{x}_i - \mathbf{x}_j|$ the distance between the i th and the j th monomer. The bond length between adjacent monomers in the chain is identical with the spacing of the used regular lattice with coordination number q . These covalent bonds are thus not stretchable. A monomer and its

nonbonded nearest neighbors may form the so-called contacts. Therefore, the maximum number of contacts of a monomer within the chain is $(q - 2)$ and $(q - 1)$ for the monomers at the ends of the chain. To account for the excluded volume, lattice proteins are self-avoiding, i.e., two monomers cannot occupy the same lattice site. The total energy for an HP protein reads in energy units of ε_0 (we set $\varepsilon_0 = 1$ in the following):

$$E_{\text{HP}} = \varepsilon_0 \sum_{\langle i,j \rangle > i+1} C_{ij} U_{\sigma_i \sigma_j}, \quad (8.1)$$

where $C_{ij} = (1 - \delta_{i+1j})\Delta(x_{ij} - 1)$ with

$$\Delta(z) = \begin{cases} 1, & z = 0 \\ 0, & z \neq 0 \end{cases} \quad (8.2)$$

is a symmetric $N \times N$ matrix called *contact map* and

$$U_{\sigma_i \sigma_j} = \begin{pmatrix} u_{HH} & u_{HP} \\ u_{HP} & u_{PP} \end{pmatrix} \quad (8.3)$$

is the 2×2 interaction matrix. Its elements $u_{\sigma_i \sigma_j}$ correspond to the energy of HH , HP , and PP contacts. For labeling purposes, we shall adopt the convention that $\sigma_i = 0 \hat{=} P$ and $\sigma_i = 1 \hat{=} H$.

In the simplest formulation [9], only the attractive hydrophobic interaction is nonzero, $u_{HH}^{\text{HP}} = -1$, while $u_{HP}^{\text{HP}} = u_{PP}^{\text{HP}} = 0$. Therefore, $U_{\sigma_i \sigma_j}^{\text{HP}} = -\delta_{\sigma_i H} \delta_{\sigma_j H}$. This parameterization, which we will traditionally call the *HP model* in the following, has been extensively used to identify ground states of HP sequences, some of which are believed to show up qualitative properties comparable with realistic proteins whose 20-letter sequence was transcribed into the 2-letter code of the HP model [16, 18, 37, 38, 39].

This simple form of the standard HP model suffers, however, from the fact that the lowest-energy states are usually highly degenerate, and therefore the number of designing sequences (i.e., sequences with unique ground state – up to the usual translational, rotational, and reflection symmetries) is very small, at least on the three-dimensional simple cubic (sc) lattice. Incorporating additional inter-residue interactions, symmetries are broken, degeneracies are smaller, and the number of designing sequences increases [14, 15]. Based on the Miyazawa–Jernigan matrix [40] of inter-residue contact energies between real amino acids, an additional attractive nonzero energy contribution for contacts between H and P monomers is more realistic [4]. In the following, we set the elements of the interaction matrix (8.3) to $u_{HH}^{\text{MHP}} = -1$, $u_{HP}^{\text{MHP}} = -1/2.3 \approx -0.435$, and $u_{PP}^{\text{MHP}} = 0$, corresponding to [4]. The factor 2.3 is a result of an analysis for the inter-residue energies of contacts between hydrophobic amino acids and contacts between hydrophobic and polar residues [40] which motivated the relation $2u_{HP} > u_{PP} + u_{HH}$ [4]. In the following, we call this variant the *MHP model* (mixed HP model).

8.3.2 Exact Enumerations for Short HP Sequences

The most important advantage of lattice HP-type models compared with other, more complex protein models is that it allows for comprising analyses of conformation and sequence space. This is essential for systematic studies following two main strategies in understanding protein structure formation: *direct* and *inverse* folding. Direct folding is sequence-based, i.e., the amino acid sequence is given and the global free-energy minimum conformation(s) are sought. In the inverse folding problem, a target structure is given and the question is for how many sequences this structure is the global free-energy minimum conformation.

Since it is widely believed that for bioproteins the unique global free-energy minimum conformation under physiological conditions (i.e., the native fold) is identical with the conformation of lowest total (free) energy, it is assumed that qualitative folding-related properties of HP lattice protein sequences are comparable with realistic proteins if their ground state is nondegenerate. An HP sequence with a unique native fold is called *designing*. On the other hand, a target structure which is the native fold of one or more designing sequences is called a *designable conformation*.

In Table 8.1, we list for all chain lengths $N = 4, \dots, 19$ the total numbers S_N of relevant designing sequences [41] in the HP and the MHP model. These results were obtained by exhaustive exact enumerations of the complete conformation and sequence spaces of chains with up to 19 monomers on the sc lattice [14]. Note that there are for a 19-mer more than 5×10^5 HP sequences and about 2×10^{12} self-avoiding conformations on the sc lattice, which in total allows naively more than 10^{18} possible combinations. In order to achieve this, an efficient parallel implementation based on contact sets [12, 42] together with symmetry considerations had to be used [15]. As already mentioned, the number of designing sequences is rather small in the standard HP model, whereas the additional *HP* attraction in the MHP model dissolves degeneracies which consequently entails a noticeably larger number of sequences with a unique ground-state conformation.

In Table 8.2, we list for both models the number of *different* native conformations D_N on the sc lattice. Interestingly, this number is usually much smaller than the number of designing sequences in Table 8.1, i.e., several designing sequences share the same ground-state conformation. The number of designing sequences that fold into a certain given target conformation $\mathbf{X}^{(0)}$

Table 8.1. Number of designing sequences S_N (only relevant sequences [41]) in the HP and MHP model on the simple cubic lattice

N	4	5	6	7	8	9	10	11	12	13	14	15	16	17	18	19
S_N^{HP}	3	0	0	0	2	0	0	0	2	0	1	1	1	8	29	47
S_N^{MHP}	7	0	0	6	13	0	11	8	124	14	66	97	486	2196	9491	4885

Table 8.2. Number of designable conformations D_N (without conformations trivially symmetric by translations, rotations, and reflections) in the HP and MHP model on the simple cubic lattice

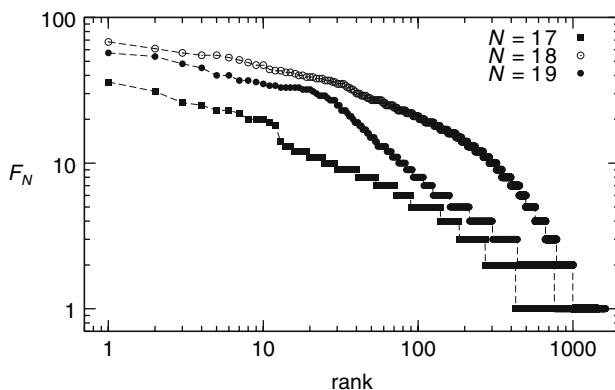
N	4	5	6	7	8	9	10	11	12	13	14	15	16	17	18	19
D_N^{HP}	1	0	0	0	2	0	0	0	2	0	1	1	1	8	28	42
D_N^{MHP}	1	0	0	2	2	0	5	6	30	8	31	58	258	708	1447	1623

(or conformations being trivially symmetric to this by translations, rotations, and reflections) is called *designability* [43]:

$$F_N(\mathbf{X}^{(0)}) = \sum_{\sigma \in \mathbf{S}_N} \Delta(\mathbf{X}_{\text{gs}}(\sigma) - \mathbf{X}^{(0)}) , \quad (8.4)$$

where $\mathbf{X}_{\text{gs}}(\sigma)$ is the native (ground-state) conformation of a designing sequence σ in the set of all designing sequences \mathbf{S}_N of length N . The function $\Delta(\mathbf{Z})$ is the generalization of (8.2) to $3N$ -dimensional vectors. It is unity for $\mathbf{Z} = \mathbf{0}$ and zero otherwise.

The designability is plotted in Fig. 8.1 for all native conformations that HP proteins with $N = 17, 18$, and 19 monomers can form in the MHP model. In this figure, the abscissa is the rank of the conformations, ordered according to their designability. The conformation with the lowest rank is therefore the most designable structure, and we see that most of the designing sequences fold into a few number of highly designable conformations, while only a small number of designing sequences possesses a native conformation with low designability (note that the plot is logarithmic). Similar results were found, for example in [44], where the designability of compact conformations on cuboid

**Fig. 8.1.** Designability F_N of native conformations in the MHP model for $N = 17, 18$, and 19 . The abscissa is the rank obtained by ordering all designable conformations according to their designability

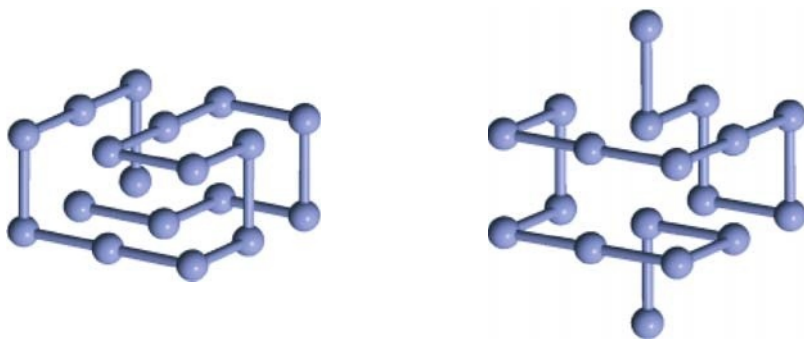


Fig. 8.2. Structure ($N = 18$) with the highest designability of all native conformations (*left*) and most compact structure with minimal radius of gyration (*right*)

lattices was investigated in detail. The *left picture* in Fig. 8.2 shows the conformation with the lowest rank (or highest designability) with $N = 18$ monomers. Note that this is not the most compact structure, i.e., the conformation with minimal gyration radius, which is also shown for $N = 18$ in Fig. 8.2 (*right*).

8.3.3 Chain-Growth Methods for Long HP Sequences

Combined exact enumeration studies of conformation *and* sequence space for lattice peptides noticeably longer than 19 monomers are currently computationally out of reach which is due to the exponential growth of the state space. Therefore, for longer sequences, primarily the direct folding problem is studied using computer simulation methods: Low-lying energetic conformations and thermodynamic properties governing the folding kinetics are identified and analyzed for a given HP sequence.

Computer simulations of lattice peptides, which are modeled as self-avoiding walks on the underlying lattice, are demanding. The reason is that the native fold, i.e., the ground-state or lowest-energy conformation, plays an essential role in protein science and that it is, in the discrete lattice representation, non- or low-degenerate. Monte Carlo simulations with move sets consisting of semilocal conformational updates such as end flips, corner flips, and “crank shafts” [23, 24, 25, 26], as well as nonlocal pivot updates [45], are inefficient in sampling the dominating dense conformations in the low-temperature region. It turned out that a different method, Rosenbluth chain growth [28] combined with a “Go with the winners” strategy [29], is much more efficient in sampling highly dense conformations.

Pruned-Enriched Rosenbluth Chain-Growth Method

In naive chain-growth methods based on simple sampling, a polymer grows by attaching the n th monomer at a randomly chosen nearest-neighbor site of the $(n - 1)$ th monomer. The growth is stopped, if the total length N of

the chain is reached or the randomly selected continuation of the chain is already occupied. In both cases, the next chain is started to grow from the first monomer. This simple chain growth is not yet very efficient, since the number of discarded chains grows exponentially with the chain length.

The performance can be improved with the Rosenbluth chain growth method [28], where first the free next neighbors of the $(n - 1)$ th monomer are determined and then the new monomer is placed to one of the unoccupied sites. Since the probability for the next monomer to be set varies with the number of free neighbors, this implies a bias given by

$$p_n = \left(\prod_{l=2}^n m_l \right)^{-1}, \quad (8.5)$$

where m_l is the number of free neighbors to place the l th monomer. The bias is corrected by assigning a Rosenbluth weight factor $W_n^R = p_n^{-1}$ to each chain that has been generated by this procedure. An illustrative example for the bias in the Rosenbluth chain-growth method is shown in Fig. 8.3. The two depicted linear chains are grown on a square lattice from either of the two ends (labeled by “1”). According to Rosenbluth sampling, the chain is continued if the number of free neighbor sites is $m \geq 1$. Since the number of free nearest-neighbor places varies, different probabilities for the continuation of the chain occur. Since both conformations are identical, the probability of creation should be the same. This requires the introduction of the correction weights. Although this biased growth is more efficient than simple sampling, this method suffers from attrition too: If all nearest neighbors are occupied, i.e., the chain was running into a “dead end” (attrition point), the complete chain has to be discarded and the growth process has to be started anew.

Combining the Rosenbluth chain growth method with population control, however, as is done in PERM (Pruned-Enriched Rosenbluth Method) [30, 31, 32], leads to a further considerable improvement of the efficiency by increasing the number of successfully generated chains. This method renders particularly useful for studying the θ point of polymers, since then the

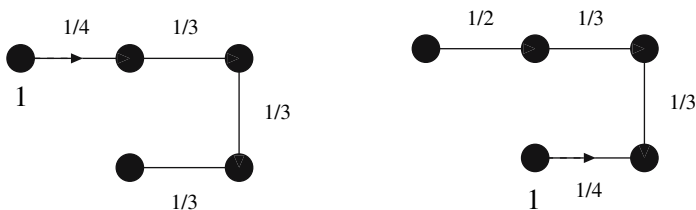


Fig. 8.3. Square lattice example for the bias implied by Rosenbluth sampling. Both walks shown are grown from the monomer labeled “1”. Although the shapes are identical, they are created with different probabilities (*left*: $p = 1/108$, *right*: $p = 1/72$)

Rosenbluth weights of the statistically relevant chains approximately cancel against their Boltzmann probability. The (a-thermal) Rosenbluth weight factor W_n^R is therefore replaced by

$$W_n^{\text{PERM}} = \prod_{l=2}^n m_l e^{-(E_l - E_{l-1})/k_B T}, \quad 2 \leq n \leq N \quad (E_1 = 0, W_1^{\text{PERM}} = 1), \quad (8.6)$$

where T is the temperature and E_l is the energy of the partial chain $\mathbf{X}_l = (\mathbf{x}_1, \dots, \mathbf{x}_l)$ created with Rosenbluth chain growth. In PERM, population control works as follows. If a chain has reached length n , its weight W_n^{PERM} is calculated and compared with suitably chosen upper and lower threshold values, $W_n^>$ and $W_n^<$, respectively. For $W_n^{\text{PERM}} > W_n^>$, *identical* copies are created which then grow independently. The weight is equally divided among them. If $W_n^{\text{PERM}} < W_n^<$, the chain is pruned with some probability, say 1/2, and in case of survival, its weight is doubled. For a value of the weight lying between the thresholds, the chain is simply continued without enriching or pruning the sample. The upper and lower thresholds $W_n^>$ and $W_n^<$ are empirically parameterized. Although their values do not influence the validity of the method, a careful choice can drastically improve the efficiency of the method (the “worst” case is $W_n^> = \infty$ and $W_n^< = 0$, in which case PERM is simply identical with Rosenbluth sampling). An efficient way of parameterization is dynamical adaption of the values [30, 31, 32, 33, 34, 35] with respect to the actual number of generated chains c_n with length n and their estimated partition sum

$$Z_n = \frac{1}{c_1} \sum_t W_n^{\text{PERM}}(t), \quad (8.7)$$

where c_1 is the number of growth starts (also called “tours”) and t counts the generated conformations with n monomers. Useful choices of the threshold values are

$$W_n^> = C_1 Z_n \frac{c_n^2}{c_1^3}, \quad W_n^< = C_2 W_n^>, \quad (8.8)$$

where $C_1, C_2 \leq 1$ are constants. For the first tour, $W_n^> = \infty$ and $W_n^< = 0$, i.e., no pruning and enriching.

In the recently developed new variants nPERMss and nPERMis [33], the number of copies is not constant and depends on the ratio of the weight W_n^{PERM} compared to the upper threshold value $W_n^>$, and the copies are necessarily chosen to be different. The method of selecting the copies is based on simple sampling (ss) in nPERMss and a kind of importance sampling (is) in nPERMis. This proves quite useful in producing highly compact polymers, and therefore these new methods are very powerful in determining lowest-energy states of lattice proteins.

Results of a simple application of PERM to self-avoiding walks on a simple-cubic lattice are plotted in Fig. 8.4, where the scaling behavior $\langle R_{\text{gyr,ee}}^2 \rangle$

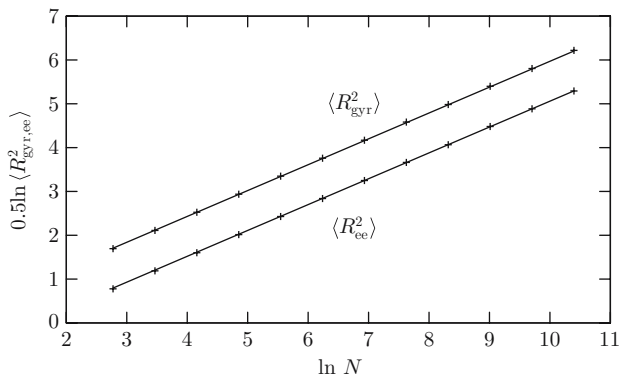


Fig. 8.4. Scaling of mean square radius of gyration $\langle R_{\text{gyr}}^2 \rangle$ and end-to-end distance $\langle R_{\text{ee}}^2 \rangle$ for self-avoiding walks. Data points refer to results from PERM runs for $N = 16, 32, \dots, 32768$ steps. Lines manifest the respective power-law behaviors

$\sim N^{2\nu}$ of the mean square radius of gyration $\langle R_{\text{gyr}}^2 \rangle$ and end-to-end distance $\langle R_{\text{ee}}^2 \rangle$ with the number of steps N is shown. Data were obtained for chains of $N = 16, 32, \dots, 32768$ steps. For both quantities, the slope of the lines in the logarithmic plot is $\nu = 0.59$, which is close to the precisely known critical exponent $\nu = 0.588 \dots$ [46].

Multicanonical Chain-Growth Algorithm

The efficiency of PERM depends on the simulation temperature. Therefore, a precise estimation of the density of states requires separate simulations at different temperatures. Then, the density of states can be constructed by means of the multiple-histogram reweighting method [47]. Although being a powerful method, it is difficult to keep track of the statistical errors involved in the individual histograms obtained in the simulations.

An alternative approach, in which the density of states $g(E)$ is obtained within a *single* simulation without the necessity of a subsequent multi-histogram reweighting, is the combination of PERM with multicanonical sampling, the so-called multicanonical chain-growth method [34, 35].

The general idea of multicanonical sampling [48, 49] is to simulate the thermodynamic behavior of the system in a generalized (multicanonical) ensemble, where the energetic macrostates are distributed uniformly, $p_{\text{muca}}(E) = \text{const}$, which implies the introduction of multicanonical weight factors $W_{\text{muca}}(E)$. In typical multicanonical Monte Carlo simulations, the dynamics is therefore governed by a random walk in energy space. Hence, the sampling of entropically rare events is, in principle, as frequent as the sampling of highly degenerate energetic states. The acceptance probability for a new system configuration \mathbf{X}' with energy E' is $w_{\text{muca}}(\mathbf{X} \rightarrow \mathbf{X}') = \min\{1, \exp[S(E(\mathbf{X}')) - S(E(\mathbf{X}))]\}$, where $S(E(\mathbf{X})) = -\ln W_{\text{muca}}(E(\mathbf{X}))$ is the microcanonical entropy. The canonical

energy distribution $p_{\text{can}}(E) \sim g(E) \exp(-E/k_{\text{B}}T)$ for a given temperature T is related with the multicanonical histogram via

$$p_{\text{can}}(E) \sim W_{\text{muca}}^{-1}(E) p_{\text{muca}}(E) e^{-E/k_{\text{B}}T}, \quad (8.9)$$

which implies that the multicanonical weights are proportional to the inverse density of states, $W_{\text{muca}}(E) \sim g^{-1}(E)$. Since $g(E)$ is unknown, the determination of the weights $W_{\text{muca}}(E)$ is not straightforward and must be performed in the first stage of the simulation in an iterative procedure [49].

The multicanonical extension of PERM requires two main changes compared to standard PERM. Firstly, the expression (8.6) for the weight factor is replaced by

$$W_n^{\text{MPERM}}(E_n) = W_{\text{muca},n}(E_n) \prod_{l=2}^n m_l, \quad W_{\text{muca},1} = 1, \quad (8.10)$$

where, according to multicanonical sampling, the multicanonical weight of the chain of current length n is related to the appropriate inverse density of states, $W_{\text{muca},n}(E) \sim g_n^{-1}(E)$. Note that the possibility to rewrite (8.10) in the recursive factorized form

$$W_n^{\text{MPERM}}(E_n) = \prod_{l=2}^n m_l \frac{W_{\text{muca},l}(E_l)}{W_{\text{muca},l-1}(E_{l-1})} = W_{n-1}^{\text{MPERM}} m_n \frac{W_{\text{muca},n}(E_n)}{W_{\text{muca},n-1}(E_{n-1})} \quad (8.11)$$

is mainly responsible for the efficiency of this method as it ensures that rare-event (flat-histogram) sampling is performed in *all* intermediate steps of the growth process. This means that for a chain of length N all energy histograms are “flat”, $H_n(E) \approx \text{const.}$ with $n \leq N$. The pruning-enriching scheme of PERM is completely carried over and remains unchanged, with the exception that the thresholds (8.8) are reexpressed as

$$W_n^> = C_1 Z_n^{\text{MPERM}} \frac{c_n^2}{c_1^3}, \quad W_n^< = C_2 W_n^>, \quad (8.12)$$

i.e., in terms of the partition sum of the multicanonical ensemble, $Z_n^{\text{MPERM}} = (1/c_1) \sum_t W_n^{\text{MPERM}}(t)$.

The second difference compared with the original PERM is the estimation of the multicanonical weights, as the densities of states $g_n(E)$, $n \leq N$, are unknown in the beginning of the simulation. Therefore, the multicanonical weight factors $W_{\text{muca},n}(E)$ must be determined iteratively for all stages $n \leq N$ of the growth process [35]. The initial choice for the multicanonical weights is typically $W_{\text{muca},n}^{(0)}(E) = 1 \forall n, E$, making the zeroth recursion a pure PERM run at infinite temperature. The energy histograms are initialized with $H_n^{(0)}(E) = 0$. Performing the multicanonical chain growth according to the

method described above, the histograms are accumulated by summing up the weights (8.11) of successively generated chains:

$$H_n^{(0)}(E) = \frac{1}{c_1} \sum_t W_{n,t}^{\text{MPERM}} \delta_{E_t E} , \quad (8.13)$$

where t labels the chain reaching length n in the growth process. Since this histogram is a first estimate for the density of states, the multicanonical weights for the following iteration are set to $W_{\text{muca},n}^{(1)}(E) = 1/H_n^{(0)}(E)$. Before starting the new recursion, Z_n^{MPERM} , c_n , $W_n^<$ are reset to zero, and $W_n^>$ to infinity (i.e., to the upper limit of the data type used to store this quantity). The iterative procedure is repeated until the weights $W_{\text{muca},n}^{(i)}(E) = W_{\text{muca},n}^{(i-1)}(E)/H_n^{(i-1)}(E)$ are stabilized. In a long final production run $i = I$, the densities of states are then determined from

$$g_n^{(I)}(E) = \frac{H_n^{(I)}(E)}{W_{\text{muca},n}^{(I)}(E)} , \quad n \leq N . \quad (8.14)$$

For practical applications of this algorithm, in particular for studies of heteropolymers, it is more favorable to replace the original pruning-enrichment core, i.e., PERM [30], by the modern, improved variants nPERMss or nPERMis [33]. The combination of this more efficient chain-growth strategy with multicanonical sampling is straightforward. The details are explained in [34, 35]. In Fig. 8.5, estimates for $g^{(i)}(E)$ after the iterations $i = 0, 1, 6$, and 9 are shown for an exemplified heteropolymer with 42 monomers, whose thermodynamic properties will be discussed in more detail in Sect. 8.3.4. The zeroth

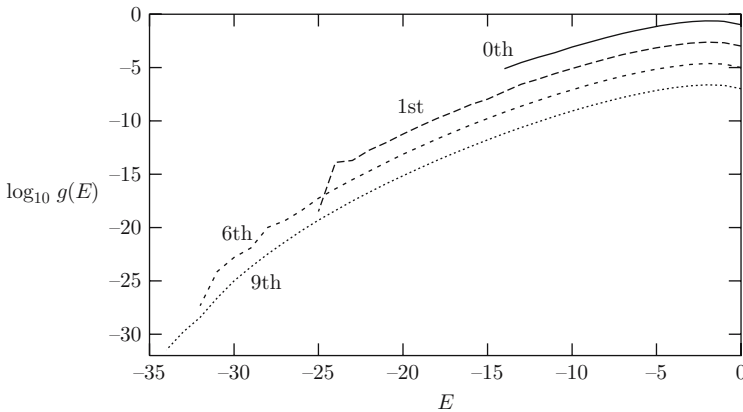


Fig. 8.5. Estimates for the density of states $g^{(i)}(E)$ for an exemplified heteropolymer with 42 monomers after several recursion levels. Since the curves would fall on top of each other, we have added, for better distinction, a suitable offset to the curves of the 1st, 6th, and 9th run. The estimate of the 0th run is normalized to unity

run is a pure PERM estimate with a reliable precision over 5 orders of magnitude. As the simulations were effectively performed in the purely entropic regime at infinite temperature (i.e., $\beta = 0$), low-energy states are rarely sampled. In this case, chain growth is governed only by the weights (8.6) which are only products of free nearest-neighbor sites and therefore identical with the Rosenbluth weights for self-avoiding walks. The model-dependent energetic influence on the growth is thus irrelevant. The efficiency is improved in the successive recursions, where the multicanonical weights (8.11) are gradually refined and allow for a sampling of larger regions of the energy space. After only ten recursions, the estimate for $g(E)$ covers the whole accessible energy space (including the ground state) and ranges over 25 orders of magnitude.

It is worth noticing that the obtained density of states is *absolute*, i.e., estimates for the degeneracies of energetic states, in particular for the important ground state, can directly be read off. Furthermore, the partition function is also absolutely estimated via $Z = \sum_E g(E) \exp(-E/k_B T)$. The reason is that chain-growth methods perform a “biased” simple sampling instead of importance sampling as is used in most Markov chain Monte Carlo methods [50]. With Markov chain importance sampling, it is usually not possible to obtain an absolute estimate for $g(E)$.

The probability for energetic states in a canonical ensemble at temperature T is obtained from the density of states by Boltzmann reweighting via $p_{\text{can}}(T) = g(E) \exp(-E/k_B T)/Z$. Thus, statistical expectation values of energetic observables $O(E)$ are simply given by $\langle O \rangle = \sum_E O(E) p_{\text{can}}(E)$. Thermal fluctuations of these quantities, e.g., defined by $d\langle O \rangle/dT = (\langle O^2 \rangle - \langle O \rangle^2)/k_B T^2$, are of particular interest for identifying temperature regions of thermodynamic activity. A very convenient measure for quantifying the cooperative behavior of a complex system is, e.g., the specific heat $C_V = (\langle E^2 \rangle - \langle E \rangle^2)/k_B T^2$.

Decoupling Energy Scales: An Instructive Example

For systems, where different energy scales decouple, the density of states $g(E)$ as a distribution of states with given *total* energy E is not the most useful quantity. As an important example, we consider the adsorption of a polymer to a substrate. In simple lattice models, only the number of intrinsic nearest-neighbor contacts between nonadjacent monomers, n_m , and the number of nearest-neighbor contacts of the polymer with the substrate, n_s , are counted. For the discussion of conformational transitions in the adsorption process later on, it is quite useful to rate intrinsic and binding forces against each other and therefore it is useful to introduce different energy scales ε_m and ε_s corresponding to the contact numbers n_m and n_s , respectively. A minimalistic model could then, for example, be defined by [51]

$$E(n_m, n_s) = -\varepsilon_m n_m - \varepsilon_s n_s \equiv -\varepsilon_0 (s n_m + n_s), \quad (8.15)$$

where the ratio $s = \varepsilon_m/\varepsilon_s$ can be considered as a kind of reciprocal solvent parameter (the larger s , the worse the quality of the solvent). The overall energy scale is simply $\varepsilon_0 \equiv \varepsilon_s$. Since the total energy E of the system depends on s , it would be necessary to fix its value in the previously described multicanonical chain-growth variant. Instead of determining the density of states $g(E)$, it would be more favorable to calculate the *contact density* $g(n_m, n_s)$ which is independent of s . Knowing the contact density, the canonical probability for a system conformation with n_m monomer–monomer and n_s monomer–substrate contacts is given by $p_{T,s}(n_m, n_s) = g(n_m, n_s) \exp[-E(n_m, n_s)/k_B T]/Z_{T,s}$, where temperature T and solubility s are considered as fixed parameters. The statistical average of a quantity $O(n_m, n_s)$ is then obtained as $\langle O(n_m, n_s) \rangle = \sum_{n_m, n_s} O(n_m, n_s) p_{T,s}(n_m, n_s)$. For the discussion of the conformational phase diagram of the hybrid polymer–substrate system in solvent, it is useful to consider the dependence of fluctuations on temperature *and* solubility. As an example, the specific heat can be expressed as

$$C_V(T, s) = k_B \left(\frac{\varepsilon_0}{k_B T} \right)^2 (s \ 1) \begin{pmatrix} \langle n_s^2 \rangle_c & \langle n_s n_m \rangle_c \\ \langle n_s n_m \rangle_c & \langle n_m^2 \rangle_c \end{pmatrix} \begin{pmatrix} s \\ 1 \end{pmatrix}, \quad (8.16)$$

where $\langle xy \rangle_c = \langle xy \rangle - \langle x \rangle \langle y \rangle$ ($x, y = n_m, n_s$) are the variances and covariances of the contact numbers. Note that the knowledge of $g(n_m, n_s)$ enables reweighting of the specific heat to any pair of parameters T and s .

Contact Density Chain-Growth Method

The determination of the contact density $g(n_m, n_s)$ follows similar lines as the multicanonical chain-growth method for the estimation of the density of states. In fact, the only change in the algorithm described in the previous section is that the weights $W_n^{\text{MPERM}}(E_n)$ defined in (8.11) are replaced by

$$W_n^{\text{CDPERM}}(n_m^{(n)}, n_s^{(n)}) = \prod_{l=2}^n m_l \frac{W_{\text{cd},l}(n_m^{(l)}, n_s^{(l)})}{W_{\text{cd},l-1}(n_m^{(l-1)}, n_s^{(l-1)})}, \quad (8.17)$$

where the multi-contact weights $W_{\text{cd},l}(n_m^{(l)}, n_s^{(l)}) \sim 1/g(n_m^{(l)}, n_s^{(l)})$ have to be determined again recursively.

The extension of this method incorporating more than two system parameters is straightforward, but the efficiency of flattening the high-dimensional histograms at all levels of the growth process decreases, whereas the storage requirements for these fields rapidly increase.

8.3.4 Bulk Behavior of HP Lattice Proteins

Before embarking into the discussion of hybrid peptide–substrate systems, we investigate first the bulk behavior of HP peptides. In the folding process from a random-coil conformation toward the native fold, the protein experiences

in many cases conformational transitions. These transitions typically require passing or circumventing of barriers in the free-energy landscape, which slows down the folding dynamics. Similar to thermodynamic phase transitions, conformational transitions can be identified by noticeable changes in the behavior of fluctuating quantities. Peaks and “shoulders” in specific-heat curves are, for example, typical signals for cooperative activity, because in the vicinity of the peak temperatures entropic changes separate qualitatively different classes of conformations (e.g., random coils and globular shapes). Since peptides are always of finite length due to their well-defined amino acid sequence, conformational transitions are not phase transitions in the strict thermodynamic sense. In consequence, fluctuations of different thermodynamic quantities typically do not exhibit the same peak structure, i.e., there is no “data collapse” which would allow the definition of a uniform transition temperature, where the phases are uniquely separated. Since for peptides different fluctuating quantities predict different transition temperatures, it is only possible to identify a temperature interval of conformational activity. This makes a precise quantitative analysis and a qualitative classification of such transitions difficult [34, 35].

In the following, we discuss ground-state properties and thermodynamics for exemplified HP sequences. These results were obtained by employing the aforementioned multicanonical chain-growth method [34, 35] for the standard version of the HP model [9]. An interesting example is the 42-monomer HP sequence representing the parallel β -helix protein *pectate lyase C* [52], which reads $\text{PH}_2\text{PHPH}_2\text{PHPHP}_2\text{H}_3\text{PHPH}_2\text{PHPH}_3\text{P}_2\text{HHPHPH}_2\text{PHPH}_2\text{P}$ [16]. Although it is not believed that specific protein properties such as the folding behavior and thermodynamics are conserved in a one-to-one transcription of an amino acid sequence into the hydrophobic–polar two-letter code, this example shows surprising coincidences of the real protein and the model, as the (low-degenerate) ground-state conformations in the HP model also exhibit two parallel helical segments. More interesting is, however, that the ground-state degeneracy is only $g_0 = 4$ without trivial rotational symmetries [16]. With multicanonical chain-growth simulations [34], the ground-state degeneracy was precisely estimated as $g_0 = 3.9 \pm 0.4$ [35]. In this simulation, ten recursions were performed and in the production run, about 5×10^7 chains entered into statistics.

The low ground-state degeneracy is indeed remarkable, as it is extremely difficult to find *designing* sequences (which possess a nondegenerate ground state) with the standard HP model (cf. Table S.1), in particular for comparatively long sequences. For a statistical analysis of the folding behavior of this 42-mer, the density of states, as has already been shown in Fig. S.5, as well as the thermodynamic quantities and their fluctuations were calculated [34]. In Fig. S.6, the specific heat C_V and fluctuations of the structural quantities radius of gyration R_{gyr} and end-to-end distance R_{ee} are plotted as functions of temperature. Two temperature regions of conformational activity (shaded in

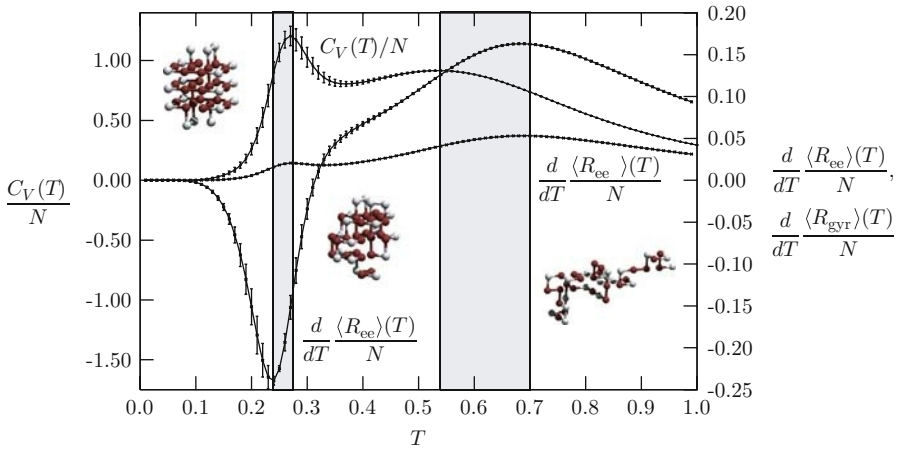


Fig. 8.6. Specific heat C_V and respective fluctuations of gyration radius and end-to-end distance, $d\langle R_{\text{gyr}}\rangle/dT$ and $d\langle R_{\text{ee}}\rangle/dT$, as functions of temperature for the 42-mer

gray), where the curves of the fluctuating quantities exhibit extremal points, can clearly be separated.

For high temperatures, random conformations are favored. In consequence, in the corresponding, rather entropy-dominated ensemble, the high-degenerate high-energy structures govern the thermodynamic behavior of the macrostates. A typical representative is shown as an inset in the high-temperature pseudophase in Fig. 8.6. Annealing the system (or, equivalently, decreasing the solvent quality), the heteropolymer experiences a conformational transition toward globular macrostates. A characteristic feature of these intermediary “molten” globules is the compactness of the dominating conformations as expressed by a small gyration radius. Nonetheless, the conformations do not exhibit a noticeable internal long-range symmetry and behave rather like a fluid. Local conformational changes are not hindered by strong free-energy barriers. The situation changes by entering the low-temperature (or poor-solvent) conformational phase. In this region, energy dominates over entropy and the effectively attractive hydrophobic force favors the formation of a maximally compact core of hydrophobic monomers. Polar residues are expelled to the surface of the globule and form a shell that screens the core from the (fictitious) aqueous environment. In Fig. 8.7, we have plotted canonical energy distributions $p_{\text{can}}(E)$ for several temperatures near the hydrophobic-core collapse transition. For temperatures above the transition region (which is between $T^{(1)} = 0.24$ and $T^{(2)} = 0.28$, cf. Fig. 8.6), globular conformations are more probable, whereas for smaller temperatures hydrophobic-core states dominate. From the two-peak structure of the distributions in the transition region, it can be concluded that this transition is first-order-like, i.e., both types of macrostates coexist in this temperature region.

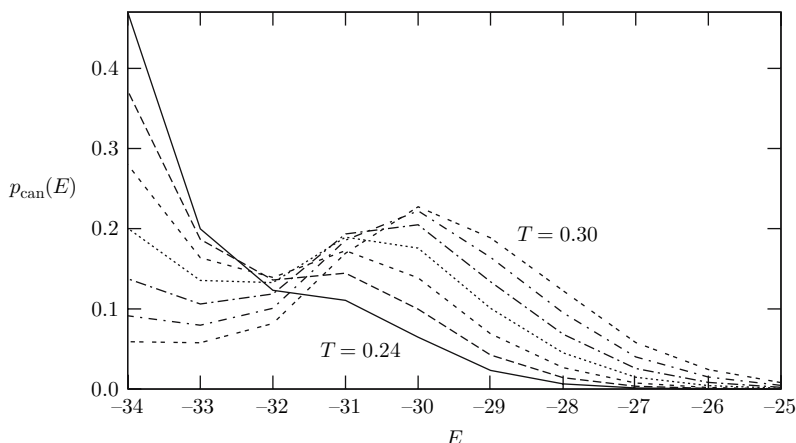


Fig. 8.7. Canonical energy distributions of the 42-mer for temperatures $T = 0.24, 0.25, \dots, 0.30$ close to the hydrophobic-core collapse transition

The existence of the hydrophobic-core collapse renders the folding behavior of a heteropolymer different from crystallization or amorphous transitions of homopolymers [53, 54]. The reason is the disorder induced by the sequence of different monomer types. The hydrophobic-core formation is the main co-operative conformational transition which accompanies the tertiary folding process of a single-domain protein.

A very important aspect in the discussion of ground-state properties and conformational transitions toward the native fold is the influence of the heteropolymer sequence. For this purpose, we analyze ten designed sequences with 48 monomers, listed in Table 8.3, as given in [16]. The ratio between the numbers of hydrophobic and polar residues is one half for these HP proteins, i.e., the hydrophobicity is $n_H = 24$. The minimum energies we found from multicanonical chain-growth simulations [35] coincide with the values given in [16, 33]. Also listed in Table 8.3 are the estimates for the degeneracies g_0 of the respective ground-state energies. For comparison, previously given lower bounds $g_{\text{CHCC}}^<$ [37] are listed, which were obtained by means of the constraint-based hydrophobic core construction (CHCC) method [16]. Utilizing the idea of a highly compact hydrophobic core in the native fold, the hydrophobic monomers are in this method arranged in frames of maximal compactness. The number of the associated so-called Hamiltonian walks that connect the monomers, respecting the nonchangeable HP sequence, gives a lower bound for the degeneracy of the ground state. If, due to the sequence, a matching walk cannot be constructed, the compactness of the frame is relaxed and the search starts anew. The exact ground-state degeneracy would be obtained by scanning all frames and searching for conformations with the ground-state energy. Since the method is of exact enumeration type, the efforts of determining the precise ground-state degeneracy are enormous and, therefore, the

main power of this method lies in the identification of native folds and the possibility to give a lower bound for its degeneracy.

For the 48-mers, the g_0 values obtained within the multicanonical chain-growth simulation lie indeed above these lower bounds or include it within the range of statistical errors. Notice that for the sequences 48.1, 48.5, and 48.8, the estimates for the ground-state degeneracy are much higher than the bounds $g_{\text{CHCC}}^<$. In these cases, the smallest frame containing the entire hydrophobic core is rather large (cube containing $4 \times 3 \times 3 = 36$ monomers with surface area $A = 32$ [bond length]²) such that enumeration of this frame is cumbersome. For 48.5 and 48.8, we further found ground-state conformations lying in less compact frames (48.5: $A = 32, 40, 42, 48, 52, 54$ [bond length]², 48.8: $A = 32, 40, 42$ [bond length]²), and those conformations would require still more effort to be identified with the CHCC algorithm, which was designed to locate global energy minima and therefore starts the search with the most compact hydrophobic frames. The ground-state energies of these examples are rather high ($E_{\min} = -31$ for 48.8 and $E_{\min} = -32$ for 48.1 and 48.5), and therefore, a higher degeneracy seems to be natural. This is, however, only true if there does not exist a conformational barrier that separates the compact H-core low-energy states from the general compact globules. Comparing the ground-state degeneracies and the low-temperature behavior of the specific heats for the sequences 48.1, 48.5, 48.6, and 48.7 (all of them having global energy minima with $E_{\min} = -32$) as shown in Fig. 8.8, we observe that 48.6 and 48.7 with rather low ground-state degeneracy actually possess a pronounced low-temperature peak in the specific heat, while the higher-degenerate proteins 48.1 and 48.5 only show up a weak indication of a structural transition at low temperatures. The HP proteins 48.2, 48.3, and 48.9, which have the lowest minimum energy $E_{\min} = -34$ among the examples in Table 8.3, have also the lowest ground-state degeneracies. These three candidates seem indeed to exhibit a rather strong ground-state/globule transition, as can be read off from the associated specific heats in Fig. 8.8.

In Fig. 8.8, also the mean end-to-end distances and mean radii of gyration are plotted as functions of temperature. Both quantities usually serve to interpret the conformational compactness of polymers. For HP proteins, the end-to-end distance is strongly influenced, however, by the types of monomers attached to the ends of the chain. It is easily seen from the figures that the 48-mers with sequences starting and ending with a hydrophobic residue (48.1, 48.2, and 48.6) have a smaller mean end-to-end distance at low temperatures than the other examples from Table 8.3. The reason is that the ends can form hydrophobic contacts and therefore a reduction of the energy can be achieved. Thus, in these cases, contacts between ends are usually favorable and the mean end-to-end distance is close to the mean radius of gyration. Interestingly, there exists indeed a crossover region, where $\langle R_{\text{ee}} \rangle < \langle R_{\text{gyr}} \rangle$. Comparing with the behavior of the specific heat, this interval is close to the region, where the phase dominated by low-energy states crosses over to the globule-favored phase. The hydrophobic contact between the ends is strong

Table 8.3. Ground-state energies E_{\min} and degeneracies g_0 as estimated with the multicanonical chain-growth method [34, 35] for ten HP sequences with 48 monomers

No.	Sequence	E_{\min}	$g_0 (\times 10^3)$	$g_{\text{CHCC}}^< (\times 10^3)$
48.1	HPH ₂ P ₂ H ₄ PH ₃ P ₂ H ₂ P ₂ HPH ₃ PHHPH ₂ P ₂ H ₂ P ₃ HP ₈ H ₂	-32	5226 ± 812	1500
48.2	H ₄ PH ₂ PH ₅ P ₂ HP ₂ H ₂ P ₂ HP ₆ HP ₂ HP ₃ HP ₂ H ₂ P ₂ H ₃ PH	-34	17 ± 8	14
48.3	PHPH ₂ PH ₆ P ₂ HPHP ₂ HPH ₂ PHHPH ₃ HP ₂ H ₂ P ₂ H ₂ P ₂ HPHP ₂ HP	-34	6.6 ± 2.8	5.0
48.4	PHPH ₂ P ₂ HPH ₃ P ₂ H ₂ PH ₂ P ₂ H ₅ P ₂ HPH ₂ PHHPH ₄ HP ₂ HPHP	-33	60 ± 13	62
48.5	P ₂ HP ₃ HPH ₄ P ₂ H ₄ PH ₂ PH ₃ P ₂ HPHPHP ₂ HP ₆ H ₂ PH ₂ PH	-32	1200 ± 332	54
48.6	H ₃ P ₃ H ₂ PHPH ₂ PH ₂ PH ₂ PH ₇ HPHP ₂ HP ₃ HP ₂ H ₆ PH	-32	96 ± 19	52
48.7	PHP ₄ HPH ₃ PHPH ₄ PH ₂ PH ₂ P ₃ HPHP ₃ H ₃ P ₂ H ₂ P ₂ H ₂ P ₃ H	-32	58 ± 21	59
48.8	PH ₂ PH ₃ PH ₄ P ₂ H ₃ P ₆ HPH ₂ P ₂ H ₂ PHP ₃ H ₂ PHHPH ₂ P ₃	-31	22201 ± 6594	306
48.9	PHHPH ₄ HPHPHP ₂ HPH ₆ P ₃ H ₃ PHP ₂ HPH ₂ P ₂ HPH ₃ P ₄ H	-34	1.4 ± 0.5	1.0
48.10	PH ₂ P ₆ H ₂ P ₃ PHP ₂ HPH ₂ P ₂ HP ₂ HP ₂ H ₂ P ₂ H ₇ P ₂ H ₂	-33	187 ± 87	188

For comparison, we have also quoted the lower bounds on native degeneracies $g_{\text{CHCC}}^<$ obtained by means of the CHCC (constraint-based hydrophobic core construction) method [16] as given in [37]. In both cases, the constant factor 48 from rotational and reflection symmetries of conformations spreading into all three spatial directions was divided out

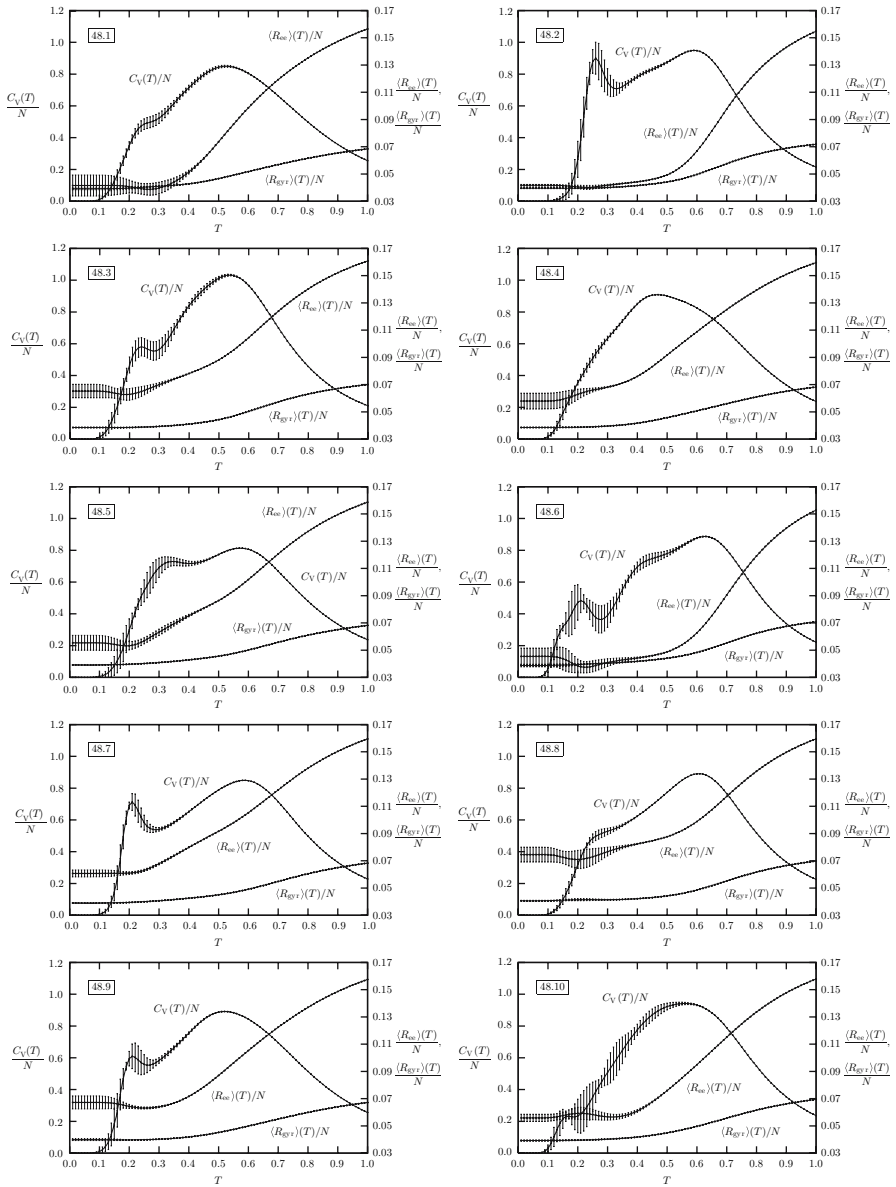


Fig. 8.8. Specific heat, mean radius of gyration, and mean end-to-end distance for the ten 48-mers listed in Table [8.3](#) [35](#)

enough to resist the thermal fluctuations in that temperature interval. The reason is that, once such a hydrophobic contact between the ends is established, usually other in-chain hydrophobic monomers are attracted and form a hydrophobic core surrounding the end-to-end contact. Thus, before the contact between the ends is broken, an increase of the temperature first leads to a melting of the surrounding contacts. The entropic freedom to form new conformations is large since the low-energy states are all relatively high degenerate and do not possess symmetries requiring an appropriate amount of heat to be broken. For sequences possessing mixed or purely polar ends, the mean end-to-end distance and mean radius of gyration differ much stronger, as there is no energetic reason why the ends occupy nearest-neighbor positions.

In conclusion, we see that for longer chains the strength of the low-temperature transition not only depends on low ground-state degeneracies as it does for short chains [34]. Rather, the influence of the higher-excited states cannot be neglected. A striking example is sequence 48.4 with rather low ground-state degeneracy, but only weak signals for a low-temperature transition.

8.3.5 Specificity of Protein Adsorption to Selective Solid Substrates

In this section, we discuss results of a simple lattice model similar to (8.15) for analyzing the conformational behavior of HP proteins in adsorption processes to different, specific solid substrates. The objective is the determination of a pseudophase diagram, which allows for the classification of conformational subphases in dependence of the external parameters temperature and solubility of the surrounding (implicit) solvent.

The recent developments in single molecule experiments at the nanometer scale, e.g., by means of atomic force microscopy (AFM) [55] and optical tweezers [56], allow now for a more detailed exploration of structural properties of polymers in the vicinity of adsorbing substrates [57]. The possibility to perform such studies is of essential biological and technological significance. From the biological point of view, the understanding of the binding and docking mechanisms of proteins at cell membranes is important for the reconstruction of biological cell processes. Similarly, specificity of peptides and binding affinity to selected substrates could be of great importance for future electronic nanoscale circuits and pattern recognition nanosensory devices [58]. The study of hybrid interface models has considerable applications for a broad variety of problems, e.g., understanding the mechanisms of protein–ligand binding [59], prewetting and layering transitions in polymer solutions as well as dewetting of polymer films [60, 61], molecular pattern recognition [62], electrophoretic polymer deposition and growth [63]. Recently, the influence of adhesion and steric hindrance for polymers grafted to a flat substrate [51, 64, 65, 66, 67, 68], conformational pseudophase transitions for nongrafted polymers and peptides in a cavity with attractive substrate [69, 70, 71, 72], the shape response to

pulling forces [73, 74] or external fields [75] were subject of computer simulations and analytical approaches of different models. The question how a flexible substrate, e.g., a cell membrane, bends as a reaction of a grafted polymer was, for example, addressed in [76]. Proteins exhibit a strong specificity as the affinity of peptides to adsorb at surfaces depends on the amino acid sequence, solvent properties, and substrate shape. This was experimentally and numerically studied, e.g., for peptide–metal [77, 78] and peptide–semiconductor [79, 80] interfaces. Binding/folding and docking properties of lattice heteropolymers at an adsorbing surface were also subject of numerical studies [81].

Lattice Model for Hybrid Peptide–Substrate Interfaces

For the study of hybrid peptide–substrate models, we use the HP transcription of the 103-residue protein *cytochrome c*, which was extensively studied in the past [33, 35, 38, 39]. The HP sequence contains 37 hydrophobic and 66 polar residues. A conformation with a highly compact hydrophobic-core, exhibiting 56 hydrophobic contacts, is shown in Fig. 8.9. This lattice peptide resides in a cavity with an attractive substrate (see Fig. 8.10). For regularization of the upper halfspace, an additional steric wall in a distance z_w is introduced. The value of z_w is chosen sufficiently large to keep the influence on the unbound heteropolymer small (in the actual example, $z_w = 200$ was used). In order to study the specificity of residue binding, we distinguish three substrates with different affinities to attract the peptide monomers: (a) the type-independent attractive, (b) the hydrophobic, and (c) the polar substrates. The number of corresponding nearest-neighbor contacts between monomers and substrate shall be denoted as n_s^{H+P} , n_s^H , and n_s^P , respectively. In analogy to the polymer–substrate model (8.15), we express the energy of the hybrid peptide–substrate system simply by

$$E_s(n_s, n_{HH}) = -\varepsilon_0(n_s + sn_{HH}) , \quad (8.18)$$

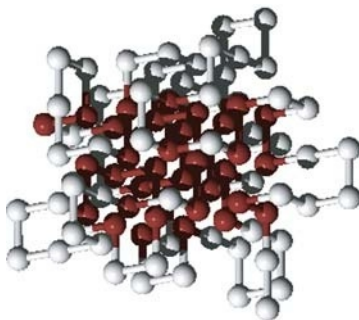


Fig. 8.9. Compact hydrophobic-core conformation of the 103-mer [35] used in the peptide adsorption study [71, 72]. Dark spheres correspond to hydrophobic monomers and light spheres mark polar residues

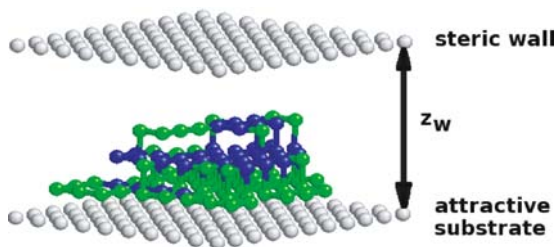


Fig. 8.10. Lattice model used in the peptide-substrate adsorption study

where $n_s = n_s^{H+P}$, n_s^P , or n_s^H depending on the substrate (we set $\varepsilon_0 = 1$ in the following). The solubility (or reciprocal solvent parameter) s is, as well as the temperature T , an external parameter. It controls the quality of the solvent (the larger the value of s , the worse the solvent). This model was investigated by means of the contact-density chain-growth algorithm (see Sect. 8.3.3), which allows a direct estimation of the degeneracy (or density) $g(n_s, n_{HH})$ of macrostates of the system with given contact numbers n_s and n_{HH} [71, 72]. In contrast to move set-based Metropolis Monte Carlo or conventional chain-growth methods which would require many separate simulations to obtain results for different parameter pairs (T, s) and which frequently suffer from slowing down in the low-temperature sector, the contact-density chain-growth method allows the computation of the *complete* contact density for each system within a *single* simulation run. Since the contact density is independent of temperature and solubility, energetic quantities such as specific heat (8.16) can easily be calculated for all values of T and s . Nonenergetic quantities require accumulated densities to be measured within the simulation, but this is also no problem.

Conformational Adsorption Behavior in Dependence of Temperature and Solubility

In Fig. 8.11(a)–(c), the color-coded profiles of the specific heats for the different substrates are shown (the brighter the larger the value of C_V). We interpret the ridges (for accentuation marked by white and gray lines) as the boundaries of the pseudophases. The gray lines indicate the main transition lines, while the white lines separate pseudophases that strongly depend on specific properties of the heteropolymer, such as its exact number and sequence of hydrophobic and polar monomers. With its degeneracy $g(n_s, n_{HH})$, we define the contact free energy as $F_{T,s}(n_s, n_{HH}) = E_s(n_s, n_{HH}) - T \ln g(n_s, n_{HH})$ and the probability for a macrostate with n_s substrate and n_{HH} hydrophobic contacts as $p_{T,s}(n_s, n_{HH}) \sim g(n_s, n_{HH}) \exp(-E_s/T)$. Assuming that the minimum of the free-energy landscape $F_{T,s}(n_s^{(0)}, n_{HH}^{(0)}) \rightarrow \min$ for given external parameters s and T is related to the class of macrostates with $n_s^{(0)}$ surface and $n_{HH}^{(0)}$ hydrophobic contacts, this class dominates the phase the system resides

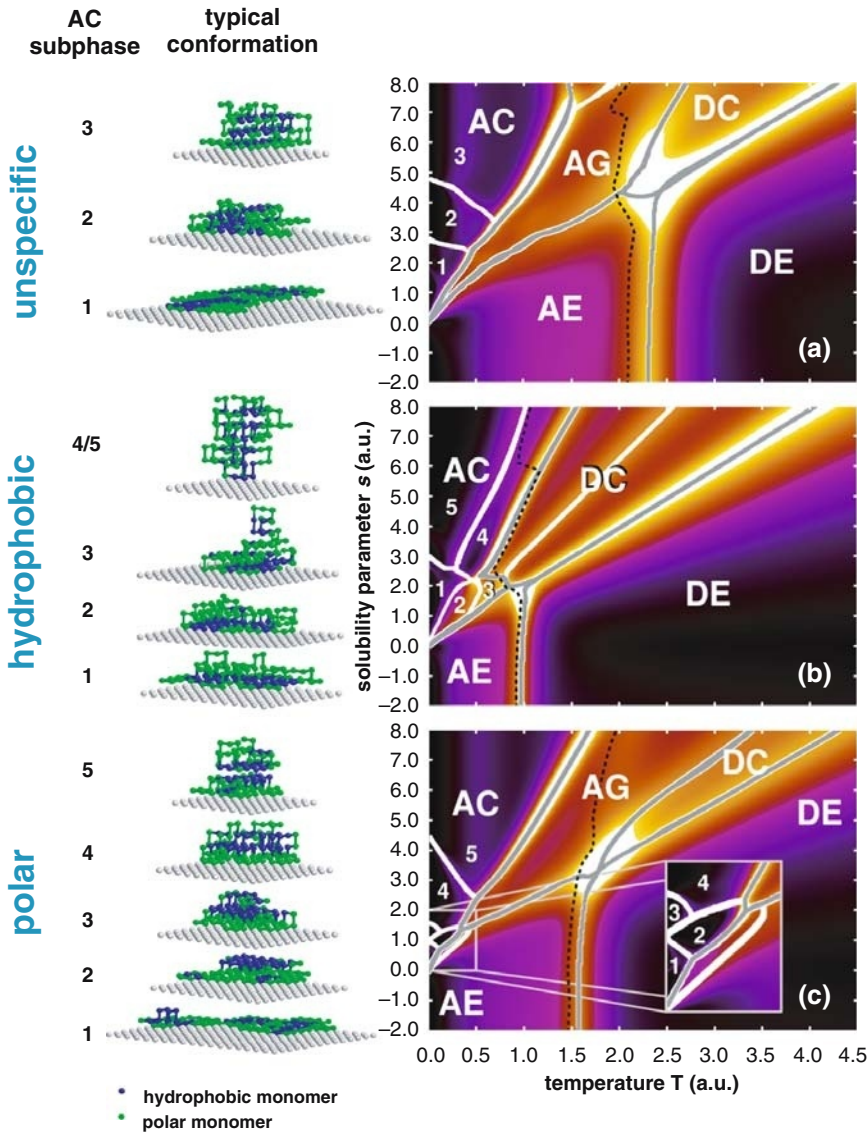


Fig. 8.11. Specific-heat profiles as a function of temperature T and solubility parameter s of the 103-mer near three different substrates that are attractive for (a) all, (b) only hydrophobic, and (c) only polar monomers. *White lines* indicate the ridges of the profile. *Gray lines* mark the main “phase boundaries”. The *dashed black line* represents the first-order-like binding/unbinding transition state, where the contact free energy possesses two minima (the adsorbed state and the desorbed state). In the *left panel*, typical conformations dominating the associated AC phases of the different systems are shown

in. For this reason, it is instructive to calculate all minima of the contact free energy and to determine the associated contact numbers in a wide range of values for the external parameters.

The map of all possible free-energy minima in the range of external parameters $T \in [0, 10]$ and $s \in [-2, 10]$ is shown in Fig. 8.12 for the peptide in the vicinity of a substrate that is equally attractive for both hydrophobic and polar monomers. Solid lines visualize “paths” through the free-energy landscape when changing temperature under constant solvent ($s = \text{const}$) conditions. Let us follow the exemplified trajectory for $s = 2.5$. Starting at very low temperatures, we know from the pseudophase diagram in Fig. 8.11(a) that the system resides in pseudophase AC1. This means that the macrostate of the peptide is dominated by the class of compact, film-like single-layer conformations. The system obviously prefers surface contacts at the expense of hydrophobic contacts. Nonetheless, the formation of compact hydrophobic domains in the two-dimensional topology is energetically favored, but maximal compactness is hindered by the steric influence of the substrate-binding polar residues. Increasing the temperature, the system experiences close to $T \approx 0.35$, a sharp first-order-like conformational transition, and a second layer forms (AC2). This is a mainly entropy-driven transition as the extension into the third dimension perpendicular to the substrate surface increases the number of possible peptide conformations. Furthermore, the loss of energetically favored substrate contacts of polar monomers is partly compensated by the energetic gain due to the more compact hydrophobic domains. Increasing the temperature further, the density of the hydrophobic domains reduces and overall compact conformations dominate in the globular pseudophase AG. Reaching AE, the number of hydrophobic contacts decreases further, and also the total number of substrate contacts. Extended, dissolved conformations dominate. The transitions from AC2 to AE via AG are comparatively “smooth”, i.e., no immediate changes in the contact numbers passing the transition lines are noticed. Therefore, these conformational transitions could be classified as second-order-like. The situation is different when approaching the unbinding transition line from AE close to $T \approx 2.14$. This transition is accompanied by a dramatic loss of substrate contacts – the peptide desorbs from the substrate and behaves in pseudophase DE like a free peptide, i.e., the substrate and the opposite neutral wall regularize the translational degree of freedom perpendicular to the walls, but rotational symmetries are unbroken (at least for conformations not touching one of the walls). As the probability distribution in Fig. 8.12 shows, the unbinding transition is also first-order-like, i.e., close to the transition line, there is a coexistence of adsorbing and desorbing classes of conformations.

Despite the surprisingly rich and complex phase behavior, there are main “phases” that can be distinguished in all three systems. These are separated in Fig. 8.11(a)–(c) by gray lines. Comparing the three systems, we find that they all possess pseudophases, where adsorbed compact (AC), adsorbed expanded (AE), desorbed compact (DC), and desorbed expanded (DE) conformations

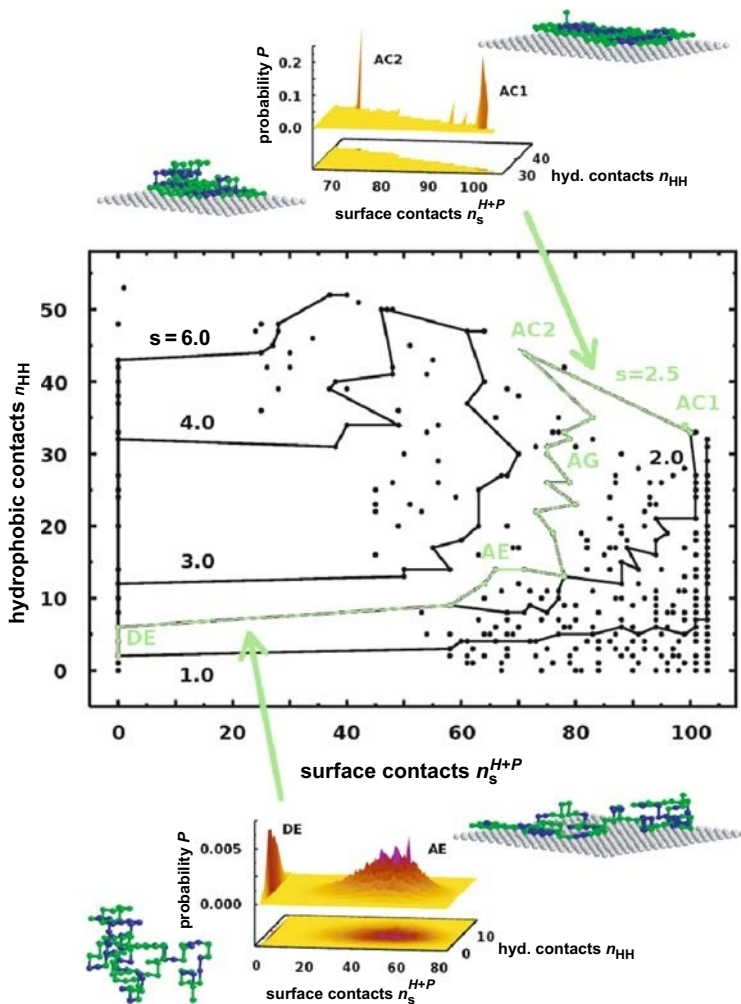


Fig. 8.12. Contact-number map of all free-energy minima for the 103-mer and substrate equally attractive to all monomers. *Full circles* correspond to minima of the contact free energy $F_{T,s}(n_s^{H+P}, n_{HH})$ in the parameter space $T \in [0, 10]$, $s \in [-2, 10]$. Lines illustrate how the contact free energy changes with the temperature at constant solvent parameter s . For the exemplified solvent with $s = 2.5$, the peptide experiences near $T = 0.35$, a sharp first-order-like layering transition between single- to double-layer conformations (AC1,2). Passing the regimes of adsorbed globules (AG) and expanded conformations (AE), the discontinuous binding/unbinding transition from AE to DE happens near $T = 2.14$. In the DE phase, the ensemble is dominated by desorbed, expanded conformations. Representative conformations of the phases are shown next to the respective peaks of the probability distributions

dominate. “Compact” here means that the heteropolymer has formed a dense hydrophobic core, while expanded conformations are dissolved, random-coil like. The sequence and substrate specificity of heteropolymers generates, of course, a rich set of new interesting and selective phenomena not available for homopolymers. One example is the pseudophase of adsorbed globules (AG), which is noticeably present only in those systems, where all monomers are equally attractive to the substrate (Fig. 8.11(a)) and where polar monomers favor contact with the surface (Fig. 8.11(b)). In this phase, the conformations are intermediates in the binding/unbinding region. This means that monomers currently desorbed from the substrate have not yet found their position within a compact conformation. Therefore, the hydrophobic core, which is smaller than in the respective adsorbed phase (i.e., at constant solubility s), appears as a loose cluster of hydrophobic monomers.

In Fig. 8.13(a)–(c), we have plotted, exemplified for $s = 2$, the statistical averages of the contact numbers n_s and n_{HH} as well as their variances and covariances for the three systems. For comparison, we have also included the specific heat, whose peaks correspond to the intersected transition lines of Fig. 8.11(a)–(c) at $s = 2$. From Fig. 8.13(a) and (c), we read off that the transition from AC to AG near $T \approx 0.4$ is mediated by fluctuations of the intrinsic hydrophobic contacts. The very dense hydrophobic domains in the AC subphases lose their compactness. This transition is absent in the hydrophobic-substrate system (Fig. 8.13(b)). The signal seen belongs to a hydrophobic layering AC subphase transition, which influences mainly the number of surface contacts n_s^H . The second peak of the specific heats belongs to the transition between adsorbed compact or globular (AC/AG) and expanded (AE) conformations. This behavior is similar in all three systems. Remarkably, it is accompanied by a strong anti-correlation between surface and intrinsic contact numbers, n_s and n_{HH} . Not surprisingly, the hydrophobic contact number n_{HH} fluctuates stronger than the number of surface contacts, but apparently in a different way. Dense conformations with hydrophobic core (and therefore many hydrophobic contacts) possess a relatively small number of surface contacts. Vice versa, conformations with many surface contacts cannot form compact hydrophobic domains. Finally, the third specific heat peak marks the binding/unbinding transition, which is, as expected, due to a strong fluctuation of the surface contact number.

The strongest difference between the three systems is their behavior in pseudophase AC, which is roughly parameterized by $s > 5T$. If hydrophobic and polar monomers are equally attracted by the substrate (Fig. 8.11(a)), we find three AC subphases in the parameter space plotted. In subphase AC1, film-like conformations dominate, i.e., all 103 monomers are in contact with the substrate. Due to the good solvent quality in this region, the formation of a hydrophobic core is less attractive than the maximal deposition of all monomers at the surface; the ground state is $(n_s^{H+P}, n_{HH})_{\min} = (103, 32)$. In fact, instead of a single compact hydrophobic core there are nonconnected hydrophobic clusters. At least on the used simple cubic lattice and the chosen

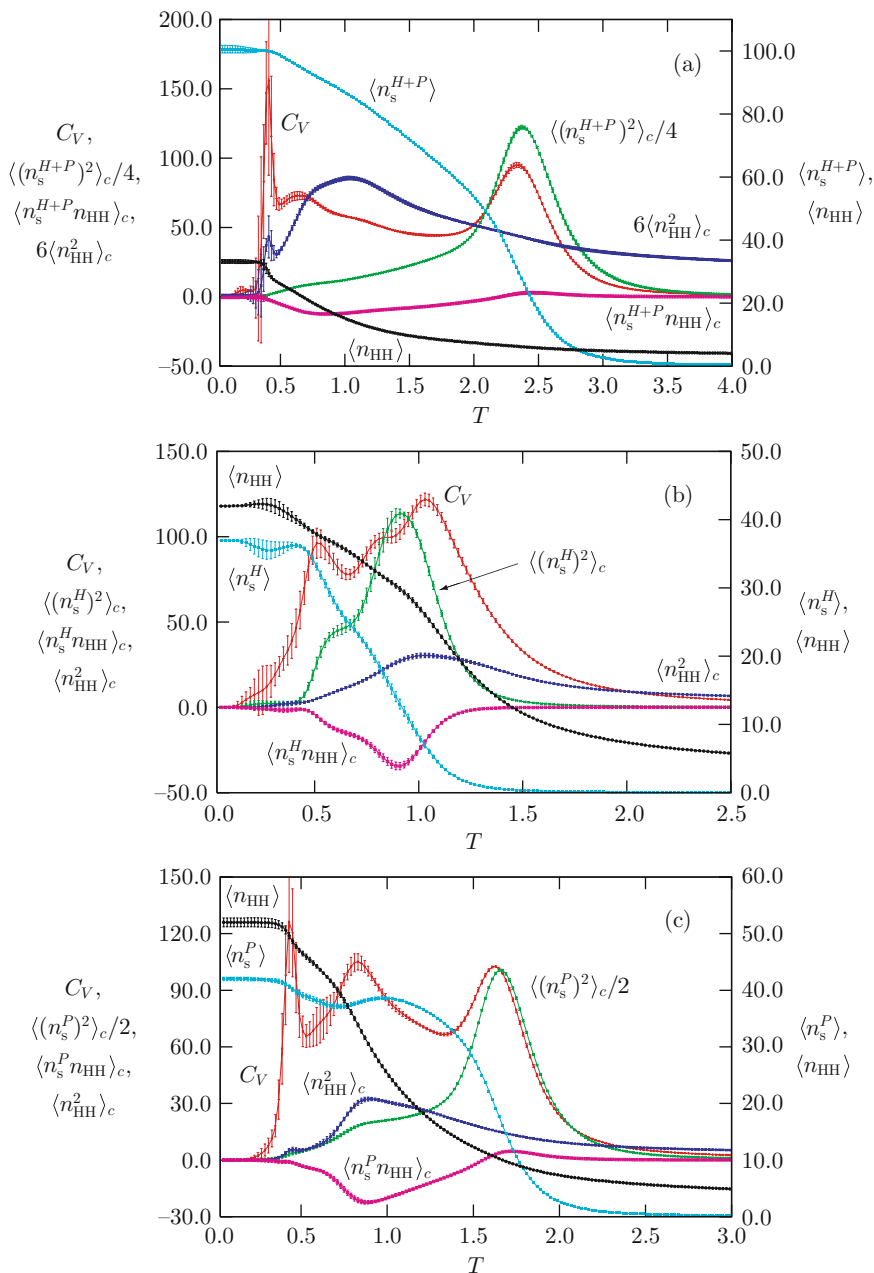


Fig. 8.13. Temperature dependence of specific heat, correlation matrix components, and contact number expectation values of the 103-mer for surfaces attractive for (a) all, (b) only hydrophobic, and (c) only polar monomers at $s = 2$

sequence, the formation of a single hydrophobic core is necessarily accompanied by an unbinding of certain polar monomers and, in consequence, an extension of the conformation into the third spatial dimension. In fact, this happens when entering AC2 $[(n_s^{H+P}, n_{HH})_{\min} = (64, 47)]$, where a single hydrophobic two-layer domain has formed at the expense of losing surface contacts. In AC3, the heteropolymer has maximized the number of hydrophobic contacts, and only local arrangements of monomers on the surface of the very compact structure lead to the still possible maximum number of substrate contacts. $F_{T,s}$ is minimal for $(n_s^{H+P}, n_{HH})_{\min} = (40, 52)$.

The behavior of the heteropolymer adsorbed at a surface that is only attractive to hydrophobic monomers (Fig. 8.11(b)) is apparently different in the AC phase. Since surface contacts of polar monomers are energetically not favored, the subphase structure is determined by the competition of two hydrophobic forces: substrate attraction and formation of intrinsic contacts. In AC1, the number of hydrophobic substrate contacts is maximal for the single hydrophobic layer, $(n_s^{HH}, n_{HH})_{\min} = (37, 42)$. The *single* two-dimensional hydrophobic domain is also maximally compact, at the expense of displacing polar monomers into a second layer. In subphase AC2, intrinsic contacts are entropically broken with minimal free energy for $35 \leq n_{HH} \leq 40$, while $n_s^{HH} = 37$ remains maximal. Another AC subphase, AC3, exhibits a hydrophobic layering transition at the expense of hydrophobic substrate contacts. Much more interesting is the subphase transition from AC1 to AC5. The number of hydrophobic substrate contacts n_s^{HH} of the ground-state conformation dramatically decreases (from 37 to 4), and the hydrophobic monomers collapse in a one-step process from the compact two-dimensional domain to the maximally compact three-dimensional hydrophobic core. The conformations are mushroom-like structures grafted at the substrate. AC4 is similar to AC5, with advancing desorption.

Not less exciting is the subphase structure of the heteropolymer interacting with a polar substrate (Fig. 8.11(c)). For small values of s and T , the behavior of the heteropolymer is dominated by the competition between polar monomers contacting the substrate and hydrophobic monomers favoring the formation of a hydrophobic core, which, however, also requires cooperativity of the polar monomers. In AC1, film-like conformations $(n_s^P = 66, n_{HH} = 31)$ with disconnected hydrophobic clusters dominate. Entering AC2, hydrophobic contacts are energetically favored and a second hydrophobic layer forms at the expense of a reduction of polar substrate contacts $[(n_s^P, n_{HH})_{\min} = (61, 37)]$. In AC3, the upper layer is mainly hydrophobic $[(n_s^P, n_{HH})_{\min} = (53, 45)]$, while the poor quality of the solvent (s large) and the comparatively strong hydrophobic force let the conformation further collapse [AC4: $(n_s^P, n_{HH})_{\min} = (42, 52)]$ and the steric cooperativity forces more polar monomers to break the contact to the surface and to form a shell surrounding the hydrophobic core $[(n_s^P, n_{HH})_{\min} = (33, 54)]$ in AC5].

8.4 Going Off-Lattice: Folding Behavior of Heteropolymers in the AB Continuum Model

The lattice models discussed in the previous sections suffer from the fact that the results for the finite-length heteropolymers typically depend on the underlying lattice type. It is difficult to separate realistic effects from artifacts induced by the use of a certain lattice structure. This problem can be avoided, in principle, by studying off-lattice heteropolymers, where the degrees of freedom are continuous. On the other hand, this advantage is partly counter-balanced by the increasing computational efforts for sampling the relevant regions of the conformational state space. In consequence, a precise analysis of statistical properties of off-lattice heteropolymers by means of generalized-ensemble methods can reliably be performed only for chains much shorter than those considered in the lattice studies. In the following, we focus on hydrophobic–polar heteropolymers with 20 monomers employing the so-called AB model [82], where A monomers are hydrophobic and residues of type B are polar (or hydrophilic).

8.4.1 Modeling and Updating

We denote the spatial position of the i th monomer in a heteropolymer consisting of N residues by \mathbf{r}_i , $i = 1, \dots, N$, and the vector connecting nonadjacent monomers i and j by \mathbf{r}_{ij} . For covalent bond vectors, we set $|\mathbf{b}_i| \equiv |\mathbf{r}_{i\ i+1}| = 1$. The bending angle between monomers k , $k+1$, and $k+2$ is ϑ_k ($0 \leq \vartheta_k \leq \pi$) and $\sigma_i = A, B$ symbolizes the type of the monomer. In the AB model [82], the energy of a conformation is given by

$$E = \frac{1}{4} \sum_{k=1}^{N-2} (1 - \cos \vartheta_k) + 4 \sum_{i=1}^{N-2} \sum_{j=i+2}^N \left(\frac{1}{r_{ij}^{12}} - \frac{C(\sigma_i, \sigma_j)}{r_{ij}^6} \right), \quad (8.19)$$

where the first term is the bending energy and the sum runs over the $(N-2)$ bending angles of successive bond vectors. The second term partially competes with the bending barrier by a potential of Lennard-Jones type. It depends on the distance between monomers being nonadjacent along the chain and accounts for the influence of the AB sequence on the energy. The long-range behavior is attractive for pairs of like monomers and repulsive for AB pairs of monomers:

$$C(\sigma_i, \sigma_j) = \begin{cases} +1, & \sigma_i, \sigma_j = A, \\ +1/2, & \sigma_i, \sigma_j = B, \\ -1/2, & \sigma_i \neq \sigma_j. \end{cases} \quad (8.20)$$

The Monte Carlo simulation of this model is not straightforward as strictly local updates are not possible. A simple nonlocal update of a given conformation can be performed by using the procedure displayed in Fig. 8.14. Since the length of the bonds is fixed ($|\mathbf{b}_k| = 1$, $k = 1, \dots, N-1$), the $(i+1)$ th

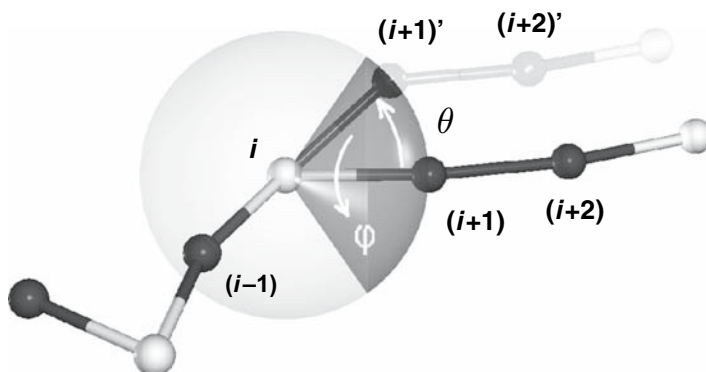


Fig. 8.14. Spherical update of the bond vector between the i th and $(i + 1)$ th monomer

monomer lies on the surface of a sphere with radius unity around the i th monomer. Therefore, spherical coordinates are the natural choice for calculating the new position of the $(i + 1)$ th monomer on this sphere. For the reason of efficiency, we do not select any point on the sphere but restrict the choice to a spherical cap with maximum opening angle $2\theta_{\max}$ (the dark area in Fig. 8.14). Thus, to change the position of the $(i + 1)$ th monomer to $(i + 1)'$, we select the angles θ and φ randomly from the respective intervals $\cos \theta_{\max} \leq \cos \theta \leq 1$ and $0 \leq \varphi \leq 2\pi$, which ensure a uniform distribution of the $(i + 1)$ th monomer position on the associated spherical cap. After updating the position of the $(i + 1)$ th monomer, the following monomers in the chain are simply translated according to the corresponding bond vectors which remain unchanged in this type of update. Only the bond vector between the i th and the $(i + 1)$ th monomers is rotated, all others keep their direction. This is similar to single spin updates in local-update Monte Carlo simulations of the classical Heisenberg model, with the difference that in addition to local energy changes, long-range interactions of the monomers, changing their relative position to each other, have to be computed anew after the update. For simulations in the state space of dense conformations, it is recommendable to choose a rather small opening angle, e.g., $\cos \theta_{\max} = 0.99$, in order to be able to sample also very narrow and deep valleys in the landscape of angles.

For the following discussion of folding channels of 20-mers [88], these updates were used in combination with multicanonical sampling [48, 49].

8.4.2 Characteristic Protein Folding Channels and Free-Energy Landscapes from Coarse-Grained Modeling

The folding process of proteins is necessarily accompanied by cooperative conformational changes. Although not phase transitions in the strict sense, it should be expected that one or a few parameters can be defined that enable

the description of the structural ordering process [83, 84]. The number of degrees of freedom in most all-atom models is given by the dihedral torsional backbone and side-chain angles. In coarse-grained C^α models as the AB model used in this study, the original dihedral angles are replaced by a set of virtual torsional and bond angles. In fact, the number of degrees of freedom is not necessarily reduced in simplified off-lattice models. Therefore, the complexity of the space of degrees of freedom is comparable with more realistic models, and it is also a challenge to identify a suitable order parameter for the folding in such minimalistic heteropolymer models.

In analogy to studies of the specific folding behavior in all-atom protein models [85, 86], it is suitable to define a generalized variant of an angular overlap order parameter as introduced in [87]. The idea is to define a simple and computationally low-cost measure for the similarity of two conformations, where the differences of the angular degrees of freedom are calculated. In order to consider this parameter as a kind of order parameter, it is useful to compare conformations $\mathbf{X} = (\mathbf{r}_1, \dots, \mathbf{r}_N)$ of the actual ensemble with a suitable reference conformation, which is preferably chosen to be the global-energy minimum conformation $\mathbf{X}^{(0)}$. We define the overlap parameter as follows:

$$Q(\mathbf{X}) = 1 - d(\mathbf{X}) . \quad (8.21)$$

With $N_b = N - 2$ and $N_t = N - 3$ being the respective numbers of bond angles θ_i and torsional angles ϕ_i , the angular deviation between the conformations is calculated according to

$$d(\mathbf{X}) = \frac{1}{\pi(N_b + N_t)} \left[\sum_{i=1}^{N_b} d_b(\theta_i) + \min_{r=\pm} \left(\sum_{i=1}^{N_t} d_t^r(\phi_i) \right) \right] , \quad (8.22)$$

where

$$d_b(\theta_i) = |\theta_i - \theta_i^{(0)}| , \quad (8.23)$$

$$d_t^\pm(\phi_i) = \min \left(|\phi_i \pm \phi_i^{(0)}|, 2\pi - |\phi_i \pm \phi_i^{(0)}| \right) . \quad (8.24)$$

Here it is taken into account that the AB model is invariant under the reflection symmetry $\phi_i \rightarrow -\phi_i$. Thus, it is not useful to distinguish between reflection-symmetric conformations and therefore only the larger overlap is considered. Since $-\pi \leq \phi_i \leq \pi$ and $0 \leq \theta_i \leq \pi$, the overlap is unity, if all angles of the conformations \mathbf{X} and $\mathbf{X}^{(0)}$ coincide, else $0 \leq Q < 1$. It should be noted that the average overlap of a random conformation with the corresponding reference state is for the sequences considered close to $\langle Q \rangle \approx 0.66$. As a rule of thumb, it can be concluded that values $Q < 0.8$ indicate weak or no significant similarity of a given structure with the reference conformation.

For the qualitative discussion of the folding characteristics, we consider the multicanonical histograms of energy E and angular overlap Q , $H_{\text{muca}}(E, Q) = \sum_t \delta_{E, E(\mathbf{x}_t)} \delta_{Q, Q(\mathbf{x}_t)}$, where the sum runs over all Monte Carlo sweeps t in

the multicanonical simulation, which yields a constant energy distribution $h_{\text{muca}}(E) = \int_0^1 dQ H_{\text{muca}}(E, Q) \approx \text{const}$. In consequence, $H_{\text{muca}}(E, Q)$ is useful for identifying the folding channels, independently of temperature. Restricting the canonical partition function at temperature T to the “microoverlap” ensemble with overlap Q , $Z(Q) = \int \mathcal{D}\mathbf{X} \delta(Q - Q(\mathbf{X})) \exp[-E(\mathbf{X})/k_B T]$, where the functional integral is over all possible conformations \mathbf{X} , we define the overlap free energy as $F(Q) = -k_B T \ln Z(Q)$.

Figure 8.15 shows the thus obtained multicanonical histograms $H_{\text{muca}}(E, Q)$ (left) and the overlap free-energy landscapes $F(Q)$ (right) at different

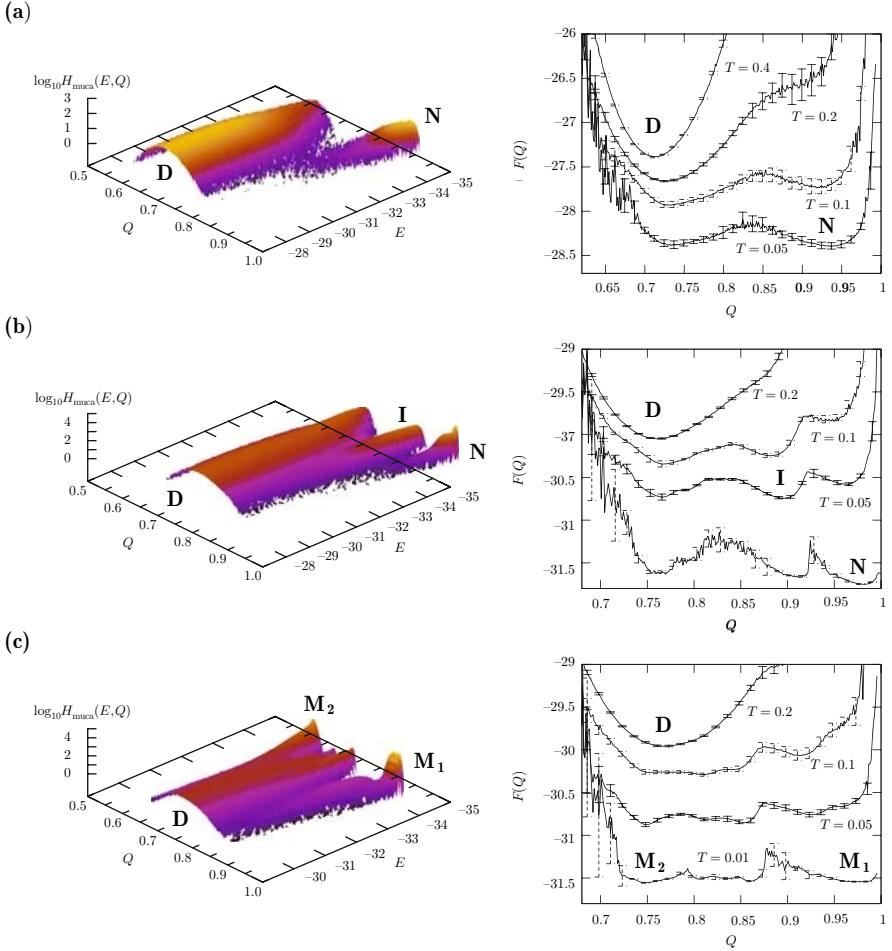


Fig. 8.15. Multicanonical histograms $H_{\text{muca}}(E, Q)$ of energy E and angular overlap parameter Q and free-energy landscapes $F(Q)$ at different temperatures for the three sequences (a) S1, (b) S2, and (c) S3. The reference folds reside at $Q = 1$ and $E = E_{\text{min}}$ [88]

Table 8.4. The three AB 20-mers studied and the values of the associated (putative) global energy minima

Label	Sequence	Global energy minimum [88]
S1	BA ₆ BA ₄ BA ₂ BA ₂ B ₂	−33.8236
S2	A ₄ BA ₂ BABA ₂ B ₂ A ₃ BA ₂	−34.4892
S3	A ₄ B ₂ A ₄ BA ₂ BA ₃ B ₂ A	−33.5838, −33.5116

Note that the given values for sequence S3 belong to two different, almost degenerate folds (cf. Fig. [8.16](#))

temperatures for the three sequences listed in Table [8.4](#). The different branches of $H_{\text{muca}}(E, Q)$ indicate the channels the heteropolymer can follow in the folding process toward the reference structure. The heteropolymers, whose sequences differ only by permutations, exhibit noticeable differences in the folding behavior toward the native conformations. The first interesting observation is that the minimalistic model used is capable of revealing the different folding behaviors of the wild-type and permuted sequences. The second remarkable result is that the angular overlap parameter Q is a surprisingly manifest measure for the peptide macrostate.

From Fig. [8.15\(a\)](#), we conclude that folding of sequence S1 exhibits typical two-state characteristics. Above the transition temperature, i.e., in the regime of denatured conformations D, conformations possess a random-coil-like overlap $Q \approx 0.7$, i.e, there is no significant similarity with the reference structure. Close to $T \approx 0.1$, the global minimum of the corresponding overlap free energy $F(Q)$ changes discontinuously toward larger Q values, and at the transition state the denatured (D) and the folded macrostates (N) are equally probable. The existence of this pronounced transition state is a characteristic indication for first-order-like two-state folding. Decreasing the temperature further, the native-fold-like conformations ($Q > 0.95$) dominate and fold smoothly toward the $Q = 1$ reference structure, i.e., the lowest-energy conformation found for sequence S1.

The folding behavior of sequence S2 is significantly different, as Fig. [8.15\(b\)](#) shows, and is a typical example for a folding event through an intermediate macrostate. The main channel D bifurcates and a side channel I branches off continuously. For smaller energies (or lower temperatures), this branching is followed by the formation of a third channel N, which ends in the native fold. The characteristics of folding-through-intermediates is also reflected by the free-energy landscapes. Starting at high temperatures in the pseudophase of denatured conformations D with $Q \approx 0.76$, the intermediary phase I with $Q \approx 0.9$ is reached close to the temperature $T \approx 0.05$. Decreasing the temperature further below the native-folding threshold close to $T = 0.01$, the hydrophobic-core formation is finished, and stable native-fold-like conformations with $Q > 0.97$ dominate in regime N.

The most extreme behavior of the three exemplified sequences is found for sequence S3, where the main channel D does not decay in favor of a single native-fold channel. In fact, in Fig. 8.15(c), we observe both, *two* separate native-fold channels, M_1 and M_2 , and a bifurcating main channel. Above the folding transition ($T = 0.2$), the typical sequence-independent denatured conformations in D ($Q \approx 0.77$) dominate. Annealing below the glass-transition threshold, several channels form and coexist. The two most prominent channels (to which the lowest-energy conformations belong that we found in the simulations) eventually lead for $T \approx 0.01$ to ensembles of states M_1 with $Q > 0.97$, which are similar to the reference structure shown in Fig. 8.16(a), and conformations M_2 with $Q \approx 0.75$. The lowest-energy conformation found in this regime is shown in Fig. 8.16(b). It is structurally different but energetically almost degenerate compared with the reference structure. It should also be noted that the lowest-energy main-channel conformations have only slightly larger energies than the two native folds. Thus, the folding of this heteropolymer is accompanied by very complex, amorphous folding characteristics. In fact, the multiple-peaked distribution $H_{\text{muca}}(E, Q)$ near minimum energies is a strong indication for metastability. A native fold in the natural sense does not exist; the $Q = 1$ conformation is only a reference structure but the folding toward this structure is not distinguished as it is in the folding characteristics of sequences S1 and S2.

These results demonstrate that it is possible to find clear indications for three different folding characteristics known from real proteins by analyzing macrostates based on an angular overlap parameter within a minimalistic heteropolymer frame. The physical objective is not only on establishing a quantitative one-to-one correspondence between model and real peptides (which, in general, is not in the focus of minimalistic, effective models) but also on a more comprehensive, qualitative understanding of universal aspects of protein folding. We find that for selected hydrophobic-polar heteropolymer sequences, characteristic folding behaviors such as two-state folding, folding through intermediates, and metastability can be observed which are qualitatively comparable with real folding events in nature. Beyond the general interest in understanding complex aspects of protein folding, the preparation

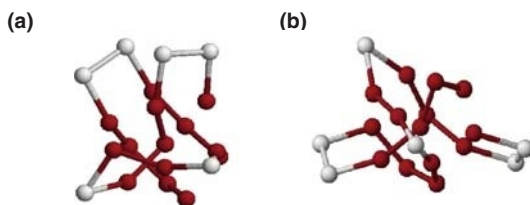


Fig. 8.16. Lowest-energy conformations for sequence S3, considered as (a) reference structure $\mathbf{X}^{(0)}$ and (b) alternative metastable conformation, whose angular overlap with $\mathbf{X}^{(0)}$ is $Q \approx 0.75$

of synthetic peptide macrostates in future applications, e.g., in the design of substrate- or pattern-selective polymers, is strongly connected with the understanding of such conformational folding transitions.

8.5 Peptide Aggregation

Another important, because biologically relevant, example for cooperative structure formation processes is the aggregation of proteins. A prominent example, where this process has disastrous effects, is the oligomerization of the A β protein which is associated with Alzheimer’s disease.

A mesoscopic model for the aggregation of multiple chains can simply be defined by assuming that the same type-dependent Lennard-Jones-like potentials used in the single-chain form (8.19) describe also the inter-monomeric interaction, i.e., the interaction among monomers of different chains [89]. For the analysis of the aggregation transition, let us consider the example of a complex of two identical AB peptides with sequence $AB_2AB_2ABAB_2AB$ [89, 90]. We suppose that the aggregation of the peptides should be signaled by strong fluctuations of the relative distance of the centers of masses of the individual chains. Thus, we define for systems consisting of M peptides:

$$\Gamma^2 = \frac{1}{2M^2} \sum_{\mu, \nu=1}^M \left(\mathbf{r}_{\text{COM}}^{(\mu)} - \mathbf{r}_{\text{COM}}^{(\nu)} \right)^2, \quad (8.25)$$

where $\mathbf{r}_{\text{COM}}^{(\mu)}$ is the center of mass of the μ th chain (in our example $M = 2$). Actually, a multicanonical computer simulation reveals very clear indications for a single conformational transition, the aggregation transition [89, 90]. This means that the peptide–peptide aggregation and the folding into a compact peptide complex are not separate transitions (at least in this example). This is illustrated in Fig. 8.17(a), where the color-coded multicanonical histogram as a function of energy E and the aggregation parameter Γ is shown. Qualitatively, two separate main branches (which are “channels” in the corresponding free-energy landscape) are apparent between which a noticeable transition occurs. In the vicinity of the energy $E_{\text{sep}} \approx -3.15$, both channels overlap, i.e., the associated macrostates coexist. Since Γ is an effective measure for the spatial distance between the two peptides, it is obvious that conformations with separated or fragmented peptides belong to the dominating channel in the regime of high energies and large Γ values, whereas the aggregates are accumulated in the narrow low-energy and small- Γ channel. Thus, the main observation from the multicanonical, comprising point of view is that the aggregation transition is a phase separation process which, even for this small system, already appears in a surprisingly clear fashion.

The high precision of the multicanonical method allows us even to see further details in the lowest-energy aggregation regime, which is usually a

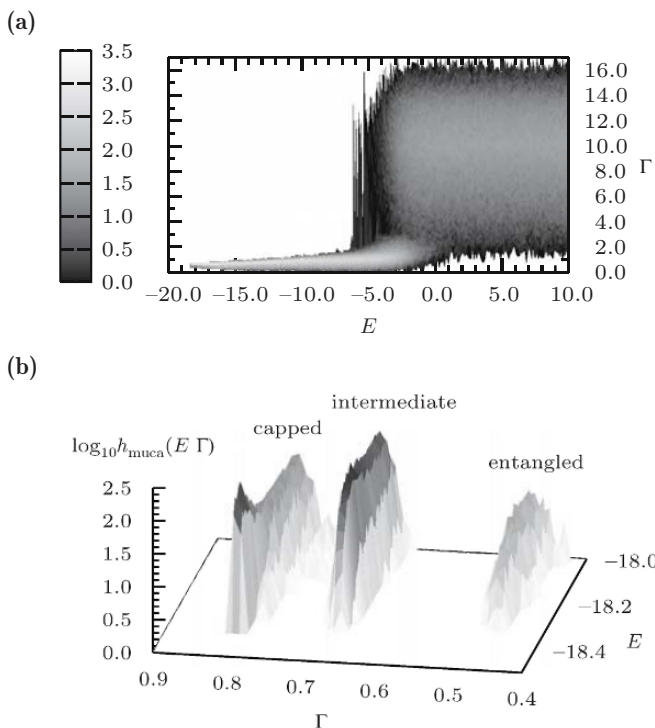


Fig. 8.17. (a) Multicanonical histogram $\log_{10} h_{\text{muca}}$ as a function of energy E and aggregation parameter Γ , (b) section of $\log_{10} h_{\text{muca}}$ in the low-energy tail [90]

notoriously difficult sampling problem. Fig. 8.17(b) shows that the tight aggregation channel splits into three separate, almost degenerate subchannels at lowest energies. From the analysis of the conformations in this region, one finds that representative conformations with smallest Γ values, $\Gamma \approx 0.45$, are typically entangled, while those with $\Gamma \approx 0.8$ have a spherically capped shape. Examples are shown in Fig. 8.18. The also highly compact conformations belonging to the intermediate subphase do not exhibit such characteristic features and are rather globules without noticeable internal symmetries. In all cases, the aggregates contain a single compact core of hydrophobic residues. This also confirms that the aggregation is not a simple docking process of two prefolded peptides but a complex cooperative folding-binding process. The general aggregation behavior is similar also for larger systems of more peptides with the same sequence [90].

Finally, from a methodological point of view, it is worth mentioning that the signals for the aggregation (and presumably also the folding) transition are much more pronounced in a *microcanonical* analysis [89, 90]. This observation might be of conceptual importance also for all-atom protein aggregation/folding studies.

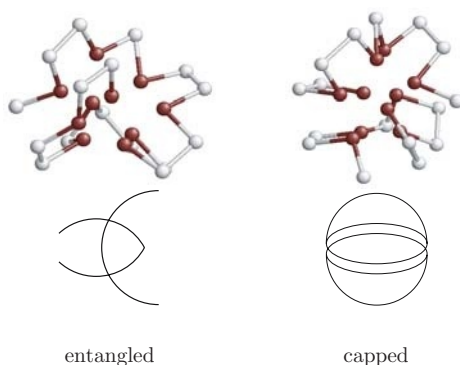


Fig. 8.18. Representatives and schematic characteristics of entangled and spherically capped conformations dominating the lowest-energy branches in the multi-canonical histogram shown in Fig. 8.17(b). *Dark spheres* correspond to hydrophobic (A), *light* ones to polar (B) residues

8.6 Summary

For the qualitative analysis of phase transitions, it is often sufficient to perform statistical studies of simplified effective models, where the natural complexity of the realistic system is broken down to the essential, irreducible level of cooperative behavior. The probably most famous example is the Ising model of ferromagnetism. In this model, a local short-range spin–spin interaction – which in essence is a consequence of the quantum-mechanical exchange mechanism between magnetic moments – triggers in two and more dimensions a nontrivial second-order phase transition between the ordered ferromagnetic macrostate and the disordered, random paramagnetic phase. The generalization of the description of phase transitions is highly successfully achieved within the framework of Ginzburg-Landau theories, which are not only restricted to transitions of second order but also allow investigations of symmetry breaking typically forcing first-order phase transitions. In any case, the idea is to introduce collective coordinates or, more specific, order parameters that allow for a unique identification of the actual macrostate of the system.

The characterization of conformational (structural) transitions during the folding process of proteins is more involved as no general theory of phase transitions for finite systems is available. In fact, the finiteness of the amino acid sequence length contradicts the demand of a thermodynamic limit, which is the essential condition for thermodynamic phase transitions to occur. Nonetheless, there is hope that following a similar strategy as in the theory for phase transitions, a classification of characteristic tertiary folding transitions (e.g.,

single-exponential folding, two-state folding, folding through weakly stable intermediary states, metastability) is possible. If so, then it should be possible to construct simple models at a raw, coarse-grained level that allow firstly the introduction of unique conformational (“order”) parameters and secondly to qualitatively reproduce the known folding characteristics of classes of proteins.

As the Ising model will not be an adequate model for precise questions regarding a *specific* ferromagnet, it is also not expected that a simple, coarse-grained model will reveal the folding behavior of a *specific* protein. This means, for explaining the folding characteristics of a *specific* protein, doubtlessly a microscopic all-atom model incorporating interactions acting over all length and energy scales is required.

In this lecture, we have demonstrated, however, that results obtained from simple lattice and off-lattice heteropolymer models are indeed capable of revealing characteristic features of proteins (stability of designing sequences, designable conformations) and protein folding (folding channels, free-energy landscapes). As far as important qualitative features of peptides and proteins on intermediate length scales are concerned, such models are thus of comparable significance as the more detailed atomic descriptions.

Acknowledgements

We are grateful to Peter Grassberger and Hsiao-Ping Hsu for detailed informations about PERM and its improved variants. We are also indebted to Anders Irbäck, Sandipan Mohanty, and Simon Mitternacht for discussions on coarse-grained and simplified variants of microscopic protein models and to Bernd A. Berg, Ulrich H. E. Hansmann, Yuko Okamoto, Tarık Çelik, and Gökhan Gökoğlu for discussions on general aspects of protein folding. We thank Handan Arkin, Reinhard Schiemann, Thomas Vogel, Stefan Schnabel, Anna Kallias, Jakob Schluttig, and Christoph Junghans for cooperation in studies of coarse-grained lattice and off-lattice heteropolymer models. The investigations of hybrid interfaces were inspired by semiconductor experiments of Karsten Goede and Marius Grundmann and by peptide synthesis and analysis of Kai Holland-Nell and Annette G. Beck-Sickinger, whom we would like to thank for close collaboration. This work is partially supported by the DFG (German Science Foundation) grant under contract no. JA 483/24-1 and by the DAAD-STINT Personnel Exchange Programme with Sweden. M. B. thanks the DFG and the Wenner-Gren Foundation for research fellowships. Support by the JUMP supercomputer time grant no. h1z11 of the John von Neumann Institute for Computing (NIC), Forschungszentrum Jülich, is also gratefully acknowledged.

References

1. T. E. Creighton: *Proteins: Structure and Molecular Properties* (Freeman, New York, 1993), 2nd ed. [204](#)
2. C. Branden, J. Tooze: *Introduction to Protein Structure* (Garland, New York, 1999), 2nd ed. [204](#)
3. K. A. Dill: *Protein Sci.* **8**, 1166 (1999) [204](#)
4. C. Tang: *Physica A* **288**, 31 (2000) [204](#), [207](#), [208](#)
5. See also the contributions of U. H. E. Hansmann (Chap. [111](#)), A. Irback (Chap. [10](#)), and Y. Okamoto (Chap. [14](#)) to simulations of all-atom protein models in this volume [204](#)
6. B. L. de Groot, T. Frigato, V. Helms, H. Grubmüller: *J. Mol. Biol.* **333**, 279 (2003) [204](#)
7. R. A. Böckmann, H. Grubmüller: *Biophys. J.* **85**, 1482 (2003) [204](#)
8. U. H. E. Hansmann: *Physica A* **254**, 15 (1998); T. Nagasima, Y. Sugita, A. Mitsutake, Y. Okamoto: *Comput. Phys. Commun.* **146**, 69 (2002) [204](#)
9. K. A. Dill: *Biochemistry* **24**, 1501 (1985); K. F. Lau, K. A. Dill: *Macromolecules* **22**, 3986 (1989) [207](#), [208](#), [219](#)
10. B. Berger, T. Leighton: *J. Comput. Biol.* **5**, 27 (1998); P. Crescenzi, D. Goldman, C. Papadimitriou, A. Piccolboni, M. Yannakakis: *J. Comput. Biol.* **5**, 423 (1998) [207](#)
11. A. Irback, E. Sandelin: *J. Chem. Phys.* **108**, 2245 (1998) [207](#)
12. A. Irback, C. Troein: *J. Biol. Phys.* **28**, 1 (2002) [207](#), [209](#)
13. H. Cejtin, J. Edler, A. Gottlieb, R. Helling, H. Li, J. Philbin, C. Tang, N. Wingreen: *J. Chem. Phys.* **116**, 352 (2002) [207](#)
14. R. Schiemann, M. Bachmann, W. Janke: *J. Chem. Phys.* **122**, 114705 (2005) [207](#), [208](#), [209](#)
15. R. Schiemann, M. Bachmann, W. Janke: *Comput. Phys. Commun.* **166**, 8 (2005) [207](#), [208](#), [209](#)
16. K. Yue, K. A. Dill: *Phys. Rev. E* **48**, 2267 (1993); K. Yue, K. A. Dill: *Proc. Natl. Acad. Sci. USA* **92**, 146 (1995) [207](#), [208](#), [219](#), [221](#), [223](#)
17. T. C. Beutler, K. A. Dill: *Protein Sci.* **5**, 2037 (1996) [207](#)
18. R. Unger, J. Moult: *J. Mol. Biol.* **231**, 75 (1993) [207](#), [208](#)
19. N. Krasnogor, W. E. Hart, J. Smith, D. A. Pelta: *Proceedings of Genetic and Evolutionary Computation Conference (GECCO99)*, Orlando (1999), p. 1596 [207](#)
20. Y. Cui, W. H. Wong, E. Bornberg-Bauer, H. S. Chan: *Proc. Natl. Acad. Sci. USA* **99**, 809 (2002) [207](#)
21. N. Lesh, M. Mitzenmacher, S. Whitesides: *International Conference on Research in Computational Molecular Biology (RECOMB'03)*, Berlin (2003), p. 188 [207](#)
22. T. Jiang, Q. Cui, G. Shi, S. Ma: *J. Chem. Phys.* **119**, 4592 (2003) [207](#)
23. F. Seno, M. Vendruscolo, A. Maritan, J. R. Banavar: *Phys. Rev. Lett.* **77**, 1901 (1996) [207](#), [211](#)
24. R. Ramakrishnan, B. Ramachandran, J. F. Pekny: *J. Chem. Phys.* **106**, 2418 (1997) [207](#), [211](#)
25. A. Irback, C. Peterson, F. Potthast, E. Sandelin: *Phys. Rev. E* **58**, R5249 (1998) [207](#), [211](#)
26. L. W. Lee, J.-S. Wang: *Phys. Rev. E* **64**, 056112 (2001) [207](#), [211](#)
27. G. Chikenji, M. Kikuchi, Y. Iba: *Phys. Rev. Lett.* **83**, 1886 (1999), and references therein [207](#)
28. M. N. Rosenbluth, A. W. Rosenbluth: *J. Chem. Phys.* **23**, 356 (1955) [207](#), [211](#), [212](#)
29. D. Aldous, U. Vazirani: "Go with the winners" algorithms, 35th Annual Symposium on Foundations of Computer Science, Santa Fe (1994), p. 492 [207](#), [211](#)

30. P. Grassberger: Phys. Rev. E **56**, 3682 (1997) [207](#), [212](#), [213](#), [216](#)
31. H. Frauenkron, U. Bastolla, E. Gerstner, P. Grassberger, W. Nadler: Phys. Rev. Lett. **80**, 3149 (1998); U. Bastolla, H. Frauenkron, E. Gerstner, P. Grassberger, W. Nadler: Proteins **32**, 52 (1998) [207](#), [212](#), [213](#)
32. P. Grassberger, W. Nadler: “*Go with the winners*” simulations. In *Computational Statistical Physics – From Billiards to Monte Carlo*, edited by K. H. Hoffmann, M. Schreiber (Springer, Berlin, 2002), p. 169, and references therein [207](#), [212](#), [213](#)
33. H.-P. Hsu, V. Mehra, W. Nadler, P. Grassberger: J. Chem. Phys. **118**, 444 (2003); H.-P. Hsu, V. Mehra, W. Nadler, P. Grassberger: Phys. Rev. E **68**, 21113 (2003) [207](#), [213](#), [216](#), [221](#), [226](#)
34. M. Bachmann, W. Janke: Phys. Rev. Lett. **91**, 208105 (2003) [207](#), [213](#), [214](#), [216](#), [219](#), [223](#), [224](#)
35. M. Bachmann, W. Janke: J. Chem. Phys. **120**, 6779 (2004) [207](#), [213](#), [214](#), [215](#), [216](#), [219](#), [221](#), [222](#)
36. R. J. Najmanovich, J. L. deLyra, V. B. Henriques: Physica A **249**, 374 (1998) [207](#)
37. K. Yue, K. M. Fiebig, P. D. Thomas, H. S. Chan, E. I. Shakhnovich, K. A. Dill: Proc. Natl. Acad. Sci. USA **92**, 325 (1995) [208](#), [221](#), [223](#)
38. E. E. Lattman, K. M. Fiebig, K. A. Dill: Biochemistry **33**, 6158 (1994) [208](#), [226](#)
39. L. Toma, S. Toma: Protein Sci. **5**, 147 (1996) [208](#), [226](#)
40. S. Miyazawa, R. L. Jernigan: J. Mol. Biol. **256**, 623 (1996) [208](#)
41. Two sequences are only distinguished, if they are not symmetric under reversal of their residues. For a chain with length $N = 4$, for example, there are ten relevant sequences instead of $2^4 = 16$ [209](#)
42. M. Vendruscolo, E. Domany: Folding Design **2**, 295 (1997); M. Vendruscolo, E. Domany: Folding Design **3**, 329 (1998) [209](#)
43. E. G. Emberly, J. Miller, C. Zeng, N. S. Wingreen, C. Tang: Proteins **47**, 295 (2002) [210](#)
44. H. Li, R. Helling, C. Tang, N. Wingreen: Science **273**, 666 (1996) [210](#)
45. N. Madras, A. D. Sokal: J. Stat. Phys. **50**, 109 (1988) [211](#)
46. J. C. Guillou, J. Zinn-Justin: Phys. Rev. Lett. **39**, 95 (1977); J. C. Guillou, J. Zinn-Justin: Phys. Rev. B **21**, 3976 (1980); A. Pelissetto, E. Vicari: Phys. Rep. **368**, 549 (2002) [214](#)
47. A. M. Ferrenberg, R. H. Swendsen: Phys. Rev. Lett. **63**, 1195 (1989) [214](#)
48. B. A. Berg, T. Neuhaus: Phys. Lett. B **267**, 249 (1991); B. A. Berg, T. Neuhaus: Phys. Rev. Lett. **68**, 9 (1992) [214](#), [235](#)
49. W. Janke: Physica A **254**, 164 (1998); B. A. Berg: Fields Inst. Comm. **26**, 1 (2000) [214](#), [215](#), [235](#)
50. B. A. Berg: In Chap. [12](#) of this volume [217](#)
51. T. Vrbová, S. G. Whittington: J. Phys. A **29**, 6253 (1996); T. Vrbová, S. G. Whittington: J. Phys. A **31**, 3989 (1998); T. Vrbová, K. Procházka: J. Phys. A **32**, 5469 (1999) [217](#), [225](#)
52. M. D. Yoder, N. T. Keen, F. Jurnak: Science **260**, 1503 (1993) [219](#)
53. F. Rampf, W. Paul, K. Binder: Europhys. Lett. **70**, 628 (2005); F. Rampf, W. Paul, K. Binder: J. Polym. Sci.: Part B: Polym. Phys. **44**, 2542 (2006) [221](#)
54. T. Vogel, M. Bachmann, W. Janke: preprint (2007), submitted to Phys. Rev. E [221](#)
55. M. Rief, H. Clausen-Schaumann, H. Gaub: Nat. Struct. Biol. **6**, 346 (1999) [225](#)
56. D. E. Smith, S. Tans, S. Smith, S. Grimes, D. L. Anderson, C. Bustamante: Nature **413**, 748 (2001) [225](#)
57. J. J. Gray: Curr. Opin. Struct. Biol. **14**, 110 (2004) [225](#)
58. E. Nakata, T. Nagase, S. Shinkai, I. Hamachi: J. Am. Chem. Soc. **126**, 490 (2004) [225](#)

59. E. Balog, T. Becker, M. Oettl, R. Lechner, R. Daniel, J. Finney, J. C. Smith: Phys. Rev. Lett. **93**, 028103 (2004); M. Ikeguchi, J. Ueno, M. Sato, A. Kidera: Phys. Rev. Lett. **94**, 078102 (2005) [225](#)
60. J. Forsman, C. E. Woodward: Phys. Rev. Lett. **94**, 118301 (2005); G. Reiter: Phys. Rev. Lett. **87**, 186101 (2001) [225](#)
61. S. Metzger, M. Müller, K. Binder, J. Baschnagel: J. Chem. Phys. **118**, 8489 (2003) [225](#)
62. T. Bogner, A. Degenhard, F. Schmid: Phys. Rev. Lett. **93**, 268108 (2004) [225](#)
63. G. M. Foo, R. B. Pandey: Phys. Rev. Lett. **80**, 3767 (1998); G. M. Foo, R. B. Pandey: Phys. Rev. E **61**, 1793 (2000) [225](#)
64. R. Hegger, P. Grassberger: J. Phys. A **27**, 4069 (1994) [225](#)
65. Y. Singh, D. Giri, S. Kumar: J. Phys. A **34**, L67 (2001); R. Rajesh, D. Dhar, D. Giri, S. Kumar, Y. Singh: Phys. Rev. E **65**, 056124 (2002) [225](#)
66. M. S. Causo: J. Chem. Phys. **117**, 6789 (2002) [225](#)
67. J. Krawczyk, T. Prellberg, A. L. Owczarek, A. Rechnitzer: Europhys. Lett. **70**, 726 (2005) [225](#)
68. J.-H. Huang, S.-J. Han: J. Zhejiang Univ. Sci. **5**, 699 (2004) [225](#)
69. M. Bachmann, W. Janke: Phys. Rev. Lett. **95**, 058102 (2005) [225](#)
70. M. Bachmann, W. Janke: Phys. Rev. E **73**, 041802 (2006) [225](#)
71. M. Bachmann, W. Janke: Phys. Rev. E **73**, 020901(R) (2006) [225](#), [226](#), [227](#)
72. M. Bachmann, W. Janke: *Chain-growth simulations of lattice-peptide adsorption to attractive substrates*. In Proceedings of the NIC Symposium 2006, John von Neumann Institute for Computing, Jülich, NIC Series vol. **32**, edited by G. Münster, D. Wolf, M. Kremer (NIC, Jülich, 2006), p. 245 [225](#), [226](#), [227](#)
73. F. Celestini, T. Frisch, X. Oyharcabal: Phys. Rev. E **70**, 012801 (2004) [226](#)
74. J. Krawczyk, T. Prellberg, A. L. Owczarek, A. Rechnitzer: J. Stat. Mech. P10004 (2004) [226](#)
75. P. Benetatos, E. Frey: Phys. Rev. E **70**, 051806 (2004) [226](#)
76. M. Breidenreich, R. R. Netz, R. Lipowsky: Europhys. Lett. **49**, 431 (2000); M. Breidenreich, R. R. Netz, R. Lipowsky: Eur. Phys. J. E **5**, 403 (2001) [226](#)
77. S. Brown: Nature Biotechnol. **15**, 269 (1997) [226](#)
78. R. Braun, M. Sarikaya, K. Schulten: J. Biomater. Sci. Polym. Ed. **13**, 747 (2002) [226](#)
79. S. R. Whaley, D. S. English, E. L. Hu, P. F. Barbara, A. M. Belcher: Nature (London) **405**, 665 (2000) [226](#)
80. K. Goede, P. Busch, M. Grundmann: Nano Lett. **4**, 2115 (2004) [226](#)
81. N. Gupta, A. Irbäck: J. Chem. Phys. **120**, 3983 (2004) [226](#)
82. F. H. Stillinger, T. Head-Gordon, C. L. Hirshfeld: Phys. Rev. E **48**, 1469 (1993); F. H. Stillinger, T. Head-Gordon: Phys. Rev. E **52**, 2872 (1995) [234](#)
83. R. Du, V. S. Pande, A. Yu. Grosberg, T. Tanaka, E. S. Shakhnovich: J. Chem. Phys. **108**, 334 (1998) [236](#)
84. V. S. Pande, D. S. Rokhsar: Proc. Natl. Acad. Sci. USA **96**, 1273 (1999) [236](#)
85. U. H. E. Hansmann, M. Masuya, Y. Okamoto: Proc. Natl. Acad. Sci. USA **94**, 10652 (1997) [236](#)
86. B. A. Berg, H. Noguchi, Y. Okamoto: Phys. Rev. E **68**, 036126 (2003) [236](#)
87. M. Bachmann, H. Arkin, W. Janke: Phys. Rev. E **71**, 031906 (2005) [236](#)
88. S. Schnabel, M. Bachmann, W. Janke: Phys. Rev. Lett. **98**, 048103 (2007); S. Schnabel, M. Bachmann, W. Janke: J. Chem. Phys. **126**, 105102 (2007) [235](#), [237](#), [238](#)
89. C. Junghans, M. Bachmann, W. Janke: Phys. Rev. Lett. **97**, 218103 (2006) [240](#), [241](#)
90. C. Junghans, M. Bachmann, W. Janke: preprint (2007), submitted to J. Chem. Phys. [240](#), [241](#)

Exact Energy Landscapes of Proteins Using a Coarse-Grained Model

Frank Dressel^{1,2} and Sigismund Kobe¹

¹ Institut für Theoretische Physik, Technische Universität Dresden, D-01062 Dresden, Germany

kobe@theory.phy.tu-dresden.de

² Biotechnologisches Zentrum, Technische Universität Dresden, D-01062 Dresden, Germany

frank.dressel@biotec.tu-dresden.de

Abstract. The understanding of the relation between the amino acid sequence and the spatial structure of the protein is an open task since many decades. Some tools for the prediction of protein structures from known ones were developed, but they let unanswered fundamental questions about properties of folded proteins and the folding process itself. Recently, coarse-grained models were developed, which are able to predict protein structures with an acceptable level of accuracy using probabilistic algorithms. In this paper, we introduce a new coarse-grained model, which neglects details on the amino acid level and uses structure elements of successive amino acids as building blocks instead. Within this approximation, we use a deterministic branch and bound algorithm, which is able to find the exact ground state and the complete low-energy landscape. The agreement of the calculated ground state with the native protein structure is shown. A possible application of the model to explain experiments with membrane proteins using dynamic force microscopy is sketched.

9.1 Introduction

Since many decades, the problem how proteins achieve their native form is unsolved. Although unknown protein structures can be predicted quite accurately on the basis of already known protein structures (see, e.g., [1]), the principles behind protein folding are not fully understood. Nowadays, more and more accurate ab initio methods, which could shed light on this issue, are under development (see, e.g., [2]). In the following, we will sketch a simple ab initio approach for protein structure and landscape prediction, which is able to capture relevant features of protein native structures.

Proteins are assembled in the ribosomes of a cell by translating RNA (ribonucleic acid) in an unstructured chain of amino acids. A single amino acid consists of a so-called backbone and a side chain. The amino acid backbones are connected via a peptide bond to form the whole protein. Proteins fold

within some split seconds into a stable three-dimensional (3d) complex, the native state. This folding is done in most cases (especially for proteins with less than 200 amino acids) without the help of catalysts. This means the 3d structure of a protein is somehow encoded in the sequence of the amino acids:

Chain of
amino acids \longrightarrow 3d structure

This fact is confirmed by mechanical unfolding experiments. After the unfolding, the proteins will refold into their native form [3].

Since the beginning of the 1990s, the number of experimentally analyzed protein structures grew in a nearly exponential fashion (see the Protein Data Bank (PDB) [4]). Today, there are more than 40 000 known structures available. Together with improvements in computational power, this leads to a raised interest in predicting protein structures. The most important point within this context is the question how the protein reaches its native state.

In 1969, Cyrus Levinthal formulated a paradox [5], which leads to the formulation of the energy-landscape theory for protein folding. If a protein with 100 amino acids has around three states per amino acid (this could be argued by Ramachandran maps, see Fig. 9.1), it ends up with around 10^{47} possible configurations. By probing 10^{13} structures per second (which is magnitudes beyond nature), it would take 10^{27} years to search all states for the ground state, more than the age of the universe. This paradox can be solved by assuming structured energy landscapes. If the structure of the energy landscape is not flat but has a broad funnel leading to the native state, folding can occur in reasonable times [7].

Minimal frustration with respect to packing of amino acids and interactions between them seems to be needed in this picture for reaching the native state of a protein in reasonable times [8]. Additionally, a small roughness can enhance folding times [9]. Thus, folding is more or less a downhill process without trapping in (deep) minima. This means that energy barriers occurring in the folding process should be more or less smaller than thermal excitation. With the knowledge of the energy landscape, thermodynamic aspects could be examined (see, e.g., [10]). Thus, calculating not only the ground state of a protein model but also the excited states with the correct energies with respect to the real structures is a promising but still challenging task because of the inherent complexity of the system.

To tackle this problem, we used a branch and bound algorithm to map the whole landscape below a certain energy threshold. This gives us on the one hand all states and all transitions between them. On the other hand, it demands discretization to handle the complexity of the problem.

This article is structured in the following way: Firstly, we discuss discretization in the context of protein models. Secondly, we introduce a fragmentation scheme followed by the energy calculation and an explanation of

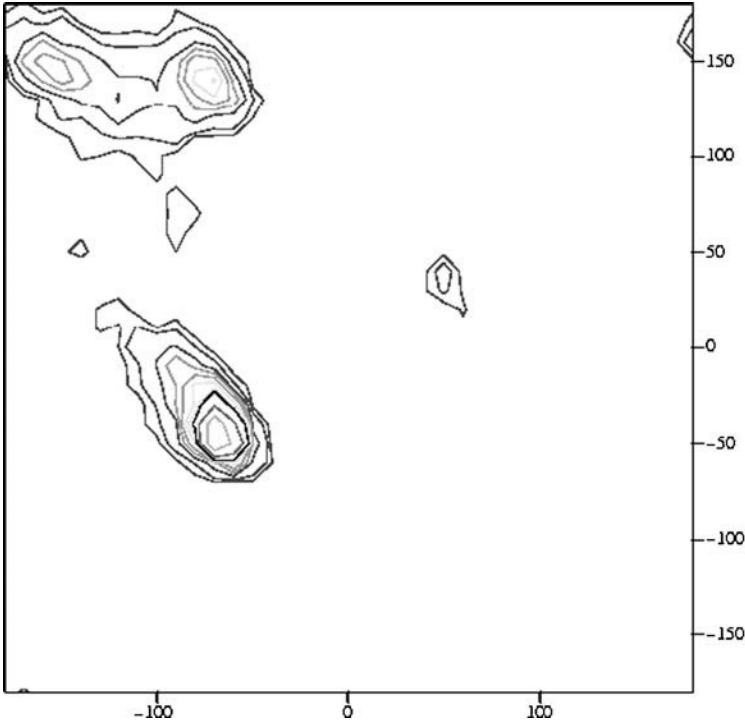


Fig. 9.1. Exemplary Ramachandran contour plot, the representation of the two main degrees of freedom (φ , ψ) in an amino acid. Three clusters exist with centers at $(-100, 140)$, $(-80, -45)$ and $(50, 45)$ [6]

the used branch and bound algorithm. This is used to calculate ground states and energy landscapes of both globular and membrane proteins in the framework of the model. Relations to the experiment are presented, e.g., for atomic force microscopy (AFM) on membrane proteins.

9.2 Structural Discretization

An amino acid consists of a backbone (N, C, O and H atoms) and a side chain (Fig. 9.2). The backbone is the same for all 20 proteinogenic amino acids, whereas their side chains differ. Thus, differentiation between amino acids is just due to the side chains.

Mostly, structural discretization has been done with respect to the torsional angles φ and ψ , (Fig. 9.3 [11]). Additionally, some models assume only one or two pseudo atoms, although an amino acid consists of many atoms. The strongest discretization is the neglecting of any detail of an amino acid. In such a way, a protein is just a collection of beads on a string

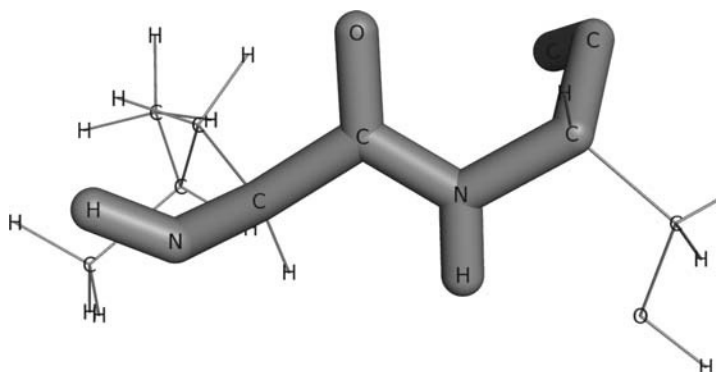


Fig. 9.2. Representation of two connected amino acids. The backbone structure is shown in *bold*. The side chains are shown as *lines*. The canonical ordering of the main backbone atoms of one amino acid is the following: N, C_α (where the side chain is attached), C. The first carbon atom of the side chain is named C_β

with regular spacing. Such an approach is used, e.g., to model proteins on cubic lattices. This procedure leads to a discretization on an amino acid level.

Further studies show that there is another way of possible discretization. For fragments of up to ten amino acids, a strong correlation between sequence and structure has been found [12]. Clustering on the basis of PDB structures leads, e.g., to approximately 30 different structural motifs for fragments of seven amino acids more or less independent of the sequence [13]. Fragments are used, e.g., for protein structure prediction algorithms such as Rosetta [14] or Robetta [15].

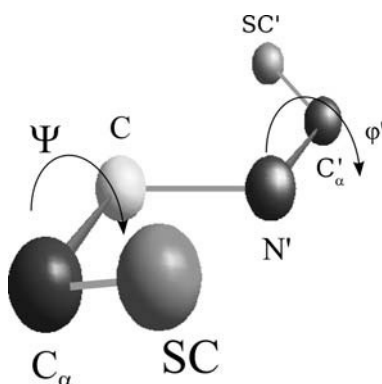


Fig. 9.3. Linkage section of two consecutive amino acids in a protein. SC denotes the side chain, the dash refers to the subsequent amino acid

9.3 Fragmentation of Protein Structures

On the basis of [13], one could think about fragmentation of protein structures to reduce the complexity. This means reference structures of m amino acids can be used as templates for the local structure of the target protein. We generate the fragments by scanning a subset of the PDB [16] with a sliding window of $m = 7\text{--}10$ amino acids. All these local PDB structures are grouped according to their first two amino acids and the last amino acid of the previous fragment. Then, the fragments within a group are clustered by k -means into 14–30 clusters using RMSD (root mean square deviation between two structures) as distance function with

$$\text{RMSD} = \sqrt{\frac{\sum_{i=1}^n (\mathbf{r}_{\text{struct. 1}, i} - \mathbf{r}_{\text{struct. 2}, i})^2}{n}}. \quad (9.1)$$

The structure with the lowest RMSD to all other structures in each cluster is used as the cluster representative. For the following results, we used a seven-amino-acid-long template set with 14 structures for every fragment.

It is possible that similar local structures are oriented in different ways in different proteins. Nevertheless, similar structures should be clustered independent of their orientation. For this issue, a canonical orthogonal coordinate system can be introduced in the following way:

$$\mathbf{e}_x = \frac{\mathbf{a}}{|\mathbf{a}|}, \quad (9.2)$$

$$\mathbf{e}_y = \frac{\mathbf{b} - (\mathbf{b} \cdot \mathbf{e}_x) \mathbf{e}_x}{|\mathbf{b} - (\mathbf{b} \cdot \mathbf{e}_x) \mathbf{e}_x|}, \quad (9.3)$$

$$\mathbf{e}_z = \mathbf{e}_x \times \mathbf{e}_y, \quad (9.4)$$

where \mathbf{a} and \mathbf{b} are vectors connecting C_{α} s (see Fig. 9.4). While scanning, every local structure from a PDB file is transformed to such a canonical coordinate system. This approach clusters such structures together, which are similar in spatial structure and orientation.

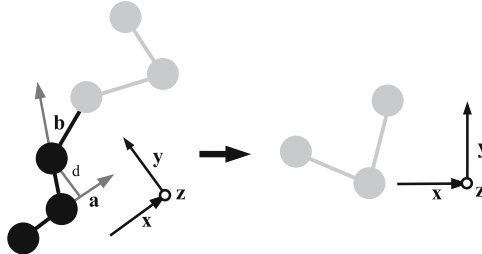


Fig. 9.4. The canonical coordinate system is defined by three amino acids (*black*). The C_{α} s are shown as circles. The coordinates of the following amino acids (*gray*) are unambiguously defined in this coordinate system



Fig. 9.5. Fragmentation of a protein. The whole structure is build up by fragments of seven amino acids. Each fragment is represented by another gray scale. The arrows and spirals denote two kinds of secondary structure: β -strands and helices [17]

The transformation ensures additionally a correct connection of neighboring fragments: Every fragment is a part of a valid PDB structure. This means that each fragment provides a valid canonical coordinate system for the next one. No alignment techniques or covering fragments are needed, cp. [18]. This procedure reduces simulation times remarkably.

One can understand this model as an extended lattice model: The fragments can be placed at a limited number of discrete places depending on the position and orientation of the previous ones. Finally, the protein structures are built up by connecting the fragments (see Fig. 9.5).

9.4 Energy Function

In real proteins, interactions between amino acids favor a few native-like structures from the huge number of alternative protein conformations. It is obvious, that discretizing in space leads automatically to deviations in distances between amino acids compared to those in the native structure. This reduces the specificity of the energy function. Although stepwise pair potentials look very naive, in some cases they are the right choice, ranging from HP models (dividing the amino acids into two classes: hydrophobic and hydrophilic, see [19, 20, 21]) to more sophisticated ones. Nevertheless, depending on the model type, the form of the energy function can be very different (see, e.g., [22, 23] for an all-atom force field).

The energy function has to be very robust in terms of distance due to the coarse-grained spatial structure of the model. This means a criteria which is independent of (small) structural deviations is needed. The required robustness circumvents a detailed dependency of the interaction scheme on the distance. One way to enhance robustness is the use of a criteria, which depends on single amino acids instead of pairs of amino acids, because deviations in the pairing of amino acids (due to local structure biases such as helices, etc.) are eliminated¹.

For determining a robust interaction scheme, we choose an inside/outside criterion for each amino acid. A similar approach was used by Wertz and Scheraga [24] for determining hydrophobicity. A subset of the PDB consisting of proteins in the SCOP (structural classification of proteins, [25]) class $\alpha+\beta$ with less than 30 % sequence similarity was scanned with respect to residues being inside or on the surface of the protein (outside). The properties “inside” or “outside” are defined for an amino acid in the following way:

$$\left\{ \begin{array}{c} \text{inside} \\ \text{outside} \end{array} \right\} \text{ if } \left\{ \begin{array}{l} |\mathbf{C}_\alpha - \mathbf{c}| < 5\text{\AA} \text{ or } (\mathbf{C}_\alpha - \mathbf{C}_\beta) \cdot (\mathbf{C}_\alpha - \mathbf{c}) < 0 \\ \text{else} \end{array} \right\} . \quad (9.5)$$

$\mathbf{C}_{\alpha/\beta}$ are the positions of the $\mathbf{C}_{\alpha/\beta}$ atoms, \mathbf{c} is the center of mass with respect to the \mathbf{C}_α s of a surrounding sphere with radius 10 Å. With this criteria, a clear separation between “inside” and “outside” of a protein is possible. The results are shown in Fig. 9.6 and Table 9.1.

The energy for bringing a single amino acid i from outside to inside can be calculated by

$$e_i = -k_B T \ln \left(\frac{n_{i,\text{in}}}{n_{i,\text{out}}} \right) , \quad (9.6)$$

where $n_{i,\text{in}}$ and $n_{i,\text{out}}$ are the number of inside and outside occurrences of amino acid i , respectively (see, e.g., [24]). The temperature is denoted by T and the Boltzmann constant by k_B . Figure 9.7 shows experimental data for amino acid solvation energies [26] compared to the calculated energies (9.6). There is a clear correlation in sign and magnitude between the experiment and the inside/outside approach. Thus, the inside/outside property reflects the ability of an amino acid to be surrounded by or shielded from water.

The interaction e_{ij} between two amino acids i and j can be described by the sum over the single amino acid solvation energy

$$e_{ij} = \alpha (e_i + e_j) , \quad (9.7)$$

where α is reciprocally proportional to the difference of numbers of nearest neighbors between inside and outside amino acids. α is approximately 1/3, this means the e_i is generated by about three surrounding amino acids. It should

¹ On the other hand, one needs a much bigger reference set for deriving significant pair interactions than for deriving properties of single amino acids.



Fig. 9.6. Inside (*dark shade*) and outside (*light shade*) amino acids in an exemplary protein (N-terminal domain of *Saccharomyces cerevisiae* RNase HI). The thin lines denote the side chains

Table 9.1. Number of occurrences for an amino acid to be inside or outside in the used set

amino acid	number inside	number outside
CYS	4582	1016
ILE	20 370	4141
SER	12 576	10 411
GLN	7373	7752
LYS	9285	15 193
ASN	8225	8928
PRO	9135	9423
THR	12 537	9622
PHE	13 353	2813
ALA	22 725	11 052
HIS	6419	3366
GLY	16 698	14 326
ASP	10 001	14 327
LEU	30 615	7107
ARG	11 327	10 441
TRP	4001	1193
VAL	23 562	6551
GLU	11 165	18 091
TYR	11 228	3529
MET	7003	1723

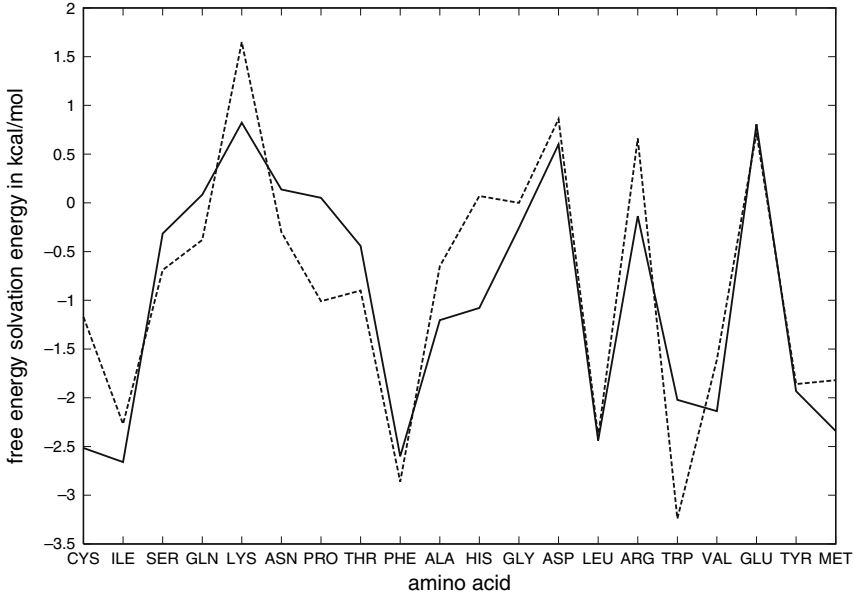


Fig. 9.7. Comparison of the experimental solvation energies taken from [26] (dotted) with the calculated energies (9.6) (straight line). The correlation coefficient between these two energies is 0.86

be noted that this ansatz gives both repulsive and attractive interactions. For Lysine, e.g., e_{Lys} is $0.5 k_B T$.

The Hamiltonian of the model protein is finally the sum over all pairwise interactions:

$$H = \sum_{\langle i,j \rangle} e_{ij} f(r_{ij}) =: \sum_{\langle i,j \rangle} e'_{ij}(r_{ij}), \quad (9.8)$$

with

$$f(r_{ij}) = \begin{cases} 1 & r_{ij} < 8 \text{ \AA} \\ 0 & \text{else} \end{cases}, \quad (9.9)$$

where r_{ij} is the distance between the C_β s of amino acids i and j . The coordinates of the C_β s are calculated according to [23]. For glycine, a virtual C_β is used. The summation over all possible pairs of two amino acids is denoted by $\langle i, j \rangle$. Interactions between direct neighbors along the chain are neglected.

It should be noted that this inside/outside approach is also applicable for nonglobular proteins, e.g., for membrane proteins.

9.5 Branch and Bound

Let us assume a system of N interacting objects (spins, atoms, amino acids, etc.). The interaction can be both repulsive and attractive. One of the most important questions is: What is the ground state of the given system?

If every object i in the system can adopt q_i different states independently of the other objects, one encounters a so-called NP complete problem. A realization of the whole system is characterized by a combination of certain states of the N objects. There is no algorithm known, which shows less than exponential behavior of CPU time consumption in dependency of system size while finding and *verifying* the exact ground state, although there are fast methods to find energetically low-lying states and local minima. Even if we cannot find and prove the ground state in less than exponential time, it is possible to reduce the magnitude of the exponent. It could be achieved by discarding as many realizations of the system as possible by a branch and bound strategy [27, 28]. This method is explained in the following on the basis of a toy example.

Assume that the interaction energy can be written as

$$e'_{ij}(r_{ij}) = e_{ij} f(r_{ij}) , \quad (9.10)$$

where $f(r_{ij})$ can be in general a function in the range between 0 and 1. Let us define E_{ideal} as the energy of the system, if all attracting interactions are totally fulfilled, this means $f(r_{ij}) = 1$:

$$E_{\text{ideal}} = - \sum_{\langle i,j \rangle} e_{ij} [\theta(e_{ij}) - 1] , \quad (9.11)$$

where $\theta(x)$ is the Heaviside step function. By placing one particle after the other at certain positions, one gets a specific realization of the system after N steps. The emerging question is: Where should each particle be placed to minimize the overall energy (9.8)? Let us assume a discretization in space to get q possible positions for the particles. Because this should give a sufficient fine discretization, already for moderate system sizes this gives an incredible amount of possible realizations of the system to be searched for the ground state. For the first particle, one has to take q possibilities into account. Because two particles cannot be at the same position, one has $q(q-1)$ possibilities for the second one, and so on. It is obvious that the search space grows enormously while adding more particles. If one knows as early as possible that adding more particles to an incomplete system will never result in the lowest energy of the complete system, one could stop and try another positioning of the placed particles.

While adding particles one by one, two possibilities emerge every time a new particle is added:

- the particle fulfills every attracting interaction with all other particles in the full strength,

- the particle misses some attractive interaction with other particles or it does not interact with the full strength or it goes into some repulsive interactions with other particles.

In the first case, the interaction energy for this particle is already accounted in E_{ideal} . In the second case, E_{ideal} is too optimistic with respect to the added particle. How could this help to fasten the search? Let us assign E_{ideal} to the subsystem consisting of one particle. The energy of the subsystem with k particles is denoted by $E(k)$, thus $E(1) = E_{\text{ideal}}$. While adding more particles, $E(k)$ becomes

$$E(k) = E(k-1) + \Delta E. \quad (9.12)$$

According to (9.11), the energy difference ΔE is positive:

$$\Delta E(k) = \sum_{i=0}^{k-1} \{e'_{ik} + e_{ik} [\theta(e_{ik}) - 1]\} \geq 0, \quad (9.13)$$

where the second term reflects the contribution of amino acid k to the ideal energy. This results in the following relation, which is crucial in understanding branch and bound:

$$E(k) \geq E(k-1) \quad \forall k. \quad (9.14)$$

If $E(k)$ is greater than a threshold energy E_{bound} , one can skip all realizations with this arrangement of the first k particles because it will never result in an energy lower than E_{bound} .

Figure 9.8 shows an example of branch and bound, applied to a simple protein (Tryptophan cage protein, 20 amino acids) in our model. Here, a certain state is assigned to each (protein) fragment (seven amino acids in length). This state determines the structure of the fragment and also the spatial orientation of the next fragment because it is connected to the previous one, see Sect. 9.3.

We start with calculating the ideal energy of the whole system, $E_{\text{ideal}} = -10.0$ (arbitrary units) according to (9.11). Now we consider the first fragment. As in the toy example mentioned above, the ideal energy is assigned to the subsystem without any possible interactions, which is the system with one particle. Otherwise, in the case of protein fragments, which can interact with itself, E_{ideal} has to be assigned to the empty system: $E(0) = E_{\text{ideal}}$. Thus,

$$E(1) = E_{\text{ideal}} + \sum_{\langle i,j \rangle}^{i=6} \{e'_{ij} + e_{ij} [\theta(e_{ij}) - 1]\}. \quad (9.15)$$

In Fig. 9.8, two paths to complete structures are shown, whereas the rest of the conformational tree is just sketched. Let us consider the path to the ground state with an arbitrarily chosen bounding energy $E_{\text{bound}} = -2.0$. $E(1)$ is $-9.2 < E_{\text{bound}}$; thus the second fragment is attached resulting in $E(2) = -6.3$. $E(2)$ is still below E_{bound} ; therefore, we attach the last fragment. This gives

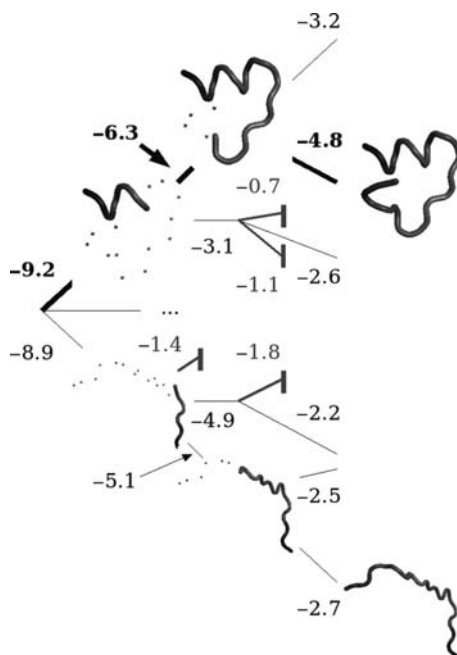


Fig. 9.8. Branch and bound tree for an exemplary protein. The *bold lines* denote the path to the ground state. The *stars* denote the remaining amino acids belonging to the complete structures at the end of the corresponding branch. Cut branches are denoted by *bars*

an energy of $E(3) = -4.8$, which is the energy of the whole structure. Let us consider a second path: $E(1) = -8.9$, $E(2) = -1.4$. Because -1.4 is above the bounding energy, the rest of this branch can be skipped (denoted by a bar). With this algorithm, all structures with energies below $E_{\text{bound}} < -2.0$ are calculated. Among them the ground state can be identified.

9.6 Results

By applying the above-mentioned method, we can calculate the ground state for proteins of up to 70 amino acids. Figure 9.9 shows the ground state of the beta subunit of translation initiation factor 2 from the archaeon *Methanococcus jannaschii* (PDBid: 1K8B) in the model and the according experimental structure. Twenty-two of the 52 residues can be aligned within 6.5 \AA RMSD (calculated with TM-score [29]) to the native state, which means 42% of the structure is correctly predicted. The secondary structure, consisting of the two helices and four β -strands, is resembled at least for the last helix and the last two β -strands.



Fig. 9.9. Ground state structure of 1K8B. The simulated structure is shown in *dark shade* and the PDB structure in *light shade*. The overall RMSD to the experimental structure is 8.9 Å

Figure 9.10 shows the N-terminal domain of *Saccharomyces cerevisiae* RNase HI (PDB id: 1QHK). Nineteen out of 47 amino acids can be aligned to the native state with an RMSD below 6.5 Å. The global RMSD is 8.3 Å. The secondary structure is recognizable as well as the tertiary structure. A further interesting example is the Tryptophan cage protein (PDBid: 1L2Y, see also Fig. 9.8). It folds faster than other proteins and has a defined secondary and tertiary structure, regardless of its small size of 20 amino acids. Its ground state is shown in Fig. 9.11.

The ground state alone does not characterize a whole protein. For understanding protein structures, it is important to look also at excited states, which

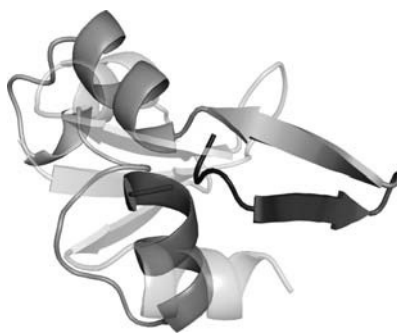


Fig. 9.10. Ground state structure of 1QHK. The simulated structure is shown in *dark shade* and the PDB structure in *light shade*. All secondary structure elements are present, although the tertiary structure shows some deviations resulting in the observed global RMSD of 8.3 Å

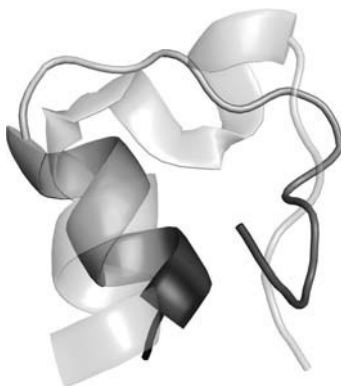


Fig. 9.11. Ground state structure of 1L2Y. The simulated structure is shown in *dark shade* and the PDB structure in *light shade*. The secondary and tertiary structures are completely resembled. The RMSD to the experimental structure is 4.4 Å

can have a nonzero probability of occurrence. The flexibility of a protein's native state can be experimentally determined, e.g., by NMR (see Fig. 9.12). The intrinsic flexibility at room temperature constrains in most cases to the loop and end regions of a protein, whereas the secondary structure elements are more or less stable. But this holds just for low temperature. If one increases the temperature (thermal denaturation) or applies a force (mechanical denaturation), also strongly excited states become important. This means on the other hand: The knowledge of structure and energy of not only the ground state but of all excited states (the energy landscape) is needed.

If the energy landscape is known, the partition function can be calculated by

$$Z = \sum_i e^{-\frac{E_i}{k_B T}}, \quad (9.16)$$



Fig. 9.12. Overlay of five NMR structures of 1AE5. The flexibility increases dramatically at the ends (unstructured regions *right* and *left*) and at loop regions of the protein

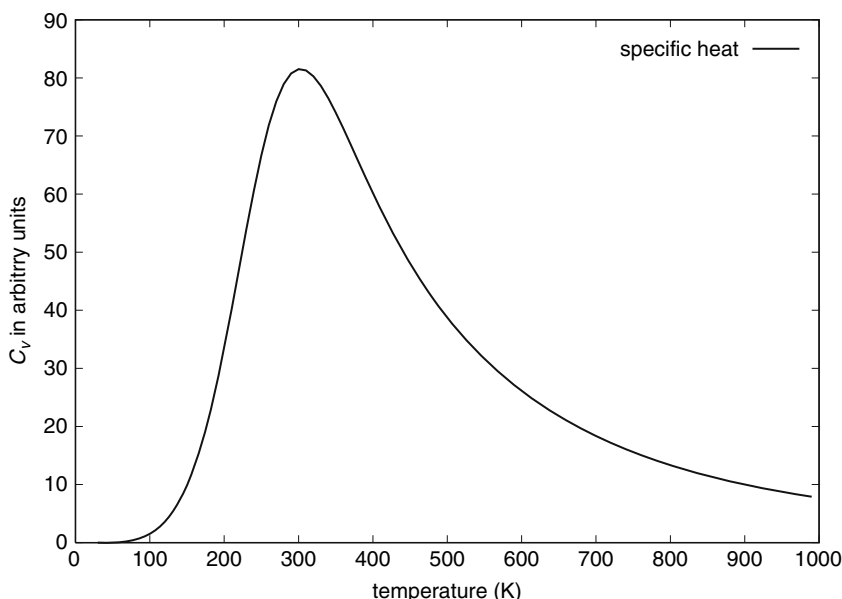


Fig. 9.13. Dependency of specific heat (in arbitrary units) of 1L2Y on the temperature

where the sum runs over all possible protein structures i . With the partition function all thermodynamic properties can be calculated. As an example, the dependency of the specific heat on the temperature is sketched for Tryptophan cage protein (PDB id: 1L2Y) in Fig. 9.13. The corresponding energy landscape for this protein is shown in Fig. 9.14 [11].

A very important field in protein science is the task to understand membrane protein structures. Membrane proteins are involved in many important functions in cells such as ion transport and signal perception. Mutations in the sequence and/or misfolding can lead to serious diseases such as Alzheimer's disease, diabetes and blindness (see, e.g., [30]). Because it is very difficult to determine the structure of membrane proteins directly, not so many structures are known. As of the beginning of 2007, there are approximately 80 structures of membrane proteins in the PDB with less than 30% sequence similarity, which means that membrane proteins are extremely underrepresented (see, e.g., [31]).

With an appropriate energy function, which is generated by applying (9.6) to a reference set of membrane proteins, we are able to model membrane proteins (see Fig. 9.15). In the case of 1X9B, e.g., the secondary structure is resembled correctly as well as the tertiary structure; the RMSD is 7.1 Å. This protein was part of the sixth CASP competition (critical assessment of structure prediction) 2004 [32]. Our model structure would be ranked with respect to RMSD as 11th out of 43 different predictions for the structure.

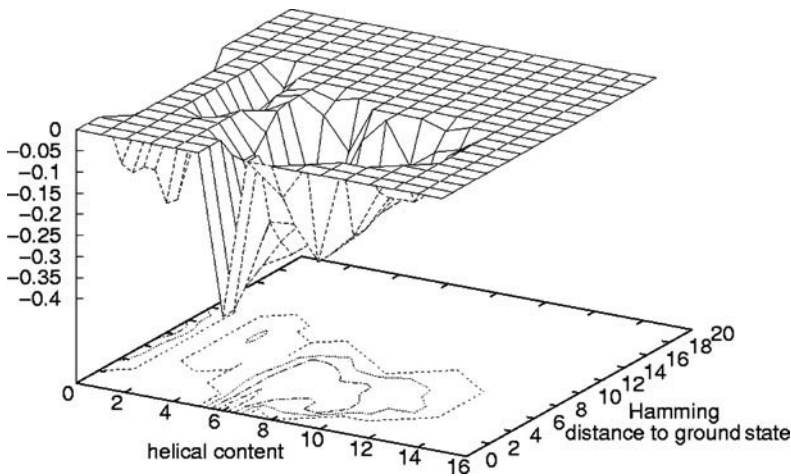


Fig. 9.14. Energy landscape of Tryptophan cage protein. The energy (in arbitrary units) is shown over Hamming distance (how many constituents of the protein model have a different state with respect to the ground state) and helical content

Because of the difficulties in membrane protein structure determination, new experimental methods such as atomic force microscopy (AFM) [33] are applied. A common experiment in this context is pulling with constant velocity on one end of the membrane protein and measuring the forces in dependency of the pulled distance. An exemplary force–distance curve is shown in Fig. 9.16 above. The hope is that with such an experiment, insight into the structural properties of the protein can be gained. In the context of the worm-like chain model [34], e.g., the increasing flank of such an AFM peak can be interpreted

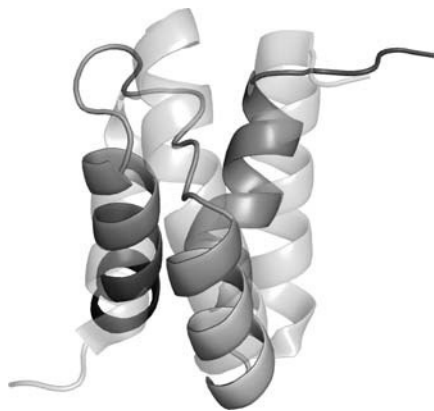


Fig. 9.15. Ground state structure of the membrane protein 1X9B (*dark shade*) and the corresponding PDB structure (*light shade*)

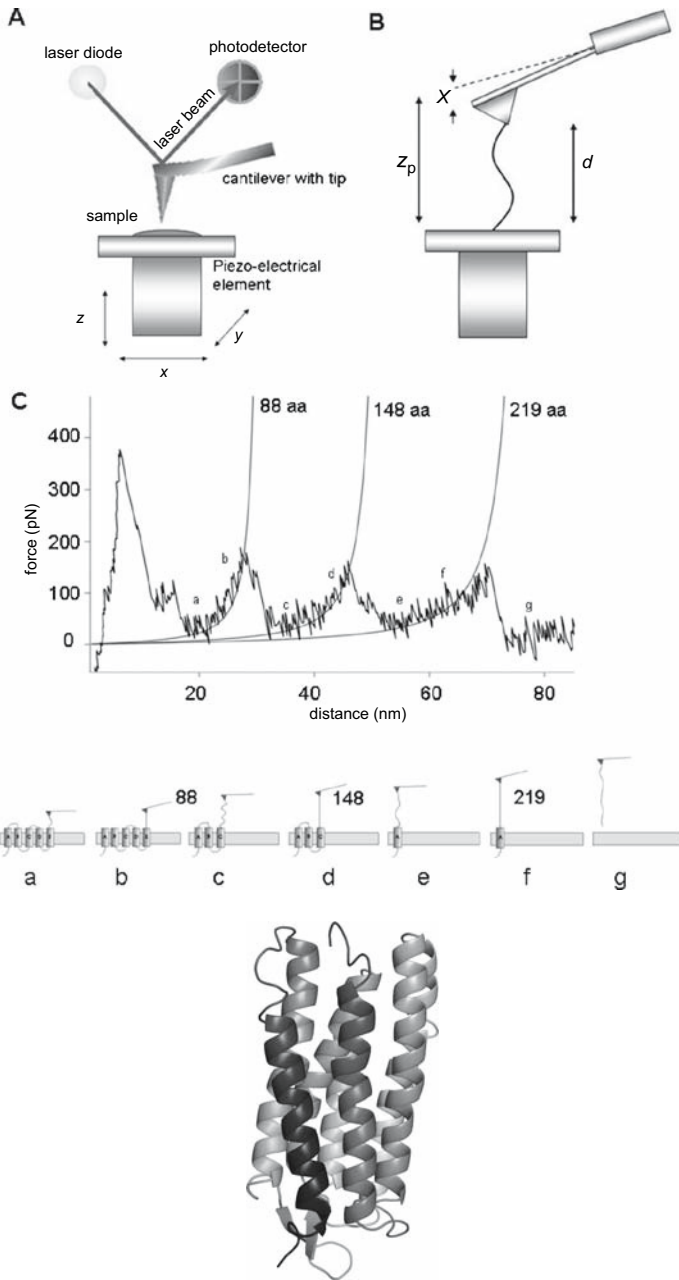


Fig. 9.16. Above: Sketch of an AFM experiment [35]. **A** and **B**: Experimental setting, **C**: Resulting force curves and interpretation. Below: X-ray structure of Bacteriorhodopsin (PDB id: 1BRR)

as the stretching of a (more or less unfolded) part of the protein, whereas the decreasing flank of a peak can be interpreted as the rapid (and cooperative) unfolding of a part of the protein, (e.g., helices, β -sheets, etc.).

We simulated the mechanical unfolding of the first helix (helix A) of Bacteriorhodopsin (PDB id: 1BRR, see Fig. 9.16, below) by calculating the ground state as well as the whole energy landscape. Within the model context this results in ca. 16 000 different structures. The energy landscape of helix A is shown in Fig. 9.17. The principal experimental setting is shown in Fig. 9.16. While moving the cantilever, it is obvious that the force applied to a structure i can be written as

$$F_i(t) = -k[v \cdot t + (d_{\text{gs}} - d_i)] , \quad (9.17)$$

where d_i is the end-to-end distance of structure i and k is the spring constant. It is assumed that the cantilever at time $t = 0$ is at the position d_{gs} , the subscript “gs” denotes the ground state with zero force. Thus, the energy for the structure i is

$$E_i = \sum_{\langle i,j \rangle} e'_{ij} + \frac{k}{2} [v \cdot t + (d_{\text{gs}} - d_i)]^2 . \quad (9.18)$$

For simulating the pulling process a Monte Carlo algorithm (MC) is applied. Although the energy in our model and the spring constant as well as

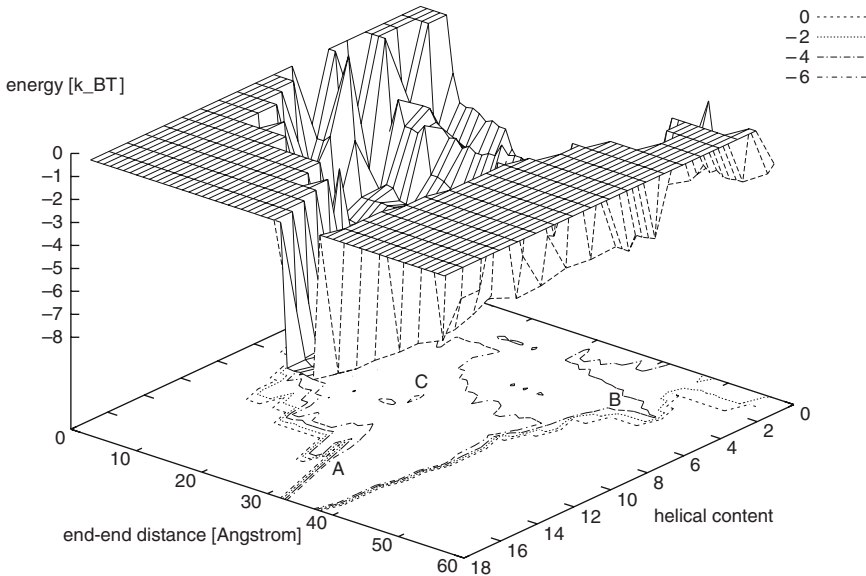


Fig. 9.17. Energy landscape of helix A of Bacteriorhodopsin (PDB id: 1BRR): energy versus helical content and end-to-end distance. The end-to-end distance is discretized in intervals of length 1 Å. Ground state basin (A), extended conformations (B) and excited states (C) are marked

the velocity v in the experiment [36] are known, there is a problem concerning the time scales in MC simulations. In principle, for every MC step, a term

$$p = e^{-\frac{\Delta E_{ij}}{k_B T}} \quad (9.19)$$

is compared to a random variable r between 0 and 1. If r is less than p , then the system goes from state i to state j . Nevertheless, the pulling velocity v connects the real time interval Δt with the number of MC steps. This can be easily seen: If the pulling speed goes to zero, there is nearly no change in the force applied to the protein in the time interval Δt , the system will equilibrate. This can be reflected by using many MC steps for the time interval Δt . If, on the other hand, the pulling speed is very high, the force will change rapidly in the time interval Δt . The system will not reach equilibrium and thus just a few MC steps are needed to simulate the time interval Δt .

Therefore, we use the following approach for the time interval Δt :

$$\Delta t = \frac{D}{vm}, \quad (9.20)$$

where m is the number of MC steps for each run and D is the maximal pulling distance. With this approach, the dependency of (9.17) and (9.18) on velocity v and real time t is replaced by a dependency on the simulation parameters D and m . By varying D and m we can assess different pulling speeds in the simulation. The results are presented in Fig. 9.18, showing that the force increases with increasing pulling speed. This corresponds with experiments [36].

A similar effect is observed using different spring constants. Figure 9.19 shows the results of our simulation. A large k leads to a strong force even within small pulling distances and so it has the same effect on the magnitude of forces like increased pulling speeds. Also a shift of the maximum toward smaller pulling distances is observed. This could be understood because a stiff cantilever would force the proteins more to change to higher end-to-end distances than a softer one. The presented results are in good agreement with experiments regarding the position of the peak in the force-distance curve (see [36]). But the simulated forces are by a factor of two smaller than in the experiment.

The whole mechanical unfolding can be understood as an interplay between entropy in state space, free energy of the structures and pulling forces, see Fig. 9.17. Without force, the protein will stay more or less in the ground state basin (A). When the protein is pulled, it moves from the ground state basin (A) to structures with higher energy and higher end-to-end distance (B). From states with higher energy more structures with lower end-to-end distances are accessible (C). This results in higher forces because the cantilever is stronger bended.

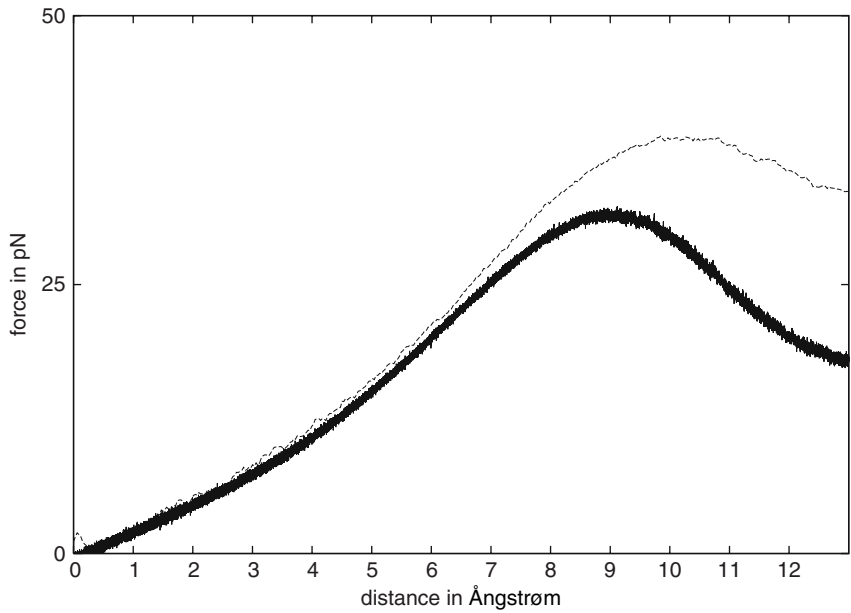


Fig. 9.18. Dependency of force from distance at constant velocity for the model of helix A of a protein (PDB id: 1BRR). High and low pulling velocities are represented by *dashed* and *straight* curves, respectively

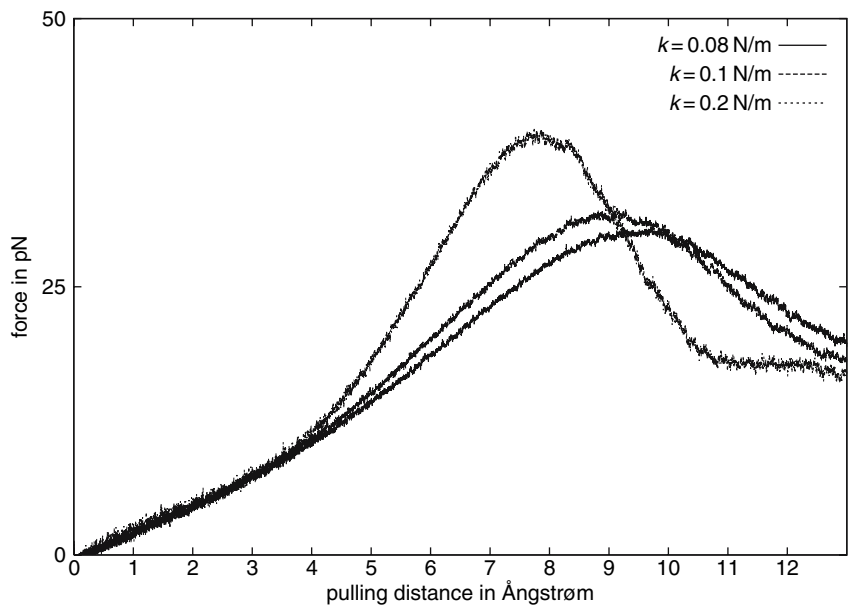


Fig. 9.19. Effect of different spring constants k on the force–distance curve. The maximum forces increase with increasing k

9.7 Summary

The energy landscape concept is used to investigate different aspects of protein structures, e.g., specific heat and force–distance behavior under external forces. For mapping complete energy landscapes, on the one hand an adequate discretization of protein structures is needed. On the other hand, algorithms, have to be applied which can handle the huge amount of possible structures. The proposed coarse-grained model is able to reproduce ground states, which are similar to measured native states as well for globular as for membrane proteins.

The presented approach is capable of coarse graining protein structures in such a way that exact optimization techniques can be applied. This opens up the possibility to examine the complete low energy landscape with all the possible transitions between two states in the framework of the model. In this context, it is possible to follow the folding/unfolding process dynamically. Some of the still unsolved problems are the following:

- Connecting the transition rates in simulation with those from experiment
- Following the whole mechanical unfolding of proteins, especially for membrane proteins
- Comparing simulation with experiments on mutants: explaining different native structures and stability

Acknowledgements

The authors are indebted to A. Marsico and D. Labudde for discussions on the AFM experiments. We are grateful to U. Büttner, N. Hlubek, V. Lankau and M. Schroeder for many useful discussions and for critical reading of the manuscript.

References

1. Y. Zhang, J. Skolnick: Proc. Natl. Acad. Sci. USA **101**, 7594 (2004) [247](#)
2. J. S. Yang, W. W. Chen, J. Skolnick, E. I. Shakhnovich: Structure **15**, 53 (2007) [247](#)
3. B. Samori, G. Zuccheri, P. Baschieri: ChemPhysChem **6**, 29 (2004) [248](#)
4. H. M. Berman, J. Westbrook, Z. Feng, G. Gilliland, T. N. Bhat, H. Weissig, I. N. Shindyalov, P. E. Bourne: Nucleic Acids Res. **28**, 235 (2000) [248](#)
5. C. Levinthal: How to fold graciously. In *Mossbauer Spectroscopy in Biological Systems: Proceedings of a Meeting Held at Allerton House*, edited by J. T. P. DeBrunner, E. Munck (University of Illinois Press, Monticello, IL, 1969), pp. 22–24 [248](#)
6. G. J. Kleywegt, T. A. Jones: Structure **4**, 1395 (1996) [249](#)
7. J. D. Bryngelson, J. N. Onuchic, N. D. Socci, P. G. Wolynes: Proteins Struct. Funct. Genet. **21**, 167 (1995) [248](#)

8. J. D. Bryngelson, P. G. Wolynes: Proc. Natl. Acad. Sci. USA **84**, 7524 (1987) [248](#)
9. I. Shrivastava, S. Vishveshwara, M. Cieplak, A. Maritan, J. R. Banavar: Proc. Natl. Acad. Sci. USA **92**, 9206 (1995) [248](#)
10. A. Irbäck, S. Mohanty: Biophys. J. **88**, 1560 (2005) [248](#)
11. F. Dressel, S. Kobe: Chem. Phys. Lett. **424**, 369 (2006) [249](#), [261](#)
12. C. Bystroff, K. T. Simons, K. F. Han, D. Baker: Curr. Opin. Biotechnol. **7**, 417 (1996) [250](#)
13. O. Sander, I. Sommer, T. Lengauer: BMC Bioinformatics **7**, 14 (2006) [250](#), [251](#)
14. K. T. Simons, C. Kooperberg, E. Huang, D. Baker: J. Mol. Biol. **268**, 209 (1997) [250](#)
15. D. Chivian, D. E. Kim, L. Malmstroem, J. Schonbrun, C. A. Rohl, D. Baker: Proteins **61** (Suppl. 7) 157 (2005) [250](#)
16. U. Hobohm, M. Scharf, R. Schneider, C. Sander: Protein Sci. **1**, 409 (1992) [251](#)
17. All pictures showing protein structures are generated with PyMol, see W. L. DeLano: The PyMOL User's Manual, DeLano Scientific, Palo Alto, CA, USA (2002) [252](#)
18. J. Lee, S. Y. Kim, K. Joo, I. Kim, J. Lee: Proteins Struct. Funct. Bioinform. **56**, 704 (2004) [252](#)
19. M. T. Wolfinger, S. Will, I. L. Hofacker, R. Backofen, P. F. Stadler: Europhys. Lett. **74**, 726 (2006) [252](#)
20. F. L. Custodio, H. J. C. Barbosa, L. E. Dardenne: Genet. Mol. Biol. **27**, 611 (2004) [252](#)
21. M. Bachmann, W. Janke: *Thermodynamics of protein folding from coarse-grained models' perspectives*, Chap. [8](#) of this volume [252](#)
22. S. Miyazawa, R. L. Jernigan: Macromolecules **18**, 534 (1985)
23. C. Micheletti, F. Seno, J. R. Banavar, A. Maritan: Proteins Struct. Funct. Genet. **42**, 422 (2001) [255](#)
24. D. H. Wertz, H. A. Scheraga: Macromolecules **11**, 9 (1978) [253](#)
25. A. G. Murzin, S. E. Brenner, T. Hubbard, C. Chothia: J. Mol. Biol. **247**, 536 (1995) [253](#)
26. W. C. Wimley, T. P. Creamer, S. H. White: Biochemistry **35**, 5109 (1996) [253](#), [255](#)
27. S. Kobe, A. Hartwig: Comput. Phys. Commun. **16**, 1 (1978)
28. S. Kobe, J. Krawczyk: Ground states, energy landscape and low-temperature dynamics in $\pm J$ spin glasses. In *Computational Complexity and Statistical Physics*, edited by A. Percus, G. Istrate, C. Moore (Oxford University Press, Oxford, 2006), pp. 141–155
29. Y. Zhang, J. Skolnick: Proteins **57**, 702 (2004) [258](#)
30. C. R. Sanders, J. K. Myers: Annu. Rev. Biophys. Biomol. Struct. **33**, 35 (2004) [261](#)
31. P. Walian, T. A. Cross, B. K. Jap: Genome Biol. **5**, 215 (2004) [261](#)
32. CASP6: 6th Community Wide Experiment on the Critical Assessment of Techniques for Protein Structure Prediction, Gaeta (Italy), December 4–8, 2004 [261](#)
33. G. Binnig, C. F. Quate, Ch. Gerber: Phys. Rev. Lett. **56**, 930 (1986) [262](#)
34. O. Kratky, G. Porod: Rec. Trav. Chim. Pays-Bas. **68**, 1106 (1949) [262](#)
35. A. Marsico, D. Labudde, T. Sappra, D. J. Muller, M. Schroeder: Bioinformatics **23**, 231 (2006) [263](#)
36. H. Janovjak, J. Struckmeier, M. Hubain, A. Kedrov, M. Kessler, D. J. Muller: Structure **12**, 871 (2004) [265](#)

Protein Folding, Unfolding and Aggregation Studied Using an All-Atom Model with a Simplified Interaction Potential

Anders Irbäck

Computational Biology and Biological Physics Group, Department of Theoretical Physics, Lund University, Sölvegatan 14A, S-223 62, Sweden
anders@thep.lu.se

Abstract. Finding a suitable transferable energy function for modeling of how different proteins fold into their respective native states is a major challenge in biophysics. Here, we discuss an all-atom protein model with implicit water and some studies based on this model. The model has a simplified and computationally convenient energy function. Despite its simplicity, the model has been found to quite successfully describe the structure and melting behavior of several peptides with about 20 amino acids. The same model, with unchanged parameters, has also been used to investigate the aggregation behavior of a fragment of Alzheimer's A β peptide and the mechanical properties of the 76-residue protein ubiquitin.

10.1 Introduction

How a protein interacts with other biological molecules, and therefore how it functions, depends crucially on its three-dimensional structure [1]. Knowledge of protein structures is therefore central to understanding biology. A protein structure is, on the other hand, not a completely static object, so having a single picture of the structure need not be sufficient. In fact, there are proteins that are unstructured or only partially structured and yet functional [2]. Bioinformatic analyses of genomes suggest that such proteins, which may adopt a specific structure upon binding to their biological targets, are more common than previously thought [3]. Another manifestation of the flexibility of protein chains is when misfolded proteins aggregate to form so-called amyloid fibrils [4]. Amyloid fibrils have been observed in many human disorders, including Alzheimer's disease and type II diabetes.

These examples clearly illustrate that being able to simulate protein dynamics on the computer is important in itself and not “only” as a means for structure prediction. Protein simulations are, however, notoriously difficult. The mere size of a protein molecule makes a quantum-mechanical calculation

unfeasible, so the models currently used are classical, and their level of detail varies. Studies at different levels of resolution serve complementary roles. Coarse-grained approaches, in the form of lattice or reduced off-lattice models, offer computational convenience and transparency and have been used to gain many useful insights into general aspects of protein folding (for a review, see [5]; see also the contribution by Bachmann and Janke in Chap. 8 of this volume). To study more detailed questions regarding specific proteins, it is often natural, and perhaps even necessary, to turn to atomistically detailed models. For all-atom simulations of proteins, there exists a number of widely used force fields, including AMBER [6], CHARMM [7], GROMOS [8] and OPLS-AA [9]. These force fields contain a large number of parameters, which typically are determined using experimental data or quantum-mechanical calculations on smaller molecules. The surrounding water molecules¹ are sometimes explicitly included in the calculations, but far from always, because it is computationally very expensive.

All-atom protein simulations are being used to study a wide range of problems, from ligand binding to unfolding and refolding studies. To fold an arbitrary amino acid sequence to its native state, from a random initial conformation, remains, however, a challenge. Such simulations are nontrivial also for small proteins [10], or peptides, for which the calculations are feasible from a purely computational perspective, which indicates that force-field development and refinement is a problem that needs continued attention.

This article discusses a simplified all-atom model for protein folding studies [11, 12, 13]. The model is based on a simple ansatz for the interaction potential. The determination of the potential is different compared to many other models because the potential is calibrated against data pertaining to folding properties of whole chains rather than properties of small groups of atoms. The calibration involves high-statistics folding simulations for a set of experimentally well-characterized peptides. The idea is to successively refine the potential by studying more and more sequences, which will impose new constraints on the model. It should be stressed that changes of the potential are accepted only if they are backward compatible, so that the model does not lose its ability to fold previously studied sequences.

The current version of this model is able to fold several sequences with about 20 amino acids. There are also examples of sequences of this size that the model fails to fold. One example is the tryptophan zipper β -hairpins [14], which make β -hairpins in the model but with the wrong topology. The set of sequences that the model can fold includes both α -helical and β -sheet peptides. Furthermore, for these sequences, the model provides a good description not only of the folded structure but also of the folded population and its temperature dependence [13]. Without changing any parameters, the model was also used to study the aggregation properties of the 7-amino acid fragment

¹ Throughout the article, it is assumed that the proteins are in aqueous solution. Membrane proteins are not considered.

A β_{16-22} of the amyloid- β peptide associated with Alzheimer's disease, with very promising results [15]. Recently, the mechanical [16] and the thermal [17] unfolding of ubiquitin, a protein with 76 amino acids, was investigated, again using exactly the same model. All the simulations of this model were performed using Monte Carlo methods.

The article is organized as follows. Section 10.2 gives a brief description of the model and the Monte Carlo methods used. Section 10.3 discusses the results obtained in the different studies mentioned above. A brief summary can be found in Sect. 10.4.

10.2 Model and Methods

The model studied contains all atoms of the protein chains, including hydrogen atoms, but no explicit water molecules. It assumes fixed bond lengths, bond angles and peptide torsion angles (180°), so that each amino acid has only the Ramachandran torsion angles ϕ , ψ and a number of side-chain torsion angles as its degrees of freedom.

The energy function of the model is intended to provide an effective description of the most relevant interactions. Many electrostatic interactions are ignored; they are assumed to be less important due to screening by the surrounding water. In the future, the energy function may be further developed with the inclusion of new terms such as Coulomb interactions between side-chain charges, but not before it becomes clear that they are needed.

A basic and somewhat unusual feature of the model is that its energy function is determined by studying folding properties of whole chains. For this approach to be computationally feasible, it is desirable to work with a simple potential with relatively few parameters to tune. At first glance, it may seem strange to combine such a potential with a detailed all-atom description of the protein chains; why spend time on a complicated all-atom description when the potential anyhow is simplified? It should therefore be stressed that including more atoms generally tends to make the potential simpler. To illustrate this point, consider the local interactions along the backbone, which are known to be important for the overall shape of the energy landscape [18]. It is well known that simple steric clashes explain much of the shape of the Ramachandran ϕ , ψ map [19]. In a model where some atoms are missing, the corresponding clashes must be accounted for through effective and generally more complicated interactions.

10.2.1 Energy Function

The energy function

$$E = E_{\text{loc}} + E_{\text{ev}} + E_{\text{hb}} + E_{\text{hp}} \quad (10.1)$$

is composed of four terms. The term E_{loc} is local in sequence and represents an electrostatic interaction between adjacent peptide units along the chain. The other three terms are nonlocal in sequence. The excluded volume term E_{ev} is a $1/r^{12}$ repulsion between pairs of atoms.

The terms responsible for driving folding in this model are E_{hb} and E_{hp} , which represent hydrogen bonds and an effective hydrophobic attraction between nonpolar side chains, respectively. E_{hb} contains two kinds of hydrogen bonds, backbone–backbone bonds and bonds between charged side chains and the backbone. The functional form of the hydrogen bond potential is $u(r)v(\alpha, \beta)$, where the radial part is a 12,10-Lennard-Jones potential:

$$u(r) = 5 \left(\frac{\sigma}{r} \right)^{12} - 6 \left(\frac{\sigma}{r} \right)^{10}. \quad (10.2)$$

The angular dependence, $v(\alpha, \beta)$, has the form

$$v(\alpha, \beta) = \begin{cases} (\cos \alpha \cos \beta)^{1/2} & \text{if } \alpha, \beta > 90^\circ, \\ 0 & \text{otherwise} \end{cases} \quad (10.3)$$

where $\alpha = \beta = 180^\circ$ corresponds to a perfectly aligned hydrogen bond.

The effective hydrophobic attraction, E_{hp} , has the pairwise additive form

$$E_{\text{hp}} = - \sum_{I < J} M_{IJ} C_{IJ}, \quad (10.4)$$

where C_{IJ} is a measure of the degree of contact between side chains I and J , and M_{IJ} sets the energy that a pair in full contact gets. Specifically, C_{IJ} is defined as

$$C_{IJ} = \frac{1}{N_I + N_J} \left[\sum_{i \in A_I} f(\min_{j \in A_J} r_{ij}^2) + \sum_{j \in A_J} f(\min_{i \in A_I} r_{ij}^2) \right], \quad (10.5)$$

where A_I and A_J are predetermined sets of nonpolar side-chain atoms and $f(x)$ is a piecewise linear function which is 1 if $x < (3.5 \text{ \AA})^2$ and 0 if $x > (4.5 \text{ \AA})^2$. Roughly speaking, C_{IJ} is the fraction of atoms in A_I or A_J that are in contact with some atom from the other side chain.

The energy parameters of the model, like the M_{IJ} s in (10.4), are internally in the simulations numbers on a dimensionless scale. The correspondence (a constant factor) of this scale to the physical energy scale is not obvious due to the effective character of the interaction terms. It can be determined by using the model prediction of the dimensionless energy value for an observable and the experimental value for the same. We chose to use the melting temperature of the Trp cage for this calibration, so the calculated melting temperature of this peptide was set to its experimental value, $T_m = 315 \text{ K}$ [20]. It must be emphasized that the energy scale was left unchanged when studying the other peptides.

For simplicity, this description of the potential was for a single protein chain. The model can be easily extended to multichain systems. Different chains then interact by excluded-volume interactions, hydrogen bonding and hydrophobic attraction between nonpolar side chains. The interchain interactions have the same form as the corresponding intrachain interactions.

10.2.2 Monte Carlo Methods

The thermodynamics of this model can be simulated by using simple single-variable Monte Carlo updates. The torsion angles are then turned one by one, and each change is followed by a Metropolis accept/reject question. This update can be applied to both backbone and side-chain degrees of freedom. However, when applied to a backbone angle, this method tends to lead to a large nonlocal deformation of the chain, which is likely to be rejected if the chain is compact.

Therefore, it is desirable to also include a backbone update less drastic than the single-angle update. One possibility is to use a strictly local method such as the concerted-rotation algorithm [21]. For long chains, such an update has the advantage of leaving a large part of the energy function unchanged. However, strictly local methods tend to be quite complex, and the proteins amenable to atomic-level simulations are in any case not very large. Instead, we have therefore chosen to use biased Gaussian steps [22], a semi-local method that is flexible and easy to implement. This method simultaneously turns n adjacent torsion angles τ_i along the backbone, where n typically is 7 or 8. Let $\boldsymbol{\tau} = (\tau_1, \dots, \tau_n)$. A tentative new set of angles, $\boldsymbol{\tau}'$, is generated with a bias toward local deformations. Specifically, using a conformation-dependent $n \times n$ matrix \mathbf{G} such that $(\boldsymbol{\tau}' - \boldsymbol{\tau})^T \mathbf{G} (\boldsymbol{\tau}' - \boldsymbol{\tau}) \approx 0$ for changes corresponding to local deformations, $\boldsymbol{\tau}'$ is drawn from the Gaussian distribution

$$W(\boldsymbol{\tau} \rightarrow \boldsymbol{\tau}') = \frac{(\det \mathbf{A})^{1/2}}{\pi^3} \exp [-(\boldsymbol{\tau}' - \boldsymbol{\tau})^T \mathbf{A} (\boldsymbol{\tau}' - \boldsymbol{\tau})], \quad (10.6)$$

$$\mathbf{A} = \frac{a}{2}(1 + b\mathbf{G}), \quad (10.7)$$

where $\mathbf{1}$ denotes the $n \times n$ unit matrix and a and b are tunable parameters. The parameter a controls the acceptance rate, whereas b sets the degree of bias toward local deformations. Typical values are $a = 300 (\text{rad})^{-2}$ and $b = 10 (\text{rad}/\text{\AA})^{-2}$. Finally, the new conformation $\boldsymbol{\tau}'$ is subject to an accept/reject step, with probability

$$P_{\text{acc}}(\boldsymbol{\tau} \rightarrow \boldsymbol{\tau}') = \min \left(1, \frac{W(\boldsymbol{\tau}' \rightarrow \boldsymbol{\tau})}{W(\boldsymbol{\tau} \rightarrow \boldsymbol{\tau}')} \exp[-(E' - E)/kT] \right) \quad (10.8)$$

for acceptance (k is Boltzmann's constant and T is the temperature). The factor $W(\boldsymbol{\tau}' \rightarrow \boldsymbol{\tau})/W(\boldsymbol{\tau} \rightarrow \boldsymbol{\tau}')$ is needed for detailed balance to be fulfilled, since \mathbf{G} is conformation-dependent and W thereby asymmetric.

These two updates, the single-variable update and the biased Gaussian step, are updates for simulations in the canonical ensemble. In recent years, there has been an increasing interest in generalized-ensemble techniques for protein folding simulations [23]. The aim of these methods is to make it easier for the system to jump between different free-energy minima and thereby speed up the exploration of conformational space. A method of this type that has been used for the present model is simulated tempering [24, 25, 26]. In this method, the temperature is a dynamical variable that can take on a set of predetermined values, T_k . The extended ensemble studied by this method is defined by the partition function

$$Z = \sum_k e^{-g_k} Z(T_k), \quad (10.9)$$

where the g_k s are tunable parameters and $Z(T_k)$ denotes the canonical partition function at temperature T_k . The temperature jumps are controlled by a Metropolis accept/reject question.

10.2.3 Software

The program package PROFASI (PROtein Folding and Aggregation Simulator) implements the model and Monte Carlo methods described above [27] and is freely available to academic users. This package, written in C++, is designed to handle both single chains and multichain systems in a flexible and efficient manner. Using this package, the folding studies below require roughly a day on a cluster of 10 2.2 GHz processors for each peptide.

10.3 Results

This section presents results obtained using the model described above. The number of sequences that this model can fold is limited. On the other hand, it should be stressed that all the different sequences are studied for one and the same choice of model parameters. In other words, the only input to the calculations is the amino acid sequence. All our calculations, except in the unfolding studies of ubiquitin, were started from random initial configurations.

10.3.1 Peptide Folding

Folding studies based on this model have been performed [13] for the following set of peptides: the α -helical Trp cage [20] and F_s [28], the β -hairpins GB1p [29] and GB1m2/GB1m3 [30], and the three-stranded β -sheets Betanova [31] and LLM [32]. These peptides are schematically illustrated in Fig. 10.1.



Fig. 10.1. Schematic illustration of the different geometries of the peptides studied. Shown from *left to right* are the Trp cage, F_s , a β -hairpin (GB1p, GB1m2 and GB1m3) and a three-stranded β -sheet (Betanova and LLM). Drawn with RasMol [33]

A common measure of similarity between protein conformations is the root-mean-square deviation (RMSD), minimized over rigid-body translations and rotations. Below, Δ_b and Δ denote RMSD values calculated over backbone atoms and all nonhydrogen atoms, respectively.

Trp Cage

The 20-amino acid Trp cage is a “miniprotein” with a compact folded state and a melting temperature of 315 K [20]. Its NMR-derived native structure [20] contains an α -helix (amino acids 2–8), a single turn of 3_{10} -helix (amino acids 11–14) and a hydrophobic core consisting of three prolines (Pro12, Pro18, Pro19) and two aromatic amino acids (Tyr3, Trp6). The Trp cage has been studied using several different models [34, 35, 36, 37, 38]. Many groups obtained structures similar to the experimental structure, but it was not shown that the melting behavior is well described by any of these models. Figures 10.2 and 10.3 show results obtained using the model of this article. The first of these figures shows the free energy $F(\Delta_b, E)$ calculated as a function of backbone RMSD from the experimental structure, Δ_b , and energy, E , at 275 K. $F(\Delta_b, E)$ has a simple shape with one dominating minimum located at $\Delta_b \approx 2.3$ Å, showing that this peptide, in the model, adopts a structure similar to the experimental structure. Figure 10.3 illustrates the melting behavior. The melting temperature of the Trp cage was, as mentioned earlier, used to set the energy scale of the model and is therefore by construction equal to its experimental value. The rate at which the native structure melts with temperature is, by contrast, a prediction of the model. Figure 10.3(a) shows the temperature dependence of the helix content. A simple two-state fit provides an excellent description of the data. Figure 10.3(b) shows the native population obtained from this fit along with experimental data. The calculated native population agrees very well with experimental data over the entire temperature range, although the agreement is not perfect at low temperature. The model thus gives a realistic melting behavior.

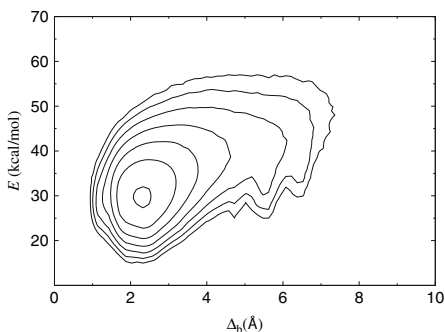


Fig. 10.2. Free energy $F(\Delta_b, E)$ calculated as a function of backbone RMSD (amino acids 2–19), Δ_b , and energy, E , for the Trp cage at 275 K. The contours are spaced at intervals of $1kT$. Contours more than $6kT$ above the minimum free energy are not shown. The free energy $F(\Delta_b, E)$ is defined by $\exp[-F(\Delta_b, E)/kT] \propto P(\Delta_b, E)$, where $P(\Delta_b, E)$ denotes the joint probability distribution of Δ_b and E at temperature T

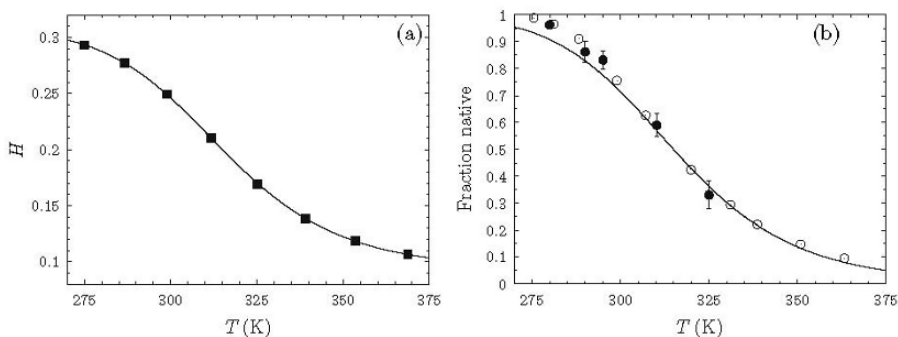


Fig. 10.3. Melting behavior of the Trp cage. (a) Helix content H against temperature. The line is a fit to the two-state expression $H(T) = (H_u + H_n K(T))/(1 + K(T))$, where H_u and H_n are the values in the unfolded and native states, respectively, and $K(T)$ is the effective equilibrium constant. $K(T)$ is given by $K(T) = \exp[(1/kT - 1/kT_m)\Delta E]$, where T_m is the melting temperature and ΔE is the energy difference between the unfolded and native states. The helix content H is, for an N -amino acid chain, defined as the fraction of the $N - 2$ inner amino acids with their Ramachandran (ϕ, ψ) pair in the α -helix region $-90^\circ < \phi < -30^\circ$, $-77^\circ < \psi < -17^\circ$. (b) Native population against temperature. The line represents the model and was obtained from the fit of data for H . Plot symbols show experimental results [20] based on CD (\circ) and NMR (\bullet), respectively

F_s

The F_s peptide is a designed alanine-based peptide with 21 amino acids, which makes an α -helix [28]. It has been extensively studied both experimentally [28, 39, 40] and theoretically [41, 42, 43]. Its melting behavior was investigated experimentally using circular dichroism (CD) as well as infrared (IR) spectroscopy, with slightly different results. The melting temperature measured by IR was 334 K [39], whereas two CD-based studies obtained $T_m = 308$ K [28] and $T_m = 303$ K [40].

Figure 10.4(a) shows a $F(\Delta_b, E)$ plot for F_s, analogous to that in Fig. 10.2 for the Trp cage. In the calculations for F_s, Δ_b denotes backbone RMSD from an ideal α -helix. The free energy has its global minimum at $\Delta_b \approx 0.5$ Å, which indeed corresponds to an α -helix. In addition, there are two local minima with $\Delta_b \approx 7$ Å and $\Delta_b \approx 11$ Å, respectively, both of which correspond to β -sheet structures. These two local minima are very weakly populated compared to the α -helix minimum.

Figure 10.4(b) shows the temperature dependence of the helix content. A two-state fit of the data gave a melting temperature of $T_m = 304 \pm 1$ K and an energy difference of $\Delta E = 11.9 \pm 0.3$ kcal/mol. This melting temperature is lower than what was found by IR, but in good agreement with the CD-based results. The result for ΔE is furthermore in perfect agreement with the CD-based result of Thompson et al. [40], namely $\Delta E = 12 \pm 2$ kcal/mol. The helix-coil transition of F_s is thus very similar in both location and sharpness to what was found in this experimental study.

GB1p, GB1m2 and GB1m3

Let us now turn from α -helical structure to β -sheet structure. The GB1p, GB1m2 and GB1m3 peptides make β -hairpins, which is the minimal unit of β -sheet structure. A β -hairpin has two strands which are connected by hydrogen

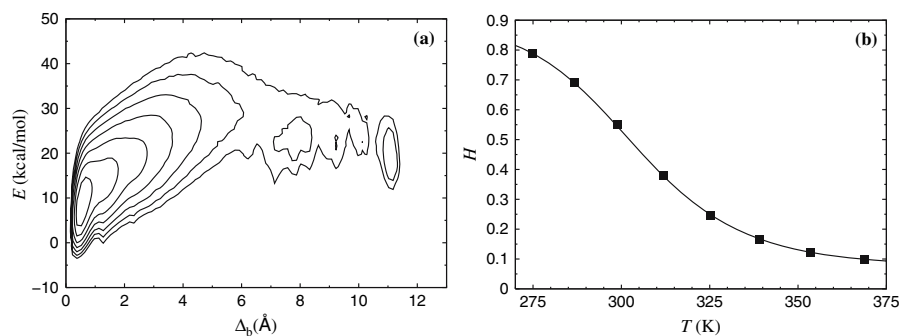


Fig. 10.4. The F_s peptide. (a) Free energy $F(\Delta_b, E)$ (see Fig. 10.2). (b) Helix content H versus temperature (see Fig. 10.3(a))

bonds. GB1p is a fragment from the protein G B1 domain (amino acids 41–56) and is known to make a β -hairpin on its own [29]. Many groups have performed simulations of this particular peptide [44, 45, 46, 47, 48, 49, 50, 51, 52, 53, 54]. GB1m2 and GB1m3 are two sequences recently derived from GB1p [30]. By CD and NMR, it was found that the folded populations of GB1p, GB1m2 and GB1m3 at 298 K are ~ 30 , 74 ± 5 and $86 \pm 3\%$, respectively [30]. The stability of GB1p was also studied using Trp fluorescence [55]. A two-state analysis of these data gave $T_m = 297$ K and $\Delta E = 11.6$ kcal/mol [55]. These values correspond to a native population higher than that found by CD and NMR.

Figure 10.5 shows the free energy $F(\Delta, E)$ for GB1p and GB1m3 at 275 K, as obtained using the model of this article. Here, an RMSD Δ calculated over all heavy atoms is needed because the backbone RMSD Δ_b cannot distinguish between the two possible β -hairpin topologies (with similar backbone folds but oppositely oriented side chains). A complete three-dimensional structure has not been determined for any of these peptides. Reference structures for the RMSD calculation were therefore derived from the NMR structure for the full protein G B1 domain [56]. For GB1p, the free energy $F(\Delta, E)$ has two low-lying minima, both of which are similar to the reference structure ($\Delta \approx 2.0$ Å and $\Delta \approx 3.2$ Å, respectively). Both these minima correspond to a β -hairpin with native hydrogen bonds. The difference between the two minima lies in the shape of the turn region. In addition to these minima, there are two weakly populated local minima at $\Delta \approx 5.3$ Å and $\Delta \approx 8-10$ Å, which correspond to a β -hairpin with the opposite topology (flipped side chains) and α -helix, respectively. The free-energy plot for GB1m3 (see Fig. 10.5(b)) has a simpler shape with only one detectable minimum. This sequence is more stable than the original GB1p sequence, as it should. The results for GB1m2 (not shown) are very similar to those for GB1m3.

Different experiments on GB1p have, as mentioned above, obtained different results for the native population. To see whether the model can explain this discrepancy, two different analyses were performed. First, the temperature

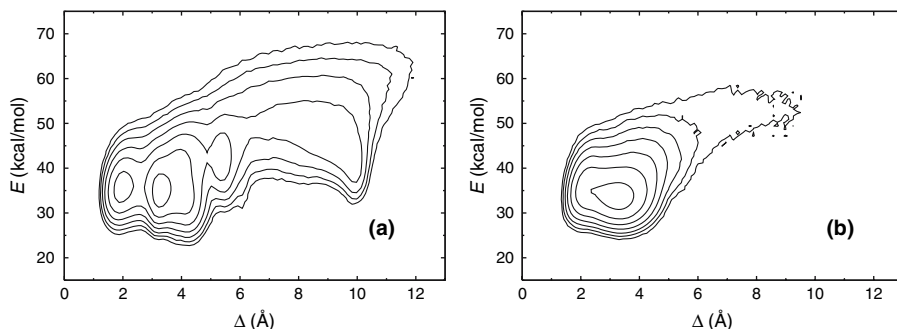


Fig. 10.5. Free energy $F(\Delta, E)$ at 275 K for (a) GB1p and (b) GB1m3. Contour levels are as in Fig. 10.2

dependence of the hydrophobicity energy E_{hp} was studied. This quantity should be strongly correlated with Trp fluorescence because the Trp amino acid (Trp43) is part of a hydrophobic cluster in the folded structure. A two-state fit of the E_{hp} data (see Fig. 10.6(a)) gave $T_{\text{m}} = 297 \pm 1$ K and $\Delta E = 14.2 \pm 0.2$ kcal/mol, which indeed is in good agreement with the Trp fluorescence results. Figure 10.6a also shows the corresponding results for GB1m3. As expected, the melting curve is shifted toward higher temperature for GB1m3. A second and independent estimate of the native population can be obtained by studying native hydrogen bonds. The number of native hydrogen bonds should be strongly correlated with the native population as obtained by CD and NMR. For a given conformation, let $N_{\text{hb}}^{\text{nat}}$ denote the number of native hydrogen bonds that are present (a hydrogen bond is considered formed if its energy is lower than a cutoff). Figure 10.6(b) shows the probability distribution of $N_{\text{hb}}^{\text{nat}}$ for GB1p and GB1m3 at 299 K. The distribution has a clear bimodal shape for both peptides, with one native and one unfolded peak. The folded population can be directly estimated from the area of the native peak. With $N_{\text{hb}}^{\text{nat}} \geq 3$ as criterion for native, one finds that GB1p and GB1m3 have folded populations of 27 ± 2 and 82 ± 1 %, respectively. These results are in good agreement with the above-mentioned CD- and NMR-based results at 298 K [30] (~ 30 % for GB1p; 86 ± 3 % for GB1m3).

The discrepancy between the experimental results for the native population of GB1p is thus very similar to what one finds in the model when analyzing different observables. This finding suggests that the difference between the experimental results reflects a true dependence of the apparent folded population on the observable studied. Such a dependence does not occur for ideal two-state systems, but a simple two-state picture might very well be inadequate for a small peptide such as GB1p. For GB1m3, there is no Trp

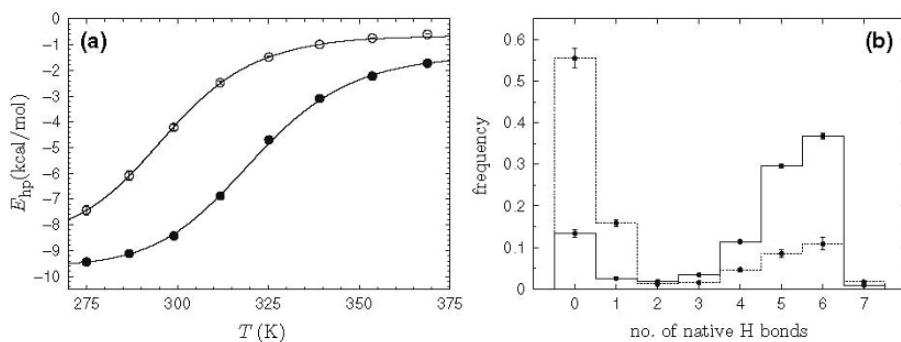


Fig. 10.6. (a) The hydrophobicity energy E_{hp} against temperature for GB1p (○) and GB1m3 (●). The lines are two-state fits ($T_{\text{m}} = 297 \pm 1$ K, $\Delta E = 14.2 \pm 0.2$ kcal/mol for GB1p; $T_{\text{m}} = 321 \pm 1$ K, $\Delta E = 15.0 \pm 0.4$ kcal/mol for GB1m3). (b) Probability distribution of the number of native hydrogen bonds, $N_{\text{hb}}^{\text{nat}}$, for GB1p (dotted line) and GB1m3 (full line) at 299 K

fluorescence study available. The simulation results suggest that the difference between results based on Trp fluorescence and results based on CD and NMR should be smaller for this peptide. Whether or not this prediction is correct remains to be seen.

Betanova and LLM

Betanova is a designed three-stranded β -sheet peptide with 20 amino acids [31]. It is only marginally stable, but Betanova mutants with higher stability have been developed, such as the triple mutant LLM (Val5Leu, Asn12Leu, Thr17Met) [32]. Betanova has been studied by both NMR [32] and computer simulations [57, 58, 59]. The NMR-based native populations of Betanova and LLM are 9 and 36%, respectively, at 283 K.

It turns out that Betanova and LLM make three-stranded β -sheets similar to the experimental structures in the model of this article. Both peptides have low stability, as they should, as can be seen from Fig. 10.7. This figure shows the probability distribution of $N_{\text{hb}}^{\text{nat}}$ for these peptides at 287 K, $N_{\text{hb}}^{\text{nat}}$ being the number of native hydrogen bonds. In both cases, the distribution exhibits three peaks: a native peak at high $N_{\text{hb}}^{\text{nat}}$, an unfolded peak at low $N_{\text{hb}}^{\text{nat}}$ and a third peak at $N_{\text{hb}}^{\text{nat}} \approx 4$. It was found that conformations in the intermediate state with $N_{\text{hb}}^{\text{nat}} \approx 4$ tend to contain the first (N-terminal) β -hairpin but not the second (C-terminal) one, which is in agreement with experimental data [32]. With $N_{\text{hb}}^{\text{nat}} \geq 6$ as the definition of native, one finds that Betanova and LLM are 6 ± 1 and 38 ± 2 % folded, respectively, at this temperature. These values are in good agreement with the NMR-based native populations.

Table 10.1 gives a summary of calculated and experimental native populations for the five β -sheet peptides studied. The model results are based on the number of native hydrogen bonds, whereas the experimental results are based on CD and NMR. The overall agreement is very good, and it should be

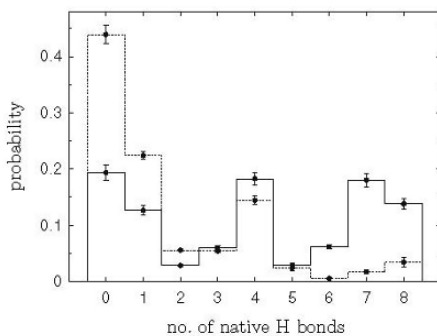


Fig. 10.7. Probability distribution of the number of native backbone hydrogen bonds, $N_{\text{hb}}^{\text{nat}}$, for Betanova (*dotted line*) and LLM (*full line*) at 287 K

Table 10.1. Experimental and calculated native populations of the β -sheet peptides studied

	exp.	model
GB1p	$\sim 30\%$ (298 K)	$27 \pm 2\%$ (299 K)
GB1m2	$74 \pm 5\%$ (298 K)	$84 \pm 1\%$ (299 K)
GB1m3	$86 \pm 3\%$ (298 K)	$82 \pm 1\%$ (299 K)
Betanova	9% (283 K)	$6 \pm 1\%$ (287 K)
LLM	36% (283 K)	$38 \pm 2\%$ (287 K)

stressed that this agreement was achieved without having to tune any model parameters. Good agreement with experimental stability data was also seen for the α -helical Trp cage and F_s peptides. This quantitative agreement indicates that factors such as Coulomb interactions between charged amino acids play a quite limited role in the folding thermodynamics of these peptides, compared to hydrogen bonding and hydrophobic attraction, which are the main driving forces of this model.

10.3.2 Aggregation of $A\beta_{16-22}$ Peptides

The fibrillar aggregates that characterize amyloid diseases are formed by specific proteins, but many other proteins are capable of forming similar aggregated structures [4, 60].

Among the known fibril-forming proteins are several fragments of the amyloid $A\beta$ peptide associated with Alzheimer's disease. One such fragment is the 7-amino acid $A\beta_{16-22}$ peptide [61]. This peptide contains the hydrophobic 16–20-amino acid segment (Lys-Leu-Val-Phe-Phe), which is known to be important in the $A\beta$ – $A\beta$ interaction [62]. Its small size makes $A\beta_{16-22}$ well suited as a model system for studying the mechanisms of fibril formation. Computer simulations of $A\beta_{16-22}$ systems have been reported by several groups [63, 64, 65, 66].

An amyloid fibril is composed of β -sheets whose strands run perpendicular to the fibril axis [67]. For $A\beta_{16-22}$ fibrils, there is evidence from solid-state NMR that the β -strands have an antiparallel organization [61, 68].

The exact role of protein aggregation in amyloid diseases remains to be clarified. However, there is increasing evidence suggesting that the full fibrils are not the neurotoxic agent, whereas there are studies linking $A\beta$ oligomers to neurotoxicity [69, 70, 71].

Using the model of this article, a study of small $A\beta_{16-22}$ systems was performed [15]. The energy function was exactly the same as in the folding studies above. Systems of one, three and six $A\beta_{16-22}$ peptides were studied by Monte Carlo simulations, which were started from random (nonaggregated) structures. The $N_c = 3$ and $N_c = 6$ systems, N_c being the number of chains, were contained in periodic boxes. The box sizes were $(35 \text{ \AA})^3$ and $(44 \text{ \AA})^3$ for

$N_c = 3$ and $N_c = 6$, corresponding to a constant peptide concentration. To the set of Monte Carlo moves, rigid-body translations and rotations of whole chains were added.

Secondary Structure

Figure 10.8 shows the α -helix and β -strand contents H and S against temperature for different N_c . For $N_c = 1$, both H and S are small at all temperatures studied. So, in this model, the $A\beta_{16-22}$ monomer is mainly a random coil throughout this temperature range. The $N_c = 3$ and $N_c = 6$ systems show a qualitatively different behavior; S increases sharply with decreasing temperature, to values of $S = 0.6$ and higher, whereas H is small. These results show that unless the temperature is too high, the three- and six-chain systems self-assemble into ordered structures with a high β -strand content.

The results for $N_c = 1$ and $N_c = 3$ can be compared with results from molecular dynamics simulations with explicit water by Klimov and Thirumalai [64]. The conclusion that the isolated $A\beta_{16-22}$ peptide is mainly a random coil is in agreement with their results. However, the $N_c = 3$ results disagree with theirs because they found a lower β -strand content for $N_c = 3$ than for $N_c = 1$.

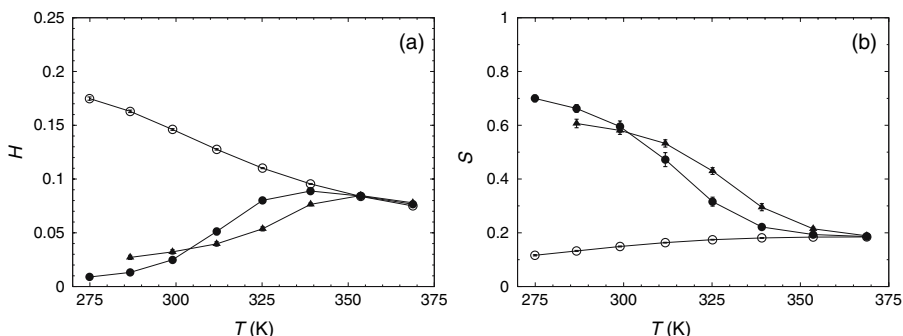


Fig. 10.8. Secondary structure of $A\beta_{16-22}$ systems. For a chain with N amino acids, the α -helix and β -strand contents are defined as the fractions of the $N-2$ inner amino acids with their (ϕ, ψ) pair in the α -helix and β -strand regions of the Ramachandran space, assuming that α -helix corresponds to $-90^\circ < \phi < -30^\circ$, $-77^\circ < \psi < -17^\circ$ and that β -strand corresponds to $-150^\circ < \phi < -90^\circ$, $90^\circ < \psi < 150^\circ$. The average α -helix and β -strand contents, over all the chains of the system, are denoted by H and S , respectively. (a) The α -helix content H against temperature T for $N_c = 1$ (\circ), $N_c = 3$ (\bullet) and $N_c = 6$ (\blacktriangle). Lines joining data points are only a guide for the eye. (b) Same for the β -strand content S

β -Strand Organization

As mentioned above, there is experimental evidence [61, 68] that the β -strands in full $A\beta_{16-22}$ fibrils have an antiparallel organization. To examine the β -strand organization in the model, parallel and antiparallel pairs of strands were identified and counted. Given a multichain configuration, all pairs of chains were identified such that (i) their interchain hydrogen bond energy was less than a cutoff (roughly corresponding to 2–3 hydrogen bonds), and (ii) both chains had a β -strand content higher than 0.5. For each such pair of chains, the scalar product of their normalized end-to-end unit vectors was calculated. If this scalar product was greater than 0.7 (less than -0.7), the two chains were taken as parallel (antiparallel). The numbers of such parallel and antiparallel pairs are denoted by n_+ and n_- , respectively.

Table 10.2 shows the joint probability distribution $P(n_+, n_-)$ for the $N_c = 6$ system at $T = 287$ K. From this table, it can be seen that many configurations contain mixed β -sheet structure. Nevertheless, there is a clear asymmetry between n_+ and n_- ; large n_- values are much more probable than large n_+ values. The combination $(n_+, n_-) = (4, 0)$ is, e.g., very unlikely to occur, whereas $(n_+, n_-) = (0, 4)$ does occur with a significant frequency.

The results in Table 10.2 were obtained at the lowest temperature studied. With increasing temperature, the average n_+ and n_- steadily decrease. At the highest temperature studied, 369 K, about 99% of the conformations have $n_+ = n_- = 0$.

A clear trend seen in Table 10.2 is that large n_+ values are suppressed, which means that large parallel β -sheets are unlikely to form. The probability of having large antiparallel β -sheets is higher. Compared to purely antiparallel β -sheet structures, it is possible that mixed β -sheet structures are more difficult to extend to large stable structures. To be able to check whether or not this is the case, simulations of larger systems are required.

Why are antiparallel β -sheets favored over parallel ones? Klimov and Thirumalai [64] concluded that $A\beta_{16-22}$ peptides make antiparallel β -sheets because of Coulomb interactions between charged side chains; the two end

Table 10.2. The probability distribution $P(n_+, n_-)$ for $N_c = 6$ $A\beta_{16-22}$ peptides at $T = 287$ K (entries smaller than 10^{-3} are omitted)

n_+	n_-				
	0	1	2	3	4
0	0.028 (5)	0.059 (11)	0.08 (2)	0.06 (2)	0.030 (15)
1	0.038 (6)	0.12 (2)	0.16 (3)	0.10 (3)	0.006 (3)
2	0.026 (11)	0.11 (5)	0.14 (5)	0.004 (2)	
3	0.008 (5)	0.013 (9)	0.015 (12)		

n_+ and n_- are the numbers of parallel and antiparallel pairs of β -strands (see text). The numbers in parentheses are the statistical errors in the last digits

side chains of the $A\beta_{16-22}$ peptide carry opposite charges, which indeed should make the antiparallel orientation electrostatically favorable. However, our model completely ignores Coulomb interactions between side-chain charges and still strongly favors the antiparallel organization. Other mechanisms than Coulomb interactions between side-chain charges might therefore play a significant role, such as the geometry of backbone–backbone hydrogen bonds, steric effects, and the precise distribution of hydrophobicity along the chains.

Examples of Low-Energy Structures

What is the typical shape of the aggregated structures? In the $N_c = 6$ simulations, no single dominating shape was observed, but rather a number of more or less degenerate local free-energy minima. Figure 10.9 shows two snapshots of such minima.

In the simplest class of typical structures observed in the simulations, five of the chains form a relatively flat β -sheet, whereas the remaining chain is a random coil and held in contact with the β -sheet by hydrophobic attraction. Six-stranded β -sheets also occurred in the simulations, but with a very low frequency. Furthermore, for the six-chain system, there were new nontrivial structures with no analogs in the three-chain simulations. The second structure in Fig. 10.9 illustrates this. Here, stability is achieved by stacking two different, three-stranded, β -sheets together, which brings hydrophobic side chains from the two β -sheets in close contact. Such “sandwiches” occurred with a nonnegligible frequency in the simulations, although not as frequently as five-stranded β -sheets.

10.3.3 Mechanical Unfolding of Ubiquitin

The same model has also been used to study the mechanical unfolding of ubiquitin [16, 17], a protein with 76 amino acids. The unfolding behavior of

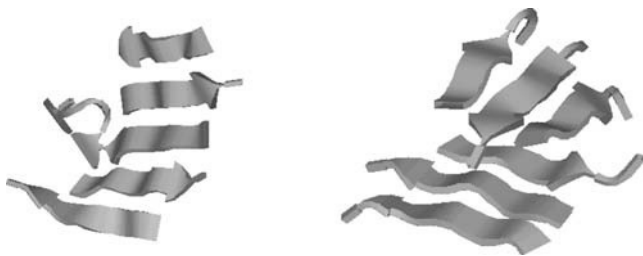


Fig. 10.9. Two typical low-energy structures from the simulations of six $A\beta_{16-22}$ peptides: a five-stranded β -sheet (*left*), and two three-stranded β -sheets “sandwiching” several of their hydrophobic side chains between them (*right*). Drawn with RasMol [33]

ubiquitin under the influence of a stretching force was recently investigated experimentally by single-molecule constant-force methods [72]. Many observed unfolding traces had a simple two-state character, whereas others showed clear evidence of intermediate states. The quantity monitored was the end-to-end distance. This quantity alone provides only limited information about the unfolding behavior and the structure of the intermediate states.

More detailed experimental information is available about the pathway followed by this protein in temperature-induced unfolding. In its native form, ubiquitin contains an α -helix packed against a five-stranded β -sheet (see Fig. 10.10). The thermally most stable parts of the native structure seem to be the α -helix and the first (N-terminal) β -hairpin [74, 75], which is part of the β -sheet. There is also evidence that the same two secondary-structure elements, the α -helix and the first β -hairpin, form early as ubiquitin folds to its native conformation. An extensive ϕ -value analysis, based on 27 mutations throughout the protein, found that both these structures are present in the transition state but that the rest of the molecule remains largely unstructured at this stage of folding [76]. Another study suggested that two additional β -strands are present in the transition state [77].

The simulations of the mechanical unfolding of ubiquitin were carried out at constant force [16]. As in the constant-force experiments [72], the forces acted on the chain ends. In the presence of these forces, the energy function becomes $\tilde{E} = E - \mathbf{F} \cdot \mathbf{R}$, where E is given by (10.1), \mathbf{F} is the force, and \mathbf{R} denotes the end-to-end vector. The forces studied were 100, 140 and 200 pN. For each force, a set of more than 500 unfolding simulations were carried out using Monte Carlo dynamics. For the backbone angles, to avoid large unphysical deformations of the chain, the single-variable update was not used, but only the semi-local biased-Gaussian-step method. All simulations were started from the native structure but with different random number seeds.

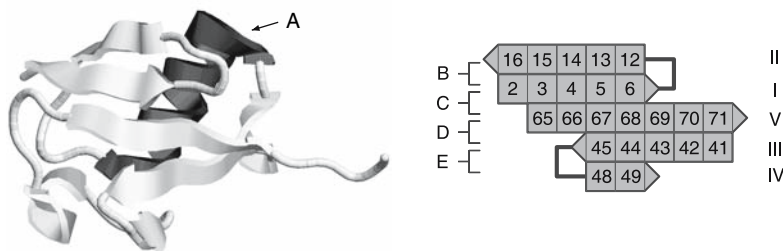


Fig. 10.10. Schematic illustrations of the native structure of ubiquitin with labels A–E for the secondary-structure elements. (*Left*) A 3D model (Protein Data Bank code 1d3z [73]) drawn with RasMol [33]. (*Right*) The organization of the β -sheet. Amino acid numbers, strand labels (I–V) and two β -hairpin turns are indicated

End-to-End Distance

Figure 10.11 shows the time evolution of the end-to-end distance $r = |\mathbf{R}|$ in two typical runs at 100 pN. From this figure, it can be seen that unfolding proceeds in a stepwise fashion in the simulations, although the steps are not as sharp as in the experiments. In many runs, the unfolding occurred in a single step, as in run R1 in Fig. 10.11. However, in agreement with the experiments [72], there were also several examples of unfolding via intermediate states, as in run R2 in Fig. 10.11. So, both one-step unfolding and unfolding through intermediate states indeed occurred in the simulations.

Also, properties such as the size of the unfolding step, the frequency of occurrence of intermediate states and the position of the typical intermediate state were all found to be in reasonable agreement with experimental data [72]. For the range of forces studied, it was found that the size of the unfolding step increased with force, whereas intermediate states occurred more frequently at lower force. These dependencies on the strength of the applied force remain to be verified experimentally.

The comparison of these results with experimental data serve as an important test of the model; the model was developed by folding studies of much smaller chains, and it is not at all clear that it can fold ubiquitin. Unfolding is, however, easier to simulate than folding to a unique native state, and atomic-level simulations of force-induced unfolding have been performed before for several proteins including ubiquitin [78] and the I27 Ig domain from titin [79, 80]. The results above suggest that the model of this article indeed is able to capture key features of the mechanical unfolding of ubiquitin. Having verified these properties, more detailed measurements were performed, which in particular aimed at characterizing the typical intermediate state.

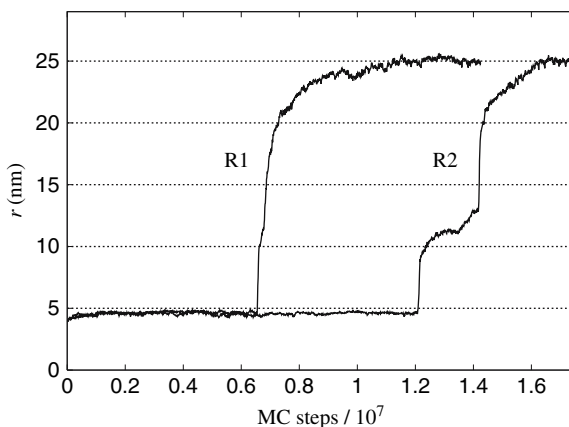


Fig. 10.11. Monte Carlo evolution of the end-to-end distance r in two representative runs. The protein chain unfolds in a single step in run R1 and via an intermediate state in run R2. The pulling force is 100 pN in both runs

Unfolding Pathway

To delineate the unfolding process, five key elements of the native structure, labeled A–E, were followed (see Fig. 10.10). The structure A is the α -helix, whereas B–E are the four different pairs of adjacent strands in the β -sheet. To examine the order in which the structures A–E break, the presence of their native hydrogen bonds was followed as a function of the end-to-end distance r (r shows an essentially monotonic increase with time). Figure 10.12 shows the result of this analysis for all the native backbone hydrogen bonds in the structures A–E at 100 pN. From this figure, it is immediately clear that the structures do not break in a random order but instead in a statistically preferred order, namely CBDEA. The structures C and B tend to break below the typical r for intermediate states, $r_I \approx 12$ nm, whereas D, E and A tend to break above r_I . The data in Fig. 10.12 thus suggest that the typical intermediate is composed of A, D and E.

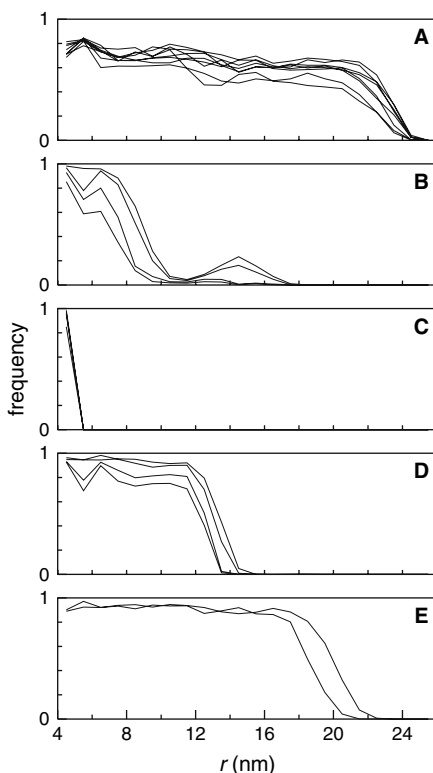


Fig. 10.12. The frequency of occurrence as a function of the end-to-end distance r for all native backbone hydrogen bonds in the respective structures A–E, at 100 pN. Each curve represents one hydrogen bond

This analysis does not tell how strong the statistical preference is for the unfolding order CBDEA, since it is based on averages over all events. To check this, the time of breaking of the structures A–E was directly analyzed, so that an unfolding path (a permutation of ABCDE) was obtained for each individual event. Disregarding interchanges of B and D due to partial refolding of the β -hairpin B, it was found that more than 80 % of the events followed the same unfolding path, CBDEA. The order was the same in events with and without intermediate states, and neither did it change between the three different forces studied.

This predicted unfolding order does not agree with the zero-force experiments mentioned above, in which A and B were found to be the most stable structures. Therefore, it should be stressed that the fact that B breaks early in the simulations appears physically reasonable. That C breaks first is inevitable because the other parts cannot sense the force until C is broken (see Fig. 10.10). The native state is mechanically resistant because C is pulled longitudinally so that several bonds must break simultaneously. Once C is gone, nothing keeps the β -hairpin B from unzipping, one bond at a time. Unzipping requires less force than separation by longitudinal pulling [81, 82], which makes B likely to break soon after C.

Recently, the thermal unfolding of ubiquitin was studied using the same model [17] to see whether the model actually predicts a different unfolding order in this case. This was found to be the case. In fact, in these simulations, the most long-lived structures were A and B, which experimentally have been found to be the thermally most stable parts of the molecule [74, 75]. A previous computational study compared thermal unfolding, folding and mechanical unfolding for the I27 Ig domain from titin [83].

10.4 Summary

With improved algorithms and faster computers, it is becoming computationally feasible to simulate how small proteins fold to their native states. This is an exciting development that will lead to a better understanding not only of protein folding but also of the interaction of proteins with other molecules and materials. For all-atom simulations of proteins, a number of interaction potentials, at different levels of sophistication, have been developed. The model discussed in this article has a crude but computationally convenient potential, which was developed through folding studies of selected peptides. It is encouraging that this model, despite its simplicity, could be used to study peptide folding and aggregation as well as the mechanical unfolding of ubiquitin, without changing any parameter of the model. The model will be further developed by studying new amino acid sequences, which will impose new conditions on the interaction potential. Hopefully, this will extend the applicability of the model to new interesting problems.

References

1. C. Brändén, J. Tooze: *Introduction to Protein Structure* (Garland, New York, 1991) [269](#)
2. H. J. Dyson, P. E. Wright: *Curr. Opin. Struct. Biol.* **12**, 54 (2002) [269](#)
3. A. K. Dunker, J. D. Lawson, C. J. Brown, R. M. Williams, P. Romero, J. S. Oh, C. J. Oldfield, A. M. Campen, C. R. Ratliff, K. W. Hipps, J. Ausio, M. S. Nissen, R. Reeves, C. H. Kang, C. R. Kissinger, R. W. Bailey, M. D. Griswold, M. Chiu, E. C. Garner, Z. Obradovic: *J. Mol. Graph. Modell.* **19**, 26 (2001) [269](#)
4. C. M. Dobson: *Nature* **426**, 884 (2003) [269](#), [281](#)
5. H. S. Chan, H. Kaya, S. Shimizu: Computational methods for protein folding: scaling a hierarchy of complexities. In *Current Topics in Computational Molecular Biology*, edited by T. Jiang, Y. Xu, M. Q. Zhang (MIT press, Cambridge, Massachusetts, USA, 2002), pp. 403–447 [270](#)
6. J. M. Wang, P. Cieplak, P. A. Kollman: *J. Comput. Chem.* **21**, 1049 (2000) [270](#)
7. A. D. MacKerell, D. Bashford, M. Bellott, R. L. Dunbrack, J. D. Evanseck, M. J. Field, S. Fischer, J. Gao, H. Guo, S. Ha, D. Joseph-McCarthy, L. Kuchnir, K. Kuczera, F. T. K. Lau, C. Mattos, S. Michnick, T. Ngo, D. T. Nguyen, B. Prodhom, W. E. Reiher, B. Roux, M. Schlenkrich, J. C. Smith, R. Stote, J. Straub, M. Watanabe, J. Wiorkiewicz-Kuczera, D. Yin, M. Karplus: *J. Phys. Chem. B* **102**, 3586 (1998) [270](#)
8. U. Stocker, W. F. van Gunsteren: *Proteins* **40**, 145 (2000) [270](#)
9. G. Kaminski, W. L. Jorgensen: *J. Phys. Chem.* **100**, 18010 (1996) [270](#)
10. T. Yoda, Y. Sugita, Y. Okamoto: *Chem. Phys.* **307**, 269 (2004) [270](#)
11. A. Irbäck, B. Samuelsson, F. Sjunnesson, S. Wallin: *Biophys. J.* **85**, 1466 (2003) [270](#)
12. A. Irbäck, F. Sjunnesson: *Proteins* **56**, 110 (2004) [270](#)
13. A. Irbäck, S. Mohanty: *Biophys. J.* **88**, 1560 (2005) [270](#), [274](#)
14. A. G. Cochran, N. J. Skelton, M. A. Starovasnik: *Proc. Natl. Acad. Sci. USA* **98**, 5578 (2001) [270](#)
15. G. Favrin, A. Irbäck, S. Mohanty: *Biophys. J.* **87**, 3657 (2004); erratum **89**, 754 (2005) [271](#), [281](#)
16. A. Irbäck, S. Mitternacht, S. Mohanty: *Proc. Natl. Acad. Sci. USA* **102**, 13427 (2005) [271](#), [284](#), [285](#)
17. A. Irbäck, S. Mitternacht: *Proteins* **65**, 759 (2006) [271](#), [284](#), [288](#)
18. G. Chikenji, Y. Fujitsuka, S. Takada: *Proc. Natl. Acad. Sci. USA* **103**, 3141 (2006) [271](#)
19. G. N. Ramachandran, V. Sasisekharan: *Adv. Protein Chem.* **23**, 283 (1968) [271](#)
20. J. W. Neidigh, R. M. Fesinmeyer, N. H. Andersen: *Nat. Struct. Biol.* **9**, 425 (2002) [272](#), [274](#), [275](#), [276](#)
21. L. R. Dodd, T. D. Boone, D. N. Theodorou: *Mol. Phys.* **78**, 961 (1993) [273](#)
22. G. Favrin, A. Irbäck, F. Sjunnesson: *J. Chem. Phys.* **114**, 8154 (2001) [273](#)
23. U. H. E. Hansmann, Y. Okamoto: *Curr. Opin. Struct. Biol.* **9**, 177 (1999) [274](#)
24. A. P. Lyubartsev, A. A. Martsinovski, S. V. Shevkunov, P. N. Vorontsov-Velyaminov: *J. Chem. Phys.* **96**, 1776 (1992) [274](#)
25. E. Marinari, G. Parisi: *Europhys. Lett.* **19**, 451 (1992) [274](#)
26. A. Irbäck, F. Potthast: *J. Chem. Phys.* **103**, 10298 (1995) [274](#)
27. A. Irbäck, S. Mohanty: *J. Comput. Chem.* **27**, 1548 (2006) [274](#)
28. D. J. Lockhart, P. S. Kim: *Science* **260**, 198 (1993) [274](#), [277](#)

29. F. J. Blanco, G. Rivas, L. Serrano: *Nat. Struct. Biol.* **1**, 584 (1994) [274](#), [278](#)
30. R. M. Fesinmeyer, F. M. Hudson, N. H. Andersen: *J. Am. Chem. Soc.* **126**, 7238 (2004) [274](#), [278](#), [279](#)
31. T. Kortemme, M. Ramírez-Alvarado, L. Serrano: *Science* **281**, 253 (1998) [274](#), [280](#)
32. M. López de la Paz, E. Lacroix, M. Ramírez-Alvarado, L. Serrano: *J. Mol. Biol.* **312**, 229 (2001) [274](#), [280](#)
33. R. Sayle, E. J. Milner-White: *Trends Biochem. Sci.* **20**, 374 (1995) [275](#), [284](#), [285](#)
34. C. D. Snow, B. Zagrovic, V. S. Pande: *J. Am. Chem. Soc.* **124**, 14548 (2002) [275](#)
35. C. Simmerling, B. Strockbine, A. E. Roitberg: *J. Am. Chem. Soc.* **124**, 11258 (2002) [275](#)
36. J. W. Pitera, W. Swope: *Proc. Natl. Acad. Sci. USA* **100**, 7587 (2003) [275](#)
37. R. Zhou: *Proc. Natl. Acad. Sci. USA* **100**, 13280 (2003) [275](#)
38. A. Schug, W. Wenzel, U. H. E. Hansmann: *J. Chem. Phys.* **122**, 194711 (2005) [275](#)
39. S. Williams, T. P. Causgrove, R. Gilmanshin, K. S. Fang, R. H. Callender, W. H. Woodruff, R. B. Dyer: *Biochemistry* **35**, 691 (1996) [277](#)
40. P. A. Thompson, W. A. Eaton, J. Hofrichter: *Biochemistry* **36**, 9200 (1997) [277](#)
41. J. A. Vila, D. R. Ripoll, H. A. Scheraga: *Proc. Natl. Acad. Sci. USA* **97**, 13075 (2000) [277](#)
42. A. E. García, K. Y. Sanbonmatsu: *Proc. Natl. Acad. Sci. USA* **99**, 2782 (2002) [277](#)
43. H. Nymeyer, A. E. García: *Proc. Natl. Acad. Sci. USA* **100**, 13934 (2003) [277](#)
44. D. Roccatano, A. Amadei, A. Di Nola, H. J. C. Berendsen: *Protein Sci.* **8**, 2130 (1999) [278](#)
45. V. S. Pande, D. S. Rokhsar: *Proc. Natl. Acad. Sci. USA* **96**, 9062 (1999) [278](#)
46. A. R. Dinner, T. Lazaridis, M. Karplus: *Proc. Natl. Acad. Sci. USA* **96**, 9068 (1999) [278](#)
47. A. E. García, K. Y. Sanbonmatsu: *Proteins* **42**, 345 (2001) [278](#)
48. B. Zagrovic, E. J. Sorin, V. Pande: *J. Mol. Biol.* **313**, 151 (2001) [278](#)
49. R. Zhou, B. J. Berne, R. Germain: *Proc. Natl. Acad. Sci. USA* **98**, 14931 (2001) [278](#)
50. E. Kussell, J. Shimada, E. I. Shakhnovich: *Proc. Natl. Acad. Sci. USA* **99**, 5343 (2002) [278](#)
51. R. Zhou: *Proteins* **53**, 148 (2003) [278](#)
52. P. G. Bolhuis: *Proc. Natl. Acad. Sci. USA* **14**, 12129 (2003) [278](#)
53. G. Wei, N. Mousseau, P. Derreumaux: *Proteins* **56**, 464 (2004) [278](#)
54. P. H. Nguyen, G. Stock, E. Mittag, C. K. Hu, M. S. Li: *Proteins* **61**, 795 (2005) [278](#)
55. V. Muñoz, P. A. Thompson, J. Hofrichter, W. A. Eaton: *Nature* **390**, 196 (1997) [278](#)
56. A. M. Gronenborn, D. R. Filpula, N. Z. Essig, A. Achari, M. Whitlow, P. T. Wingfield, G. M. Clore: *Science* **253**, 657 (1991) [278](#)
57. B. D. Bursulaya, C. L. Brooks III: *J. Am. Chem. Soc.* **121**, 9947 (1999) [280](#)
58. G. Colombo, D. Roccatano, A. E. Mark: *Proteins* **46**, 380 (2002) [280](#)
59. S. Y. Kim, J. Lee, J. Lee: *J. Chem. Phys.* **120**, 8271 (2004) [280](#)
60. J. C. Rochet, P. T. Lansbury Jr.: *Curr. Opin. Struct. Biol.* **10**, 60 (2000) [281](#)
61. J. J. Balbach, Y. Ishii, O. N. Antzutkin, R. D. Leapman, N. W. Rizzo, F. Dyda, J. Reed, R. Tycko: *Biochemistry* **39**, 13748 (2000) [281](#), [283](#)
62. L. O. Tjernberg, J. Näslund, F. Lindqvist, J. Johansson, A. R. Karlström, J. Thyberg, L. Terenius, C. Nordstedt: *J. Biol. Chem.* **271**, 8545 (1996) [281](#)
63. B. Ma, R. Nussinov: *Proc. Natl. Acad. Sci. USA* **99**, 14126 (2002) [281](#)

64. D. K. Klimov, D. Thirumalai: *Structure* **11**, 295 (2003) [281](#), [282](#), [283](#)
65. S. Santini, N. Mousseau, P. Derreumaux: *J. Am. Chem. Soc.* **126**, 11509 (2004) [281](#)
66. S. Gnanakaran, R. Nussinov, A. E. García: *J. Am. Chem. Soc.* **128**, 2158 (2006) [281](#)
67. M. Sunde, C. Blake: *Adv. Protein Chem.* **50**, 123 (1997) [281](#)
68. D. J. Gordon, J. J. Balbach, R. Tycko, S. C. Meredith: *Biophys. J.* **86**, 428 (2004) [281](#), [283](#)
69. M. P. Lambert, A. K. Barlow, B. A. Chromy, C. Edwards, R. Freed, M. Liosatos, T. E. Morgan, I. Rozovsky, B. Trommer, K. L. Viola, P. Wals, C. Zhang, C. E. Finch, G. A. Krafft, W. L. Klein: *Proc. Natl. Acad. Sci. USA* **95**, 6448 (1998) [281](#)
70. D. M. Walsh, D. M. Hartley, Y. Kusumoto, Y. Fezoui, M. M. Condrón, A. Lomakin, G. B. Benedek, D. J. Selkoe, D. B. Teplow: *J. Biol. Chem.* **274**, 25945 (1999) [281](#)
71. D. M. Walsh, I. Klyubin, J. V. Fadeeva, W. K. Cullen, R. Anwyl, M. S. Wolfe, M. J. Rowan, D. J. Selkoe: *Nature* **416**, 535 (2002) [281](#)
72. M. Schlierf, H. Li, J. M. Fernandez: *Proc. Natl. Acad. Sci. USA* **101**, 7299 (2004) [285](#), [286](#)
73. G. Cornilescu, J. L. Marquardt, M. Ottiger, A. Bax: *J. Am. Chem. Soc.* **120**, 6836 (1998) [285](#)
74. F. Cordier, S. Grzesiek: *J. Mol. Biol.* **317**, 739 (2002) [285](#), [288](#)
75. H. S. Chung, M. Khalil, A. W. Smith, Z. Ganim, A. Tokmakoff: *Proc. Natl. Acad. Sci. USA* **102**, 612 (2005) [285](#), [288](#)
76. H. M. Went, S. E. Jackson: *Protein Eng. Des. Sel.* **18**, 229 (2005) [285](#)
77. B. A. Krantz, R. S. Dothager, T. R. Sosnick: *J. Mol. Biol.* **337**, 463 (2004) [285](#)
78. P. C. Li, D. E. Makarov: *J. Chem. Phys.* **121**, 4826 (2004) [286](#)
79. H. Lu, K. Schulten: *Biophys. J.* **79**, 51 (2000) [286](#)
80. S. B. Fowler, R. B. Best, J. L. T. Herrera, T. J. Rutherford, A. Steward, E. Paci, M. Karplus, J. Clarke: *J. Mol. Biol.* **322**, 841 (2002) [286](#)
81. R. Rohs, C. Etchebest, R. Lavery: *Biophys. J.* **76**, 2760 (1999) [288](#)
82. D. J. Brockwell, E. Paci, R. C. Zinober, G. S. Beddard, P. D. Olmsted, D. A. Smith, R. N. Perham, S. E. Radford: *Nat. Struct. Biol.* **10**, 731 (2003) [288](#)
83. M. Cieplak, J. Sułkowska: *J. Chem. Phys.* **123**, 194908 (2005) [288](#)

All-Atom Simulations of Proteins

Ulrich H. E. Hansmann^{1,2}

¹ John von Neumann Institute für Computing (NIC), Forschungszentrum Jülich,
52425 Jülich, Germany

u.hansmann@fz-juelich.de

² Department of Physics, Michigan Technological University, Houghton,
MI 49931, USA

hansmann@mtu.edu

Abstract. The successful deciphering of the human genome has highlighted an old challenge in protein science: For most of the resolved protein sequences, we do not know the corresponding structures and functions. Neither do we understand in detail the mechanism by which a protein folds into its biologically active form. Computer experiments offer one way to evaluate the sequence–structure relationship and the folding process but are extremely difficult for detailed protein models. Only over the last few years have algorithms been developed that allow an efficient sampling of relevant protein configurations. Important examples of these new techniques will be introduced in the context of all-atom simulations of small proteins. For these molecules, the folding mechanism and the relation between secondary structure formation and folding are explored. Limitations of current energy functions are discussed.

11.1 Introduction

Proteins are one of the most common and important class of molecules in living systems forming, for instance, muscles and connective tissues, or as enzymes catalyze and regulate biochemical reactions in the cell. While the differences in size and structure are enormous, all proteins are chemically linear chain molecules with the 20 naturally occurring amino acids as monomers. Regular elements such as helices, sheets and turns are formed locally, but the biological function of a protein is decided by its unique overall three-dimensional shape which is determined by the sequence of amino acids as given in the genome. Hence, after the successful completion of the human genome project, the chemical composition of all proteins in the human body is in principal known. However, for most of the resolved protein sequences, one does not know the corresponding structures. Since proteins are functional only if they fold into their specific shape, it is important to understand how the structure and function of proteins emerge from their sequence of amino acids.

Computer experiments offer a possibility to unveil the sequence–structure (function) relationship. Most proteins exist at room temperature in a *unique* structure that one can identify with the lowest *potential* energy conformation [1]. Hence, structure prediction of proteins is a global optimization problem. Both deterministic methods such as the $\alpha\mathbf{BB}$ algorithm [2] and stochastic methods such as Monte Carlo minimization [3], simulated annealing [4] or genetic algorithms [5] are often exploited.

As calorimetric measurements show that a protein in its native state is only by a free-energy difference of $\approx 10\text{--}20$ kcal/mol more stable than the ensemble of the denatured conformations, it is important to use realistic models taking the interactions among all atoms into account. The resulting potential energy $E_{\text{tot}} = E_{\text{protein}} + E_{\text{solv}}$ (given in kcal/mol) can be written as a sum of two terms. The first term, E_{protein} , describes the forces within a protein, and the second term, E_{solv} , the interaction of a protein with the surrounding water. Since inclusion of water molecules is computationally demanding, one often has to rely on implicit solvent models. One example is the introduction of a solvent-accessible surface term that approximates the hydrophobic forces on the protein [6]:

$$E_{\text{solv}} = \sum_i \sigma_i A_i . \quad (11.1)$$

Here A_i is the solvent-accessible surface area of the i th atom in a given configuration and σ_i is the empirically determined solvation parameter of the atom i .

An example for the atomic force fields that model the interactions between the atoms within a protein is the ECEPP energy function [7]. It is defined by the sum of an electrostatic term E_{es} , a van der Waals energy E_{vdW} and a hydrogen bond term E_{hb} for all pairs of atoms in the peptide together with a torsion term E_{tors} for all torsion angles:

$$\begin{aligned} E_{\text{ECEPP}} &= E_{\text{es}} + E_{\text{vdW}} + E_{\text{hb}} + E_{\text{tors}} , \\ E_{\text{es}} &= \sum_{(i,j)} \frac{332q_i q_j}{\epsilon r_{ij}} , \\ E_{\text{vdW}} &= \sum_{(i,j)} \left(\frac{A_{ij}}{r_{ij}^{12}} - \frac{B_{ij}}{r_{ij}^6} \right) , \\ E_{\text{hb}} &= \sum_{(i,j)} \left(\frac{C_{ij}}{r_{ij}^{12}} - \frac{D_{ij}}{r_{ij}^{10}} \right) , \\ E_{\text{tors}} &= \sum_l U_l (1 \pm \cos(n_l \alpha_l)) . \end{aligned} \quad (11.2)$$

Here, r_{ij} is the distance between the atoms i and j , and α_l is the torsion angle for the chemical bond l . The parameters (q_i , A_{ij} , B_{ij} , C_{ij} , D_{ij} , U_l and n_l) are calculated from crystal structures of amino acids. Since the bond lengths and

bond angles are set constant, the true degrees of freedom are rotations around these bonds characterized by dihedral angles ϕ , ψ , ω and χ_i .

Unfortunately, all-atom models of proteins lead to a very rough energy landscape with a huge number of local minima separated by high-energy barriers. For this reason, sampling of low-energy conformations becomes a hard computational task, and physical quantities cannot be calculated accurately from simple low-temperature molecular dynamics or Monte Carlo simulations. Only recently has progress been in alleviating the above-stated multiple-minima problem. For a review, see, for instance, [8]. In the following, I will describe some of these methods that proved to be successful in numerical simulations. Some recent applications will be presented that illustrate the success and limitations of current protein simulations.

11.2 Energy Landscape Paving

A general characteristic of successful optimization techniques is that they avoid entrapment in local minima and continue to search for further solutions. One example that proved very promising in protein studies is energy landscape paving (ELP) [9]. In this technique, one performs low-temperature Monte Carlo simulations with an effective energy designed to steer the search away from regions that have been already explored:

$$w(\tilde{E}) = e^{-\tilde{E}/k_B T} \quad \text{with} \quad \tilde{E} = E + f(H(q, t)) . \quad (11.3)$$

Here, T is a (low) temperature, \tilde{E} serves as a replacement of the energy E and $f(H(q, t))$ is a function of the histogram $H(q, t)$ in a pre-chosen “order parameter” q . This may be a “natural” quantity for the system under study or the energy itself.

The weight of a local minimum state decreases with the time the system stays in that state, i.e., ELP deforms the energy landscape locally till the local minimum is no longer favored, and the system will explore higher energies. It will then either fall in a new local minimum or walk through this high-energy region till the corresponding histogram entries all have similar frequencies, and the system again has a bias toward low energies. Since the weight factor is time dependent, it follows that ELP violates detailed balance. Hence, the method cannot be used to calculate thermodynamic averages. Note, however, that for $f(H(q, t)) = f(H(q))$ detailed balance is fulfilled, and ELP reduces to the *generalized-ensemble* methods [10] discussed later.

The small peptide Met-Enkephalin is used to illustrate the search process in ELP [9]. This pentapeptide has the sequence Tyr-Gly-Gly-Phe-Met and is a frequently used benchmark model to examine new algorithms. Its ground state is known for the ECEPP/2 field (see [11, 2]), as implemented in the computer code SMMP [11], and has an energy $E_0 = -10.7$ kcal/mol. Since the next higher local minimum has an energy of $E_1 = -9.8$ kcal/mol [12], one can

easily identify any configuration with energy below $E = -9.8$ kcal/mol as a representative of the ground state. As in our algorithmic presentation of ELP, we use the potential energy itself as an order parameter. Thus, the deformed energy landscape of Met-enkephalin is generated by $\tilde{E} = E + H(E, t)$, where $H(E, t)$ is the histogram in energy at MC sweep t . We chose a bin size $E_{bin} = 0.25$ kcal/mol in the histogram and set the temperature to $T = 50$ K.

Figure 11.1 illustrates the search process in energy landscape paving. The starting configuration has an energy of $E_{\text{start}} = -5.1$ kcal/mol and was obtained from a random configuration through quenching in initial 100 sweeps. The simulation soon gets trapped in a local minimum of $E \approx -7.8$ kcal/mol (after only 250 MC sweeps). Through the following MC sweeps, entries in the corresponding histogram bin are accumulated and the energy landscape locally deformed, until after about 750 MC sweeps the simulation escapes this local minimum to find a lower local minimum after 2000 MC sweeps. This process is repeated till the simulation finds the global minimum conformation for the first time after 7260 sweeps. Within the 50 000 sweeps of our simulation, the ground state region ($E < -9.8$ kcal/mol) was reached five times, each time separated by explorations in the high-energy region. Note that the range of energies covered increases with MC time: ELP starts with filling up the small “potholes” in the energy landscape, but fills up also large valleys as the simulation continues.

We have tested the efficiency of ELP by performing 20 independent ELP runs of each 50 000 MC sweeps. The results of the ELP runs are compared with 20 simulated annealing [4] runs of equal statistics using the annealing schedule that proved to be optimal for Met-enkephalin in [13]. However, even with this optimized annealing schedule, the ground state is found only in $8/20 = 40\%$ of the simulations and the average value of the lowest energy conformation ($\langle E_{\text{min}} \rangle = -8.5$ kcal/mol) is above our threshold for ground

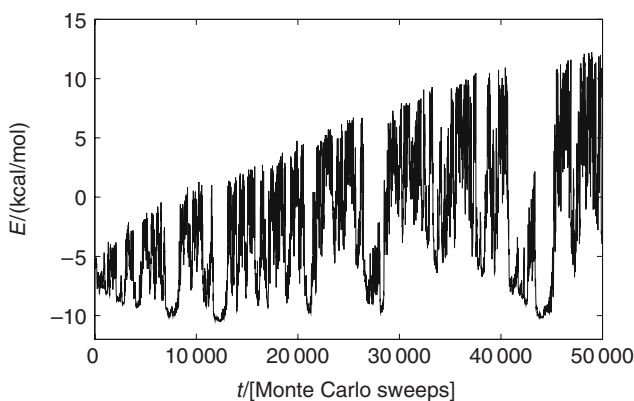


Fig. 11.1. “Time series” of energy for an ELP simulation of the peptide Met-enkephalin. The figure is taken from [9]

state configurations (-9.8 kcal/mol). On the other hand, with ELP we find the ground state in each of the 20 runs. As a consequence, the average of lowest energy states $\langle E_{\min} \rangle = -10.3$ kcal/mol is well below our threshold for ground state configurations.

Note also that ELP allows even the possibility of zero-temperature simulations [14]. For $T \rightarrow 0$ only moves with $\Delta\tilde{E} \leq 0$ will be accepted. If we choose $\tilde{E} = E + cH(E, t)$, we find as acceptance criterion

$$\Delta E + c\Delta H(q, t) \leq 0 \leftrightarrow c\Delta H(q, t) \leq -\Delta E, \quad (11.4)$$

where E is the physical energy. Hence, within ELP the system can overcome even at $T = 0$ any energy barrier. The waiting time for such a move is proportional to the height of the barrier that needs to be crossed. Note that the factor c sets now only the time scale and in this sense the $T = 0$ form of ELP is parameter-free.

11.3 Parallel Tempering

Structure prediction by means of global optimization requires the use of an energy function that describes the interactions within a protein and between the protein and the surrounding water. Hence, any global optimization approach to structure prediction of proteins is limited by the accuracy of the force fields. Global optimization techniques are also not suitable for investigations of the structural transitions in proteins that are a key issue for understanding the folding and biological function of a number of proteins. As with structure prediction, it is necessary to go beyond global optimization techniques such as ELP and to measure thermodynamic quantities, i.e., to sample a set of configurations from a canonical ensemble and take an average of the chosen quantity over this ensemble.

Such sampling is hampered by the roughness of the energy landscape. One popular method to overcome the resulting slow thermalization at low temperatures is parallel tempering [15] (also known as replica exchange method or Multiple Markov chains), a technique that was first applied to protein studies in [16].

In its most common form, one considers in parallel tempering an artificial system built up of N *noninteracting* replicas of the molecule, each at a different temperature T_i . In addition to standard Monte Carlo or molecular dynamics moves that act only on one replica (i.e., the molecule at a fixed temperature), an exchange of conformations between two copies i and $j = i + 1$ is allowed with probability

$$w(\mathbf{C}^{\text{old}} \rightarrow \mathbf{C}^{\text{new}}) = \min\{1, \exp[-\beta_i E(C_j) - \beta_j E(C_i) + \beta_i E(C_i) + \beta_j E(C_j)]\}. \quad (11.5)$$

The exchange of conformations will at low temperatures lead to a faster convergence of the Markov chain than is observed in regular canonical simulations

with only local moves. This is because the resulting random walk in temperatures allows the configurations to move out of local minima and cross energy barriers. Note that parallel tempering does not require Boltzmann weights. The method can be combined easily with other generalized-ensemble techniques as was demonstrated first in [16].

Met-enkephalin is used again to illustrate the parallel tempering algorithm. Simulations with seven copies were performed [16]. The corresponding temperatures are $T_1 = 1000$ K, $T_2 = 500$ K, $T_3 = 330$ K, $T_4 = 250$ K, $T_5 = 170$ K, $T_6 = 100$ K and $T_7 = 50$ K. The simulation consists of 144 000 sweeps for each copy. After each sweep, an exchange of conformations between pairs of copies at neighboring temperatures was tried. The “time series” of temperatures for one of the seven copies is shown in Fig. 11.2. Due to the exchange

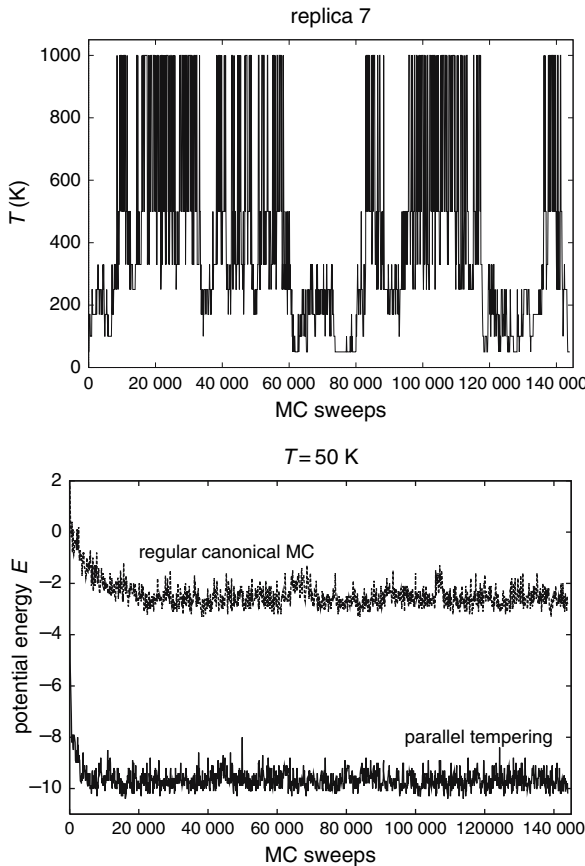


Fig. 11.2. “Time series” of temperature for one copy of Met-enkephalin (*top*) and energy at temperature $T = 50$ K (*bottom*) as obtained from a parallel tempering simulation. The figure is taken from [16]

move, the configuration walks randomly between low temperatures and high temperatures. The resulting random walk in energy ensures – as in the case of ELP – that any energy barrier can be overcome, and the molecule will thermalize at all seven temperatures. The faster convergence can be seen in Fig. 11.2 where also the “time series” in energy is displayed for both a regular canonical simulation at $T = 50$ K and for the copy with $T = 50$ K of a parallel tempering simulation. Obviously, the regular canonical Monte Carlo got trapped in a local minimum and was not able to thermalize. From previous simulations (see 11.7), it is known that even 1 000 000 sweeps are not enough to thermalize Met-enkephalin at $T = 50$ K. On the other hand, with the exchange of configurations by parallel tempering, the simulation thermalizes at $T = 50$ K in less than 10 000 sweeps.

A long-standing problem is how to optimize the temperature distribution of a parallel tempering run 11.8. Commonly, it is assumed that equilibration is fastest if the *local* acceptance rate of swaps is the same for all pairs of neighboring temperatures T_i and T_{i+1} . However, the convergence of a parallel tempering run is given by the relaxation at lowest temperature and can be gauged by the frequency n_{rt} of statistically independent visits at this temperature. Hence, it is this quantity that one has to maximize in order to optimize a parallel tempering simulation. For this purpose, we can add a “up” or “down” to the replica that indicates which of the two extremal temperatures, T_{\min} or T_{\max} , respectively, the replica has visited most recently. For each temperature point in the temperature set $\{T_i\}$, we record two histograms $n_{\text{up}}(T_i)$ and $n_{\text{down}}(T_i)$. For each temperature point, this allows us to evaluate the average fraction of replicas which diffuse from the lowest to the highest temperature as

$$f(T) = \frac{n_{\text{up}}(T)}{n_{\text{up}}(T) + n_{\text{down}}(T)}. \quad (11.6)$$

The so-labeled replicas define a steady-state current from T_{\min} to T_{\max} that is proportional to the round-trip rate n_{rt} and therefore independent of temperature. This current is given by

$$j = D(T)\eta(T)\frac{df}{dT}, \quad (11.7)$$

where $D(T)$ is the local diffusivity at temperature T and $\eta(T)$ is the probability distribution for a replica to reside at temperature T , where the temperature T is now assumed to be a continuous variable (and not limited to the points of the current temperature set). For a given temperature set, we approximate this probability distribution with a step function $\eta(T) = C/\Delta T$, where $\Delta T = T_{i+1} - T_i$ is the length of the temperature interval around temperature $T_i < T < T_{i+1}$ in the current temperature set. The normalization constant C is chosen as

$$\int_{T_1}^{T_N} \eta(T) dT = C \int_{T_1}^{T_N} \frac{dT}{\Delta T} = 1. \quad (11.8)$$

In order to speed up equilibration, we want to maximize the rate of round trips which each replica performs between the two extremal temperatures, or equivalently the diffusive current j , by varying the temperature set $\{T_i\}$ and thus the probability distribution $\eta(T)$. This goal is achieved by minimizing the integral

$$\frac{1}{j} = \int \left[\frac{1}{D(T)\eta(T)} + \lambda\eta(T) \right] dT, \quad (11.9)$$

where we have added a Lagrange multiplier λ which ensures that $\eta(T)$ remains a normalized probability distribution. Varying the probability distribution $\eta(T)$, the integrand in (11.9) is minimized for

$$\eta^{(\text{opt})}(T) = \frac{C'}{\Delta T'} = C' \sqrt{\frac{1}{\Delta T} \frac{df}{dT}} \sim \frac{1}{\sqrt{D(T)}}, \quad (11.10)$$

where the normalization C' is again chosen according to the normalization condition in (11.8). For the optimal temperature set, the temperature points are thus rearranged in such a way that the probability distribution $\eta^{(\text{opt})}(T)$ becomes inversely proportional to the square root of the local diffusivity. Measuring the local diffusivity $D(T)$ for an initial temperature set, we can determine the optimized probability distribution $\eta^{(\text{opt})}(T)$ approximated as a step function in the original temperature set. The *optimized* temperature set $\{T'_i\}$ is then found by choosing the n th temperature point T'_n such that

$$\int_{T'_1}^{T'_n} \eta^{(\text{opt})}(T) dT = n/N, \quad (11.11)$$

where $1 < n < N$ and the two extremal temperatures $T'_1 = T_1$ and $T'_N = T_N$ remain fixed. This feedback of the local diffusivity is then iterated for increasingly long simulation runs until convergence of the optimized temperature set is found [18].

An interesting variant of the parallel tempering idea is “model hopping” (MH) [19] where the random walk in temperatures is replaced by one through an ensemble of models with slightly altered energy functions. For this we assume that the energy function can be separated into two terms: $E = E_A + aE_B$. As in parallel tempering, MH considers N noninteracting copies of the molecule, but copies are now exchanged according to

$$\begin{aligned} w(\mathbf{C}^{\text{old}} \rightarrow \mathbf{C}^{\text{new}}) &= \min\{1, \exp(-\beta [E_A(C_j) + a_i E_B(C_j) \\ &\quad + E_A(C_i) + a_j E_B(C_i) \\ &\quad - E_A(C_i) - a_i E_B(C_i) \\ &\quad - E_A(C_j) - a_j E_B(C_j)])]\} \\ &= \min\{1, \exp(\beta \Delta a \Delta E_B)\}. \end{aligned} \quad (11.12)$$

Here, $\Delta a = a_j - a_i$ and $\Delta E_B = E_B(C_j) - E_B(C_i)$.

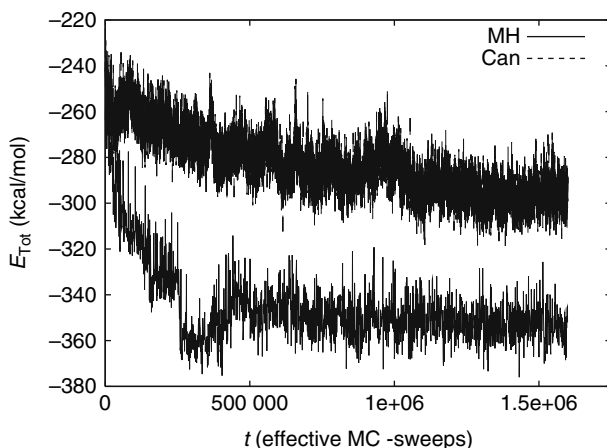


Fig. 11.3. “Time series” of total energy as obtained in an MH run (for $a = 1$) at $T = 300$ K and in a regular canonical Monte Carlo simulation. The figure is taken from [19]

Due to this exchange move, configurations perform a random walk on a ladder of models with $a_1 = 1 > a_2 > a_3 > \dots > a_N$ that differ by the relative contributions of E_B to the total energy E of the molecule. For instance, barriers in the energy landscape of proteins often arise from van der Waals repulsion between atoms that come too close. In MH, the protein walks randomly up and down on a ladder of models with successively smaller contributions from the van der Waals energy. While the “physical” system is on one side of the ladder (at $a_1 = 1$), the (nonphysical) model on the other end of the ladder (at $a_N \ll 1$) may allow atoms to share the same position in space. As the protein “tunnels” in this way through energy barriers, sampling of low-energy configurations will be enhanced in the “physical” model (at $a_1 = 1$). That the resulting random walk in the strength of the vdW-term leads to a faster convergence of the system can be seen in Fig. 11.3 where we draw the time series in energy (for $a_i = 1.0$) and contrast it with a regular canonical simulation at $T = 300$ K. We have plotted here the energies as a function of “effective” MC sweeps taking into account that one sweep in MH corresponds to $N = 8$ sweeps in regular Monte Carlo. Note that the energies in the MH run are on average 70 kcal/mol lower than that of the regular MC run that got trapped in a local minimum.

11.4 Multicanonical Sampling

Generalized-ensemble simulations [10] offer another possibility to overcome the multiple minima problem and to calculate reliable low-temperature quantities. The idea is again to ensure that a simulation does not get trapped in

local minima but samples both low- and high-energy states with sufficient probability. Such movement in and out of local minima is obtained by requiring that a Monte Carlo or molecular dynamics simulation shall lead to a uniform distribution of a pre-chosen physical quantity. Probably the earliest realization of this idea is *umbrella sampling* [20], but it has been lately rediscovered in various forms such as multicanonical sampling [21] and simulated tempering [22]. The first application of these new techniques to protein simulations can be found in [23] where a Monte Carlo technique was used. Later, a formulation for the molecular dynamics method was also developed [24].

In the *multicanonical algorithm* [21], configurations with energy E are assigned a weight $w(E)$ such that the distribution of energies

$$P_{\text{mu}}(E) \propto n(E)w_{\text{mu}}(E) = \text{const} , \quad (11.13)$$

where $n(E)$ is the spectral density. Since all energies appear with the equal probability, a free random walk in the energy space is enforced: the simulation can overcome *any* energy barrier and will not get trapped in one of the many local minima. In order to demonstrate the latter point, the “time series” of energy is shown in Fig. 11.4 as a function of Monte Carlo sweeps for both a regular canonical Monte Carlo simulation at temperature $T = 50$ K (dotted curve) and a multicanonical simulation. The displayed data are again from a simulation of the pentapeptide Met-enkephalin using a slightly modified version [13] of the ECEPP/2 force field. Starting from a random configuration the two simulations continued for 1 000 000 Monte Carlo sweeps. For the canonical run, the curve stays around the value $E = -7$ kcal/mol, with small thermal

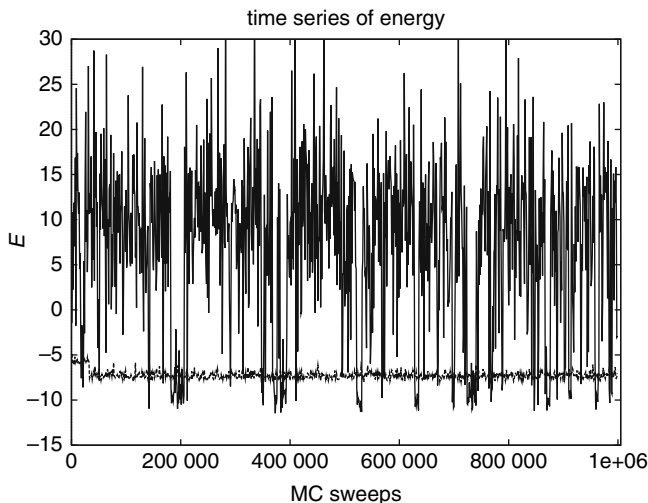


Fig. 11.4. “Time series” of energy for the pentapeptide Met-enkephalin. The results from both a canonical simulation at $T = 50$ K (*dotted line*) and a multicanonical simulation are shown

fluctuations reflecting the low-temperature nature. The run has apparently been trapped in a local minimum, since the mean energy at this temperature is $\langle E \rangle = -11.1$ kcal/mol as found in [13]. On the other hand, the multicanonical simulation covers a much wider energy range than the canonical run. It is a random walk in energy space, which keeps the simulation from getting trapped in a local minimum. From such a multicanonical simulation, one can not only locate the energy global minimum but also calculate the expectation value of any physical quantity \mathcal{O} at temperature T by reweighting techniques [25]:

$$\langle \mathcal{O} \rangle_T = \frac{\int dE \mathcal{O}(E) P_{\text{mu}}(E) w_{\text{mu}}^{-1}(E) e^{-E/k_{\text{B}}T}}{\int dE P_{\text{mu}}(E) w_{\text{mu}}^{-1}(E) e^{-E/k_{\text{B}}T}}, \quad (11.14)$$

$$= \frac{\int dx \mathcal{O}(x) w_{\text{mu}}^{-1}(E(x)) e^{-\beta E(x)}}{\int dx w_{\text{mu}}^{-1}(E(x)) e^{-\beta E(x)}} \quad (11.15)$$

where x stands for configurations.

Unlike in the canonical ensemble, the weights $w_{\text{mu}}(E) \propto n^{-1}(E)$ are not a priori known and one needs their estimates for a numerical simulation. Hence, multicanonical sampling consists of three steps: Calculation of the multicanonical (and other generalized-ensemble weights) is usually done by an iterative procedure [13, 23]. We remark that calculation of the weights can be slow (about 40% of the total CPU time was spent in [23] on this point), and several attempts were made to obtain generalized-ensemble weights in a faster way; see, for instance, [26].

11.5 Other Generalized-Ensemble Techniques

In multicanonical simulations, the computational effort increases with the number of residues like $\approx N^4$ (when measured in Metropolis updates) [27]. In general, the computational effort in simulations increases with $\approx X^2$ where X is the variable in which one wants a flat distribution. This is because generalized-ensemble simulations realize by construction of the ensemble a 1D random walk in the chosen quantity X . In the multicanonical algorithm, the reaction coordinate X is the potential energy $X = E$. Since $E \propto N^2$, the above scaling relation for the computational effort $\approx N^4$ is recovered. Hence, multicanonical sampling is not always the optimal generalized-ensemble algorithm in protein simulations. A better scaling of the computer time with size of the molecule may be obtained by choosing a more appropriate reaction coordinate for our ensemble than the energy.

One often used choice is *simulated tempering* [22] where the temperature itself becomes a dynamic variable and is sampled uniformly. Temperature and configuration are both updated with a weight

$$w_{\text{ST}}(T, E) = e^{-E/k_{\text{B}}T - g(T)}. \quad (11.16)$$

Here, the function $g(T)$ is chosen so that the probability distribution of temperature is given by

$$P_{\text{ST}}(T) = \int dE \, n(E) \, e^{-E/k_{\text{B}}T - g(T)} = \text{const} . \quad (11.17)$$

Physical quantities have to be sampled for each temperature point separately, and expectation values at intermediate temperatures are calculated by reweighting techniques [25].

As common in generalized-ensemble simulations, the weight $w_{\text{ST}}(T, E)$ is not a priori known (since it requires knowledge of the parameters $g(T)$) and their estimator has to be calculated. They can be again obtained by an iterative procedure as described in Sect. 11.4. In the simplest version, the improved estimator for $g^{(i)}(T)$ for the i th iteration is calculated from the histogram of *temperature* distribution $H_{\text{ST}}^{(i-1)}(T)$ of the preceding simulation as follows:

$$g^{(i)}(T) = g^{(i-1)}(T) + \log H_{\text{ST}}^{(i-1)}(T) . \quad (11.18)$$

In this procedure, one uses that the histogram of the i th iteration is given by

$$H_{\text{ST}}(T) = e^{-g_{i-1}(T)} Z_i(T) , \quad (11.19)$$

where $Z_i(T) = \int dE n(E) \exp(-E/k_{\text{B}}T)$ is an estimate for the canonical partition function at temperature T . Setting $\exp(g_i(T)) = Z_i(T)$ leads to the iterative relationship of (11.18).

11.6 Helix Versus Sheet Formation

It has become clear over the last years that misfolding of proteins, often involving formation of β -sheets instead of α -helices, is the cause of various illnesses including Alzheimer's disease, bovine spongiform encephalopathy (BSE) and other Prion diseases. In order to research the $\alpha \rightarrow \beta$ transition we have chosen a peptide, whose sequence of amino acids in one letter code is EKAYLRT and that appears in naturally occurring proteins with significant frequency at positions of both α -helices and β -sheets. Our results rely on multicanonical simulations of peptides in a detailed representation where the interactions between all atoms are taken into account. The interactions between the atoms are described by a standard force field, ECEPP/2 [7], as implemented in the program package SMMP [11]. A more detailed account of our results and the technical details of the simulations is published in [28].

We start with presenting our results for the isolated EKAYLRT peptide and display its average helicity $\langle n_{\text{H}} \rangle$ as a function of temperature in Fig. 11.5. Data obtained in gas phase (GP) and for the soluted peptide (ASA) are shown. In both cases, we observe a steep helix-coil transition that separates a high-temperature region with little helicity from a low-temperature region where

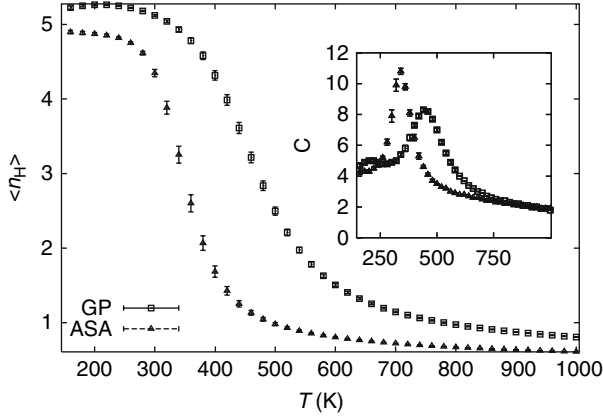


Fig. 11.5. The average number $\langle n_H \rangle$ of helical residues as a function of temperature T for EKAYLRT in gas phase (GP) and simulated with an implicit solvent term (ASA). The specific heat $C(T)$ as function of temperature T is displayed in the inset. The figure is taken from [28]

most of the residues are part of an α -helix. The location of this helix-coil transition can be determined from the corresponding peaks in the specific heat $C(T)$ that are drawn in the inset of Fig. 11.5. The more pronounced peak for the solvated molecule indicates a temperature $T_{\text{hc}}^{\text{ASA}} = 340 \pm 10$ K that is considerably lower than the one in gas phase: $T_{\text{hc}}^{\text{GP}} = 445 \pm 15$ K.

Our results indicate that the peptide EKAYLRT has an intrinsic tendency to form helices. Since EKAYLRT appears *within* proteins in both helices and β -sheets, sheet formation must be due to the interaction of the peptide with its surrounding. We conjecture that EKAYLRT forms a β -sheet if it is in the proximity of another strand. Since the present version of SMMP does not allow the simulation of two interacting proteins, we have studied instead the peptide EKAYLRT-GGGG-EKAYLRT, with the C-terminal EKAYLRT residues kept as β -strand. The four glycine residues form a flexible chain that holds the two EKAYLRT units together but allows their relative positions to vary.

In Fig. 11.6, we display the helicity and sheetness of the N-Terminal EKAYLRT at $T = 300$ K. Both quantities are shown as functions of the end-to-end distance $d_{\text{e-e}}$ which is a measure for the separation of the two EKAYLRT chains. For $d_{\text{e-e}} \gtrsim 16$ Å the N-terminal EKAYLRT chain forms a complete helix and strands are rarely observed. Hence, for these distances, the N-terminal chain has a similar behavior as the isolated EKAYLRT peptide. However, the helicity decreases with end-to-end distance and vanishes for $d_{\text{e-e}} \lesssim 10$ Å. At the same time, the sheetness increases and the peptide forms a β -sheet for $d_{\text{e-e}} \approx 5 - 6$ Å. Examples of configurations that correspond to the two minima are shown in Fig. 11.7.

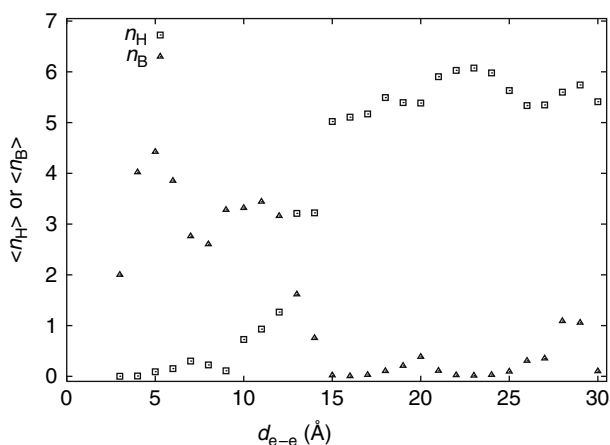


Fig. 11.6. The average helicity $\langle n_H \rangle$ and sheetness $\langle n_B \rangle$ at $T = 300$ K of the N-terminal EKAYLRT residues as a function of the end-to-end distance d_{e-e} . The figure is taken from [28]

Our results [28] suggest autocatalytic properties for EKAYLRT: if the peptide forms a strand, it becomes favorable for other nearby EKAYLRT molecules to transform themselves into a sheet. The behavior of EKAYLRT is similar to the mechanism thought to be responsible for the outbreak of neuro-degenerative illnesses such as Alzheimer's or the Prion diseases. Outbreak of these illnesses is associated with the appearance of a misfolded structure that

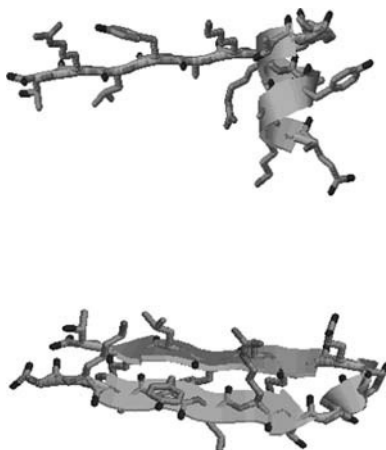


Fig. 11.7. Low-energy configurations of the interacting EKAYLRT molecule. The one in the upper plot is the lowest energy configuration where the EKAYLRT-residues form an α -helix; the one in the lower plot where they form a β -sheet. The figure is taken from [28]

differs from the correctly folded one by a β -sheet instead of an α -helix. The misfolded structure is thought to be autocatalytic; that is, its presence leads to a structural transition by which the correctly folded (helical) structure changes into the harmful β -sheet form. Hence, peptides based on the sequence of amino acids EKAYLRT can serve as simple models to study $\alpha \rightarrow \beta$ transitions and the mechanism of Prion diseases.

11.7 Structure Predictions of Small Proteins

Computational protein studies are limited not only by the availability of effective search algorithms but also on the accuracy of current protein models. In order to test the latter point, one needs to study sufficiently large molecules. Our example is the 36-residue villin headpiece subdomain HP-36, one of the smallest peptides that can fold autonomously. HP-36 was chosen by Duan and Kollman for a 1-microsecond molecular dynamics simulation of protein folding [29]. The experimental structure was determined by NMR analysis [30]. Luc Wille (Florida Atlantic University) and I have used this protein to study the efficiency of the ELP algorithm. We have used the approach of [11.1] to approximate the interaction between protein and water, with the parameters σ_i chosen from [31].

Built up only out of α -helices as secondary structure elements, HP-36 allows in a simple way the definition of an order parameter to characterize configurations other than by their energy. This natural order parameter is the number n_H of residues in the peptide which are part of an α -helix. Throughout the search process, we try to deform the energy landscape by means of a histogram $H(E, n_H, t)$ in *both* helicity and energy: $\tilde{E} = E + H(E, n_H, t)$. Operating again at a temperature $T = 50$ K, we find as weights for the search algorithm

$$w(E, n_H, t) = e^{-\beta(E+H(E, n_H, t))} . \quad (11.20)$$

Using this weight, we performed simulations with 50 000 MC sweeps (starting from random configurations), keeping track of the lowest energy configuration during the search process.

The structure of HP-36 as obtained from the Protein Data Bank (PDB code 1vii) is shown in Fig. 11.8. The structure consists of three helices between residues 4–8, 15–18 and 23–32, respectively, which are connected by a loop and a turn. We find for this structure in our model an energy (ECEPP/2 + solvation term) $E_{\text{nat}} = -276$ kcal/mol. Our approach led to a configuration with the lowest energy $E_{\text{min}} = -277$ kcal/mol which we show also in Fig. 11.8 [9]. The above structure consists of three helices where the first helix stretches from residue 2 to residue 11 and is more elongated than the corresponding one in the native structure (residues 4–8). The second helix consists of residues 13–17 (compared to residues 15–18 in the native structure) and the third helix stretches from residue 23–33 (residues 23–32 in the PDB



Fig. 11.8. *Top:* Experimental structure of HP-36 as deposited in the PDB data-bank. *Middle:* Lowest energy structure as obtained in a simulation of the solvated peptide. *Bottom:* Lowest energy structure of HP-36 as obtained in a simulation in gas phase

structure). The structure has 95% of the native helical content and a radius of gyration $R_g = 10.1 \text{ \AA}$ which indicates that the numerically obtained structure is slightly less compact than the experimental structure ($R_g = 9.6 \text{ \AA}$); 60% of native contacts are formed. These values are comparable with the results in [29] (but required orders of magnitude less computer time) where the optimal structure of a 1-microsecond molecular dynamic folding simulation showed 80% of native helical content and 62% of native contacts. Similarly comparable were the values of the root-mean-square deviation (RMSD) of both numerically determined conformers to the native structure: 5.8 \AA versus 5.7 \AA in [29] (counting only backbone atoms). On the other hand, an ELP simulation of 50 000 sweeps relying only on the ECEPP/2 force field led to a structure with an ECEPP energy of $E_{GP} = -192 \text{ kcal/mol}$. That structure, shown at the bottom of Fig. 11.8, is built out of two helices (between residues 2–16 and 23–33) connected by a loop and differs significantly from the regularized PDB structure with the higher potential energy $E_{nat} = -176$

kcal/mol. Hence, the native structure of the peptide HP-36 is *not* the global minimum configuration in ECEPP/2 in gas phase.

In order to understand more the differences between the gas-phase results and that with a solvent accessible surface term, Chai-Yu Lin, Chin-Ku Hu (both Academia Sinica, Taiwan) and I have simulated recently HP-36 with parallel tempering on 20 nodes of a cluster of IBM 4-ways 375 MHz SMP Thin Nodes [32]. We have chosen as temperatures $T = 1000, 900, 800, 700, 610, 560, 530, 510, 495, 485, 475, 465, 450, 420, 390, 360, 330, 300, 275$ and 250 K. On each node, we performed 150 000 MC sweeps, and a replica exchange move was attempted after each sweep. Both gas-phase simulations and such relying on a solvent-accessible surface term with the parameter set OONS of [6] were performed.

From these parallel tempering simulations, we have calculated the number of helical residues as function of temperature. Figure 11.9 displays our results. Little difference is found at high temperatures. However, below the transition temperature $T \approx 490$ K the data for both simulations diverge. The helicity grows rapidly with decreasing temperature in the OONS simulation while it stays small in gas phase. Configurations in gas phase and in OONS simulations differ also in their compactness. We display in Fig. 11.10 for HP-36 two quantities that measure the compactness of protein configurations. The main graph is a plot of the average radius of gyration $\langle r_{\text{gy}} \rangle(T)$ as a function of temperature. The corresponding values for the total number of contacts $\langle n_{\text{TC}}(T) \rangle$ are shown in the inset. Both plots indicate that configurations in gas phase are substantially more compact than the ones in the OONS simulation. For instance, at $T = 300$ K, we find $r_{\text{gy}} = 9.6(1)$ Å in gas phase compared to $r_{\text{gy}} = 12.5(1)$ Å in OONS simulations. Note that even at

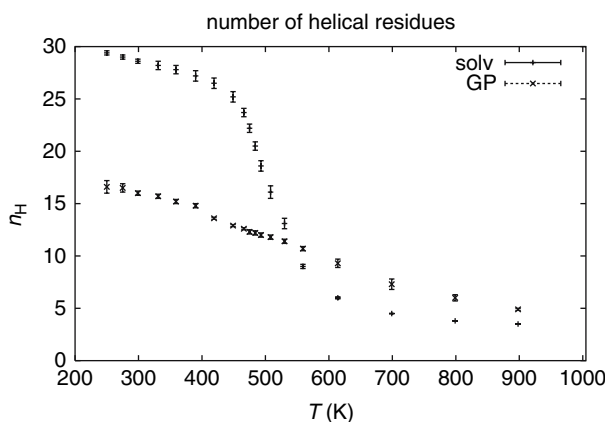


Fig. 11.9. Average number of helical residues $\langle n_{\text{H}} \rangle(T)$ of HP-36 as a function of temperature for both the solvated protein and in gas phase. The figure is taken from [32]

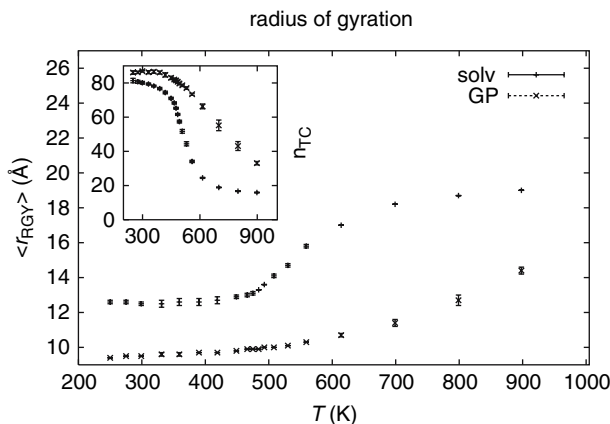


Fig. 11.10. Average radius of gyration $\langle r_{gy} \rangle(T)$ of HP-36 as a function of temperature for both the solvated protein and in gas phase. The figure is taken from [32]

$T = 1000$ K, the peptide in gas phase has a radius of gyration $r_{gy} = 15.6(1)$ Å and is substantially more compact than in OONS simulation ($r_{gy} = 19.2$ Å). We conjecture that this bias toward compact configurations inhibits the formation of α -helices and that the low-energy states of HP-36 in gas phase are characterized by large density and low helicity.

Our simulations of HP-36 demonstrate that the simulation techniques described in this review allow one not only to predict the structure of small peptides but also to evaluate the limitations of the utilized energy functions. For instance, in our example, we were able to determine the reasons behind the failure of gas-phase simulations when compared to such with simple solvent approximations. Since presently available energy functions are often parametrized for small molecules, their limitations will become more obvious as one proceeds toward larger systems. Modern simulation techniques may open ways to unveil and finally overcome these limitations.

This can also be seen in our investigations of the 46-residue-long 10–55 fragment of the B domain of staphylococcal protein A. This three-helix bundle [33] has been studied extensively with both coarse-grained [34, 35, 36] and all-atom models [37]. The experimentally observed structure (PDB code 1BDD) of the protein is displayed in Fig. 11.11, with the three helices marked I, II and III, respectively. After minimization in our force field, energy of the protein is $E_{tot} = -596.9$ kcal/mol.

Figure 11.11 also displays the configuration with lowest energy obtained in our MH simulation. After minimization, its energy of $E_{tot} = -666.5$ kcal/mol is 70 Kcal/mol lower than that of the PDB structure. The radius of gyration $r_{gy} = 10.7$ Å and solvent accessible surface $A = 3804$ Å² are larger than the values found for the PDB structure ($r_{gy} = 9.7$ Å and $A = 3333$ Å²). All three helices are formed. However, the middle helix II is broken up by the GLY₂₁

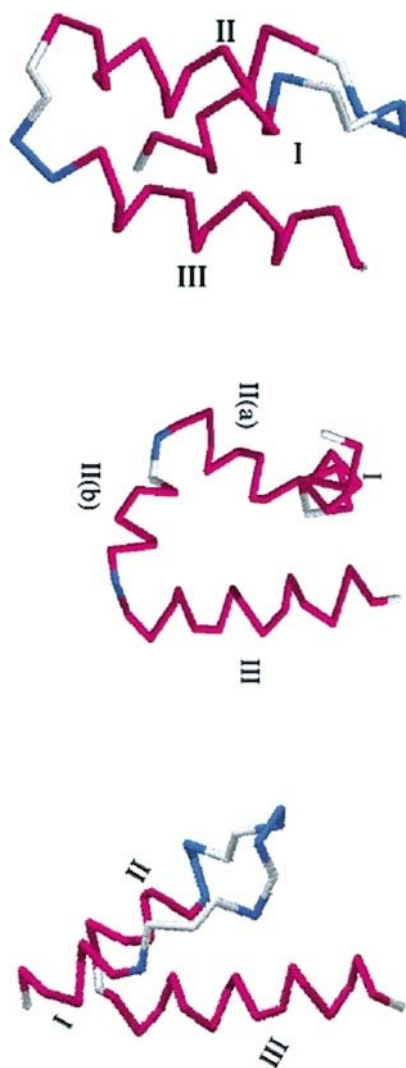


Fig. 11.11. *Top:* Experimental observed structure of the fragment 10–55 of the B domain of staphylococcal protein A (PDB-code 1BDD). *Middle:* Lowest energy configuration of the B domain as obtained in our MH simulation. *Bottom:* Lowest energy configuration of the B domain as obtained with a modified solvation parameter set

residue into helices II(a) and II(b), and this configuration is therefore built out of four helices. The total helicity, defined as the number of residues that are part of an α -helix, is 85% higher than for the PDB structure (74%). The root-mean-square deviation (RMSD) between both configurations (calculated over backbone atoms) is 6.8 Å. Modifying our implicit solvent in a simulation of protein A of 100 000 sweeps, we find indeed a lowest energy configuration

(Fig. 11.11) that differs from the native structure by only 3.2 Å [19] and has a radius of gyration $r_{\text{gy}} = 10.0$ Å and a solvent accessible surface area of $A = 3553$ Å².

11.8 Conclusions

I gave a brief introduction into some techniques used in simulations of the protein folding problem. These examples demonstrate that modern simulation algorithms are well suited for investigations of both the thermodynamics of proteins and the prediction of their structure. It seems now that all-atom simulations of proteins are rather restricted by the accuracy of the present energy functions than by the efficiency of the search algorithms.

Acknowledgements

The presented work was partially supported by research grants of the National Science Foundation (CHE-0313618) and the National Institutes of Health (GM62838), both USA.

References

1. C. B. Anfinsen: *Science* **181**, 223 (1973) [294]
2. I. P. Androulakis, C. D. Maranas, C. A. Floudas: *J. Glob. Opt.* **11**, 1 (1997) [294]
3. Z. Li, H. A. Scheraga: *Proc. Natl. Acad. Sci. USA* **84**, 6611 (1987) [294]
4. S. Kirkpatrick, C. D. Gelatt, Jr., M. P. Vecchi: *Science* **220**, 671 (1983) [294, 296]
5. J. Holland, University of Michigan Press, 1975 [294]
6. T. Ooi, M. Obatake, G. Nemethy, H. A. Scheraga: *Proc. Natl. Acad. Sci. USA* **8**, 3086 (1987) [294, 309]
7. M. J. Sippl, G. Némethy, H. A. Scheraga: *J. Phys. Chem.* **88**, 6231 (1984), and references therein [294, 304]
8. U. H. E. Hansmann, Y. Okamoto: *Curr. Opin. Struct. Biol.* **9**, 177 (1999) [295]
9. U. H. E. Hansmann, L. T. Wille: *Phys. Rev. Lett.* **88**, 068105 (2002) [295, 296, 307]
10. U. H. E. Hansmann, Y. Okamoto: In *Annual Reviews in Computational Physics VI*, edited by D. Stauffer (World Scientific, Singapore, 1999), p. 129 [295, 301]
11. F. Eisenmenger, U. H. E. Hansmann, Sh. Hayryan, C.-K. Hu: *Comput. Phys. Commun.* **138**, 192 (2001) [295, 304]
12. F. Eisenmenger, U. H. E. Hansmann: *J. Phys. Chem. B* **101**, 3304 (1997) [295]
13. U. H. E. Hansmann, Y. Okamoto: *Physica A* **212**, 415 (1994) [296, 302, 303]
14. A. Schug, W. Wenzel, U. H. E. Hansmann: *J. Chem. Phys.* **122** 194711 (2005) [297]
15. K. Hukushima, K. Nemoto: *J. Phys. Soc. Jpn.* **65**, 1604 (1996); G. J. Geyer: *J. Am. Stat. Assoc.* **90** (431), 909 (1995) [297]
16. U. H. E. Hansmann: *Chem. Phys. Lett.* **281**, 140 (1997) [297, 298]
17. U. H. E. Hansmann, Y. Okamoto: *Phys. Rev. E* **56**, 2228 (1997) [299]
18. S. Trebst, M. Troyer, U. H. E. Hansmann: *J. Chem. Phys.* **124**, 174903 (2006) [299, 300]

19. W. Kwak, U. H. E. Hansmann: *Phys. Rev. Lett.* **95**, 138102 (2005) [300](#), [301](#), [312](#)
20. G. M. Torrie, J. P. Valleau: *J. Comput. Phys.* **23**, 187 (1977) [302](#)
21. B. A. Berg, T. Neuhaus: *Phys. Lett. B* **267**, 249 (1991) [302](#)
22. A. P. Lyubartsev, A. A. Martinovski, S. V. Shevkunov, P. N. Vorontsov-Velyaminov: *J. Chem. Phys.* **96**, 1776 (1992); E. Marinari, G. Parisi: *Europhys. Lett.* **19**, 451 (1992) [302](#), [303](#)
23. U. H. E. Hansmann, Y. Okamoto: *J. Comp. Chem.* **14**, 1333 (1993) [302](#), [303](#)
24. U. H. E. Hansmann, Y. Okamoto, F. Eisenmenger: *Chem. Phys. Lett.* **259**, 321 (1996) [302](#)
25. A. M. Ferrenberg, R. H. Swendsen: *Phys. Rev. Lett.* **61**, 2635 (1988); A. M. Ferrenberg, R. H. Swendsen: *Phys. Rev. Lett.* **63**, 1658(E) (1989); and references given in the erratum [303](#), [304](#)
26. F. Wang, D. P. Landau: *Phys. Rev. Lett.* **86**, 2050 (2001) [303](#)
27. U. H. E. Hansmann, Y. Okamoto: *J. Chem. Phys.* **110**, 1267 (1999); U. H. E. Hansmann, Y. Okamoto: *J. Chem. Phys.* **111**, 1339(E) (1999) [303](#)
28. Y. Peng, U. H. E. Hansmann: *Phys. Rev. E* **68**, 041911 (2003) [304](#), [305](#), [306](#)
29. Y. Duan, P. A. Kollman: *Science* **282**, 740 (1998) [307](#), [308](#)
30. C. J. McKnight, D. S. Doehring, P. T. Matsudaria, P. S. Kim: *J. Mol. Biol.* **260**, 126 (1996) [307](#)
31. L. Wesson, D. Eisenberg: *Protein Sci.* **1**, 227 (1992) [307](#)
32. C.-Y. Lin, C.-K. Hu, U. H. E. Hansmann: *Proteins* **52**, 436 (2003) [309](#), [310](#)
33. H. Gouda, H. Torigoe, A. Saito, M. Sato, Y. Arata, I. Shimada: *Biochemistry* **31**, 9665 (1992) [310](#)
34. G. Favrin, A. Irbäck, S. Wallin: *Proteins* **47**, 99 (2002) [310](#)
35. J. Lee, A. Liwo, H. A. Scheraga: *Proc. Natl. Acad. Sci. USA* **96**, 2025 (1999) [310](#)
36. A. Ghosh, R. Elber, H. A. Scheraga: *Proc. Natl. Acad. Sci. USA* **99**, 10394 (2002) [310](#)
37. E. M. Boczeko, Ch. L. Brooks, III: *Science* **269**, 393 (1995) [310](#)

Algorithmic Developments

Markov Chain Monte Carlo Methods for Simulations of Biomolecules

Bernd A. Berg^{1,2}

¹ School of Computational Science (SCS), Florida State University, Tallahassee, FL 32306-4120, USA

berg@scs.fsu.edu

² Department of Physics, Florida State University, Tallahassee, FL 32306-4350, USA

berg@hep.fsu.edu

Abstract. The computer revolution has been driven by a sustained increase of computational speed of approximately one order of magnitude (a factor of ten) every 5 years since about 1950. In natural sciences, this has led to a continuous increase of the importance of computer simulations. Major enabling techniques are Markov Chain Monte Carlo (MCMC) and molecular dynamics (MD) simulations.

This article deals with the MCMC approach. First, basic simulation techniques as well as methods for their statistical analysis are reviewed. Afterwards, the focus is on generalized ensembles and biased updating. These are two advanced techniques, which are of relevance for simulations of biomolecules or are expected to become relevant in that respect. In particular, we consider the multicanonical ensemble and the replica exchange method (also known as parallel tempering or method of multiple Markov chains).

12.1 Introduction

Markov chain Monte Carlo (MCMC) calculations started in earnest with the 1953 paper by Nicholas Metropolis, Arianna Rosenbluth, Marshall Rosenbluth, Augusta Teller and Edward Teller [1]. Since then, MCMC simulations have become an indispensable tool with applications in many branches of science. Some of those are reviewed in the proceedings [2] of the 2003 Los Alamos conference, which celebrated the 50th birthday of Metropolis simulations.

The purpose of this article is to give a concise overview ranging from statistical preliminaries and plain Monte Carlo (MC) calculations over basic techniques for MCMC simulations to advanced methods, which are indispensable when it comes to the simulations of complex systems with frustrated interactions. For such systems, rugged free-energy landscapes are typical. Here, our focus is on biomolecules such as peptides (small proteins) in an all-atom approach defined by a model energy function. At a given temperature, this

energy function determines in principle the Gibbs ensemble of the molecule. In practice, equilibrium is sometimes hard to reach in MCMC simulations of the canonical ensemble. Considerable improvements can be made by using generalized ensembles and biased sampling.

The first part of this article gives a treatment of the MCMC fundamentals that is largely based on the author's book [3] on the subject, which gives many more details and contains extensive additional material. The book comes with computer code that can be downloaded from the web. The solutions of numerous numerical assignments are reproducible by compiling and running the corresponding computer programs. Information and a link to the computer code are presently found on the web at <http://www.scs.fsu.edu/~berg>.

The second part of this article builds on original literature of generalized ensemble methods [4, 5, 6, 7, 8, 9, 10, 11, 12]. We start with a brief history and elaborate on the underlying ideas. Subsequently, we turn to biophysics, where generalized ensembles were introduced in [13, 14]. Finally, a scheme for biasing the Metropolis updating proposals [15] is considered, which can be combined with generalized ensembles.

As our emphasis is on explaining MCMC methods, we restrict ourselves to simple models, which are well suited for illustrating the essence of a method. Our article is organized as follows. Section 12.2 introduces the MCMC method. Section 12.3 discusses the statistical analysis of autocorrelated MCMC data. Section 12.4 deals with generalized ensembles and Sect. 12.5 with biased MCMC updating. A short outlook and conclusions are given in Sect. 12.6. It should be noted that these lecture notes are not supposed to be an unbiased review but are based on work in which the author has been involved or is particularly interested.

12.2 Markov Chain Monte Carlo

12.2.1 Statistical Preliminaries

Let $f(x)$ be a probability density and x^r its associated random variable. The (*cumulative*) *distribution function* (CDF) of the random variable x^r is defined as

$$F(x) = P(x^r \leq x) = \int_{-\infty}^x f(x) dx, \quad (12.1)$$

where $P(x^r \leq x)$ is the probability for $x^r \leq x$. A particularly simple and important case is the *uniform probability distribution* for random numbers between $[0, 1)$:

$$u(x) = \begin{cases} 1 & \text{for } 0 \leq x < 1; \\ 0 & \text{elsewhere.} \end{cases} \quad (12.2)$$

Remarkably, the uniform distribution allows for the construction of general probability distributions. Let

$$y = F(x) = \int_{-\infty}^x f(x') dx'$$

and assume that the inverse function $x = F^{-1}(y)$ exists. For y^r being a uniformly distributed random variable in the range $[0, 1)$, it follows that

$$x^r = F^{-1}(y^r) \quad (12.3)$$

is distributed according to the probability density $f(x)$. To generate the uniform distribution on a computer, one relies on pseudo-random number generators. Desirable properties are randomness according to statistical tests, a long period, computational efficiency, repeatability, portability and homogeneity (all subsets of bits are random). Our purposes are reasonably well served by the generator of Marsaglia and collaborators [16], which comes as part of the code of [3].

12.2.2 Partition Function and Potts Models

MC simulations of systems described by the Gibbs canonical ensemble aim at calculating estimators of physical observables at temperature T . In the following, we choose units so that the Boltzmann constant becomes one, i.e., $\beta = 1/T$. Let us consider the calculation of the *expectation value* of an *observable* \mathcal{O} . Mathematically all systems on a computer are discrete because a finite word length has to be used. Hence, the expectation value is given by the sum

$$\hat{\mathcal{O}} = \hat{\mathcal{O}}(\beta) = \langle \mathcal{O} \rangle = Z^{-1} \sum_{k=1}^K \mathcal{O}^{(k)} e^{-\beta E^{(k)}}, \quad (12.4)$$

where

$$Z = Z(\beta) = \sum_{k=1}^K e^{-\beta E^{(k)}} \quad (12.5)$$

is the *partition function*. The index $k = 1, \dots, K$ labels the *configurations* of the system, and $E^{(k)}$ is the (internal) energy of configuration k . The configurations are also called *microstates*. To distinguish the configuration index from other indices, it is put in parenthesis.

We introduce generalized Potts models on d -dimensional hypercubic lattices with periodic boundary conditions (i.e., the models are defined on a torus in d dimensions). Without being overly complicated, these models are general enough to illustrate the essential features of MCMC simulations. Various subcases are by themselves of physical interest. See F. Y. Wu [17] for a review of Potts models. We define the energy function of the system by

$$E^{(k)} = -2 \sum_{\langle ij \rangle} \delta(q_i^{(k)}, q_j^{(k)}) + \frac{2dN}{q} \quad \text{where} \quad \delta(q_i, q_j) = \begin{cases} 1 & \text{for } q_i = q_j \\ 0 & \text{for } q_i \neq q_j \end{cases}. \quad (12.6)$$

The sum $\langle ij \rangle$ is over the nearest neighbor lattice sites and $q_i^{(k)}$ is called the *Potts spin* or *Potts state* of configuration k at site i . For the q -state Potts model, $q_i^{(k)}$ takes on the values $1, \dots, q$. The case $q = 2$ becomes equivalent to the Ising ferromagnet. In $d = 2$ dimensions, the phase transition is second order for $q \leq 4$ and first order for $q \geq 5$. The exact infinite-volume latent heats Δe_s and entropy discontinuities Δs were calculated by Baxter [18], and the interface tensions f_s were derived later, see [19] and references therein.

12.2.3 Sampling, Reweighting and Important Configurations

For the Ising model (2-state Potts), it is straightforward to *sample statistically independent configurations*. We simply have to generate N spins, each either 0 or 1 with 50% likelihood. This is called *random sampling*. In Fig. [12.1], a thus obtained histogram for the 2d Ising model *energy per spin* is depicted.

Note that it is important to distinguish the energy measurements on single configurations from the expectation value. The expectation value \hat{e}_s is a single number, while e_s fluctuates. From the measurement of many e_s values, one finds an estimator of the mean, \bar{e}_s , which fluctuates with a reduced variance.

The histogram entries at $\beta = 0$ can be *reweighted* so that they correspond to other β values. We simply have to multiply the entry corresponding to energy E by $\exp(-\beta E)$. Similarly, histograms corresponding to the Gibbs ensemble at some value β_0 can be reweighted to other β values. Care has to be taken to ensure that the involved arguments of the exponential function

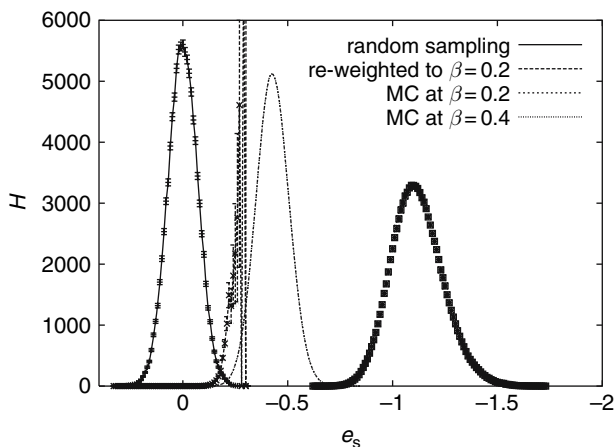


Fig. 12.1. Energy histograms of 100 000 entries each for the Ising model on a 20×20 lattice: random sampling gives statistically independent configurations at $\beta = 0$. Histograms at $\beta = 0.2$ and $\beta = 0.4$ are generated with Markov chain MC. Reweighting of the $\beta = 0$ random configurations to $\beta = 0.2$ is shown to fail. These are assignments a0301_02 and a0303_02 of [3]

do not become too large [3]. Reweighting has a long history, which we discuss in Sect. 12.4.1.

In Fig. 12.1, reweighting is done from $\beta_0 = 0$ to $\beta = 0.2$. But, by comparison to the histogram from a Metropolis MC calculation at $\beta = 0.2$, the result is seen to be disastrous. The reason is easily identified: In the range where the $\beta = 0.2$ histogram takes on its maximum, the $\beta = 0$ histogram has not a single entry. Our random sampling procedure misses the important configurations at $\beta = 0.2$. Reweighting to new β values works only in a range $\beta_0 \pm \Delta\beta$, where $\Delta\beta \rightarrow 0$ in the infinite-volume limit. Details are given in Sect. 12.4.1.

Let us determine the important contributions to the partition function. The partition function can be rewritten as a sum over energies

$$Z = Z(\beta) = \sum_E n(E) e^{-\beta E}, \quad (12.7)$$

where the unnormalized spectral density $n(E)$ is defined as the number of microstates k with energy E . For a fixed value of β , the energy probability density

$$P_\beta(E) = c_\beta n(E) e^{-\beta E} \quad (12.8)$$

is peaked around the average value $\hat{E}(\beta)$, where c_β is a normalization constant determined by $\sum_E P_\beta(E) = 1$. The important configurations at temperature $T = 1/\beta$ are at the energy values for which the probability density $P_\beta(E)$ is large. To sample them efficiently, one needs a procedure which generates the configurations with their Boltzmann weights

$$w_B^{(k)} = e^{-\beta E^{(k)}}. \quad (12.9)$$

The number of configurations $n(E)$ and the weights combine then so that the probability to generate a configuration at energy E becomes $P_\beta(E)$ as given by (12.8).

12.2.4 Importance Sampling and Markov Chain Monte Carlo

For the canonical ensemble, *importance sampling* generates configurations k with probability

$$P_B^{(k)} = c_B w_B^{(k)} = c_B e^{-\beta E^{(k)}}, \quad (12.10)$$

where the constant c_B is determined by the normalization condition $\sum_k P_B^{(k)} = 1$. The vector $(P_B^{(k)})$ is called *Boltzmann state*. When configurations are stochastically generated with probability $P_B^{(k)}$, the expectation value becomes the *arithmetic average*:

$$\hat{\mathcal{O}} = \hat{\mathcal{O}}(\beta) = \langle \mathcal{O} \rangle = \lim_{N \rightarrow \infty} \frac{1}{N} \sum_{n=1}^N \mathcal{O}^{(k_n)}. \quad (12.11)$$

Truncating the sum at some finite value of N , we obtain an *estimator of the expectation value*

$$\overline{\mathcal{O}} = \frac{1}{N} \sum_{n=1}^N \mathcal{O}^{(k_n)} . \quad (12.12)$$

Normally, we cannot generate configurations k directly with the probability (12.10), but they may be found as members of the equilibrium distribution of a dynamic process. A *Markov process* is a particularly simple dynamic process, which generates configuration k_{n+1} stochastically from configuration k_n , so that no information about previous configurations k_{n-1}, k_{n-2}, \dots is needed. The elements of the Markov process *time series* are the configurations. Assume that the configuration k is given. Let the transition probability to create the configuration l in one step from k be given by $W^{(l)(k)} = W[k \rightarrow l]$. The *transition matrix*

$$W = \left(W^{(l)(k)} \right) \quad (12.13)$$

defines the Markov process. Note that this matrix is very big (never stored in the computer) because its labels are the configurations. To generate configurations with the desired probabilities, the matrix W needs to satisfy the following properties:

(i) *Ergodicity*:

$$e^{-\beta E^{(k)}} > 0 \text{ and } e^{-\beta E^{(l)}} > 0 \text{ imply} \quad (12.14)$$

an integer number $n > 0$ exists so that $(W^n)^{(l)(k)} > 0$ holds.

(ii) *Normalization*:

$$\sum_l W^{(l)(k)} = 1 . \quad (12.15)$$

(iii) *Balance*:

$$\sum_k W^{(l)(k)} e^{-\beta E^{(k)}} = e^{-\beta E^{(l)}} . \quad (12.16)$$

The Boltzmann state (12.10) is an eigenvector with eigenvalue 1 of the matrix $W = (W^{(l)(k)})$.

An *ensemble* is a collection of configurations for which to each configuration k a probability $P^{(k)}$ is assigned, $\sum_k P^{(k)} = 1$. The *Gibbs or Boltzmann ensemble* E_B is defined to be the ensemble with the probability distribution (12.10).

An *equilibrium ensemble* E_{eq} of the Markov process is defined by its probability distribution P_{eq} satisfying

$$W P_{\text{eq}} = P_{\text{eq}} , \text{ in components } P_{\text{eq}}^{(l)} = \sum_k W^{(l)(k)} P_{\text{eq}}^{(k)} . \quad (12.17)$$

Statement: Under conditions (i), (ii) and (iii), the Boltzmann ensemble is the *only* equilibrium ensemble of the Markov process and an *attractive fixed point*. Applying the transition matrix n times gives rise to an ensemble E^n .

For $n \rightarrow \infty$, the distance between E^n and the Boltzmann ensemble decreases asymptotically like

$$\|E^n - E_B\| \leq \exp(-\lambda n) \|E^0 - E_B\|, \quad (12.18)$$

where E^0 is the initial ensemble and $\lambda > 0$ a constant.

For a proof the readers are referred to [3]. There are many ways to construct a Markov process satisfying (i), (ii) and (iii). A stronger condition than balance (12.16) is

(iii') *Detailed balance*:

$$W^{(l)(k)} e^{-\beta E^{(k)}} = W^{(k)(l)} e^{-\beta E^{(l)}}. \quad (12.19)$$

Using the normalization $\sum_k W^{(k)(l)} = 1$, detailed balance implies balance.

At this point, we have succeeded in replacing the canonical ensemble average by a time average over an artificial dynamics. Calculating averages over large times, like one does in real experiments, is equivalent to calculating averages of the ensemble.

12.2.5 Metropolis and Heat-Bath Algorithm for Potts Models

The *Metropolis algorithm* can be used whenever one knows how to calculate the energy of a configuration. Given a configuration k , the Metropolis algorithm proposes a configuration l with probability

$$f(l, k) \text{ normalized to } \sum_l f(l, k) = 1. \quad (12.20)$$

The new configuration l is accepted with probability

$$w^{(l)(k)} = \min \left[1, \frac{P_B^{(l)}}{P_B^{(k)}} \right] = \begin{cases} 1 & \text{for } E^{(l)} < E^{(k)} \\ \exp[-\beta(E^{(l)} - E^{(k)})] & \text{for } E^{(l)} > E^{(k)} \end{cases} \quad (12.21)$$

If the new configuration is rejected, the old configuration has to be counted again. The *acceptance rate* is defined as the ratio of accepted changes over proposed moves. With this convention, we do not count a move as accepted when it proposes the at-hand configuration.

The Metropolis procedure gives rise to the transition probabilities:

$$W^{(l)(k)} = f(l, k) w^{(l)(k)} \quad \text{for } l \neq k \quad (12.22)$$

and

$$W^{(k)(k)} = f(k, k) + \sum_{l \neq k} f(l, k) (1 - w^{(l)(k)}) \quad (12.23)$$

Therefore, the ratio $(W^{(l)(k)}/W^{(k)(l)})$ satisfies detailed balance (12.19) if

$$f(l, k) = f(k, l) \text{ holds.} \quad (12.24)$$

Otherwise the probability density $f(l, k)$ is unconstrained. So there is an amazing flexibility in the choice of the transition probabilities $W^{(l)(k)}$. Also, the algorithm generalizes immediately to arbitrary weights.

If sites are chosen with the uniform probability distribution $1/N$ per site, where N is the total number of spins, it is obvious that the algorithm fulfills detailed balance. It is noteworthy that the procedure remains valid when the spins are chosen in the systematic order $1, \dots, N$. Balance (12.16) still holds, whereas detailed balance (12.19) is violated (an exercise of [3]).

If one performs multiple hits with the Metropolis algorithm at the same spin (*multi-hit Metropolis algorithm*), the local Boltzmann distribution defined by its nearest neighbors is approached for an increasing number of hits. The *heat-bath algorithm* (HBA) chooses a state q_i directly with the local Boltzmann distribution defined by its nearest neighbors. The state q_i can take on one of the values $1, \dots, q$ and, with all other states set, determines a value of the energy function (12.6). We denote this energy by $E(q_i)$, and the Boltzmann probabilities are

$$P_B(q_i) = \text{const } e^{-\beta E(q_i)}, \quad (12.25)$$

where the constant is determined by the normalization condition

$$\sum_{q_i=1}^q P_B(q_i) = 1. \quad (12.26)$$

In (12.25), we can define $E(q_i)$ to be just the contribution of the interaction of q_i with its nearest neighbors to the total energy and absorb the other contributions into the overall constant. Here, we give a generic HBA which works for arbitrary values of q and d (other solutions can be more efficient). We calculate the CDF of the heat-bath probabilities

$$P_{HB}(q_i) = \sum_{q'_i=1}^{q_i} P_B(q'_i). \quad (12.27)$$

The normalization condition (12.26) implies $P_{HB}(q) = 1$. Comparison of these cumulative probabilities with a uniform random number x^r yields the heat-bath update $q_i \rightarrow q'_i$. Note that in the heat-bath procedure the original value q_i^{in} does not influence the selection of q_i^{new} .

12.2.6 Heat-Bath Algorithm for a Continuous System

We give the $O(3)$ σ model as an example of a model with a continuous energy function. Expectation values are calculated with respect to the partition function

$$Z = \int \prod_i ds_i e^{-\beta E(\{s_i\})} \quad \text{of spins } \mathbf{s}_i = \begin{pmatrix} s_{i,1} \\ s_{i,2} \\ s_{i,3} \end{pmatrix} \quad (12.28)$$

which are normalized to lie on the unit sphere, $(\mathbf{s}_i)^2 = 1$. The measure ds_i is defined by

$$\int ds_i = \frac{1}{4\pi} \int_{-1}^{+1} d\cos(\theta_i) \int_0^{2\pi} d\phi_i, \quad (12.29)$$

where the polar (θ_i) and azimuth (ϕ_i) angles define the spin s_i on the unit sphere. The energy is

$$E = - \sum_{\langle ij \rangle} \mathbf{s}_i \mathbf{s}_j, \quad (12.30)$$

where the sum goes over the nearest neighbor sites of the lattice and $\mathbf{s}_i \mathbf{s}_j$ is the dot product of the vectors. The 2d version of the model is of interest to field theorists because of its analogies with the four-dimensional Yang-Mills theory. In statistical physics, the d -dimensional model is known as the *Heisenberg ferromagnet* (references can be found in [3]).

We would like to update a single spin \mathbf{s} . The sum of its 2d neighbors is

$$\mathbf{S} = \mathbf{s}_1 + \mathbf{s}_2 + \cdots + \mathbf{s}_{2d-1} + \mathbf{s}_{2d}.$$

Hence, the contribution of spin \mathbf{s} to the energy is $-\mathbf{s}\mathbf{S}$. We may propose a new spin \mathbf{s}' with the measure (12.29) by drawing two uniformly distributed random numbers

$$\phi^r \in [0, 2\pi) \quad \text{for the azimuth angle}$$

and

$$\cos(\theta^r) = x^r \in [-1, +1) \quad \text{for the cosine of the polar angle.}$$

This defines the probability function $f(\mathbf{s}', \mathbf{s})$ of the Metropolis process, which accepts the proposed spin \mathbf{s}' with probability

$$w(\mathbf{s} \rightarrow \mathbf{s}') = \begin{cases} 1 & \text{for } \mathbf{S}\mathbf{s}' > \mathbf{S}\mathbf{s}, \\ \exp[-\beta(\mathbf{S}\mathbf{s} - \mathbf{S}\mathbf{s}')] & \text{for } \mathbf{S}\mathbf{s}' < \mathbf{S}\mathbf{s}. \end{cases}$$

One would prefer to choose \mathbf{s}' directly with the probability

$$W(\mathbf{s} \rightarrow \mathbf{s}') = P(\mathbf{s}'; \mathbf{S}) = \text{const} e^{\beta \mathbf{s}' \mathbf{S}}.$$

The HBA creates this distribution. Implementation of it should be considered when the energy function allows for an efficient explicit calculation of the probability $P(\mathbf{s}'; \mathbf{S})$. This is the case for the $O(3)$ σ -model. Let

$$\alpha = \text{angle}(\mathbf{s}', \mathbf{S}), \quad x = \cos(\alpha) \quad \text{and} \quad S = \beta |\mathbf{S}|.$$

For $S = 0$, a new spin \mathbf{s}' is obtained by random sampling and we assume in the following $S > 0$. The Boltzmann weight becomes $\exp(xS)$ and the normalization constant follows from

$$\int_{-1}^{+1} dx e^{xS} = \frac{2}{S} \sinh(S) .$$

Therefore, the desired probability is

$$P(\mathbf{s}'; \mathbf{S}) = \frac{S}{2 \sinh(S)} e^{xS} =: f(x)$$

and (12.3) can be used to generate events with the probability density $f(x)$. A uniformly distributed random number $y^r \in [0, 1)$ translates into

$$x^r = \cos \alpha^r = \frac{1}{S} \ln [\exp(+S) - y^r \exp(+S) + y^r \exp(-S)] . \quad (12.31)$$

To give \mathbf{s}' a direction in the plane orthogonal to \mathbf{S} , one chooses a uniformly distributed angle β^r in the range $0 \leq \beta^r < 2\pi$. Then, $x^r = \cos \alpha^r$ and β^r completely determine \mathbf{s}' with respect to \mathbf{S} . Before storing \mathbf{s}' in the computer memory, we have to calculate coordinates of \mathbf{s}' with respect to a Cartesian coordinate system, which is globally used for all spins of the lattice. This amounts to a linear transformation, which is explicitly given in [3].

12.3 Statistical Errors of MCMC Data

In large-scale MC simulation, it may take months, possibly years, to collect the necessary statistics. For such data, a thorough error analysis is a must. A typical MC simulation falls into two parts:

1. *Equilibration:* Initial sweeps are performed to reach the equilibrium distribution. During these sweeps, measurements are either not taken at all or they have to be discarded when calculating equilibrium expectation values.
2. *Data Production:* Sweeps with measurements are performed. Equilibrium expectation values are calculated from this statistics.

A rule of thumb is, *Do not spend more than 50% of your CPU time on measurements*. The reason for this rule is that one cannot be off by a factor worse than 2 ($\sqrt{2}$ in the statistical error).

How many sweeps should be discarded for reaching equilibrium? In some situations, this question can be rigorously answered with the *Coupling from the Past* method [20] (for a review see [21]). The next best thing to do is to measure the integrated autocorrelation time and to discard, after reaching a visually satisfactory situation, a number of sweeps which is larger than

the integrated autocorrelation time. In practice, even this can often not be achieved.

Therefore, it is reassuring that it is sufficient to pick the number of discarded sweeps approximately right. With increasing statistics the contribution of the nonequilibrium data dies out like $1/N$, where N is the number of measurements. This is eventually swallowed by the statistical error, which declines only like $1/\sqrt{N}$. The point of discarding the equilibrium configurations is that the factor in front of $1/N$ can be large.

However, there can be involved situations, like that the Markov chain ends up in a metastable configuration, which may even stay unnoticed (this tends to happen in complex systems such as spin glasses or proteins).

12.3.1 Autocorrelations

We like to estimate the expectation value \hat{f} of some physical observable. We assume that the system has reached equilibrium. How many MC sweeps are needed to estimate \hat{f} with some desired accuracy? To answer this question, one has to understand the autocorrelations within the Markov chain.

Given is a *time series* of N measurements from a Markov process

$$f_i = f(x_i), \quad i = 1, \dots, N, \quad (12.32)$$

where x_i are the configurations generated. The label $i = 1, \dots, N$ runs in the temporal order of the Markov chain and the elapsed time (measured in updates or sweeps) between subsequent measurements f_i, f_{i+1} is always the same. The estimator of the expectation value \hat{f} is

$$\bar{f} = \frac{1}{N} \sum f_i. \quad (12.33)$$

With the notation

$$t = |i - j|,$$

the definition of the *autocorrelation function* of the observable \hat{f} is

$$\hat{C}(t) = \hat{C}_{ij} = \langle (f_i - \langle f_i \rangle) (f_j - \langle f_j \rangle) \rangle = \langle f_i f_j \rangle - \langle f_i \rangle \langle f_j \rangle = \langle f_0 f_t \rangle - \hat{f}^2 \quad (12.34)$$

where we used that translation invariance in time holds for the equilibrium ensemble. The asymptotic behavior for large t is

$$\hat{C}(t) \sim \exp\left(-\frac{t}{\tau_{\text{exp}}}\right) \quad \text{for } t \rightarrow \infty, \quad (12.35)$$

where τ_{exp} is called *exponential autocorrelation time* and is related to the second largest eigenvalue λ_1 of the transition matrix by $\tau_{\text{exp}} = -\ln \lambda_1$ under the assumption that f has a nonzero projection on the corresponding eigenstate. Superselection rules are possible so that different autocorrelation times reign for different operators.

The variance of f is a special case of the autocorrelations (12.34)

$$\widehat{C}(0) = \sigma^2(f) . \quad (12.36)$$

Some algebra [3] shows that the variance of the estimator \bar{f} (12.33) for the mean and the autocorrelation functions (12.34) are related by

$$\sigma^2(\bar{f}) = \frac{\sigma^2(f)}{N} \left[1 + 2 \sum_{t=1}^{N-1} \left(1 - \frac{t}{N} \right) \widehat{c}(t) \right] \quad \text{with} \quad \widehat{c}(t) = \frac{\widehat{C}(t)}{\widehat{C}(0)} . \quad (12.37)$$

This equation ought to be compared with the corresponding equation for uncorrelated random variables: $\sigma^2(\bar{f}) = \sigma^2(f)/N$. The difference is the factor in the bracket of (12.37), which defines the *integrated autocorrelation time*

$$\tau_{\text{int}} = \left[1 + 2 \sum_{t=1}^{N-1} \left(1 - \frac{t}{N} \right) \widehat{c}(t) \right] . \quad (12.38)$$

For correlated data, the variance of the mean is by the factor τ_{int} larger than the corresponding variance for uncorrelated data. In most simulations, one is interested in the limit $N \rightarrow \infty$ and (12.38) becomes

$$\tau_{\text{int}} = 1 + 2 \sum_{t=1}^{\infty} \widehat{c}(t) . \quad (12.39)$$

The numerical estimation of the integrated autocorrelation time faces difficulties. The variance of the estimator for (12.39) diverges, because for large t each $\widehat{c}(t)$ adds a constant amount of noise, whereas the signal dies out like $\exp(-t/\tau_{\text{exp}})$. To obtain nevertheless an estimate, one considers the t -dependent estimator

$$\bar{\tau}_{\text{int}}(t) = 1 + 2 \sum_{t'=1}^t \bar{c}(t') \quad (12.40)$$

and looks out for a *window* in t for which $\bar{\tau}_{\text{int}}(t)$ is flat.

12.3.2 Integrated Autocorrelation Time and Binning

Using binning (also called blocking), the integrated autocorrelation time can also be estimated via the variance ratio. We bin the time series (12.32) into $N_{\text{bs}} \leq N$ bins of

$$N_{\text{b}} = \text{NBIN} = \left\lfloor \frac{N}{N_{\text{bs}}} \right\rfloor = \left\lfloor \frac{\text{NDAT}}{\text{NBINS}} \right\rfloor \quad (12.41)$$

data each. Here $\lfloor \cdot \rfloor$ stands for Fortran integer division, i.e., $N_{\text{b}} = \text{NBIN}$ is the largest integer $\leq N/N_{\text{bs}}$, implying $N_{\text{bs}} \cdot N_{\text{b}} \leq N$. It is convenient to choose the values of N and N_{bs} so that N is a multiple of N_{bs} . The binned data are the averages

$$f_j^{N_b} = \frac{1}{N_b} \sum_{i=1+(j-1)N_b}^{jN_b} f_i \text{ for } j = 1, \dots, N_{bs} . \quad (12.42)$$

For $N_b > \tau_{\text{exp}}$, the autocorrelations are essentially reduced to those between nearest neighbor bins and even these approach zero under further increase of the bin size.

For a set of N_{bs} binned data $f_j^{N_b}$ ($j = 1, \dots, N_{bs}$), we may calculate the mean with its naive error bar. Assuming for the moment an infinite time series, we find the integrated autocorrelation time (12.38) from the following ratio of sample variances

$$\tau_{\text{int}} = \lim_{N_b \rightarrow \infty} \tau_{\text{int}}^{N_b} \text{ with } \tau_{\text{int}}^{N_b} = \left(\frac{s_{f^{N_b}}^2}{s_f^2} \right) . \quad (12.43)$$

In practice, the $N_b \rightarrow \infty$ limit will be reached for a sufficiently large, finite value of N_b . The statistical error of the τ_{int} estimate (12.43) is, in the first approximation, determined by the errors of $s_{f^{N_b}}^2$. The typical situation is then that, due to the central limit theorem, the binned data are approximately Gaussian, so that the error of $s_{f^{N_b}}^2$ is analytically known from the χ^2 distribution. Finally, the fluctuations of the denominator s_f^2 give rise to a small correction which can be worked out [3].

Numerically, most accurate estimates of τ_{int} are obtained for the finite bin size N_b which is just large enough so that the binned data (12.42) are practically uncorrelated. While the Student distribution shows that the confidence intervals of the error bars from 16 uncorrelated normal data are reasonable approximations to those of the Gaussian standard deviation, about 1000 independent data are needed to provide a decent estimate of the corresponding variance (at the 95% confidence level with an accuracy of slightly better than 10%). It makes sense to work with error bars from 16 binned data, but the error of the error bar, and hence a reliable estimate of τ_{int} , requires far more data.

12.3.3 Comparison of MCMC Algorithms

Figure 12.2 illustrates 2d Ising model simulations at the critical point of its second-order phase transition, $\beta = \beta_c = \ln(1 + \sqrt{2})/2$. *Critical slowing down* is observed: An increase $\tau_{\text{int}} \sim L^z$ with lattice size, where $z \approx 2.17$, is the *dynamic critical exponent* of the 2d Ising model. Estimates of z are compiled in [22]. Using another MC dynamics, the critical slowing down can be overcome by cluster updating [23, 24].

Figure 12.3 exhibits the *improvements of heat-bath over Metropolis updating* for the 10-state $d = 2$ Potts model at $\beta = 0.62$. For this first-order phase

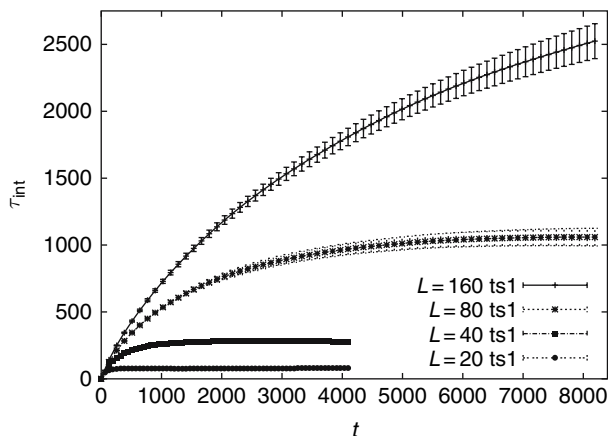


Fig. 12.2. One-hit Metropolis algorithm with sequential updating: Lattice size dependence of the integrated autocorrelation time for the $d = 2$ Ising model at its critical temperature (assignment a0402_02 D of [3]). The ordering of the curves is identical with the ordering of the labels in the figure

transition, there is practically no lattice size dependence of the integrated autocorrelation time once the lattices are large enough. We see that the 2-hit Metropolis updating reduces τ_{int} by about a factor of 2 and the heat-bath updating reduces it by about a factor of 5.

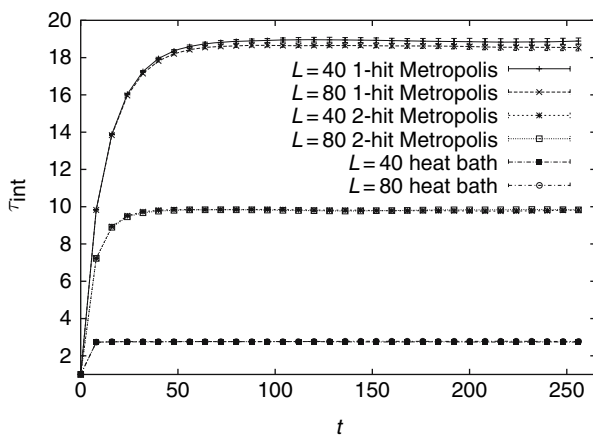


Fig. 12.3. Systematic updating: Comparison of the integrated autocorrelation times of the 1-hit and 2-hit Metropolis algorithms and the heat-bath algorithm for the 10-state Potts model on $L \times L$ lattices at $\beta = 0.62$ (assignment a0402_06). The $L = 40$ and $L = 80$ curves lie almost on top of one another

12.3.4 Jackknife Estimators

Often, one wants to estimate a nonlinear function of the mean \hat{x} of some statistical variables $\hat{f} = f(\hat{x})$ where the estimators of \hat{x} and \hat{f} are

$$\bar{x} = \frac{1}{N} \sum_{i=1}^N x_i, \quad \bar{f} = f(\bar{x}). \quad (12.44)$$

Typically, the bias is of order $1/N$:

$$\text{bias}(\bar{f}) = \hat{f} - \langle \bar{f} \rangle = \frac{a_1}{N} + \frac{a_2}{N^2} + O\left(\frac{1}{N^3}\right), \quad (12.45)$$

where a_1 and a_2 are constants. For the biased estimator, we lost the ability to estimate the variance $\sigma^2(\bar{f}) = \sigma^2(f)/N$ via the standard equation

$$s^2(\bar{f}) = \frac{1}{N} s^2(f) = \frac{1}{N(N-1)} \sum_{i=1}^N (f_i - \bar{f})^2, \quad (12.46)$$

because $f_i = f(x_i)$ is not a valid estimator of \hat{f} . The error bar problem for the estimator \bar{f} is conveniently overcome by using *jackknife estimators* \bar{f}^J , f_i^J , defined by

$$\bar{f}^J = \frac{1}{N} \sum_{i=1}^N f_i^J \quad \text{with} \quad f_i^J = f\left(x_i^J\right) \quad \text{and} \quad x_i^J = \frac{1}{N-1} \sum_{k \neq i} x_k. \quad (12.47)$$

The estimator for the variance $\sigma^2(\bar{f}^J)$ is

$$s_J^2(\bar{f}^J) = \frac{N-1}{N} \sum_{i=1}^N \left(f_i^J - \bar{f}^J\right)^2. \quad (12.48)$$

Straightforward algebra shows that in the unbiased case, the estimator of the jackknife variance (12.48) reduces to the normal variance (12.46). Notably, only order N (not N^2) operations are needed to construct the jackknife averages x_i^J , $i = 1, \dots, N$ from the original data.

The jackknife method was introduced in the 1950s [25, 26]. For a review see [3]. It is recommended as the standard for error bar calculations of biased estimators.

12.3.5 Self-consistent Versus Reasonable Error Analysis

By visual inspection of the time series, one may get an impression about the length of the out-of-equilibrium part of the simulation. On top of this, one should still choose

$$\text{nequi} > \tau_{\text{int}} , \quad (12.49)$$

to allow the system to settle. That is a first reason why it appears necessary to control the integrated autocorrelation time of an MC simulation. A second reason is that we have to control the error bars of the equilibrium part of our simulation. Ideally, the error bars are calculated as

$$\Delta \bar{f} = \sqrt{\sigma^2(\bar{f})} \quad \text{with} \quad \sigma^2(\bar{f}) = \tau_{\text{int}} \frac{\sigma^2(f)}{N} . \quad (12.50)$$

This constitutes a *self-consistent error analysis* of an MC simulation.

However, the calculation of the integrated autocorrelation time may be out of reach. Many more than the about 20 independent data are needed, which according to the Student distribution are sufficient to estimate mean values with reasonably reliable error bars.

In practice, one has to be content with what can be done. *Often this means to rely on the binning method.* We simply calculate error bars of our ever increasing statistics with respect to a fixed number of

$$\text{NBINS} \geq 16 . \quad (12.51)$$

In addition, we may put 10% of the initially planned simulation time away for reaching equilibrium. A posteriori, this can always be increased. Once the statistics is large enough, our small number of binned data become effectively independent and our error analysis is justified.

How do we know that the statistics has become large enough? In applications, there can be indirect arguments, such as finite-size scaling (FSS) estimates, which tell us that the integrated autocorrelation time is in fact (much) smaller than the achieved bin length. This is no longer self-consistent, as we perform no explicit measurement of τ_{int} , but it is a *reasonable error analysis*.

12.4 Generalized Ensembles for MCMC Simulations

The MCMC schemes discussed so far simulate the Gibbs canonical ensemble. Mean values of physical observables at the temperature chosen are obtained as arithmetic averages of the measurements. However, in statistical physics, one would like to control the partition function, which allows to calculate observables at all temperatures and for the proper normalization of the entropy and free energy. Also configurations can be of physical interest, which are rare in the canonical but well represented in another ensemble. Finally, the efficiency of the Markov process, i.e., the computer time needed for the convergence of an estimator of a physical quantity to a desired accuracy can depend greatly on the ensemble in which the simulations are performed.

12.4.1 Reweighting of the Canonical Ensemble

A first attempt to calculate the partition function by MCMC simulations dates back to a 1959 paper by Salsburg et al. [27]. As was already noticed by the authors, their method is restricted to very small lattices. The reason is that their approach relies on what one calls in the modern language *reweighting* of the Gibbs canonical ensemble. It extrapolates data from a canonical simulation at one temperature to the canonical ensemble at another temperature.

The reweighting method has a long history. McDonald and Singer [28] were the first to use the equations of [27] to evaluate physical quantities over a range of temperatures. But thereafter the method was essentially forgotten and a rediscovery in lattice gauge theory [29, 30] focused on calculating complex zeros of the partition function. It remained to the paper by Ferrenberg and Swendsen [31] to formulate crystal clear for what the method is particularly good and for what not: It allows to focus on peaks of appropriate observables like the specific heat, but it does not allow to cover a finite temperature range in the infinite-volume limit. Off critical points the reweighting range $\Delta\beta$ in $\beta = 1/(kT)$ decreases like $\Delta\beta \sim 1/\sqrt{N}$, where N is the number of degrees of freedom, which parametrizes the size of the system (e.g., the number of atoms). This follows from the fact that the energy is an extensive thermodynamic quantity, $E \sim N$ with fluctuations $\sim \sqrt{N}$. As β multiplies the energy, the change stays within the fluctuations as long as $\Delta\beta N \sim \sqrt{N}$, so that $\Delta\beta \sim 1/\sqrt{N}$ follows.

At second-order phase transitions, the reweighting range actually increases because critical fluctuations are larger than noncritical fluctuations. One has then $\Delta E \sim N^x$, with $1/2 < x < 1$, and the requirement $\Delta\beta N \sim N^x$ yields $\Delta\beta \sim N^{x-1}$. For first-order phase transitions, one has a latent heat $\Delta E \sim N$, but this does not mean that the reweighting range becomes of order one. In essence, the fluctuations collapse because the two phases become separated by an interface. One is back to fluctuations within either of the two phases where $\Delta\beta \sim 1/\sqrt{N}$ holds.

To estimate the partition function over a finite range Δe in the energy density $e = E/N$, i.e., $\Delta E \sim N$, one can patch the histograms from canonical simulations at several temperatures. Such *multi-histogram methods* have a long tradition too. In 1972, Valleau and Card [32] proposed the use of overlapping bridging distributions and called their method “multistage sampling”. Free-energy and entropy calculations become possible when one can link the temperature region of interest with a point in configuration space for which exact values of these quantities are known. Reference [31] stimulated a renaissance of this approach. Modern work [33, 34, 35] developed efficient techniques to combine the overlapping distributions into one estimate of the spectral density and to control the statistical errors of the estimate. However, the patching of histograms from canonical simulations faces a number of limitations:

1. The number of canonical simulations diverges like \sqrt{N} when one wants to cover a finite, noncritical range of the energy density.
2. At first-order phase transition points, the canonical probability of configurations with an interface decreases $\sim \exp(-f_s A)$. Here, f_s is the interfacial surface tension and A the minimal area of an interface, which divides the system into subsystems of distinct phases. For a system of volume L^d , the area A diverges $\sim L^{d-1}$ in the infinite-volume limit $L \rightarrow \infty$.

12.4.2 Generalized Ensembles

One can cope with the difficulties of multi-histogram methods by allowing arbitrary sampling distributions instead of just the Gibbs–Boltzmann ensemble. This was first recognized by Torrie and Valleau [4] when they introduced *umbrella sampling*. However, for the next 13 years, applications of this idea remained mainly confined to a narrow range of physical chemistry. That there is a potentially very broad range of applications for the basic idea remained unrecognized. A major barrier, which prevented researchers from trying such extensions, was certainly the apparent lack of direct and straightforward ways of determining suitable weighting functions for problems at hand. In the words of Li and Scheraga [36]: *The difficulty of finding such weighting factors has prevented wide applications of the umbrella sampling method to many physical systems.*

The turnaround came with the introduction of the *multicanonical ensemble* [7, 8, 9]. These papers focused on one well-defined weight function, up to a normalization constant the inverse spectral density,

$$w_{\text{muca}}(E) \sim 1/n(E) \quad \text{for } E_{\min} \leq E \leq E_{\max}, \quad (12.52)$$

where $n(E)$ is the number of states, and offered a variety of methods to find a “*working approximation*” of the weight function. Here, a working approximation is defined as being accurate enough so that the desired energy range will indeed be covered after the weight factors are fixed. A typical multicanonical simulation consists then of three parts:

1. Construct a working approximation of the weight function w_{muca} .
2. Perform a conventional MCMC simulation with these weight factors.
3. Reweight the data to the Gibbs–Boltzmann ensemble at desired temperatures to obtain estimates of canonical expectation values for observables of physical interest.

For instance, for the $2d$ 10-state Potts model considered in [8], the FSS allows to construct the weight function on a larger lattice in one step from the information about the spectral density on the already simulated smaller lattices. This is a solution to step (1) in this particular case. The simulation and data analysis (see [3] for details) is then rather straightforward. Still, such conceptual simplifications might have changed little on the situation that

noncanonical ensembles were rarely used, if there were not other favorable circumstances.

One was that the paper by Berg and Neuhaus [8] estimated the interfacial tension of the $2d$ 10-state Potts model and produced a result, which was an order of magnitude smaller than previous numerical estimate by renown computational scientists. Normally this would have been followed by an extended debate of the advantages and disadvantages of the competing methods. However, shortly after publication of the numerical estimates, it turned out that the interfacial tension of the $2d$ 10-state Potts models can be calculated analytically [19], and the multicanonical estimate was within 3% of the rigorous value. This attracted attention and gave researchers confidence in the method.

Another phenomenon was that from 1991 on many papers emerged in the literature, which all aimed at improving MCMC calculations by extending the confines of the canonical ensemble. References [6, 10, 11, 12] are a small subset of those. Widely used nowadays is the *replica exchange method*, which is also known under the names *parallel tempering* and *multiple Markov chains*. In the context of spin glass simulations, an exchange of partial lattice configurations at different temperatures was proposed by Swendsen and Wang [5]. But it was, essentially by rediscovery, only in later works [6, 12] recognized that the special case for which entire configurations at distinct temperatures are exchanged is of utmost importance.

In the successful replica exchange method, one performs n canonical MC simulations at different β -values with Boltzmann weight factors

$$w_{B,i}(E^{(k)}) = e^{-\beta_i E^{(k)}} = e^{-H}, \quad i = 0, \dots, n-1, \quad (12.53)$$

where $\beta_0 < \beta_1 < \dots < \beta_{n-2} < \beta_{n-1}$, and exchanges neighboring β -values:

$$\beta_{i-1} \longleftrightarrow \beta_i \quad \text{for } i = 1, \dots, n-1. \quad (12.54)$$

Their joint Boltzmann factor is

$$e^{-\beta_{i-1} E_{i-1} - \beta_i E_i} = e^{-H} \quad (12.55)$$

and the $\beta_{i-1} \leftrightarrow \beta_i$ exchange leads to

$$\begin{aligned} -\Delta H &= \left(-\beta_{i-1} E_i^{(k)} - \beta_i E_{i-1}^{(k')} \right) - \left(-\beta_i E_i^{(k)} - \beta_{i-1} E_{i-1}^{(k')} \right), \quad (12.56) \\ &= (\beta_i - \beta_{i-1}) (E_i^{(k)} - E_{i-1}^{(k')}) \end{aligned}$$

which is accepted or rejected according to the Metropolis algorithm, i.e., with probability one for $\Delta H \leq 0$ and with probability $\exp(-\Delta H)$ for $\Delta H > 0$. The β_i -values should be determined so that an appropriate large acceptance rate is obtained for *each* β exchange. This can be done by recursions [3], which are straightforward modifications of a method introduced in [37].

Finally, and perhaps most important: From about 1992, applications of generalized ensemble methods diversified tremendously. This is documented in a number of reviews [38, 39, 40, 41]. Recently, it was demonstrated that generalized ensembles are also advantageous in the realm of second-order phase transition [42], for which canonical simulations had remained the standard. In the next section, we focus on the use of generalized ensembles in biophysics.

12.4.3 Generalized Ensembles and Biophysics

In [43], the multicanonical ensemble was for the first time used for simulations of complex systems with frustrated interactions, in that case the Edwards-Anderson Ising spin glass. Multicanonical simulations of biologically relevant molecules followed [13, 14], in [14] under the name “entropic sampling”, but this is just identical with multicanonical sampling [44].

The interactions defined by an energy function are frustrated if one cannot align all variables simultaneously toward their local energy minima due to conflicting constraints, which one cannot fulfill simultaneously. So one gets “frustrated”, a situation well known to all political decision makers. In physical models, frustrated interactions lead to a rugged free-energy landscape. Canonical MCMC simulations tend to get stuck in free-energy barriers. In a nutshell, another ensemble may smoothen out such barriers, jump them, or at least allow to escape from them, for instance through a disordered phase. This can accelerate the overall convergence of the MCMC process considerably. If all parameters are chosen right, reweighting will finally allow to reconstruct canonical ensemble expectation values at desired temperatures.

The parallel tempering (replica exchange) method was introduced in [45] to the simulation of biomolecules. In particular, its extension to molecular dynamics (MD) [46] has subsequently been tremendously successful. Nowadays folding of small proteins is achieved using PC clusters, and it appears that all these simulations rely on some form of the replica exchange method.

12.4.4 Overcoming Free-Energy Barriers

Basic mechanisms for overcoming energy barriers are easily illustrated for first-order phase transitions. There, one deals with the simplified situation of a single barrier, which is visualized by plotting histograms of an appropriate observable. To give an example, Fig. 12.4 shows for the $2d$ 10-state Potts model the canonical energy histogram at a pseudo-critical temperature versus the energy histogram of a multicanonical simulation on a 70×70 lattice [8]. The energy barrier is overcome by enhancing the probabilities for configurations, which are suppressed in the canonical ensemble due to an interfacial tension.

The same barrier can be overcome by a parallel tempering simulation, but in a quite different way. Figure 12.5 shows the histograms from a parallel tempering simulation with eight processes on 20×20 lattices. Each histogram corresponds to a fixed temperature, given by the β values in the figure. The

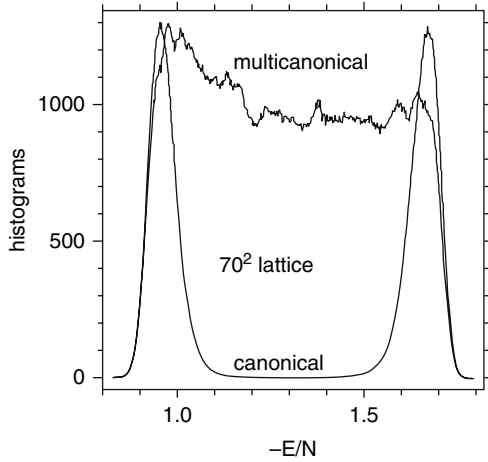


Fig. 12.4. Multicanonical $P_{mu}(E)$ together with canonical $P(E)$ energy distribution as obtained in [8] for the 2d 10-state Potts model on a 70×70 lattice

β_4 and β_5 values produce the clearest double peak histograms. For β_4 , the higher peak is in the disordered region and for β_5 it is in the ordered region. So the barrier can be “jumped” when there are at least two temperatures in the ensemble, which are sufficiently close to the particular pseudo-critical temperature for which the two peaks of the histogram assume equal heights (pseudo-critical temperatures may also be defined by giving equal weights to the two parts of the histogram [47]). One of these two temperatures has to be

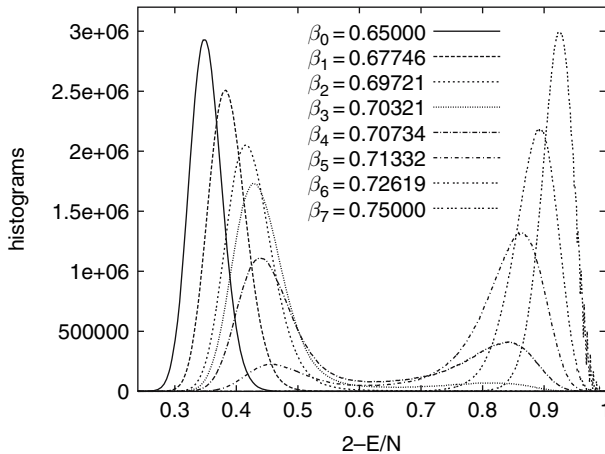


Fig. 12.5. Energy histograms from a parallel tempering simulation with eight processes for the 2d 10-state Potts model on 20×20 lattices (assignment a0603_04 in [3])

in the ordered phase, the other in the disordered phase, and their start configurations have to be in the corresponding phases. The barrier can be jumped by an exchange of these two temperatures. If the barrier is high enough, so that a single canonical simulations does not cross it during the simulation time, the jumping process determines the relative weight of the two phases at the temperatures used. Adding more close-by temperatures to the ensemble will increase to the accuracy. Additional complications can occur if a rare canonical tunneling process (crossing of the barrier) actually takes place.

Let us compare with a multicanonical simulation. The multicanonical method flattens the barrier, whereas the parallel tempering simulation allows to jump it. Using larger lattices, the multicanonical method is well suited for calculations of the interface tensions from energy histograms [8]. For parallel tempering, this is not the case because the sampling of each histogram is still canonical. Neuhaus and Hager [48] have shown that this problem can be overcome by a Gaussian variant of simulated tempering.

In complex systems with a rugged free-energy landscape, the barriers can no longer be explicitly controlled. Nevertheless, it has turned out that switching to generalized ensembles can greatly enhance the MCMC efficiency. A variety of biologically relevant applications are reviewed in [39, 41] and in some of the lectures of this volume. Here we confine ourselves to showing a particularly nice example in Fig. 12.6: the folding of poly-alanine into its α -helix coil [49]. No a priori information about the ground state conformation is used. Whereas in a canonical simulation one would in essence get stuck in a configuration like the second of the first row of this figure, the multicanonical simulation finds its way in and out of the helix structure.

Variations of the basic idea introduce weights in other variables than the energy (or even in several variables). For instance, weights in the magnetic field of spin systems were introduced quite some while ago [50]. For spin

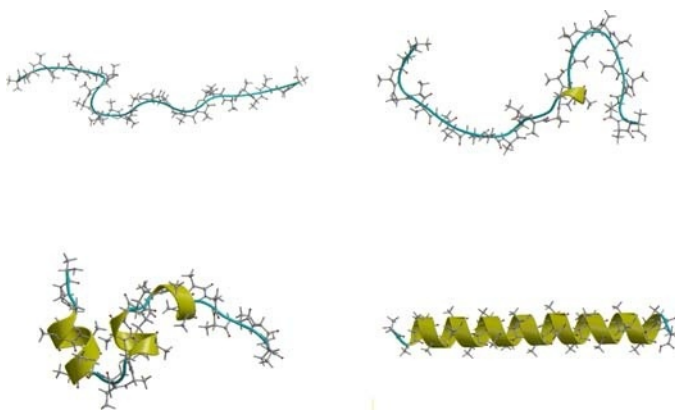


Fig. 12.6. Example configurations from a multicanonical simulation of poly-alanine [49] (courtesy Ulrich Hansmann and Yuko Okamoto)

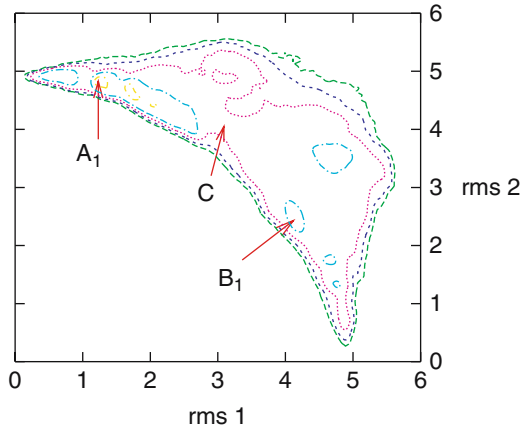


Fig. 12.7. Free-energy landscape of Met-enkephalin at $T = 250$ K with respect to rms distances (\AA) from two reference configurations [52]

glasses, weights in the Parisi overlap variable are used [51]. The overlap of the configuration at hand with two reference configurations allows one to determine the transition state efficiently [52]. Figure 12.7 shows a transition state located by this method in the free-energy landscape of a simple peptide (Met-enkephalin, which is discussed in the next section). In this figure, contour lines are drawn every $2k_B T$. The labels A_1 and B_1 indicate the positions for the local-minimum states that originate from the reference configuration 1 and the reference configuration 2, respectively. The label C stands for the saddle point that corresponds to the transition state.

12.4.5 Weight Factor Recursions

For systems with rugged free-energy landscapes, FSS methods for estimating the weight factors are normally not available because the systems are either of one particular size (e.g., biomolecules) or change too much when the system size is increased (e.g., spin glasses). In view of this, one has to rely on ad hoc per hand estimates of the weights or, more conveniently, on general purpose recursions. Designs for the latter were reported in a number of papers [53, 54, 55, 56].

The recursions discussed in the following have in common that they intend to create weight factors which are inversely proportional to the spectral density of the system at hand. Modifications to target other weights, which may lead to even more efficient simulations [57, 58], are straightforward. The Wang–Landau (WL) recursion [56, 59] differs fundamentally from the other approaches by iterating the weight factor at energy E multiplicatively instead of additively. At a first glance, the WL approach is counterintuitive because the correct iteration of the weight factor after a sufficiently long simulation is

obviously proportional to 1 over the number of histogram entries $H(E)$ and not $1/(f_{\text{WL}})^{H(E)}$ with $f_{\text{WL}} > 1$. The advantage of the WL recursion is that it moves right away rapidly through the targeted energy range. Once this energy range is sufficiently covered, the WL method refines its iteration factor by $f_{\text{WL}} \rightarrow \sqrt{f_{\text{WL}}}$, so that it approaches 1. In this way, the working approximations to the desired weight factors can be obtained for any finite energy range. In the following, we give details for a variant [3] of the multicanonical recursion [53] (the modifications rely on work with W. Janke) and the WL recursion [56].

The multicanonical recursion uses the parameterization [7]

$$w(a) = e^{-S(E_a)} = e^{-b(E_a) E_a + a(E_a)}$$

of the weights, where (for ϵ smallest stepsize)

$$b(E) = [S(E + \epsilon) - S(E)] / \epsilon$$

and

$$a(E - \epsilon) = a(E) + [b(E - \epsilon) - b(E)] E .$$

After some algebra and other considerations [3], the recursion reads

$$\begin{aligned} b^{n+1}(E) &= b^n(E) + \hat{g}_0^n(E) [\ln H^n(E + \epsilon) - \ln H^n(E)] / \epsilon , \\ \hat{g}_0^n(E) &= g_0^n(E) / [g^n(E) + \hat{g}_0^n(E)] , \\ g_0^n(E) &= H^n(E + \epsilon) H^n(E) / [H^n(E + \epsilon) + H^n(E)] , \\ g^{n+1}(E) &= g^n(E) + g_0^n(E), \quad g^0(E) = 0 . \end{aligned}$$

For continuous systems like biomolecules, some modification is required, see [60].

For the WL recursion, updates are performed with estimators $\rho(E)$ of the density of states

$$p(E_1 \rightarrow E_2) = \min \left[\frac{\rho(E_1)}{\rho(E_2)}, 1 \right] .$$

Each time an energy level is visited, one updates the estimator multiplicatively

$$\rho(E) \rightarrow \rho(E) f_{\text{WL}} ,$$

where, initially, $\rho(E) = 1$ and $f_{\text{WL}} = f_0 = e^1$. Once the desired energy range is covered, the factor f_{WL} is refined to

$$f_1 = \sqrt{f_0} , \quad f_{n+1} = \sqrt{f_n}$$

until some small value like $f_{\text{WL}} = e^{-8} = 1.00000001$ is reached. For f_{WL} very close to 1, the difference to a simulation with fixed weights becomes negligible, so that one may just keep on iterating $f_{\text{WL}} \rightarrow \sqrt{f_{\text{WL}}}$. However, it appears that such a continued iteration is less efficient than switching to a simulation with fixed weights as soon as a working estimate is found. Surprisingly, there appears to be only one comparative study [61] of the different recursions, finding that overall performances are similar.

12.5 Biased Markov Chain Monte Carlo

Consider a random variable y which is sampled with a probability density function (PDF) $P(y)$ on an interval $[y_1, y_2]$. The cumulative distribution function (CDF) is defined by

$$z = F(y) = \int_{y_1}^y P(y') dy' \quad \text{and} \quad P(y) = \frac{dF(y)}{dy}, \quad (12.57)$$

where $P(y)$ is properly normalized so that $F(\infty) = 1$ holds.

The HBA generates y by converting a uniformly distributed random number $0 \leq z < 1$ into

$$y = F^{-1}(z). \quad (12.58)$$

As the *acceptance rate* is defined by the number of accepted changes divided by the total number of proposed moves, the acceptance rate of the HBA is in continuous systems always 1 as a new value of y is generated in *every* step (the likelihood to propose the at-hand configuration is of measure zero). In simulations, the inversion of the CDF (12.57) can be unacceptably slow or the CDF itself may not be a priori known. Then one has to rely on other approaches than the HBA.

In the conventional Metropolis scheme, y_{new} is generated uniformly in a range $[y_1, y_2]$ (we refer to this as *proposal*) and accepted with probability

$$p_{\text{Met}} = \min \left\{ 1, \frac{P(y_{\text{new}})}{P(y_{\text{old}})} \right\}. \quad (12.59)$$

This *accept/reject step* can have a low acceptance rate in the region of interest. Possible remedies are to decrease the proposal range, which makes the moves small, or to use multi-hit Metropolis. Excluding CPU time considerations for the moment, measured by the integrated autocorrelation time both remedies are normally less efficient than a HBA.

Hastings [62] identified proposal probabilities, which are more general than those of the conventional Metropolis scheme, but gave no guidance whether some probabilities may be preferable over others. If one does not propose y_{new} uniformly anymore, the name *biased Metropolis algorithm (BMA)* is often used. Some biased Metropolis simulations can be found in the literature where the bias is introduced to match special situations [63, 64, 65, 66, 67]. In the following, we discuss a general biased Metropolis scheme [15, 68], which aims at approximating heat-bath probabilities.

Let us discretize y into n bins as

$$y_1 = y^0 < y^1 < y^2 < \dots < y^n = y_2, \quad (12.60)$$

where the lengths of the bins are

$$\Delta y^j = y^j - y^{j-1}, \quad \text{with } j = 1, \dots, n. \quad (12.61)$$

A BMA can then be defined by the following steps:

- Propose a new value y_{new} by randomly picking a bin j_{new} and then proposing y_{new} uniformly in the given bin. Two uniform random numbers r_1, r_2 are needed:

$$j_{\text{new}} = 1 + \text{Int}[n r_1] \quad \text{and} \quad y_{\text{new}} = y^{j_{\text{new}}-1} + \Delta y^{j_{\text{new}}} r_2, \quad (12.62)$$

where $\text{Int}[n r_1]$ denotes rounding to the largest integer $\leq n r_1$.

- Locate the bin j_{old} to which y_{old} belongs:

$$y^{j_{\text{old}}-1} \leq y_{\text{old}} \leq y^{j_{\text{old}}}. \quad (12.63)$$

- Accept y_{new} with probability:

$$p_{\text{BMA}} = \min \left\{ 1, \frac{P(y_{\text{new}})}{P(y_{\text{old}})} \frac{\Delta y^{j_{\text{new}}}}{\Delta y^{j_{\text{old}}}} \right\}. \quad (12.64)$$

p_{BMA} in (12.64) differs from p_{Met} in (12.59) by the *bias* $\Delta y^{j_{\text{new}}} / \Delta y^{j_{\text{old}}}$. The scheme outlined in (12.62)–(12.64) satisfies balance or detailed balance in the same way as the original Metropolis algorithm, while the bias changes the acceptance rate.

So far the partitioning y^j has not been introduced explicitly. A particular choice is

$$\frac{j}{n} = F(y^j) \quad \text{or} \quad y^j = F^{-1} \left(\frac{j}{n} \right). \quad (12.65)$$

This equation achieves equidistant partitioning on the CDF ordinate. Let us pick a bin initially labeled j and take the limit $n \rightarrow \infty$ so that this bin collapses into a point labeled z . Then this BMA approaches the HBA and the acceptance rate converges to 1:

$$\frac{P(y_{\text{new}})}{P(y_{\text{old}})} \frac{\Delta y^{j_{\text{new}}}}{\Delta y^{j_{\text{old}}}} \rightarrow \frac{P(y_{\text{new}})}{P(y_{\text{old}})} \frac{1/P(y_{\text{new}})}{1/P(y_{\text{old}})} = 1. \quad (12.66)$$

Therefore, we call a BMA with the partitioning (12.65) *biased Metropolis-heat-bath algorithm (BMHA)*. Restricted to the updating of one dynamical variable, the improvements are similar to those seen in Fig. 12.3, where the gain is a factor of 5. Having in mind that realistic simulations often take months of computer time, such factors are highly welcome. Extending the biased method to simultaneous updating of more than one variable, larger improvement factors can be anticipated. But extensions to more than two variables face technical difficulties.

12.5.1 Application to a Continuous Model

Following [68], we illustrate the BMHA for a system with a continuous energy function: Pure lattice gauge theory calculations with the $U(1)$ gauge group for which the “matrices” are complex numbers on the unit circle, parameterized

by an angle $\phi \in [0, 2\pi)$. After defining the theory on the links of a four-dimensional lattice and going through some algebra, the PDF

$$P_\alpha(\phi) = N_\alpha e^{\alpha \cos(\phi)} \quad (12.67)$$

has to be sampled, where α is a parameter associated to the interaction of the link being updated with its environment. The corresponding CDF is

$$F_\alpha(\phi) = N_\alpha \int_0^\phi d\phi' e^{\alpha \cos(\phi')}, \quad (12.68)$$

where N_α ensures the normalization $F_\alpha(2\pi) = 1$. In the following, we consider $U(1)$ gauge theory at a coupling close to the critical point for which one finds $0 \leq \alpha \leq 6$.

Let us discretize the parameter α into $m = 2^{n_1} = 16$ ($n_1 = 4$) bins, choosing equidistant partitioning. In each α^i bin, we discretize ϕ using the condition (12.65) with $n = 2^{n_2} = 16$ ($n_2 = 4$). Two two-dimensional arrays are needed: one for storing $\phi^{i,j}$ and another for $\Delta\phi^{i,j} = \phi^{i,j} - \phi^{i,j-1}$ (distances between levels), see Fig. 12.8. For a given α^i , it is straightforward to apply BMA step (12.62). For example, for $\alpha = \alpha^{11}$, the cross section of the $F_\alpha(\phi)$ surface plane is shown in Fig. 12.9. To determine the bin label j_{old} which belongs to the (known) value $\phi_{0,\text{old}}$ (BMA step (12.63)), one may use the n_2 -step recursion $j \rightarrow j + 2^{i_2} \text{sign}(\phi - \phi^{i,j})$, $i_2 \rightarrow i_2 - 1$. Once j_{old} is known, it gives the length of the bin: $\Delta\phi^{i,j_{\text{old}}}$ and the final accept/reject step (12.64) can be applied:

$$p_{\text{BMA}} = \min \left\{ 1, \frac{\exp(\alpha \cos \phi_{0,\text{new}})}{\exp(\alpha \cos \phi_{0,\text{old}})} \frac{\Delta\phi_0^{i,j_{\text{new}}}}{\Delta\phi_0^{i,j_{\text{old}}}} \right\}. \quad (12.69)$$

In this example the CDF is known. Sampling with the BMHA is essentially equivalent to using the HBA, but can be numerically faster, as is the case for $U(1)$. $SU(2)$ lattice gauge theory with the fundamental-adjoint action allows

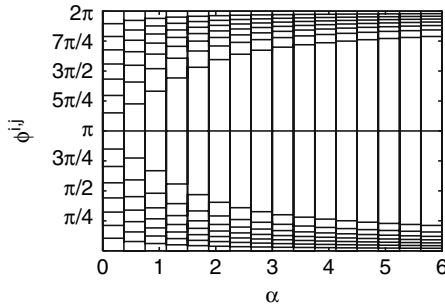


Fig. 12.8. $m \times n$ partitioning of $\Delta\phi^{i,j}$ for $U(1)$ at the coupling constant value discussed in the text

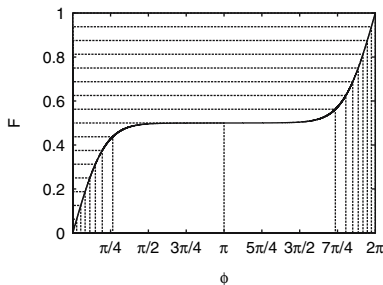


Fig. 12.9. Discretization of the CDF $F_{\alpha^{11}}(\phi)$ for $U(1)$ corresponding to the 11th bin of Fig. 12.8

for substantial speedups by using a BMHA [69]. In the next section, we show how a similar biasing procedure can be used when the CDF is not known (making a HBA impossible) and extend it to two variables.

12.5.2 Rugged Metropolis – A Biasing Scheme for Biophysics

We consider biomolecule models for which the energy E is a function of a number of dynamical variables v_i , $i = 1, \dots, n$. The fluctuations in the Gibbs canonical ensemble are described by a probability density function $\rho(v_1, \dots, v_n; T) = \text{const} \exp[-\beta E(v_1, \dots, v_n)]$, where T is the temperature, $\beta = 1/(k_B T)$ and E is the energy of the system. To be consistent with the notation of [15], we now use $\rho(v_1, \dots, v_n; T)$ instead of $P(y)$. A HBA is only possible when the CDF of the PDF can be controlled. In particular, this requires the normalization constant in front of the $\exp[-\beta E(v_1, \dots, v_n)]$ Boltzmann factor, which is often unknown. Then the following strategy can provide a useful approximation.

For a range of temperatures

$$T_1 > T_2 > \dots > T_r > \dots > T_{f-1} > T_f, \quad (12.70)$$

the simulation at the highest temperature, T_1 , is performed with the usual Metropolis algorithm and the data are used to construct an *estimator*

$$\bar{\rho}(v_1, \dots, v_n; T_1)$$

which is used to bias the simulation at T_2 . Recursively, the estimated PDF

$$\bar{\rho}(v_1, \dots, v_n; T_{r-1})$$

is expected to be a useful approximation of $\rho(v_1, \dots, v_n; T_r)$. So we use for the BMA acceptance step (12.64) at temperature T_r :

$$P_{\text{RM}} = \min \left\{ 1, \frac{\exp(-\beta E')}{\exp(-\beta E)} \frac{\bar{\rho}(v_1, \dots, v_n; T_{r-1})}{\bar{\rho}(v'_1, \dots, v'_n; T_{r-1})} \right\}. \quad (12.71)$$

For this type of BMA, the bias is constructed by using information from a higher temperature. It is called *rugged Metropolis (RM)* algorithm in [15].

In the following, our test case will be the small brain peptide Met-enkephalin (Tyr-Gly-Gly-Phe-Met) in vacuum, which features 24 dihedral angles as dynamical variables. Its global energy minimum was determined some time ago by Li and Scheraga [70]. Ever since, this molecule is often used for testing new computational methods. We rely on the all-atom energy function ECEPP/2 (Empirical Conformational Energy Program for Peptides) [71] as implemented in the SMMP (Simple Molecular Mechanics for Proteins) [72] program package. Besides the ϕ , ψ angles, we keep also the ω angles unconstrained, which are usually restricted to $[\pi - \pi/9, \pi + \pi/9]$. This allows us to illustrate RM for a particularly simple case.

To get things started, we need to construct an estimator $\bar{\rho}(v_1, \dots, v_n; T_r)$ from the numerical data of an RM simulation at temperature T_r . This is not straightforward and approximations are used.

RM₁ Approximation

In [15], the factorization

$$\bar{\rho}(v_1, \dots, v_n; T_r) = \prod_{i=1}^n \bar{\rho}_i^1(v_i; T_r) \quad (12.72)$$

was investigated, where $\bar{\rho}_i^1(v_i; T_r)$ are estimators of reduced one-variable PDFs defined by

$$\rho_i^1(v_i; T) = \int_{-\pi}^{+\pi} \prod_{j \neq i} dv_j \rho(v_1, \dots, v_n; T) . \quad (12.73)$$

The resulting algorithm, called RM₁, constitutes the simplest RM scheme. The CDFs are defined by

$$F_i(v) = \int_{-\pi}^v dv' \rho_i^1(v') . \quad (12.74)$$

The estimate of F_{10} , the CDF for the dihedral angle Gly-3 ϕ (v_{10}), from the simulations at our highest temperature, $T_1 = 400$ K, is shown in Fig. [12.10]. For our plots we use degrees, while we use radiant in our theoretical discussions and in the computer programs. Figure [12.10] is obtained by sorting all n_{dat} values of v_{10} in our time series in ascending order and increasing the values of F_{10} by $1/n_{\text{dat}}$ whenever a measured value of v_{10} is encountered. Using a heapsort approach [3], the sorting is done in $n_{\text{dat}} \log_2(n_{\text{dat}})$ steps.

Figure [12.11] shows the CDF for v_9 (Gly-2 ω) at 400 K, which is the angle of lowest acceptance rate in the conventional Metropolis updating. This distribution function corresponds to a histogram narrowly peaked around $\pm\pi$, which is explained by the specific electronic hybridization of the CO-N peptide

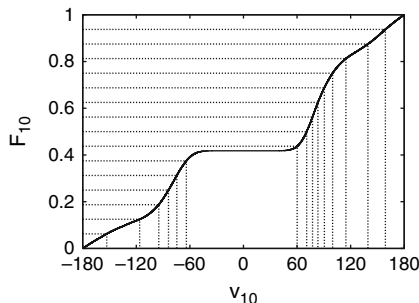


Fig. 12.10. Estimate of the cumulative distribution function for the Met-enkephalin dihedral angle v_{10} (Gly-3 ϕ) at 400 K

bond. From the grid shown in Fig. 12.11, it is seen that the RM_1 updating has automatically a similar effect as the often used restriction to the range $[\pi - \pi/9, \pi + \pi/9]$, which is the default implementation in SMMP.

After the empirical CDFs are constructed for each angle v_i , they are discretized using the condition (12.65). Here we denote the differences (12.61) by

$$\Delta v_{i,j} = v_{i,j} - v_{i,j-1} \quad \text{with } v_{i,0} = -\pi. \quad (12.75)$$

The RM_1 updating of each dihedral angle v_i follows then the BMA procedure (12.62)–(12.64). The accept/reject step in the $v_{i,j}$ notation is

$$p_{\text{RM}_1} = \min \left\{ 1, \frac{\exp(-\beta E')}{\exp(-\beta E)} \frac{\Delta v_{i,j_{\text{new}}}}{\Delta v_{i,j_{\text{old}}}} \right\}. \quad (12.76)$$

RM₂ Approximation

In [73], the RM_1 scheme of (12.76) was generalized to the *simultaneous* updating of two dihedral angles. For $i_1 \neq i_2$, reduced two-variable PDFs are defined by

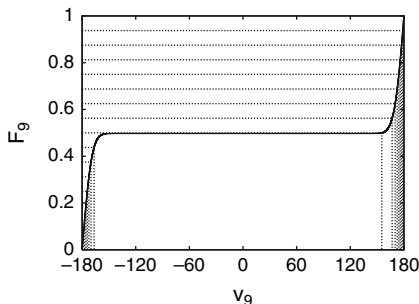


Fig. 12.11. Estimate of the cumulative distribution function for the Met-enkephalin dihedral angle v_9 (Gly-2 ω) at 400 K

$$\rho_{i_1, i_2}^2(v_{i_1}, v_{i_2}; T) = \int_{-\pi}^{+\pi} \prod_{j \neq i_1, i_2} dv_j \rho(v_j, \dots, v_n; T) . \quad (12.77)$$

We define conditional CDFs by

$$F_{i_1, i_2; j}(v) = \int_{-\pi}^v dv_{i_2} \int_{v_{i_1, j-1}}^{v_{i_1, j}} dv_{i_1} \rho_{i_1, i_2}^2(v_{i_1}, v_{i_2}) \quad (12.78)$$

for which the normalization $F_{i_1, i_2; j}(\pi) = 1/n$ holds. To extend the RM₁ updating to two variables, we define $F_{i_1, i_2; j, k} = k/n^2$ for each integer $k = 1, \dots, n$, $v_{i_1, i_2; j, k}$ through $F_{i_1, i_2; j, k} = F_{i_1, i_2; j}(v_{i_1, i_2; j, k})$ and also the differences

$$\Delta v_{i_1, i_2; j, k} = v_{i_1, i_2; j, k} - v_{i_1, i_2; j, k-1} \quad \text{with} \quad v_{i_1, i_2; j, 0} = -\pi . \quad (12.79)$$

The RM₂ procedure for the simultaneous update of (v_{i_1}, v_{i_2}) is then specified as follows:

- Propose a new value $v_{i_1, \text{new}}$ using two uniform random numbers r_1, r_2 (BMA step (12.62) for the angle i_1):

$$j_{\text{new}} = [nr_1] \quad \text{and} \quad v_{i_1, \text{new}} = v_{i_1, j_{\text{new}}-1} + \Delta v_{i_1, j_{\text{new}}} r_2. \quad (12.80)$$

- Propose a new value $v_{i_2, \text{new}}$ using two uniform random numbers r_3, r_4 (BMA step (12.62) for the angle i_2):

$$k_{\text{new}} = [nr_3] \quad \text{and} \quad v_{i_2, \text{new}} = v_{i_1, i_2; j_{\text{new}}, k_{\text{new}}-1} + \Delta v_{i_1, i_2; j_{\text{new}}, k_{\text{new}}} r_4. \quad (12.81)$$

- Find the bin index j_{old} for the present angle $v_{i_1, \text{old}}$ through $v_{i_1, j_{\text{old}}-1} \leq v_{i_1, \text{old}} \leq v_{i_1, j_{\text{old}}}$, just like for RM₁ updating (BMA step (12.63) for v_{i_1}).
- Find the bin index k_{old} for the present angle $v_{i_2, \text{old}}$ through $v_{i_1, i_2; j_{\text{old}}, k_{\text{old}}-1} \leq v_{i_2, \text{old}} \leq v_{i_1, i_2; j_{\text{old}}, k_{\text{old}}}$ (again step (12.63) but for v_{i_2}).
- Accept $(v_{i_1, \text{new}}, v_{i_2, \text{new}})$ with the probability

$$p_{\text{RM}_2} = \min \left\{ 1, \frac{\exp(-\beta E')}{\exp(-\beta E)} \frac{\Delta v_{i_1, j_{\text{new}}}}{\Delta v_{i_1, j_{\text{old}}}} \frac{\Delta v_{i_1, i_2; j_{\text{new}}, k_{\text{new}}}}{\Delta v_{i_1, i_2; j_{\text{old}}, k_{\text{old}}}} \right\} . \quad (12.82)$$

As for RM₁, first estimates of the conditional CDFs and the intervals $\Delta v_{i_1, i_2; j, k}$ are obtained from a conventional Metropolis simulation at 400 K. In the following, we focus on the pairs (v_7, v_8) , (v_{10}, v_{11}) and (v_{15}, v_{16}) . These angles correspond to the largest integrated autocorrelation times of the RM₁ procedure and are expected to be strongly correlated with one another because they are pairs of dihedral angles around a C $_{\alpha}$ atom.

The bias of the acceptance probability given in (12.82) is governed by the areas

$$\Delta A_{i_1, i_2; j, k} = \Delta v_{i_1, j} \Delta v_{i_1, i_2; j, k} .$$

For $i_1 = 7$ and $i_2 = 8$, our 400 K estimates of these areas are depicted in Fig. 12.12. For the RM₂ procedure, these areas take the role which the intervals on the abscissa of Fig. 12.10 play for RM₁ updating. The small and the

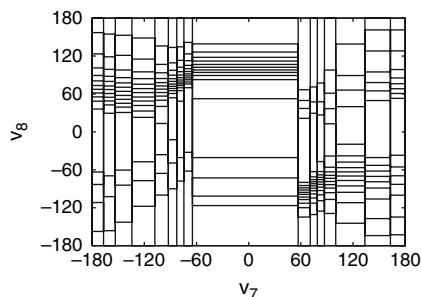


Fig. 12.12. Areas of equal probabilities (sorting v_7 then v_8)

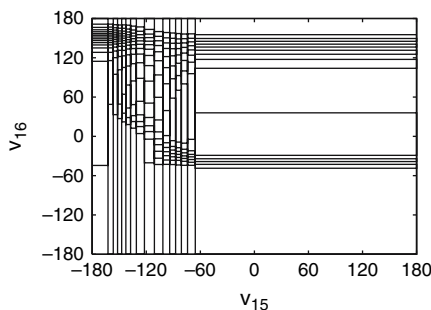


Fig. 12.13. Areas of equal probabilities (sorting v_{15} then v_{16})

large areas are proposed with equal probabilities, so the a priori probability for our two angles is high in a small area and low in a large area. Areas of high probability correspond to allowed regions in the Ramachandran map of a Gly residue [74]. In Fig. [12.12], the largest area is 503.4 times the smallest area. Note that the order in which the angles are sorted introduces some differences. Figure [12.13] gives a plot for (v_{15}, v_{16}) pairs in which the angle with the smaller subscript is sorted first. There the ratio of the largest area over the smallest area is 2565.8. The large value is related to the fact that (v_{15}, v_{16}) is the pair of ϕ, ψ angles around the C_α atom of Phe-4, for which positive ϕ values are disallowed [74].

Reductions in the integrated autocorrelation times of the angles vary and are again similar to those observed in Fig. [12.3] when moving from the ordinary Metropolis to the HBA.

12.6 Conclusions and Outlook

Spin systems, lattice gauge theory and biophysics models are certainly far apart in their scientific objectives. Nevertheless, quite similar computational techniques allow for efficient MCMC simulations in either field. Cross-fertilization may spread in both directions. For instance, generalized ensemble

techniques propagated from lattice gauge theory [7] over statistical physics [43] into biophysics [13], while it appears that biased Metropolis techniques [15, 63, 64, 65, 66] propagate in the opposite direction [68].

It is rather straightforward to combine the biased techniques of Sect. 12.5 with generalized ensembles, and some work on this topic has just begun. In [15, 75], combinations with parallel tempering have been studied and the improvements were approximately multiplicative. An implementation into the multicanonical ensemble has recently been worked out [76] and applied in a study of the deconfining phase transition of $U(1)$ lattice gauge theory. The basic ideas of the rugged MC may also be useful in MD simulations [77]. As this leads into ongoing research, it is a good point to conclude these lecture notes at this point.

References

1. N. Metropolis, A. W. Rosenbluth, M. N. Rosenbluth, A. H. Teller, E. Teller: J. Chem. Phys. **21**, 1087 (1953) [317]
2. J. Gubernatis (ed.): *The Monte Carlo Method in the Physical Sciences: Celebrating the 50th Anniversary of the Metropolis Algorithm* (AIP Conference Proceedings, Vol. 690, Melville, NY, 2003) [317, 350]
3. B. A. Berg: *Markov Chain Monte Carlo Simulations and Their Statistical Analysis* (World Scientific, Singapore, 2004) [318, 319, 320, 321, 323, 324, 325, 326, 328, 329, 330, 331, 332, 333, 334, 335, 336, 337, 338, 339, 340, 341, 342, 343, 344, 345, 346, 347, 348, 349, 350, 351, 352, 353, 354, 355, 356, 357, 358, 359, 360, 361, 362, 363, 364, 365, 366, 367, 368, 369, 370, 371, 372, 373, 374, 375, 376, 377, 378, 379, 380, 381, 382, 383, 384, 385, 386, 387, 388, 389, 390, 391, 392, 393, 394, 395, 396, 397, 398, 399, 400, 401, 402, 403, 404, 405, 406, 407, 408, 409, 410, 411, 412, 413, 414, 415, 416, 417, 418, 419, 420, 421, 422, 423, 424, 425, 426, 427, 428, 429, 430, 431, 432, 433, 434, 435, 436, 437, 438, 439, 440, 441, 442, 443, 444, 445, 446, 447, 448, 449, 450, 451, 452, 453, 454, 455, 456, 457, 458, 459, 460, 461, 462, 463, 464, 465, 466, 467, 468, 469, 470, 471, 472, 473, 474, 475, 476, 477, 478, 479, 480, 481, 482, 483, 484, 485, 486, 487, 488, 489, 490, 491, 492, 493, 494, 495, 496, 497, 498, 499, 500, 501, 502, 503, 504, 505, 506, 507, 508, 509, 510, 511, 512, 513, 514, 515, 516, 517, 518, 519, 520, 521, 522, 523, 524, 525, 526, 527, 528, 529, 530, 531, 532, 533, 534, 535, 536, 537, 538, 539, 540, 541, 542, 543, 544, 545, 546, 547, 548, 549, 550, 551, 552, 553, 554, 555, 556, 557, 558, 559, 560, 561, 562, 563, 564, 565, 566, 567, 568, 569, 570, 571, 572, 573, 574, 575, 576, 577, 578, 579, 580, 581, 582, 583, 584, 585, 586, 587, 588, 589, 590, 591, 592, 593, 594, 595, 596, 597, 598, 599, 600, 601, 602, 603, 604, 605, 606, 607, 608, 609, 610, 611, 612, 613, 614, 615, 616, 617, 618, 619, 620, 621, 622, 623, 624, 625, 626, 627, 628, 629, 630, 631, 632, 633, 634, 635, 636, 637, 638, 639, 640, 641, 642, 643, 644, 645, 646, 647, 648, 649, 650, 651, 652, 653, 654, 655, 656, 657, 658, 659, 660, 661, 662, 663, 664, 665, 666, 667, 668, 669, 670, 671, 672, 673, 674, 675, 676, 677, 678, 679, 680, 681, 682, 683, 684, 685, 686, 687, 688, 689, 690, 691, 692, 693, 694, 695, 696, 697, 698, 699, 700, 701, 702, 703, 704, 705, 706, 707, 708, 709, 710, 711, 712, 713, 714, 715, 716, 717, 718, 719, 720, 721, 722, 723, 724, 725, 726, 727, 728, 729, 730, 731, 732, 733, 734, 735, 736, 737, 738, 739, 740, 741, 742, 743, 744, 745, 746, 747, 748, 749, 750, 751, 752, 753, 754, 755, 756, 757, 758, 759, 760, 761, 762, 763, 764, 765, 766, 767, 768, 769, 770, 771, 772, 773, 774, 775, 776, 777, 778, 779, 780, 781, 782, 783, 784, 785, 786, 787, 788, 789, 790, 791, 792, 793, 794, 795, 796, 797, 798, 799, 800, 801, 802, 803, 804, 805, 806, 807, 808, 809, 810, 811, 812, 813, 814, 815, 816, 817, 818, 819, 820, 821, 822, 823, 824, 825, 826, 827, 828, 829, 830, 831, 832, 833, 834, 835, 836, 837, 838, 839, 840, 841, 842, 843, 844, 845, 846, 847, 848, 849, 850, 851, 852, 853, 854, 855, 856, 857, 858, 859, 860, 861, 862, 863, 864, 865, 866, 867, 868, 869, 870, 871, 872, 873, 874, 875, 876, 877, 878, 879, 880, 881, 882, 883, 884, 885, 886, 887, 888, 889, 890, 891, 892, 893, 894, 895, 896, 897, 898, 899, 900, 901, 902, 903, 904, 905, 906, 907, 908, 909, 910, 911, 912, 913, 914, 915, 916, 917, 918, 919, 920, 921, 922, 923, 924, 925, 926, 927, 928, 929, 930, 931, 932, 933, 934, 935, 936, 937, 938, 939, 940, 941, 942, 943, 944, 945, 946, 947, 948, 949, 950, 951, 952, 953, 954, 955, 956, 957, 958, 959, 960, 961, 962, 963, 964, 965, 966, 967, 968, 969, 970, 971, 972, 973, 974, 975, 976, 977, 978, 979, 980, 981, 982, 983, 984, 985, 986, 987, 988, 989, 990, 991, 992, 993, 994, 995, 996, 997, 998, 999, 1000]
4. G. M. Torrie, J. P. Valleau: J. Comput. Phys. **23**, 187 (1977) [318, 334]
5. R. H. Swendsen, J.-S. Wang: Phys. Rev. Lett. **57**, 2607 (1986) [318, 335]
6. G. J. Geyer: Markov chain Monte Carlo maximum likelihood. In *Computing Science and Statistics*, Proceedings of the 23rd Symposium on the Interface, edited by E. M. Keramidas (Interface Foundation, Fairfax, VA, 1991), pp. 156–163 [318, 335]
7. B. A. Berg, T. Neuhaus: Phys. Lett. B **267**, 249 (1991) [318, 334, 340, 349]
8. B. A. Berg, T. Neuhaus: Phys. Rev. Lett. **68**, 9 (1992) [318, 334, 335, 336, 337, 338]
9. B. A. Berg: Int. J. Mod. Phys. **3**, 1083 (1992) [318, 334]
10. A. P. Lyubartsev, A. A. Martsinovski, S. V. Shevkanov, P. N. Vorontsov-Velyaminov: J. Chem. Phys. **96**, 1776 (1992) [318, 335]
11. E. Marinari, G. Parisi: Europhys. Lett. **19**, 451 (1992) [318, 335]
12. K. Hukushima, K. Nemoto: J. Phys. Soc. Jpn. **65**, 1604 (1996) [318, 335]
13. U. H. Hansmann, Y. Okamoto: J. Comput. Chem. **14**, 1333 (1993) [318, 336, 349]
14. M.-H. Hao, H. A. Scheraga: J. Phys. Chem. **98**, 4940 (1994) [318, 336]
15. B. A. Berg: Phys. Rev. Lett. **90**, 180601 (2003) [318, 341, 344, 345, 349]
16. G. Marsaglia, A. Zaman, W. W. Tsang: Stat. Prob. **8**, 35 (1990) [319]
17. F. Y. Wu: Rev. Mod. Phys. **54**, 235 (1982) [319]
18. R. J. Baxter: J. Phys. C **8**, L445 (1973) [320]
19. C. Borgs, W. Janke: J. Phys. I (France) **2**, 2011 (1992) [320, 335]
20. J. Propp, D. Wilson: DIMACS Series in Discrete Mathematics and Theoretical Computer Science (AMS) **41**, 181 (1998) [326]
21. W. S. Kendall: Notes on perfect simulation. In *Markov Chain Monte Carlo: Innovations and Applications* (Lecture Notes Series, Institute for Mathematical Sciences, National University of Singapore), edited by W. S. Kendall, F. Liang, J.-S. Wang (World Scientific, Singapore, 2005) [326]

22. D. P. Landau, K. Binder: *A Guide to Monte Carlo Simulations in Statistical Physics* (Cambridge University Press, Cambridge, MA 2000) [329](#)
23. R. H. Swendsen, J.-S. Wang: Phys. Rev. Lett. **58**, 86 (1987) [329](#)
24. U. Wolff: Phys. Rev. Lett. **62**, 361 (1989) [329](#)
25. M. H. Quenouille: Biometrika **43**, 353 (1956) [331](#)
26. J. W. Tukey: Ann. Math. Stat. **29**, 614 (1958) [331](#)
27. Z. W. Salsburg, J. D. Jacobson, W. S. Fickett, W. W. Wood: J. Chem. Phys. **30**, 65 (1959) [333](#)
28. I. R. McDonald, K. Singer: Discuss. Faraday Soc. **43**, 40 (1967) [333](#)
29. M. Falcioni, E. Marinari, L. Paciello, G. Parisi, B. Taglienti: Phys. Lett. B **108**, 331 (1982) [333](#)
30. E. Marinari: Nucl. Phys. B **235**, 123 (1984) [333](#)
31. A. M. Ferrenberg, R. H. Swendsen: Phys. Rev. Lett. **61**, 2635 (1988); A. M. Ferrenberg, R. H. Swendsen: Phys. Rev. Lett. **63**, 1658(E) (1989) [333](#)
32. J. P. Valleau, D. N. Card: J. Chem. Phys. **57**, 5457 (1972) [333](#)
33. A. M. Ferrenberg, R. H. Swendsen: Phys. Rev. Lett. **63**, 1195 (1989) [333](#)
34. N. A. Alves, B. A. Berg, R. Villanova: Phys. Rev. B **41**, 383 (1990) [333](#)
35. N. A. Alves, B. A. Berg, S. Sanielevici: Nucl. Phys. B **376**, 218 (1992) [333](#)
36. Z. Li, H. A. Scheraga: J. Mol. Struct. (Theochem) **179**, 333 (1988) [334](#)
37. W. Kerler, P. Rehberg: Phys. Rev. E **50**, 4220 (1994) [335](#)
38. W. Janke: Physica A **254**, 164 (1998) [336](#)
39. U. H. Hansmann, Y. Okamoto: Ann. Rev. Comp. Phys. **6**, 129 (1999) [336](#), [338](#)
40. B. A. Berg: Fields Inst. Commun. **26**, 1 (2000) [cond-mat/990923] [336](#)
41. A. Mitsutake, Y. Sugita, Y. Okamoto: Biopolymers (Peptide Science) **60**, 96 (2001) [336](#), [338](#)
42. B. A. Berg, W. Janke: Phys. Rev. Lett. **98**, 040602 (2007) [336](#)
43. B. A. Berg, T. Celik: Phys. Rev. Lett. **69**, 2292 (1992) [336](#), [349](#)
44. B. A. Berg, U.H. Hansmann, Y. Okamoto: J. Phys. Chem. **99**, 2236 (1995) [336](#)
45. U. H. Hansmann: Chem. Phys. Lett. **281**, 140 (1997) [336](#)
46. Y. Sugita, Y. Okamoto: Chem. Phys. Lett. **314**, 141 (1999) [336](#)
47. C. Borgs, S. Kappler: Phys. Lett. A **171**, 37 (1992) [337](#)
48. T. Meuhaus, J. S. Hager: Phys. Rev. E **74**, 036702 (2006) [338](#)
49. U. H. Hansmann, Y. Okamoto: J. Chem. Phys. **110**, 1267 (1999) [338](#)
50. B. A. Berg, U. H. Hansmann, T. Neuhaus: Phys. Rev. B **47**, 497 (1993) [338](#)
51. B. A. Berg, W. Janke: Phys. Rev. Lett. **80**, 4771 (1998) [339](#)
52. B. A. Berg, H. Noguchi, Y. Okamoto: Phys. Rev. E **68**, 036126 (2003). [339](#)
53. B. A. Berg: J. Stat. Phys. **82**, 323 (1996) [339](#), [340](#)
54. B. A. Berg, A. Billoire, W. Janke: Phys. Rev. B **61**, 12143 (2000) [339](#)
55. Y. Sugita, Y. Okamoto: Chem. Phys. Lett. **329**, 261 (2000) [339](#)
56. F. Wang, D. P. Landau: Phys. Rev. Lett. **86**, 2050 (2001) [339](#), [340](#)
57. B. Hesselbo, R. Stinchcombe: Phys. Rev. Lett. **74**, 2151 (1995) [339](#)
58. S. Trebst, D. A. Huse, M. Troyer: Phys. Rev. E **70**, 046701 (2004) [339](#)
59. F. Wang, D. P. Landau: Phys. Rev. E **64**, 056101 (2001) [339](#)
60. F. Yasar, T. Celik, B. Berg, H. Meirovitch: J. Comput. Chem. **21**, 1251 (2000) [340](#)
61. Y. Okamoto: In [2](#), p. 248 [cond-mat/0308119] [340](#)
62. W. K. Hastings: Biometrika **57**, 97 (1970) [341](#)
63. A. D. Bruce: J. Phys. A **18**, L873 (1985) [341](#), [349](#)
64. A. Milchev, D. W. Heermann, K. Binder: J. Stat. Phys. **44**, 749 (1986) [341](#), [349](#)

- 65. M. W. Deem, J. S. Bader: *Mol. Phys.* **87**, 1245 (1996) [341](#), [349](#)
- 66. G. Favrin, A. Irbäck, F. Sjunnesson: *J. Chem. Phys.* **114**, 8154 (2001) [341](#), [349](#)
- 67. J. P. Ulmschneider, W. L. Jorgensen: *J. Chem. Phys.* **118**, 4261 (2003) [341](#)
- 68. A. Bazavov, B. A. Berg: *Phys. Rev. D* **71** 114506 (2005) [341](#), [342](#), [349](#)
- 69. A. Bazavov, B. A. Berg, U. M. Heller: *Phys. Rev. D* **72**, 117501 (2005) [344](#)
- 70. Z. Li, H. A. Scheraga: *Proc. Natl. Acad. Sci. USA* **85**, 6611 (1987) [345](#)
- 71. M. J. Sippl, G. Nemethy, H. A. Scheraga: *J. Phys. Chem.* **88**, 6231 (1984) [345](#)
- 72. F. Eisenmenger, U. H. Hansmann, S. Hayryan, C.-K. Hu: *Comput. Phys. Commun.* **138**, 192 (2001) [345](#)
- 73. B. A. Berg, H.-X. Zhou: *Phys. Rev. E* **72**, 016712 (2005) [346](#)
- 74. G. E. Schultz, R. H. Schirmer: *Principle of Protein Structure* (Springer, New York, 1979) [348](#)
- 75. B. A. Berg, H.-P. Hsu: *Phys. Rev. E* **69**, 026703 (2004) [349](#)
- 76. A. Bazavov, B. A. Berg: *Phys. Rev. D* **74**, 094502 (2006) [349](#)
- 77. H. Li, G. Li, B. A. Berg, W. Yang: *J. Chem. Phys.* **125**, 144902 (2006) [349](#)

A Different Approach to Monte Carlo Simulations in Systems with Complex Free-Energy Landscapes

David P. Landau

Center for Simulation Physics, The University of Georgia, Athens, GA 30602, USA

dlandau@hal.physast.uga.edu

Abstract. We describe a new Monte Carlo algorithm that produces results of high accuracy with reduced simulational effort. In the simplest application of the algorithm, a random walk is performed in energy space, and the resultant density of states is modified continuously to produce a “flat” histogram. This method permits us to directly access the entropy and free energy, is independent of temperature, and is efficient for the study of both first-order and second-order phase transitions as well as complex systems with a rough energy landscape. The method may be extended to random walks in more than one variable.

13.1 Introduction

In recent decades the power of computer simulation methods has grown tremendously. Consequently, the traditional “scientific method”, in which theory is tested by experiment the results of which may be used to improve the theory, has been replaced by a new paradigm in which in addition to these traditional forms of investigation of physical systems computer simulation must now be considered as another equally important means of investigation. This new paradigm is portrayed schematically in Fig. 13.1

Monte Carlo methods have played a pivotal role in the rise of computer simulations as a serious scientific tool [1]. For the past half century, the Metropolis Monte Carlo method [2] has been used to study a wide variety of different problems in statistical physics. In essence, it performs a random walk in probability space to explore the different “important” states of the system. The method is flexible and straightforward to implement and has consequently been used extensively. Other importance sampling methods have been devised in which entire clusters, intelligently chosen, are flipped to produce new states. As we shall show in the next section, however, there are situations in which it becomes exceedingly difficult to obtain reliable results using these algorithms.

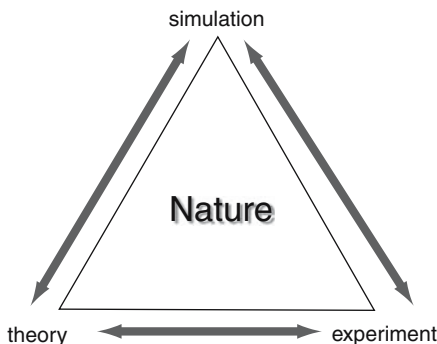


Fig. 13.1. Schematic representation of methods of scientific investigation appropriate for the study of problems in statistical physics. Arrows indicate interaction between different approaches

The purpose of this article is to describe an alternative approach which circumvents many of the difficulties of the Metropolis method as well as more sophisticated methods that generate states at a constant temperature. This approach has already shown itself to be both powerful and broadly applicable. We will first show applications to several simple models for which exact results are available, and then results for several models with rough energy landscapes will be described.

13.2 Method

13.2.1 Problems and Challenges

Within the context of statistical mechanics, the thermodynamic properties of any classical model can be extracted from the partition function

$$Z = \sum_{\{\text{states}\}} e^{-\beta E}, \quad (13.1)$$

where $\beta = 1/k_B T$ and the sum is over ALL states of the system. Simple Monte Carlo sampling of the states is impractical because of the large number of states. Importance sampling Monte Carlo approaches, e.g., the Metropolis method, for which states are sampled according to their canonical probability provide a vast improvement; nonetheless, near a second-order phase transition very long time scales develop (“critical slowing down”) so that successive configurations are strongly correlated. As a consequence, very long runs are needed. Near first order transitions, both the ordered and disordered states may coexist (with different probabilities except exactly at the transition) and pronounced metastability may occur. This represents a difficulty that also requires very long simulations to surmount. Another challenge for Monte Carlo

simulations is systems with complex energy landscapes. At low temperatures, it becomes quite difficult to sample a sufficient number of states to explore all of the local minima to determine which is actually the global minimum. This background sets the stage for the description of a method that takes a fundamentally different approach to Monte Carlo sampling of systems in statistical physics and can also be used as a general optimization tool for many other problems.

13.2.2 The Algorithm

One solution to the difficulties outlined in the previous subsection is to estimate the density of states $g(E)$ directly and then to use that result to calculate thermodynamic properties for all temperatures without performing additional simulations. Rewriting the partition function Z in terms of the density of states, i.e., sum over all energies instead of over all states, we quickly realize that there are many fewer different values of energy than the total number of states. Furthermore, the density of states is independent of temperature, so once it is determined, all thermodynamic properties may be calculated by weighting each value of $g(E)$ by the appropriate Boltzmann factor:

$$Z = \sum_{\{\text{states}\}} e^{-\beta E} = \sum_E g(E) e^{-\beta E} .$$

The approach that we describe here will then be to estimate $g(E)$ through an iterative procedure that relies on random walks in energy space instead of probability space. Originally entitled the “random walk with a flat histogram” method [3, 4, 5], this approach has become known as “Wang–Landau sampling” and we will use this shorthand designation. (We emphasize at the outset that the algorithm can be applied to densities of states of multiple parameters, but at the moment, for pedagogical reasons, the discussion will be limited to use of a single variable.) This algorithm is based on the observation that a random walk performed in energy space, e.g., for a spin system by flipping spins randomly, subject to a probability of visiting a given energy level E that is proportional to the reciprocal of the density of states, $[g(E)]^{-1}$, should lead to a flat histogram for the energy distribution. The “Wang–Landau algorithm” does this by modifying the estimated density of states systematically to produce a “flat” histogram over the allowed range of energy and simultaneously a density of states that converges to the true value. The density of states is modified constantly during each step of the random walk and the updated density of states is used to perform a further random walk in energy space. This “modification factor” is controlled carefully, and at the end of simulation, it should be very close to unity, i.e. the ideal case of the random walk with the true density of states.

Initially, $g(E)$ is a priori unknown, so one can simply set all entries to $g(E) = 1$ for all possible energies E . (Of course, a more intelligent initial

choice may speed up convergence of the algorithm, but even quite simple choices turn out to be adequate.) Then, one begins a random walk in energy space by flipping spins randomly, and the probability for a given energy E is proportional to $[g(E)]^{-1}$. In general, if E_1 and E_2 are energies before and after a spin is flipped, the transition probability from energy E_1 to E_2 is

$$p(E_1 \rightarrow E_2) = \min \left(\frac{g(E_1)}{g(E_2)}, 1 \right). \quad (13.2)$$

Each time an energy level E is visited, the existing value in the histogram is multiplied by a modification factor $f > 1$, i.e., $g(E) \rightarrow g(E) \times f$. (As a practical matter, it is generally beneficial to use the formula $\ln(g(E)) \rightarrow \ln(g(E)) + \ln(f)$ in order to fit all possible $g(E)$ into double precision numbers.) If the random walk rejects a trial move and stays at the same energy level, the existing $g(E)$ is also multiplied by the same modification factor. Although in the original publication [3] in which the algorithm was first proposed, an initial modification factor of $f = f_0 = e^1 \simeq 2.718 \dots$ was used because it was a simple choice yet allowed the system to reach all possible energy levels very quickly, even for large systems, this choice is not essential to the success of the algorithm. Nevertheless, some care must be exercised since if f_0 is too small, the random walk will take too long to reach all possible energies, and if it is too large, pronounced statistical errors will result. During the random walk, a histogram, $H(E)$, is also accumulated for the number of visits at each energy level E in energy space at that level of iteration. When the histogram is approximately “flat” over the energy range of the random walk, the density of states will have converged to the true value with an accuracy proportional to that modification factor $\ln(f)$. Then, the modification factor is reduced to a smaller value using some simple procedure, e.g., $f_1 = \sqrt{f_0}$, and the histogram is re-zeroed. The next iteration random walk begins during which the density of states is modified with this finer modification factor, f_1 , during each step and a new histogram is accumulated. When the histogram is again “flat”, the random walk stops, the histogram is again reset, the modification factor is again reduced, and the next iteration, i.e., random walk, begins. The algorithm continues until the modification factor is smaller than some predefined value (e.g., $f_{\text{final}} = \exp(10^{-8}) \simeq 1.00000001$), and a high-quality estimate for $g(E)$ has been then produced by this iterative procedure. It is very clear that the modification factor acts as a control parameter for the accuracy of the density of states during the simulation and also determines how many Monte Carlo sweeps are necessary for the simulation. It is impossible to obtain a perfectly flat histogram; the term “flat histogram” means simply that the histogram $H(E)$ for all possible E is at least $x\%$ of the average histogram $\langle H(E) \rangle$, where $x\%$ is chosen according to the size and complexity of system and the desired accuracy of the density of states. For the $L = 32$, two-dimensional Ising model with only nearest-neighbor couplings, this percentage can be chosen as high as 95%, but for large systems, the criterion for “flatness” may never be satisfied if this percentage is chosen to be too high. (The program might then run

forever.) Typically $x\%$ is in the range of 80–90%, but it may also be varied adaptively during the simulation. (A description of this algorithm that has appeared elsewhere [6] also includes additional pedagogical material.)

The accuracy of the density of states is proportional to $\ln(f)$ at that iteration; however, $\ln(f_{\text{final}})$ cannot be chosen arbitrarily small or the modified $\ln(g(E))$ will not differ sufficiently from the unmodified one. In this case, the algorithm no longer converges to the true value, and the program may again run “forever”.

The reduction of the modification factor by taking the square root after each iteration is also not essential to the functioning of the algorithm. Any function may be used as long as it decreases f monotonically to 1. A simple and efficient formula is $f_{i+1} = f_i^{1/n}$, where $n > 1$. The value of n can be chosen according to the available CPU time and expected accuracy of the simulation. Generally, the choice of $n = 2$ yielded good accuracy in a relatively short time, even for relatively large systems; however, Zhou and Bhatt [7] showed that it might even be preferable to begin with a larger value of f and to reduce it much faster than with a square root.

The method can be further enhanced by performing multiple random walks, each for a different range of energy, either serially or in parallel fashion. When the random walk is being carried out over some fixed subinterval of energy, a decision must be made about what to do when a spin flip takes the system outside of the range. The initial choice [3, 4] was to reject the spin-slip trial and leave the histogram and density of states unchanged. This led to spurious “boundary effects” at the limits of the energy range. It was later shown [8] that by rejecting the move and also updating $H(E)$ and $g(E)$ for that energy value, the “boundary effects” were suppressed. The different ranges of energy do not all have to be of the same extent, and larger ranges can be used for those regions that are less likely to be important to the final canonical properties. The resultant pieces of the density of states can then be joined together to produce a complete $g(E)$ which can then be used to produce canonical averages for the calculation of thermodynamic quantities for any temperature.

The reader should be aware that during the early iterations the algorithm does not satisfy the detailed balance condition exactly, since the density of states is modified constantly during the random walk. However, after many iterations, $g(E)$ converges to the true value very quickly as the modification factor approaches 1 and detailed balance is recovered to a high degree of precision. If $p(E_1 \rightarrow E_2)$ is the transition probability from the energy level E_1 to level E_2 , from (13.2), the ratio of the transition probabilities from E_1 to E_2 and from E_2 to E_1 can be calculated very easily as

$$\frac{p(E_1 \rightarrow E_2)}{p(E_2 \rightarrow E_1)} = \frac{g(E_1)}{g(E_2)}, \quad (13.3)$$

where $g(E)$ is the density of states. In other words, the random walk algorithm satisfies detailed balance:

$$\frac{1}{g(E_1)}p(E_1 \rightarrow E_2) = \frac{1}{g(E_2)}p(E_2 \rightarrow E_1), \quad (13.4)$$

where $\frac{1}{g(E_1)}$ is the probability at the energy level E_1 and $p(E_1 \rightarrow E_2)$ is the transition probability from E_1 to E_2 for the random walk. We conclude that the detailed balance condition is satisfied with accuracy proportional to $\ln(f)$.

The idea of using a histogram generated from the states that are visited is not new. “Histogram reweighting” [9] has been proven to be invaluable, but since it involves extracting the density of states indirectly from a canonical distribution generated during a simulation, the results can be used only over a quite narrow range of temperatures nearby the temperature at which the simulation was performed. Methods based on the accumulation of histogram entries have had the problem of scalability for large systems [10, 11, 12, 13]. In “Wang–Landau sampling” the density of states is modified at each step of the random walk, and this permits a much faster approach to the true density of states, especially for large systems. (An alternative approach to the simulation of systems that have complex energy landscapes is the multicanonical method [14, 15, 16, 17, 18, 19, 20, 21, 22], but it is sometimes unwieldy to implement.)

We emphasize here that the total number of configurations increases exponentially with the size of the system, whereas the total number of possible energy levels increases linearly with system size. Thus, it is comparatively easier to calculate $g(E)$ with a random walk in energy space for a large system even though only a small fraction of the states can be generated. Later in this manuscript, we will consider the Q -state Potts model on an $L \times L$ lattice with nearest-neighbor interactions [23]. For $Q \geq 3$, the number of possible energy levels is about $2N$, where $N = L^2$ is the total number of the lattice site. However, the average number of possible states (or configurations) for each energy may be as large as $\frac{Q^N}{2N}$, where Q^N is the total number of possible configurations of the system. Therefore, most models in statistical physics may be well defined but are not amenable to brute force calculation of thermodynamic quantities by enumerating all states. This is also the reason why efficient and fast simulational algorithms are required instead.

Note that the algorithm only produces relative values for the density of states, since the density of states can be modified at each time it is visited. The final result then needs to be normalized, e.g., using the condition that the total number of possible states for the Q -state Potts model is Q^N , or that the number of ground states is Q , to get the absolute density of states from the raw data.

Finally, we mention that Zhou and Bhatt [7] have provided a numerical analysis of the method and shown that it converges to the correct answer. They have also provided an upper bound on the errors. Thus, the foundation underpinning the method is now firmly in place.

13.3 Applications

13.3.1 Two-Dimensional Ising Model

The power of the method just described can be clearly demonstrated by performing simulations for the two-dimensional Ising lattice, a model for which exact values for the density of states can be obtained for relatively small systems.

The Hamiltonian for the Ising model is

$$\mathcal{H} = -J \sum_{\langle ij \rangle} \sigma_i \sigma_j, \quad (13.5)$$

where the spins $\sigma_i = \pm 1$. In Fig. 13.2, the results of a “Wang–Landau simulation” for two different size Ising square lattices with periodic boundary conditions are compared with exact values. The agreement is startlingly good. In the main part of the figure, it is impossible to distinguish the results from the simulation from the exact values. From the density of states, the thermodynamic properties may be calculated as a function of temperature and are also in excellent agreement with exact answers.

We do not expect, of course, that the density of states will be important for positive energies since such high energy states will have quite low probability at most temperatures of interest. Nevertheless, the determination of $g(E)$ for the *entire* energy range demonstrates the performance of the method. By breaking up the energy range into multiple pieces as described earlier, it is relatively easy to obtain quite precise values for $g(E)$ for systems of size 256 for which the exact density of states cannot be calculated. One particularly

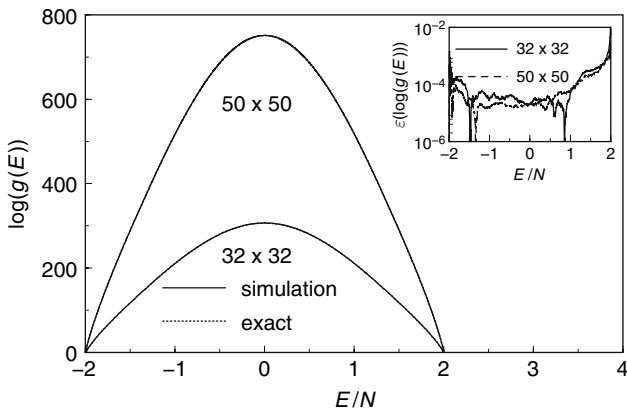


Fig. 13.2. Comparison of the density of states obtained by “Wang–Landau sampling” for the 2D Ising model and the exact results calculated by the method developed by Beale [24]. After Wang and Landau [3]

interesting quantity is the free energy, since this would normally require a thermodynamic integration. With the density of states, one can instead calculate it directly, and the curve shown in Fig. 13.3 gives the result for $L = 256$. The inset shows the relative error as compared with the exact results, and clearly the values in the “interesting region” near the phase transition are extremely good. Furthermore, it is easy to see that, as expected for a second-order transition, the free energy shows no discontinuity in slope near the transition.

13.3.2 The Two-Dimensional Potts Model: The Next Step in Complexity

In this section, we shall show that this algorithm also works quite well for a system with a first-order phase transition. The two-dimensional Potts model is known to have a first-order, temperature-driven transition if the number of states $Q > 4$. For such cases, the canonical probability distribution should show two peaks near the phase transition, one for the ordered state and one for the disordered state. Between these peaks the probability should be quite low, and standard, e.g., Metropolis, Monte Carlo simulations tend to get trapped near one maximum or the other. (This scenario corresponds to having a substantial free-energy barrier separating two free-energy minima.) In order to obtain high-quality equilibrium values for thermodynamic properties, the simulation must “tunnel” often from one peak to another. This process would require an extremely long time using standard methods.

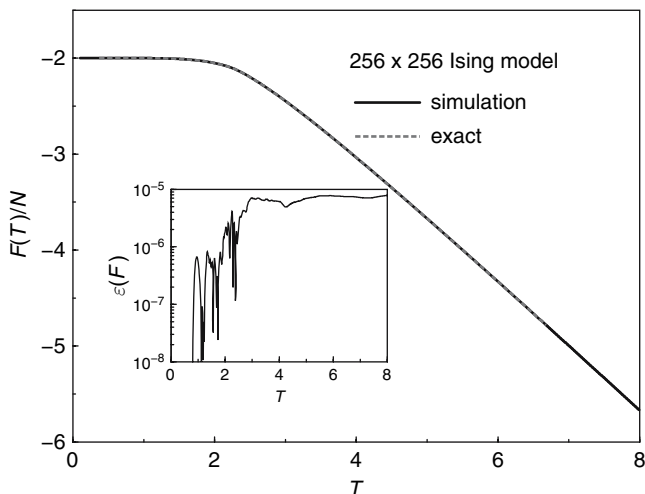


Fig. 13.3. Free energy for the Ising square lattice obtained using “Wang–Landau sampling”. The inset shows the relative error between the exact values and results from simulations. After Wang and Landau [4]

We now focus on the two-dimensional $Q = 10$ Potts model on $L \times L$ square lattice with nearest-neighbor interactions and periodic boundary conditions. The Hamiltonian for this model can be written as

$$\mathcal{H} = -J \sum_{\langle ij \rangle} \delta(q_i, q_j) \quad (13.6)$$

and $q_i = 1, 2, \dots, Q$. An efficient vectorized program had been used to perform large-scale Metropolis Monte Carlo simulations for this model and help test a finite-size scaling theory appropriate for a temperature-driven first-order transition [25]. Despite quite long runs, it was not possible to get reliable results for large lattices because of the long times needed to tunnel between the ordered and disordered states. However, “Wang–Landau sampling” can be used for this model and, as expected, it encounters fewer difficulties because of the lack of the energy barrier problem. At the end of the simulations, the density of states for different energies could be normalized either by using the fact that the total number of possible states is Q^N or that the number of ground states is Q , where $N = L^2$ is the total number of lattice sites. (Either one of these conditions can be used to get the absolute density of states and then the other condition can be used to check the accuracy of the result.) In the following, the number of ground states Q is used to help insure the accuracy of thermodynamic quantities at low temperatures. The maximum density of states for $L = 200$ then turns out to be very close to $10^{40\,000}$!

From the simulation result for $g(E)$, one can calculate the canonical distribution by the above formula at essentially any temperature without performing multiple simulations. In Fig. 13.4, we show the resultant double-peaked canonical distribution [25] at the transition temperature T_c for the first-order transition of the $Q = 10$ Potts model. (The “transition temperatures” $T_c(L)$ are 0.70171 for $L = 60$, 0.70143 for $L = 80$, and 0.70135 for

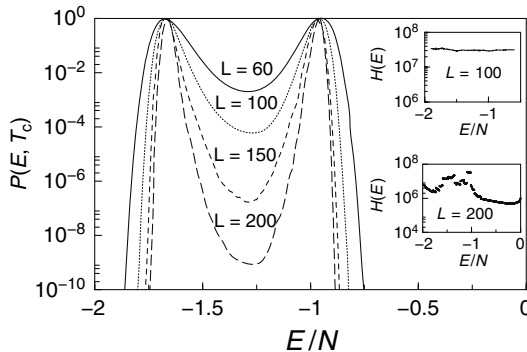


Fig. 13.4. Canonical probability function for the Potts model at the transition temperature. Values are determined from estimates of the density of states obtained by “Wang–Landau sampling”. After Wang and Landau [4]

$L = 100$, i.e., the temperatures where the peaks are of the same height). Note that the peaks of the distributions are normalized to 1 in this figure. The valley between two peaks is quite deep, e.g., 7×10^{-5} for $L = 100$. The latent heat for this (temperature-driven) first-order phase transition can be estimated from the energy difference between the double peaks, and the results for the locations of the peaks are consistent with those obtained by the multicanonical method [26, 27] and multibondic cluster algorithm [28, 29] for those lattice sizes for which these other methods are able to generate estimates. However, “Wang–Landau sampling” produces values for substantially larger systems than have been studied by these other approaches.

With this algorithm, all possible energy levels are visited with approximately equal probability, so the tunnelling barrier between the coexisting phases in the conventional Monte Carlo simulations presents no difficulty. The histograms for $L = 100$ and 200 are shown in the inset of Fig. 13.4. Each is the overall histogram defined by the total number of visits on each energy level for the random walk. Here, too, the initial modification factor was $f_0 = e^1$, and the final one as $\exp(10^{-8}) \simeq 1.00000001$. (The total number of iterations was 27.) In the simulation, there was no predetermined number of MC sweeps for each iteration but rather a “stopping” criterion was set for which the program checks periodically. Generally, the number of MC sweeps needed to satisfy the criterion increases as we reduce the modification factor, but one cannot predict the exact number of MC sweeps needed for each iteration ahead of time. This also guarantees that sufficiently flat histograms result from the random walks which, in turn, determine the accuracy of the final estimate for $g(E)$. Nonetheless, it is advisable to perform some test runs to insure that the program will finish within a reasonable time.

To speed up the simulation, one need not be constrained to perform a single random walk over the entire energy range with high accuracy. If we are only interested in a specific temperature range, e.g., near T_c , we could first perform a low-precision unrestricted random walk, i.e., over all energies, to estimate the “important” range of energy and then perform an accurate random walk for the appropriate energy region. The canonical probabilities in Fig. 13.4 only show values resulting from extensive random walks in the energy range between $E/N = -1.90$ and -0.60 . If one wanted to know $g(E)$ more accurately for some energies, one could perform separate simulations, one for low energies, one for high energies, and one for an intermediate energy range which includes the double peaks of the canonical distribution at T_c . This scheme not only speeds up the simulation but also increases the probability of accessing the energies for which both maximum and minimum values of the distributions occur by performing the individual random walks within relatively small energy ranges. If one performs single random walk over all possible energies, it will take a long time to generate rare spin configurations. Improbable energy levels include the ground state energy or low energy levels for which only a few spins have different values and high energy levels where all, or most, adjacent Potts spins are different.

If the system is not larger than 100×100 , the random walk over important energy regions (e.g., including the two peaks of the canonical distribution at T_c) can be carried out using a single processor and give an accurate estimate for the density of states within about 10^7 visits per energy level. The results for the smaller lattices shown in Fig. 13.4 were obtained using a single processor; however, for a larger system, we can use a parallelized algorithm by performing random walks over different energy regions, each using a different processor. (In the early studies, this was implemented using PVM with a simple master-slave model and yielded an accurate estimate for the density of states with relatively short runs on each processor. Using MPI to accomplish the same task today would be straightforward.) The densities of states for 150×150 and 200×200 were obtained by joining together the pieces obtained from 21 independent random walks, each constrained within a different region of energy. The histograms from individual random walks are shown in the inset of Fig. 13.4 for both 100×100 and 200×200 lattices. In this case, we only require that the histogram of the random walk in the individual energy segments is sufficiently flat without regard to the relative flatness over the entire energy range. In Fig. 13.4, the results for large lattices show clear double peaks for the canonical distributions at temperatures $T_c(L) = 0.70127$ for $L = 150$ and $T_c(L) = 0.701243$ for $L = 200$. The exact result is $T_c = 0.701232\dots$ for the infinite system. Considering that the valley which appears for $L = 200$ is as deep as 9×10^{-10} , we can easily understand why conventional Monte Carlo algorithms are unable to overcome the tunneling barrier with available computational resources.

If we compare the histogram for $L = 100$ in the inset of Fig. 13.4 with that for $L = 200$, we see that the simulation effort for $L = 200$ (9.8×10^6 visit per energy level) is even less than the effort for $L = 100$. It is more efficient to perform random walks in relatively small energy segments and to satisfy the flatness criterion than it is for a single random walk over all energies. This is because the random walk is a local walk, which means for a given E_1 , the energy level for the next step only can be one of nine levels in the energy range $[E_1 - 4, E_1 + 4]$ (for the Potts model discussed in this section). The algorithm itself only requires that the histogram on such local transitions be flat, whereas a single random walk, subject to the requirement of a flat histogram for all energy levels, will take quite long. For random walks in small energy segments, one must be very careful to make sure that all spin configurations with energies in the desired range can be equally accessed so the random walk may be restarted periodically from independent spin configurations.

13.3.3 Systems with Complex Energy Landscapes

There are numerous interesting problems in statistical physics for which there are more than two states with, at least local, free-energy minima, and in such instances the free-energy landscape may become quite rough. Determining

the global minimum at low temperatures becomes quite challenging because of the difficulty in passing over multiple, local, free-energy barriers to find the global minimum. (Spin-glass models have long been known to fall into this category and have been the subject of substantial scrutiny [30].) One such “classic” example is a simple extension of the Ising model known as the Edwards–Anderson (EA) spin glass. The model consists of Ising spins on a lattice with exchange constants J_{ij} between neighbors i and j that vary randomly from $+J$ to $-J$ with equal probability. The Hamiltonian for the Edwards–Anderson (EA) spin-glass model [31] is

$$\mathcal{H} = - \sum_{\langle ij \rangle} J_{ij} \sigma_i \sigma_j . \quad (13.7)$$

The density of states for this model was determined as described above, but here using a two-dimensional random walk in both energy and order parameter space. A histogram generated for a single distribution of bonds is shown in Fig. 13.5.

It is important to note that there is a correlation between the values of order parameter and energy that can simultaneously exist for a state so that some values of q and E never appear.

The final estimate for $g(E, q)$ was used to calculate canonical probabilities, seen in Fig. 13.6 and these showed dramatic differences in values over the range of different order parameters. This plot provides an excellent view of the complex variations of probability in a system with a rough energy landscape.

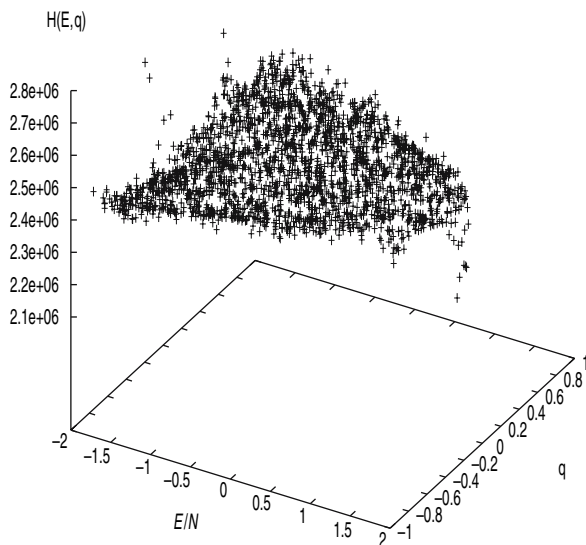


Fig. 13.5. Typical histogram for a two-dimensional random walk for the EA spin-glass model using “Wang–Landau sampling”

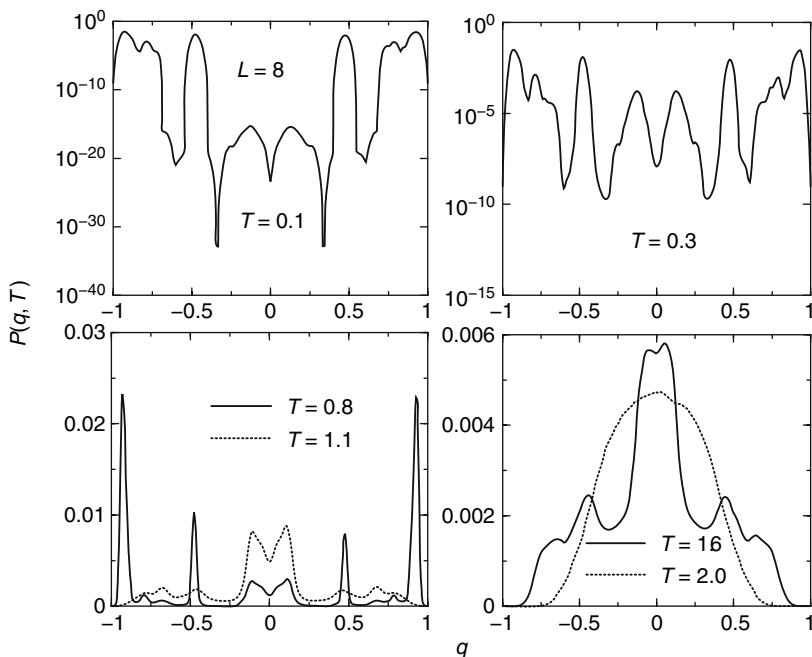


Fig. 13.6. Variation of the canonical probability with order parameter q for the Edwards–Anderson spin glass on an $L \times L \times L$ simple cubic lattice. Data for the underlying density of states were obtained for a single bond distribution using “Wang–Landau sampling”. After Wang and Landau [4]

At high temperature, the probability is rather smooth with a maximum for $q = 0$. As the temperature is lowered, however, multiple peaks appear, and at the lowest temperature, not only does the maximum probability occur for $q \neq 0$ but there are over 30 orders of magnitude difference between the largest and smallest probabilities. With this algorithm, it was possible to obtain estimates for the internal energy and entropy at essentially zero temperature for lattices as large as $L = 20$, and from crossing points in the fourth-order cumulants the transition temperature for a spin-glass transition was estimated to be $T_g \sim 1.2J$. While this study was not intended to be exhaustive, we emphasize that it was accomplished with quite modest computer resources. The behavior of the Edwards–Anderson spin glass is still controversial (see the discussion in [4]), and a more detailed application of this algorithm might prove to be extremely valuable.

“Wang–Landau sampling” has also now been used successfully for many other applications in physical, biological, and mathematical science. In some of these cases, the systems under investigation also possess complex energy landscapes. One such area of increasing importance is protein folding: Given the primary structure, i.e., the sequence of amino acids, what is the structure of

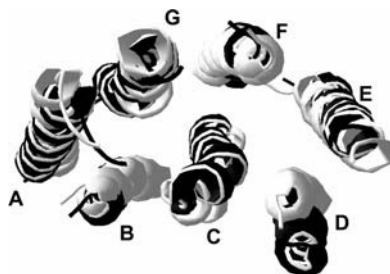


Fig. 13.7. “Optimized” folded state for Bacteriorhodopsin (1QHJ) using “Wang–Landau sampling”. Each α -helix is labeled with a letter. From Z. Chen [32]

the protein in the native state? Protein models must include quite short-range (bonded) interactions as well as weaker, longer-range (nonbonded) couplings and are hence nontrivial to simulate. Different structures may have different folds yet have quite similar energies, and the determination of the “optimum” state is non-trivial. Chen [32] examined the folding of the seven helix bundle Bacteriorhodopsin (1QHJ). This protein has 174 residues with a total of 1619 atoms. In the simulation the side chains were kept rigid, and the interactions included a van der Waals nonbonded coupling along with a lipid-helix potential. Starting from a rather random state, the algorithm successfully allowed the system to reach a state in which seven, well-formed α -helices are produced and correctly oriented as shown in Fig. 13.7. Substantial computing time was nonetheless needed, although “standard”, importance sampling Monte Carlo methods were unable to provide an acceptable solution.

Agreement with experiment could be improved still further, but, of course, it is not known if remaining differences have their origin in the numerics or in deficiencies in the Hamiltonian field used. Work on this problem is continuing. Of course, there is nothing that limits this method to single particle trial moves (spin-flips), and “Wang–Landau sampling” has already been performed with other kinds of moves. Other implementations have ranged from diverse problems in statistical mechanics [33, 34], fluids [35], polymers [36, 37], and proteins [38, 39] to optimization [40] and computational number theory [41]. Even quantum models [42, 43, 44] have permitted the use of “Wang–Landau sampling”. When studying new problems, it is important to consider what the appropriate thermodynamic parameters for the random walk might be. Whereas for a simple ferromagnet one might perform a two-dimensional random walk in energy and magnetization, for a polymer chain the bonded and nonbonded energies might prove to be more suitable. In the end, some experimentation might be helpful. The consideration of systems with continuous degrees of freedom, and thus continuous variation of the energy, poses a special problem because of singularities in the logarithm of the density of states at very low energies. A very nice way of treating such systems that also enhances performance by about an order of magnitude has been recently demonstrated

by Zhou et al. [45]. Even for systems with discrete variable, improvements are possible. Lee et al. [46] have shown how the method can be “refined” by choosing an appropriate stopping point and then “correcting” $g(E)$. Trial updates other than single spin flips can be used, and an adaptive algorithm that biases the random walk so as to improve the system rate of “round trips” in energy has also been proposed [47]. The future will surely see other inventive modifications of the algorithm that will improve performance still further.

13.4 Conclusions

In this manuscript, we have reviewed a recently developed algorithm that approaches Monte Carlo simulations of models in statistical physics from a different perspective. This method, termed “Wang–Landau sampling”, is an iterative approach that performs a random walk in energy space at each level of iteration and estimates the density of states quite accurately. Thus, from a single simulation, thermodynamic properties may then be calculated for all temperatures. The method is flexible, can be readily extended to random walks in multiple parameter dimension, and provides a powerful means for the examination of systems with rough energy landscapes. By adapting the method to different problems, yet further acceleration in performance will often be possible.

Acknowledgements

We thank F. Wang and S.-H. Tsai for fruitful collaborations and discussions. This work was supported in part by NSF grant DMR-0341874.

References

1. D. P. Landau, K. Binder: *A Guide to Monte Carlo Methods in Statistical Physics*, (Cambridge University Press, Cambridge, 2005) 2nd ed. [353]
2. N. Metropolis, A. W. Rosenbluth, M. N. Rosenbluth, A. H. Teller, E. Teller: *J. Chem. Phys.* **21**, 1087 (1953) [353]
3. F. Wang, D. P. Landau: *Phys. Rev. Lett.* **86**, 2050 (2001) [355, 356, 357, 359]
4. F. Wang, D. P. Landau: *Phys. Rev. E* **64**, 056101 (2001) [355, 357, 360, 361, 365]
5. D. P. Landau, F. Wang: *Comput. Phys. Commun.* **147**, 674 (2002) [355]
6. D. P. Landau, S.-H. Tsai, M. Exler: *Am. J. Phys.* **72**, 1294 (2004) [357]
7. C. Zhou, R. N. Bhatt: *Phys. Rev. E* **72**, 025701 (2005) [357, 358]
8. B. J. Schulz, K. Binder, M. Müller, D. P. Landau: *Phys. Rev. E* **67**, 067102 (2003) [357]
9. A. M. Ferrenberg, R. H. Swendsen: *Phys. Rev. Lett.* **61**, 2635 (1988); A. M. Ferrenberg, R. H. Swendsen: *Phys. Rev. Lett.* **63**, 1195 (1989) [358]

10. P. M. C. de Oliveira, T. J. P. Penna, H. J. Herrmann: Braz. J. Phys. **26**, 677 (1996); P. M. C. de Oliveira, T. J. P. Penna, H. J. Herrmann: Eur. Phys. J. B **1**, 205 (1998) [358](#)
11. J.-S. Wang: Eur. Phys. J. B **8**, 287 (1998) [358](#)
12. J. Lee: Phys. Rev. Lett. **71**, 211 (1993) [358](#)
13. A. R. Lima, P. M. C. de Oliveira, T. J. P. Penna: J. Stat. Phys. **99**, 691 (2000) [358](#)
14. B. A. Berg, T. Neuhaus: Phys. Rev. Lett. **68**, 9 (1992) [358](#)
15. B. A. Berg, T. Celik: Phys. Rev. Lett. **69**, 2292 (1992) [358](#)
16. B. A. Berg, U. Hansmann, T. Neuhaus: Phys. Rev. B **47**, 497 (1993) [358](#)
17. B. A. Berg: Nucl. Phys. (Proc. Suppl.) **63**, 982 (1998) [358](#)
18. B. A. Berg, T. Celik, U. Hansmann: Europhys. Lett. **22**, 63 (1993) [358](#)
19. B. A. Berg, U. Hansmann: Eur. Phys. J. B **6**, 395 (1998) [358](#)
20. U. Hansmann: Phys. Rev. B **56**, 6200 (1997) [358](#)
21. U. Hansmann, Y. Okamoto: Phys. Rev. E **54**, 5863 (1996) [358](#)
22. W. Janke, B. A. Berg, A. Billoire: Comput. Phys. Commun. **121–122**, 176 (1999) [358](#)
23. F. Y. Wu: Rev. Mod. Phys. **54**, 235 (1982) [358](#)
24. P. D. Beale: Phys. Rev. Lett. **76**, 78 (1996) [359](#)
25. M. S. S. Challa, D. P. Landau, K. Binder: Phys. Rev. B **34**, 1841 (1986) [361](#)
26. B. A. Berg, T. Neuhaus: Phys. Lett. B **267**, 249 (1991) [362](#)
27. W. Janke: Int. J. Mod. Phys. C **3**, 375 (1992) [362](#)
28. W. Janke: Physica A **254**, 164 (1998) [362](#)
29. W. Janke, S. Kappler: Phys. Rev. Lett. **74**, 212 (1995) [362](#)
30. K. Binder, A. P. Young: Rev. Mod. Phys. **58**, 801 (1986) [364](#)
31. S. F. Edwards, P. W. Anderson: J. Phys. F Metal Phys. **5** 965 (1975) [364](#)
32. Z. Chen: Unpublished [366](#)
33. C. Yamaguchi, Y. Okabe: J. Phys. A **34**, 8781 (2001) [366](#)
34. Y. Okabe, Y. Tomita, C. Yamaguchi: Comput. Phys. Commun. **146**, 63 (2002) [366](#)
35. Q. L. Yan, R. Faller, J. J. de Pablo: J. Chem. Phys. **116**, 8745 (2002) [366](#)
36. T. S. Jain, J. J. de Pablo: J. Chem. Phys. **116**, 7238 (2002) [366](#)
37. F. Rampf, W. Paul, K. Binder: Europhys. Lett. **70**, 628 (2005) [366](#)
38. N. Rathore, J. J. de Pablo: J. Chem. Phys. **116**, 7225 (2002) [366](#)
39. N. Rathore, T. A. Knotts, J. J. de Pablo: J. Chem. Phys. **118**, 4285 (2003) [366](#)
40. M. A. de Menezes, A. R. Lima: Phys. Lett. A **323**, 428 (2003) [366](#)
41. V. Mustonen, R. Rajesh: J. Phys. A **36**, 6651 (2003) [366](#)
42. M. Troyer, S. Wessel, F. Alet: Phys. Rev. Lett. **90**, 120201 (2003) [366](#)
43. P. N. Vorontsov-Velyaminov, A. P. Lyubartsev: J. Phys. A **36**, 685 (2003) [366](#)
44. W. Koller, A. Prüll, H. G. Evertz, W. von der Linden: Phys. Rev. B **67**, 104432 (2003) [366](#)
45. C. Zhou, T. C. Schulthess, S. Torbrügge, D. P. Landau: Phys. Rev. Lett. **96**, 120201 (2006) [367](#)
46. H.-K. Lee, Y. Okabe, D. P. Landau: Comput. Phys. Commun. **175**, 36 (2006) [367](#)
47. S. Trebst, D. A. Huse, M. Troyer: Phys. Rev. E **70**, 046701 (2004) [367](#)

Generalized-Ensemble Algorithms for Protein Folding Simulations

Yuji Sugita¹, Ayori Mitsutake² and Yuko Okamoto³

¹ Theoretical Biochemistry Laboratory, Discovery Research Institute, RIKEN, Wako-shi, Saitama 351-0198, Japan
sugita@riken.jp

² Department of Physics, Keio University, Yokohama, Kanagawa 223-8522, Japan
ayori@rk.phys.keio.ac.jp

³ Department of Physics, Nagoya University, Nagoya, Aichi 464-8602, Japan
okamoto@phys.nagoya-u.ac.jp

Abstract. Conventional simulations of complex systems in the canonical ensemble suffer from the quasi-ergodicity problem. A simulation in generalized ensemble overcomes this difficulty by performing a random walk in potential energy space and other parameter space. From only one simulation run, one can obtain canonical-ensemble averages of physical quantities as functions of temperature by the single-histogram and/or multiple-histogram reweighting techniques. In this article, we review the generalized-ensemble algorithms. Three well-known methods, namely multicanonical algorithm, simulated tempering, and replica-exchange method, are described first. Both Monte Carlo and molecular dynamics versions of the algorithms are given. We then present further extensions of the above three methods.

14.1 Introduction

Canonical fixed-temperature simulations of complex systems such as spin glasses and biopolymers are greatly hampered by the multiple-minima problem, or the quasi-ergodicity problem. Because simulations at low temperatures tend to get trapped in a few of a huge number of local-minimum-energy states which are separated by high-energy barriers, it is very difficult to obtain accurate canonical distributions at low temperatures by conventional Monte Carlo (MC) and molecular dynamics (MD) methods. One way to overcome this multiple-minima problem is to perform a simulation in a *generalized ensemble* where each state is weighted by an artificial, non-Boltzmann probability weight factor so that a random walk in potential energy space may be realized (for reviews see, e.g., [1, 2, 3, 4, 5, 6, 7]). The random walk allows the simulation to escape from any energy barrier and to sample much wider configurational space than by conventional methods. Monitoring the energy in a single simulation run, one can obtain not only the global-minimum-energy

state but also canonical ensemble averages as functions of temperature by the single-histogram [8] and/or multiple-histogram [9, 10] reweighting techniques (an extension of the multiple-histogram method is also referred to as *weighted histogram analysis method* (WHAM) [10]). Besides generalized-ensemble algorithms, which are usually based on local updates, methods based on nonlocal updates such as cluster algorithms and their generalizations have also been widely used [11, 12, 13]. In this article, we focus our discussion on generalized-ensemble algorithms.

One of the most well-known generalized-ensemble methods is perhaps *multicanonical algorithm* (MUCA) [14, 15] (for reviews see, e.g., [16, 17]). (The method is also referred to as *entropic sampling* [18] and *adaptive umbrella sampling* [19] of the potential energy [20]. MUCA can also be considered as a sophisticated ideal realization of a class of algorithms called *umbrella sampling* [21]. Also closely related methods are *transition matrix methods* reviewed in [4, 22] and *random walk algorithm* [23, 24], which is also referred to as *density of states Monte Carlo* [25]. See also [26].) MUCA and its generalizations have been applied to spin systems (see, e.g., [27, 28, 29, 30, 31, 32]). MUCA was also introduced to the molecular simulation field [33]. Since then, MUCA and its generalizations have been extensively used in many applications in protein and related systems [34, 35, 36, 37, 38, 39, 40, 41, 42, 43, 44, 45, 46, 47, 48, 49, 50, 51, 52, 53, 54, 55, 56, 57, 58, 59, 60, 61, 62, 63, 64]. Molecular dynamics version of MUCA has also been developed [20, 41, 44] (see also [41, 65] for Langevin dynamics version). MUCA has been extended so that flat distributions in other parameters instead of potential energy may be obtained [28, 29, 40, 45, 47, 62]. Moreover, multidimensional (or multicomponent) extensions of MUCA can be found in [40, 45, 46, 64].

While a simulation in multicanonical ensemble performs a free 1D random walk in potential energy space, that in *simulated tempering* (ST) [66, 67] (the method is also referred to as the *method of expanded ensemble* [66]) performs a free random walk in temperature space (for a review, see, e.g., [68]). This random walk, in turn, induces a random walk in potential energy space and allows the simulation to escape from states of local energy minima. ST has also been applied to protein folding problem [42, 43, 69, 70].

The generalized-ensemble algorithms are powerful, but in the above two methods, the probability weight factors are not a priori known and have to be determined by iterations of short trial simulations. This process can be non-trivial and very tedious for complex systems with many degrees of freedom. Therefore, there have been attempts to accelerate the convergence of the iterative process for MUCA weight factor determination [20, 27, 40, 71, 72, 73] (see also [16, 74]).

In the *replica-exchange method* (REM) [75, 76, 77], the difficulty of weight factor determination is greatly alleviated. (A closely related method was independently developed in [78]. Similar methods in which the same equations are used but emphasis is laid on optimizations have been developed [79, 80]. REM is also referred to as *multiple Markov chain method* [81] and *parallel tempering*

[68]. Details of literature about REM and related algorithms can be found in recent reviews [2, 82].) In this method, a number of noninteracting copies (or replicas) of the original system at different temperatures are simulated independently and simultaneously by the conventional MC or MD method. Every few steps, pairs of replicas are exchanged with a specified transition probability. The weight factor is just the product of Boltzmann factors, and so it is essentially known.

REM has already been used in many applications in protein systems [70, 83, 84, 85, 86, 87, 88, 89, 90, 91, 92, 93, 94, 95, 96, 97]. Other molecular simulation fields have also been studied by this method in various ensembles [98, 99, 100, 101, 102, 103]. Moreover, REM was applied to cluster studies in quantum chemistry field [104]. The details of molecular dynamics algorithm have been worked out for REM in [84] (see also [83, 101]). This led to a wide application of replica-exchange MD method in the protein folding problem [105, 106, 107, 108, 109, 110, 111, 112].

However, REM also has a computational difficulty: As the number of degrees of freedom of the system increases, the required number of replicas also greatly increases, whereas only a single replica is simulated in MUCA or ST. This demands a lot of computer power for complex systems. Our solution to this problem is: Use REM for the weight factor determinations of MUCA or ST, which is much simpler than previous iterative methods of weight determinations, and then perform a long MUCA or ST production run. The first example is the *replica-exchange multicanonical algorithm* (REMUC) [88, 93, 94]. In REMUC, a short replica-exchange simulation is performed, and the multicanonical weight factor is determined by the multiple-histogram reweighting techniques [9, 10]. Another example of such a combination is the *replica-exchange simulated tempering* (REST) [89]. In REST, a short replica-exchange simulation is performed, and the simulated tempering weight factor is determined by the multiple-histogram reweighting techniques [9, 10].

We have introduced two further extensions of REM, which we refer to as *multicanonical replica-exchange method* (MUCAREM) [88, 93, 94] (see also [113, 114]) and *simulated tempering replica-exchange method* (STREM) [115] (see also [116] for a similar idea). In MUCAREM, a replica-exchange simulation is performed with a small number of replicas each in multicanonical ensemble of different energy ranges. In STREM, on the other hand, a replica-exchange simulation is performed with a small number of replicas in “simulated tempering” ensemble of different temperature ranges.

Finally, one is naturally led to a multidimensional (or multivariable) extension of REM, which we refer to as *multidimensional replica-exchange method* (MREM) [86] (see also [92, 99, 117, 118, 112, 119]). A special realization of MREM is *replica-exchange umbrella sampling* (REUS) [86], and it is particularly useful in free-energy calculations (see also [87] for a similar idea).

In this article, we describe the generalized-ensemble algorithms mentioned above, namely we first review the three familiar methods: MUCA, ST, and REM. We then present further extensions of the three methods.

14.2 Generalized-Ensemble Algorithms

14.2.1 Multicanonical Algorithm and Simulated Tempering

Let us consider a system of N atoms of mass m_k ($k = 1, \dots, N$) with their coordinate vectors and momentum vectors denoted by $q \equiv \{\mathbf{q}_1, \dots, \mathbf{q}_N\}$ and $p \equiv \{\mathbf{p}_1, \dots, \mathbf{p}_N\}$, respectively. The Hamiltonian $H(q, p)$ of the system is the sum of the kinetic energy $K(p)$ and the potential energy $E(q)$:

$$H(q, p) = K(p) + E(q) , \quad (14.1)$$

where

$$K(p) = \sum_{k=1}^N \frac{\mathbf{p}_k^2}{2m_k} . \quad (14.2)$$

In the canonical ensemble at temperature T , each state $x \equiv (q, p)$ with the Hamiltonian $H(q, p)$ is weighted by the Boltzmann factor:

$$W_B(x; T) = \exp(-\beta H(q, p)) , \quad (14.3)$$

where the inverse temperature β is defined by $\beta = 1/k_B T$ (k_B is the Boltzmann constant). The average kinetic energy at temperature T is then given by

$$\langle K(p) \rangle_T = \left\langle \sum_{k=1}^N \frac{\mathbf{p}_k^2}{2m_k} \right\rangle_T = \frac{3}{2} N k_B T . \quad (14.4)$$

Because the coordinates q and momenta p are decoupled in (14.1), we can suppress the kinetic energy part and can write the Boltzmann factor as

$$W_B(x; T) = W_B(E; T) = \exp(-\beta E) . \quad (14.5)$$

The canonical probability distribution of potential energy $P_B(E; T)$ is then given by the product of the density of states $n(E)$ and the Boltzmann weight factor $W_B(E; T)$:

$$P_B(E; T) \propto n(E) W_B(E; T) . \quad (14.6)$$

Since $n(E)$ is a rapidly increasing function and the Boltzmann factor decreases exponentially, the canonical ensemble yields a bell-shaped distribution which has a maximum around the average energy at temperature T . The conventional MC or MD simulations at constant temperature are expected to yield $P_B(E; T)$. An MC simulation based on the Metropolis algorithm [120] is performed with the following transition probability from a state x of potential energy E to a state x' of potential energy E' :

$$w(x \rightarrow x') = \min \left(1, \frac{W_B(E'; T)}{W_B(E; T)} \right) = \min (1, \exp(-\beta \Delta E)) , \quad (14.7)$$

where

$$\Delta E = E' - E . \quad (14.8)$$

An MD simulation, on the other hand, is based on the following Newton equations of motion:

$$\dot{\mathbf{q}}_k = \frac{\mathbf{p}_k}{m_k} , \quad (14.9)$$

$$\dot{\mathbf{p}}_k = -\frac{\partial E}{\partial \mathbf{q}_k} = \mathbf{f}_k , \quad (14.10)$$

where \mathbf{f}_k is the force acting on the k th atom ($k = 1, \dots, N$). This set of equations actually yield the microcanonical ensemble, and we have to add a thermostat in order to obtain the canonical ensemble at temperature T . Here, we just follow Nosé's prescription [121, 122], and we have

$$\dot{\mathbf{q}}_k = \frac{\mathbf{p}_k}{m_k} , \quad (14.11)$$

$$\dot{\mathbf{p}}_k = -\frac{\partial E}{\partial \mathbf{q}_k} - \frac{\dot{s}}{s} \mathbf{p}_k = \mathbf{f}_k - \frac{\dot{s}}{s} \mathbf{p}_k , \quad (14.12)$$

$$\dot{s} = s \frac{P_s}{Q} , \quad (14.13)$$

$$\dot{P}_s = \sum_{k=1}^N \frac{\mathbf{p}_k^2}{m_k} - 3Nk_B T = 3Nk_B (T(t) - T) , \quad (14.14)$$

where s is Nosé's scaling parameter, Q is its mass, P_s is its conjugate momentum, and the "instantaneous temperature" $T(t)$ is defined by

$$T(t) = \frac{1}{3Nk_B} \sum_{k=1}^N \frac{\mathbf{p}_k(t)^2}{m_k} . \quad (14.15)$$

However, in practice, it is very difficult to obtain accurate canonical distributions of complex systems at low temperatures by conventional MC or MD simulation methods. This is because simulations at low temperatures tend to get trapped in one or a few of local-minimum-energy states.

In the multicanonical ensemble [14, 15], on the other hand, each state is weighted by a non-Boltzmann weight factor $W_{\text{mu}}(E)$ (which we refer to as the *multicanonical weight factor*) so that a uniform potential energy distribution $P_{\text{mu}}(E)$ is obtained:

$$P_{\text{mu}}(E) \propto n(E)W_{\text{mu}}(E) \equiv \text{const} . \quad (14.16)$$

The flat distribution implies that a free random walk in the potential energy space is realized in this ensemble. This allows the simulation to escape from any local minimum-energy states and to sample the configurational space much more widely than the conventional canonical MC or MD methods.

The definition in (14.16) implies that the multicanonical weight factor is inversely proportional to the density of states, and we can write it as follows:

$$W_{\text{mu}}(E) \equiv \exp[-\beta_0 E_{\text{mu}}(E; T_0)] = \frac{1}{n(E)} , \quad (14.17)$$

where we have chosen an arbitrary reference temperature, $T_0 = 1/k_B\beta_0$, and the “multicanonical potential energy” is defined by

$$E_{\text{mu}}(E; T_0) \equiv k_B T_0 \ln n(E) = T_0 S(E) . \quad (14.18)$$

Here, $S(E)$ is the entropy in the microcanonical ensemble. Since the density of states of the system is usually unknown, the multicanonical weight factor has to be determined numerically by iterations of short preliminary runs [14, 15].

A multicanonical MC simulation is performed, for instance, with the usual Metropolis criterion [120]: The transition probability of state x with potential energy E to state x' with potential energy E' is given by

$$\begin{aligned} w(x \rightarrow x') &= \min \left(1, \frac{W_{\text{mu}}(E')}{W_{\text{mu}}(E)} \right) = \min \left(1, \frac{n(E)}{n(E')} \right) \\ &= \min(1, \exp(-\beta_0 \Delta E_{\text{mu}})) , \end{aligned} \quad (14.19)$$

where

$$\Delta E_{\text{mu}} = E_{\text{mu}}(E'; T_0) - E_{\text{mu}}(E; T_0) . \quad (14.20)$$

The MD algorithm in the multicanonical ensemble also naturally follows from (14.17), in which the regular constant temperature MD simulation (with $T = T_0$) is performed by replacing E by E_{mu} in (14.12) [41, 44]:

$$\dot{\mathbf{p}}_k = - \frac{\partial E_{\text{mu}}(E; T_0)}{\partial \mathbf{q}_k} - \frac{\dot{s}}{s} \mathbf{p}_k = \frac{\partial E_{\text{mu}}(E; T_0)}{\partial E} \mathbf{f}_k - \frac{\dot{s}}{s} \mathbf{p}_k . \quad (14.21)$$

From (14.18), this equation can be rewritten as

$$\dot{\mathbf{p}}_k = \frac{T_0}{T(E)} \mathbf{f}_k - \frac{\dot{s}}{s} \mathbf{p}_k , \quad (14.22)$$

where the following thermodynamic relation gives the definition of the “effective temperature” $T(E)$:

$$\left. \frac{\partial S(E)}{\partial E} \right|_{E=E_a} = \frac{1}{T(E_a)} , \quad (14.23)$$

with

$$E_a = \langle E \rangle_{T(E_a)} . \quad (14.24)$$

If the exact multicanonical weight factor $W_{\text{mu}}(E)$ is known, one can calculate the ensemble averages of any physical quantity A at any temperature T ($= 1/k_B\beta$) as follows:

$$\langle A \rangle_T = \frac{\sum_E A(E) P_B(E; T)}{\sum_E P_B(E; T)} = \frac{\sum_E A(E) n(E) \exp(-\beta E)}{\sum_E n(E) \exp(-\beta E)}, \quad (14.25)$$

where the density of states is given by (see (14.17))

$$n(E) = \frac{1}{W_{\text{mu}}(E)}. \quad (14.26)$$

The summation instead of integration is used in (14.25) because we often discretize the potential energy E with step size ϵ ($E = E_i, i = 1, 2, \dots$). Here, the explicit form of the physical quantity A should be known as a function of potential energy E . For instance, $A(E) = E$ gives the average potential energy $\langle E \rangle_T$ as a function of temperature, and $A(E) = \beta^2 \langle E - \langle E \rangle_T \rangle^2$ gives specific heat.

In general, the multicanonical weight factor $W_{\text{mu}}(E)$, or the density of states $n(E)$, is not a priori known, and one needs its estimator for a numerical simulation. This estimator is usually obtained from iterations of short trial multicanonical simulations. The details of this process are described, for instance, in [27, 36]. However, the iterative process can be nontrivial and very tedious for complex systems.

In practice, it is impossible to obtain the ideal multicanonical weight factor with completely uniform potential energy distribution. The question is when to stop the iteration for the weight factor determination. Our criterion for a satisfactory weight factor is that as long as we do get a random walk in potential energy space, the probability distribution $P_{\text{mu}}(E)$ does not have to be completely flat with a tolerance of, say, an order of magnitude deviation. In such a case, we usually perform with this weight factor a multicanonical simulation with high statistics (production run) in order to get even better estimate of the density of states. Let $N_{\text{mu}}(E)$ be the histogram of potential energy distribution $P_{\text{mu}}(E)$ obtained by this production run. The best estimate of the density of states can then be given by the single-histogram reweighting techniques [8] as follows (see the proportionality relation in (14.16)):

$$n(E) = \frac{N_{\text{mu}}(E)}{W_{\text{mu}}(E)}. \quad (14.27)$$

By substituting this quantity into (14.25), one can calculate ensemble averages of physical quantity $A(E)$ as a function of temperature. Moreover, ensemble averages of any physical quantity A (including those that cannot be expressed as functions of potential energy) at any temperature T ($= 1/k_B\beta$) can now be obtained as long as one stores the “trajectory” of configurations (and A) from the production run, namely we have

$$\langle A \rangle_T = \frac{\sum_{k=1}^{n_0} A(x(k)) W_{\text{mu}}^{-1}(E(x(k))) \exp[-\beta E(x(k))]}{\sum_{k=1}^{n_0} W_{\text{mu}}^{-1}(E(x(k))) \exp[-\beta E(x(k))]} , \quad (14.28)$$

where $x(k)$ is the configuration at the k th MC (or MD) step and n_0 is the total number of configurations stored. Note that when A is a function of E , (14.28) reduces to (14.25) where the density of states is given by (14.27).

Equations (14.25) and (14.28) or any other equations which involve summations of exponential functions often encounter with numerical difficulties such as overflows. These can be overcome by using, for instance, the following equation [123, 124]: For $C = A + B$ (with $A > 0$ and $B > 0$), we have

$$\begin{aligned} \ln C &= \ln \left[\max(A, B) \left(1 + \frac{\min(A, B)}{\max(A, B)} \right) \right] \\ &= \max(\ln A, \ln B) + \ln \{1 + \exp[\min(\ln A, \ln B) - \max(\ln A, \ln B)]\} . \end{aligned} \quad (14.29)$$

We now briefly review the original *simulated tempering* (ST) method [66, 67]. In this method temperature itself becomes a dynamical variable, and both the configuration and the temperature are updated during the simulation with a weight:

$$W_{\text{ST}}(E; T) = \exp(-\beta E + a(T)) , \quad (14.30)$$

where the function $a(T)$ is chosen so that the probability distribution of temperature is flat:

$$P_{\text{ST}}(T) = \int dE n(E) W_{\text{ST}}(E; T) = \int dE n(E) \exp(-\beta E + a(T)) = \text{const} . \quad (14.31)$$

Hence, in simulated tempering, the *temperature* is sampled uniformly. A free random walk in temperature space is realized, which in turn induces a random walk in potential energy space and allows the simulation to escape from states of energy local minima.

In the numerical work, we discretize the temperature in M different values, T_m ($m = 1, \dots, M$). Without loss of generality, we can order the temperature so that $T_1 < T_2 < \dots < T_M$. The lowest temperature T_1 should be sufficiently low so that the simulation can explore the global-minimum-energy region, and the highest temperature T_M should be sufficiently high so that no trapping in an energy-local-minimum state occurs. The probability weight factor in (14.30) is now written as

$$W_{\text{ST}}(E; T_m) = \exp(-\beta_m E + a_m) , \quad (14.32)$$

where $a_m = a(T_m)$ ($m = 1, \dots, M$). Note that from (14.31) and (14.32), we have

$$\exp(-a_m) \propto \int dE \, n(E) \exp(-\beta_m E) . \quad (14.33)$$

The parameters a_m are therefore “dimensionless” Helmholtz free energy at temperature T_m (i.e., the inverse temperature β_m multiplied by the Helmholtz free energy). We remark that the density of states $n(E)$ (and hence, the multicanonical weight factor) and the simulated tempering weight factor a_m are related by a Laplace transform [42]. The knowledge of one implies that of the other, although in numerical work the inverse Laplace transform of (14.33) is nontrivial.

Once the parameters a_m are determined and the initial configuration and the initial temperature T_m are chosen, a simulated tempering simulation is then realized by alternately performing the following two steps [66, 67]:

1. A canonical MC or MD simulation at the fixed temperature T_m (based on (14.7) or (14.11)–(14.14)) is carried out for certain steps.
2. The temperature T_m is updated to the neighboring values $T_{m\pm 1}$ with the configuration fixed. The transition probability of this temperature-updating process is given by the Metropolis criterion (see (14.32)):

$$w(T_m \rightarrow T_{m\pm 1}) = \min \left(1, \frac{W_{\text{ST}}(E; T_{m\pm 1})}{W_{\text{ST}}(E; T_m)} \right) = \min(1, \exp(-\Delta)) , \quad (14.34)$$

where

$$\Delta = (\beta_{m\pm 1} - \beta_m) E - (a_{m\pm 1} - a_m) . \quad (14.35)$$

Note that in Step 2 we exchange only pairs of neighboring temperatures in order to secure sufficiently large acceptance ratio of temperature updates.

As in multicanonical algorithm, the simulated tempering parameters $a_m = a(T_m)$ ($m = 1, \dots, M$) are also determined by iterations of short trial simulations (see, e.g., [43, 68, 69] for details). This process can be nontrivial and very tedious for complex systems.

After the optimal simulated tempering weight factor is determined, one performs a long simulated tempering run once. The canonical expectation value of a physical quantity A at temperature T_m ($m = 1, \dots, M$) can be calculated by the usual arithmetic mean as follows:

$$\langle A \rangle_{T_m} = \frac{1}{n_m} \sum_{k=1}^{n_m} A(x_m(k)) , \quad (14.36)$$

where $x_m(k)$ ($k = 1, \dots, n_m$) are the configurations obtained at temperature T_m and n_m is the total number of measurements made at $T = T_m$. The expectation value at any intermediate temperature can also be obtained from (14.25), where the density of states is given by the multiple-histogram reweighting techniques [9, 10] as follows. Let $N_m(E)$ and n_m be, respectively, the potential energy histogram and the total number of samples obtained at temperature $T_m = 1/k_B \beta_m$ ($m = 1, \dots, M$). The best estimate of the density of states is then given by [9, 10]

$$n(E) = \frac{\sum_{m=1}^M g_m^{-1} N_m(E)}{\sum_{m=1}^M g_m^{-1} n_m \exp(f_m - \beta_m E)}, \quad (14.37)$$

where we have for each m ($= 1, \dots, M$)

$$\exp(-f_m) = \sum_E n(E) \exp(-\beta_m E). \quad (14.38)$$

Here, $g_m = 1 + 2\tau_m$, and τ_m is the integrated autocorrelation time at temperature T_m . For many systems, the quantity g_m can safely be set to be a constant in the reweighting formulae [10], and hereafter we set $g_m = 1$.

Note that (14.37) and (14.38) are solved self-consistently by iteration [9, 10] to obtain the density of states $n(E)$ and the dimensionless Helmholtz free energy f_m , namely we can set all the f_m ($m = 1, \dots, M$) to, e.g., zero initially. We then use (14.37) to obtain $n(E)$, which is substituted into (14.38) to obtain next values of f_m and so on.

Moreover, ensemble averages of any physical quantity A (including those that cannot be expressed as functions of potential energy) at any temperature T ($= 1/k_B\beta$) can now be obtained from the “trajectory” of configurations of the production run. We first obtain f_m ($m = 1, \dots, M$) by solving (14.37) and (14.38) self-consistently, and then we have [93]

$$\langle A \rangle_T = \frac{\sum_{m=1}^M \sum_{k=1}^{n_m} A(x_m(k)) \frac{1}{\sum_{\ell=1}^M n_\ell \exp[f_\ell - \beta_\ell E(x_m(k))]} \exp[-\beta E(x_m(k))]}{\sum_{m=1}^M \sum_{k=1}^{n_m} \frac{1}{\sum_{\ell=1}^M n_\ell \exp[f_\ell - \beta_\ell E(x_m(k))]} \exp[-\beta E(x_m(k))]}, \quad (14.39)$$

where $x_m(k)$ ($k = 1, \dots, n_m$) are the configurations obtained at temperature T_m .

14.2.2 Replica-Exchange Method

The *replica-exchange method* (REM) [75, 76, 77] was developed as an extension of simulated tempering [75] (thus it is also referred to as *parallel tempering* [68]) (see, e.g., [84] for a detailed description of the algorithm). The system for REM consists of M *noninteracting* copies (or replicas) of the original system in the canonical ensemble at M different temperatures T_m ($m = 1, \dots, M$).

We arrange the replicas so that there is always exactly one replica at each temperature. Then there exists a one-to-one correspondence between replicas and temperatures; the label i ($i = 1, \dots, M$) for replicas is a permutation of the label m ($m = 1, \dots, M$) for temperatures, and vice versa:

$$\begin{cases} i = i(m) \equiv f(m) , \\ m = m(i) \equiv f^{-1}(i) , \end{cases} \quad (14.40)$$

where $f(m)$ is a permutation function of m and $f^{-1}(i)$ is its inverse.

Let $X = \{x_1^{[i(1)]}, \dots, x_M^{[i(M)]}\} = \{x_{m(1)}^{[1]}, \dots, x_{m(M)}^{[M]}\}$ stand for a “state” in this generalized ensemble. Each “substate” $x_m^{[i]}$ is specified by the coordinates $q^{[i]}$ and momenta $p^{[i]}$ of N atoms in replica i at temperature T_m :

$$x_m^{[i]} \equiv \left(q^{[i]}, p^{[i]} \right)_m . \quad (14.41)$$

Because the replicas are noninteracting, the weight factor for the state X in this generalized ensemble is given by the product of Boltzmann factors for each replica (or at each temperature):

$$\begin{aligned} W_{\text{REM}}(X) &= \prod_{i=1}^M \exp \left\{ -\beta_{m(i)} H \left(q^{[i]}, p^{[i]} \right) \right\} = \prod_{m=1}^M \exp \left\{ -\beta_m H \left(q^{[i(m)]}, p^{[i(m)]} \right) \right\} \\ &= \exp \left\{ -\sum_{i=1}^M \beta_{m(i)} H \left(q^{[i]}, p^{[i]} \right) \right\} = \exp \left\{ -\sum_{m=1}^M \beta_m H \left(q^{[i(m)]}, p^{[i(m)]} \right) \right\} , \end{aligned} \quad (14.42)$$

where $i(m)$ and $m(i)$ are the permutation functions in (14.40).

We now consider exchanging a pair of replicas in the generalized ensemble. Suppose we exchange replicas i and j which are at temperatures T_m and T_n , respectively:

$$X = \{ \dots, x_m^{[i]}, \dots, x_n^{[j]}, \dots \} \longrightarrow X' = \{ \dots, x_m^{[j]'}, \dots, x_n^{[i]'}, \dots \} . \quad (14.43)$$

Here, i , j , m , and n are related by the permutation functions in (14.40), and the exchange of replicas introduces a new permutation function f' :

$$\begin{cases} i = f(m) \longrightarrow j = f'(m) , \\ j = f(n) \longrightarrow i = f'(n) . \end{cases} \quad (14.44)$$

The exchange of replicas can be written in more detail as

$$\begin{cases} x_m^{[i]} \equiv (q^{[i]}, p^{[i]})_m \longrightarrow x_m^{[j]'} \equiv (q^{[j]}, p^{[j]'})_m , \\ x_n^{[j]} \equiv (q^{[j]}, p^{[j]})_n \longrightarrow x_n^{[i]'} \equiv (q^{[i]}, p^{[i]'})_n , \end{cases} \quad (14.45)$$

where the definitions for $p^{[i]'}$ and $p^{[j]'}$ will be given below. We remark that this process is equivalent to exchanging a pair of temperatures T_m and T_n for the corresponding replicas i and j as follows:

$$\begin{cases} x_m^{[i]} \equiv (q^{[i]}, p^{[i]})_m \longrightarrow x_n^{[i]'} \equiv (q^{[i]}, p^{[i]'})_n , \\ x_n^{[j]} \equiv (q^{[j]}, p^{[j]})_n \longrightarrow x_m^{[j]'} \equiv (q^{[j]}, p^{[j]'})_m . \end{cases} \quad (14.46)$$

In the original implementation of the *replica-exchange method* (REM) [75, 76, 77], MC algorithm was used, and only the coordinates q (and the potential energy function $E(q)$) had to be taken into account. In molecular dynamics algorithm, on the other hand, we also have to deal with the momenta p . We proposed the following momentum assignment in (14.45) (and in (14.46)) [84]:

$$\begin{cases} p^{[i]'} \equiv \sqrt{\frac{T_n}{T_m}} p^{[i]} , \\ p^{[j]'} \equiv \sqrt{\frac{T_m}{T_n}} p^{[j]} , \end{cases} \quad (14.47)$$

which we believe is the simplest and the most natural. This assignment means that we just rescale uniformly the velocities of all the atoms in the replicas by the square root of the ratio of the two temperatures so that the temperature condition in (14.4) may be satisfied.

In order for this exchange process to converge toward an equilibrium distribution, it is sufficient to impose the detailed balance condition on the transition probability $w(X \rightarrow X')$:

$$\frac{W_{\text{REM}}(X)}{Z} w(X \rightarrow X') = \frac{W_{\text{REM}}(X')}{Z} w(X' \rightarrow X) , \quad (14.48)$$

where Z is the partition function of the entire system. From (14.1), (14.2), (14.42), (14.47), and (14.48), we have

$$\begin{aligned} \frac{W_{\text{REM}}(X')}{W_{\text{REM}}(X)} &= \exp \left\{ -\beta_m [K(p^{[j]'}) + E(q^{[j]})] - \beta_n [K(p^{[i]'}) + E(q^{[i]})] \right. \\ &\quad \left. + \beta_m [K(p^{[i]}) + E(q^{[i]})] + \beta_n [K(p^{[j]}) + E(q^{[j]})] \right\} \\ &= \exp \left\{ -\beta_m \frac{T_m}{T_n} K(p^{[j]}) - \beta_n \frac{T_n}{T_m} K(p^{[i]}) + \beta_m K(p^{[i]}) + \beta_n K(p^{[j]}) \right. \\ &\quad \left. - \beta_m [E(q^{[j]}) - E(q^{[i]})] - \beta_n [E(q^{[i]}) - E(q^{[j]})] \right\} \\ &= \exp(-\Delta) , \end{aligned} \quad (14.49)$$

where

$$\Delta = \beta_m (E(q^{[j]}) - E(q^{[i]})) - \beta_n (E(q^{[j]}) - E(q^{[i]})) , \quad (14.50)$$

$$= (\beta_m - \beta_n) (E(q^{[j]}) - E(q^{[i]})) , \quad (14.51)$$

and i, j, m , and n are related by the permutation functions in (14.40) before the exchange:

$$\begin{cases} i = f(m) , \\ j = f(n) . \end{cases} \quad (14.52)$$

This can be satisfied, for instance, by the usual Metropolis criterion [120] (see also (14.7), (14.19), and (14.34)):

$$w(X \rightarrow X') \equiv w\left(x_m^{[i]} \mid x_n^{[j]}\right) = \min(1, \exp(-\Delta)) \quad , \quad (14.53)$$

where in the second expression (i.e., $w(x_m^{[i]}|x_n^{[j]})$) we explicitly wrote the pair of replicas (and temperatures) to be exchanged. Note that this is exactly the same criterion that was originally derived for Monte Carlo algorithm [75, 76, 77].

Without loss of generality, we can again assume $T_1 < T_2 < \dots < T_M$. A simulation of the *replica-exchange method* (REM) [75, 76, 77] is then realized by alternately performing the following two steps:

1. Each replica in canonical ensemble of the fixed temperature is simulated *simultaneously* and *independently* for certain MC or MD steps.
2. A pair of replicas at neighboring temperatures, say $x_m^{[i]}$ and $x_{m+1}^{[j]}$, are exchanged with the probability $w\left(x_m^{[i]} \mid x_{m+1}^{[j]}\right)$ in (14.53).

Note that in Step 2 we exchange only pairs of replicas corresponding to neighboring temperatures because the acceptance ratio of the exchange process decreases exponentially with the difference of the two β s (see (14.51) and (14.53)). Note also that whenever a replica exchange is accepted in Step 2, the permutation functions in (14.40) are updated.

The REM simulation is particularly suitable for parallel computers. Because one can minimize the amount of information exchanged among nodes, it is best to assign each replica to each node (exchanging pairs of temperature values among nodes is much faster than exchanging coordinates and momenta). This means that we keep track of the permutation function $m(i; t) = f^{-1}(i; t)$ in (14.40) as a function of MC or MD step t during the simulation. After parallel canonical MC or MD simulations for certain steps (Step 1), $M/2$ pairs of replicas corresponding to neighboring temperatures are simultaneously exchanged (Step 2), and the pairing is alternated between the two possible choices, i.e., (T_1, T_2) , (T_3, T_4) , \dots and (T_2, T_3) , (T_4, T_5) , \dots .

The major advantage of REM over other generalized-ensemble methods such as multicanonical algorithm [14, 15] and simulated tempering [66, 67] lies in the fact that the weight factor is a priori known (see (14.42)), while in the latter algorithms the determination of the weight factors can be very tedious and time-consuming. A random walk in “temperature space” is realized for each replica, which in turn induces a random walk in potential energy space. This alleviates the problem of getting trapped in states of energy local minima. In REM, however, the number of required replicas increases as the system size N increases (according to \sqrt{N}) [75]. This demands a lot of computer power for complex systems.

14.2.3 Replica-Exchange Multicanonical Algorithm and Replica-Exchange Simulated Tempering

The *replica-exchange multicanonical algorithm* (REMUCA) [88, 93, 94] overcomes the difficulties of both MUCA (the multicanonical weight factor determination is nontrivial) and REM (a lot of replicas, or computation time, is required). In REMUCA, we first perform a short REM simulation (with M replicas) to determine the multicanonical weight factor and then perform with this weight factor a regular multicanonical simulation with high statistics. The first step is accomplished by the multiple-histogram reweighting techniques [9, 10]. Let $N_m(E)$ and n_m be, respectively, the potential energy histogram and the total number of samples obtained at temperature T_m ($= 1/k_B\beta_m$) of the REM run. The density of states $n(E)$ is then given by solving (14.37) and (14.38) self-consistently by iteration.

Once the estimate of the density of states is obtained, the multicanonical weight factor can be directly determined from (14.17) (see also (14.18)). Actually, the density of states $n(E)$ and the multicanonical potential energy, $E_{\text{mu}}(E; T_0)$, thus determined are only reliable in the following range:

$$E_1 \leq E \leq E_M, \quad (14.54)$$

where

$$\begin{aligned} E_1 &= \langle E \rangle_{T_1}, \\ E_M &= \langle E \rangle_{T_M}, \end{aligned} \quad (14.55)$$

and T_1 and T_M are, respectively, the lowest and the highest temperatures used in the REM run. Outside this range, we extrapolate the multicanonical potential energy linearly [88]:

$$\mathcal{E}_{\text{mu}}^{\{0\}}(E) \equiv \begin{cases} \left. \frac{\partial E_{\text{mu}}(E; T_0)}{\partial E} \right|_{E=E_1} (E - E_1) + E_{\text{mu}}(E_1; T_0), & \text{for } E < E_1, \\ E_{\text{mu}}(E; T_0), & \text{for } E_1 \leq E \leq E_M, \\ \left. \frac{\partial E_{\text{mu}}(E; T_0)}{\partial E} \right|_{E=E_M} (E - E_M) + E_{\text{mu}}(E_M; T_0), & \text{for } E > E_M. \end{cases} \quad (14.56)$$

The multicanonical MC and MD runs are then performed, respectively, with the Metropolis criterion of (14.19) and with the modified Newton equation in (14.21), in which $\mathcal{E}_{\text{mu}}^{\{0\}}(E)$ in (14.56) is substituted into $E_{\text{mu}}(E; T_0)$. We expect to obtain a flat potential energy distribution in the range of (14.54). Finally, the results are analyzed by the single-histogram reweighting techniques as described in (14.27) (and (14.25)).

Some remarks are now in order. From (14.18), (14.23), (14.24), and (14.55), Eq. (14.56) becomes

$$\mathcal{E}_{\text{mu}}^{\{0\}}(E) = \begin{cases} \frac{T_0}{T_1}(E - E_1) + T_0 S(E_1) = \frac{T_0}{T_1}E + \text{const}, & \text{for } E < E_1, \\ T_0 S(E), & \text{for } E_1 \leq E \leq E_M, \\ \frac{T_0}{T_M}(E - E_M) + T_0 S(E_M) = \frac{T_0}{T_M}E + \text{const}, & \text{for } E > E_M. \end{cases} \quad (14.57)$$

The Newton equation in (14.21) is then written as (see (14.22)–(14.24))

$$\dot{\mathbf{p}}_k = \begin{cases} \frac{T_0}{T_1} \mathbf{f}_k - \frac{\dot{s}}{s} \mathbf{p}_k, & \text{for } E < E_1, \\ \frac{T_0}{T(E)} \mathbf{f}_k - \frac{\dot{s}}{s} \mathbf{p}_k, & \text{for } E_1 \leq E \leq E_M, \\ \frac{T_0}{T_M} \mathbf{f}_k - \frac{\dot{s}}{s} \mathbf{p}_k, & \text{for } E > E_M. \end{cases} \quad (14.58)$$

Because only the product of inverse temperature β and potential energy E enters in the Boltzmann factor (see (14.5)), a rescaling of the potential energy (or force) by a constant, say α , can be considered as the rescaling of the temperature by $1/\alpha$ [41, 101]. Hence, our choice of $\mathcal{E}_{\text{mu}}^{\{0\}}(E)$ in (14.56) results in a canonical simulation at $T = T_1$ for $E < E_1$, a multicanonical simulation for $E_1 \leq E \leq E_M$ and a canonical simulation at $T = T_M$ for $E > E_M$. Note also that the above arguments are independent of the value of T_0 , and we will get the same results regardless of its value.

For Monte Carlo method, the above statement follows directly from the following equation, namely our choice of the multicanonical potential energy in (14.56) gives (by substituting (14.57) into (14.17))

$$W_{\text{mu}}(E) = \exp \left[-\beta_0 \mathcal{E}_{\text{mu}}^{\{0\}}(E) \right] = \begin{cases} \exp(-\beta_1 E + \text{const}), & \text{for } E < E_1, \\ \frac{1}{n(E)}, & \text{for } E_1 \leq E \leq E_M, \\ \exp(-\beta_M E + \text{const}), & \text{for } E > E_M. \end{cases} \quad (14.59)$$

We now present another effective method of the multicanonical weight factor determination [3], which is closely related to REMUCA. We first perform a short REM simulation as in REMUCA and calculate $\langle E \rangle_T$ as a function of T by the multiple-histogram reweighting techniques (see (14.37) and (14.38)). Let us recall the Newton equation of (14.22) and the thermodynamic relation of (14.23) and (14.24). The effective temperature $T(E)$, or the derivative $\frac{\partial E_{\text{mu}}(E; T_0)}{\partial E}$, can be numerically obtained as the inverse function of (14.24), where the average $\langle E \rangle_{T(E)}$ has been obtained from the results of the REM simulation by the multiple-histogram reweighting techniques. Given its derivative, the multicanonical potential energy can then be obtained by numerical integration (see (14.18) and (14.23)) [3]:

$$E_{\text{mu}}(E; T_0) = T_0 \int_{E_1}^E \frac{\partial S(E)}{\partial E} dE = T_0 \int_{E_1}^E \frac{dE}{T(E)}. \quad (14.60)$$

We remark that the same equation was used to obtain the multicanonical weight factor in [72], where $\langle E \rangle_T$ was estimated by simulated annealing instead of REM. Essentially the same formulation was also recently used in [61] to obtain the multicanonical potential energy, where $\langle E \rangle_T$ was calculated by conventional canonical simulations.

We finally present the new method which we refer to as the *replica-exchange simulated tempering* (REST) [89]. In this method, just as in REMUCA, we first perform a short REM simulation (with M replicas) to determine the simulated tempering weight factor and then perform with this weight factor a regular ST simulation with high statistics. The first step is accomplished by the multiple-histogram reweighting techniques [9, 10], which give the dimensionless Helmholtz free energy f_m (see (14.37) and (14.38)).

Once the estimate of the dimensionless Helmholtz free energy f_m is obtained, the simulated tempering weight factor can be directly determined by using (14.32) where we set $a_m = f_m$ (compare (14.33) with (14.38)). A long simulated tempering run is then performed with this weight factor. Let $N_m(E)$ and n_m be respectively the potential-energy histogram and the total number of samples obtained at temperature $T_m (= 1/k_B\beta_m)$ from this simulated tempering run. The multiple-histogram reweighting techniques of (14.37) and (14.38) can be used again to obtain the best estimate of the density of states $n(E)$. The expectation value of a physical quantity A at any temperature $T (= 1/k_B\beta)$ is then calculated from (14.25).

The formulations of REMUCA and REST are simple and straightforward, but the numerical improvement is great because the weight factor determination for MUCA and ST becomes very difficult by the usual iterative processes for complex systems.

14.2.4 Multicanonical Replica-Exchange Method and Simulated Tempering Replica-Exchange Method

In the previous subsection, we presented REMUCA, which uses a short REM run for the determination of the multicanonical weight factor. Here, we present two modifications of REM and refer the new methods as multicanonical replica-exchange method (MUCAREM) [88, 93, 94] and simulated tempering replica-exchange method (STREM) [115]. In MUCAREM, the production run is a REM simulation with a few replicas not in the canonical ensemble but in the multicanonical ensemble, i.e., different replicas perform MUCA simulations with different energy ranges. Likewise, in STREM, the production run is a REM simulation with a few replicas that performs ST simulations with different temperature ranges. While MUCA and ST simulations are usually based on local updates, a replica-exchange process can be considered to be a global update, and global updates enhance the sampling further.

We first describe MUCAREM. Let \mathcal{M} be the number of replicas. Here, each replica is in one-to-one correspondence not with temperature but with

multicanonical weight factors of different energy range. Note that because multicanonical simulations cover much wider energy ranges than regular canonical simulations, the number of required replicas for the production run of MUCAREM is much less than that for the regular REM ($\mathcal{M} \ll M$). The weight factor for this generalized ensemble is now given by (see (14.42))

$$W_{\text{MUCAREM}}(X) = \prod_{i=1}^{\mathcal{M}} W_{\text{mu}}^{\{m(i)\}} \left(E \left(x_{m(i)}^{[i]} \right) \right) = \prod_{m=1}^{\mathcal{M}} W_{\text{mu}}^{\{m\}} \left(E \left(x_m^{[i(m)]} \right) \right), \quad (14.61)$$

where we prepare the multicanonical weight factor (and the density of states) separately for m regions (see (14.17)):

$$W_{\text{mu}}^{\{m\}} \left(E \left(x_m^{[i]} \right) \right) = \exp \left[-\beta_m \mathcal{E}_{\text{mu}}^{\{m\}} \left(E \left(x_m^{[i]} \right) \right) \right] \equiv \frac{1}{n^{\{m\}} \left(E \left(x_m^{[i]} \right) \right)}. \quad (14.62)$$

Here, we have introduced \mathcal{M} arbitrary reference temperatures $T_m = 1/k_B \beta_m$ ($m = 1, \dots, \mathcal{M}$), but the final results will be independent of the values of T_m , as one can see from the second equality in (14.62) (these arbitrary temperatures are necessary only for MD simulations).

Each multicanonical weight factor $W_{\text{mu}}^{\{m\}}(E)$, or the density of states $n^{\{m\}}(E)$, is defined as follows. For each m ($m = 1, \dots, \mathcal{M}$), we assign a pair of temperatures $(T_L^{\{m\}}, T_H^{\{m\}})$. Here, we assume that $T_L^{\{m\}} < T_H^{\{m\}}$ and arrange the temperatures so that the neighboring regions covered by the pairs have sufficient overlaps. Without loss of generality, we can assume $T_L^{\{1\}} < \dots < T_L^{\{\mathcal{M}\}}$ and $T_H^{\{1\}} < \dots < T_H^{\{\mathcal{M}\}}$. We define the following quantities:

$$\begin{cases} E_L^{\{m\}} = \langle E \rangle_{T_L^{\{m\}}}, \\ E_H^{\{m\}} = \langle E \rangle_{T_H^{\{m\}}}, \end{cases} \quad (m = 1, \dots, \mathcal{M}). \quad (14.63)$$

Suppose that the multicanonical weight factor $W_{\text{mu}}(E)$ (or equivalently, the multicanonical potential energy $E_{\text{mu}}(E; T_0)$ in (14.18)) has been obtained as in REMUCA or by any other methods in the entire energy range of interest ($E_L^{\{1\}} < E < E_H^{\{\mathcal{M}\}}$). We then have for each m ($m = 1, \dots, \mathcal{M}$) the following multicanonical potential energies (see (14.56)) [88]:

$$\mathcal{E}_{\text{mu}}^{\{m\}}(E) = \begin{cases} \frac{\partial E_{\text{mu}}(E_L^{\{m\}}; T_m)}{\partial E} (E - E_L^{\{m\}}) + E_{\text{mu}}(E_L^{\{m\}}; T_m), & \text{for } E < E_L^{\{m\}}, \\ E_{\text{mu}}(E; T_m), & \text{for } E_L^{\{m\}} \leq E \leq E_H^{\{m\}}, \\ \frac{\partial E_{\text{mu}}(E_H^{\{m\}}; T_m)}{\partial E} (E - E_H^{\{m\}}) + E_{\text{mu}}(E_H^{\{m\}}; T_m), & \text{for } E > E_H^{\{m\}}. \end{cases} \quad (14.64)$$

Finally, a MUCAREM simulation is realized by alternately performing the following two steps.

1. Each replica of the fixed multicanonical ensemble is simulated *simultaneously* and *independently* for certain MC or MD steps.
2. A pair of replicas, say i and j , which are in neighboring multicanonical ensembles, say m th and $(m+1)$ th, respectively, are exchanged:

$$X = \left\{ \dots, x_m^{[i]}, \dots, x_{m+1}^{[j]}, \dots \right\} \longrightarrow X' = \left\{ \dots, x_m^{[j]}, \dots, x_{m+1}^{[i]}, \dots \right\}.$$

The transition probability of this replica exchange is given by the Metropolis criterion:

$$w(X \rightarrow X') = \min(1, \exp(-\Delta)) , \quad (14.65)$$

where we now have (see (14.50)) [88]

$$\begin{aligned} \Delta = & \beta_m \left\{ \mathcal{E}_{\text{mu}}^{\{m\}}(E(q^{[j]})) - \mathcal{E}_{\text{mu}}^{\{m\}}(E(q^{[i]})) \right\} \\ & - \beta_{m+1} \left\{ \mathcal{E}_{\text{mu}}^{\{m+1\}}(E(q^{[j]})) - \mathcal{E}_{\text{mu}}^{\{m+1\}}(E(q^{[i]})) \right\} . \end{aligned} \quad (14.66)$$

Here, $E(q^{[i]})$ and $E(q^{[j]})$ are the potential energy of the i th replica and the j th replica, respectively.

Note that in (14.66) we need to newly evaluate the multicanonical potential energy, $\mathcal{E}_{\text{mu}}^{\{m\}}(E(q^{[j]}))$ and $\mathcal{E}_{\text{mu}}^{\{m+1\}}(E(q^{[i]}))$, because $\mathcal{E}_{\text{mu}}^{\{m\}}(E)$ and $\mathcal{E}_{\text{mu}}^{\{n\}}(E)$ are, in general, different functions for $m \neq n$.

In this algorithm, the m th multicanonical ensemble actually results in a canonical simulation at $T = T_L^{\{m\}}$ for $E < E_L^{\{m\}}$, a multicanonical simulation for $E_L^{\{m\}} \leq E \leq E_H^{\{m\}}$ and a canonical simulation at $T = T_H^{\{m\}}$ for $E > E_H^{\{m\}}$, while the replica-exchange process samples states of the whole energy range ($E_L^{\{1\}} \leq E \leq E_H^{\{\mathcal{M}\}}$).

For obtaining the canonical distributions at any intermediate temperature T , the multiple-histogram reweighting techniques [9, 10] are again used. Let $N_m(E)$ and n_m be, respectively, the potential energy histogram and the total number of samples obtained with the multicanonical weight factor $W_{\text{mu}}^{\{m\}}(E)$ ($m = 1, \dots, \mathcal{M}$). The expectation value of a physical quantity A at any temperature $T (= 1/k_B\beta)$ is then obtained from (14.25), where the best estimate of the density of states is obtained by solving the WHAM equations, which now read [88]

$$n(E) = \frac{\sum_{m=1}^{\mathcal{M}} N_m(E)}{\sum_{m=1}^{\mathcal{M}} n_m \exp(f_m) W_{\text{mu}}^{\{m\}}(E)} = \frac{\sum_{m=1}^{\mathcal{M}} N_m(E)}{\sum_{m=1}^{\mathcal{M}} n_m \exp\left(f_m - \beta_m \mathcal{E}_{\text{mu}}^{\{m\}}(E)\right)} , \quad (14.67)$$

and for each $m = 1, \dots, \mathcal{M}$

$$\exp(-f_m) = \sum_E n(E) W_{\text{mu}}^{\{m\}}(E) = \sum_E n(E) \exp\left(-\beta_m \mathcal{E}_{\text{mu}}^{\{m\}}(E)\right). \quad (14.68)$$

Note that $W_{\text{mu}}^{\{m\}}(E)$ is used instead of the Boltzmann factor $\exp(-\beta_m E)$ in (14.37) and (14.38).

Moreover, ensemble averages of any physical quantity A (including those that cannot be expressed as functions of potential energy) at any temperature $T (= 1/k_B\beta)$ can now be obtained from the “trajectory” of configurations of the production run, namely, we first obtain f_m ($m = 1, \dots, \mathcal{M}$) by solving (14.67) and (14.68) self-consistently, and then we have [93]

$$\langle A \rangle_T = \frac{\sum_{m=1}^{\mathcal{M}} \sum_{k=1}^{n_m} A(x_m(k)) \frac{1}{\sum_{\ell=1}^{\mathcal{M}} n_{\ell} \exp(f_{\ell}) W_{\text{mu}}^{\{\ell\}}(E(x_m(k)))} \exp[-\beta E(x_m(k))]}{\sum_{m=1}^{\mathcal{M}} \sum_{k=1}^{n_m} \frac{1}{\sum_{\ell=1}^{\mathcal{M}} n_{\ell} \exp(f_{\ell}) W_{\text{mu}}^{\{\ell\}}(E(x_m(k)))} \exp[-\beta E(x_m(k))]}}, \quad (14.69)$$

where the trajectories $x_m(k)$ ($k = 1, \dots, n_m$) are taken from each multicanonical simulation with the multicanonical weight factor $W_{\text{mu}}^{\{m\}}(E)$ ($m = 1, \dots, \mathcal{M}$) separately.

As seen above, both REMUCA and MUCAREM can be used to obtain the multicanonical weight factor, or the density of states, for the entire potential energy range of interest. For complex systems, however, a single REMUCA or MUCAREM simulation is often insufficient. In such cases, we can iterate MUCA (in REMUCA) and/or MUCAREM simulations in which the estimate of the multicanonical weight factor is updated by the single- and/or multiple-histogram reweighting techniques, respectively.

To be more specific, this iterative process can be summarized as follows. The REMUCA production run corresponds to a MUCA simulation with the weight factor $W_{\text{mu}}(E)$. The new estimate of the density of states can be obtained by the single-histogram reweighting techniques of (14.27). On the other hand, from the MUCAREM production run, the improved density of states can be obtained by the multiple-histogram reweighting techniques of (14.67) and (14.68).

The improved density of states thus obtained leads to a new multicanonical weight factor (see (14.17)). The next iteration can be either a MUCA production run (as in REMUCA) or MUCAREM production run. The results of this production run may yield an optimal multicanonical weight factor that yields a sufficiently flat energy distribution for the entire energy range of interest. If not, we can repeat the above process by obtaining the third estimate

of the multicanonical weight factor either by a MUCA production run (as in REMUCA) or by a MUCAREM production run, and so on.

We remark that as the estimate of the multicanonical weight factor becomes more accurate, one is required to have a less number of replicas for a successful MUCAREM simulation because each replica will have a flat energy distribution for a wider energy range. Hence, for a large, complex system, it is often more efficient to first try MUCAREM and iteratively reduce the number of replicas so that eventually one needs only one or a few replicas (instead of trying REMUCA directly from the beginning and iterating MUCA simulations).

In the following, we describe the simulated tempering replica-exchange method (STREM) [115]. Suppose that the simulated tempering weight factor $W_{\text{ST}}(E; T_n)$ (or equivalently, the dimensionless Helmholtz free energy a_n in (14.32)) has been obtained as in REST or by any other methods in the entire temperature range of interest ($T_1 \leq T_n \leq T_M$). We divide the overlapping temperature ranges into \mathcal{M} regions ($\mathcal{M} \ll M$). Suppose each temperature range m has \mathcal{N}_m temperatures: $T_k^{\{m\}}$ ($k = 1, \dots, \mathcal{N}_m$) for $m = 1, \dots, \mathcal{M}$. We assign each temperature range to a replica: each replica i is in one-to-one correspondence with a different temperature range m of ST run, where $T_1^{\{m\}} \leq T_k^{\{m\}} \leq T_{\mathcal{N}_m}^{\{m\}}$ ($k = 1, \dots, \mathcal{N}_m$). We then introduce the replica-exchange process between neighboring temperature ranges. This works when we allow sufficient overlaps between the temperature regions.

A STREM simulation is then realized by alternately performing the following two steps [115]:

1. Each replica performs a ST simulation within the fixed temperature range *simultaneously* and *independently* for certain MC or MD steps.
2. A pair of replicas, say i and j , which are at, say $T = T_k^{\{m\}}$ and $T = T_\ell^{\{m+1\}}$, neighboring temperature ranges, say m th and $(m+1)$ th, respectively, are exchanged: $X = \{\dots, x_k^{[i]}, \dots, x_\ell^{[j]}, \dots\} \longrightarrow X' = \{\dots, x_k^{[j]}, \dots, x_\ell^{[i]}, \dots\}$. The transition probability of this replica exchange is given by the Metropolis criterion:

$$w(X \rightarrow X') = \min(1, \exp(-\Delta)) , \quad (14.70)$$

where

$$\Delta \equiv (\beta_k^{\{m\}} - \beta_\ell^{\{m+1\}}) \left(E(q^{[j]}) - E(q^{[i]}) \right) . \quad (14.71)$$

While in MUCAREM each replica performs a random walk in multicanonical ensemble of finite energy range, in STREM each replica performs a random walk by simulated tempering of finite temperature range. These “local” random walks are made “global” to cover the entire energy range of interest by the replica-exchange process.

14.2.5 Multidimensional Replica-Exchange Method

We now present our multidimensional extension of REM, which we refer to as *multidimensional replica-exchange method* (MREM) [86]. The crucial observation that led to the new algorithm is: As long as we have M *noninteracting* replicas of the original system, the Hamiltonian $H(q, p)$ of the system does not have to be identical among the replicas and it can depend on a parameter with different parameter values for different replicas, namely we can write the Hamiltonian for the i th replica at temperature T_m as

$$H_m(q^{[i]}, p^{[i]}) = K(p^{[i]}) + E_{\lambda_m}(q^{[i]}) , \quad (14.72)$$

where the potential energy E_{λ_m} depends on a parameter λ_m and can be written as

$$E_{\lambda_m}(q^{[i]}) = E_0(q^{[i]}) + \lambda_m V(q^{[i]}) . \quad (14.73)$$

This expression for the potential energy is often used in simulations. For instance, in umbrella sampling [21], $E_0(q)$ and $V(q)$ can be, respectively, taken as the original potential energy and the “biasing” potential energy with the coupling parameter λ_m . In simulations of spin systems, on the other hand, $E_0(q)$ and $V(q)$ (here, q stands for spins) can be respectively considered as the zero-field term and the magnetization term coupled with the external field λ_m .

While replica i and temperature T_m are in one-to-one correspondence in the original REM, replica i and “parameter set” $\Lambda_m \equiv (T_m, \lambda_m)$ are in one-to-one correspondence in the new algorithm. Hence, the present algorithm can be considered as a multidimensional extension of the original replica-exchange method where the “parameter space” is one-dimensional (i.e., $\Lambda_m = T_m$). Because the replicas are noninteracting, the weight factor for the state X in this new generalized ensemble is again given by the product of Boltzmann factors for each replica (see (14.42)):

$$\begin{aligned} W_{\text{MREM}}(X) &= \exp \left\{ - \sum_{i=1}^M \beta_{m(i)} H_{m(i)} \left(q^{[i]}, p^{[i]} \right) \right\} \\ &= \exp \left\{ - \sum_{m=1}^M \beta_m H_m \left(q^{[i(m)]}, p^{[i(m)]} \right) \right\} , \end{aligned} \quad (14.74)$$

where $i(m)$ and $m(i)$ are the permutation functions in (14.40). Then the same derivation that led to the original replica-exchange criterion follows, and the transition probability of replica exchange is given by (14.53), where we now have (see (14.50)) [86]

$$\Delta = \beta_m \left(E_{\lambda_m} \left(q^{[j]} \right) - E_{\lambda_m} \left(q^{[i]} \right) \right) - \beta_n \left(E_{\lambda_n} \left(q^{[j]} \right) - E_{\lambda_n} \left(q^{[i]} \right) \right) . \quad (14.75)$$

Here, E_{λ_m} and E_{λ_n} are the total potential energies (see (14.73)). Note that we need to newly evaluate the potential energy for exchanged coordinates, $E_{\lambda_m}(q^{[j]})$ and $E_{\lambda_n}(q^{[i]})$, because E_{λ_m} and E_{λ_n} are in general different functions.

For obtaining the canonical distributions, the multiple-histogram reweighting techniques [9, 110] are particularly suitable. Suppose we have made a single run of the present replica-exchange simulation with M replicas that correspond to M different parameter sets $\Lambda_m \equiv (T_m, \lambda_m)$ ($m = 1, \dots, M$). Let $N_m(E_0, V)$ and n_m be, respectively, the potential-energy histogram and the total number of samples obtained for the m th parameter set Λ_m . The WHAM equations that yield the canonical probability distribution $P_{T,\lambda}(E_0, V) = n(E_0, V) \exp(-\beta E_\lambda)$ with any potential energy parameter value λ at any temperature $T = 1/k_B\beta$ are then given by [86]

$$n(E_0, V) = \frac{\sum_{m=1}^M N_m(E_0, V)}{\sum_{m=1}^M n_m \exp(f_m - \beta_m E_{\lambda_m})}, \quad (14.76)$$

and for each m ($= 1, \dots, M$)

$$\exp(-f_m) = \sum_{E_0, V} n(E_0, V) \exp(-\beta_m E_{\lambda_m}). \quad (14.77)$$

Here, $n(E_0, V)$ is the generalized density of states. Note that $n(E_0, V)$ is independent of the parameter sets $\Lambda_m \equiv (T_m, \lambda_m)$ ($m = 1, \dots, M$). The density of states $n(E_0, V)$ and the “dimensionless” Helmholtz free energy f_m in (14.76) and (14.77) are solved self-consistently by iteration.

We can use MREM for free-energy calculations. We first describe the free-energy perturbation case. The potential energy is given by

$$E_\lambda(q) = E_I(q) + \lambda(E_F(q) - E_I(q)), \quad (14.78)$$

where E_I and E_F are the potential energy for a “wild-type” molecule and a “mutated” molecule, respectively. Note that this equation has the same form as (14.73).

Our replica-exchange simulation is performed for M replicas with M different values of the parameters $\Lambda_m = (T_m, \lambda_m)$. Since $E_{\lambda=0}(q) = E_I(q)$ and $E_{\lambda=1}(q) = E_F(q)$, we should choose enough λ_m values distributed in the range between 0 and 1 so that we may have sufficient acceptance of replica exchange. From the simulation, M histograms $N_m(E_I, E_F - E_I)$, or equivalently $N_m(E_I, E_F)$, are obtained. The Helmholtz free energy difference of “mutation” at temperature T ($= 1/k_B\beta$), $\Delta F \equiv F_{\lambda=1} - F_{\lambda=0}$, can then be calculated from

$$\exp(-\beta\Delta F) = \frac{Z_{T,\lambda=1}}{Z_{T,\lambda=0}} = \frac{\sum_{E_I, E_F} P_{T,\lambda=1}(E_I, E_F)}{\sum_{E_I, E_F} P_{T,\lambda=0}(E_I, E_F)} , \quad (14.79)$$

where $P_{T,\lambda}(E_I, E_F) = n(E_I, E_F) \exp(-\beta E_\lambda)$ are obtained from the WHAM equations of (14.76) and (14.77).

We now describe another free-energy calculation based on MREM applied to umbrella sampling [21], which we refer to as *replica-exchange umbrella sampling* (REUS). The potential energy is a generalization of (14.73) and is given by

$$E_{\boldsymbol{\lambda}}(q) = E_0(q) + \sum_{\ell=1}^L \lambda^{(\ell)} V_\ell(q) , \quad (14.80)$$

where $E_0(q)$ is the original unbiased potential, $V_\ell(q)$ ($\ell = 1, \dots, L$) are the biasing (umbrella) potentials, and $\lambda^{(\ell)}$ are the corresponding coupling constants ($\boldsymbol{\lambda} = (\lambda^{(1)}, \dots, \lambda^{(L)})$). Introducing a “reaction coordinate” ξ , the umbrella potentials are usually written as harmonic restraints:

$$V_\ell(q) = k_\ell (\xi(q) - d_\ell)^2 , \quad \ell = 1, \dots, L , \quad (14.81)$$

where d_ℓ are the midpoints and k_ℓ are the strengths of the restraining potentials. We prepare M replicas with M different values of the parameters $\boldsymbol{\Lambda}_m = (T_m, \boldsymbol{\lambda}_m)$, and the replica-exchange simulation is performed. Since the umbrella potentials $V_\ell(q)$ in (14.81) are all functions of the reaction coordinate ξ only, we can take the histogram $N_m(E_0, \xi)$ instead of $N_m(E_0, V_1, \dots, V_L)$. The WHAM equations of (14.76) and (14.77) can then be written as [86]

$$n(E_0, \xi) = \frac{\sum_{m=1}^M N_m(E_0, \xi)}{\sum_{m=1}^M n_m \exp(f_m - \beta_m E_{\boldsymbol{\lambda}_m})} \quad (14.82)$$

and for each m ($= 1, \dots, M$)

$$\exp(-f_m) = \sum_{E_0, \xi} n(E_0, \xi) \exp(-\beta_m E_{\boldsymbol{\lambda}_m}) . \quad (14.83)$$

The expectation value of a physical quantity A with any potential energy parameter value $\boldsymbol{\lambda}$ at any temperature T ($= 1/k_B\beta$) is now given by

$$\langle A \rangle_{T, \boldsymbol{\lambda}} = \frac{\sum_{E_0, \xi} A(E_0, \xi) P_{T, \boldsymbol{\lambda}}(E_0, \xi)}{\sum_{E_0, \xi} P_{T, \boldsymbol{\lambda}}(E_0, \xi)} , \quad (14.84)$$

where $P_{T,\boldsymbol{\lambda}}(E_0, \xi) = n(E_0, \xi) \exp(-\beta E_{\boldsymbol{\lambda}})$ is obtained from the WHAM equations of (14.82) and (14.83).

The potential of mean force (PMF), or free energy as a function of the reaction coordinate, of the original, unbiased system at temperature T is given by

$$\mathcal{W}_{T,\boldsymbol{\lambda}=\{0\}}(\xi) = -k_B T \ln \left[\sum_{E_0} P_{T,\boldsymbol{\lambda}=\{0\}}(E_0, \xi) \right], \quad (14.85)$$

where $\{0\} = (0, \dots, 0)$.

We now present two examples of realization of REUS. In the first example, we use only one temperature, T , and L umbrella potentials. We prepare replicas so that the potential energy for each replica includes exactly one umbrella potential (here, we have $M = L$), namely in (14.80) for $\boldsymbol{\lambda} = \boldsymbol{\lambda}_m$, we set

$$\lambda_m^{(\ell)} = \delta_{\ell,m}, \quad (14.86)$$

where $\delta_{k,l}$ is Kronecker's delta function, and we have

$$E_{\boldsymbol{\lambda}_m}(q^{[i]}) = E_0(q^{[i]}) + V_m(q^{[i]}). \quad (14.87)$$

We exchange replicas corresponding to “neighboring” umbrella potentials, V_m and V_{m+1} . The acceptance criterion for replica exchange is given by (14.53), where (14.75) now reads (with the fixed inverse temperature $\beta = 1/k_B T$) [86]

$$\Delta = \beta \left(V_m(q^{[j]}) - V_m(q^{[i]}) - V_{m+1}(q^{[j]}) + V_{m+1}(q^{[i]}) \right), \quad (14.88)$$

where replicas i and j , respectively, have umbrella potentials V_m and V_{m+1} before the exchange.

In the second example, we prepare N_T temperatures and L umbrella potentials, which makes the total number of replicas $M = N_T \times L$. We can introduce the following relabeling for the parameters that characterize the replicas:

$$\begin{aligned} \Lambda_m = (T_m, \boldsymbol{\lambda}_m) &\longrightarrow \Lambda_{I,J} = (T_I, \boldsymbol{\lambda}_J) . \\ (m = 1, \dots, M) &\quad (I = 1, \dots, N_T, J = 1, \dots, L) \end{aligned} \quad (14.89)$$

The potential energy is given by (14.87) with the replacement $m \rightarrow J$. We perform the following replica-exchange processes alternately:

1. Exchange pairs of replicas corresponding to neighboring temperatures, T_I and T_{I+1} (i.e., exchange replicas i and j that respectively correspond to parameters $\Lambda_{I,J}$ and $\Lambda_{I+1,J}$). (We refer to this process as T -exchange.)
2. Exchange pairs of replicas corresponding to “neighboring” umbrella potentials, V_J and V_{J+1} (i.e., exchange replicas i and j that respectively correspond to parameters $\Lambda_{I,J}$ and $\Lambda_{I,J+1}$). (We refer to this process as λ -exchange.)

The acceptance criterion for these replica exchanges is given by (14.53), where (14.75) now reads [86]

$$\Delta = (\beta_I - \beta_{I+1}) \left(E_0(q^{[j]}) + V_J(q^{[j]}) - E_0(q^{[i]}) - V_J(q^{[i]}) \right) , \quad (14.90)$$

for T -exchange, and

$$\Delta = \beta_I \left(V_J(q^{[j]}) - V_J(q^{[i]}) - V_{J+1}(q^{[j]}) + V_{J+1}(q^{[i]}) \right) , \quad (14.91)$$

for λ -exchange. By this procedure, the random walk in the reaction coordinate space as well as in the temperature space can be realized.

14.2.6 From Multidimensional REM to Multidimensional MUCA and ST

The formulations of MREM give multidimensional/multivariable extensions of REMUCA and REST, where the results of MREM can be used to determine the weight factors for multidimensional MUCA and multidimensional ST, respectively [5]. In REMUCA and REST, the multicanonical weight factor and the simulated tempering weight factor are determined from the results of a short REM simulation, respectively. The results of a short MREM simulation can therefore be used to determine the weight factors for multidimensional/multivariable MUCA and ST simulations, where random walks in multidimensional “energy” and “parameter” space are realized [5]. Here, we give more details.

We consider a simple example with the following potential energy:

$$E_\lambda(q) = E_0(q) + \lambda V(q) . \quad (14.92)$$

In the two-dimensional multicanonical ensemble, each state is weighted by the multicanonical weight factor $W_{\text{mu}}(E_0, V)$ so that a uniform potential energy distribution in both E_0 and V may be obtained:

$$P_{\text{mu}}(E_0, V) \propto n(E_0, V) W_{\text{mu}}(E_0, V) \equiv \text{const} , \quad (14.93)$$

where $n(E_0, V)$ is the two-dimensional density of states. This implies that

$$W_{\text{mu}}(E_0, V) \equiv \exp[-\beta_0 E_{\text{mu}}(E_0, V; T_0)] = \frac{1}{n(E_0, V)} , \quad (14.94)$$

where we have chosen an arbitrary reference temperature, $T_0 = 1/k_B\beta_0$, and the “multicanonical potential energy” is defined by

$$E_{\text{mu}}(E_0, V; T_0) \equiv k_B T_0 \ln n(E_0, V) . \quad (14.95)$$

The two-dimensional MUCA MC simulation can be performed with the following transition probability from state x with potential energy $E_0 + \lambda V$ to state x' with potential energy $E_0' + \lambda V'$ (see (14.19)):

$$w(x \rightarrow x') = \min \left(1, \frac{W_{\text{mu}}(E_0', V')}{W_{\text{mu}}(E_0, V)} \right) = \min \left(1, \frac{n(E_0, V)}{n(E_0', V')} \right) . \quad (14.96)$$

The MD algorithm in the two-dimensional multicanonical ensemble also naturally follows from (14.17), in which the regular constant temperature MD simulation (with $T = T_0$) is performed by replacing E by E_{mu} in (14.12) (see (14.21)):

$$\dot{\mathbf{p}}_k = - \frac{\partial E_{\text{mu}}(E_0, V; T_0)}{\partial \mathbf{q}_k} - \frac{\dot{s}}{s} \mathbf{p}_k . \quad (14.97)$$

In the two-dimensional simulated tempering, the parameter set (T, λ) become dynamical variables, and both the configuration and the parameter set are updated during the simulation with a weight (see (14.30)):

$$W_{\text{ST}}(E_\lambda; T, \lambda) = \exp(-\beta E_\lambda + f(T, \lambda)) , \quad (14.98)$$

where the function $f(T, \lambda)$ is chosen so that the probability distribution of the two-dimensional parameter set is flat (see (14.31)):

$$\begin{aligned} P_{\text{ST}}(T, \lambda) &= \int dE_0 dV n(E_0, V) W_{\text{ST}}(E_\lambda; T, \lambda) \\ &= \int dE_0 dV n(E_0, V) \exp(-\beta E_\lambda + f(T, \lambda)) = \text{const} . \end{aligned} \quad (14.99)$$

In the numerical work, we discretize the parameter set in $M = N_T \times L$ different values, (T_I, λ_J) ($I = 1, \dots, N_T, J = 1, \dots, L$). Without loss of generality, we can order the parameters so that $T_1 < T_2 < \dots < T_{N_T}$ and $\lambda_1 < \lambda_2 < \dots < \lambda_L$. The free energy f is now written as $f_{I,J} = f(T_I, \lambda_J)$. Once the initial configuration and the initial parameter set are chosen, the two-dimensional ST is then realized by alternately performing the following two steps:

1. A canonical MC or MD simulation at the fixed parameter set (T_I, λ_J) is carried out for certain steps.
2. One of the parameters in the parameter set (T_I, λ_J) is updated to the neighboring values with the configuration and the other parameter fixed. The transition probability of this parameter-updating process is given by the following Metropolis criterion:

$$w(T_I \rightarrow T_{I\pm 1}) = \min \left(1, \frac{W_{\text{ST}}(E_{\lambda_J}; T_{I\pm 1}, \lambda_J)}{W_{\text{ST}}(E_{\lambda_J}; T_I, \lambda_J)} \right) = \min(1, \exp(-\Delta)) , \quad (14.100)$$

where

$$\Delta = (\beta_{I\pm 1} - \beta_I) E_{\lambda_J} - (f_{I\pm 1, J} - f_{I, J}) , \quad (14.101)$$

for T -update, and

$$w(\lambda_J \rightarrow \lambda_{J\pm 1}) = \min \left(1, \frac{W_{\text{ST}}(E_{\lambda_{J\pm 1}}; T_I, \lambda_{J\pm 1})}{W_{\text{ST}}(E_{\lambda_J}; T_I, \lambda_J)} \right) = \min(1, \exp(-\Delta)) , \quad (14.102)$$

where

$$\begin{aligned}\Delta &= \beta_I (E_{\lambda_{J\pm 1}} - E_{\lambda_J}) - (f_{I,J\pm 1} - f_{I,J}) \\ &= \beta_I (\lambda_{J\pm 1} - \lambda_J) V - (f_{I,J\pm 1} - f_{I,J}) ,\end{aligned}\quad (14.103)$$

for λ -update.

Finally, we present the corresponding MREM. We prepare N_T temperatures and L λ parameters, which makes the total number of replicas $M = N_T \times L$. We perform the following replica-exchange processes alternately:

1. Exchange pairs of replicas corresponding to neighboring temperatures, T_I and T_{I+1} . (We refer to this process as T -exchange.)
2. Exchange pairs of replicas corresponding to “neighboring” λ parameters, λ_J and λ_{J+1} . (We refer to this process as λ -exchange.)

The acceptance criterion for these replica exchanges is given by (14.53), where (14.75) now reads

$$\Delta = (\beta_I - \beta_{I+1}) \left(E_{\lambda_J} \left(q^{[j]} \right) - E_{\lambda_J} \left(q^{[i]} \right) \right) , \quad (14.104)$$

for T -exchange, and

$$\begin{aligned}\Delta &= \beta_I \left(E_{\lambda_J} \left(q^{[j]} \right) - E_{\lambda_J} \left(q^{[i]} \right) - E_{\lambda_{J+1}} \left(q^{[j]} \right) + E_{\lambda_{J+1}} \left(q^{[i]} \right) \right) \\ &= \beta_I (\lambda_J - \lambda_{J+1}) \left(V \left(q^{[j]} \right) - V \left(q^{[i]} \right) \right) ,\end{aligned}\quad (14.105)$$

for λ -exchange.

After a short MREM simulation, we can use the multiple-histogram reweighting techniques to obtain $n(E_0, V)$ and $f_{I,J}$. Let $N_{I,J}(E_0, V)$ and $n_{I,J}$ be, respectively, the potential energy histogram and the total number of samples obtained for the parameter set (T_I, λ_J) . The WHAM equations are then given by

$$n(E_0, V) = \frac{\sum_{I=1}^{N_T} \sum_{J=1}^L N_{I,J}(E_0, V)}{\sum_{I=1}^{N_T} \sum_{J=1}^L n_{I,J} \exp(f_{I,J} - \beta_I E_{\lambda_J})} , \quad (14.106)$$

and for each I and J ($I = 1, \dots, N_T, J = 1, \dots, L$)

$$\exp(-f_{I,J}) = \sum_{E_0, V} n(E_0, V) \exp(-\beta_I E_{\lambda_J}) . \quad (14.107)$$

These equations are solved self-consistently by iteration for $n(E_0, V)$ and $f_{I,J}$.

Hence, we can determine the multidimensional multicanonical weight factor $W_{\text{mu}}(E_0, V)$ in (14.94) and the multidimensional simulated tempering weight factor $W_{\text{ST}}(E_{\lambda_J}; T_I, \lambda_J)$ in (14.98). The former is given by

$$W_{\text{mu}}(E_0, V) = \frac{1}{n(E_0, V)} \, , \tag{14.108}$$

and the latter is given by

$$W_{\text{ST}}(E_{\lambda_J}; T_I, \lambda_J) = \exp(-\beta_I E_{\lambda_J} + f_{I,J}) \, . \tag{14.109}$$

14.3 Simulation Results

We first compare the performances of REM, MUCAREM, and REMUCA. The accuracy of average quantities calculated depends on the “quality” of the random walk in the potential energy space, and the measure for this quality can be given by the number of tunneling events [15, 94]. One tunneling event is defined by a trajectory that goes from E_{H} to E_{L} and back, where E_{H} and E_{L} are the values near the highest energy and the lowest energy, respectively, which the random walk can reach. If E_{H} is sufficiently high, the trajectory gets completely uncorrelated when it reaches E_{H} . On the other hand, when the trajectory reaches near E_{L} , it tends to get trapped in local-minimum states. We thus consider that the more tunneling events we observe during a fixed number of MC/MD steps, the more efficient the method is as a generalized-ensemble algorithm (or, the average quantities obtained by the reweighting techniques are more reliable).

The first example is Monte Carlo simulations of the system of a 17-residue fragment of ribonuclease T1 in implicit solvent (expressed by the solvent accessible surface area) [94]. The amino-acid sequence is Ser-Ser-Asp-Val-Ser-Thr-Ala-Gln-Ile-Ala-Ala-Tyr-Lys-Leu-His-Glu-Asp. The energy function E_{TOT} that we used is the sum of the conformational energy term of the solute E_{P} and the solvation free-energy term E_{SOL} for the interaction of the peptide with the surrounding solvent: $E_{\text{TOT}} = E_{\text{P}} + E_{\text{SOL}}$. Here, the solvation term E_{SOL} is given by the sum of the terms that are proportional to the solvent-accessible surface area of the atomic groups of the solute. The parameters in

Table 14.1. Number of tunneling events in the MC simulations of a fragment of ribonuclease T1 for REM, MUCAREM, and REMUCA simulations

total MC sweeps	REM	MUCAREM	REMUCA
2×10^6	2	9	18
3×10^6	5	16	29
4×10^6	9	22	38

the conformational energy as well as the molecular geometry were taken from ECEPP/2. The parameters of the solvent term were adopted from [125]. The computer code KONF90 [126, 127] was used, and MC simulations based on the REM, MUCAREM, and REMUCA were performed. For the calculation of a solvent-accessible surface area, we used the computer code NSOL [128]. The dihedral angles ϕ and ψ in the main chain and χ in the side chain constituted the variables to be updated in the MC simulations. The number of degrees of freedom for the peptide is 80. One MC sweep consists of updating all these angles once with Metropolis evaluation for each update. The simulations were started from randomly generated conformations. In Table [4.1], we list the number of tunneling events in REM, MUCAREM, and REMUCA simulations of the same system [94]. Hence, REMUCA is the most efficient, then MUCAREM, and finally REM.

The next systems are small peptides in explicit water [129]. When we consider explicit water molecules, the problem becomes order-of-magnitude more difficult than the case with implicit water models. They are alanine dipeptide with 132 water molecules, alanine trimer with 278 water molecules, and Met-enkephalin with 526 water molecules. The force field, or the potential energy, that we used is AMBER parm96 [130] for the peptides and TIP3P [131] for water molecules. The peptides were placed inside the spheres of water molecules, and the harmonic constraining forces were imposed in order to prevent the water molecules from flying apart. The unit time step, Δt , was set to 0.5 fs. The modified version [132, 133] of the software PRESTO version 2 [134] was used. In Table [4.2], we list the number of tunneling events in these systems. From the Table we find again that the rank order of efficiency is REMUCA, MUCAREM, and REM.

The last system is the C-peptide of ribonuclease A in explicit water [135]. In the model of simulations, the N-terminus and the C-terminus of the C-peptide analogue were blocked with the acetyl group and the N-methyl group, respectively. The number of amino acids is 13 and the amino-acid sequence is Ace-Ala-Glu⁻-Thr-Ala-Ala-Ala-Lys⁺-Phe-Leu-Arg⁺-Ala-His⁺-Ala-Nme [136, 137]. The initial configuration of our simulation was first generated by a high-temperature MD simulation (at $T = 1000$ K) in gas phase, starting from a fully extended conformation. We randomly selected one of the structures that do not have any secondary structures such as α -helix and β -sheet.

Table 14.2. Number of tunneling events in the MD simulations of three peptides in explicit water for REM, MUCAREM, and REMUCA simulations

peptide	no. of atoms	total MD steps	REMD	MUCAREM	REMUCA
alanine dipeptide	418	4×10^6	11	40	59
alanine trimer	876	5×10^6	1	20	29
Met-enkephalin	1662	8×10^6	0	12	27

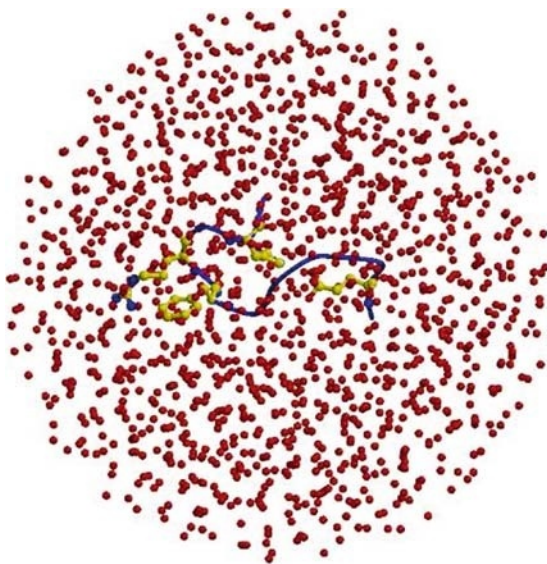


Fig. 14.1. The initial configuration of C-peptide in explicit water, which was used in all of the 32 replicas of the first REMD simulation (REMD1 in Table 14.3). The red filled circles stand for the oxygen atoms of water molecules. The number of water molecules is 1387, and they are placed in a sphere of radius 22 Å. As for the peptide, besides the backbone structure (in black), side chains of only Glu⁻-2, Phe-8, Arg⁺-10, and His⁺-12 are shown (in light gray). The figure was created with Molscript [140] and Raster3D [141]

The peptide was then solvated in a sphere of radius 22 Å, in which 1387 water molecules were included (see Fig. 14.1). Harmonic restraint was applied to prevent the water molecules from going out of the sphere. The total number of atoms is 4365. The dielectric constant was set equal to 1.0. The force-field parameters for peptide were taken from the all-atom version of AMBER parm99 [138], which was found to be suitable for studying helical peptides [139], and TIP3P model [131] was used for water molecules. The unit time step, Δt , was set to 0.5 fs.

In Table 14.3, the essential parameters in the simulations performed are summarized. We first performed a REMD simulation with 32 replicas for 100 ps per replica (REMD1 in Table 14.3). During this REMD simulation, replica exchange was tried every 200 MD steps. Using the obtained potential energy histogram of each replica as input data to the multiple-histogram analysis in (14.37) and (14.38), we obtained the first estimate of the multicanonical weight factor, or the density of states. We divided this multicanonical weight factor into four multicanonical weight factors that cover different energy regions [88, 93, 94] and assigned these multicanonical weight factors into four replicas (the weight factors cover the potential energy ranges from -13 791.5 to -11 900.5

Table 14.3. Summary of parameters in REMD, MUCAREM, and REMUCA simulations of C-peptide

	number of replicas, M	temperature, T_m (K) ($m = 1, \dots, M$)	MD steps per replica
REMD1 ^a	32	250, 258, 267, 276, 286, 295, 305, 315, 326, 337, 348, 360, 372, 385, 398, 411, 425, 440, 455, 470, 486, 502, 519, 537, 555, 574, 593, 613, 634, 655, 677, 700	2.0×10^5
MUCAREM1	4	360, 440, 555, 700	2.0×10^6
REMUCA1	1	700	3.0×10^7

^a REMD1 stands for the replica-exchange molecular dynamics simulation, MUCAREM1 stands for the multicanonical replica-exchange molecular dynamics simulation, and REMUCA1 stands for the final multicanonical molecular dynamics simulation (the production run) of REMUCA. The results of REMD1 were used to determine the multicanonical weight factors for MUCAREM1, and those of MUCAREM1 were used to determine the multicanonical weight factor for REMUCA1

kcal/mol, from -12962.5 to -10796.5 kcal/mol, from -11900.5 to -9524.5 kcal/mol, and from -10796.5 to -8293.5 kcal/mol). We then carried out a MUCAREM simulation with four replicas for 1 ns per replica (MUCAREM1 in Table 14.3), in which replica exchange was tried every 1000 MD steps. We again used the potential energy histogram of each replica as the input data to the multiple-histogram analysis and finally obtained the multicanonical weight factor with high precision. As a production run, we carried out a 15 ns multicanonical MD simulation with one replica (REMUCA1 in Table 14.3), and the results of this production run were analyzed in detail.

In Fig. 14.2, we show the probability distributions of potential energy that were obtained from the above three generalized-ensemble simulations, namely REMD1, MUCAREM1, and REMUCA1. We see in Fig. 14.2(a) that there are enough overlaps between all pairs of neighboring canonical distributions, suggesting that there were sufficient numbers of replica exchange in REMD1. We see in Fig. 14.2(b) that there are good overlaps between all pairs of neighboring multicanonical distributions, implying that MUCAREM1 also performed properly. Finally, the multicanonical distribution in Fig. 14.2(c) is completely flat between around -13000 kcal/mol and around -8000 kcal/mol. The results suggest that a free random walk was realized in this energy range.

In Fig. 14.3(a) we show the time series of potential energy from REMUCA1. We indeed observe a random walk covering as much as 5000 kcal/mol of energy range (note that 23 kcal/mol ≈ 1 eV). We show in Fig. 14.3(b) the average potential energy as a function of temperature, which was obtained from the trajectory of REMUCA1 by the reweighting techniques. The average potential energy monotonically increases as the temperature increases.

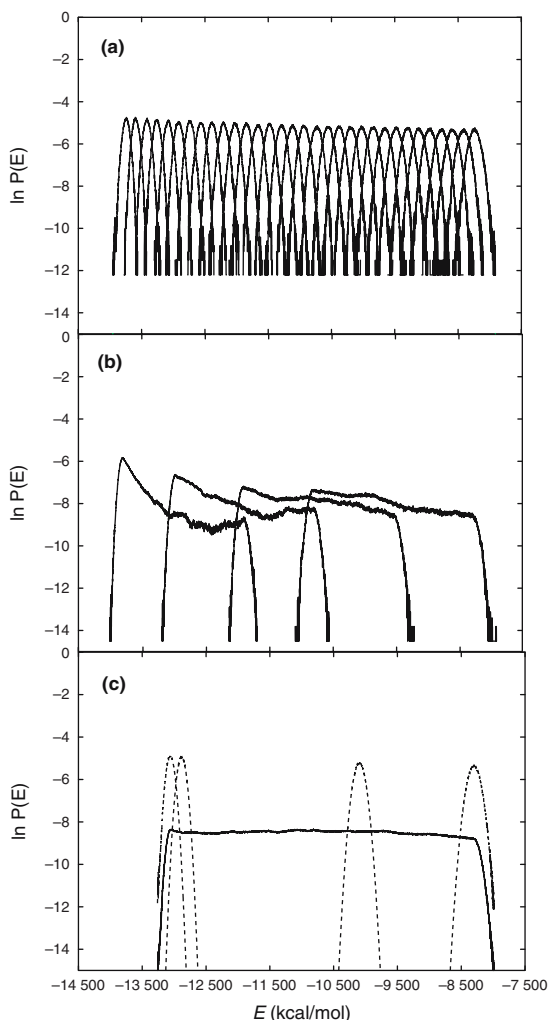


Fig. 14.2. Probability distributions of potential energy of the C-peptide system obtained from (a) REMD1, (b) MUCAREM1, and (c) REMUCA1. See Table 14.3 for the parameters of the simulations. Dashed curves in (c) are the reweighted canonical distributions at 290, 300, 500, and 700 K (from left to right)

The random walk in REMUCA1 yielded as many as 55 tunneling events in 15 ns. Here, we took $E_H = -8250$ kcal/mol and $E_L = -12850$ kcal/mol for the measurement of the tunneling events. The corresponding numbers of tunneling events for REMD1 and MUCAREM1 were 0 in 3.2 ns and 5 in 4 ns, respectively. Hence, REMUCA is again the most efficient and reliable among the three generalized-ensemble algorithms.

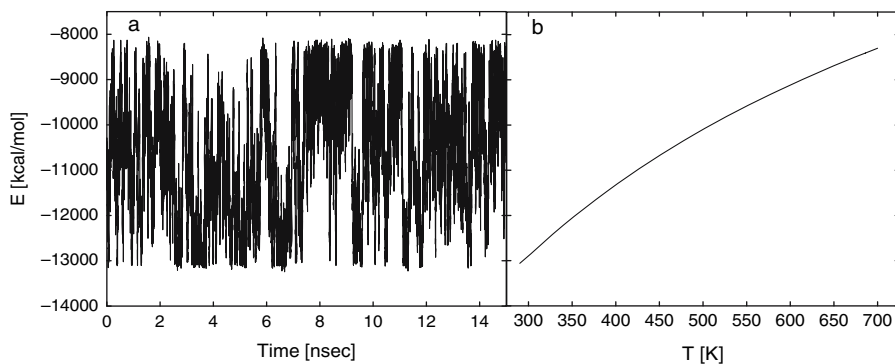


Fig. 14.3. Time series of potential energy of the C-peptide system from the REMUCA production run (REMUCA1 in Table 14.3) (a) and the average potential energy as a function of temperature (b). The latter was obtained from the trajectory of REMUCA1 by the single-histogram reweighting techniques

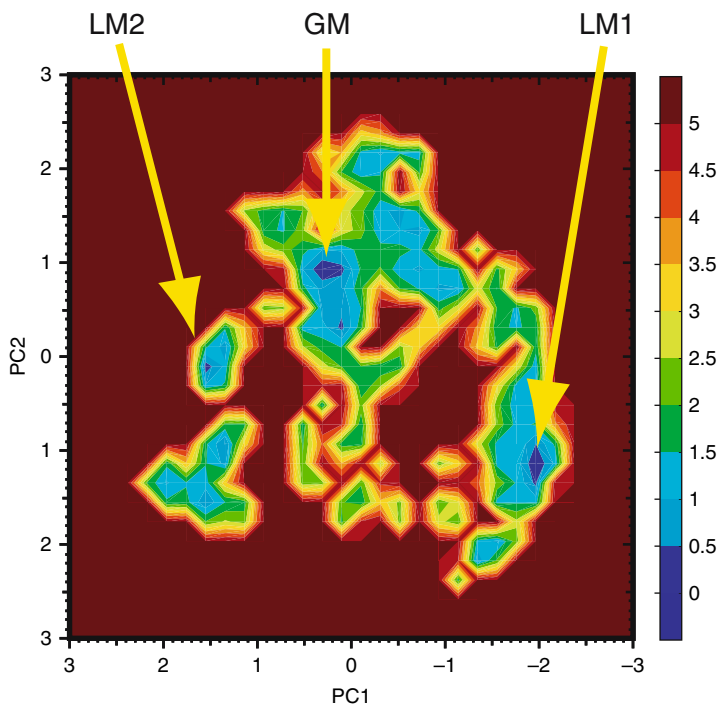


Fig. 14.4. Potential of mean force (kcal/mol) of the C-peptide system along the first two principal components at 300 K. The free energy was calculated from the results of REMUCA production run (REMUCA1 in Table 14.3) by the single-histogram reweighting techniques and normalized so that the global-minimum state (GM) has the value zero. GM, LM1, and LM2 represent three distinct local-minimum free-energy states

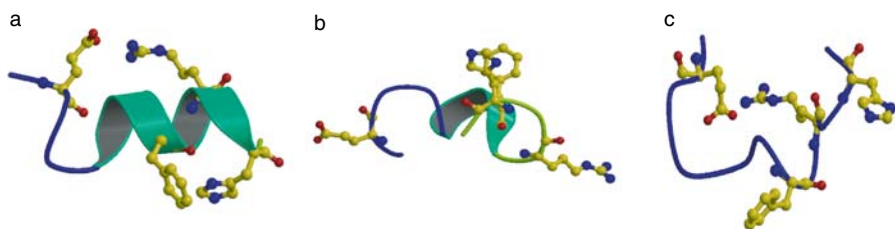


Fig. 14.5. The representative structures at the global-minimum free-energy state ((a) GM) and the two local-minimum states ((b) LM1 and (c) LM2). As for the peptide structures, besides the backbone structure, side chains of only Glu⁻-2, Phe-8, Arg⁺-10, and His⁺-12 are shown in ball-and-stick model

In Fig. 14.4, the potential of mean force (PMF), or free energy, along the first two principal component axes at 300 K is shown. There exist three distinct minima in the free-energy landscape, which correspond to three local-minimum-energy states. We show representative conformations at these minima in Fig. 14.5. The structure of the global-minimum free-energy state (GM) has a partially distorted α -helix with the salt bridge between Glu⁻-2 and Arg⁺-10. The structure is in good agreement with the experimental structure obtained by both NMR and X-ray experiments. In this structure, there also exists a contact between Phe-8 and His⁺-12. This contact is again observed in the corresponding residues of the X-ray structure. At LM1 the structure has a contact between Phe-8 and His⁺-12, but the salt bridge between Glu⁻-2 and Arg⁺-10 is not formed. On the other hand, the structure at LM2 has this salt bridge, but it does not have a contact between Phe-8 and His⁺-12. Thus, only the structures at GM satisfy all of the interactions that have been observed by the X-ray and other experimental studies.

Finally, we remark that the largest peptide in explicit water that we have succeeded in folding into the native structure from random initial conformations is so far the 16-residue C-terminal β -hairpin of streptococcal protein G B1 domain, which was accomplished by MUCAREM simulations with eight replicas 142.

14.4 Conclusions

In this article, we have reviewed some of powerful generalized-ensemble algorithms for both Monte Carlo simulations and molecular dynamics simulations. A simulation in generalized ensemble realizes a random walk in potential energy space, alleviating the multiple-minima problem that is a common difficulty in simulations of complex systems with many degrees of freedom.

Detailed formulations of the three well-known generalized-ensemble algorithms, namely, multicanonical algorithm (MUCA), simulated tempering (ST), and replica-exchange method (REM), were given.

We then introduced several new generalized-ensemble algorithms that combine the merits of the above three methods.

The question is then which method is the most recommended. Our criterion for the effectiveness of generalized-ensemble algorithms was how many random walk cycles (tunneling events) in potential energy space between the high-energy region and low-energy region are realized within a fixed number of total MC (or MD) steps. We found that once the optimal MUCA weight factor is obtained, MUCA (and REMUCA) is the most effective (i.e., has the most number of tunneling events), and REM is the least [93]. We also found that once the optimal ST weight factor is obtained, ST (and REST) has more tunneling events than REM [89, 115]. Moreover, we compared the efficiency of Berg’s recursion [73], Wang–Landau method [23, 24], and REMUCA/MUCAREM as methods for the multicanonical weight factor determination in two-dimensional 10-state Potts model and found that the three methods are about equal in efficiency [143, 144, 145].

Hence, the answer to the above question will depend on how much time one is willing to (or forced to) spend in order to determine the MUCA or ST weight factors. Given a problem, the first choice is REM because of its simplicity (no weight factor determination is required). If REM turns out to be insufficient or too much time-consuming (like the case with first-order phase transitions), then other more powerful algorithms such as MUCAREM and STREM are recommended.

Acknowledgements

This work was supported, in part, by Grants-in-Aid for Scientific Research in Priority Areas (“Water and Biomolecules” and “Membrane Interface”) and for the Next Generation Super Computing Project, Nanoscience Program from the Ministry of Education, Culture, Sports, Science and Technology (MEXT), Japan.

References

1. U. H. E. Hansmann, Y. Okamoto: Generalized-ensemble approach for protein folding simulations. In *Annual Reviews of Computational Physics VI*, edited by D. Stauffer (World Scientific, Singapore, 1999), pp. 129–157 [369]
2. A. Mitsutake, Y. Sugita, Y. Okamoto: *Biopolymers (Peptide Science)* **60**, 96–123 (2001) [369, 371]
3. Y. Sugita, Y. Okamoto: Free-energy calculations in protein folding by generalized-ensemble algorithms. In *Lecture Notes in Computational Science and Engineering*, edited by T. Schlick, H. H. Gan (Springer-Verlag, Berlin, 2002), pp. 304–332 [cond-mat/0102296] [369, 383]
4. B. A. Berg: *Comput. Phys. Commun.* **147**, 52–57 (2002) [369, 370]

5. Y. Okamoto: *J. Mol. Graphics Mod.* **22**, 425–439 (2004) [[cond-mat/0308360](#)] [369](#), [393](#)
6. H. Kokubo, Y. Okamoto: *Mol. Sim.* **32**, 791–801 (2006) [369](#)
7. S. G. Itoh, H. Okumura, Y. Okamoto: *Mol. Sim.* **33**, 47–56 (2007) [369](#)
8. A. M. Ferrenberg, R. H. Swendsen: *Phys. Rev. Lett.* **61**, 2635–2638 (1988);
A. M. Ferrenberg, R. H. Swendsen: *Phys. Rev. Lett.* **63**, 1658 (1989)
9. A. M. Ferrenberg, R. H. Swendsen: *Phys. Rev. Lett.* **63**, 1195–1198 (1989)
10. S. Kumar, D. Bouzida, R. H. Swendsen, P. A. Kollman, J. M. Rosenberg: *J. Comput. Chem.* **13**, 1011–1021 (1992) [370](#), [375](#)
11. R. H. Swendsen, J. S. Wang: *Phys. Rev. Lett.* **58**, 86–88 (1987) [370](#), [371](#), [377](#), [378](#), [382](#), [383](#)
12. U. Wolff: *Phys. Rev. Lett.* **62**, 361–364 (1989) [370](#), [371](#), [377](#), [378](#), [382](#), [384](#), [386](#), [390](#)
13. H. G. Evertz, G. Lana, M. Marcu: *Phys. Rev. Lett.* **70**, 875–879 (1993) [370](#)
14. B. A. Berg, T. Neuhaus: *Phys. Lett. B* **267**, 249–253 (1991) [370](#)
15. B. A. Berg, T. Neuhaus: *Phys. Rev. Lett.* **68**, 9–12 (1992) [370](#)
16. B. A. Berg: *Fields Inst. Commun.* **26**, 1–24 (2000) [[cond-mat/9909236](#)] [370](#), [373](#), [374](#), [383](#)
17. W. Janke: *Physica A* **254**, 164–178 (1998) [370](#), [373](#), [374](#), [381](#), [396](#)
18. J. Lee: *Phys. Rev. Lett.* **71**, 211–214 (1993); J. Lee: *Phys. Rev. Lett.* **71**, 2353(E) (1993) [370](#)
19. M. Mezei: *J. Comput. Phys.* **68**, 237–248 (1987) [370](#)
20. C. Bartels, M. Karplus: *J. Phys. Chem. B* **102**, 865–880 (1998) [370](#)
21. G. M. Torrie, J. P. Valleau: *J. Comput. Phys.* **23**, 187–199 (1977) [370](#)
22. J. S. Wang, R. H. Swendsen: *J. Stat. Phys.* **106**, 245–285 (2002) [370](#)
23. F. Wang, D. P. Landau: *Phys. Rev. Lett.* **86**, 2050–2053 (2001) [370](#), [389](#), [391](#)
24. F. Wang, D. P. Landau: *Phys. Rev. E* **64**, 056101 (2001) [370](#)
25. Q. Yan, R. Faller, J. J. de Pablo: *J. Chem. Phys.* **116**, 8745–8749 (2002) [370](#), [403](#)
26. S. Trebst, D. A. Huse, M. Troyer: *Phys. Rev. E* **70**, 046701 (2004) [370](#), [403](#)
27. B. A. Berg, T. Celik: *Phys. Rev. Lett.* **69**, 2292–2295 (1992) [370](#)
28. B. A. Berg, U. H. E. Hansmann, T. Neuhaus: *Phys. Rev. B* **47**, 497–500 (1993) [370](#)
29. W. Janke, S. Kappler: *Phys. Rev. Lett.* **74**, 212–215 (1995) [370](#), [375](#)
30. B. A. Berg, W. Janke: *Phys. Rev. Lett.* **80**, 4771–4774 (1998) [370](#)
31. N. Hatano, J. E. Gubernatis: *Prog. Theor. Phys. (Suppl.)* **138**, 442–447 (2000) [370](#)
32. B. A. Berg, A. Billoire, W. Janke: *Phys. Rev. B* **61**, 12143–12150 (2000) [370](#)
33. U. H. E. Hansmann, Y. Okamoto: *J. Comput. Chem.* **14**, 1333–1338 (1993) [370](#)
34. U. H. E. Hansmann, Y. Okamoto: *Physica A* **212**, 415–437 (1994) [370](#)
35. M. H. Hao, H. A. Scheraga: *J. Phys. Chem.* **98**, 4940–4948 (1994) [370](#)
36. Y. Okamoto, U. H. E. Hansmann: *J. Phys. Chem.* **99**, 11276–11287 (1995) [370](#)
37. N. B. Wilding: *Phys. Rev. E* **52**, 602–611 (1995) [370](#)
38. A. Kolinski, W. Galazka, J. Skolnick: *Proteins* **26**, 271–287 (1996) [370](#), [375](#)
39. N. Urakami, M. Takasu: *J. Phys. Soc. Jpn.* **65**, 2694–2699 (1996) [370](#)
40. S. Kumar, P. Payne, M. Vázquez: *J. Comput. Chem.* **17**, 1269–1275 (1996) [370](#)
41. U. H. E. Hansmann, Y. Okamoto, F. Eisenmenger: *Chem. Phys. Lett.* **259**, 321–330 (1996) [370](#)
42. U. H. E. Hansmann, Y. Okamoto: *Phys. Rev. E* **54**, 5863–5865 (1996) [370](#)
43. U. H. E. Hansmann, Y. Okamoto: *J. Comput. Chem.* **18**, 920–933 (1997) [370](#), [374](#), [383](#)
44. N. Nakajima, H. Nakamura, A. Kidera: *J. Phys. Chem. B* **101**, 817–824 (1997) [370](#), [377](#)
45. C. Bartels, M. Karplus: *J. Comput. Chem.* **18**, 1450–1462 (1997) [370](#), [377](#)
46. J. Higo, N. Nakajima, H. Shirai, A. Kidera, H. Nakamura: *J. Comput. Chem.* **18**, 2086–2092 (1997) [370](#), [374](#)

47. Y. Iba, G. Chikenji, M. Kikuchi: J. Phys. Soc. Jpn. **67**, 3327–3330 (1998) [370](#)
48. A. Mitsutake, U. H. E. Hansmann, Y. Okamoto: J. Mol. Graph. Mod. **16**, 226–238; 262–263 (1998) [370](#)
49. U. H. E. Hansmann, Y. Okamoto: J. Phys. Chem. B **103**, 1595–1604 (1999) [370](#)
50. H. Shimizu, K. Uehara, K. Yamamoto, Y. Hiwatari: Mol. Sim. **22**, 285–301 (1999) [370](#)
51. S. Ono, N. Nakajima, J. Higo, H. Nakamura: Chem. Phys. Lett. **312**, 247–254 (1999) [370](#)
52. A. Mitsutake, Y. Okamoto: J. Chem. Phys. **112**, 10638–10647 (2000) [370](#)
53. K. Sayano, H. Kono, M. M. Gromiha, A. Sarai: J. Comput. Chem. **21**, 954–962 (2000) [370](#)
54. F. Yasar, T. Celik, B. A. Berg, H. Meirovitch: J. Comput. Chem. **21**, 1251–1261 (2000) [370](#)
55. A. Mitsutake, M. Kinoshita, Y. Okamoto, F. Hirata: Chem. Phys. Lett. **329**, 295–303 (2000) [370](#)
56. M. S. Cheung, A. E. Garcia, J. N. Onuchic: Proc. Natl. Acad. Sci. USA **99**, 685–690 (2002) [370](#)
57. N. Kamiya, J. Higo, H. Nakamura: Protein Sci. **11**, 2297–2307 (2002) [370](#)
58. S. W. Jang, Y. Pak, S. M. Shin: J. Chem. Phys. **116**, 4782–4786 (2002) [370](#)
59. J. G. Kim, Y. Fukunishi, H. Nakamura: Phys. Rev. E **67**, 011105 (2003) [370](#)
60. N. Rathore, T. A. Knotts, IV, J. J. de Pablo: J. Chem. Phys. **118**, 4285–4290 (2003) [370](#)
61. T. Terada, Y. Matsuo, A. Kidera: J. Chem. Phys. **118**, 4306–4311 (2003) [370](#)
62. B. A. Berg, H. Noguchi, Y. Okamoto: Phys. Rev. E **68**, 036126 (2003) [370](#)
63. M. Bachmann, W. Janke: Phys. Rev. Lett. **91**, 208105 (2003) [370](#), [384](#)
64. H. Okumura, Y. Okamoto: Chem. Phys. Lett. **383**, 391–396 (2004) [370](#)
65. T. Munakata, S. Oyama: Phys. Rev. E **54**, 4394–4398 (1996) [370](#)
66. A. P. Lyubartsev, A. A. Martinovski, S. V. Shevkunov, P. N. Vorontsov-Velyaminov: J. Chem. Phys. **96**, 1776–1783 (1992) [370](#)
67. E. Marinari, G. Parisi: Europhys. Lett. **19**, 451–458 (1992) [370](#)
68. E. Marinari, G. Parisi, J. J. Ruiz-Lorenzo: In *Spin Glasses and Random Fields*, edited by A. P. Young (World Scientific, Singapore, 1998), pp. 59–98 [370](#), [376](#), [377](#), [381](#)
69. A. Irbäck, F. Potthast: J. Chem. Phys. **103**, 10298–10305 (1995) [370](#), [376](#), [377](#), [381](#)
70. A. Irbäck, E. Sandelin: J. Chem. Phys. **110**, 12256–12262 (1999) [370](#), [371](#), [377](#), [378](#)
71. G. R. Smith, A. D. Bruce: Phys. Rev. E **53**, 6530–6543 (1996) [370](#), [377](#)
72. U. H. E. Hansmann: Phys. Rev. E **56**, 6200–6203 (1997) [370](#), [371](#)
73. B. A. Berg: Nucl. Phys. B (Proc. Suppl.) **63A-C**, 982–984 (1998) [370](#)
74. W. Janke: Histograms and all that. In *Computer Simulations of Surfaces and Interfaces V*, NATO Science Series, II Mathematics, Physics and Chemistry Vol. **114**, Proceedings of the NATO Advanced Study Institute, edited by B. Dünweg, D. P. Landau, A. I. Milchev (Kluwer, Dordrecht, 2003), pp. 137–157 [370](#), [384](#)
75. K. Hukushima, K. Nemoto: J. Phys. Soc. Jpn. **65**, 1604–1608 (1996) [370](#), [403](#)
76. K. Hukushima, H. Takayama, K. Nemoto: Int. J. Mod. Phys. C **7**, 337–344 (1996) [370](#)
77. C. J. Geyer: In *Computing Science and Statistics: Proceedings of the 23rd Symposium on the Interface*, edited by E. M. Keramidas (Interface Foundation, Fairfax Station, 1991), pp. 156–163 [370](#), [378](#), [380](#), [381](#)
78. R. H. Swendsen, J.-S. Wang: Phys. Rev. Lett. **57**, 2607–2609 (1986) [370](#), [378](#), [380](#), [381](#)

79. K. Kimura, K. Taki: In *Proceedings of the 13th IMACS World Congress on Computation and Applied Mathematics (IMACS '91)*, edited by R. Vichnevetsky, J. J. H. Miller, Vol. 2, pp. 827–828 [370](#) [378](#) [380](#) [381](#)
80. D. D. Frantz, D. L. Freeman, J. D. Doll: *J. Chem. Phys.* **93**, 2769–2784 (1990) [370](#)
81. M. C. Tesi, E. J. J. van Rensburg, E. Orlandini, S. G. Whittington: *J. Stat. Phys.* **82**, 155–181 (1996) [370](#)
82. Y. Iba: *Int. J. Mod. Phys. C* **12**, 623–656 (2001) [370](#)
83. U. H. E. Hansmann: *Chem. Phys. Lett.* **281**, 140–150 (1997) [370](#)
84. Y. Sugita, Y. Okamoto: *Chem. Phys. Lett.* **314**, 141–151 (1999) [371](#)
85. M. G. Wu, M. W. Deem: *Mol. Phys.* **97**, 559–580 (1999) [371](#)
86. Y. Sugita, A. Kitao, Y. Okamoto: *J. Chem. Phys.* **113**, 6042–6051 (2000) [371](#) [378](#) [380](#)
87. C. J. Woods, J. W. Essex, M. A. King: *J. Phys. Chem. B* **107**, 13703–13710 (2003) [371](#)
88. Y. Sugita, Y. Okamoto: *Chem. Phys. Lett.* **329**, 261–270 (2000) [371](#) [389](#) [390](#) [391](#) [392](#) [393](#)
89. A. Mitsutake, Y. Okamoto: *Chem. Phys. Lett.* **332**, 131–138 (2000) [371](#)
90. D. Gront, A. Kolinski, J. Skolnick: *J. Chem. Phys.* **113**, 5065–5071 (2000). [371](#) [382](#) [384](#)
91. G. M. Verkhivker, P. A. Rejto, D. Bouzida, S. Arthurs, A. B. Colson, S. T. Freer, D. K. Gehlhaar, V. Larson, B. A. Luty, T. Marrone, P. W. Rose: *Chem. Phys. Lett.* **337**, 181–189 (2001) [371](#) [384](#) [403](#)
92. H. Fukunishi, O. Watanabe, S. Takada: *J. Chem. Phys.* **116**, 9058–9067 (2002) [371](#)
93. A. Mitsutake, Y. Sugita, Y. Okamoto: *J. Chem. Phys.* **118**, 6664–6675 (2003) [371](#)
94. A. Mitsutake, Y. Sugita, Y. Okamoto: *J. Chem. Phys.* **118**, 6676–6688 (2003) [371](#)
95. A. Sikorski, P. Romiszowski: *Biopolymers* **69**, 391–398 (2003) [371](#) [378](#) [382](#) [384](#) [387](#) [398](#)
96. C. Y. Lin, C. K. Hu, U. H. E. Hansmann: *Proteins* **52**, 436–445 (2003) [371](#) [382](#) [384](#) [396](#)
97. G. La Penna, A. Mitsutake, M. Masuya, Y. Okamoto: *Chem. Phys. Lett.* **380**, 609–619 (2003) [371](#)
98. M. Falcioni, M. W. Deem: *J. Chem. Phys.* **110**, 1754–1766 (1999) [371](#)
99. Q. Yan, J. J. de Pablo: *J. Chem. Phys.* **111**, 9509–9516 (1999) [371](#)
100. T. Nishikawa, H. Ohtsuka, Y. Sugita, M. Mikami, Y. Okamoto: *Prog. Theor. Phys. (Suppl.)* **138**, 270–271 (2000) [371](#)
101. R. Yamamoto, W. Kob: *Phys. Rev. E* **61**, 5473–5476 (2000) [371](#)
102. D. A. Kofke: *J. Chem. Phys.* **117**, 6911–6914 (2002) [371](#)
103. T. Okabe, M. Kawata, Y. Okamoto, M. Mikami: *Chem. Phys. Lett.* **335**, 435–439 (2001) [371](#) [383](#)
104. Y. Ishikawa, Y. Sugita, T. Nishikawa, Y. Okamoto: *Chem. Phys. Lett.* **333**, 199–206 (2001) [371](#)
105. A. E. Garcia, K. Y. Sanbonmatsu: *Proteins* **42**, 345–354 (2001) [371](#)
106. R. H. Zhou, B. J. Berne, R. Germain: *Proc. Natl. Acad. Sci. USA* **98**, 14931–14936 (2001) [371](#)
107. A. E. Garcia, K. Y. Sanbonmatsu: *Proc. Natl. Acad. Sci. USA* **99**, 2782–2787 (2002) [371](#)
108. R. H. Zhou, B. J. Berne: *Proc. Natl. Acad. Sci. USA* **99**, 12777–12782 (2002) [371](#)
109. M. Feig, A. D. MacKerell, C. L. Brooks, III: *J. Phys. Chem. B* **107**, 2831–2836 (2003) [371](#)
110. Y. M. Rhee, V. S. Pande: *Biophys. J.* **84**, 775–786 (2003) [371](#)
111. J. W. Pitera, W. Swope: *Proc. Natl. Acad. Sci. USA* **100**, 7587–7592 (2003) [371](#)
112. M. K. Fenwick, F. A. Escobedo: *Biopolymers* **68**, 160–177 (2003) [371](#)
113. H. F. Xu, B. J. Berne: *J. Chem. Phys.* **112**, 2701–2708 (2000) [371](#)

114. R. Faller, Q. Yan, J. J. de Pablo: *J. Chem. Phys.* **116**, 5419–5423 (2002) [371](#)
115. A. Mitsutake, Y. Okamoto: *J. Chem. Phys.* **121**, 2491–2504 (2004) [371](#)
116. M. K. Fenwick, F. A. Escobedo: *J. Chem. Phys.* **119**, 11998–12010 (2003) [371](#)
117. K. Hukushima: *Phys. Rev. E* **60**, 3606–3614 (1999) [371](#), [384](#), [388](#), [403](#)
118. T. W. Whitfield, L. Bu, J. E. Straub: *Physica A* **305**, 157–171 (2002) [371](#)
119. W. Kwak, U. H. E. Hansmann: *Phys. Rev. Lett.* **95**, 138102 (2005) [371](#)
120. N. Metropolis, A. W. Rosenbluth, M. N. Rosenbluth, A. H. Teller, E. Teller: *J. Chem. Phys.* **21**, 1087–1092 (1953) [371](#)
121. S. Nosé: *Mol. Phys.* **52**, 255–268 (1984) [371](#)
122. S. Nosé: *J. Chem. Phys.* **81**, 511–519 (1984) [372](#), [374](#), [381](#)
123. B. A. Berg: *Markov Chain Monte Carlo Simulations and Their Statistical Analysis* (World Scientific, Singapore, 2004), p. 253 [373](#)
124. B. A. Berg: *Comput. Phys. Commun.* **153**, 397–406 (2003) [373](#)
125. T. Ooi, M. Oobatake, G. Némethy, H. A. Scheraga: *Proc. Natl. Acad. Sci. USA* **84**, 3086–3090 (1987) [376](#)
126. H. Kawai, Y. Okamoto, M. Fukugita, T. Nakazawa, T. Kikuchi: *Chem. Lett.* **1991**, 213–216 (1991) [376](#)
127. Y. Okamoto, M. Fukugita, T. Nakazawa, H. Kawai: *Protein Eng.* **4**, 639–647 (1991) [397](#)
128. M. Masuya: Manuscript in preparation; see also <http://biocomputing.cc/nsol/> [397](#)
129. Y. Sugita, Y. Okamoto: Unpublished [397](#)
130. P. A. Kollman, R. Dixon, W. Cornell, T. Fox, C. Chipot, A. Pohorille: In *Computer Simulation of Biomolecular Systems*, Vol. 3, edited by A. Wilkinson, P. Weiner, W. F. van Gunsteren (Kluwer, Dordrecht, 1997), pp. 83–96 [397](#)
131. W. L. Jorgensen, J. Chandrasekhar, J. D. Madura, R. W. Impey, M. L. Klein: *J. Chem. Phys.* **79**, 926–935 (1983) [397](#)
132. Y. Sugita, A. Kitao: *Proteins* **30**, 388–400 (1998) [397](#)
133. A. Kitao, S. Hayward, N. Gō: *Proteins* **33**, 496–517 (1998) [397](#), [398](#)
134. K. Morikami, T. Nakai, A. Kidera, M. Saito, H. Nakamura: *Comput. Chem.* **16**, 243–248 (1992) [397](#)
135. Y. Sugita, Y. Okamoto: *Biophys. J.* **88**, 3180–3190 (2005) [397](#)
136. K. R. Shoemaker, P. S. Kim, E. J. York, J. M. Stewart, R. L. Baldwin: *Nature* **326**, 563–567 (1987) [397](#)
137. K. R. Shoemaker, R. Fairman, D. A. Schultz, A. D. Robertson, E. J. York, J. M. Stewart, R. L. Baldwin: *Biopolymers* **29**, 1–11 (1990) [397](#)
138. J. Wang, P. Cieplak, P. A. Kollman: *J. Comput. Chem.* **21**, 1049–1074 (2000) [397](#)
139. T. Yoda, Y. Sugita, Y. Okamoto: *Chem. Phys. Lett.* **386**, 460–467 (2004) [397](#)
140. P. J. Kraulis: *J. Appl. Crystallogr.* **24**, 946–950 (1991) [398](#)
141. E. A. Merritt, D. J. Bacon: *Methods Enzymol.* **277**, 505–524 (1997) [398](#)
142. T. Yoda, Y. Sugita, Y. Okamoto: *Proteins* **66**, 846–859 (2007) [398](#)
143. T. Nagasima, Y. Sugita, A. Mitsutake, Y. Okamoto: Unpublished [398](#)
144. T. Nagasima, Y. Sugita, A. Mitsutake, Y. Okamoto: *Comput. Phys. Commun.* **146**, 69–76 (2002) [402](#)
145. Y. Okamoto: Metropolis algorithms in generalized ensemble. In *The Monte Carlo Method in the Physical Sciences: Celebrating the 50th Anniversary of the Metropolis Algorithm*, edited by J. E. Gubernatis (American Institute of Physics, Melville, 2003), pp. 248–260 [[cond-mat/0308119](#)] [403](#)

Index

- p*-spin model, 29
- AB model, 205, 234
- accept/reject step, 341
- acceptance rate, 323
- adsorption, 225
- aggregation, 240
- aging, 69–71, 74, 191
- algorithm
 - biased Metropolis, 341
 - biased Metropolis heat-bath, 342
 - branch and bound, 256
 - Dijkstra, 78, 84, 86
 - ground state, 79–87
 - matching, 92
 - Metropolis, 323
 - parallel tempering, 29
 - shortest path, 76, 78, 84, 86
- amino acid, 249
- amyloid fibrils, 269, 281
- Anfinsen conjecture, 294
- atomic force microscopy, 225, 262
- autocorrelations, 327, 328
- balance, 322
- biased Gaussian steps, 273
- biased Metropolis algorithm, 341
- biased Metropolis heat-bath, 342
- binning, 328
- biopolymer, 369
- blocking, 328
- Boltzmann
 - constant, 319
 - ensemble, 322
 - state, 321
 - weights, 321
- bond, 72, 77
 - hard, 92
- boundary conditions, 75, 79–81, 86, 87, 89, 91, 99
- branch and bound algorithm, 256
- canonical ensemble, 319
- CASP, 261
- chain-growth
 - contact density, 218, 227
 - multicanonical, 214, 219
 - pruned-enriched, 211
 - Rosenbluth, 211
- complex systems, 336
- configuration, 319
- configurational entropy, 54
- convergence of MCMC, 323
- coupling from the past, 326
- critical slowing down, 53, 329
- cumulative distribution function, 318
- Curie-Weiss law, 52
- data production, 326
- designability, 210
- detailed balance, 323
- Dijkstra algorithm, 78, 84, 86
- distribution function, 318
- domain wall, 88–91
- droplet, 75, 88, 96, 99
 - single-bond, 93, 94
- droplet picture, 75, 76
- dynamic critical exponent, 50, 329

dynamical transition, [51](#), [53](#)

ECEPP/[2](#), [345](#)

Edwards-Anderson model, [12](#)

effective hydrophobic attraction, [272](#)

energy barrier, [96](#)–[103](#)

energy landscape paving (ELP), [295](#), [296](#), [307](#)

ensemble, [322](#)

entropic sampling, [336](#)

entropy discontinuities, [320](#)

equal heights/weights, [337](#)

equilibrium ensemble, [322](#)

ergodic components, [53](#)

ergodicity, [322](#)

error analysis, [326](#), [332](#)

error bar, [332](#)

estimator, [322](#)

expanded ensemble, [370](#)

expectation value, [322](#), [327](#)

exponential autocorrelation time, [327](#)

ferromagnet, [320](#)

fixed point, [322](#)

free-energy barriers, [336](#)

frustrated interactions, [336](#)

frustrated plaquette, [79](#), [80](#), [82](#)–[87](#), [92](#)

frustration, [72](#), [79](#), [80](#), [82](#)–[87](#), [92](#), [93](#)

gauge glass, [196](#)

generalized ensemble, [295](#), [302](#), [303](#), [369](#)

generalized-ensemble algorithm, [370](#)

Gibbs ensemble, [319](#), [322](#)

glass susceptibility, [52](#), [55](#)

go with the winners, [211](#)

gonihedric Potts model, [195](#)

graph, [76](#)

planar, [77](#), [86](#)

ground state, [67](#), [75](#), [76](#), [79](#), [88](#), [89](#), [91](#)–[95](#), [99](#)–[102](#)

ground state algorithm, [79](#)–[87](#)

GS, *see* ground state

hard bond, [92](#)

heapsort, [345](#)

heat-bath algorithm, [324](#), [325](#), [329](#)

Heisenberg ferromagnet, [325](#)

HP model, [205](#), [207](#), [208](#), [252](#)

HP-[36](#), [307](#), [309](#), [310](#)

hydrogen bond potential, [272](#)

hydrophobicity, [253](#)

importance sampling, [321](#)

integrated autocorrelation time, [328](#)

interface tensions, [320](#)

inverted hard bond, [93](#)

Ising model, [320](#)

jackknife estimators, [331](#)

Kauzmann temperature, [52](#), [63](#)

latent heat, [320](#)

LEDA library, [85](#)

Levinthal paradox, [248](#)

library

LEDA, [85](#)

Markov process, [322](#)

matching, [78](#), [84](#)

maximum-cardinality, [78](#)

maximum-weight, [79](#)

minimum-weight perfect, [84](#)

perfect, [78](#), [84](#)

weighted, [79](#)

matching algorithm, [92](#)

maximum-cardinality matching, [78](#)

maximum-weight matching, [79](#)

MC, [369](#)

MD, [369](#)

mechanical denaturation, [260](#)

mechanical unfolding, [264](#), [271](#), [284](#)

membrane protein, [261](#)

Met-enkephalin, [295](#), [296](#), [298](#), [302](#), [344](#)

Metropolis

algorithm, [323](#)

proposal, [341](#)

microcanonical analysis, [241](#)

microstate, [319](#)

minimum-weight perfect matching, [84](#)

mode-coupling theory (MCT), [50](#), [165](#)

molecular dynamics (MD), [150](#), [369](#)

Monte Carlo (MC), [369](#)

MREM, [371](#)

MUCA, [370](#)

MUCAREM, [371](#)

multi-histogram methods, [333](#)

multi-hit Metropolis, [324](#)

- multicanonical
 - algorithm, 370
 - ensemble, 334, 336
 - recursion, 340
 - replica-exchange method, 371
 - sampling, 214, 237, 302, 303
 - weights, 215, 216, 339
- multidimensional replica-exchange
 - method, 371
- multiple Markov chain method, 335, 370
- multiple minima, 295, 301
- multistage sampling, 333

- Nambu-Goto action, 175
- nonergodicity parameter, 51
- NP complete, 256
- NP hard, 76

- $O(3)$ σ -model, 325
- optimization, 294, 297
- overlap of configurations, 339
- overlap parameter, 236

- parallel tempering, 29, 297, 298, 309, 335, 336, 370
- Parisi overlap variable, 339
- partition function, 319
- peptide
 - aggregation, 270, 281
 - folding, 270, 274
- perfect matching, 78, 84
- PERM, 211, 212
- planar graph, 77, 86
- plaquette, 79
 - frustrated, 79, 80, 82, 87, 92
- Potts model, 319
 - gonihedric, 195
 - simplex representation, 51
- probability density, 318
- PROFASI, 274
- protein
 - folding, 204, 206, 207, 235, 243, 269, 370
 - fragments, 250, 251
 - models, 294, 310
 - structure, 293, 295, 307, 310
- Protein Data Bank, 248
- pseudophase, 205, 225

- Ramachandran map, 248
- random number generator, 319
- random walk, 369
- reaction coordinate, 97-99
- REM, 370
- REMUCA, 371
- replica symmetry breaking, 55
- replica trick, 15
- replica-exchange
 - method, 335, 370
 - multicanonical algorithm, 371
 - simulated tempering, 371
 - umbrella sampling, 371
- REST, 371
- REUS, 371
- reweighting, 320, 333, 336
- reweighting techniques, 370
- RKKY interaction, 71
- Robetta, 250
- Rosenbluth chain growth, 211
- Rosenbluth weights, 212
- Rosetta, 250
- rugged free-energy landscape, 336
- rugged Metropolis, 344

- self-avoiding walks, 211
- Sherrington-Kirkpatrick model, 14, 56
- shortest-path algorithm, 76, 78, 84, 86
- sigma model, 325
- simulated annealing, 294
- simulated tempering, 274, 303, 370
- simulated tempering replica-exchange
 - method, 371
- single-bond droplet, 93, 94
- SMMP, 345
- sorting, 345
- spectral density, 321
- Spherical Sherrington-Kirkpatrick
 - model, 28
- spin glass, 67-76, 79-103, 369
- ST, 370
- statistical errors, 326
- Steiner action, 175
- STREM, 371
- structure factor, 153

- tempering, 335
- thermal denaturation, 260
- thermal unfolding, 271, 288

time series, [322](#)

transition

adsorption, [225](#)

aggregation, [240](#)

conformational, [217](#), [219](#), [225](#), [240](#),
[242](#)

folding, [205](#), [239](#), [240](#), [242](#)

glass, [239](#)

transition matrix, [322](#)

transition probability, [322](#)

transition state, [339](#)

U(1) lattice gauge theory, [342](#)

umbrella sampling, [334](#), [370](#)

uniform distribution, [318](#)

variance, [328](#)

variance ratio, [328](#)

vertex, [76](#)

Wang–Landau recursion, [339](#)

weighted matching, [79](#)

weights

multicanonical, [215](#), [216](#), [339](#)

Rosenbluth, [212](#)

WHAM, [370](#)

working approximation, [334](#)